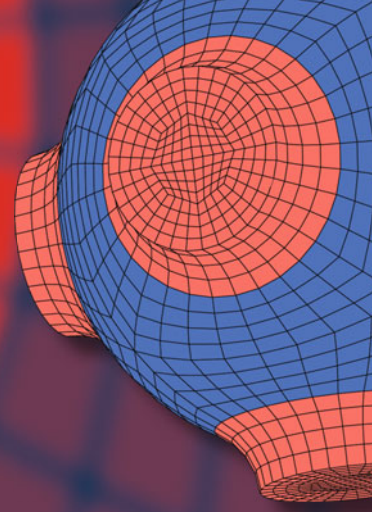Holm Altenbach
Hans Irschik
Alexey V. Porubov *Editors*

Progress in Continuum Mechanics

Springer

Advanced Structured Materials

Volume 196

Series Editors

Andreas Öchsner, Faculty of Mechanical Engineering, Esslingen University of Applied Sciences, Esslingen, Germany

Lucas F. M. da Silva, Department of Mechanical Engineering, Faculty of Engineering, University of Porto, Porto, Portugal

Holm Altenbach ⓘ, Faculty of Mechanical Engineering, Otto von Guericke University Magdeburg, Magdeburg, Sachsen-Anhalt, Germany

Common engineering materials are reaching their limits in many applications, and new developments are required to meet the increasing demands on engineering materials. The performance of materials can be improved by combining different materials to achieve better properties than with a single constituent, or by shaping the material or constituents into a specific structure. The interaction between material and structure can occur at different length scales, such as the micro, meso, or macro scale, and offers potential applications in very different fields.

This book series addresses the fundamental relationships between materials and their structure on overall properties (e.g., mechanical, thermal, chemical, electrical, or magnetic properties, etc.). Experimental data and procedures are presented, as well as methods for modeling structures and materials using numerical and analytical approaches. In addition, the series shows how these materials engineering and design processes are implemented and how new technologies can be used to optimize materials and processes.

Advanced Structured Materials is indexed in Google Scholar and Scopus.

Holm Altenbach · Hans Irschik · Alexey V. Porubov
Editors

Progress in Continuum Mechanics

Springer

Editors
Holm Altenbach 🆔
Institut für Mechanik
Otto-von-Guericke-Universität Magdeburg
Magdeburg, Germany

Hans Irschik 🆔
Institut für Technische Mechanik
Johannes-Kepler-Universität
Linz, Austria

Alexey V. Porubov 🆔
Russian Academy of Sciences
Institute for Problems in Mechanical
Engineering
St. Petersburg, Russia

Paper in this product is recyclable.

Preface

This book is dedicated to our colleague, and for many of us a friend and a comrade Alexander Belyaev. He turns 70 on August 13, 2023. In this regard, we can state that he has done a lot already. He is a universal scientist in the field of mechanics, who is able to describe operation of any mechanism and structure in the form of a mathematical model. That is, almost a relationship describing a certain approximation of the nature. He is one of the founders of mechatronics, the author of the theory of high-frequency vibrations of structures, of models of hydrogen brittleness and one of the creators of the method of acoustic damage. This book reflects not only our achievements related to the research fields of our jubilee, but also the unique breadth of the spectrum of interests and studies conducted by Alexander Belyaev and his scientific results.

Fig. 1: Alexander Konstantinovich Belyaev.

The great Leonhard Euler was known for his active help to colleagues and inventors. For example, he helped Ivan Kulibin in testing a scale model of the first arched wooden bridge 200 m long. Alexander Belyaev, as a real scientists, also helped actively other scientists and engineers solving difficult problems in solid mechanics and mechatronics. He himself is both a Doctor of physical and mathematical sciences and a certified engineer.

He is an active participant in many scientific and engineering projects. He obtained various honours and awards, such as the Thomas A. Jaeger Prize (an award which promotes young scientists working in the field of nuclear engineering) of the

International Association for Structural Mechanics in Reactor Technology in 1993, the Michail A. Lavrentiev Award in Mathematics and Mechanics of the RAS in 2016 and the Pafnuty L. Chebyshev Award in Mathematics and Mechanics of St. Petersburg in 2018.

Alexander Belyaev is an author/co-author of many scientific publications highly reflected by the community. As the editor of the journal **Acta Mechanica** and the editor-in-chief of the journal **Vestnik of Saint Petersburg University. Mathematics. Mechanics. Astronomy**, he contributed to the appearance of truly new and original articles in these journals. Alexander Belyaev translated several fundamental books of Soviet and Russian mechanicist of the 20th century for the Springer publishing house.

Alexander Belyaev is a real connecting link of European mechanics, he worked at Austrian, German, and Russian universities. He was awarded a Doctor Honoris Causa in 2012 at the Johannes Kepler University of Linz. In 2016, he was awarded as a Foreign Member of the Austrian Academy of Sciences and in 2019, he was awarded as a Member of the Russian Academy of Sciences. He has initiated a large number of scientific contacts all over the world, and he served as Chairman and Co-Chairman of various international conferences and symposia. Currently, he works as a Member of Advisory Board of European Mechanics Society (EUROMECH), as a Member of the Symposia Panel of International Union for Theoretical and Applied Mechanics (IUTAM) and as a Member of Presidium of Russian National Committee for Theoretical and Applied Mechanics.

Alexander Belyaev continues all his activities, teaches at three universities (Johannes Kepler University of Linz, St. Petersburg University and Peter the Great St. Petersburg Polytechnic University) simultaneously, directs graduate students, edits journals, organizes conferences, he is the co-head of a megagrant. We wish him further creative success.

Magdeburg,   *Holm Altenbach*,
Linz,   *Hans Irschik*
St. Petersburg,   *Vladimir Polyanskiy*
Juli 2023   *Alexey Porubov*

Contents

List of Contributors

Andrei K. Abramian
Institute for Problems in Mechanical Engineering of the Russian Academy of
Sciences, Bolshoy prospekt 61, V.O., 199178 St. Petersburg, Russian Federation,
e-mail: andabr33@yahoo.co.uk

Christoph Adam
Universität Innsbruck, Unit of Applied Mechanics, Technikerstr. 13, 6020 Innsbruck,
Austria,
e-mail: christoph.adam@uibk.ac.at

Vladislav O. Alexenko
Institute of Strength Physics and Materials Science, Siberian Branch of the Russian
Academy of Sciences, 2/4, prospekt Akademicheskii, 634055 Tomsk, Russian
Federation,
e-mail: vl.aleksenko@mail.ru

Holm Altenbach
Institut für Mechanik, Otto-von-Guericke-Universität Magdeburg, 39106 Magdeburg,
Germany,
e-mail: holm.altenbach@ovgu.de

Dmitry G. Arseniev
Institute for Problems in Mechanical Engineering of the Russian Academy of
Sciences, Bolshoy prospekt 61, V.O., 199178 St. Petersburg, Russian Federation,
e-mail: adg@ipme.ru

Larisa A. Avershina
Cheboksary branch of N.S. Fyodorov National Medical Research Center "MNTH
"Eye Microsurgery", 10 Traktostrostroiteley av., 428028 Cheboksary, Russian
Federation,
e-mail: avershina@mntkcheb.ru

Alexey V. Babenko
National Research Centre "Kurchatov Institute", Ploshchad' Akademika Kurchatova, 1, 123098 Moscow, Russian Federation,
e-mail: svpma91@mail.ru

Ludmila Ya. Banakh
Mechanical Engineering Research Institute of Russian Academy of Sciences, 4 Mal. Kharitonjevsky str., 101990 Moscow & Mechanical Engineering Research Institute of the Russian Academy of Sciences– Branch of Federal Research Center "Institute of Applied Physics of the RAS", 85 Belinsky str., 603024 Nizhny Novgorod, Russian Federation,
e-mail: banl@inbox.ru

Svetlana M. Bauer
St. Petersburg State University, 7/9 Universitetskaya Emb., 1999034 St. Petersburg, Russian Federation,
e-mail: s.bauer@spbu.ru

Nikolai M. Bessonov
Institute for Problems in Mechanical Engineering of the Russian Academy of Sciences, Bolshoy prospekt 61, V.O., 199178 St. Petersburg, Russian Federation,
e-mail: nickbessonov1@gmail.com

Sergey A. Bochkarev
Institute of Continuous Media Mechanics, Ural Branch of Russian Academy of Sciences, 1, Acad. Korolev str., 614068 Perm, Russian Federation,
e-mail: bochkarev@icmm.ru

Svetlana A. Bochkareva
Institute of Strength Physics and Materials Science, Siberian Branch of the Russian Academy of Sciences2/4, prospekt Akademicheskii, 634055 Tomsk & Tomsk State University of Control Systems and Radioelectronics, 40, prospect Lenina, 634050 Tomsk, Russian Federation,
e-mail: svetlanab7@yandex.ru

Marina Botogova
Belarusian State University, 4, Nezavisimosti Ave., 220030 Minsk, Belarus,
e-mail: Batahova@bsu.by

Roman Buchta
Institute of Energy Systems and Thermodynamics, TU Wien, Getreidemarkt 9, 1060 Wien, Austria,
e-mail: roman.buchta@tuwien.ac.at

Anton V. Byakov
Institute of Strength Physics and Materials Science, Siberian Branch of the Russian Academy of Sciences, 2/4, prospekt Akademicheskii, 634055 Tomsk, Russian Federation,
e-mail: bjakov@ispms.ru

Anastasiia A. Chevrychkina
Institute for Problems in Mechanical Engineering of the Russian Academy of
Sciences, Bolshoy prospekt 61, V.O., 199178 St. Petersburg, Russian Federation,
e-mail: Anastasiia.Che@gmail.com

Galeb El Chabaan
Institute of Structural Engineering, Research Unit of Mechanics and Structural
Dynamics, TU Wien, Vienna, Austria,
e-mail: galeb.el.chabaan@tuwien.ac.at

Peter Eberhard
Institute of Engineering and Computational Mechanics, University of Stuttgart,
Germany,
e-mail: peter.eberhard@itm.uni-stuttgart.de

Victor A. Eremeyev
DICAAR, University of Cagliari, Via Marengo, 2, 09123 Cagliari, Italy
e-mail: victor.eremeev@unica.it

Vladimir Erofeev
Mechanical Engineering Research Institute of Russian Academy of Sciences, 85
Belinskogo str., 603024 Nizhny Novgorod, Russian Federation,
e-mail: erof.vi@yandex.ru

Ksenia Frolova
Institute for Problems in Mechanical Engineering of the Russian Academy of
Sciences, Bolshoy prospekt 61, V.O., 199178 St. Petersburg, Russian Federation,
e-mail: kspfrolova@gmail.com

Thomas Furtmüller
Universität Innsbruck, Unit of Applied Mechanics, Technikerstr. 13, 6020 Innsbruck,
Austria,
e-mail: thomas.furtmueller@uibk.ac.at

Elena F. Grekova
Institute for Problems in Mechanical Engineering of the Russian Academy of
Sciences, Bolshoy prospekt 61, V.O., 199178 St. Petersburg, Russian Federation,
e-mail: elgreco@pdmi.ras.ru

Markus A. Hartmann
Ludwig Boltzmann Institute of Osteology at Hanusch Hospital of OEGK and AUVA
Trauma Centre Meidling, Vienna, Austria,
e-mail: markus.hartmann@osteologie.lbg.ac.at

Christian Hellmich
Institute for Mechanics of Materials and Structures, TU Wien, Austria,
e-mail: christian.hellmich@tuwien.ac.at

Rudolf Heuer
Institute of Structural Engineering, Research Unit of Mechanics and Structural
Dynamics, TU Wien, Vienna, Austria,
e-mail: rudolf.heuer@tuwien.ac.at

Hans Irschik
Institute of Technical Mechanics, Johannes Kepler University Linz, Altenberger Str.
69, 4040 Linz, Austria,
e-mail: hans.irschik@jku.at

Sabina M. Isaeva
Scientific and Education center Gazpromneft-Politech, Polytechnicheskaya, 29AF,
Tehnopolis Politeh A 2.24, 195251 St. Petersburg, Russian Federation,
e-mail: sabinca98@list.ru

Bernhard Jakoby
Institute for Microelectronics and Microsensors, Johannes Kepler University Linz,
4040 Linz, Austria,
e-mail: Bernhard.Jakoby@jku.at

Nabor Jiménez Segura
Institute for Mechanics of Materials and Structures, TU Wien, Austria,
e-mail: nabor.segura@tuwien.ac.at

Vladimir V. Kornikov
St. Petersburg State University, 7/9 Universitetskaya Emb., 199034 St. Petersburg,
Russian Federation,
e-mail: v.kornikov@spbu.ru

Michael Krommer
Institute of Technical Mechanics, Johannes Kepler University Linz, Altenberger Str.
69, 4040 Linz, Austria,
e-mail: michael.krommer@jku.at

Boris Lampsi (Jr.)
Nizhny Novgorod State University of Architecture and Civil Engineering, 65
Ilinskaya str., 603950 Nizhny Novgorod, Russian Federation,
e-mail: boris-lampsi@yandex.ru

Nguyen Le
Belarusian State University, 4 Nezavisimosti Ave., 220030 Minsk, Belarus,
e-mail: dinhnguyen081017@gmail.com

Sergey V. Lekomtsev
Institute of Continuous Media Mechanics, Ural Branch of Russian Academy of
Sciences, 1, Acad. Korolev str., 614068 Perm, Russian Federation,
e-mail: lekomtsev@icmm.ru

Anna Leonteva
Mechanical Engineering Research Institute of Russian Academy of Sciences, 85
Belinskogo str., 603024 Nizhny Novgorod, Russian Federation
e-mail: aleonav@mail.ru

Yaroslava I. Litvinova
Peter the Great St. Petersburg Polytechnic University, Polytechnicheskaya, 29,
195251 St.Petersburg, Russian Federation,
e-mail: yailitvinova@gmail.com

Boris A. Lyukshin
Institute of Strength Physics and Materials Science Siberian Branch of the Russian
Academy of Sciences, 2/4, prospekt Akademicheskii, 634055 Tomsk, Tomsk State
University of Control Systems and Radioelectronics, 40, prospect Lenina, 634050
Tomsk & National Research Tomsk State University, Lenin Ave 36, 634050 Tomsk,
Russian Federation,
e-mail: lba2008@yandex.ru

Valerii P. Matveenko
Institute of Continuous Media Mechanics, Ural Branch of Russian Academy of
Sciences, 1, Acad. Korolev str., 614068 Perm, Russian Federation,
e-mail: mvp@icmm.ru

Gennadi Mikhasev
Belarusian State University, 4 Nezavisimosti Ave., 220030 Minsk, Belarus & Harbin
Institute of Technology, 92 West Dazhi Street, Nangang District, 150001 Harbin,
P.R. China,
e-mail: mikhasev@bsu.by

Wolfgang H. Müller
Institute of Mechanics, Chair of Continuum Mechanics and Constitutive Theory,
Technische Universität Berlin, Sekr. MS. 2, Einsteinufer 5, 10587 Berlin, Germany,
e-mail: wolfgang.h.mueller@tu-berlin.de

Chigbogu Ozoegwu
Department of Mechanical Engineering, University of Nigeria, Nsukka, Nigeria,
e-mail: chigbogug@yahoo.com

Sergey V. Panin
Institute of Strength Physics and Materials Science, Siberian Branch of the Russian
Academy of Sciences, 2/4, prospekt Akademicheskii, 634055 Tomsk & National
Research Tomsk Polytechnic University, Lenin Ave, 30, 634050 Tomsk, Russian
Federation,
e-mail: svp@ispms.ru

Iliya L. Panov
Institute of Strength Physics and Materials Science, Siberian Branch of the Russian
Academy of Sciences, 2/4, prospekt Akademicheskii, 634055 Tomsk & National
Research Tomsk State University, Lenin Ave 36, 634050 Tomsk, Russian Federation,
e-mail: panov.iliya@mail.ru

Ivan Paulmichl
Universität Innsbruck, Unit of Applied Mechanics, Technikerstr. 13, 6020 Innsbruck,
Austria,

e-mail: ivan.paulmichl@uibk.ac.at

Dmitry Pashkovsky
Peter the Great St. Petersburg Polytechnic University, St.Petersburg, Polytechnic-eskaya, 29, 195251, Russian Federation,
e-mail: mr.vivivilka@icloud.com

Igor S. Pavlov
Mechanical Engineering Research Institute of the Russian Academy of Sciences–Branch of Federal Research Center "Institute of Applied Physics of the RAS", 85 Belinsky str., Nizhny Novgorod 603024 & National Research Lobachevsky State University of Nizhny Novgorod, 23 Gagarin av., Nizhny Novgorod 603950, Russian Federation, e-mail: ispavlov@mail.ru

Yuri V. Pavlov
Institute for Problems in Mechanical Engineering of the Russian Academy of Sciences, Bolshoy prospekt 61, V.O., 199178 St. Petersburg, Russian Federation,
e-mail: yuri.pavlov@mail.ru

Astrid S. Pechstein
Institute of Technical Mechanics, Johannes Kepler University Linz, Altenberger Str. 69, 4040 Linz, Austria,
e-mail: astrid.pechstein@jku.at

Bernhard L.A. Pichler
Institute for Mechanics of Materials and Structures, TU Wien, Austria,
e-mail: bernhard.pichler@tuwien.ac.at

Oksana R. Polyakova
Public Organization of Scientific Research "Metagalactic Sciences" of Moscow region, Russian Federation,
e-mail: ksenpolyaor@yandex.ru

Vladimir A. Polyanskiy
Institute for Problems in Mechanical Engineering of the Russian Academy of Sciences, Bolshoy prospekt 61, V.O., 199178 St. Petersburg, Russian Federation,
e-mail: vapol@mail.ru

Alexey V.Porubov
Institute for Problems in Mechanical Engineering of the Russian Academy of Sciences, Bolshoy prospekt 61, V.O., 199178 St. Petersburg, Russian Federation,
e-mail: alexey.porubov@gmail.com

Franz G. Rammerstorfer
Institute of Lightweight Design and Structural Biomechanics, TU Wien, Vienna, Austria,
e-mail: franz.rammerstorfer@tuwien.ac.at

Michael Ruttmann
TU Wien, Getreidemarkt 9, 1060 Wien, Austria,
e-mail: e11909827@student.tuwien.ac.at

Nadezhda Semerikova
National Research Lobachevsky State University of Nizhny Novgorod, 23 Gagarina
av., 603022 Nizhny Novgorod, Russian Federation
e-mail: nadezhda.semerikova@yandex.ru

Alexander N. Senin
Institute of Continuous Media Mechanics, Ural Branch of Russian Academy of
Sciences, 1, Acad. Korolev str., 614068 Perm, Russian Federation,
e-mail: senin.a@icmm.ru

Alois Steindl
TU Wien, Institute for Mechanics and Mechatronics, Getreidemarkt 9, 1060 Wien,
Austria,
e-mail: Alois.Steindl@tuwien.ac.at

Anna E. Terentyeva
Cheboksary branch of N.S. Fyodorov National Medical Research Center "MNTH
"Eye Microsurgery", 10 Traktostrostroiteley av., 428028 Cheboksary, Russian
Federation,
e-mail: anyaterentieva@yandex.ru

Melanie Todt
Institute of Lightweight Design and Structural Biomechanics, TU Wien, Vienna,
Austria,
e-mail: melanie.todt@tuwien.ac.at

Tatiana P. Tovstik
Institute for Problems in Mechanical Engineering of the Russian Academy of
Sciences, Bolshoy prospekt 61, V.O., 199178 St. Petersburg, Russian Federation,
e-mail: tovstik_t@mail.ru

Sergey A. Vakulenko
Institute for Problems in Mechanical Engineering of the Russian Academy of
Sciences, Bolshoy prospekt 61, V.O., 199178 St. Petersburg, Russian Federation,
e-mail: vakulenfr@mail.ru

Liudmila A. Venatovskaya
St. Petersburg State University, 7/9 Universitetskaya Emb., 199034 St. Petersburg,
Russian Federation,
e-mail: l.venatovskaya@spbu.ru

Yury Vetyukov
TU Wien, Institute for Mechanics and Mechatronics, Getreidemarkt 9, 1060 Wien,
Austria,
e-mail: Yury.Vetyukov@tuwien.ac.at

Elena N. Vilchevskaya
Flugsnapparegatan 6, Mölndal, Sweden,
e-mail: Vilchevska@gmail.com

Thomas Voglhuber-Brunnmaier
Institute for Microelectronics and Microsensors, Johannes Kepler University Linz,
4040 Linz, Austria,
e-mail: thomas.voglhuber-brunnmaier@jku.at

Eva B. Voronkova
St. Petersburg State University, 7/9 Universitetskaya Emb., 199034 St. Petersburg,
Russian Federation,
e-mail: e.voronkova@spbu.ru

Yuri A. Yakovlev
Institute for Problems in Mechanical Engineering of the Russian Academy of
Sciences, Bolshoy prospekt 61, V.O., 199178 St. Petersburg, Russian Federation,
e-mail: yura.yakovlev@gmail.com

Yuting Zhao
Peter the Great St. Petersburg Polytechnic University, Polytechnicheskaya, 29,
195251 St.Petersburg, Russian Federation,
e-mail: chzhao13.yu@edu.spbstu.ru

Chapter 1
A Semi-Empirical Fluid Force Model for Vortex-Induced Vibration of an Elastic Structure

Andrei K. Abramian and Sergey A. Vakulenko

Abstract A new semi-empirical model is presented for the vortex-induced vibration of structures. The lift force on a structure is assumed to consist of two components. The first component is a non-linear force that has a polynomial dependence on the velocity of the structure. The second component is a harmonic force with the Strouhal frequency. Only the crossflow motion of the structure is considered. The maximum response amplitude of the structure is estimated as well as the phase difference between the structural displacement and the periodic component of the lift force. The model predictions are compared with experimental results available in literature to show good qualitative agreement.

1.1 Introduction

Many flexible engineering structures, such as marine cables towing instruments, flexible risers used in petroleum production and mooring lines are prone to Vortex Induced Vibration (VIV), see [1–6]. The VIV can have considerable amplitude and significantly accelerate fatigue of the structures. This makes VIV one of the most undesirable phenomena in offshore engineering. If the structure (or its segments) vibrates at nearly the forcing frequency, the structure and the wake will be in the state of "synchronization" or lock-in as termed in the classical work of [7]. This state occurs in a narrow band of cylinder oscillation frequencies which includes the Strouhal frequency. About three decades ago, several investigators began employing nonlinear oscillator equations of the van der Pol type to represent the fluctuating lift force acting on the cylinder [8–10]. The modeling was continued in [11, 12]. The representation for the lift force in this papers was based on the similarity between

Andrei K. Abramian · Sergey A. Vakulenko
Institute for Problems in Mechanical Engineering of the Russian Academy of Sciences, Bolshoy prospekt 61, V.O., 199178 St. Petersburg, Russian Federation,
e-mail: andabr33@yahoo.co.uk, vakulenfr@mail.ru

the vortex-shedding process and the behavior of nonlinear oscillators rather than on the underlying fluid dynamics. In [12] under the assumption of a sinusoidal lift and drag force at a single frequency for a stationary cylinder in a cross flow, higher harmonics that represent non-linearity in the fluid-structure interaction process were presented. The force model in [12] was developed based on an iterative process and the modal analysis approach. For other types of the modeling of VIV process see a review in [13]. In [14] authors explores the accuracy of the semi-empirical wake oscillator models for VIV based on the optimization of (a) the damping term and (b) empirical coefficients in the fluid equation. Nevertheless, some fundamental features of VIV of an elastic cylinder are still not fully understood. For example, what is the maximum possible amplitude attainable for a cylinder undergoing VIV, for conditions of extremely small mass and damping? What modes of structural response exist, and how does the system jump between the different modes? The objective of this paper is to answer the above questions using an analytical approach and simple numerical computations with the help of a new semi-empirical model of the lift force. In this model, the lift force on the structure resulting from the shedding process consists of two components. The first component is a force that depends non-linearly on the velocity of the structure across the flow. The second component is a harmonic force with the vortex-shedding frequency. Only the cross-flow vibration of the structure is considered.

1.2 A Fluid Force Model

1.2.1 Formulation of the Problem

Consider a flexible, circular cylindrical structure subjected to a uniform cross-flow of velocity V_0 and mass density ρ. For long structures where tension dominates bending, the PDE governing geometrically linear transversal vibrations can be written in the form:

$$\partial_t (M \partial_t u_y) + \varsigma \partial_t u_y = T_0 \partial_{xx} u_y + F, \qquad (1.1)$$

where $M = m_c + m_{\text{add}}$ is the mass per unit length of the structure including the added fluid mass, m_{add} is the added mass per unit length, m_c is the mass of the structure per unit length, u_y is the transversal displacement, ς is the structural damping, T_0 is the tension in the structure (assumed to be constant), F is the fluid force, ∂_t is a partial derivative with respect to time, ∂_x is a partial derivative with respect to the coordinate. It is proposed to represent the fluid force as follows:

$$F = \frac{1}{2} c_n \rho d V_0^2 \left[-b_1 \frac{\partial_t u_y}{V_0} + b_3 \left(\frac{\partial_t u_y}{V_0} \right)^3 - b_5 \left(\frac{\partial_t u_y}{V_0} \right)^5 + f_0 \sin(\omega_s t + \beta) \right], \qquad (1.2)$$

where d is the diameter of the structure, c_n, b_1, b_3, b_5 are coefficients to be found from experiments, f_0 is the amplitude of the periodic part of the force, ω_s is the Strouhal

angular frequency; β is the phase of the periodic force. Equation (1.1) should be supplemented with the boundary conditions.

In the model, the force F acting on the structure in the cross flow direction as a result of the shedding process consists of two components. The first component is a force depending non-linearly on the velocity of the structural motion in the crossflow direction. The force is such, that at small velocities it adds to the hydrodynamic resistance force and is directed opposite to the velocity, this insures the structural stability. With the velocity rise the force becomes co-directed with the velocity, which leads to the growth of the vibration amplitude. But with the further velocity rise the force becomes again directed opposite to the velocity, which limits the vibration amplitude. Such a nature of the force dependence on the cable velocity is proved experimentally for marine cables [15]. With the flow velocity rise the frequency of the force grows, and when it becomes close to the first natural frequency of the structural vibration, the intensive eigenmode vibration is exited. The non-linear force/velocity dependence leads to the limitation of the oscillation amplitude. The structure gets into a self-oscillation regime with the mode close to the eigenmode. With further increase of the flow velocity, the force frequency continues to grow, and when it is approaching to the second natural frequency, the intensive vibration is exited at the second eigenmode. The self-oscillation regime with the mode close to the first eigenmode ends and the structure gets into the self-oscillation regime with the mode close to the second eigenmode. With the further increase of the velocity the jump to the third natural frequency occurs and, correspondingly, to the third eigenmode. In Eq. (1.2) the non-linear component of the force differs from the model of classical forced Rayleigh-type oscillator by the additional term $(\partial_t u_y/V_0)^5$ and the signs in front of the linear and the first non-linear terms. The term $(\partial_t u_y/V_0)^5$ allows describing the stabilization of the structural vibration when the vibrating structure velocity rises. The second component of the lift force is a harmonic force with the vortex-shedding frequency. It reflects the following experimental result: at small values of the oscillation amplitudes the lift coefficient varies according to the sinusoidal law [15]. Inserting Eq. (1.2) into Eq.(1.1), one obtains:

$$\partial_t((m_c + m_{\text{add}})\partial_t u_y) + \varsigma \partial_t u_y = T_0 \partial_{xx} u_y$$
$$+ \frac{1}{2} c_n \rho d V_0^2 \left[-b_1 \partial_t u_y/V_0 + b_3 (\partial_t u_y/V_0)^3 - b_5 (\partial_t u_y/V_0)^5 + f_0 \sin(\omega_s t + \beta) \right]).$$

$$(1.3)$$

Equation (1.3) allows to take into account the possible variation of the added mass of the fluid in time according to the variation of reduced velocity

$$V_r = \frac{V_0}{d\nu},$$

where ν is natural frequency of the structure. The dependence of added mass on time and on the reduced velocity for small mass ratio cylinders was studied experimentally in [15–17]. The obtained results show that there are significant cycle-to cycle variations in added mass and vibration period as shown in [17]. The added mass

dependence on time was observed for $V_r = 4$. Once the lock-in commences, at approximately $V_r = 4$, then the natural frequency of the cylinder increases with increasing reduced velocity, enabling lock-in to persist, in this case up to approximately $V_r = 12$, because the mass ratio

$$\mu = \frac{m_c}{\rho d^2 L}$$

was quite low ($\mu = 3$, L is the length of the cylinder). On the basis of results obtained in [17], in the present paper the behaviour of the system is described in the following way. The model of the system behaviour in the upper and lower branches of the lock-in range takes into account the dependence of the added mass on the reduced velocity and outside that regions will not. It was also shown in [17] that the added mass is influenced by components of the cylinder displacement at frequencies which are different from the natural vortex-induced vibration response. This fact is not taken into account in this paper, but will be shortly discussed in the conclusion. Analytical research of the elastic structure dynamics described by Eq. (1.3) has not been performed in the past. Such a research can be carried out by perturbations methods and averaging techniques. The present paper presents preliminary results of such a research. Let us first consider the structural behaviour when the added mass is assumed to be constant. Then, Eq. (1.3) can be reduced to the equation for a single degree of freedom (SDOF) oscillator. SDOF models use a single ordinary differential equation to describe the behaviour of the structural oscillator (see for references [13]). Such a model can be obtained for elastic systems that could be described by the one dimensional damped wave equation (e.g. wires, cables). The results obtained in [12] indicate that for a particular pure response mode, the equations describing the system response reduced to those obtained for a rigid cylinder. Using Galerkin procedure, and seeking the solution of Eq. (1.4) in the form

$$u_y = \sum_{i=0}^{\infty} y_i(t) Z_i(x),$$

one can come to the solution of the infinite system of ODES for determining time dependent coefficients $y_i(t)$. Neglecting interaction of modes, which is of course, the strong assumption, and dividing both parts of Eq. (1.3) by η, one has the following equation for i-th mode:

$$\frac{d^2 y_i}{dt^2} + \eta \frac{dy_i}{dt} + \Omega_i^2 y_i = F(\dot{y}_i, t), \tag{1.4}$$

where η is the damping coefficient, y_i is the modal coefficient of the transverse displacement of the elastic system, $F(\dot{y}_i, t)$ is the hydroelastic forcing function, Ω_i is the natural circular frequency of the i-th mode. In Eq. (1.3), the expression for the added mass is as follows:

$$m_{ad} = \frac{\chi \pi d^2}{4};$$

χ is the coefficient depending on the structure design.

1.2.2 Solution of the Structure Motion Equation

Although cables and wires very often are made of synthetic fibers, for example Capron and Kevlar, some cables are made of stainless steel. Underwater cables also can be armored or have a metal braiding. Thus, deepwater cables contain armor elements like a compacted conductor or a metal tube for optical modules/optical fibers. Since the density of the fluid is smaller then the density of the structure material it is natural to introduce there ratio as a small parameter ε; then the right hand side of Eq. (1.4) can be represented as follows:

$$F(\dot{y},t) = \varepsilon f(\dot{y},t),$$

where ε is a small parameter,

$$f(\dot{y},t) = c_n \frac{V_0^2 d}{2\delta(1+m_c/m_{\mathrm{add}})} \Big[-b_1(\dot{y}/V_0) + b_3(\dot{y}/V_0)^3 - b_5(\dot{y}/V_0)^5 \\ + f_0 \sin(\omega_s t + \beta) \Big],$$

$\varepsilon = \rho/\rho_c$, ρ_c is the density of the cylinder material; δ is the area of the structure cross section. Here and in the following we omit the index i in the frequency and the displacement notations.

Since the lift coefficient frequency does not coincide with the natural frequency of the structure, the approximation of the solution of Eq. (1.4) will be constructed in the form:

$$y = A(\tau)\sin(\omega t + \psi(\tau)), \tag{1.5}$$

where A is the displacement amplitude, ψ is the displacement phase, ω is the circular frequency of the structural vibration. In Eq. (1.5) the amplitude and the phase are time functions slowly changing. In Eq. (1.5) the slow time $\tau = \varepsilon t$ is introduced. Then, the standard averaging procedure (see for an example [18] is used. To eliminate the secular terms in the approximation of the solution of Eq.(1.5) it is necessary to multiply Eq. (1.5) by $\sin(\omega t + \psi)$ and $\cos(\omega t + \psi)$, and integrate over t from 0 to T. One can get, up to the order of $O(\varepsilon^2)$:

$$\begin{cases} -\omega A \psi_\tau = \dfrac{1}{T} \displaystyle\int_0^T g(\dot{y},t)\sin(\omega t + \psi)\,dt, \\[4mm] \omega A_\tau = \dfrac{1}{T} \displaystyle\int_0^T g(\dot{y},t)\cos(\omega t + \psi)\,dt, \end{cases} \tag{1.6}$$

where $g(\dot{y},t) = R(\dot{y}) + F_0$; $R(\dot{y}) = -b_1\dot{y} + b_3\dot{y}^3 - b_5\dot{y}^5$; $F_0 = f_0\sin(\omega_s t + \beta)$.

The function $g(\dot{y},t)$ gives two different contributions in the first equation of Eqs. (1.6). The first is related to $R(\dot{y})$ and the second to F_0. Calculating the contribution from $R(\dot{y})$ we assume that $\dot{y} \approx A\omega\cos(\omega t + \psi)$ up to $O(\varepsilon^2)$. Then, the

contribution of $R(\dot{y})$ is equal to zero. At $A > 0$ the phase ψ is changing so, that either $\psi \to \infty$ or, if the contribution of F_0 has roots $\psi_0, \psi_1, \dots \psi_\infty$, then $\psi \to \psi_\infty(\tau \to \infty)$. It means that the equilibrium values of ψ_∞ are the roots of the contribution from F_0. These roots satisfy the following equation:

$$\frac{1}{T(\omega_s+\omega)} \cos\left[\frac{(\omega_s+\omega)T}{2} + \beta + \psi)\right] \sin\frac{(\omega_s+\omega)T}{2}$$
$$+ \frac{1}{\Delta\omega T} \sin\frac{\Delta\omega T}{2} \cos\left(\frac{\Delta\omega T}{2} + \beta - \psi\right), \quad (1.7)$$

where $\Delta\omega = \omega_s - \omega$.

Let us consider the pure resonance case, the near resonance and the non-resonance cases. The near resonance behavior (detuning) is not considered in all details in the present paper, it is a subject of a future research which can be done with a help of the more accurate averaging technique presented in [18].

1.2.2.1 Pure Resonance Case

At resonance, substituting $T = 2\pi/\omega$ into Eq. (1.7) one obtains:

$$\cos(\beta - \psi) = 0. \qquad (1.8)$$

Consequently, $\beta - \psi = \frac{\pi}{2}(2k+1)$, $k = 0, \pm1, \pm2, \dots$ with the accuracy $O(\varepsilon^2)$. Therefore, the phase of the displacement reads:

$$\psi_\infty = \beta - \frac{\pi}{2}(2k+1). \qquad (1.9)$$

So, one can conclude that the difference in phases between the force and the displacement is equal to $\pm\frac{\pi}{2}$. In experiments the phase difference close to $\frac{\pi}{2}$ was also found (see [13]). To satisfy the second equation of Eqs. (1.6) it is necessary to substitute the found values of ψ_∞, Eq. (1.9), into the equation for A_τ. The steady-state values of the cable amplitudes are determined from the roots of

$$\frac{1}{T}\int_0^T g(\dot{y},t)\cos(\omega t + \psi)dt$$

where $\psi = \psi_\infty$. The integration of $R(\dot{y})$ as a part of $g(\dot{y},t)$ gives the following expression in dimensionless variables:

$$R(\bar{A},\bar{\omega}) = -\frac{1}{2}(2\pi St)b_1(\bar{A}\bar{\omega}) + \frac{3}{8}(2\pi St)^3 b_3(\bar{A}\bar{\omega})^3 - \frac{5}{16}(2\pi St)^5 b_5(\bar{A}\bar{\omega})^5,$$
$$R\left(\frac{\bar{A}}{V_r}\right) = -\frac{1}{2}(2\pi)b_1\left(\frac{\bar{A}}{V_r}\right) + \frac{3}{8}(2\pi)^3 b_3\left(\frac{\bar{A}}{V_r}\right)^3 - \frac{5}{16}(2\pi)^5 b_5\left(\frac{\bar{A}}{V_r}\right)^5,$$

where $\bar{A} = A/d$ is the dimensionless amplitude with respect to the diameter of the cable; $\bar{\omega} = \omega/\omega_s$, $\bar{\omega} = 1$ at the resonance; St is the Strouhal number. The remaining part of the

$$\frac{1}{T} \int_0^T g(\dot{y}, t) \cos(\omega t + \psi) dt$$

which came from F_0, gives the expression: $(-1)^k \bar{f}_0$, where $\bar{f}_0$ is the dimensionless amplitude of the periodic part of the lift coefficient. So, finally the equation for finding the dimensionless amplitude of the structure has the form:

$$(-1)^k \bar{f}_0 + R(\bar{A}) = 0. \tag{1.10}$$

The solution of Eq. (1.10) can be found numerically or graphically. For values of $k = 1, 3, 5, \ldots$, Eq. (1.10) has a form:

$$\bar{f}_0 = R(\bar{A}). \tag{1.11}$$

The different values of k correspond to different values of the phase ψ obtained from the Eq. (1.8). The solution of the Eq. (1.11) is represented in Fig. 1.1. It is seen that depending on the value of the force amplitude $\bar{f}_0$ it is possible to have one, two or three values of the resonant displacement amplitudes. It is because the different values of $\bar{f}_0$ correspond to different shifts of the $R(\bar{A})$ curve up or down with respect
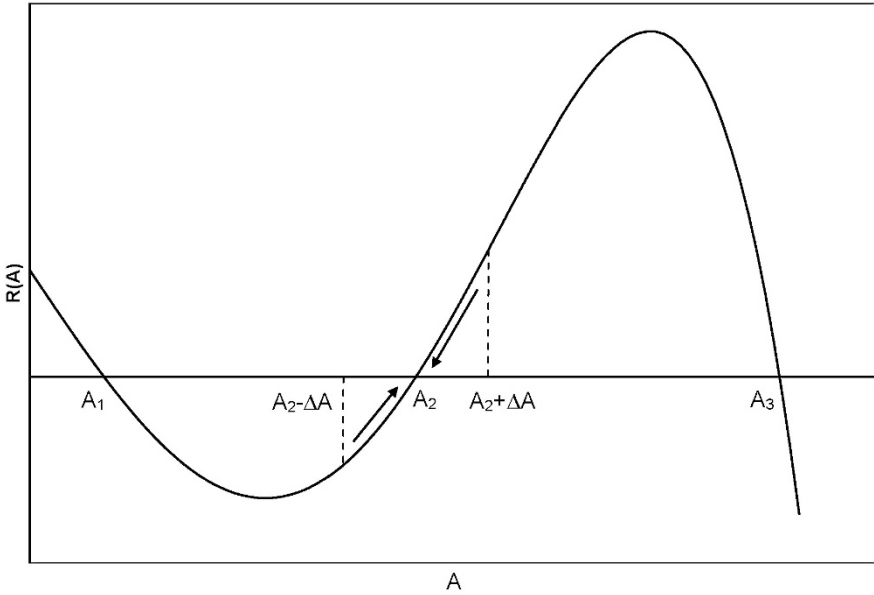
Fig. 1.1: The solution to Eq. (1.11).

to the ordinate axis. The possibility to have more then one value of the amplitude of the structural vibration corresponds to the so called hysteresis. Let us consider the stability of the found solution for the amplitude. Let A_1, A_2, A_3 be the roots of Eq. (1.11) shown in Fig. 1.1. If $A < A_2$, then in the first equation of Eqs. (1.6) the right hand side of equation is positive which can be satisfied if $A_\tau > 0$ which means that $A \rightarrow A_2$. If $A > A_2$ then the sign of the right hand side of the first Eq. (1.6) is negative and from this follows: $A \rightarrow A_2$. In the same way it is possible to show that A_1, A_3 are unstable. So, the values of the amplitudes of structural vibration belonging to the positive slope of the $R(\bar{A})$ curve correspond to the stable oscillations of the cable. If the value of the amplitude of the periodic component of the lift coefficient is bigger than $R(\bar{A}\bar{\omega})$: $\bar{f}_0 > R(\bar{A}\bar{\omega})$, the oscillations of this mode became impossible. The same effect appears if the velocity of the flow and the frequency of the shedding change. Then one can get in the vicinity of resonance the case when

$$\bar{f}_0 \frac{\sin \Delta \omega T}{\Delta \omega T} \rightarrow \bar{f}_0,$$

and as a result of that one can get the inequality: $\bar{f}_0 > R(\bar{A}\bar{\omega})$, and oscillations vanish. The energy which is transferred to the oscillating structure from the fluid can not be accumulated by that one mode only. As a result, the structure will start to oscillate on the next mode. For this mode another curve $R(\bar{A}\bar{\omega})$ can be obtained and if the velocity of the flow continues to grow, the jump to the next mode occurs. For $k = 0, 2, 4, \ldots$, the equation for determination of the structure amplitude can be analyzed in the same way as for Eq. (1.11).

1.2.2.2 Near Resonance Case

Let us consider the case when $\omega = \omega_s + \varepsilon \alpha$, it is the lock-in region, its lower branch if $\alpha > 0$. Then the system of Eqs. (1.6) with the accuracy $O(\varepsilon^2)$ becomes:

$$\begin{cases} 2\bar{A}\theta_\tau = 2\bar{A}\alpha + \bar{f}_0 \cos \theta, \\ -\bar{A}_\tau = R(\bar{A}) + \bar{f}_0 \sin \theta, \end{cases} \tag{1.12}$$

where $\theta = \beta - \psi + \alpha \varepsilon t = \beta - \psi + \alpha \tau$.

Let us now consider the behavior of the system when ω is closed to ω_s and detuning parameter α is small. For the steady state we have: $\theta_\tau = 0$, $A_\tau = 0$, and then the system of Eqs. (1.6) takes the form:

$$\begin{cases} 2\bar{A}\alpha + \bar{f}_0 \cos \theta = 0, \\ R(\bar{A}) + \bar{f}_0 \sin \theta = 0. \end{cases} \tag{1.13}$$

Therefore, the $\bar{A}$ and θ are given as:

$$R(\bar{A}) \pm \bar{f}_0 \sqrt{1 - 4\alpha^2 \frac{\bar{A}^2}{\bar{f}_0^2}} = 0,$$

$$\cos\theta = -2\alpha \frac{\bar{A}}{\bar{f}_0}.$$

Let us determine the types of the critical points which satisfy the steady state conditions (1.13). In the vicinity of $\theta_0 = \frac{\pi}{2}$, $R(\bar{A}_0) = \pm\bar{f}_0$ one can get the following decomposition:

$$\begin{aligned} \theta &= \theta_0 + \alpha\theta_1 + ..., \\ A &= A_0 + \alpha A_1 + ... \end{aligned} \qquad (1.14)$$

Substituting (1.14) into (1.13) for the small α one can get :

$$\begin{cases} \theta_1 = \dfrac{2\omega A_0}{f_0}, \\[2mm] A_1 = \dfrac{-f_0}{R'(A_0)}, \end{cases}$$

where $R'(A_0)$ is a derivative with respect to A_0. For the following investigation of the stability let us rewrite Eq. (1.6) in the form:

$$\begin{cases} \theta_\tau = \dfrac{1}{2\omega A}(2\alpha\omega A + f_0\cos\theta) = g_1(A,\theta), \\[2mm] A_\tau = -\dfrac{1}{\omega}(R(A) + f_0\sin\theta) = g_2(A,\theta). \end{cases}$$

The types of the critical points depend on the eigenvalues of the Jakobian:

$$J = \begin{vmatrix} \dfrac{\partial g_1}{\partial\theta} & \dfrac{\partial g_1}{\partial A} \\[3mm] \dfrac{\partial g_2}{\partial\theta} & \dfrac{\partial g_2}{\partial A} \end{vmatrix}$$

After standard manipulations one can get the following eigenvalues of J (when $\alpha > 0$):

$$\lambda_1 = \frac{(-1)^k f_0}{2\omega A_0}, \quad \lambda_2 = -\frac{1}{\omega}R'(A_0)$$

If $\lambda_1, \lambda_2 > 0$ then we have unstable node; if $\lambda_1, \lambda_2 < 0$, then the node is stable, and if $\lambda_1 < 0, \lambda_2 > 0$ or $\lambda_1 > 0, \lambda_2 < 0$ one has saddle. So, if the eigenvalues of the critical point of the averaged Eqs. (1.6) all have negative real parts, the corresponding periodic solution of Eq. (1.4) is asymptotically stable for small ε. If one of the eigenvalues has a positive real part then the solution of Eq. (1.4) is unstable [18]. If α is not small but f_0 is small then the first equation of Eqs. (1.6) can be reduced to the equation: $\theta_\tau = \alpha$ and from this follows $\theta = \alpha\tau$ and $-\omega A_\tau = R(A) + f_0\sin\alpha\tau$, then one has small oscillations near the equilibrium point.

1.2.2.3 Non-Resonant Case

Let us consider Eq. (1.7) for the case when $\Delta\omega$ is not in the near resonance zone. After some algebraic manipulation, taking into account that $\omega T = 2\pi$, one can get from Eq. (1.7) the following expression for the condition of the steady state solution:

$$\frac{\omega}{\pi(\omega_s^2 - \omega^2)} \sin\pi\frac{\omega_s}{\omega}\left[\omega_s\cos(\pi\frac{\omega_s}{\omega}+\beta)\cos\psi + \omega\sin(\pi\frac{\omega_s}{\omega}+\beta)\sin\psi\right] = 0. \quad (1.15)$$

Then, if $\cos(\frac{\omega_s}{\omega}\pi+\beta) \neq 0$, for the phase ψ which make the expression (1.15) equal to 0 one has:

$$\psi = -\arctg\left[\frac{\omega_s}{\omega}ctg(\pi\frac{\omega_s}{\omega}+\beta)\right]+\pi s \text{ and } s = 0; \pm1; .... \quad (1.16)$$

Note that Eq. (1.16) will be satisfied also if: $\sin\pi\frac{\omega_s}{\omega} = o \Rightarrow \omega_s = \omega l$, $l = 0, \pm1, ...$. It means that sub-harmonics can lead to the stable periodic solutions of Eq. (1.4). From Eq. (1.16) one can see that the phase angle can change its value by π including the case when $\frac{\omega_s}{\omega} = 1$. That can be caused by vortex switching which was observed experimentally in [13]. Let us consider in addition 4 cases:

(a) $\cos(\frac{\omega_s}{\omega}\pi+\beta) = 0$ and $\sin\psi = 0$,

(b) $\sin(\frac{\omega_s}{\omega}\pi+\beta) = 0$ and $\cos\psi = 0$,

(c) $\sin(\frac{\omega_s}{\omega}\pi+\beta) = 0$ and $\cos\psi = 0$, $\sin\frac{\pi\omega_s}{\omega} = 0$,

(d) $\cos(\frac{\omega_s}{\omega}\pi+\beta) = 0$ and $\sin\psi = 0$, $\sin\frac{\pi\omega_s}{\omega} = 0$.

For the case (a) one can get:

$$\pi\frac{\omega_s}{\omega}+\beta = \frac{\pi}{2}(2j+1), \quad \psi = \pi n, \quad \beta-\psi = \pi\left(j-n-\frac{\omega_s}{\omega}+\frac{1}{2}\right),$$
$$n = \pm1; \pm2; ..., \quad j = 0; \pm1; ...$$

For the case (b) one has:

$$\pi\frac{\omega_s}{\omega}+\beta = \pi j, \quad \psi = \frac{\pi}{2}(2n+1), \quad \beta-\psi = \pi\left(j-n-\frac{\omega_s}{\omega}-\frac{1}{2}\right),$$
$$n, j = 0; \pm1; ...$$

For the case (c) one has:

$$\beta-\psi = \pi(j-n-l-\frac{1}{2}), \quad j, n, l = 0; \pm1; ..., \quad \omega_s = \omega l.$$

For the case (d) one has:

$$\beta - \psi = \pi\left(j - n - l + \frac{1}{2}\right), \quad j,n,l = 0; \pm 1; \ldots, \quad \omega_s = \omega l.$$

To find the steady state amplitudes of the displacement it is necessary to substitute the found values of ψ from Eq. (1.16) in the equation for A_τ. Then, for determination of the displacement amplitude one can get the equation in the form:

$$\frac{\bar{\omega}\left[\sin(\frac{\pi}{\bar{\omega}} + \beta)\cos\psi - \bar{\omega}\cos(\frac{\pi}{\bar{\omega}} + \beta)\sin\psi\right]}{\pi(1 - \bar{\omega}^2)}\bar{f}_0\sin\frac{\pi}{\bar{\omega}} + R(\bar{A}\bar{\omega}) = 0. \qquad (1.17)$$

Analysis of the possible existence of the displacement amplitude can be carried out in the same way as above using numerical or graphical methods. For the case when $\omega_s = \omega l$ (sub-resonances) the input of $\bar{f}_0$ is zero, and for the amplitudes of oscillations one can get:

$$R(\bar{A}\bar{\omega}) = 0. \qquad (1.18)$$

For that case the roots of $R(\bar{A}\bar{\omega}) = 0$ are as follows:

$$z_{1,2} = \frac{-\bar{b}_3 \pm \sqrt{\bar{b}_3^2 - 4\bar{b}_5\bar{b}_1}}{2\bar{b}_5} \qquad (1.19)$$

where

$$\bar{b}_1 = \frac{1}{2}(2\pi\mathrm{St})b_1, \quad \bar{b}_3 = \frac{3}{8}(2\pi\mathrm{St})^3 b_3, \quad \bar{b} = \frac{5}{16}(2\pi\mathrm{St})^5 b_5.$$

From Eqs. (1.18) and (1.19) one can conclude that the amplitudes of the structural oscillations do not depend on the amplitude of the periodic component of the force. To find the influence of the force on the structural oscillation amplitude in this case it is necessary to keep the terms of order higher then $O(\varepsilon)$ in Eq. (1.4). For the cases a, b, c, d the amplitudes can be found from Eq. (1.17).

1.2.3 Effect of Variation of an Added Mass with the Reduced Velocity

The mean value of the added mass over one period of oscillations as a function of the reduced velocity was found in [17]. Using that data it is possible to find the frequency of vibrations in the lock-in region for its lower branch more accurately. Variation of the mass as a function of the reduced velocity on the basis of data from [17] can be approximated by the following expression:

$$m_{\mathrm{add}} = m_0 e^{-aV_r} - 1, \qquad (1.20)$$

where $m_0 = 14.135$ and $a = 0.331$. If we substitute Eq. (1.20) into Eq. (1.3) then one can get that not only the natural frequency of the structure but also the structural damping is influenced by the variation of the added mass and the coefficients of the

right hand side of the Eq. (1.4) as well. If we take into account the variation of the mass according to Eq. (1.20) then all formulas obtained in Subsect. 1.2.2 are still valid.

1.3 An Example

The results obtained in the presented work are compared in this section with experimental results available in literature [15, 19]. Coefficients b_1, b_3, b_5 in the Eq. (1.3) can be determined by using the measured accelerations and the structure displacement amplitudes following the technique given in [15]. Measurements given in [15] have shown that for calculations of elastic cylinder oscillations or oscillations of some types of cables the same b_i coefficients can be used for particular parameters of the fluid flow and structures. The cylinders (straight and bent) used in that experiments were from 1 to 5m length and have diameters from 0.1–0.4 m. Maximum bend cylinder deflection was in the range of $0.23 - 0.66$ m, Re $= 6000 - 50000$; the Strouhal number corresponded St $=$ St $\sin\alpha$, (where α is the angle of attack), was practically constant (for bent cylinders) when attack angles were smaller then $50°$, and is equal to St $= 0.19$ for Re $<$ Re$_{\text{critical}}$.Those experiments have been performed for flows with the values of velocities $V_0 = 0.1 - 3$ m/s. For determination of the lift force parameters the following method was suggested. The lift force as was mentioned above consists of two non-correlated components. The first one can be estimated from the data obtained from the tests with fixed cylinder. The value of the second component, caused by the changing of the type of vortex shedding, can be found using the method suggested in [15] on the basis of knowledge of the dispersion of the cylinder oscillation amplitudes and spectrum, for different Reynolds numbers and for different ranges of the cylinder length and diameters. For the given range of the flow and structure parameters the above mentioned $b_i, \bar{f}_0, c_n$ coefficients can be taken as follows for an elastically mounted cylinder:

$$b_1 = 0.17, \quad b_3 = 1.4, \quad b_5 = 0.7, \quad \bar{f}_0 = 0.6, \quad c_n = 1.2, \quad \text{St} = 0.19. \quad (1.21)$$

The coefficient $\bar{f}_0$ depends on the type of structure (elastic cylinder, cable, wire) and its value is varying in the range $0.05 - 0.6$. In the presented model the value of the mass-damping parameter $m\xi = 0.013$ and $\mu = 8.72$:

$$m = m_c/m_d, \quad m_d = \pi\rho_0 d^2 L/4, \quad \xi = \frac{\varsigma}{2\sqrt{\sigma(m_c + m_{\text{add}})}},$$

where σ is the system stiffness. Those values were taken close to those which were used in [19]. In the near resonance range when $V_r = 4.5 - 5.5$ Eqs. (1.9) and (1.11) were used for calculations of the structure response. For the lower branch of the lock-in region, when $V_r = 5.5 - 8.5$, the dependence of the added mass on the reduced velocity was taken into consideration. For the calculation of the amplitude of structure vibrations in that range Eqs. (1.16), (1.17) and (1.19) were used. The
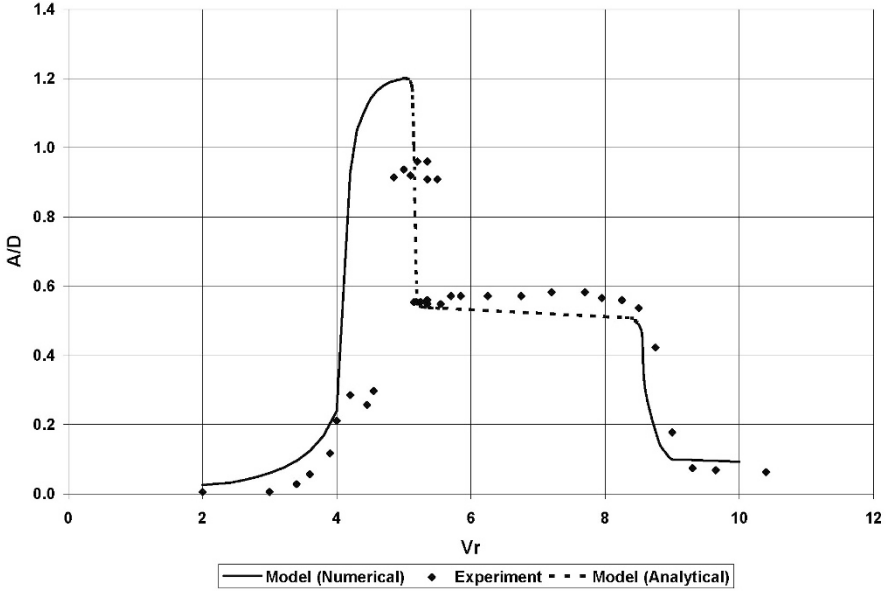
Fig. 1.2: Dependence of the amplitude of structure vibrations on V_r.

result of calculations is shown in Fig. 1.2. As can be seen from Fig. 1.2 the suggested model in the lower branch of the lock-in region has a satisfactory agreement with the experimental data from [19]. The resonance value of amplitude is 20% higher then was found in the experiment. The computer simulation for the $V_r = 2 - 4.5$ and $V_r = 8.5 - 10$ was conducted according to Eq. (1.4) with the help of the Maple 9.5 and show a good agreement with the experimental data from [19].

1.4 Conclusion and Discussion

The proposed in this paper semi-empirical model of the fluid force allows highlighting some peculiarities of the VIV of the bluff bodies. The maximum amplitude value of the structure vibrating in the flow for the parameters range indicated in the section 3 has been estimated and found to be 20% higher then the experimental one. The amplitude of vibrations in the resonance range depends on the amplitude of the forcing term. When the amplitude of the forcing term reaches a particular value and the phase difference between the structure displacement and the periodic component of the lift force is equal to $\pi/2$ then the stable oscillations became impossible even if the condition $\frac{\omega}{\omega_s} = 1$ is fulfilled. It is because the flow energy that the structure gets at some flow velocity cannot be accumulated on that one mode. As a result the system jumps between the different modes. The analytical results show that the sub-harmonical periodic regimes are possible. For estimation of the amplitude values

in the lower branch of the lock-in region the analytical solution according to Eqs. (1.16), (1.17), and (1.20) were used, and showed a good agreement with experimental data. An equation for the determination of the phase difference between the periodic component of the lift force and the structure displacement has been obtained as well. There are still however many open problems for future research which should be solved. Some of them are as follows. The case when the added mass is a varying with time function should be investigated, for example. The equation of the structural motion in this case is as follows:

$$(m + m_{\text{add}})\ddot{y} + \dot{m}_{\text{add}}\dot{y} + \varsigma\dot{y} + cy = F(\dot{y}, t). \tag{1.22}$$

This equation is different from the equation which was used in [20]. In Eq. (1.22) the additional term $\dot{m}\dot{y}$ is introduced. If the added mass is time-varying then in addition to the change of the oscillation frequency it can lead to the amplitude growth and instability of the structure. For the case when the forcing and structural damping terms vanish the exact solution of Eq. (1.22) can be obtained if the dependence of the added mass on time is a smooth function. In the following manipulation the abbreviations:

$$m + m_{\text{add}} = m_0(1 + \chi(t)), \qquad \bar{\chi} = 1 + \chi(t)$$

are used. A non-dimensional time scale τ can be introduced by:

$$\tau = \int\limits_0^t \sqrt{\frac{c}{m_0\bar{\chi}(t)}}\,dt.$$

In that case the solution of Eq. (1.22) can be found in the closed form as follows [21]:

$$y(\tau) = Z(\tau)U(\tau),$$

where

$$Z(\tau) = \frac{1}{\sqrt[4]{\bar{\chi}(\tau)}},$$

and $U(\tau)$ satisfied the equation of the form:

$$U''(\tau) + \left[1 - Z(\tau)\frac{d^2}{d\tau^2}\left(\frac{1}{Z(\tau)}\right)\right]U(\tau) = 0. \tag{1.23}$$

A closed form solution of Eq. (1.23) exists for various functions $\bar{\chi}$. For example for an exponential variation of the mass

$$\bar{\chi} = Be^{-2\alpha\omega t}$$

the solution for $y(\tau)$ has a form:

$$y(s) = \frac{1}{\sqrt[4]{B}}s\left[C_1 J_1(\frac{s}{\delta}) + C_2 Y_1(\frac{s}{\delta})\right], \quad s = 1 + \sqrt{\frac{m_0 B}{c}}\,\alpha\omega\tau = e^{\alpha\omega t}, \quad \delta = \alpha\omega\sqrt{\frac{m_0 B}{c}}.$$

From that it follows that when time increases, the oscillation amplitude grows exponentially. Then a solution for the non-homogeneous equation can be obtained with the help of the method of variation of constants. That solution will be also unbounded. Then the only possible reasons for limitation of the amplitude can be a nonlinearity of the fluid force or a large structural damping. Using the equation of the form:

$$(m + m_{\text{add}})\ddot{y} + \dot{m}_{\text{add}}\dot{y} + \varsigma\dot{y} + \Omega^2 y = F(\dot{y}, t),$$

and dividing both parts of it by $m + m_{\text{add}}$, one can get the equation which will have time-varying coefficients. For the case when m_{add} vary with time according to the harmonic law or as a piece-wise-constant function the solutions of the linear equations with variable in time coefficients were obtained in [22, 23]. Also the solution of the non-linear equation with variable in time coefficients and polynomial non-linearity with respect to the first derivative of the structure displacement of the power of three was found as well. The results obtained in [22, 23] show that solutions and regions of the stability depend on the parameters of the system. In stead of the exponentially decaying mass in the mentioned above cases the stable oscillations are possible for the particular parameters of the system under consideration. The suggested in the present paper model should be improved by introducing the added mass dependence on time for investigation of the structural behavior in the lock-in region. As a first step it is possible to assume that the second term in the Eq. (1.21) behave in the following way:

$$\dot{m}_{\text{add}}\dot{y} = \frac{dm}{d\omega} \cdot \frac{d\omega}{dt}\dot{y} = m'_\omega \phi \dot{y}$$

and

$$\phi = \frac{d\omega}{dt} = \text{const.}$$

So, finally one concludes that the type of the dependence of the added mass on time is an important issue and it is necessary to find out it experimentally for the wide range of the values of the reduced velocities. The measurements given in [15, 17] show that the lift force consists of not one but several harmonics. Usually, only the first harmonic is taken into consideration. The presence of the higher harmonics leads to the fact that the structural oscillation frequency at resonance is smaller then the natural frequency of the structure. When the amplitude of vibrations is considered the influence of the higher harmonics on the amplitude is marginal but is significant on the vibration frequency. For simplicity assume that the structure is linear and has a small structural damping which can be neglected. The average values of the potential and kinetic energies of the structure over one period at resonance should be equal:

$$\frac{1}{T}\int_0^T M\dot{y}^2 dt = \frac{1}{T}\int_0^T cy^2 dt. \tag{1.24}$$

Then, one can seek a solution of Eq.(1.23) in the form:

$$y = A_1 \sin \omega t + A_2 \sin(2\omega t + \varphi_2) + ..., \quad \dot{y} = A_1 \omega \cos \omega t + A_2 2\omega \cos(2\omega t + \varphi_2) + ...$$
$$(1.25)$$

Then, substituting Eq. (1.25) into Eq. (1.24), and taking into consideration that the harmonics are orthogonal, one can get:

$$M\omega^2 \sum_1^\infty n^2 A_n^2 = c \sum_1^\infty A_n^2,$$

where

$$\omega_0^2 = \frac{c}{M}.$$

So, finally for the frequency ω of the structural vibration one has:

$$\omega^2 = \omega_0^2 \frac{[A_1^2 + A_3^2 + ...A_n^2]}{[A_1^2 + 9A_3^2 + ... + n^2 A_n^2]}. \tag{1.26}$$

From Eq. (1.26) it follows that the vibration frequency at resonance became decreases as a result of the existence of odd harmonics in the lift force spectrum .When the amplitudes of vibration increase the frequency decreases, which coincide with experimental results obtained in [15, 17]. So, the influence of the higher harmonics should be considered and there interaction as well. It can be done with a help of a more accurate technique provided by the averaging method and a computer simulation. The next approximations of the solution of the Eq. (1.4) where the terms of the order higher than $O(\varepsilon)$ are taking into account have to be found. The coupling of the different modes of the structural oscillations in the cross-flow and inflow directions has to be considered as well. The coefficients $b_1, b_3, b_5, \bar{f}_0$ were found from the experimental data under the assumption that the lift force is uniformly distributed along the length of the tested cylinder. For such structural elements like cables and wires it is necessary to find the correction coefficients which will take into account the non-uniform distribution of the lift force along the length of the structure and its segments. The applicability of the suggested values of b_1, b_3, b_5, c_n for different types of structures has to be verified by a comparison with various experimental data. And, finally, the solution of the Eq. (1.1) should be found.

References

[1] Blevins RD (1977) Flow Induced Vibration. Van Nostrand Reinhold, New York
[2] Iwan WD (1981) The vortex-induced oscillation of non-uniform structural systems. Journal of Sound and Vibration **79**(2):291–301

[3] Alexander CM (1981) The complex vibrations and implied drag of a long oceanographic wire in cross-flow. Ocean Engineering **8**(4):379–406

[4] Ramberg SE, Griffin OM (1976) The effects of vortex coherence, spacing, and circulation on the flow-induced forces on vibrating cables and bluff structures. Interim Report Naval Research Laboratory 7945, Washington, DC

[5] Vandiver JK (1993) Dimensionless parameters important to the prediction of vortex-induced vibration of long, flexible cylinders in ocean currents. Journal of Fluids and Structures **7**(5):423–455

[6] Newman D, Karniadakis GE (1996) Simulations of flow over a flexible cable: A comparison of forced and flow-induced vibration. Journal of Fluids and Structures **10**(5):439–453

[7] Bishop RED, Hassan AY, Saunders OA (1964) The lift and drag forces on a circular cylinder oscillating in a flowing fluid. Proceedings of the Royal Society of London Series A Mathematical and Physical Sciences **277**(1368):51–75

[8] Hartlen RT, Currie IG (1970) Lift-oscillator model of vortex-induced vibration. Journal of the Engineering Mechanics Division **96**(5):577–591

[9] Skop RA, Griffin OM (1975) On a theory for the vortex-excited oscillations of flexible cylindrical structures. Journal of Sound and Vibration **41**(3):263–274

[10] Iwan WD, Blevins RD (1974) A Model for Vortex Induced Oscillation of Structures. Journal of Applied Mechanics **41**(3):581–586

[11] Skop RA, Balasubramanian S (1997) A new twist on an old model for vortex-excited vibrations. Journal of Fluids and Structures **11**(4):395–412

[12] Wang XQ, So RMC, Chan KT (2003) A non-linear fluid force model for vortex-induced vibration of an elastic cylinder. Journal of Sound and Vibration **260**(2):287–305

[13] Gabbai R, Benaroya H (2005) An overview of modeling and experiments of vortex-induced vibration of circular cylinders. Journal of Sound and Vibration **282**(3):575–616

[14] Kurushina V, Postnikov A, Franzini GR, Pavlovskaia E (2022) Optimization of the wake oscillator for transversal viv. Journal of Marine Science and Engineering **10**(2):293

[15] Devnin SI (1975) Hydroelasticity of the Bluff Bodies in a Flow (in Russ.). Sudostroenie, Leningrad

[16] Sarpkaya T (1979) Vortex-Induced Oscillations: A Selective Review. Journal of Applied Mechanics **46**(2):241–258

[17] Vikestad K, Vandiver JK, Larsen CM (2000) Added mass and oscillation frequency for a circular cylinder subjected to vortex-induced vibrations and external disturbance. Journal of Fluids and Structures **14**(7):1071–1088

[18] Verhulst F (2000) Non-linear Differential Equations and Dynamical Systems. Springer, Berlin

[19] Khalak A, Williamson CHK (1997) Fluid forces and dynamics of a hydroelastic structure with very low mass and damping. Journal of Fluids and Structures **11**(8):973–982

[20] Willden RHJ, Graham JMR (2001) Numerical prediction of viv on long flexible circular cylinders. Journal of Fluids and Structures **15**(3):659–669

[21] Holl HJ, Belyaev AK, Irschik H (1999) Simulation of the duffing-oscillator with time-varying mass by a bem in time. Computers & Structures **73**(1):177–186

[22] van der Burgh AHP, Hartono, Abramian AK (2006) A new model for the study of rain-wind-induced vibrations of a simple oscillator. International Journal of Non-Linear Mechanics **41**(3):345–358

[23] van Horssen W, Abramian A, Hartono (2006) On the free vibrations of an oscillator with a periodically time-varying mass. Journal of Sound and Vibration **298**(4):1166–1172

Chapter 2
Nonlinear Buckling and Equilibria of Layered Shallow Parabolic Arches with Interlayer Slip

Christoph Adam, Ivan Paulmichl, and Thomas Furtmüller

Abstract In this paper, the critical loads for instability and nonlinear equilibrium paths of shallow parabolic arches composed of three symmetrically arranged layers are determined. The considered members are soft-hinged and immovably supported at both ends. The interlayer slips due to the flexible bond of the layers yield a discontinuous displacement in the cross-section. Thus, the kinematic assumptions of the Euler-Bernoulli theory can only be applied layer-wise when establishing the boundary value problem. Based on the differential equations of equilibrium and an infinite series expansion of the governing kinematic variables, nonlinear analytical relationships are presented for the critical loads in limit point buckling and in bifurcation buckling. The results indicate the large influence of the interlayer slip on the critical loads and the equilibrium paths.

2.1 Introduction

In structures composed of several layers, rigid bond between the layers cannot be always achieved due to the flexibility of the fasteners. In such structures with flexibly bonded layers, the layers may be displaced relative to each other at the interface. This deformation behavior, known as interlayer slip, has long been recognized and, accordingly, numerous theories have been developed to account for interlayer slip in the analysis of the static (e.g., [1–5]) and dynamic response (e.g., [6–9]) of layered beams. Other papers deal with buckling of straight beams with flexibly bonded layers subjected to an axial compressive force (e.g., [10–12]). However, the stability analysis of shallow arches with interlayer slip has not been paid attention to until recently. From numerous studies (e.g., [13–16]) on the stability behavior of homogeneous

Christoph Adam · Ivan Paulmichl · Thomas Furtmüller
Universität Innsbruck, Unit of Applied Mechanics, Technikerstr. 13, 6020 Innsbruck, Austria,
e-mail: christoph.adam@uibk.ac.at, ivan.paulmichl@uibk.ac.at,
thomas.furtmueller@uibk.ac.at

shallow arches, it is known that these members may become unstable under radial loading in the form of limit point buckling or in the form of bifurcation buckling. In limit point buckling, the member assumes a remote equilibrium position after reaching the limit point, referred to as snap-through. If instability occurs in the form of bifurcation buckling, then an adjacent equilibrium state exists. A symmetric shallow arch subjected to a symmetrically distributed radial load structure responds symmetrically during limit point buckling, but antimetric during bifurcation buckling. Stability analysis of homogeneous shallow arches with parabolic shape can be found in [17–19].

Only recently, the authors of this paper were the first to address the stability and instability analysis of layered shallow arches with interlayer slip. In [20], the equilibrium equations for shallow arches composed of two flexibly bonded layers were derived, followed by a numerical solution procedure to determine the nonlinear equilibrium paths for buckling and post-buckling analysis. Another paper [21] is devoted to the nonlinear stability analysis of three-layer sinusoidal shallow arches with interlayer slip subjected to a sinusoidal radial load, in which analytical relations for the critical loads and the equilibrium paths for both limit point buckling and bifurcation buckling have been derived. The nonlinear buckling and post-buckling analysis of circular three-layer shallow arches with interlayer slip was performed in [22].

In order to deepen the knowledge on the stability behavior of layered shallow arches with interlayer slip, the following study investigates the symmetrically layered three-layer shallow parabolic arch that is soft-hinged supported and immovably fixed at both ends. Expressions for the critical loads and the equilibrium paths for both limit point buckling and bifurcation buckling are derived for this member. The basis is the differential equilibrium equations and boundary conditions of the three-layer shallow arch with interlayer slip and arbitrary initial deformation derived in [21]. The solution of this nonlinear boundary value problem for the considered parabolic arches subjected to radial loading is found with the methods used in [22].

2.2 Basic Equations

The considered shallow arch of length l is composed of three symmetrically arranged layers of rectangular cross-section, which are subsequently indicated from top to bottom by the subscripts $1, 2, 3$, see Fig. 2.1. Thus, the cross-sectional dimensions of the two outer layers are the same, i.e. their thickness $h_3 = h_1$ and their width $b_3 = b_1$. Moreover, these layers are made of the same material, thus the modulus of elasticity is also the same, $E_3 = E_1$. The thickness and width of the middle layer are denoted by h_2 and b_2, and its elastic modulus by E_2. Due to the symmetrical configuration, the curved member axis corresponds to the line connecting the centers of gravity of the middle layer. The arch is soft-hinged and immovably supported at both ends at the level of the member axis. The quantities of the arch are referenced to a x, y, z coordinate system whose origin is in the left support. The x coordinate extends along
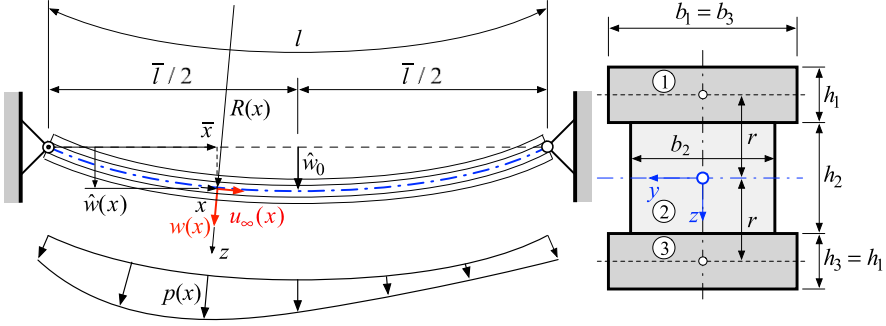
Fig. 2.1: Immovably soft-hinged supported three-layer shallow parabolic arch with interlayer slip (modified from [21]).

the member axis, the y coordinate is the out-of-plane coordinate, and the z coordinate is oriented in the radial direction, as depicted in Fig. 2.1. In the unloaded state, the member axis has the shape of a quadratic parabola,

$$\hat{w}(x) = \frac{4\hat{w}_0}{l^2} x \, (l - x) \tag{2.1}$$

Here $\hat{w}_0$ is crown height of the shallow arch, i.e. $\hat{w}(l/2) = \hat{w}_0$, which is small compared to the member length l. The curvature k of this initial deformation, which enters into the differential equilibrium equations given below, is thus constant over the entire length of the member,

$$k = -\hat{w}_{,xx} = \frac{8\hat{w}_0}{l^2} \tag{2.2}$$

Since for the shallow arch with circular initial deformation the curvature k is also constant, the procedure presented in [22] for the circular shallow arch with interlayer slip can be used for the analysis of the response of the present parabolic shallow arch with interlayer slip.

The three layers are elastically bonded in the tangential direction. The tangential stiffness of this elastic connection is captured by the slip modulus K_s. Under radial load

$$p(x) = p_0 f(x) \tag{2.3}$$

with the load amplitude p_0 and the load distribution function $f(x)$, these layers are therefore displaced relative to each other, which is referred to as interlayer slip. In the following, $\Delta u_1(x)$ denotes the interlayer slip between the top and middle layer and $\Delta u_2(x)$ the interlayer slip between the middle and bottom layer, see Fig. 2.2. In the radial direction, the interlaminar stiffness is assumed to be infinite in the model.

The cross-sectional dimensions of the layers are small compared to the length l. Therefore, the kinematic assumptions of the Euler-Bernoulli theory can be assumed to be valid layerwise. Under these assumptions, the entire deformation field of the shallow arch is captured by four kinematic variables, namely, the radial deformation
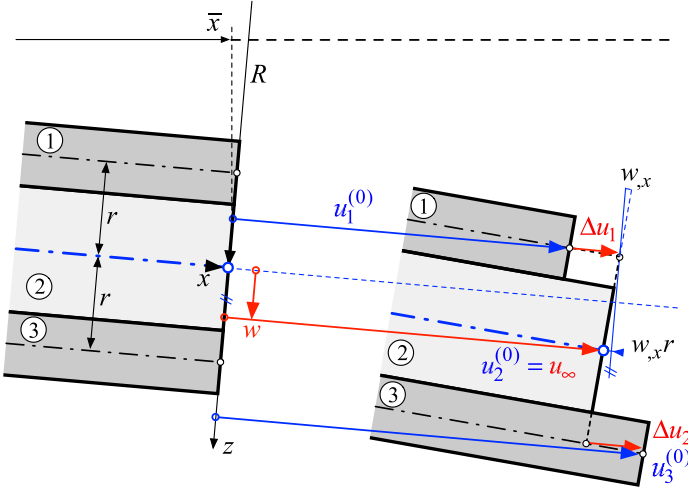
Fig. 2.2: Cross-section at x in its initial and its deformed state [21].

$w(x)$, which is the same for each fiber parallel to the member axis, the longitudinal displacement of the member axis $u_\infty(x)$, and the two interlayer slips $\Delta u_1(x)$ and $\Delta u_2(x)$ [21], see Fig. 2.2.

In [21], the differential equations of equilibrium of a shallow arch with interlayer slip with arbitrary curvature were derived, which read as follows for constant curvature $k = \text{const}$ [22],

$$\Delta u_{1,xx} + \Delta u_{2,xx} - \frac{K_s}{E_1 A_1} \left(\Delta u_1 + \Delta u_2\right) - 2w_{,xxx}r = 0 \,, \tag{2.4}$$

$$\Delta u_{1,xx} - \Delta u_{2,xx} - \frac{K_s E A_e}{E_1 A_1 E_2 A_2} \left(\Delta u_1 - \Delta u_2\right) = 0 \,, \tag{2.5}$$

$$u_{\infty,xx} + w_{,x}k + w_{,x}w_{,xx} - \frac{K_s}{E_2 A_2} \left(\Delta u_1 - \Delta u_2\right) = 0 \,, \tag{2.6}$$

$$E J_\infty w_{,xxxx} - E_1 A_1 r \left(\Delta u_{1,xxx} + \Delta u_{2,xxx}\right) - N \left(w_{,xx} - k\right) = p \tag{2.7}$$

Here r is the distance from the member axis to the center of gravity of the upper and lower layers, respectively, $A_1 = h_1 b_1$ is the cross-sectional area of the two outer layers and $A_2 = h_2 b_2$ is the cross-sectional area of the middle layer, $E A_e = 2E A_1 + E A_2$ is the extensional stiffness, $E J_\infty = E J_0 + 2r^2 E_1 A_1$ is the bending stiffness of the arch with rigid bond of the layers, and $E J_0 = 2E_1 J_1 + E_2 J_2$ is the bending stiffness without bond of the layers. The overall normal force N is constant over the length l [21],

$$N = \frac{EA_e}{l} \int_0^l \left(wk + \frac{1}{2}w_{,x}^2 \right) dx - \frac{E_1 A_1}{l} \int_0^l \left(\Delta u_{1,x} - \Delta u_{2,x} \right) dx \qquad (2.8)$$

and the overall moment $M(x)$ as a function of the kinematic variables is [21]

$$M(x) = -EJ_\infty w_{,xx} + E_1 A_1 r \left(\Delta u_{1,x} + \Delta u_{2,x} \right) \qquad (2.9)$$

For the considered hinged supports, where the interlayer slips at the boundaries is not constrained (so-called soft-hinged supports), and which are immovable in all directions, the boundary conditions as a function of the kinematic variables can be expressed as follows [21],

$$\Delta u_{1,x}(x_r) + \Delta u_{2,x}(x_r) = 0 \,, \qquad (2.10)$$

$$u_\infty(x_r) = 0 \,, \qquad (2.11)$$

$$2\left(u_{\infty,x}(x_r) + w(x_r)k(x_r) + \frac{1}{2}w_{,x}^2(x_r) \right) - \left(\Delta u_{1,x}(x_r) - \Delta u_{2,x}(x_r) \right) = 0 \,, \qquad (2.12)$$

$$w(x_r) = 0 \,, \ w_{,xx}(x_r) = 0 \qquad (2.13)$$

where $x_r = 0$ or $x_r = l$.

2.3 Solution

The solution of the present boundary value problem is based on the expansion of the deflection w into the buckling modes $\phi_i(x)$ of the associated straight beam with interlayer slip [16, 22]

$$w(x) = \sum_{i=1}^\infty q_i \phi_i(x) \qquad (2.14)$$

which, under the present boundary conditions, are simply the following sinusoidal functions [10, 21]

$$\phi_i(x) = \sin(\lambda_i x) \,, \ \lambda_i = \frac{i\pi}{l} \,, \ i = 1,...,\infty \qquad (2.15)$$

The other kinematic variables are also to be expressed as a function of the generalized coordinates q_i [5]. This is achieved by substituting the Ritz approach Eq. (2.14) into the differential equations Eqs (2.4), (2.5) and (2.6) and then solving them analytically together with the boundary conditions Eqs (2.10), (2.11) and (2.12). For the two interlayer slips, the result is

$$\Delta u_1(x) = \sum_{i=1}^\infty q_i \left[\frac{r\lambda_i^3 \cos(\lambda_i x)}{\lambda_i^2 + \frac{K_s}{E_1 A_1}} - \frac{\beta}{2}\left(\frac{1}{2}\lambda_i^2 q_i - \chi_i \right) \right] \,, \qquad (2.16)$$

$$\Delta u_2(x) = \sum_{i=1}^{\infty} q_i \left[\frac{r \lambda_i^3 \cos(\lambda_i x)}{\lambda_i^2 + \frac{K_s}{E_1 A_1}} + \frac{\beta}{2} \left(\frac{1}{2} \lambda_i^2 q_i - \chi_i \right) \right] , \qquad (2.17)$$

where

$$\chi_i = -\frac{2 \left(1 - (-1)^i \right)}{\lambda_i l} \frac{8 \hat{w}_0}{l^2} , \; i = 1, ..., \infty , \qquad (2.18)$$

$$\beta(x) = \frac{E A_e l \sinh \left(\frac{1}{2} \kappa (l - 2x) \right)}{4 E_1 A_1 \sinh \left(\frac{\kappa l}{2} \right) + E_2 A_2 \kappa l \cosh \left(\frac{\kappa l}{2} \right)} , \; \kappa = \left(\frac{K_s E A_e}{E_1 A_1 E_2 A_2} \right)^{1/2} \qquad (2.19)$$

Substituting the series expansions Eqs (2.14), (2.16), and (2.17) into Eq. (2.8) leads to the overall normal force also as a function of q_i [22]

$$N = \frac{\psi}{4} \sum_{i=1}^{\infty} q_i \left(\lambda_i^2 q_i - 2 \chi_i \right) , \; \psi = \frac{E A_e E_2 A_2 \kappa l \cosh \left(\frac{\kappa l}{2} \right)}{4 E_1 A_1 \sinh \left(\frac{\kappa l}{2} \right) + E_2 A_2 \kappa l \cosh \left(\frac{\kappa l}{2} \right)} \qquad (2.20)$$

The nonlinear equation for finding the generalized coordinates follows by application of Galerkin's method [23] to the equilibrium equation Eq. (2.7). According to this procedure, the equation where the series expansions of the kinematic variables have been inserted, is multiplied by the i-th shape function $\phi_i(x)$ and integrated over the length l [22]

$$\int_0^l \left[EJ_\infty w_{,xxxx} - E_1 A_1 r \left(\Delta u_{1,xxx} + \Delta u_{2,xxx} \right) - N \left(w_{,xx} - k \right) - p \right] \phi_i(x) dx = 0 ,$$

$$i = 1, ..., \infty \qquad (2.21)$$

Performing this operation for each shape function finally leads to the coupled equations [22],

$$h_i = \left(\lambda_i^2 q_i - \chi_i \right) N + c_i q_i - \frac{2}{l} p_0 f_i = 0 , \; i = 1, ..., \infty \qquad (2.22)$$

where c_i is the i-th generalized stiffness, α is the layer interaction coefficient, and f_i is the i-th generalized loading function [22],

$$c_i = \lambda_i^4 \left(\lambda_i^2 + \alpha^2 \right) \left(\frac{\alpha^2}{EJ_\infty} + \frac{\lambda_i^2}{EJ_0} \right)^{-1} , \; \alpha = \sqrt{\frac{K_s EJ_\infty}{E_1 A_1 EJ_0}} , \qquad (2.23)$$

$$f_i = \int_0^l f(x) \phi_i(x) dx , \; i = 1, ..., \infty \qquad (2.24)$$

2.4 Buckling and Post-Buckling Analysis

For this boundary value problem, analytical expressions for the buckling and post-buckling analysis of the shallow parabolic arch with interlayer slip are presented below, based on the derivations in [22].

2.4.1 Primary Equilibrium Path

Equation (2.22) is first solved for q_i [22],

$$q_i = \frac{2p_0 f_i + l \chi_i N}{l \left(c_i + \lambda_i^2 N \right)} \ , \ i = 1, ..., \infty \tag{2.25}$$

which is subsequently inserted into the series expansion of the overall normal force N, Eq. (2.20). This leads to a quadratic equation for the load amplitude p_0 [22],

$$\frac{4}{l^2} C_1 p_0^2 - \frac{4}{l} \left(C_4 - C_2 N \right) p_0 + N \left(C_3 N - 2C_5 - 1 \right) = 0 \tag{2.26}$$

with

$$C_1 = \frac{\psi}{4} \sum_{i=1}^{\infty} \frac{\lambda_i^2 f_i^2}{\left(c_i + \lambda_i^2 N \right)^2} \ , \ C_2 = \frac{\psi}{4} \sum_{i=1}^{\infty} \frac{\lambda_i^2 f_i \chi_i}{\left(c_i + \lambda_i^2 N \right)^2} \ , \ C_3 = \frac{\psi}{4} \sum_{i=1}^{\infty} \frac{\lambda_i^2 \chi_i^2}{\left(c_i + \lambda_i^2 N \right)^2} \ ,$$

$$C_4 = \frac{\psi}{4} \sum_{i=1}^{\infty} \frac{f_i \chi_i}{c_i + \lambda_i^2 N} \ , \ C_5 = \frac{\psi}{4} \sum_{i=1}^{\infty} \frac{\chi_i^2}{c_i + \lambda_i^2 N} \tag{2.27}$$

The solution gives p_0 as a function of the overall normal force N [22],

$$p_0(N) = \frac{l}{2C_1} \left(C_4 - C_2 N \pm \sqrt{C_4^2 + C_1 N (1 + 2C_5 - C_3 N) + C_2 N (C_2 N - 2C_4)} \right) \tag{2.28}$$

To find the primary equilibrium path for the other response variables, the above expression for p_0 is substituted into the generalized coordinates q_i, Eq. (2.25), which thus become a function of N only. This expression is inserted into the series expansions of the kinematic variables, which thus also become a function of N, e.g., $\Delta u_1(N)$. Simultaneously solving the equations for $\Delta u_1(N)$ and $p_0(N)$ (Eq. (2.28)) yields the desired representation $p_0(\Delta u_1)$. The representations $p_0(\Delta u_2)$ and $p_0(w)$ are found analogously.

2.4.2 Limit Loads and Limit Points

The critical loads are determined separately for the limit loads (critical loads for limit point buckling) and the bifurcation buckling loads. The basis for finding the limit loads is the condition that the tangent stiffness matrix at the stability limit is singular. This leads to the following simplified buckling equation for limit point buckling [22],

$$\det \boldsymbol{K} = 1 + \frac{\psi}{2} \sum_{i=1}^{\infty} \frac{\left(\chi_i - \lambda_i^2 q_i^{(lc)}\right)^2}{c_i + \lambda_i^2 N^{(lc)}} = 0. \qquad (2.29)$$

The superscript (lc) identifies variables at the stability limit for limit point buckling. Inserting the generalized coordinate $q_i^{(lc)}$ according to Eq. (2.25) into this buckling equation, a nonlinear equation for the unknown limit loads $p_0^{(lc)}$ and the corresponding critical normal forces $N^{(lc)}$ is obtained [22],

$$\frac{4}{l^2} D_1 (p_0^{(lc)})^2 - \frac{4}{l} \left(2C_2 - D_2 N^{(lc)}\right) p_0^{(lc)} + N^{(lc)} \left(D_3 N^{(lc)} - 4C_3\right) + 2C_5 + 1 = 0 \qquad (2.30)$$

with

$$D_1 = \frac{\psi}{2} \sum_{i=1}^{\infty} \frac{\lambda_i^4 f_i^2}{\left(c_i + \lambda_i^2 N^{(lc)}\right)^3} ,$$

$$D_2 = \frac{\psi}{2} \sum_{i=1}^{\infty} \frac{\lambda_i^4 f_i \chi_i}{\left(c_i + \lambda_i^2 N^{(lc)}\right)^3} ,$$

$$D_3 = \frac{\psi}{2} \sum_{i=1}^{\infty} \frac{\lambda_i^4 \chi_i^2}{\left(c_i + \lambda_i^2 N^{(lc)}\right)^3} . \qquad (2.31)$$

This equation is solved for $p_0^{(lc)}$ and $N^{(lc)}$ together with the previously determined nonlinear equation Eq. (2.26) (in which p_0 is replaced by $p_0^{(lc)}$ and N is replaced by $N^{(lc)}$).

2.4.3 Bifurcation Loads and Bifurcation Points

In a symmetrical shallow arch, bifurcation buckling is possible only if the radial load $p(x) = p_0 f(x)$ is symmetrically distributed, i.e., $f(x) = f(l-x)$ [22]. Bifurcation buckling occurs antimetrically according to an antimetric buckling mode of the associated straight beam, which in the case of the soft-hinged supported beam column with interlayer slip are the antimetric sinusoidal functions $\sin \lambda_n x$, $n = 2, 4, 6, \ldots$ [10]. The bifurcation normal forces $N_n^{(bc)}$ associated to the buckling modes are then [21],

$$N_n^{(bc)} = -\frac{c_n}{\lambda_n^2} \ , \ n = 2, 4, 6, \dots \tag{2.32}$$

Since the bifurcation point is at the primary equilibrium path, the response of the symmetrically loaded shallow arch at this point is also symmetric, i.e., the generalized coordinates associated with the antimetric shape functions are zero at this point, i.e., $q_{in}^{(bc)} = 0, i = 2, 4, 6, \dots$ To determine the bifurcation load related to the n-th buckling mode $p_n(x)^{(bc)} = p_{0n}^{(bc)} f(x) = p_{0n}^{(bc)} f(l-x)$, the nonzero generalized coordinates at the bifucation point $q_{in}^{(bc)} \neq 0, i = 1, 3, 5, \dots$ are substituted into the series expansion for the overall normal force N, Eq. (2.20). Then, in this expression, the overall normal force is replaced by the bifurcation buckling normal force $N_n^{(bc)}$ according to Eq. (2.32). The result is the following quadratic equation [22],

$$\frac{\lambda_n^4}{l^2} F_1^{(n)} \left(p_{0n}^{(bc)} \right)^2 - \frac{\lambda_n^2}{l} F_2^{(n)} p_{0n}^{(bc)} + c_n \left(\frac{1}{2} F_3^{(n)} + \frac{1}{\lambda_n^2} \right) = 0 \ , \ n = 2, 4, 6, \dots \tag{2.33}$$

with

$$F_1^{(n)} = \psi \sum_{i=1}^{\infty} \frac{\lambda_{2i-1}^2 f_{2i-1}^2}{\left(\lambda_n^2 c_{2i-1} - \lambda_{2i-1}^2 c_n \right)^2} \ ,$$

$$F_2^{(n)} = \psi \left(c_n \sum_{i=1}^{\infty} \frac{\lambda_{2i-1}^2 f_{2i-1} \chi_{2i-1}}{\left(\lambda_n^2 c_{2i-1} - \lambda_{2i-1}^2 c_n \right)^2} + \sum_{i=1}^{\infty} \frac{f_{2i-1} \chi_{2i-1}}{\lambda_n^2 c_{2i-1} - \lambda_{2i-1}^2 c_n} \right) \ ,$$

$$F_3^{(n)} = \psi \left(\frac{c_n}{2} \sum_{i=1}^{\infty} \frac{\lambda_{2i-1}^2 \chi_{2i-1}^2}{\left(\lambda_n^2 c_{2i-1} - \lambda_{2i-1}^2 c_n \right)^2} + \sum_{i=1}^{\infty} \frac{\chi_{2i-1}^2}{\lambda_n^2 c_{2i-1} - \lambda_{2i-1}^2 c_n} \right) \tag{2.34}$$

from which the two bifurcation loads for the n-th buckling mode are obtained [22],

$$p_{0n}^{(bc)(1)} = \frac{l}{2F_1^{(n)} \lambda_n^3} \left(F_2^{(n)} \lambda_n + \sqrt{\left(F_2^{(n)} \right)^2 \lambda_n^2 - 2F_1^{(n)} c_n \left(2 + F_3^{(n)} \lambda_n^2 \right)} \right) \ , \tag{2.35}$$

$$p_{0n}^{(bc)(2)} = \frac{l}{2F_1^{(n)} \lambda_n^3} \left(F_2^{(n)} \lambda_n - \sqrt{\left(F_2^{(n)} \right)^2 \lambda_n^2 - 2F_1^{(n)} c_n \left(2 + F_3^{(n)} \lambda_n^2 \right)} \right) . \tag{2.36}$$

Substituting, for example, $p_{0n}^{(bc)(1)}$ from Eq. (2.35) and $N_n^{(bc)}$ from Eq. (2.32) into Eq. (2.25) leads to the generalized coordinates $q_{in}^{(bc)(1)}$ at the bifurcation point and these in turn inserted into the corresponding series expansions lead to the kinematic variables at the bifurcation point.

2.4.4 Post-Bifurcation Equilibrium Path

Now that the bifurcation points are known, the post-bifurcation equilibrium path is determined for each of the occurring antimetric buckling modes. For better readability, subsequently the index n, which identifies the response quantity of corresponding buckling mode, is omitted where possible. For the purpose of predicting the post-bifurcation equilibrium path, the response in this path is split into the response at the bifurcation point and the response relative to that point [14, 24],

$$w = w^{(bc)} + \Delta w , \; u_\infty = u_\infty^{(bc)} + \Delta u_\infty ,$$
$$\Delta u_1 = \Delta u_1^{(bc)} + \Delta(\Delta u_1) , \; \Delta u_2 = \Delta u_2^{(bc)} + \Delta(\Delta u_2). \quad (2.37)$$

The relative response Δw etc. is thereby induced by the load relative to the bifurcation load $p^{(bc)}$ [21],

$$\Delta p(x) = p(x) - p^{(bc)}(x) = \Delta p_0 f(x) , \; \Delta p_0 = p_0 - p_0^{(bc)}. \quad (2.38)$$

Furthermore, the relative displacement Δw is split into the symmetric part $\Delta w^{(s)}$ and the antimetric part $\Delta w^{(a)}$ in the form of the bifurcation buckling mode, each of which is expanded into the corresponding shape functions [24],

$$\Delta w = \Delta w^{(s)} + \Delta w^{(a)}, \; \Delta w^{(s)} = \sum_{i=1}^{\infty} \Delta q_{2i-1} \phi_{2i-1}, \; \Delta w^{(a)} = \Delta q_n \phi_n. \quad (2.39)$$

Δq_i is the i-th generalized coordinate of the relative response. Moreover, along the post-bifurcation buckling equilibrium path, the overall normal force is constant [14, 19], i.e.

$$N = N^{(bc)} , \; \Delta N = 0. \quad (2.40)$$

Therefore, the upper and lower interlayer slip relative to the value at the bifurcation point are equal [21],

$$\Delta(\Delta u_1) = \Delta(\Delta u_2). \quad (2.41)$$

$\Delta(\Delta u_1)$ and $= \Delta(\Delta u_2)$ must also be expressed as a function of the generalized relative coordinates Δq_i. For this purpose, the equilibrium equation Eq. (2.4) is modified for the relative response in the bifurcation buckling path, which then becomes [22]

$$\Delta(\Delta u_1)_{,xx} - \frac{K_s}{E_1 A_1} \Delta(\Delta u_1) - \Delta w_{,xxx} r = 0. \quad (2.42)$$

The series expansion Eq. (2.39) is inserted into this differential equation and then solved together with the boundary conditions $\Delta(\Delta u_1)_{,x}(0) = \Delta(\Delta u_2)_{,x}(l) = 0$, resulting in [22]

$$\Delta(\Delta u_1)(x) = \Delta(\Delta u_2)(x) = \sum_{i=1}^{\infty} \frac{r\lambda_{2i-1}^3 \cos(\lambda_{2i-1}x)}{\lambda_{2i-1}^2 + \frac{K_s}{E_1 A_1}} \Delta q_{2i-1} + \frac{r\lambda_n^3 \cos(\lambda_n x)}{\lambda_n^2 + \frac{K_s}{E_1 A_1}} \Delta q_n.$$

(2.43)

The relation for the still unknown generalized coordinates of the symmetric response part, Δq_i, $i = 1, 3, 5, ...$, are derived from the equilibrium equation [22]

$$EJ_\infty \Delta w_{,xxxx} - 2E_1 A_1 r\Delta(\Delta u_1)_{,xxx} - N^{(bc)}\Delta w_{,xx} = \Delta p_0 f(x)$$

(2.44)

that follows from adaptation of the differential equilibrium condition Eq. (2.7) for the relative response. To Eq. (2.44) Galerkin's method is applied as shown in Eq. (2.21), yielding [22]

$$\Delta q_i = \frac{2\lambda_n^2}{l\lambda_i^2} \left(\frac{EJ_\infty \lambda_i^2 + EJ_0 \alpha^2}{\lambda_n^2 \lambda_i^2 EJ_0 EJ_\infty (\lambda_i^2 + \alpha^2) - c_n (EJ_\infty \lambda_i^2 + EJ_0 \alpha^2)} \right) f_i \Delta p_0,$$

(2.45)

$$i = 1, 3, 5... , \ n = 2, 4, 6....$$

(2.46)

The generalized coordinate Δq_n for the n-th bifurcation buckling mode follows from the condition that the normal force remains constant in the bifurcation buckling path, or in other words $\Delta N = 0$, see Eq. (2.40). Splitting off $N^{(bc)}$ from Eq. (2.8), taking into account Eqs (2.37) and (2.41), the following relation is obtained [22]

$$\Delta N = \frac{EA_e}{l} \int_0^l \left(\Delta wk + \frac{1}{2}\Delta w_{,x}^2 + w_{,x}^{(bc)}\Delta w_{,x} \right) dx = 0$$

(2.47)

from which, after substituting Eqs (2.14) and (2.39), the sought generalized coordinate Δq_n is obtained,

$$\Delta q_n = \pm \frac{1}{\lambda_n} \sqrt{ -\sum_{i=1}^{\infty} \left(\frac{\Delta q_{2i-1}}{\lambda_{2i-1}} \left(\lambda_{2i-1}^3 \left(\Delta q_{2i-1} + 2q_{2i-1}^{(bc)} \right) + \frac{64\hat{w}_0}{l^3} \right) \right) }.$$

(2.48)

2.5 Application

In the following, the presented beam theory is applied to shallow arches subjected to a uniformly distributed radial load $p(x) = p_0$ (i.e., $f(x) = 1$). The parabolic initial deflection is directed against the positive z coordinate, i.e., the initial deflection amplitude $\hat{w}_0$ is negative, see Fig. 2.3. The dimensions of the considered members are given by length $l = 1.0$ m and cross-sectional dimensions $b_1 = b_2 = 0.1$ m, $h_1 = 0.005$ m, $h_2 = 0.01$ m. Material parameters chosen are $E_1 = 7.0 \cdot 10^{10}$ N/m^2, $E_2 = 2.0 \cdot 10^{10}$ N/m^2 for Young's moduli, and $K_s = 1.0 \cdot 10^9$ N/m^2 for slip modulus. Then, the layer interaction coefficient αl (for α see Eq. (2.23)) becomes $\alpha l = 19.7$, which corresponds to a moderate interaction of the layers [10].
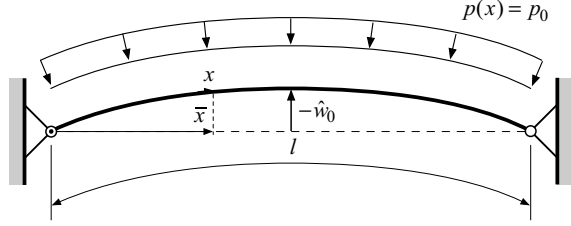
2.5.1 Example Problem 1

In the first example, the crown height is chosen as $\hat{w}_0 = -0.023$ m. At this crown
height a limit point buckling problem is present, bifurcation buckling does not occur.
The evaluation of Eqs (2.28) and (2.30) yields the two normalized limit loads of this
structure as $\bar{p}_0^{(lc)(1)} = p_0^{(lc)(1)} l^3 / EJ_\infty = 1.949$ and $\bar{p}_0^{(lc)(2)} = p_0^{(lc)(2)} l^3 / EJ_\infty = 0.846$.

In addition to the solution with the presented analytical relations, for their veri-
fication the equilibrium path is computed numerically with the finite element (FE)
method in the software suite Abaqus [25] assuming a plane stress state. For this
analysis, the three layers are discretized with plane stress 8-noded quadrilateral two-
dimensional continuum elements with reduced integration (CPS8R). As an additional
quantity, for the plane stress state, the Possion's ratio must be specified, which is
chosen as $\nu = 0.3$ for all three layers. A very thin layer of thickness $2.0 \cdot 10^{-6}$ m
is introduced between the layers to model the flexible bond, which is discretized
with 4-node two-dimensional cohesive elements (COH2D4). The horizontal stiffness
corresponds to the slip modulus K_s in the beam model. For the vertical stiffness,
which is infinite in the beam model, the very large value $1.0 \cdot 10^{13}$ has been assigned.
To model the soft-hinged boundary conditions in the FE model, the boundary nodes
of the middle layer are coupled with an additional node, which is fixed.

Figure 2.4 shows kinematic response quantities of this shallow arch. In Fig. 2.4(a),
the normalized load amplitude $\bar{p}_0 = p_0 l^3 / EJ_\infty$ is plotted versus the normalized radial
displacement $w(0.5l)/l$ at the center of the arch, which illustrates the typical response
behavior of a snap-through problem. The thick blue line is the equilibrium path of
the shallow arch with interlayer slip found with the presented analytical relations, the
thin red dashed line with cross markers is the result of the FE plane stress analyses.
The two solutions are practically identical, which is a verification of the presented
solution equations. In addition, the result of the Euler-Bernoulli theory assuming a
rigid bond of the layers (i.e. $K_s = \infty$) is shown with a thin black line. In this case, the
critical load at the first limit point $p_0^{(lc)(1)}$ is 50% larger than for the member with
interlayer slip, showing how important it is to consider the interlayer slip in the model.
Figure 2.4(b) shows the distribution of the radial displacement $w(x)/l$ of the shallow
arch with interlayer slip over x/l at the points of the equilibrium path denoted A (first
limit point), B, C (second limit point), and D in Fig. 2.4(a).

The diagram $\bar{p}_0$ over the two normalized interlayer slips $\bar{\Delta}u_1(l) = \Delta u_1(l)/l$ (black
line) and $\bar{\Delta}u_2(l) = \Delta u_2(l)/l$ (blue line) at the member end $x = l$ in Fig. 2.4(c) show
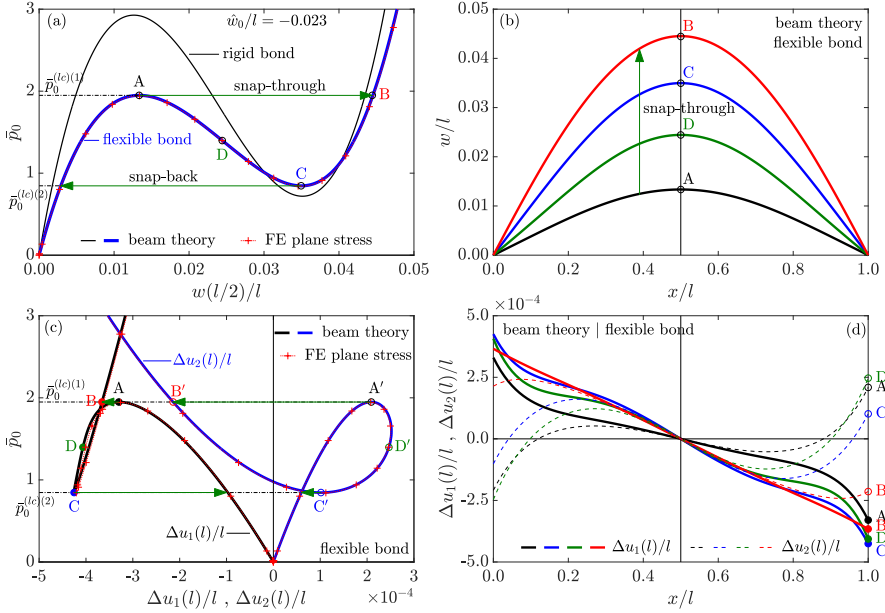
Fig. 2.4: Crown height $\hat{w}_0/l = -0.023$. Uniformly distributed load. (a) Load amplitude over radial displacement at $x/l = 0.5$; (b) radial displacement over x/l at discrete load levels; (c) load amplitude over upper/lower interlayer slip at $x/l = 1$; (d) upper/lower interlayer slip over x/l at discrete load levels. Non-dimensional representation.

a much more complex shape than that of the radial displacement. The deviation of the FE solution (thin red lines with cross markers) from the presented beam solution is very small and only visually noticeable in the region of the loop of the upper interlayer slip. The distribution of the two interlayer slips over the member axis (x/l) at points A, B, C, D (upper interlayer slip) and A', B', C', D' (lower interlayer slip), respectively, is shown in Fig. 2.4(d).

Figure 2.5 shows the equilibrium path for the normalized overall normal force (left) and for the normalized overall moment at beam center $M(l/2)/EJ_\infty$ (right) for this shallow parabolic arch with interlayer slip from the beam theory presented (blue lines), from the FE plane stress analyses (red dashed lines with cross markers), and for the shallow arch with rigid bond of the layers (thin black lines). The beam solution and FE solution also agree excellently for the internal forces. Also with the internal forces, it can be seen that in this example, neglecting the interlayer slip leads to an incorrect prediction of the response.
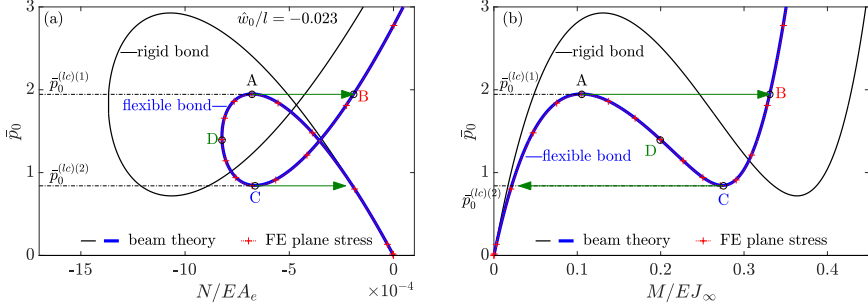
Fig. 2.5: Crown height $\hat{w}_0/l = -0.023$. Uniformly distributed load. (a) Load amplitude over overall normal force; (b) overall and layer-wise normal forces over x/l at discrete load levels; (c) load amplitude over overall bending moment at $x/l = 0.5$; (d) overall bending moment over x/l at discrete load levels. Non-dimensional representation.

2.5.2 Example Problem 2

In the second example, the crown height is increased to $\hat{w}_0/l = -0.0325$, all other quantities are the same as before. The critical loads for bifurcation buckling and $\bar{p}_0^{(bc)(2)} = 0.218$ are

$$\bar{p}_0^{(bc)(1)} = p_0^{(bc)(1)} l^3 / EJ_\infty = 3.901$$

(Eqs. (2.28) and (2.30)), and those for limit point buckling are

$$\bar{p}_0^{(lc)(1)} = 4.154 \quad \text{and} \quad \bar{p}_0^{(lc)(2)} = 0.208$$

(Eqs. (2.35) and (2.36)). Since

$$\bar{p}_0^{(bc)(1)} < \bar{p}_0^{(lc)(1)},$$

this structure becomes unstable due to bifurcation buckling.

Figures 2.6 and 2.7 show the response variables of this structure in the same way as Figs 2.4 and 2.5 for Example 1. However, in addition to the primary equilibrium path, the post-bifurcation buckling equilibrium path is plotted with dashed lines. In Figs 2.6(b) and 2.6(d), which show the distribution of radial deformation and interlayer slip, respectively, at the two bifurcation points (points A and C and A' and C', respectively), at the center of the post-bifurcation path (point E and E', respectively), and at point B on the primary equilibrium path, the symmetry of the response in the primary equilibrium path and the asymmetry in the post-bifurcation path can be seen. The comparative FE plane stress analysis with the perfect uniformly distributed load yield the primary equilibrium path. To approximate the bifurcation buckling path, a second FE analysis was performed with a perturbed distributed load in the form $f(x) = 0.99 + 0.02H(x - l/2)$, with $H(x - l/2)$ denoting the Heaviside
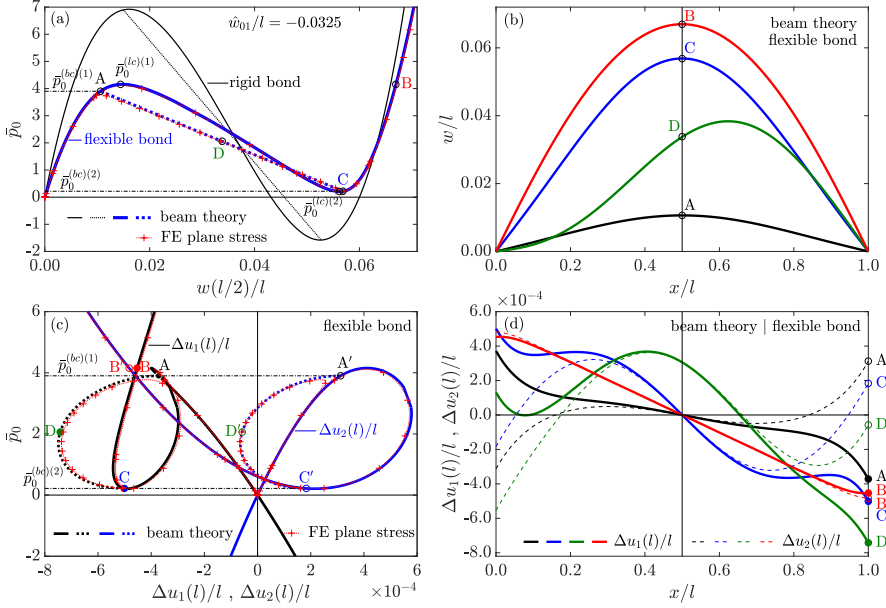
Fig. 2.6: Crown height $\hat{w}_0/l = -0.0325$. Uniformly distributed load. (a) Load amplitude over radial displacement at $x/l = 0.5$; (b) radial displacement over x/l at discrete load levels; (c) load amplitude over upper/lower interlayer slip at $x/l = 1$; (d) upper/lower interlayer slip over x/l at discrete load levels. Non-dimensional representation.
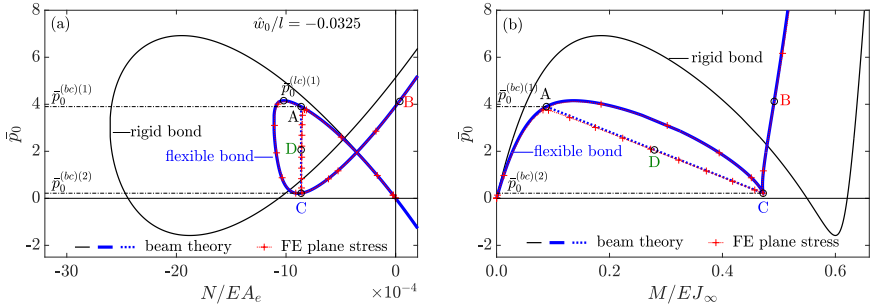
Fig. 2.7: Crown height $\hat{w}_0/l = -0.0325$. Uniformly distributed load. (a) Load amplitude over overall normal force; (b) overall and layer-wise normal forces over x/l at discrete load levels; (c) load amplitude over overall bending moment at $x/l = 0.5$; (d) overall bending moment over x/l at discrete load levels. Non-dimensional representation.

step function. As observed, the results of the presented solution equations and the comparative FE plane stress results agree excellently. Also in this example, the analysis with perfectly bonded layers overestimates the buckling loads significantly and cannot reproduce the equilibrium paths.

2.5.3 Critical Loads

Next, the critical loads of this shallow parabolic arch with interlayer slip are determined as a function of crown height according to Eqs (2.28), (2.30), (2.35) and (2.36). Figure 2.8 shows the two non-dimensional critical loads for limit point buckling, $\bar{p}_0^{(lc)(1)}$ and $\bar{p}_0^{(lc)(2)}$, and for bifurcation buckling, $\bar{p}_0^{(bc)(1)}$ and $\bar{p}_0^{(bc)(2)}$, plotted against $-\hat{w}_0/l$. The blue vertical lines indicate the two shallow arches of example problems 1 and 2. As observed, the minimum crown height for limit point buckling is $\hat{w}_0/l = 0.0148$. The black lines indicate the limit loads. With increasing crown height also the limit load $\bar{p}_0^{(lc)(1)}$ becomes larger. At crown height $\hat{w}_0/l = 0.0237$, two bifurcation buckling loads $p_0^{(bc)}$ occur in addition, depicted with red lines. The red dashed lines indicate the range where the bifurcation loads are on the unstable branch of the primary equilibrium path. This means that in this range of crown heights the structure becomes unstable due to limit point buckling, since the bifurcation points are not reached. However, for crown heights larger than the intersection of the limit point buckling and bifurcation buckling lines, bifurcation buckling occurs because the bifurcation loads are on the ascending branch of the primary equilibrium path.

2.5.4 Parabolic Shallow Arch vs. Circular Shallow Arch

The curvature of the circular shallow arch [22],

$$k = \frac{8\hat{w}_0}{4\hat{w}_0^2 + l^2} \tag{2.49}$$

is constant (i.e., independent form x), as in the case of the parabolic arch. Comparison of Eq. (2.2) and Eq. (2.49) shows that the curvatures differ only in the denominator by $4\hat{w}_0^2$. Since for the shallow arches $\hat{w}_0^2 \ll l^2$, the curvatures for the parabolic arch
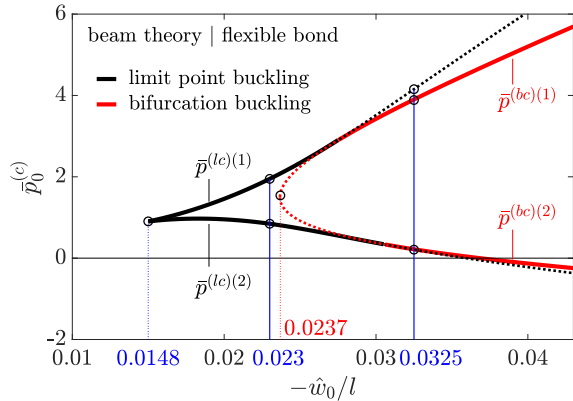
Fig. 2.8: Normalized critical loads over normalized crown height. Uniformly distributed load. Shallow parabolic arch with interlayer slip

and the circular arch are only insignificantly different. Therefore, the critical loads of the parabolic arch with interlayer slip and the circular arch with interlayer slip are virtually the same. This was verified for the present examples using both the present beam theory and FE plane stress analyses.

2.6 Summary and Conclusions

Based on the differential equations of equilibrium and an expansion of the radial displacement into the buckling modes of the corresponding straight beam, analytical relations for the critical loads, the primary and the post-bifurcation equilibrium path have been presented for the layered parabolic arch with interlayer slip. The results of example applications demonstrate the large influence of the interlayer slip on the critical loads and nonlinear response paths of these structural members with moderate layer interaction. Therefore, the classical beam theory assuming a rigid bond of the layers is not suitable to estimate the response of such shallow arches.

References

[1] Goodman JR, Popov EP (1968) Layered beam systems with interlayer slip. Journal of the Structural Division **94**:2535–2548
[2] Girhammar UA, Gopu VKA (1993) Composite beam-columns with interlayer slip-exact analysis. Journal of Structural Engineering **119**(4):1265–1282
[3] Monetto I (2015) Analytical solutions of three-layer beams with interlayer slip and step-wise linear interface law. Composite Structures **120**:543–551
[4] Gahleitner J, Schoeftner J (2021) A two-layer beam model with interlayer slip based on two-dimensional elasticity. Composite Structures **274**:114,283
[5] Adam C, Ladurner D, Furtmüller T (2022) Moderately large deflection of slightly curved layered beams with interlayer slip. Archive of Applied Mechanics **92**(5):1431–1450
[6] Girhammar UA, Pan D (1993) Dynamic analysis of composite members with interlayer slip. International Journal of Solids and Structures **30**:797–823
[7] Girhammar UA, Pan DH, Gustafsson A (2009) Exact dynamic analysis of composite beams with partial interaction. International Journal of Mechanical Sciences **51**(8):565–582
[8] Adam C, Heuer R, Jeschko A (1997) Flexural vibrations of elastic composite beams with interlayer slip. Acta Mechanica **125**:17–30
[9] Adam C, Ladurner D, Furtmüller T (2022) Free and forced small flexural vibrations of slightly curved slender composite beams with interlayer slip. Thin-Walled Structures **180**:109,857

[10] Girhammar UA, Pan DH (2007) Exact static analysis of partially composite beams and beam-columns. International Journal of Mechanical Sciences **49**(2):239 – 255

[11] Schnabl S, Planinc I (2013) Exact buckling loads of two-layer composite reissner's columns with interlayer slip and uplift. International Journal of Solids and Structures **50**(1):30–37

[12] Schnabl S, Planinc I, Turk G (2013) Buckling loads of two-layer composite columns with interlayer slip and stochastic material properties. Journal of Engineering Mechanics **139**(8):961–966

[13] Pi YL, Bradford M, Uy B (2002) In-plane stability of arches. International Journal of Solids and Structures **39**(1):105–125

[14] Kiss L (2019) Sensitivity of fgm shallow arches to loading imperfection when loaded by a concentrated radial force around the crown. International Journal of Non-Linear Mechanics **116**:62–72

[15] Pi YL, Bradford M (2013) Nonlinear analysis and buckling of shallow arches with unequal rotational end restraints. Engineering Structures **46**:615–630

[16] Zhou Y, Chang W, Stanciulescu I (2015) Non-linear stability and remote unconnected equilibria of shallow arches with asymmetric geometric imperfections. International Journal of Non-Linear Mechanics **77**:1–11

[17] Moon J, Yoon KY, Lee TH, Lee HE (2007) In-plane elastic buckling of pin-ended shallow parabolic arches. Engineering Structures **29**(10):2611–2617

[18] Moon J, Yoon KY, Lee TH, Lee HE (2009) In-plane strength and design of parabolic arches. Engineering Structures **31**(2):444–454

[19] Cai J, Xu Y, Feng J, Zhang J (2012) In-plane elastic buckling of shallow parabolic arches under an external load and temperature changes. Journal of Structural Engineering **138**(11):1300–1309

[20] Adam C, Ladurner D, Furtmüller T (2022) In-plane instability of shallow layered arches with interlayer slip. Acta Mechanica **233**(9):3813–3828

[21] Adam C, Ladurner D, Furtmüller T (2023) In-plane buckling of flexibly bonded three-layer pinned-fixed half-sine shallow arches. International Journal of Non-Linear Mechanics **151**:104,369

[22] Adam C, Paulmichl I, Furtmüller T (2023) Nonlinear buckling and equilibria of layered shallow parabolic arches with interlayer slip. Journal of Structural Stability and Dynamics (accepted for publication)

[23] Ziegler F (1995) Mechanics of Solids and Fluids, 2nd edn. Springer New York

[24] Lu H, Liu A, Pi YL, Bradford MA, Fu J, Huang Y (2018) Localized loading and nonlinear instability and post-instability of fixed arches. Thin-Walled Structures **131**:165–178

[25] Simulia (Dassault Systèmes) (2021) Abaqus FEA v. 6.21-6

Chapter 3
On the General Strategies to Formulate Shell and Plate Theories

Holm Altenbach and Victor A. Eremeyev

Abstract Different approaches exist to formulate general shell or plate theories. The approaches can be classified, for example, by the starting point of the derivation. This can be the well-known three-dimensional continuum mechanics equations. At present these equations are preferred by the engineers. In contrast, one can introduce à priory a two-dimensional deformable surface which is the basis for a more natural formulation of the two-dimensional governing equations. Here we discuss the theories based on the Cosserat approach.

3.1 Introduction

One of the basic problems in engineering mechanics is the analysis of the strength, the vibration behavior and the stability of structural elements with the help of structural models. Examples are thin-walled structures (discs, plates, shells, folded structures, etc.) which are used in various engineering applications. Their main advantage is the high load bearing capacity, combined with low weight and excellent stiffness properties. Modern thin-walled structures are made from different materials - common structural materials like steel or concrete, but also advanced materials, for example, composites like laminates, or sandwiches, metallic and polymeric foams, and functionally graded materials.

Increasing safety requirements or the need of optimization in an early design stage has lead again to a strong interest in the analysis of thin-walled structures. A common

Holm Altenbach
Institut für Mechanik, Otto-von-Guericke-Universität Magdeburg, 39106 Magdeburg, Germany,
e-mail: holm.altenbach@ovgu.de

Victor A. Eremeyev
Department of Civil, Environmental Engineering and Architecture, University of Cagliari, Via Marengo, 2, 09123 Cagliari, Italy
e-mail: victor.eremeev@unica.it

    37

modeling approach is to use shell and plate theories, which can be derived by different procedures. Here a clear classification of the approaches to model elements under consideration will be given.

For the sake of simplicity the discussions are limited by some assumptions. At first, only the linear elastic behavior is taken into account. At second, the thin-walled structure has a constant thickness. Finally, the presented equations are valid only for plates.

3.2 Classification Principles

3.2.1 Classification of Structural Models

Structural models are special cases or approximations of the general continuum theory. The structural models can be classified, for example, [1]

- by their suitability for bodies with certain geometrical (spatial) dimensions,
- by their suitability for certain applied loads,
- by the use of kinematical and/or statical hypotheses approximating its mechanical behavior.

A complex structure can be built up by different individual structural elements. The behavior of the whole structure can often be described by combining different structural models for the individual elements. Care must however be taken that the interface conditions between two neighboring elements are compatible with the assumptions and restrictions of their structural models.

Structural elements and the structural models for their analysis can be categorized into three classes, depending on the ratio of their characteristic dimensions [2]: three-dimensional structural elements with three spatial dimensions of the same order, two-dimensional structural elements, which have two spatial dimensions of comparable size, and a third spatial dimension, the so-called thickness, which is at least one order of magnitude smaller, and one-dimensional structural with two spatial dimensions, which can be related to the cross-section, having a comparable size and a third dimension, which is related to the length of the structural element and has at least one order of magnitude larger than the size of the cross-section dimensions.

In general, it is possible to introduce other classes. For example, in shipbuilding, thin-walled structural elements with a special profile are often used. If the spatial dimensions are of significantly different order and the thickness of the profile is small in comparison to the other cross-section dimensions, and the cross-section dimensions are much smaller in comparison to the length of the structure one can introduce quasi-onedimensional structural elements. Suitable theories for the analysis of quasi-onedimensional structural elements are the thin-walled beam theory (Vlasov-Theory) and the semi-membrane theory or generalized beam theory [3].

3.2.2 Classification of Theories for Two-Dimensional Structures

Since the thickness is much smaller than the characteristic length in the surface
directions, for two-dimensional structures it is tempting to look for procedures that
eliminate the thickness dimension. The mathematical consequence is obvious - instead
of a three-dimensional problem, which is represented by a system of coupled partial
differential equations with respect to three spatial coordinates, one can analyze a two-
dimensional problem considering two spatial coordinates only. These coordinates
represent a surface in the three-dimensional space, and a procedure has to be developed
that maps the real behavior in thickness direction onto the mechanical behavior of the
surface. The transition from the three-dimensional to the two-dimensional problem
is non-trivial, but once a two-dimensional theory has been obtained, the solution
effort decreases significantly, and the possibilities to solve problems analytically are
increased.

The two-dimensional equations can be established applying different approaches
[4–9]. The first one is the reduction technique, which starts from the equations of the
three-dimensional continuum and develops approximate two-dimensional continuum
theories. The second one is the direct approach, which starts from a rigorous two-
dimensional continuum theory (deformable material surface). Applying the first
approach common techniques are: the use of hypotheses on the stresses, strains
and/or displacements to approximate the three-dimensional equations, or the use of
mathematical approaches, such as series expansions, special functions or asymptotic
expansion. All these approaches have their own advantages and disadvantages, and
it is difficult to argue what is the best method for establishing the two-dimensional
equations. Note that in many cases different derivation methods result in identical
sets of governing equations.

Theories which are based on hypotheses are preferred by engineers. For example,
there is a huge number of theories which are based on displacement approximations.
Let us mention here only Kirchhoff's plate theory or Love's shell theory with the
kinematical hypothesis that an arbitrary cross-section is plane and orthogonal to
the mid-surface before and after deformation. On the base of these theories one
gets satisfying results for classical applications. But they ignore such effects like
transverse shear strains and thickness changes. From this follows the necessity to
develop improved theories, for examples, with additional degrees of freedom like
independent cross-section rotations. But the introduction of independent rotations is
in some cases not enough, since it is assumed again that any cross-section will be
plane before and after deformation. A weaker assumptions are proposed in several
papers. One example for plates is given in Levinson [10] or Reddy [11]. These refined
theories can be understood as theories with additional degrees of freedom, or as some
part of a power series expansion. A generalization of the power series approach in
the plate theory is given in Meenen and Altenbach [12], which can be extended to
shells.

The method of hypotheses considering assumptions for the stress and/or the strain
(displacement) states are also applied in many cases. It can be shown that shell
theories based on different hypothesis result in partly identical equations, but that

the coefficients take slightly different values and that their physical interpretation is partly not clear. Pure mathematical approaches are mostly based on power series, trigonometric functions, on special functions, etc. The mathematical approaches are very helpful if the accuracy of the given approximation should be checked.

The direct approach is based on the a priori introduction of a two-dimensional deformable surface. This approach is applied in Rubin [13], Zhilin [14], and Eremeyev and Zubov [15], Eremeyev and Altenbach [16], Eremeyev et al [17] among others. The main advantage of these theories is that their derivation does not rely on assumptions or series expansions and mathematically and physically they are strong and exact as the three-dimensional continuum mechanics. This approach is still under discussion [18], since the application is not trivial, and a satisfying relationship between the constitutive laws of the two-dimensional surface and the corresponding three-dimensional body up to now is not established. Further we discuss the family of the elastic shell theories based on the model of directed surface.

3.3 Direct Approach

3.3.1 General Cosserat Surface Theory

One of the most general theories of shells based on the direct approach is proposed in [19] and developed in many papers, see e.g. [13, 20]. The kinematical model of a simple shell is based on the introduction of a directed material surface $\omega(t)$, which is determined in the actual configuration by

$$\{\boldsymbol{r}(q^1, q^2, t); \boldsymbol{d}_k(q^1, q^2, t)\}; \; k = 1, \dots, p \tag{3.1}$$

with $\boldsymbol{r}(q^1, q^2, t)$ – the position vector defining the geometry of ω, $q^1, q^2 \in \omega$ and $\boldsymbol{d}_k(q^1, q^2, t)$ – a set of vectors called directors, see Fig. 3.1. In the reference configuration the following quantities are introduced

$$\{\boldsymbol{R}(q^1, q^2); \boldsymbol{D}_k(q^1, q^2)\}; \; k = 1, \dots, p. \tag{3.2}$$

On this stage each material point of the shell has $3 + 3p$ degrees of freedom.

The kinematics of the shell with p directors is too complicated. Hence, this theory is mostly formulated with the help of the introduction of one deformable director $\boldsymbol{d}$, see Rubin [13]. For the elastic Cosserat shell there exists a surface strain energy function $\mathcal{W}$

$$
\begin{aligned}
\mathcal{W} &= \mathcal{W}(\boldsymbol{F}, \boldsymbol{d}, \nabla \boldsymbol{d}), \quad \boldsymbol{F} = \nabla \boldsymbol{r}, \quad \nabla(\dots) \triangleq \boldsymbol{R}^\alpha \otimes \frac{\partial(\dots)}{\partial q^\alpha} \\
\boldsymbol{R}^\alpha \cdot \boldsymbol{R}_\beta &= \delta_\beta^\alpha, \quad \boldsymbol{R}^\alpha \cdot \boldsymbol{N} = 0, \quad \boldsymbol{R}_\beta = \frac{\partial \boldsymbol{R}}{\partial q^\beta}.
\end{aligned}
\tag{3.3}
$$

Using the principle of frame indifference, the following equation should be satisfied

Fig. 3.1 Cosserat surface with p deformable directors in the actual configuration, $\boldsymbol{n}$ is the unit normal, and $\boldsymbol{r}_\alpha = \partial \boldsymbol{r}/\partial q^\alpha$.
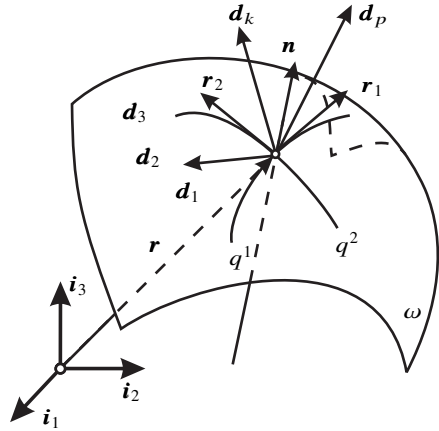
$$\mathcal{W}\,[\boldsymbol{F}\cdot\boldsymbol{O},\boldsymbol{d}\cdot\boldsymbol{O},(\nabla\boldsymbol{d})\cdot\boldsymbol{O}] = \mathcal{W}\,(\boldsymbol{F},\boldsymbol{d},\nabla\boldsymbol{d}) \tag{3.4}$$

for an arbitrary orthogonal tensor $\boldsymbol{O}$. The Lagrangian equilibrium equations have the form

$$\nabla\cdot\boldsymbol{T}+\boldsymbol{f}=\boldsymbol{0}, \quad \nabla\cdot\boldsymbol{M}-\frac{\partial\mathcal{W}}{\partial\boldsymbol{d}}+\boldsymbol{\ell}=\boldsymbol{0},$$
$$\boldsymbol{T}\triangleq\frac{\partial\mathcal{W}}{\partial\boldsymbol{F}}, \quad \boldsymbol{M}\triangleq\frac{\partial\mathcal{W}}{\partial\nabla\boldsymbol{d}}. \tag{3.5}$$

3.3.2 12-Parameter Theory

The so-called micromorphic shell theory is based on the introduction of the triad of deformable directors (Fig. 3.2). With other words, the micromorphic shell is the
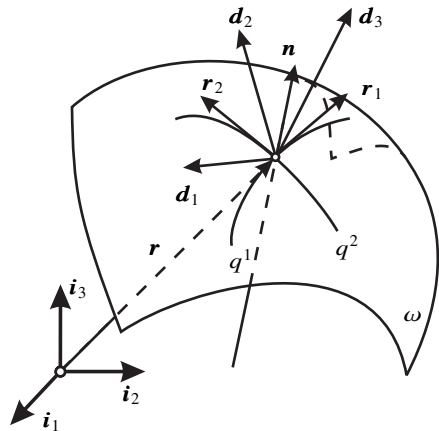
Fig. 3.2 Cosserat surface with 3 deformable directors (micromorphic shell).

two-dimensional analog of the three-dimensional micromorphic continuum [21, 22].

The strain energy function of an elastic micromorphic shell is given by the relation

$$W = W(\boldsymbol{F}, \boldsymbol{G}, \nabla \boldsymbol{G}), \quad \boldsymbol{G} \triangleq \boldsymbol{D}^k \otimes \boldsymbol{d}_k, \tag{3.6}$$

where $\boldsymbol{D}^k$ are reciprocal to $\boldsymbol{D}_k$, the second-order tensor $\boldsymbol{G}$ is the microdistorsion tensor, and the following relation holds true

$$W(\boldsymbol{F}, \boldsymbol{G}, \nabla \boldsymbol{G}) = W\left[(\boldsymbol{F} \cdot \boldsymbol{O}, \boldsymbol{G} \cdot \boldsymbol{O}, (\nabla \boldsymbol{G}) \cdot \boldsymbol{O}\right]$$
$$\forall \boldsymbol{O}^T = \boldsymbol{O}^{-1}. \tag{3.7}$$

In the theory of micromorphic shells the surface stress, couple stress tensors, and, in addition, the tensor of double stresses are present and in this theory the force dipoles are taking into account.

3.3.3 6-Parameter Theory

In contrast to the Cosserat surface theory or the micromorphic shell theory, in the 6-parameter theory of shell in each point of ω three orthonormal vectors $\boldsymbol{d}_k, k = 1, 2, 3$, are attached, i.e. $\boldsymbol{d}_k \cdot \boldsymbol{d}_m = \delta_{km}$ and $\boldsymbol{D}_k \cdot \boldsymbol{D}_m = \delta_{km}$. This variant of shell theory is also named micropolar shell theory and it is developed in [6, 7, 23], and [15] among others. A micropolar shell is a two-dimensional continuum in which the interaction between different parts of the shell is described by forces and moments only. The strain energy function of an elastic micropolar shell is given by

$$W = W(\boldsymbol{F}, \boldsymbol{H}, \nabla \boldsymbol{H}), \quad \boldsymbol{H} \triangleq \boldsymbol{D}^k \otimes \boldsymbol{d}_k. \tag{3.8}$$

$\boldsymbol{H}$ is the orthogonal tensor which is named the microrotation tensor. After application of the principle of the frame indifference W takes the form

$$W = W(\boldsymbol{E}, \boldsymbol{K}),$$
$$\boldsymbol{E} \triangleq (\nabla \boldsymbol{r}) \cdot \boldsymbol{H}^T, \quad \boldsymbol{K} \triangleq \frac{1}{2} \boldsymbol{R}^\alpha \otimes \left(\frac{\partial v \boldsymbol{H}}{\partial q^\alpha} \cdot v \boldsymbol{H}^T \right)_\times. \tag{3.9}$$

The Lagrangian equilibrium equations are given by

$$\nabla \cdot \boldsymbol{D} + \boldsymbol{f} = \boldsymbol{0}, \quad \nabla \cdot \boldsymbol{P} + \left[\boldsymbol{F}^T \cdot \boldsymbol{D} \right]_\times + \boldsymbol{l} = \boldsymbol{0},$$
$$\boldsymbol{D} \triangleq \frac{\partial W}{\partial \boldsymbol{E}} \cdot \boldsymbol{H}, \quad \boldsymbol{P} \triangleq \frac{\partial W}{\partial \boldsymbol{K}} \cdot \boldsymbol{H}. \tag{3.10}$$

Within the framework of the Cosserat-surface shell model one can discuss the material surface consisting of deformable particles on which forces and moments and some hyper-stresses act. At the same time the micropolar shell can be represented by a surface composed of rigid microparticles of arbitrary shape. The interaction between

these particles are given by forces and moments only. Now the Cosserat-surface shell model can be presented by a surface composed of microparticles of beam shape changing during the deformation its length, but they does not reflect the rotation about there axis. For the six-parameter shell theory we refer to [6, 7, 15–17, 24–26].

3.3.4 5-Parameter Theory

One of the most satisfying theories of shells based on the direct approach is the theory of simple shells [14, 27]. A simple shell is a two-dimensional continuum in which the interaction between different parts of the shell is due to forces and moments. The kinematical model of a simple shell is based on the introduction of a directed material surface ω, which is determined in the actual configuration by Eq. (3.1) considering $k = 1, 2, 3$. Now $\boldsymbol{d}_k(q^1, q^2)$ are a triad of orthonormal vectors obeying the condition $\boldsymbol{d}_3 = \boldsymbol{n}$. In the reference configuration Eq. (3.2) with $\boldsymbol{D}_k = \boldsymbol{N}$ holds true, where $\boldsymbol{N}$ is the unit normal to the shell surface in the reference configuration. On this stage each material point of the shell has 5 degrees of freedom. Making the standard derivation the linear and the angular velocities $\boldsymbol{v}(q,t)$, $\boldsymbol{\omega}(q,t)$ can be introduced.

In the case of infinitesimal deformations, the local equations of motion can be written as

$$
\begin{aligned}
\boldsymbol{\nabla} \cdot \boldsymbol{T} + \boldsymbol{f} \quad &= \rho(\boldsymbol{v} + \boldsymbol{\Theta}_1^T \cdot \boldsymbol{\omega})^{\boldsymbol{\cdot}}, \\
\boldsymbol{\nabla} \cdot \boldsymbol{M} + \boldsymbol{T}_\times + \boldsymbol{l} &= \rho(\boldsymbol{\Theta}_1 \cdot \boldsymbol{v} + \boldsymbol{\Theta}_2 \cdot \boldsymbol{\omega})^{\boldsymbol{\cdot}} + \rho \boldsymbol{v} \times \boldsymbol{\Theta}_1^T \cdot \boldsymbol{\omega},
\end{aligned}
\tag{3.11}
$$

where $\boldsymbol{T} = \boldsymbol{R}_\alpha \otimes \boldsymbol{T}^\alpha, \boldsymbol{M} = \boldsymbol{R}_\alpha \otimes \boldsymbol{M}^\alpha$ denote the force and moment tensors and $\boldsymbol{T}_\times \equiv \boldsymbol{R}_\alpha \times \boldsymbol{T}^\alpha$. The vectors $\boldsymbol{f}$ and $\boldsymbol{l}$ are the surface density of the external forces and moments, respectively.

Let $\mathcal{U}$ be the mass density of the internal energy. The local form of the balance of energy can be expressed as

$$
\rho \dot{\mathcal{U}} = \boldsymbol{T}^{\mathrm{T}} \boldsymbol{\cdot\cdot} \boldsymbol{\nabla}\boldsymbol{v} - \boldsymbol{T}_\times \cdot \boldsymbol{\omega} - \boldsymbol{M}^{\mathrm{T}} \boldsymbol{\cdot\cdot} \boldsymbol{\nabla}\boldsymbol{\omega}.
\tag{3.12}
$$

Introducing the energetic tensors we obtain another form of the balance of energy with the first and the second deformation tensors [27]. The specific elastic deformation energy $\mathcal{U}$ contains 12 scalar arguments. It can be shown that only 11 are independent. One can choose the following integrals

$$
\begin{aligned}
\mathcal{E} &= \frac{1}{2} \left[(\boldsymbol{E} + \boldsymbol{a}) \cdot \boldsymbol{a} \cdot (\boldsymbol{E} + \boldsymbol{a})^T - \boldsymbol{a} \right], \\
\boldsymbol{\Phi} &= (\boldsymbol{F} - \boldsymbol{b} \cdot \boldsymbol{c}) \cdot \boldsymbol{a} \cdot (\boldsymbol{E} + \boldsymbol{a})^T + \boldsymbol{b} \cdot \boldsymbol{c} \cdot \mathcal{E} + \boldsymbol{b} \cdot \boldsymbol{c}, \\
\boldsymbol{\gamma} &= \boldsymbol{E} \cdot \boldsymbol{n}, \quad \boldsymbol{\gamma}_* = \boldsymbol{F} \cdot \boldsymbol{n}.
\end{aligned}
\tag{3.13}
$$

$\mathcal{U}$ does not depend on $\boldsymbol{\gamma}_*$. Tensors $\mathcal{E}, \boldsymbol{\Phi}, \boldsymbol{\gamma}$ are called the reduced deformation tensors. Here $\mathcal{E}$ denote plane tensile and shear strains, $\boldsymbol{\Phi}$ - bending and torsional strains and $\boldsymbol{\gamma}$ - transverse shear.

For a shell made from an elastic material the strains are relatively small while the displacements and rotations can be relatively large. In such a case the following quadratic approximation can be introduced

$$
\begin{aligned}
2\rho_0 \mathcal{U} = {} & 2\boldsymbol{T}_0 \cdot\cdot \boldsymbol{\mathcal{E}} + 2\boldsymbol{M}_0^T \cdot\cdot \boldsymbol{\Phi} + 2\boldsymbol{N}_0 \cdot \boldsymbol{\gamma} + \boldsymbol{\mathcal{E}} \cdot\cdot {}^{(4)}\boldsymbol{C}_1 \cdot\cdot \boldsymbol{\mathcal{E}} + 2\boldsymbol{\mathcal{E}} \cdot\cdot {}^{(4)}\boldsymbol{C}_2 \cdot\cdot \boldsymbol{\Phi} \\
& + 2\boldsymbol{\Phi} \cdot\cdot {}^{(4)}\boldsymbol{C}_3 \cdot\cdot \boldsymbol{\Phi} + \boldsymbol{\gamma} \cdot \boldsymbol{\Gamma} \cdot \boldsymbol{\gamma} + 2\boldsymbol{\gamma} \cdot ({}^{(3)}\boldsymbol{\Gamma}_1 \cdot\cdot \boldsymbol{\mathcal{E}} + {}^{(3)}\boldsymbol{\Gamma}_2 \cdot\cdot \boldsymbol{\Phi}).
\end{aligned}
\tag{3.14}
$$

Here $\boldsymbol{T}_0, \boldsymbol{M}_0, \boldsymbol{N}_0$, ${}^{(4)}\boldsymbol{C}_1, {}^{(4)}\boldsymbol{C}_2, {}^{(4)}\boldsymbol{C}_3$, ${}^{(3)}\boldsymbol{\Gamma}_1, {}^{(3)}\boldsymbol{\Gamma}_2$, $\boldsymbol{\Gamma}$ denote stiffness tensors of different order. They express the effective elastic properties of the simple shell. The differences between various classes of simple shells are connected with different expressions of the stiffness tensors. The stiffness tensors do not depend on the deformations. Thus they may be found from tests based on the linear shell theory.

3.3.5 3-P arameter Theory

Finally, it is worst to mention the classical Kirchhoff-Love theory of shells. Within the discussed above director-based approach the classical shell model could be related the case when directors coincide with coordinate base vectors, and we refer to the books by [4, 26, 28–30].

3.4 Conclusions

Starting from the multipolar approach we briefly discussed some approaches based on consistent reduction of the kinematics descriptors. So in the same framework we introduced twelve-, six-, and five-parametric theories of plates and shells. For the current state of the art in the field of plates and shells we mention recent proceedings [31–34] and the review by [35].

References

[1] Altenbach H (2008) Analysis of homogeneous and non-homogeneous plates. In: de Borst R, Sadowski T (eds) Lecture Notes on Composite Materials – Current Topics and Achievements, Springer, Berlin, pp 1–36
[2] Altenbach H, Meenen J (2008) On the different possibilities to derive plate and shell theories. In: Jaiani G, Podio-Guidugli P (eds) IUTAM Symposium on

Relations of Shell, Plate, Beam, and 3D Models, Springer, Berlin, pp 37–47

[3] Altenbach J, Kissing W, Altenbach H (1994) Dünnwandige Stab- und Stabscha-lentragwerke. Vieweg, Braunschweig/Wiesbaden

[4] Naghdi P (1972) The theory of plates and shells. In: Flügge S (ed) Handbuch der Physik, vol VIa/2, Springer, pp 425–640

[5] Reissner E (1985) Reflection on the theory of elastic plates. Appl Mech Rev **38**(11):1453–1464

[6] Libai A, Simmonds JG (1998) The Nonlinear Theory of Elastic Shells, 2nd edn. Cambridge University Press, Cambridge

[7] Chróścielewski J, Makowski J, Pietraszkiewicz W (2004) Statics and Dynamics of Multifold Shells: Nonlinear Theory and Finite Element Method (in Polish). Wydawnictwo IPPT PAN, Warszawa

[8] Wisniewski K (2010) Finite Rotation Shells. Basic Equations and Finite Elements for Reissner Kinematics. Springer

[9] Aßmus M, Altenbach H (2021) On the Principles to Derive Plate Theories. In: Challamel N, Kaplunov J, Takewaki I (eds) Modern Trends in Structural and Solid Mechanics 2, Mechanical Engineering and Solid Mechanics, ISTE - WILEY, London · Hoboken, pp 29–42

[10] Levinson M (1980) An accurate, simple theory of the statics and dynamics of elastic plates. Mech Res Comm **7**(6):343–350

[11] Reddy J (1984) A simple higher–order theory for laminated composite plates. Trans ASME J Appl Mech **51**:745–752

[12] Meenen J, Altenbach H (2001) A consistent deduction of von Kármán-type plate theories from threedimensional non-linear continuum mechanics. Acta Mech **147**:1–17

[13] Rubin MB (2000) Cosserat Theories: Shells, Rods and Points. Kluwer, Dordrecht

[14] Zhilin PA (2006) Applied Mechanics. Foundations of the Theory of Shells (in Russ.). St. Petersburg State Polytechnical University, Saint Petersburg

[15] Eremeyev VA, Zubov LM (2008) Mechanics of Elastic Shells (in Russ.). Nauka, Moscow

[16] Eremeyev V, Altenbach H (2017) Basics of mechanics of micropolar shells. In: Altenbach H, Eremeyev V (eds) Shell-like Structures: Advanced Theories and Applications, CISM International Centre for Mechanical Sciences, vol 572, Springer, Cham, pp 63–111

[17] Eremeyev VA, Lebedev LP, Altenbach H (2013) Foundations of Micropolar Mechanics. Springer, Heidelberg

[18] Simmonds JG (1997) Some comments on the status of shell theory at the end of the 20th century: Complaints and correctives. In: AIAA/ASME/ASCE/AHS/ASC Structures, Structural Dynamics, and Materials Conference and Exhibit, 38th, and AIAA/ASME/AHS Adaptive Structures Forum, Kissimmee, FL, Apr. 7-10, 1997, Collection of Technical Papers, Pt. 3 (A97-24112 05-39), AIAA, pp 1912–1921

[19] Ericksen JL, Truesdell C (1958) Exact theory of stress and strain in rods and shells. Archive for Rational Mechanics and Analysis **1**(1):295–323

[20] Green AE, Naghdi PM, Wainwright WL (1965) A general theory of a Cosserat surface. Archive for Rational Mechanics and Analysis **20**(4):287–308

[21] Mindlin RD (1964) Microstructure in linear elasticity. Archive for Rational Mechanics and Analysis **16**:51–78

[22] Eringen AC (1999) Microcontinuum Field Theory. I. Foundations and Solids. Springer, New York

[23] Pietraszkiewicz W, Chróścielewski J, Makowski J (2005) On dynamically and kinematically exact theory of shells. In: Pietraszkiewicz W, Szymczak C (eds) Shell Structures: Theory and Applications, Taylor & Francis, London, pp 163–167

[24] Altenbach J, Altenbach H, Eremeyev VA (2010) On generalized Cosserat-type theories of plates and shells: a short review and bibliography. Archive of Applied Mechanics **80**(1):73–92

[25] Altenbach H, Eremeyev VA (2014) Actual developments in the nonlinear shell theory: state of the art and new applications of the six-parameter shell theory. In: Pietraszkiewicz W, Górski J (eds) Shell Structures: Theory and Applications, Taylor & Francis Group, London, vol 3, pp 3–12

[26] Eremeyev VA, Cloud MJ, Lebedev LP (2018) Applications of Tensor Analysis in Continuum Mechanics. World Scientific, New Jersey

[27] Altenbach H, Naumenko K, Zhilin PA (2005) A direct approach to the formulation of constitutive equations for rods and shells. In: Pietraszkiewicz W, Szymczak C (eds) Shell Structures - Theory and Application 2005, Taylor & Francis/Balkema, London et al., pp 87–90

[28] Novozhilov VV, Chernykh KF, Mikhailovskii EI (1991) Linear Theory of Thin Shells (in Russian). Politekhnika, Leningrad

[29] Chernykh KF (1964) Linear Theory of Shells (in Russian). University Press, 1968 English Translation by NASA-TT-F-II

[30] Ciarlet PG (2000) Mathematical Elasticity, Vol III, Theory of Shells. North-Holland

[31] Mikhasev GI, Altenbach H (2019) Thin-walled laminated structures, Advanced Structured Materials, vol 106. Springer, Cham

[32] Altenbach H, Chróścielewski J, Eremeyev VA, Wiśniewski K (2019) Recent Developments in the Theory of Shells, Advanced Structured Materials, vol 110. Springer, Cham

[33] Altenbach H, Chinchaladze N, Kienzler R, Müller WH (2020) Analysis of Shells, Plates and Beams, Advanced Structured Materials, vol 134. Springer, Cham

[34] Altenbach H, Bauer S, Eremeyev VA, Mikhasev GI, Morozov NF (2022) Recent Approaches in the Theory of Plates and Plate-Like Structures, Advanced Structured Materials, vol 151. Springer, Cham

[35] Altenbach H, Eremeyev V (2017) Thin-walled structural elements: Classification, classical and advanced theories, new applications. In: Altenbach H, Eremeyev V (eds) Shell-like Structures: Advanced Theories and Applications, Springer, Cham, CISM International Centre for Mechanical Sciences, vol 572, pp 1–62

Chapter 4
Conceptual Generalizations of the Kapitsa Problem

Alexey V. Babenko, Oksana R. Polyakova, and Tatyana P. Tovstik

Abstract The problem of an inverted pendulum stability under the action of vibration of its base for the first time was published in the works of A. Stephenson and it was analyzed in detail in the works of P.L. Kapitsa. The problem continues to interest scientists. The areas of its practical application are growing. The purpose of the work is to reveal the influence of elastic transverse and longitudinal deformations of the Kapitsa pendulum on its stability and on the pattern of oscillations at steady state. The dynamic problem of the Kapitsa pendulum movement in the generalized case for a flexible tensile rod is solved analytically and numerically. The problem of small transverse vibrations of a longitudinally compressed flexible rod on a vibrating base is solved by introducing an auxiliary boundary value problem of the static equilibrium bifurcation of a rod under its own weight with a free upper end and a hinged lower end. The problem is reduced to a system of Mathieu-type equations. For solution we used the method of two-scale asymptotic expansion into a series in powers of a small parameter, where the amplitude of the vertical oscillation of the support is small with respect to the length of the pendulum. The Pade approximation is used in numerical calculations for coefficients depending on the base vibration frequency in a complex way. The obtained results make it possible to evaluate the effects of the influence of the second and third forms of bending oscillations and four longitudinal resonances on the stability and dynamics of the pendulum. Four dimensionless parameters are

Alexey V. Babenko
National Research Centre "Kurchatov Institute", Ploshchad' Akademika Kurchatova, 1, 123098 Moscow, Russian Federation,
e-mail: svpma91@mail.ru

Oksana R. Polyakova
Public Organization of Scientific Research "Metagalactic Sciences" of Moscow region, Russian Federation,
e-mail: ksenpolyaor@yandex.ru

Tatyana P. Tovstik
Institute for Problems in Mechanical Engineering of the Russian Academy of Sciences, Bolshoy prospekt 61, V.O., 199178 St. Petersburg, Russian Federation,
e-mail: tovstik_t@mail.ru

proposed, which include all parameters of the linear dimensional problem in the general case of a flexible tensile Kapitsa pendulum. The results are shown in the graphs.

4.1 Introduction

The problem of the upper position stability of an inverted pendulum in the case of the suspension point vibration was considered at the beginning of the 20th century by A. Stephenson [1]. Stephenson found an approximate solution to the equation of motion of a pendulum with a vibrating base in the case of small deviations of the pendulum and derived the condition for the stability of the upper equilibrium position. The equation he used belongs to Mathieu-type equation and assumes a solution by series expansion. The Mathieu equation was also used in the works of the next stage in the development of the inverted pendulum problem [2–7] in the 20-30s of the last century. It is rightly points out in the article [8] that it was a time when published works went unnoticed, since the time had not yet come and the problem of a pendulum with a vibrating base was simply "waiting for its time".

A new stage began 20 years later, with the development of the stability theory, when N.N. Bogolyubov [9] solved a more general problem than Stephenson's. The resulting solution allowed us to derive the stability condition. Unlike N.N. Bogoliubov, P.L. Kapitsa [10] considers the nonlinear equation of pendulum oscillations without taking damping into account and obtains the result for the stability parameters not only for the first approximation, which coincides with the result of [9], but also for higher approximations. P.L. Kapitsa constructed a theory for calculating the pendulum oscillation period. He obtained not only the equilibrium condition, but also an estimate of the accuracy under the assumption of small amplitude of the suspension point oscillation. He also solved the problem with the deviation of the pendulum from the upper equilibrium position by a finite angle and found the restoring moment acting on the pendulum.

Along with new theoretical results obtained for the case of more complex suspension oscillations P.L. Kapitsa also conducts its an experimental study and denotes options for practical applications. P.L. Kapitsa writes [11] that "the beautiful and instructive phenomenon of the dynamic stability of an inverted pendulum has not only not been included in modern manuals on mechanics, but is even almost unknown to a wide range of specialists". The situation has changed significantly with the advent of the works of N.N. Bogolyubov and P.L. Kapitsa. The approach of L.D. Landau in relation to the problem of a pendulum with a vibrating base supposed the introduction "effective potential energy" concept. It is precisely the minimum of the effective potential energy function corresponds to the position of stable equilibrium. The problem of a pendulum with a vibrating base took pride of place in the first volume of L.D. Landau and E.M. Lifshitz [12].

Works by N.N. Bogolyubov and P.L. Kapitsa opened a new trend in vibrational dynamics. The development of this trend was continued by such prominent scientists as V.N. Chelomei [13], V.I. Arnold [14], I.I. Blekhman [15].

For today the application of the effect, which was studied in detail for the first time for the Kapitsa pendulum, is being expanded. The stability of oscillatory systems of classical mechanics [16], physics [17], microscopic particles [18] is studied. New fundamental and technological problems are being solved. At the same time, the nature of the studied high-vibration effects on a body or system of bodies can be both mechanical and electromagnetic.

4.2 Mathieu Equation

The famous Mathieu equation

$$\frac{d^2\varphi}{dt_1^2} - (q - \varepsilon \sin t_1)\,\varphi = 0, \tag{4.1}$$

to which, in the case of small deflection of the pendulum from the vertical, the Kapitsa problem is reduced, contains two parameters – q and ε, in the plane of which the stability or instability of vibrations near the equilibrium state $\varphi = 0$ is determined. On the plane of these parameters, a diagram of stability regions is constructed, known as the Ince–Strutt diagram[19], Fig. 4.1.

Let us show the physical meaning of the quantities included here. To do this, we write the equation of vibrations of an inverted mathematical pendulum of length L under the action of vertical vibrations of the base $z(t) = a \sin(\omega t + \beta)$ in the field of gravity with acceleration of free fall g

$$\ddot{\varphi} - \left(\frac{g}{L} - \frac{a\omega^2}{L}\sin(\omega t + \beta)\right)\sin\varphi = 0. \tag{4.2}$$

By introducing the dimensionless time $t_1 = \omega t + \beta$, for small deflection angles of the pendulum $\sin\varphi = \varphi$, Eq. (4.2) is reduced to (4.1), and $q = \dfrac{g}{L\omega^2}$ – is responsible for
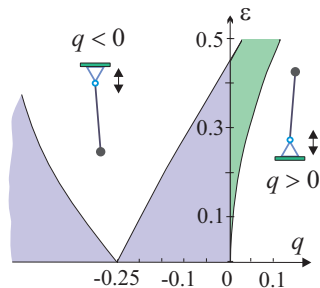
Fig. 4.1 Fragment of the Ince–Strutt diagram. The stability regions are hatched.

the contribution of gravity. For the problem of a pendulum oscillating in the lower equilibrium position, the quantity q in Eq. (4.1) is negative.

The parameter $|q|$ can be represented as the ratio of squared angular velocities

$$q = \frac{\omega_1^2}{\omega^2}, \qquad \omega_1^2 = \frac{g}{L}, \tag{4.3}$$

where ω_1 is the frequency of free vibration of the pendulum in its lower equilibrium position in the absence of vibrations of the suspension point, and ω is the specified frequency of oscillation of the base. Such an approach, which includes angular velocities in the formulation and solution of the stability problem, was developed by D.J. Acheson [20] for the case of multilink pendulums.

The parameter ε in Eq. (4.1) has the physical meaning of the dimensionless amplitude of oscillations of the base

$$\varepsilon = \frac{a}{L}. \tag{4.4}$$

The diagram (Fig. 4.1) gives an idea of the movement of the pendulum under the action of vibration of the base and gravity in the entire range of parameters. In particular, even in the lower position of the pendulum, there are modes of oscillation in which the lower equilibrium position is unstable (non hatched parts of the graph for $q < 0$).

The classical Kapitsa effect for a problem with small pendulum deflection angles $\varphi(t)$ is realized for small values of the ratio of the base oscillation amplitude to the pendulum length $\varepsilon = \frac{a}{L} \ll 1$. The equations for the boundaries of the stability region of an inverted pendulum (for $q > 0$) are known [19], and the stability conditions have the form

$$0.5\varepsilon^2 > q > 0.595(\varepsilon - 0.454). \tag{4.5}$$

The right side of the inequality holds for all small ε, the left side in dimensional variables gives

$$\frac{a^2}{2L^2} > \frac{g}{L\omega^2}. \tag{4.6}$$

Inequality (4.6) will be satisfied for sufficiently large values of the frequency ω. Thus, for the Kapitsa problem, equation (4.1) includes two parameters: the small factor ε with the oscillating term $\varphi \sin t_1$ and the factor $q \sim \varepsilon^2$, $q > 0$ of the second order of smallness with the term responsible for the destabilizing effect.

4.3 Model of the Flexible Rod of the Kapitsa Pendulum

There is a video recording of interesting experiments conducted by colleagues of our institute [21, 22]. In the first of the experiments, a rope was taken as a model of Kapitsa's pendulum. In the absence of vibrations, the rope is bent and

placed horizontally on the table. The vibration of the support is turned on and the vibration speed gradually increases until the rope becomes vertical. With an even greater increase in the frequency of vibrations, the system passes twice through areas with large amplitudes of transverse vibrations, and in the first and second cases it is visually seen that the shapes are different. Adopting the Kapitsa flexible compressible pendulum model, we investigate this phenomenon on our model. The second experiment shows a working model of an inverted pendulum with an internal degree of freedom in the form of a mass on an elastic spring.

In this section, we develop the approach started in [23–27]. Let us consider the generalized model of the Kapitsa pendulum and find what effect the condition of deformability and flexibility of the pendulum can have on its stability. Let the pendulum be a homogeneous deformable rod, the bending of which is described by the Bernoulli-Euler beam model. The rod is fixed on a hinged support that performs harmonic oscillations with a given frequency and amplitude in the vertical direction. The movement takes place in the field of gravity. We will assume that the support vibration amplitude a is small compared to the rod length L.

In the general case, to describe the motion of the Kapitsa pendulum, it is necessary to consider two boundary value problems that describe small transverse oscillations and longitudinal oscillations, respectively. The equation of transverse vibrations of a longitudinally compressed rod near the upper equilibrium position has the form [28]

$$D\frac{\partial^4 w}{\partial x^4} + \frac{\partial}{\partial x}\left(P(x,t)\frac{\partial w}{\partial x}\right) + \rho S\frac{\partial^2 w}{\partial t^2} = 0, \qquad (4.7)$$

where $w(x,t)$ – transverse deflection, $D = EI$ – bending stiffness, E – Young's modulus, ρ – mass density, S is the cross-sectional area. The upper end $x = L$ of the rod is free, and at the lower end $x = 0$ we consider the hinge support

$$\left.\frac{\partial^2 w}{\partial x^2}\right|_{x=L} = \left.\frac{\partial^3 w}{\partial x^3}\right|_{x=L} = 0, \qquad w(0,t) = \left.\frac{\partial^2 w}{\partial x^2}\right|_{x=0} = 0. \qquad (4.8)$$

The axial force P consists of two terms, the first of which is related to the weight of the rod P_0, and the second is due to the harmonic vertical vibrations of the base $a\sin(\omega t + \beta)$. For the inextensible rod model

$$P(x,t) = P_0\frac{L-x}{L} - \rho a\omega^2 S(L-x)\sin(\omega t + \beta), \quad P_0 = \rho g S L. \qquad (4.9)$$

In the case of a tensile rod model, the axial force is found from the boundary value problem of the propagation of longitudinal waves along the rod

$$\rho S\left(\frac{\partial^2 u}{\partial t^2} + g - a\omega^2\sin(\omega t + \beta)\right) = ES\frac{\partial^2 u}{\partial x^2}, \quad u(0,t) = 0, \quad \left.\frac{du}{dx}\right|_{x=L} = 0, \qquad (4.10)$$

where $u(x,t)$ is the longitudinal displacement. The axial compressive force is related to the longitudinal deformation by the formula

$$P(x,t) = -ESu_x. \tag{4.11}$$

Let us introduce dimensionless parameters ε, q, P_D and pass to dimensionless variables

$$\hat{x} = \frac{x}{L}, \quad \hat{t} = \omega t, \quad \hat{w} = \frac{w}{L}, \quad \hat{u} = \frac{u}{L}, \quad P_D = \frac{P_0 L^2}{D}, \quad \varepsilon = \frac{a}{L}, \quad q = \frac{g}{L\omega^2}. \tag{4.12}$$

In what follows, the ^ icon will be omitted.

For the model of an inextensible pendulum, the Eq. (4.7) in dimensionless variables takes the form

$$\frac{\partial^4 w}{\partial x^4} + P_D \frac{\partial}{\partial x} \left[(1-x) \frac{\partial w}{\partial x} \right] \left[1 - \frac{\varepsilon}{q} \sin(t+\beta) \right] + \frac{P_D}{q} \frac{\partial^2 w}{\partial t^2} = 0. \tag{4.13}$$

For the model of an extensible pendulum, we first find the longitudinal force from Eq. (4.10) problem, which in dimensionless variables has the form

$$\frac{\partial^2 u}{\partial t^2} + q - \varepsilon \sin(t+\beta) = \frac{E}{L^2 \rho \omega^2} \frac{\partial^2 u}{\partial x^2}, \quad u(0,t) = 0, \quad \frac{du}{dx}\bigg|_{x=1} = 0. \tag{4.14}$$

We are looking for a solution (4.14) in the form

$$u(x,t) = \frac{P_0}{ES} \left(\frac{x^2}{2} - x \right) + U(x) \sin(t+\beta), \quad P_0 = \rho g S L. \tag{4.15}$$

For the function $U(x)$ we obtain the boundary value problem

$$\frac{d^2 U}{dx^2} + v^2 (U+\varepsilon) = 0, \quad U(0) = 0, \quad \frac{dU}{dx}\bigg|_{x=1} = 0, \quad v^2 = \frac{\omega^2 L^2}{c^2}, \quad c^2 = \frac{E}{\rho}, \tag{4.16}$$

where c is the speed of sound in the rod material. We find a solution $U(x)$

$$U(x) = -\varepsilon(1 - \cos vx - \sin vx \tan v) \tag{4.17}$$

and axial force

$$P(x,t) = -ES \frac{L^2}{D} \frac{\partial u}{\partial x} = P_D \left[1 - x - \frac{\varepsilon}{q} \frac{\cos vx \tan v - \sin vx}{v} \sin(t+\beta) \right]. \tag{4.18}$$

For an inextensible rod $E \to \infty$, $c \to \infty$, $v \to 0$ and, passing to the limit in Eq. (4.18) for $v \to 0$, we find

$$P = P_D(1-x) \left[1 - \frac{\varepsilon}{q} \sin(t+\beta) \right],$$

which coincides with the formula (4.9) in its dimensionless writing.

Substituting the force $P(x,t)$ into the equation for transverse oscillations (4.7), we obtain

$$\frac{\partial^4 w}{\partial x^4} + P_D \frac{\partial}{\partial x}\left\{\left[1 - x - \frac{\varepsilon}{q}\frac{\cos \nu x \tan \nu - \sin \nu x}{\nu}\sin(t+\beta)\right]\frac{\partial w}{\partial x}\right\} +$$

$$+\frac{P_D}{q}\frac{\partial^2 w}{\partial t^2} = 0. \tag{4.19}$$

The solution to the problem of small transverse oscillations of a longitudinally compressed flexible rod on a vibrating base (4.19) is sought as the sum of the series

$$w(x,t) = \sum_{n=1}^{N}\Psi_n(x)\,w_n(t), \tag{4.20}$$

where $\Psi_n(x)$ are eigenfunctions of the auxiliary boundary value problem of the static equilibrium bifurcation of a rod under its own weight with a free upper end and a hinged lower end

$$\frac{d^4\Psi_n}{dx^4} + \lambda_n\frac{d}{dx}\left[(1-x)\frac{d\Psi_n}{dx}\right] = 0, \quad \Psi_n(0) = \Psi_n''(0) = \Psi_n''(1) = \Psi_n'''(1) = 0, \tag{4.21}$$

where the orthogonality condition is satisfied

$$\int_0^1 (1-x)\frac{d\Psi_k}{dx}\frac{d\Psi_n}{dx}dx = 0, \quad k \neq n, \tag{4.22}$$

It is convenient that the eigenfunctions Ψ_n and the dimensionless Euler critical values λ_n depend only on the pendulum fixing conditions and do not depend on the parameters of the Kapitsa problem. Integrating the equation with the boundary conditions (4.21), we arrive at the Airy equation

$$V''(x,\lambda) + \lambda(1-x)V(x,\lambda) = 0 \tag{4.23}$$

for

$$\Psi_k(x) = \int_0^x V(x,\lambda_k)dx, \tag{4.24}$$

and taking into account $V'(1,\lambda) = 0$, to the solution [19] as a series

$$V(x,\lambda) = \sum_{k=0}^{\infty}\frac{\left[-\lambda(1-x)^3\right]^k}{a_k}, \quad a_0 = 1, \quad a_k = 3k(3k-1)a_{k-1}. \tag{4.25}$$

We substitute the resulting solution (4.20) into Eq. (4.19), and taking into account the orthogonality conditions (4.22), similarly to Eq. [24], we obtain a system of differential equations with variable coefficients

$$\sum_{k=1}^{N} a_{nk} \frac{d^2 w_k}{dt^2} + q b_n \left(\frac{\lambda_n}{P_D} - 1 \right) w_n + \sum_{k=1}^{N} \varepsilon c_{nk} \sin (t + \beta) w_k = 0, \quad n = 1, \ldots, N. \quad (4.26)$$

It is convenient to write the same system in matrix form by introducing the vector $\boldsymbol{W}$ of unknown functions $\{w_k\}_{k=1,N}^{T}$ and coefficient matrices

$$\boldsymbol{A} \frac{d^2 \boldsymbol{W}}{dt^2} + q \boldsymbol{P} \cdot \boldsymbol{W} + \varepsilon \boldsymbol{C} \cdot \boldsymbol{W} \sin (t + \beta) = 0, \qquad \varepsilon = \frac{a}{L}, \qquad q = \frac{g}{L \omega^2}, \qquad (4.27)$$

where $\boldsymbol{A}$ and $\boldsymbol{C}$ are symmetric matrices, $\boldsymbol{P}$ is a diagonal matrix

$$P_{nn} = b_n \left(\frac{\lambda_n}{P_D} - 1 \right), \quad b_n = \int_0^1 (1 - x) \left(\frac{d \Psi_n}{dx} \right)^2 dx, \quad (4.28)$$

$$a_{nk} = \int_0^1 \Psi_n(x) \Psi_k(x) dx, \quad c_{nk} = \int_0^1 \frac{(\cos \nu x \tan \nu - \sin \nu x)}{\nu} \frac{d \Psi_n}{dx} \frac{d \Psi_k}{dx} dx. \quad (4.29)$$

The first eigenvalues of the problem are

$$\lambda_1 = 0, \ \lambda_2 = 25.64, \ \lambda_3 = 95.96, \ \lambda_4 = 210.68, \ \lambda_5 = 369.83. \quad (4.30)$$

From the expressions (4.28), (4.30) we see that the first principal minor of the matrix $\boldsymbol{P}$ is negative for any positive pendulum weight $P_D > 0$. This term will make a contribution that has a destabilizing effect on the motion of the pendulum. The next elements of the diagonal matrix $\boldsymbol{P}$ will be negative only for values of the pendulum weight parameter P_D exceeding the corresponding eigenvalues λ_n of the problem of static deflection of an hinged rod. The oscillating term will have a stabilizing effect.

Thus, the stability of the Kapitsa pendulum in the problem for a flexible compressible rod, in contrast to the problem for a non-deformable pendulum, is affected by four parameters. The parameters P_D and ν are added to the parameters of the dimensionless amplitude ε and the dimensionless acceleration of gravity q, which determine the dynamics of the classical Kapitsa problem (Sect. 4.2). When the bending stiffness of a rod tends to infinity, the weight parameter P_D associated with bending tends to zero. Letting the tensile-compressive stiffness tend to infinity, we obtain the zero value of the compressibility parameter ν.

By numerically solving the system (4.27), one can obtain separate results regarding the influence of certain parameter values on the stability. Next, we continue the analytical study using the asymptotic two-scale expansion in order to obtain a general picture of the stability of the pendulum with small deviations from the vertical.

4.4 Asymptotic Expansion

Previously, for a non-deformable pendulum (Sect. 4.2), an estimate was obtained

$$q \sim \varepsilon^2, \tag{4.31}$$

let's take the designation

$$\tilde{q} = \frac{q}{\varepsilon^2}. \tag{4.32}$$

Let a small deviation of the pendulum and zero initial speed be given at the initial moment of time. Then the equation (4.27) and the initial conditions for it will look like

$$A\frac{d^2W}{dt^2} + \varepsilon^2 \tilde{q} P \cdot W + \varepsilon C \cdot W \sin(t+\beta) = 0, \quad W(0) = W_0, \quad \frac{dW}{dt}\bigg|_{t=0} = 0. \tag{4.33}$$

Consider the stability of the zero solution of the system (4.33). For $\varepsilon = 0$ this system has a solution $W(\theta) = W_0$, where the components of the vector W_0 are constant. Therefore, for $\varepsilon \ll 1$, we will look for a solution to the system in the form of periodic functions with slowly varying amplitudes [19]. The vector function

$$W = W(t,\theta,\varepsilon), \qquad \theta = \varepsilon t, \tag{4.34}$$

where θ is slow time, is sought in the form of an asymptotic expansion

$$W(t,\theta,\varepsilon) = \sum_{m=0}^{\infty}(U_m(\theta) + V_m(t,\theta))\varepsilon^m, \quad \int_0^{2\pi} V_m(t,\theta)dt = 0, \quad m = 0,1,\dots \tag{4.35}$$

Taking into account the relation

$$\frac{d^2W}{dt^2} = \frac{\partial^2W}{\partial t^2} + 2\varepsilon\frac{\partial^2W}{\partial t\partial\theta} + \varepsilon^2\frac{\partial^2W}{\partial\theta^2} \tag{4.36}$$

we successively find

$$\varepsilon^0: \quad V_0(t,\theta) \equiv 0,$$

$$\varepsilon^1: \quad V_1(t,\theta) = A^{-1}\cdot C\cdot U_0\sin(t+\beta),$$

$$\varepsilon^2: \quad A\cdot\frac{d^2U_0}{d\theta^2} + D\cdot U_0 = 0, \qquad D = \tilde{q}P + \frac{1}{2}C\cdot A^{-1}\cdot C. \tag{4.37}$$

For the zero solution of Eq. (4.37) to be stable, the matrix D must be positive definite, since the matrix A is positive definite. The loss of positive definiteness D serves to determine the critical value of the parameters.

The initial conditions in the linear approximation do not affect the stability, but affect the oscillation amplitude. Let us write the initial conditions (4.33) for Eq. (4.37)

$$\boldsymbol{U}_0(0) = \boldsymbol{W}_0,$$

$$\frac{d\boldsymbol{W}}{dt} = \varepsilon \frac{d\boldsymbol{U}_0}{d\theta} + \frac{d}{dt}\left[\varepsilon \boldsymbol{A}^{-1}\cdot\boldsymbol{C}\cdot\boldsymbol{U}_0\sin(t+\beta)\right] + O\left(\varepsilon^2\right), \qquad (4.38)$$

$$\left.\frac{d\boldsymbol{W}}{dt}\right|_{t=0} = \boldsymbol{0} \quad => \quad \left.\frac{d\boldsymbol{U}_0}{d\theta}\right|_{\theta=0} = -\boldsymbol{A}^{-1}\cdot\boldsymbol{C}\cdot\boldsymbol{W}_0\cos\beta.$$

We see that for slowly varying deflections of the rod along the eigenmodes $\boldsymbol{U}_0(\theta)$, the initial conditions included the value of the initial phase of vibrations of the base β. Indeed, calculations have shown that for some values of β, the amplitude of the pendulum oscillations $w_1(t)$ is several times greater than the initial value of the deflection.

4.5 Pade Approximation

Let us write down for the first three modes of oscillations the numerical values of the coefficients (4.28), (4.29) included in Eq. (4.37). For oscillations in the first three modes, we have

$$\lambda_1 = 0, \quad \Psi_1(x) = x, \quad a_{11} = 1/3, \quad b_1 = 0.5,$$

$$a_{12} = 0.0331, \quad a_{22} = 0.02 \quad b_2 = 0.162,$$

$$a_{13} = 0.00195 \quad a_{23} = 0.00576, \quad a_{33} = 0.00633, \quad b_3 = 0.131, \qquad (4.39)$$

$$P_{11} = -0.5, \quad P_{22} = 0.162\left(\frac{25.6}{P_D} - 1\right), \quad P_{33} = 0.131\left(\frac{96}{P_D} - 1\right).$$

Here and below, we give values with an accuracy of one to three significant figures, but the calculations were made with an accuracy of six or more significant figures.

The components of the matrix $\boldsymbol{C}$ depend in a complicated way on the compressibility parameter ν. For an incompressible rod, the matrix $\boldsymbol{C}$ is diagonal, and $c_{nn} = b_n$. Graphs of coefficients $c_{ij}(\nu)$ are shown in Fig. 4.2.

These coefficients are calculated using the formulas (4.24), (4.25), (4.29). The first of the coefficients can be written out explicitly, for the rest we use the Pade approximation [29] on the interval $0.07 < \nu < 8.3$, chosen so that the relative error in the indicated region is less than 0.5%. Approximation works up to $\nu = 12$, while the error increases, but the visually accurate and approximate graphs are almost the same.

$$c_{11}(\nu) = (\tan\nu\sin\nu + \cos\nu - 1)/\nu^2, \qquad (4.40)$$

$$z = z(\nu) = \left(1 - \frac{4\nu^2}{\pi^2}\right)\left(1 - \frac{4\nu^2}{9\pi^2}\right)\left(1 - \frac{4\nu^2}{25\pi^2}\right)\left(1 - \frac{4\nu^2}{49\pi^2}\right), \qquad \pi = 3.14,$$

$$c_{22}(\nu) = 10^{-6}(162000 - 13.9\nu - 7460\nu^2 - 35.7\nu^3 + 212\nu^4 - 5.8\nu^5 - .13\nu^6 - .098\nu^7 + .004\nu^8)/z,$$

$$c_{33}(\nu) = 10^{-6}(131000 - 23.8\nu - 5970\nu^2 - 88.6\nu^3 + 169\nu^4 - 15.3\nu^5 + 2.1\nu^6 - .27\nu^7 + .01\nu^8)/z,$$

$$c_{12}(\nu) = 10^{-6}(-15 - 14.9\nu + 13500\nu^2 - 32\nu^3 - 291\nu^4 - 5.1\nu^5 + 2.6\nu^6 - .086\nu^7 + .004\nu^8)/z,$$

$$c_{13}(\nu) = 10^{-6}(32.9 - 14\nu - 1450\nu^2 - 39\nu^3 + 205\nu^4 - 6.5\nu^5 - .331\nu^6 - .11\nu^7 + .005\nu^8)/z,$$

$$c_{23}(\nu) = 10^{-6}(-18 + 1.7\nu + 5510\nu^2 + 4.06\nu^3 - 119\nu^4 + .68\nu^5 + .88\nu^6 + .013\nu^7 - .0008\nu^8)/z.$$

The obtained approximations are especially convenient when it is necessary to perform calculations in a large range of ν values.

In our previous papers, we limited ourselves to approximating the absolute values of $c_{ij}(\nu)$, since Eq. (4.37) equation included the quadratic form of these coefficients, and $c_{ij}(\nu)$ all changed sign simultaneously. Starting from the third form of oscillations, it will not be possible to limit ourselves to the approximation of modules. As we see from Fig. 4.2, the quantity $c_{13}(\nu)$, unlike the other c_{ij}, changes sign not only at resonances.

4.6 Discussion of Results

4.6.1 Resonances of Longitudinal Vibrations

Let us discuss the physical meaning of resonances of longitudinal vibrations. The first resonant frequency is the value $\nu = \pi/2$. Rewrite the formula (4.16)

$$\nu = \omega \frac{L}{c} = \frac{2\pi}{T_\omega} T_L, \tag{4.41}$$

where T_ω is the dimensional value of the support oscillation period, T_L is the travel time of the tension-compression wave along the length of the pendulum L in one direction. Equating ν to the first resonant value, we get
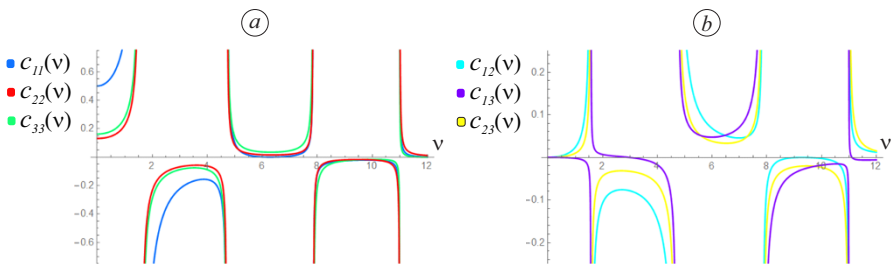
Fig. 4.2: Plot of the coefficients $c_{ij}(\nu)$. (**a**) The functions c_{11}, c_{22}, c_{33} are shown as blue, green and red lines respectively. (**b**) Functions c_{12}, c_{13}, c_{23} are shown with cyan, purple and yellow lines.

$$4T_L = T_\omega, \tag{4.42}$$

that is, during the period of one oscillation of the base, the tension-compression wave passes 4 times along the length of the rod. Note that the fourfold passage of the length of the rod by the tension-compression wave is the full period for this wave under the given conditions of the rod fixing. If at the first moment a compression wave was generated, then, having reflected from the upper free end of the rod, it becomes a tension wave. Further, reflecting from the lower boundary, the wave continues to move as a stretching wave to the upper end, and, finally, reflecting from the free upper end, then goes down as a compression wave. For the next two resonances, we get

$$4T_L = 3T_\omega, \qquad 4T_L = 5T_\omega. \tag{4.43}$$

In all these cases, energy is pumped into the system: at the moment $2T_L$, when the tension wave arrives, the support goes down, further increasing the tension of the rod; at the moment $4T_L$ when the compression wave comes down, the support goes up, increasing the compression even more (Fig. 4.3.) Naturally, the picture is much more complicated, we just followed the wave front.

4.6.2 General Picture of Stability by Asymptotic Formulas

In real structures, it is often possible to change the angular velocity in the course of one experiment. The dimensionless quantities included in the pendulum oscillation formula in the asymptotic approximation (4.37) depend on the angular velocity. The angular velocity enters into two dimensionless parameters – v and $\tilde{q}$. In the dimensionless parameter $\tilde{q}$, we single out separately the factor associated with v, and separately the factor associated with the amplitude of the oscillations and the parameters of the pendulum rod – $\hat{q}$. Using the formulas (4.16), (4.27), (4.32), we find

$$v^2 = \omega^2 \frac{L^2 \rho}{E}, \qquad \tilde{q} = \frac{1}{\omega^2} \frac{gL}{a^2} = \frac{1}{v^2} \frac{gL^3 \rho}{a^2 E}, \qquad \tilde{q} = \frac{\hat{q}}{v^2}, \quad \hat{q} = \frac{gL^3 \rho}{a^2 E}. \tag{4.44}$$
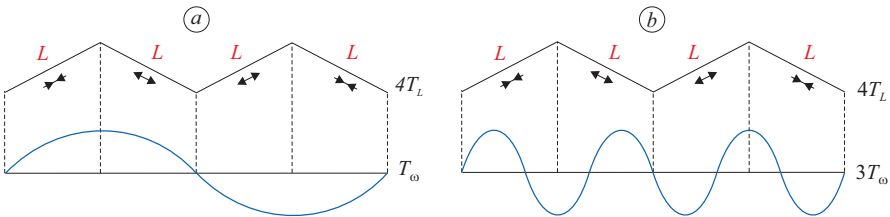
Fig. 4.3: Longitudinal resonance. (**a**). First resonance. (**b**). Second resonance.

The figures show graphs of the three principal minors of the matrix $\boldsymbol{D}$ of the equation (4.37) versus the frequency ν. Asymptotic stability requires that all three minors be positive. The value of the first minor is shown in blue, the value of the second in red and the third in green. For comparison, calculations are given when only the first two vibration modes were taken into account. In this case, the figure shows the first two minors of the $\boldsymbol{D}$ matrix, in blue and red, respectively. The results for an inflexible compressible rod are also shown, one curve in blue. And a graph is given for an inflexible compressible rod without taking into account compressibility $(c_{ij}(\nu) = c_{ij}(0) = b_i\delta_{ij})$ – a cyan line.

Graphs in Fig. 4.4(a,b,c) show the stability conditions for a rod with low flexibility $P_D = 0.1$ at $\hat{q} = 1$ in case of taking into account three, two and one mode of vibrations respectively. We see that, taking into account the three modes of oscillation, the pendulum becomes stable in the region between the first and fourth resonances, where the inflexible rod was unstable.

If at $P_D = 0.1$ we decrease the parameter $\hat{q}$ associated with the force of gravity, then for the calculation by the first form of vibrations, on the graph (Fig. 4.4(c)) between the third and fourth resonances, we obtain the stability region. Between the second and third resonances, the region of instability will remain.

Figure 4.5(a,b,c) shows the stability conditions for a highly flexible rod $P_D = 100$ at $\hat{q} = 1$. The flexibility parameter does not affect the results for the first waveform, and Fig. 4.5(c) is the same as Fig. 4(c). As P_D increases, the instability regions expand, and the negative values of the second and third principal minors increase in absolute value. Also, with the growth of P_D, an interesting effect appears – negative peaks of the graphs not far from the resonances. If we compare the magnitude of the negative green peak (D_{III}), which has the order of $\sim 10^{-3}$ (Fig. 4.5a), with the magnitude of the negative blue region (D_I) for of the first form (Fig. 4.5c), then it should be taken into account that the value of the third principal minor of the matrix is the sum of the cubes of its elements, that is, the elements themselves, on average, have the order of $\sim 10^{-1}$. Figure 4.5(d,e,f) shows the stability conditions for a large gravity parameter $\hat{q} = 10$ for a rod with medium flexibility $P_D = 10$. We see that
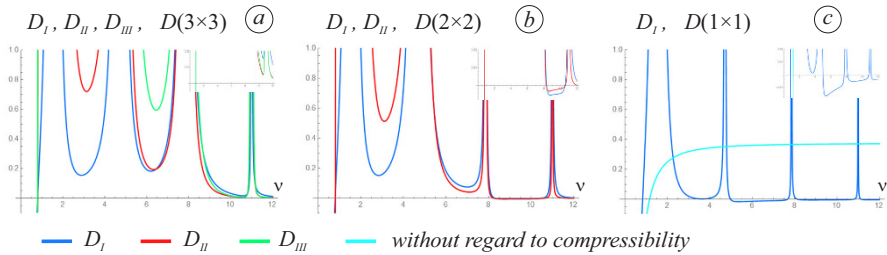
Fig. 4.4: The principal minors of the matrix $\boldsymbol{D}$. The stability condition is the positive definiteness of the matrix. (**a**) Accounting for three forms. (**b**) Accounting for two forms. (**c**) Accounting for one form according to the compressible pendulum model (blue line) and without taking into account compressibility, $c_{11}(\nu) = b_1$, (cyan line).
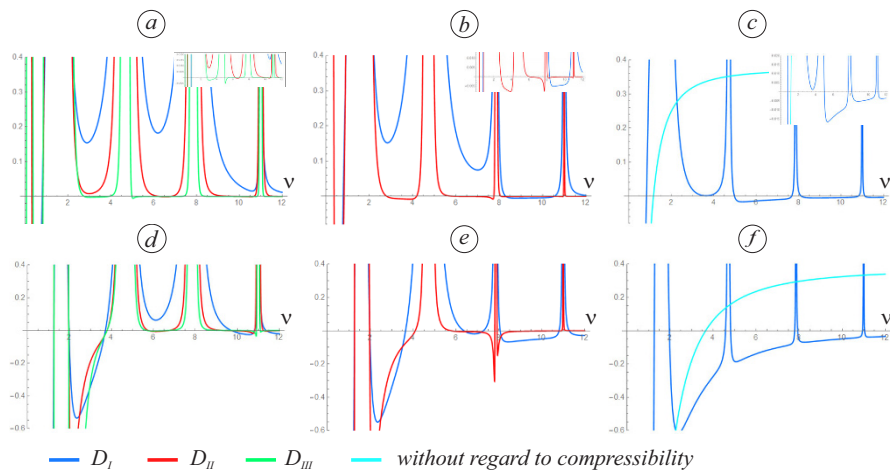
Fig. 4.5: Principal minors of the matrix $\boldsymbol{D}$. $(\boldsymbol{a}, \boldsymbol{b}, \boldsymbol{c})$ – $P_D = 100$, $\hat{q} = 1$. $(\boldsymbol{d}, \boldsymbol{e}, \boldsymbol{f})$ – $P_D = 10$, $\hat{q} = 10$.

taking into account the second and third vibration modes gives wider stability regions in the region of the second and third resonances.

4.6.3 Comparison with the Exact Solution

Comparing the results of calculation by the approximate (4.37) and exact (4.27) formulas, we found out that the value of the small parameter $\varepsilon = a/L$ of the order of 0.1 does not always ensure the agreement of the obtained results. But for $\varepsilon \sim 0.01$ the obtained results agree. Let us take the problem parameters from Fig. 4.4 and calculate the motion of the pendulum at $\nu = 7.27$ with the given dimensionless initial deviation according to the first form. Previously, we found that for a given value of ν, counting only in the first form gives the instability of the system, and when all three forms are taken into account, stability. On Fig. 4.6. graphs of fluctuations of three variables $w_i(t)$ and three averaged functions $U_{0i}(\theta)$ for $\varepsilon = 0.005$ and $\varepsilon = 0.05$ are shown. We see that for insufficiently small ε the obtained results do not coincide. When calculating taking into account only the first form, both results turned out to be unstable (not shown on the graphs), which is consistent with the result of Fig. 4.4c.

For small values of P_D, small amplitudes of the second and third vibration modes are obtained in the process of movement, if the rod is initially deflected according to the first mode. As the parameter P_D, which is responsible for the flexibility of the rod, increases, the amplitudes of higher frequencies noticeably increase. Three calculation results obtained with the same other parameters and different values of P_D are shown in the graph (Fig. 4.7).
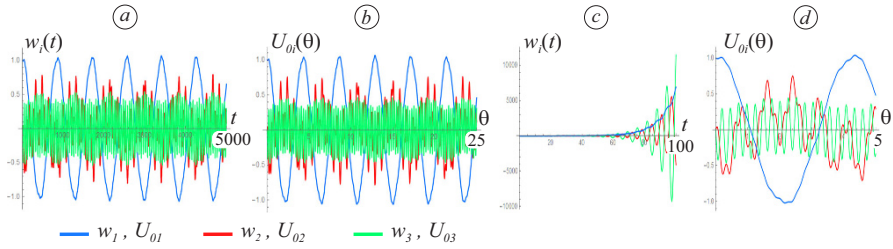
Fig. 4.6: Vibration forms of the rod at $\nu = 7.27$, $\hat{q} = 1.05$, $P_D = 0.1$, $\beta = -\pi/2$, $w_{01} = 1, w_{02} = 0, w_{03} = 0$. (**a**) $\varepsilon = 0.005$, $w_i(t)$, $t \in (0, 5000)$. (**b**) $\varepsilon = 0.005$, $U_{0i}(\theta)$, $\theta \in (0, 25)$. (**c**) $\varepsilon = 0.05$, $w_i(t)$, $t \in (0, 100)$. (**d**) $\varepsilon = 0.05$, $U_{0i}(\theta)$, $\theta \in (0, 5)$.
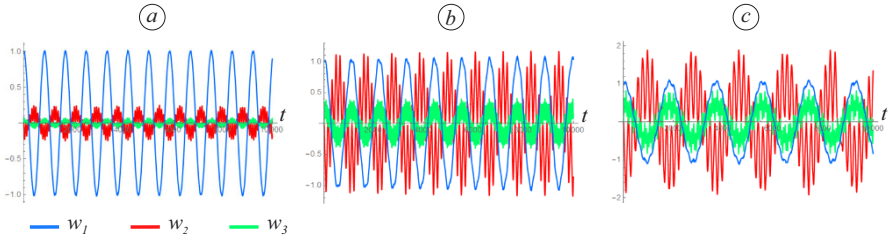
Fig. 4.7: The results of the calculation of pendulum oscillations at $\nu = 3$, $\hat{q} = 0.18$, $\varepsilon = 0.01$, $t = 10000$, $\beta = -\pi/2$, $w_{01} = 1, w_{02} = 0, w_{03} = 0$. (**a**) $P_D = 0.1$. (**b**) $P_D = 1$. (**c**) $P_D = 10$.

4.6.4 Conclusions

The problem of stability of the generalized Kapitsa pendulum for a flexible rod is solved in the zero asymptotic approximation, taking into account longitudinal resonances. The regions of stability are found taking into account three modes of oscillation of the rod, as well as the effects of the influence of the second and third forms of bending oscillations on the stability of the pendulum. Four dimensionless parameters that affect the dynamics of the pendulum model are determined. It is shown that taking into account the second and third forms of transverse oscillations can change the picture of the stability of a compressible pendulum, despite the fact that this pendulum can be rigid enough not to lose static stability in these forms.

The parameter ε affects the dynamics of the pendulum, but is not included in the asymptotic stability conditions. For insufficiently small ε, the accuracy of the asymptotic method will decrease.

Even with a sufficiently rigid pendulum that does not lose static stability in the second form, under the influence of vibrations of the base we obtain not small transverse oscillations in the second and third forms.

4.7 Some Hypotheses Regarding the Possible Application of the Kapitsa Pendulum Effect in Modern and Advanced Technology

If we look at the effect of the Kapitsa pendulum as the effect of stabilizing the system in some specific state, which requires a multifactorial impact on the system on two (or several) scales at once, both in time and in space, then what future do we see in its application? The invention of new materials and the improvement of the accuracy of manufacturing parts will make it possible to increase the speed and energy, and, consequently, the efficiency of new installations operating in a two-scale mode.

Various combinations of the Kapitsa effects with gyroscopic effects can give rise to new devices for stabilizing spacecraft while moving along a chosen course.

We see the deepening of the possibilities of mechatronics, when with the use of new materials the ability to convert mechanical motion into electrical motion and use it in various sensors and other mechatronic devices, up to the damping of mechanical vibrations by generating electrical energy, expands.

Vibration effect, perhaps, will be achieved, for example, the orientation of protein molecules in solution and the construction of protein structures of given parameters. It can be assumed that the technologies for the separation of heavy metal isotopes based on the principle of the difference in the atomic masses of the nuclei of elements will be developed with the use of combinations of vibrational effects.

In elementary particle physics, the problem of both stabilizing and compactifying a beam of charged beam and streamlining the motion of particles in a beam in circular accelerators continues to be relevant. At the moment, particle acceleration is carried out due to the synchronous acceleration effect [30], in which particles pass through the accelerating intervals of the accelerator in approximately the same phase of the accelerating phase of the magnetic field. The introduction of yet another high-frequency electric field matched to the magnetic field is a theoretically real and interesting possibility for solving this problem.

References

[1] Stephenson A (1908) XX. On induced stability. The London, Edinburgh, and Dublin Philosophical Magazine and Journal of Science **15**(86):233–236
[2] Erdélyi A (1934) Über die kleinen Schwingungen eines Pendels mit oszillierendem Aufhängepunkt. ZAMM - Journal of Applied Mathematics and Mechanics / Zeitschrift für Angewandte Mathematik und Mechanik **14**(4):235–247
[3] Hirsch P (1930) Das Pendel mit oszillierendem Aufhängepunkt. ZAMM - Journal of Applied Mathematics and Mechanics / Zeitschrift für Angewandte Mathematik und Mechanik **10**(1):41–52
[4] Lowenstern E (1932) XXXIX. The stabilizing effect of imposed oscillations of high frequency on a dynamical system. The London, Edinburgh, and Dublin

Philosophical Magazine and Journal of Science **13**(84):458–486

[5] Strutt MJ (1927) Stabiliseering en labiliseering door trillingen. Physica **7**:265–271

[6] van der Pol B (1925) Stabiliseering door kleine trillingen. Physica **5**:157–162

[7] van der Pol B, Strutt MJO (1928) II. On the stability of the solutions of Mathieu's equation. The London, Edinburgh, and Dublin Philosophical Magazine and Journal of Science **5**(27):18–38

[8] Bogatov EM, Mukhin RR (2017) The averaging method, a pendulum with a vibrating suspension: N.N. Bogolyubov, A. Stephenson, P.L. Kapitza and others (in Russ.). Izvestiya VUZ Applied Nonlinear Dynamics **25**(5):69–87

[9] Bogoliubov NN (1950) Perturbation theory in nonlinear mechanics (in Russ.). Proceedings of the Institute Builds Mechanics Academy of Sciences of the Ukrainian SSR **14**:9–34

[10] Kapitsa PL (1951) The pendulum in vibrating support (in Russ.). Uspekhi Fizicheskikh Nauk **44**(1):7–20

[11] Kapitza PL (1965) Chapter 45 - Dynamical stability of a pendulum when its point of suspension vibrates. In: Ter Haar D (ed) Collected Papers of P.L. Kapitza, vol 2, Pergamon, pp 714–725

[12] Landau LD, Lifshitz EM (1976) Mechanics, vol 1, 3rd edn. Butterworth-Heinemann

[13] Chelomei VN (1983) Mechanical paradoxes caused by vibrations (in Russ.). Doklady Akademii Nauk SSSR **270**(1):62–67

[14] Arnold VI (2014) Mathematical Understanding of Nature: Essays on Physical Phenomena and Their Understanding by Mathematicians. American Mathematical Society, Providence, RI

[15] Blekhman II (2000) Vibrational Mechanics. World Scientific, Singapore

[16] Li M, Aoyama T, Hasegawa Y (2020) Gait modification for improving walking stability of exoskeleton assisted paraplegic patient. Robomech Journal **7**(1):21

[17] Fradkov AL (2005) Application of cybernetic methods in physics. Physics-Uspekhi **48**(2):103

[18] Richards CJ, Smart TJ, Jones PH, Cubero D (2018) A microscopic Kapitza pendulum. Scientific Reports **8**(1):13,107

[19] Abramowitz M, Stegun I (eds) (1964) Handbook of Mathematical Functions, Applied Mathematics Series, vol 55. National Bureau of Standards, Gaithersburg, MD

[20] Acheson DJ (1993) A pendulum theorem. Proceedings: Mathematical and Physical Sciences **443**(1917):239–245

[21] IPME (2023) Institute for Problems in Mechanical Engineering of the Russian Academy of Sciences. Articles Laboratorys. Indian rope trick. https://ipme.ru/en/183-indiiskaja-magicheskaja-veryovka.html, accessed 19 Apr 2023

[22] IPME (2023) Institute for Problems in Mechanical Engineering of the Russian Academy of Sciences. Articles Laboratorys. Stephenson-Kapitza pendulum with an additional degree of freedom. https://ipme.ru/en/184-majatnik-

stefensona-kapicy-s-dopolnitelnoi-stepenyu-svobody.html, accessed 19 Apr 2023

[23] Belyaev AK, Morozov NF, Tovstik PE, Tovstik TP (2018) Stability of a Vertical Rod on a Vibrating Support. Vestnik St Petersburg University, Mathematics **51**(3):296–304

[24] Belyaev AK, Morozov NF, Tovstik PE, Tovstik TM, Tovstik TP (2021) Classical Kapitsa's problem of stability of an inverted pendulum and some generalizations. Acta Mechanica **323**(5):1743–1759

[25] Belyaev AK, Polyakova OR, Tovstik TP (2023) The effect of longitudinal oscillations resonance on stability and domains of attraction in the generalized kapitsa problem. In: Altenbach H, Mkhitaryan SM, Hakobyan V, Sahakyan AV (eds) Solid Mechanics, Theory of Elasticity and Creep, Advanced Structured Materials, vol 185, Springer International Publishing, Cham, pp 93–100

[26] Kulizhnikov DB, , Tovstik PE, Tovstik TP (2019) The Basin of Attraction in the Generalized Kapitsa Problem. Vestnik St Petersburg University, Mathematics **52**(3):309–316

[27] Morozov NF, Belyaev AK, Tovstik PE, Tovstik TP (2018) Stability of a Vertical Rod on a Vibrating Support. Physics - Doklady **63**(9):380–384

[28] Svetlitsky VA (2000) Mechanics of Flexible Rods (in Russ.). Publ. MAI, Moscow

[29] Andrianov IV, Barantsev RG, Manevich LI (2004) Asymptotic Mathematics and Synergetics (in Russ.). URSS, Moscow

[30] Veksler VI (1944) A new method for accelerating relativistic particles (in Russ.). Doklady Akademii Nauk SSSR **43**(8):346–348

Chapter 5
Dynamic Properties of Periodic Structures with Symmetric Inclusions

Ludmila Ya. Banakh and Igor S. Pavlov

Abstract Oscillations and waves in multisection periodic systems with symmetric subsystems are investigated. Many engineering systems, building structures, as well as models of acoustic metamaterials have a similar structure. The structure of the natural frequency spectrum for such a class of systems is found, taking into account the elastic properties of the constituent subsystems. It is shown that such systems have band gaps of a harmonic signal and the dispersion curve consists of n branches according to the number of degrees of freedom in the subsystem. The boundaries of the harmonic signal band gaps have been found in the analytical form. Vibration modes have been obtained in different frequency ranges. Modulated waves are shown to arise in the system due to modulation by lower frequencies that correspond to system oscillations without taking into account the elasticity of the constituent subsystems. In the analysis of symmetric structures, the theory of groups is used in combination with wave dispersion equations.

Ludmila Ya. Banakh

Mechanical Engineering Research Institute of Russian Academy of Sciences, 4 Mal. Kharitonjevsky str., 101990 Moscow & Mechanical Engineering Research Institute of the Russian Academy of Sciences– Branch of Federal Research Center "Institute of Applied Physics of the RAS", 85 Belinsky str., 603024 Nizhny Novgorod, Russian Federation,
e-mail: banl@inbox.ru

Igor S. Pavlov

Mechanical Engineering Research Institute of the Russian Academy of Sciences– Branch of Federal Research Center "Institute of Applied Physics of the RAS", 85 Belinsky str., 603024 Nizhny Novgorod & National Research Lobachevsky State University of Nizhny Novgorod, 23 Gagarin av., 603950 Nizhny Novgorod, Russian Federation,
e-mail: ispavlov@mail.ru

5.1 Introduction

Multisection periodic systems composed of identical subsystems are of great interest in mechanics. Generating subsystems (inclusions) can have a various structure, for example, periodic or symmetrical. Multisection systems with periodic inclusions are studied in [1]. A dispersion equation has been obtained, band gaps of a harmonic signal have been found, and vibration modes have been classified for them.

Dynamic properties of periodic systems with symmetric inclusions are investigated in this article. Such systems are widely used in engineering practice. Really, some features of the dynamic behavior of symmetric systems make their application extremely convenient. So, such systems are characterized by independence between translational and rotational displacements, moreover, there is a "calm" point during the rotational vibrations - the center of symmetry that is very important for vibration isolation of equipment.

Engineering applications of periodic systems with symmetrical inclusions are found in various fields of mechanical engineering. Layered space grids (typically double-layer and triple-layer configurations) having a high degree of symmetry are used as roofs for industrial warehouses, exhibition pavilions, and indoor sports complexes [2]. Vibrations of polygonal ducts are investigated in [3] using the group theoretic approach.

Longitudinal elastic vibrations of multistage liquid-propellant launch vehicle body are studied in [4]. The use of symmetry properties made possible to reduce the corresponding vibration modes to launch vehicle stabilization planes.

The dynamics of the planetary gearbox having a high degree of geometric symmetry is analyzed in [5]. Using the group-theoretic approach, generalized oscillation modes of the gear elements are found, including differential gear, satellites, and epicycle. It is shown that errors in engagement cause asymmetry of the system that leads to the interaction of vibration modes and degrades the quality of the gearbox. Three-dimensional, but shallow cable net, formed by two families of highly tensioned cables is considered in [6].

Structures with geometric symmetry are widely used in industrial and civil engineering as supporting and frame structures (see, for instance, [7]). Such types of structures are the frame of the bored pile (Fig. 5.1a) and frame scaffolding (Fig. 5.1b).

In [8] the group theory is extended to asymmetric systems with multiple symmetric stages. Symmetry of any component stage is arbitrary, including cyclic and dihedral symmetry. The theory of groups for elastic structural problems is discussed in [9]. As examples, classic bifurcation problems including isotropic and composite laminate panels under compression loading are investigated. The resonant vibrations in weakly coupled nonlinear identical cyclic symmetric structures are studied in [10]. A careful bifurcation analysis of the amplitude equations is performed in the fundamental resonance case for an illustrative example consisting of a three-particle system. The role of coupling strength in creating/destroying localized solutions is discussed. The paper [11] reviews the advances made in the application of group theory in areas such as bifurcation analysis, vibration analysis and finite element analysis, and summarizes the various implementation procedures currently available.

(a)
(b)
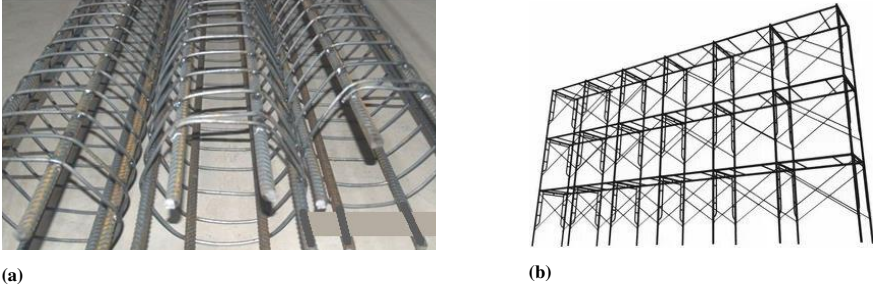
Fig. 5.1: Support and frame structures: (a) a bored pile skeleton with hexagonal frames, (b) frame scaffolding.

A wide class of systems with symmetric inclusions is also represented by systems with rotating symmetry, particularly, rotor systems with bladed-disk assemblies. A lot of references (see, for example [12–14]) are devoted to computational, experimental and theoretical investigations of oscillations of such systems. Engineering applications of periodic systems with symmetrical inclusions can be also acoustic and vibro-insulating metamaterials [15].

The dynamic model of an acoustic metamaterial representing a symmetrical one-dimensional lattice with local resonators coupled through linear springs of three types (Fig. 5.2) is considered in [16]. Such a system is shown to have three band gaps. Parameters are found to achieve the maximum total width of the band gap in the low-frequency range.

The model of an acoustic metamaterial, which represents a chain of "cantilevers-in-mass", is proposed in [17]. Analysis of this model has confirmed the efficiency of damping stress waves at a certain resonance frequency. An acoustic metamaterial beam (AMB) based on the normal square grid structure with local resonators possessing both flexible band gaps and high static stiffness is studied in [18] (Fig. 5.3). Such a structure is widely used in architectural and mechanical field for its high strength and saving material, as well as for vibration control.

In addition to one-dimensional models of acoustic metamaterials, two-dimensional models are often used. Thus, a lattice consisting of square particles has been considered in [19]. Based on the division of this lattice into two sublattices, a two-field model has been developed, within which the frequency band gaps are found.
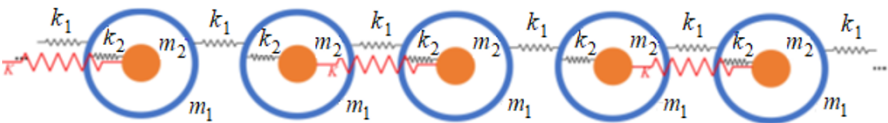
Fig. 5.2: The acoustic metamaterial model as a 1D "mass-in-mass" lattice with three types of springs [16].

Fig. 5.3: The geometry of square grid structure with internal resonators [18].

At present, the structures of metamaterials are becoming more and more compact, thin-walled, therefore approaches to the analysis of the physical and mechanical properties of such materials should be improved. They must take into account elastic properties of inclusions in various frequency ranges. In order to analyze wave processes in infinite periodic structures, impedance approaches have also been developed [20].

The purposes of this article are to study the vibrational and wave properties of periodic structures with symmetrical inclusions and to reveal the spectrum structure, taking into account an elasticity of inclusions. To this goal, the article proposes a method for deriving a dispersion equation for such systems. The combination of the mathematical apparatus of the group theory with dispersion equations, which has been presented in the article, enables one identifying the modulated oscillation modes of the entire system and finding the band gaps of the harmonic signal, as well as the frequency ranges corresponding to various modes of elastic oscillations of the constituent subsystems. In this case, it becomes possible to consider discrete models in the high-frequency range without their continualization and to identify additional frequency band gaps, furthermore, in an analytical form, using only the elastic properties of inclusions. As it will be shown below, despite the variety of components and engineering applications, periodic systems with inclusions are well predicted and, what is especially important, admit the analytical solutions.

Let us now describe the methods of analysis of symmetric systems. The universal method for studying systems with a discrete symmetry is the group representation theory [21–24]. Group-theoretic approaches are widely used in theoretical physics and chemistry. Recently, as it can be seen from the given above review, these methods have also been successfully used in problems of mechanics. Indeed, this approach enables one finding the main features of the behavior of systems using only symmetry properties without solving the motion equations. In addition, it also comprises the prediction and systematization of all possible oscillation modes provided by the symmetry of a given type, the selection of nodal lines and stationary points, as well as the separation of multiple frequencies. In this case, structural elements, which are not sensitive to the effects of certain loads, as well as multiple frequencies that cause system instability, are easily identified.

An addition from an engineering point of view the main attraction of group-theoretic methods has been their potential to reduce computational effort in the
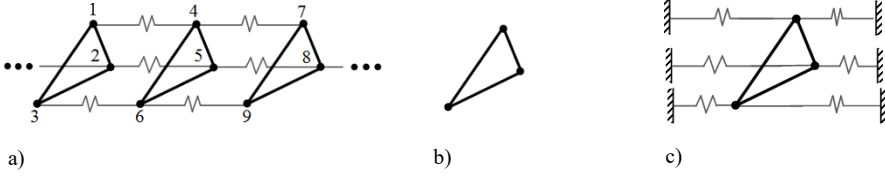
Fig. 5.4: A multi-section system with symmetrical subsystems: a) a general view, b) a subsystem with free ends, c) a subsystem with fixed ends.

analysis of large-scale problems. The use of finite element approaches is especially effective in this case.

In the group theory, projective symmetry operators $\boldsymbol{P}$ and basis vectors $\boldsymbol{V}$ are used. The coordinate transformation $\boldsymbol{V} = \boldsymbol{Px}$ decomposes the initial n-dimensional space of the problem into independent invariant subspaces, each of which corresponds to its own symmetry operation. We employed earlier the group representation theory to study oscillations of multidimensional mechanical systems [21]. The description of these approaches on the example of a mechanical system with triangle-type symmetry is given in Appendix. More detailed information about the application of group theory for mechanical systems is available, for example, in [22, 23]. In this paper, we consider multi-section systems with symmetric subsystems of the n-gon type (Fig.5.4).

5.2 Oscillations of Symmetric n-gon Frames

Before proceeding to the dynamic analysis of the multi-section system shown in Fig. 5.4, we describe the group-theoretic approach employed by us using the example of bending vibration analysis for a hexagonal frame in the (x, y)-plane (Fig. 5.5). Let the frame be made up of beam elements. In this case, it is convenient to obtain governing equations using the Finite-Element Method (FEM) in the analytical form [21]. Let us assume without loss of generality that each span of the frame 1-2-...-6 can be represented as one finite element.

The stiffness matrix for a plane beam element (Fig. 5.5c) has the form [25]-[26]:

$$
\boldsymbol{K} = \begin{bmatrix} \boldsymbol{K}^{11} & \boldsymbol{K}^{12} \\ \boldsymbol{K}^{21} & \boldsymbol{K}^{22} \end{bmatrix}, \quad \boldsymbol{K}^{11} = \begin{bmatrix} \dfrac{12EI}{l^3} & \dfrac{6EI}{l^2} \\ \dfrac{6EI}{l^2} & \dfrac{4EI}{l} \end{bmatrix},
$$

$$
\boldsymbol{K}^{12} = \boldsymbol{K}^{T21} = \begin{bmatrix} -\dfrac{12EI}{l^3} & -\dfrac{6EI}{l^2} \\ \dfrac{6EI}{l^2} & \dfrac{2EI}{l} \end{bmatrix}, \quad \boldsymbol{K}^{22} = \begin{bmatrix} \dfrac{12EI}{l^3} & -\dfrac{6EI}{l^2} \\ -\dfrac{6EI}{l^2} & \dfrac{4EI}{l} \end{bmatrix}.
\tag{5.1}
$$
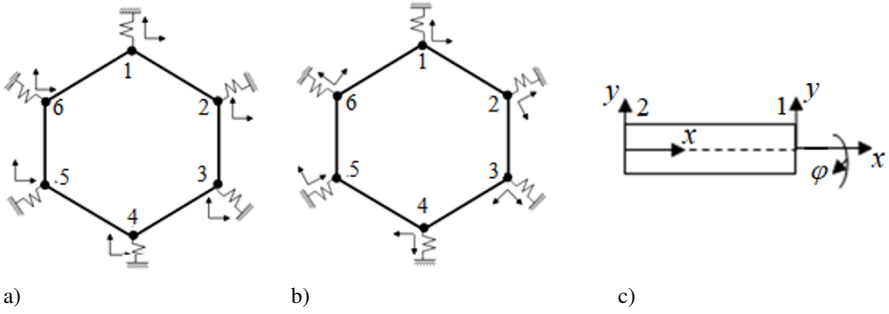
Fig. 5.5: The symmetrical frame: a) an initial coordinate system for each node, b) a coordinate system symmetrical with respect to each node, c) a beam finite element: y_1 and y_2 are displacements of the 1st and 2nd ends of the beam element, φ is the rotation angle.

K^{ij} are blocks of stiffness and inertia matrices of the finite element for the 1st and 2nd beam ends, respectively. The motion of each node is described by vector Y_s with coordinates $[y_s, \varphi_i]$, where y_s is the displacement of the i-th node and φ_s is the rotation angle. Expressions (5.1) coincide with the static stiffness matrix of the beam [21]. In the low-frequency range, it is possible to model the beam by one finite element, if the length of the finite element is $a < L/4$, where L is the wavelength.

Traditionally, the directions of the coordinate axes are chosen in FEM uniformly for each node (Fig. 5.5a). But for the practical application of group-theoretic approaches, it is much more convenient to choose a local coordinate system located symmetrically with respect to each node (Fig. 5.5b) [21]. In these axes, the matrix describing the vibrations of a symmetrical frame takes on an especially simple form. So, for a hexagonal frame shown in Fig. 5.5b it has the form

$$D = \begin{bmatrix} a_{11} & a_{12} & 0 & 0 & 0 & a_{21} \\ a_{21} & a_{11} & a_{12} & 0 & 0 & 0 \\ 0 & a_{21} & a_{11} & a_{12} & 0 & 0 \\ 0 & 0 & a_{21} & a_{11} & a_{12} & 0 \\ 0 & 0 & 0 & a_{21} & a_{11} & a_{12} \\ a_{12} & 0 & 0 & 0 & a_{21} & a_{11} \end{bmatrix} - \lambda M, \tag{5.2}$$

where $a_{11} = \theta_\vartheta^{tr} K_{11}\theta_\vartheta + \theta_{-\vartheta}^{tr} K_{22}\theta_{-\vartheta} + k$, $a_{12} = a_{21}^{tr} = \theta_\vartheta^{tr} K_{12}\theta_{-\vartheta}$, and $\vartheta = 2\pi/6$. Here

$$\theta_\vartheta = \begin{bmatrix} \cos\vartheta & -\sin\vartheta \\ \sin\vartheta & \cos\vartheta \end{bmatrix}$$

is the matrix for rotation of local coordinate axes of finite elements by angle ϑ.

The coordinates $X' = (x', y')$ in the "symmetrical" coordinate system (Fig. 5.5b) are related with the coordinates $X = (x, y)$ in the traditional coordinate system (Fig. 5.5a) by the equation

$$X' = \boldsymbol{\theta}X,$$

where

$$\boldsymbol{\theta} = \operatorname{diag} \boldsymbol{E} \quad \boldsymbol{\theta}_\vartheta \ \dots \ \boldsymbol{\theta}_{5\vartheta}.$$

The form of matrix (5.2) is quite obvious from symmetry considerations, since each node is completely identical in the chosen "symmetric" coordinate system. Further, a "symmetric" coordinate system will be used in the article.

For a hexagon, the projective operator, as follows from (5.11), has the form:

$$\boldsymbol{V}_6 = \boldsymbol{P}_6\boldsymbol{X}, \ \boldsymbol{P}_6 = \frac{1}{6} \begin{bmatrix} 1 & 1 & 1 & 1 & 1 & 1 \\ 2 & 1 & -1 & 2 & -1 & 1 \\ 1 & 2 & 1 & -1 & -2 & -1 \\ 2 & -1 & -1 & 2 & -1 & -1 \\ -1 & 2 & -1 & -1 & 2 & -1 \\ 1 & -1 & 1 & -1 & 1 & -1 \end{bmatrix} \tag{5.3}$$

It follows from the form of the operator $\boldsymbol{P}_6$ and the basis vectors $\boldsymbol{V}_i$ (5.3) that the lowest vibration mode corresponds to the motion of all nodes in phase and the highest one is in antiphase, whereas the natural frequencies of the remaining vibration modes are multiples of two. The presence of multiple roots is a characteristic feature of symmetrical structures, and this leads to their oscillation instability at these frequencies.

Applying group transformation (5.3) to matrix (5.2), one can obtain a block-diagonal matrix $\boldsymbol{D^*}_6$, i.e. splitting of the original matrix into independent blocks, that greatly simplifies both the calculation and the analysis of symmetric systems.

$$\boldsymbol{D^*} = \boldsymbol{P}^{tr}\boldsymbol{D}\boldsymbol{P} = \begin{bmatrix} \boldsymbol{A}_{11} & & & & & \\ & \boldsymbol{A}_{22} & \boldsymbol{A}_{23} & & & \\ & \boldsymbol{A}_{32} & \boldsymbol{A}_{33} & & & \\ & & & \boldsymbol{A}_{44} & \boldsymbol{A}_{45} & \\ & & & \boldsymbol{A}_{54} & \boldsymbol{A}_{55} & \\ & & & & & \boldsymbol{A}_{66} \end{bmatrix} - \lambda\boldsymbol{M^*},$$

where

$$A_{11} = a_{11} + a_{12} + a_{21}, \ \ A_{44} = 6a_{11} - a_{12} - a_{21}.$$

Here, block $\boldsymbol{A}_{11}$ describes the in-phase oscillations of all nodes and block $\boldsymbol{A}_{66}$ characterizes the anti-phase oscillations, whereas the double blocks correspond to multiple frequencies.

5.3 Oscillations of Periodic Systems Containing Symmetric Subsystems

Let us now determine a structure of frequency spectrum for an infinite periodic system with symmetrical inclusions (Fig. 5.4). First, we introduce the designations: k_1 is the stiffness along the z-axis for elastic elements connecting the frame nodes, k_2 is the rigidity of springs between the frames, and m is mass of each node. We consider the longitudinal vibrations of the system, assuming for the convenience of analytical calculations that each node has one degree of freedom. For a triangle $n = 3$, we find the basis vectors (5.12)

$$V = PX, \quad P = \frac{1}{3}\begin{bmatrix} 1 & 1 & 1 \\ 2 & -1 & -1 \\ -1 & 2 & -1 \end{bmatrix}. \tag{5.4}$$

In order to obtain the oscillation equations for the system of Fig. 5.5a, we divide the variables into three groups according to the number of disks in a section. Taking into account (5.3), we will search for a solution in the form of harmonic functions by Floquet's theorem

$$x_{3s} = b_1 e^{i(\omega t - 3s\,\mu)}, \quad x_{3s-1} = b_2 e^{i[\omega t - (3s-1)\,\mu]}, \quad x_{3s-2} = b_3 e^{i[\omega t - (3s-2)\,\mu]}, \tag{5.5}$$

where μ is the propagation constant. In the "symmetric" reference frame, the equations for the s-th subsystem take on the form:

$$\begin{aligned}
m\ddot{x}_{3s} + k_{11}x_{3s} - k_1 x_{3s-1} - k_1 x_{3s-2} - k_2 x_{3s-3} - k_2 x_{3s+3} = 0, \quad 3s = 3, 6, \dots; \\
m\ddot{x}_{3s-1} + k_{11}x_{3s-1} - k_1 x_{3s-2} - k_1 x_{3s} - k_2 x_{3s-4} - k_2 x_{3s+2} = 0, \quad 3s - 1 = 2, 5, \dots; \\
m\ddot{x}_{3s-2} + k_{11}x_{3s-2} - k_1 x_{3s-2} - k_1 x_{3s-1} - k_2 x_{3s-5} = 0, \quad 3s - 2 = 1, 4, \dots
\end{aligned} \tag{5.6}$$

$k_{11} = 2k_{12} + k_{13}$ is the total stiffness of the elements included in the i-th node ($i = 1, 2, 3$).

From (5.5) and (5.6) the characteristic equation yields:

$$D = \begin{bmatrix} A - k_2\left(e^{-3i\mu} + e^{3i\mu}\right) & -k_1 e^{-i\mu} & -k_1 e^{-2i\mu} \\ -k_1 e^{i\mu} & A - k_2\left(e^{-3i\mu} + e^{3i\mu}\right) & -k_1 e^{-i\mu} \\ -k_1 e^{2i\mu} & -k_1 e^{i\mu} & A - k_2\left(e^{-3i\mu} + e^{3i\mu}\right) \end{bmatrix} = 0, \tag{5.7}$$

where $A = -m\omega^2 + k_{11}$. Expanding the determinant in (5.7), we obtain

$$(A - 2k_2 \cos 3\mu)^3 - 2k_1^3 - 2k_1^2(A - 2k_2 \cos 3\mu) = 0. \tag{5.8}$$

The relationship (5.8) is a periodic dispersion equation. Its period equals $\pi/3$, therefore the limiting wavelength $L_{\lim}$ corresponds to $\mu = \pi/3$. For each wavelength μ there are three frequencies ω. Hence, the dispersion curve consists of three segments, each of which corresponds to its own vibration mode of the triangular frame.

Thus, the straight lines $\mu = 0$ (the ordinate axis) and $\mu = \pi/3$ are limiting for the dispersion curve. Let us find the limiting points on these axes. For $\mu = 0$, equation (5.8) can be rewritten in the form

$$\boldsymbol{D} = \begin{bmatrix} -m\omega^2 + 2k_1 & -k_1 & -k_1 \\ -k_1 & -m\omega^2 + 2k_1 & -k_1 \\ -k_1 & -k_1 & -m\omega^2 + 2k_1 \end{bmatrix} = 0, \tag{5.9}$$

which corresponds to the equation for vibrations of the frame subsystem with free ends (Fig. 5.4b). Using the basis vectors for the triangle (5.4), we reduce Eq. (5.9) to a diagonal form and find the points of the dispersion curve on the axis $\mu = 0$:

$$\omega_1 = 0, \quad \omega_2 = \omega_3 = (3k_1/m)^{1/2}.$$

In order to find the limiting points ω_1^* and $\omega_2^* = \omega_3^*$ on the axis $\mu = \pi/3$, we obtain the following equation from Eqs. (5.6) and (5.7):

$$\boldsymbol{D} = \begin{bmatrix} -m\omega^2 + 2k_1 + 4k_2 & -k_1 & -k_1 \\ -k_1 & -m\omega^2 + 2k_1 + 4k_2 & -k_1 \\ -k_1 & -k_1 & -m\omega^2 + 2k_1 + 4k_2 \end{bmatrix} = 0. \tag{5.10}$$

Equation (5.10) corresponds to oscillations of an isolated subsystem with fixed ends (Fig. 5.4c). It should be noted that for an isolated section (but not for the system as a whole) its boundary passes in the middle of the elastic element k_2 connecting the sections, therefore its stiffness equals $2k_2$. From Eq. (5.10) the limiting points are similarly determined on the straight line $\mu = \pi/3$. Thus, we have found all the limiting points of the dispersion curve without solving the system as a whole, but only using the oscillation frequencies of an isolated section under various boundary conditions.

The dispersion curves have been plotted in Fig. 5.6 using Eqs. (5.6) and (5.7), as well as the relations for limiting points. Thus, the dispersion curve consists of two branches, each of which corresponds to its own oscillation mode of the section. There is a band gap for the harmonic signal between these branches in the frequency range
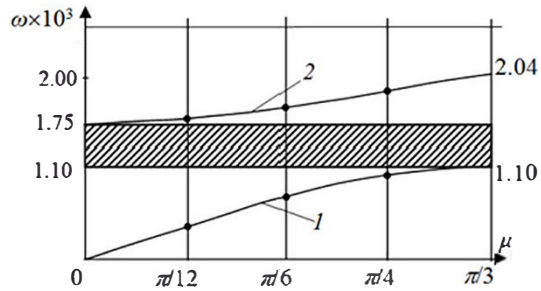
Fig. 5.6 Dispersion curves of the multi-section system shown in Fig. 5.4: 1 and 2 are parts of the dispersion curves. The shading marks the frequency band gap of the harmonic signal.

$$\omega_1^* < \omega < \omega_2.$$

Since the dispersion curve does not depend on the boundary conditions, the harmonic signal is attenuated in this range under any boundary conditions, that ensures good vibroisolation for the entire system.

5.4 An Example of Calculation of a 3-Section System with Symmetric Subsystems

Let us consider as an example a 3-section system (Fig. 5.7). The system parameters are as follows: $k_1 = 1 \times 10^5$ N/m, $k_2 = 0.3 \times 10^5$ N/m, $m = 1$ kg. Due to the Matrix Calculator program, vibration frequencies and modes have been found for this system (Table 5.1). As it is visible from the table, the three highest frequencies are multiples. The subsystem frequencies are as follows:

- for a subsystem with free ends: $\omega_1 = 0$, $\omega_2 = \omega_3 = (3k_1/m)^{1/2} = \sqrt{3}\,\text{sec}^{-1}$;
- for a subsystem with fixed ends: $\omega_1^* = 1.1\,\text{sec}^{-1}$, $\omega_2^* = \omega_3^* = 2.04\,\text{sec}^{-1}$.

Due to the multiplicity of natural frequencies, there are two branches of the dispersion curve plotted in Fig. 5.6. The low-frequency branch 1 corresponds to the system oscillations, in which the sections are not deformed. Oscillations of the
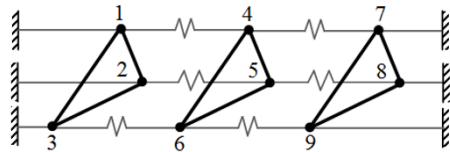
Fig. 5.7: A 3-section periodic system with symmetric subsystems of the triangle type

Table 5.1: Vibration frequencies and modes for the system given in Fig. 5.7.

Number of a node	The frequency s^{-1}								
	1	2	3	4	5	6	7	8	9
0.419	1	1	1	$\sqrt{2}$	$\sqrt{2}$	$\sqrt{2}$	1	1	1
0.77	-1	-1	-1	0	0	0	1	1	1
1.01	1	1	1	$-\sqrt{2}$	$-\sqrt{2}$	$-\sqrt{2}$	1	1	1
1.78	-1	1	0	$-\sqrt{2}$	$\sqrt{2}$	0	-1	1	0
(multiple)	-1	0	1	$-\sqrt{2}$	0	$\sqrt{2}$	-1	0	1
1.9	1	-1	0	0	0	0	-1	1	0
(multiple)	1	0	-1	0	0	0	-1	0	1
2	-1	1	0	$\sqrt{2}$	$-\sqrt{2}$	0	-1	1	0
(multiple)	-1	0	1	$\sqrt{2}$	0	$-\sqrt{2}$	-1	0	1

entire structure arise, in which the sections can be considered as a solid body. The high-frequency branch - 2 - describes modulated oscillations due to the interaction of elastic vibrations of the sections and low-frequency vibrations of the structure, without taking into account the elastic oscillations of the sections determined by the first branch of the dispersion curve. The frequency band gap of the harmonic signal in Fig. 5.6 is shaded.

In order to determine the natural frequencies, we assume that the system is rigidly fixed at the ends for $s = 1 - 3$ and $s = 7 - 9$. An equation $x_{3s} = C_1 \sin 3\mu s + C_2 \cos 3\mu s$ yields from Eq. (5.10). Assuming $x_0 = x_{3(n+1)} = 0$, one can find

$$\mu N + 1 = \pi j, \ j + 1 ... n.$$

Here $N = 3$ is the number of sections. Hence, $\mu = \pi/12, \pi/6, \pi/4$. Due to the equidistance of the spectrum of wave numbers μ, the joint solution of these equations can be easily found both numerically and graphically, as follows from Fig. 5.6. The natural frequencies (see Table 5.1) are determined by points of intersection of the lines $\mu = \pi/12, \pi/6$ and $\pi/4$ with the dispersion curve. In Fig. 5.6 they are marked with dots on the dispersion curve.

As it follows from Table 5.1, the three minimal frequencies lie on the lower branch of the dispersion curve, whereas the maximal frequencies (multiples) are located on the second branch. This fact completely corresponds to the theoretical results obtained in Sect. 5.2.

5.5 Structure of the Spectrum of Natural Frequencies of a Multisection Structure

Thus, the structure of the natural frequency spectrum is as follows:

1. the limiting points on the lines $\mu = 0$ and $\mu = \pi/3$, corresponding to the maximum and minimum wavelengths, are equal to the natural frequencies of the isolated section under different conditions of fixing;
2. the natural frequencies are divided into N groups, according to the number of sections. In each group the vibration modes have the same wavelength, but different frequencies, since they belong to various segments of the dispersion curve. In the system at issue, these are groups with frequency numbers (1, 4), (2, 5), (3, 6);
3. the dispersion curve is divided into n branches, each of which corresponds to its own vibration mode of the section.

There are two branches of the dispersion curve in the system at issue, since only two frequencies are different due to the multiplicity of the natural frequencies of the triangular frame. These are the following frequency subgroups: (1, 2, 3) and multiple frequencies (4, 5, 6). So, in the second subgroup, the oscillations of the sections occur according to the second vibration mode (Fig. 5.5).

Let us remark that there is a certain analogy in the structure of the spectrum for multisection systems with periodic subsystems considered in [1]. It should be also noted that all the results for natural vibrations of a multisection system have been obtained without calculating the system as a whole, only on the basis of an analysis of the vibrational and wave properties of a separate section under various boundary conditions (see Sect. 5.2).

Obviously, rotary systems with discs equipped with blades can also be attributed to the considered class of periodic systems. Many computational and experimental studies of such systems [27] show a close qualitative nature of oscillations for rotor systems with discs equipped with blades. There arise collective oscillations of the blades.

The oscillation modes are similarly divided into groups. The first group includes oscillation modes, in which the blade has one oscillation node (the first oscillation mode). The second group involves oscillations, in which the blade has two vibration nodes, etc. The case, when $m = 0$, corresponds to in-phase oscillations. With an odd number of blades, the n-th frequency of the in-phase oscillation mode is non-multiple. For an even number of blades, there is another non-multiple mode corresponding to $m = n/2$. In case of this oscillation mode, all adjacent blades vibrate in antiphase. Depending on the bandage rigidity, modulated oscillations arise. The specificity of such rotor systems is the occurrence of coupled flexural-torsional vibrations of the blades.

5.6 Conclusions

The main oscillatory and wave properties of multisection periodic systems with symmetrical inclusions have been revealed. Such a structure is typical for a lot of engineering systems and for many acoustic metamaterials. These systems are shown to have frequency band gaps of a harmonic signal, the number of which is one less than the number of degrees of freedom of the inclusion subsystems. The boundaries of band gaps are determined analytically as the frequencies of a separate subsystem of inclusions with fixed and free boundaries. The presence of multiple frequencies in symmetrical structures leads to their instability at these frequencies.

Natural frequencies are divided into N groups according to the number of sections. The vibration modes in each group have the same wavelength, but different frequencies. As a result, modulated vibrations of a system arise due to modulation by lower frequencies corresponding to vibrations of the system without tak-ing into account the elasticity of the constituent subsystems.

In this paper, the representation theory of discrete symmetry groups is used in combination with dispersion equations obtained under the assumption that the periodic structure is infinite. This enables one studying the discrete models of the considered systems in the high-frequency range without their continualization.

Appendix A. Application of the Group Representation Theory for Mechanical Systems

A.1. Basic Concepts of the Representation Theory of Symmetry Groups

Here we clarify the concepts introduced above and define the form of projective operators and basis vectors for mechanical systems with cyclic symmetry. In the group representation theory, a system having the triangle-type symmetry (Fig. 5.8) is denoted as C_{3v}.

In the general case, the character table is used to obtain projective symmetry operators [8–10]

$$P_k = \frac{f_k}{n} \sum_i \chi_k(g_i^* g_i), \qquad (5.11)$$

where n is the group order, f_k is the dimension of the k-th irreducible representation, χ is its character, $\chi(g^*) = \chi(g^{-1})$ for real operators, and g_i are the elements of group G. Tables of group characters are known [15, 16]. For a triangle, such a table looks like

C_{3v}	E	$2C_3$	3σ
A_1	1	1	1
A_2	1	1	-1
E_1	2	-1	0

The top line of the table shows the symmetry operators for this group: the identical transformation, two rotations by angles $\pm 2\pi/3$, and three reflections around the axes connecting vertices (1,2,3) of the triangle with its center. The characters of the corresponding symmetry operators are located in the right-hand side of the table. The left column shows the dimension of this representation.

a)   b)
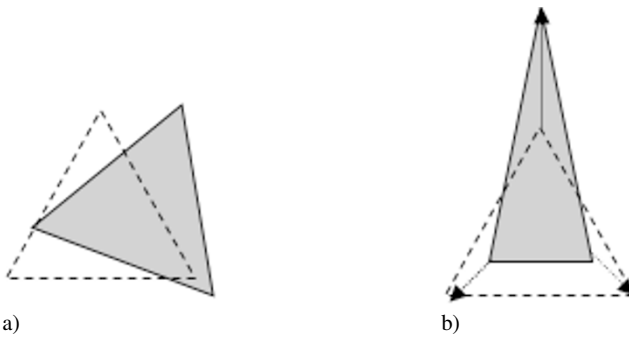
Fig. 5.8: A system with cyclic symmetry of the triagonal type: a) the first oscillation mode of the system (displacement as a rigid body); b) the second (third) oscillation mode..

Based on Eq. (5.11), we define the projective symmetry operators and basis vectors V_i:

$$V = PX, \quad P = \frac{1}{3} \begin{bmatrix} 1 & 1 & 1 \\ 2 & -1 & -1 \\ -1 & 2 & -1 \end{bmatrix}, \tag{5.12}$$

where P is a projective operator. The basis vectors V_i, in fact, determine the oscillation modes. The physical meaning of the vectors V_i in (5.12) is clear. V_1 means that all nodes 1, 2, 3 are in phase and correspond to a one-dimensional subspace. V_2 and V_3 mean that oscillations are associated with the deformation of the triangle: nodes 1 and 3 are in phase, whereas 2 is in antiphase. These operators correspond to multiple roots and any linear combination of them will also be an eigenmode.

A.2. Matrix Symmetry Operators

The application of the group representation theory to problems in mechanics has some features. So, elements or subsystems of a large dimension (for example, n) can be used as a node in mechanical systems. For taking into account these features of mechanical systems, the block projective symmetry operators are introduced, which elements related to a node with n degrees of freedom are block matrices of $n \times n$-order [1, 21].

For example, let each node in Fig. 5.8 has three degrees of freedom. Then the entire system possesses nine degrees of freedom and the generalized operator P, with account of (5.12), takes on the form of a block matrix:

$$V = PX, \quad P = \frac{1}{3} \begin{bmatrix} E & E & E \\ 2E & -E & -E \\ -E & 2E & -E \end{bmatrix}, \quad E = \begin{bmatrix} 1 & & \\ & 1 & \\ & & 1 \end{bmatrix} \tag{5.13}$$

Here E is the identity matrix, which order is equal to the number of independent coordinates in the node. Consequently, the projective operator (5.13) defines the basis vectors V_1, V_2, V_3, which will currently determine some generalized vibration modes describing the oscillations of nodes. Using the operator (5.13), the original matrix $K - \lambda M$ is reduced to a block-diagonal form, i.e. the original matrix equations are split into independent blocks.

References

[1] Banakh LY, Barmina OV, Volokhovskaya OA (2021) Oscillations and waves in multi-section rotor systems. Journal of Machinery Manufacture and Reliability **50**(5):396–404

[2] Zingoni A (2005) On the symmetries and vibration modes of layered space grids. Engineering Structures **27**(4):629–638

[3] Mohan SJ, Pratap R (2004) A natural classification of vibration modes of polygonal ducts based on group theoretic analysis. Journal of Sound and Vibration **269**(3):745–764

[4] Dyachenko MI, Pavlov AM, Temnov AN (2015) Longitudinal elastic vibrations of multistage liquid-propellant launch vehicle body (in Russ.). Vestn Mosk Gos Tekh Univ im NE Baumana (5):14–24

[5] Banakh LY, Grinkevitch VK, Ovchinnikova NF, Fedoseev YN (1988) Analysis of the dynamics of mechanisms using symmetry groups. Mashinovedenie (2):67–70

[6] Zingoni A (2014) Group-theoretic insights on the vibration of symmetric structures in engineering. Philosophical Transactions of the Royal Society A: Mathematical, Physical and Engineering Sciences **372**(2008):20120,037

[7] Ching FDK, Onouye BS, Zuberbuhler D (2014) Building Structures Illustrated: Patterns, Systems, and Design, 2nd edn. Wiley

[8] Dong B, Parker RG (2022) Vibration of multi-stage systems with arbitrary symmetry of stages: A group theory approach. Journal of Sound and Vibration **524**:116,738

[9] Zucco G, Weaver PM (2020) The role of symmetry in the post-buckling behaviour of structures. Proceedings of the Royal Society A: Mathematical, Physical and Engineering Sciences **476**(2233):20190,609

[10] Samaranayake S, Samaranayake G, Bajaj AK (2000) Resonant vibrations in harmonically excited weakly coupled mechanical systems with cyclic symmetry. Chaos, Solitons & Fractals **11**(10):1519–1534

[11] Zingoni A (2009) Group-theoretic exploitations of symmetry in computational solid and structural mechanics. International Journal for Numerical Methods in Engineering **79**(3):253–289

[12] Vakakis AF (1992) Dynamics of a nonlinear periodic structure with cyclic symmetrys. Acta Mechanica **95**(3):197–226

[13] Srinivasan AV (1984) Vibrations of Bladed-Disk Assemblies—A Selected Survey (Survey Paper). Journal of Vibration, Acoustics, Stress, and Reliability in Design **106**(2):165–168

[14] Thomas D (1974) Standing waves in rotationally periodic structures. Journal of Sound and Vibration **37**(2):288–290

[15] Bobylyov VN, Grebnev PA, Erofeev VI, Kuzmin DS, Monich DV (2020) Sound in-sulation of frameless sandwich panels with groove-type connection of the middle layer. Privolzhsky Scientific Journal **8**(3):9–18

[16] Hu G, Tang L, Das R, Gao S, Liu H (2017) Acoustic metamaterials with coupled local resonators for broadband vibration suppression. AIP Advances **7**(2):025,211

[17] Qureshi A, Li B, Tan KT (2016) Numerical investigation of band gaps in 3D printed cantilever-in-mass metamaterials. Scientific Reports **6**:28,314

[18] Zhou X, Wang J, Wang R, Lin J (2017) Band gaps in grid structure with periodic local resonator subsystems. Modern Physics Letters B **31**(25):1750,225

[19] Vasiliev AA, Pavlov IS (2021) Discrete and generalized continuum dynamical models of tetrachiral cosserat lattices with finite-sized particles. Mechanics Research Communications **115**:103,732

[20] Bobrovnitskii YI (2022) Impedance theory of wave propagation on infinite periodic structures. Journal of Sound and Vibration **525**:116,801

[21] Banakh LY, Kempner ML (2010) Vibrations of Mechanical Systems with Regular Structure. Foundations of Engineering Mechanics, Springer, Berlin Heidelberg

[22] Weyl H (2007) The Theory of Groups and Quantum Mechanics. Kessinger Publishing

[23] Hammermesh M (1962) Group Theory and its Application to Physical Problems. Addison-Wesley

[24] Zlokovic GM (1989) Group Theory and G-vector Spaces in Structural Analysis. Ellis Horwood, Group C, Chichester

[25] Zienkiewicz OC (1971) The Finite Element Method in Structural and Continuum Mechanics. McGraw-Hill, London

[26] Oden JT (19971) Finite elements: An introductions. In: Handbook of Numerical Analysis, Finite element methods (Part I), Handbook of Numerical Analysis, Finite element methods (Part I), Amsterdam, pp 3–12

[27] Ewins DJ, Imregun M (1984) Vibration Modes of Packeted Bladed Disks. Journal of Vibration, Acoustics, Stress, and Reliability in Design **106**(2):175–180

Chapter 6
Mathematical Model for Myopia Correction with MyoRing Implants

Svetlana M. Bauer, Liudmila A. Venatovskaya, Eva B. Voronkova, Vladimir V. Kornikov, Larisa A. Avershina, and Anna E. Terenteva

Abstract A finite-element simulation for the implantation of corneal rings for patients with high myopia is presented. The eyeball is modelled by joined spherical segments with different geometries and elastic properties. The ring implantation process is modelled by three surface-surface contact pairs: contact between corneal layers and contacts of the ring and with the lower and upper surface of the corneal pocket. The role of the surgical parameters (the MyoRing thickness and the implantation depth) on the stress-strain state is studied. The results of the simulation were compared with the clinical data on the change in curvature after the surgery.

6.1 Introduction

Myopia or shortsightedness is the most common refractive error. It is expected that by 2050, half of the world's population will have myopia. Laser vision correction provides safe and effective treatment for myopia by removing tissue to reshape the cornea (the transparent front part of the eye). However, complicated cases of myopia (high degree and/or thin cornea, irregular corneal surface etc.) make laser refractive surgery not eligible due to the increased risk of postoperative keratectasia or myopic regression with time [1].

Svetlana M. Bauer · Liudmila A. Venatovskaya · Eva B. Voronkova · Vladimir V. Kornikov
St. Petersburg State University, 7/9 Universitetskaya Emb., 199034 St. Petersburg, Russian Federation,
e-mail: s.bauer@spbu.ru, l.venatovskaya@spbu.ru, e.voronkova@spbu.ru, v.kornikov@spbu.ru

Larisa A. Avershina · Anna E. Terentyeva
Cheboksary branch of N.S. Fyodorov National Medical Research Center "MNTH "Eye Microsurgery", 10 Traktostrostroiteley av., 428028 Cheboksary, Russian Federation,
e-mail: avershina@mntkcheb.ru, anyaterentieva@yandex.ru

The implantation of intrastromal corneal ring segments (ICRS) or intrastromal continuous rings (ICR) is one of the alternative methods to reshape (flatten) the human cornea and improve vision. Nowadays, the use of ICRSs is one of the most common treatments for patients with keratoconus (KC) — an eye disorder caused by noninflammatory thinning of the corneal tissue [2].

A new technology, named corneal intrastromal implantation surgery (CISIS), for the surgical treatment of high myopia ($6 - 20$ diopters [D]), was presented in 2007 [1]. The procedure involves the use of a small deformable close ring (MyoRing, Dioptex GmbH) introduced into a pocket under the surface of the cornea. The MyoRing implantation consists of two main steps. First, a corneal pocket is formed with the PocketMaker microkeratome or a femtosecond laser. With a femtosecond laser ophthalmologists can make slices inside the cornea with the highest precision in terms of exposure depth and diameter. Then, a soft ring implant is inserted into the corneal pocket through a tunnel micro-incision. The tunnel incision heals independently and does not require sutures. Although MyoRing was designed for permanent wear, the procedure is reversible, and the inlay can easily be removed. It is also important to note, that the advantage of this technique is that it doesn't affect corneal biomechanics, since the PocketMaker microkeratome or femtosecond laser does not create a flap and forms a corneal pocket using incisions parallel to the collagen fibres and not through or perpendicular to the fibrils [1].

Currently, surgical planning (choosing the optimal type of ICR, depth of the implantation), as well as, achieving a certain refractive outcome, are mainly based on clinical practice and statistical studies. However, mechanical factors, such as intraocular pressure (IOP) and tissue biomechanics, play a role and should be taken into account. Finite-element simulation can help the clinician to take decisions and observe the results while modifying many factors which would not be possible to modify in a real environment.

Bagheri et al. investigated the influence of ICRS implementation techniques on the postoperative biomechanical state [3]. They developed a three-dimensional (3D) patient-specific finite-element model (FEM) of the keratoconic cornea, using clinical data of three patients with different stages and patterns of keratoconus. Then, several surgical scenarios with different ICRS designs (complete or incomplete segment) and surgical implementation techniques (tunnel incision and lamellar pocket cut) were simulated.

A patient-specific finite element (FE) model of the human cornea was used to predict the outcomes of the surgery after the ICRS implantation in real patients by Lago and coauthors [4]. They obtained the 3D geometry of the cornea of each patient from its specific topography. To characterise the mechanical behavior of the cornea a hyperelastic model was assumed. The curvature of the corneal profile predicted by FE simulation was compared with the real curvature after the surgery.

Ariza-Gracia et al. [5] used in silico models to determine the corneal shape and stresses after ring implantation. They consider generic implants with an elliptical cross-section to focus on studying the size and diameter of the implants. The study showed that implants create a local bulkening effect that regularizes the corneal shape. The authors also mentioned that for MyoRing type implants, shallower implantation

depths could provide a higher refractive correction. In the present study, we use two segments eyeball model to estimate the effect of different surgical and biomechanical parameters on the mechanical behaviour of the cornea after the MyoRing implantation.

6.2 Problem Statement

The corneoscleral coat of the eye is modelled as two joint segments of different geometric and mechanical properties [6, 7]. The average parameters were used to model the geometry of the simulated eyeball. The outer surface of the cornea is approximated by a spherical segment with radius $R_c = 7.76$ mm. We assumed that the thickness of the cornea is minimum at the apex $h_{AP} = 0.49$ mm, increases linearly along the meridional direction and achieves its maximum at the limbus where the cornea connects to the sclera $h_L = 0.75$ mm. The sclera was represented as a spherical segment with the outer radius $R_s = 12$ mm. We proposed that scleral thickness is equal to $h_E = 0.6$ mm near the equator (see Fig. 6.1).

We assume materials of the cornea and sclera are close to transversely isotropic material. Young's moduli of the cornea and sclera in the isotropic surface are taken $E_c = 0.3$ MPa, $E_s = 10.0$ MPa, corresponding Young's moduli in the normal (thickness) direction are $E'_c = E_c/20$, $E'_s = E_s/10$ [8], Poisson's ratios for all considered materials are taken as $\nu = 0.49$ in the isotropic surface and $\nu' = 0.01$ in the thickness direction.

Nonlinear analyses were performed using engineering finite element software Ansys®, Release 18. Due to symmetry, two-dimensional (2D) modelling was carried out with finite element PLANE182. The axisymmetric problem was considered with the axis of symmetry Y and the X axis was directed along the normal to the isotropic
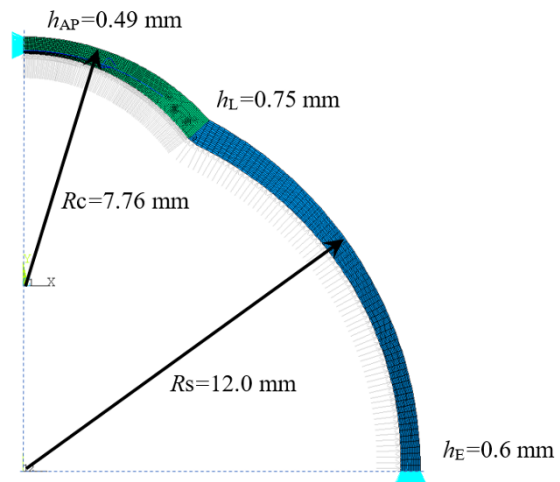
Fig. 6.1 Finite-element simulation of the corneoscleral eye shell filled by incompressible liquid.

surface. The symmetry boundary conditions were applied along the anterior-posterior axis of the eye (at the top of the cornea and the posterior pole of the sclera), and at the equator, the displacement of the sclera in a vertical direction was prohibited.

The MyoRing implants are available in different dimensions with diameters ranging from 5 to 7 mm and thicknesses ranging from 200 to 400 μm in 20 μm increments. According to the technique, the ring is implanted into a corneal pocket 9 mm in diameter, formed by femtosecond laser, to a depth of 80% of the initial corneal thickness. Figure 6.2 shows the human cornea 2 after years after MyoRing implantation surgery. The thickness of the implanted ring was 280 μm. The corneal pocket was performed with a femtosecond laser at a depth of 380 μm.

Corneal pocket modelling is performed by dividing the cornea into two separate layers. The ring implantation process is modelled by three surface-surface contact pairs (Fig. 6.3). The first contact pair sets the contact between corneal layers as a result of corneal pocket formation. The other two pairs simulate the contact of the ring with the lower and upper surface of the corneal pocket, in which the ring is inserted. Then, the nonlinear problem at large deformations is solved. In contact pairs with a ring, an initial geometrical gap is set, which gradually decreases at each step of the solution until the ring is completely installed in the pocket area. Since the elastic properties of the ring significantly exceed the elastic properties of the soft
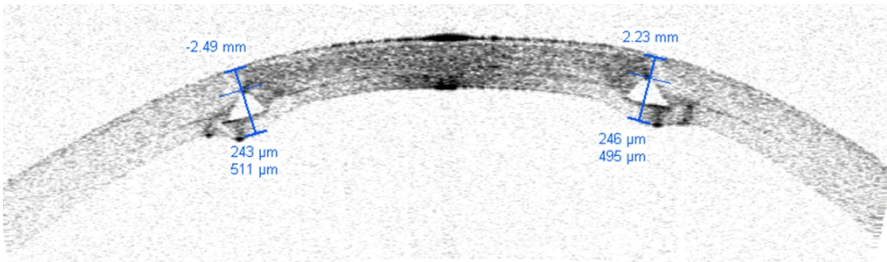
Fig. 6.2: The OCT image 2 years after MyoRing implantation.
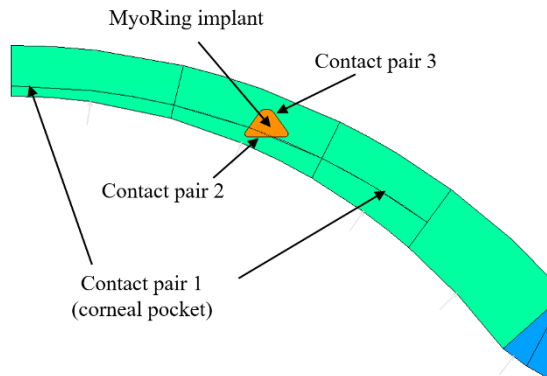
Fig. 6.3 Contact interaction between the layers: contact pair 1 — between the inner corneal layers (as a result of corneal pocket formation), contact pair 2 — between the lower corneal layer and the lower surface of the ring, contact pair 3 — between the upper corneal layer and the upper surface of the ring.

cornea, the ring can therefore be considered as an absolutely solid body compared to the cornea during the FE calculations.

6.3 Results and Discussion

Figure 6.4 shows the total displacement distribution and von Mises stress distribution of the simulated cornea at a physiological pressure of 15 mm Hg before implantation. Figures 6.5 and 6.6 depict the same mechanical characteristics for the cornea after MyoRing implantation of different thicknesses. We set the stiffness of the ring inlays as of 1800 MPa. The difference in the stress-strain states of the shells shows that the installation of thicker rings has a stronger effect on changes in the cornea profile, respectively, allowing to correct large refractive errors.

Table 6.1 presents the values of corneal curvature radii calculated from the displacement of the corneal apex during deformation in response to the application of
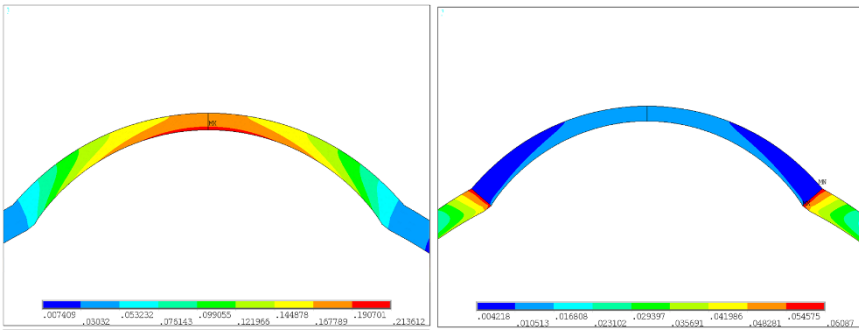
Fig. 6.4: Deformed state of the cornea under intraocular pressure of 15 mm Hg before implantation: displacements (in the left) and von Mises stress distribution (in the right).
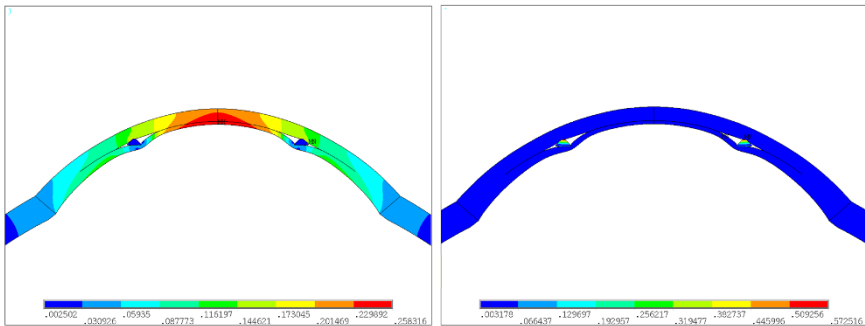
Fig. 6.5: Deformed state of the cornea at an intraocular pressure of 15 mm Hg after implantation of 200 μm ring implant.
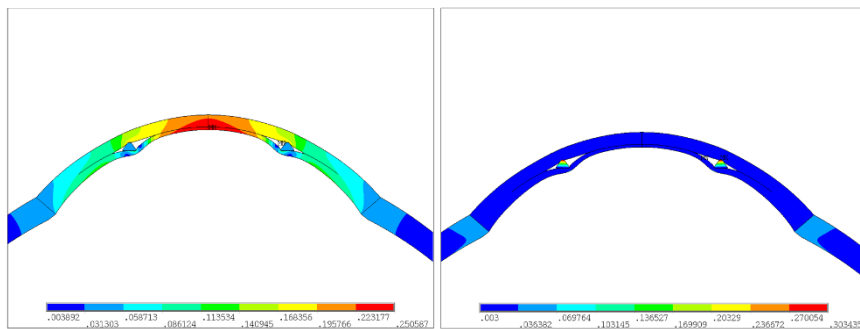
Fig. 6.6: Deformed state of the cornea at an intraocular pressure of 15 mm Hg after implantation of 280 μm ring implant.

Table 6.1: Radius of curvature at apex of cornea, mm.

	Before implantation	After implantation		
MyoRing thickness, μm	-	200	240	280
Radius of curvature at apex of cornea, mm	7,76	7,818	7,815	7,812

15 mm Hg pressure before and after MyoRing implantation simulation. Figures 6.7, 6.8 and Table 6.2 demonstrate how the corneal mechanical characteristics affect the stress-strain state both before and after MyoRing correction surgery. The distributions of corneal displacements for the corneal elastic modulus in isotropic surface varying that ranges from 0.4 MPa to 0.1 MPa. are displayed in Figs. 6.7 and 6.8. Table 6.2 compares the flattening of the corneal profile due to an increase of the apex curvature) after the surgery for different sets of mechanical parameters. One can see that the

Table 6.2: Corneal apex curvature radius values before and after implantation of a 200 μm thickness ring for corneas with different elastic moduli, mm.

Corneal elasticity moduli	$E_c = 0.4$ MPa	$E_c = 0.3$ MPa	$E_c = 0.2$ MPa	$E_c = 0.1$ MPa
Radius of curvature before implantation, mm	7.71	7.76	7.85	8.11
Radius of curvature after implantation, mm	7.76	7.82	7.93	8.21
Changes in radius of curvature before and after implantation, mm	0.05	0.06	0.08	0.10
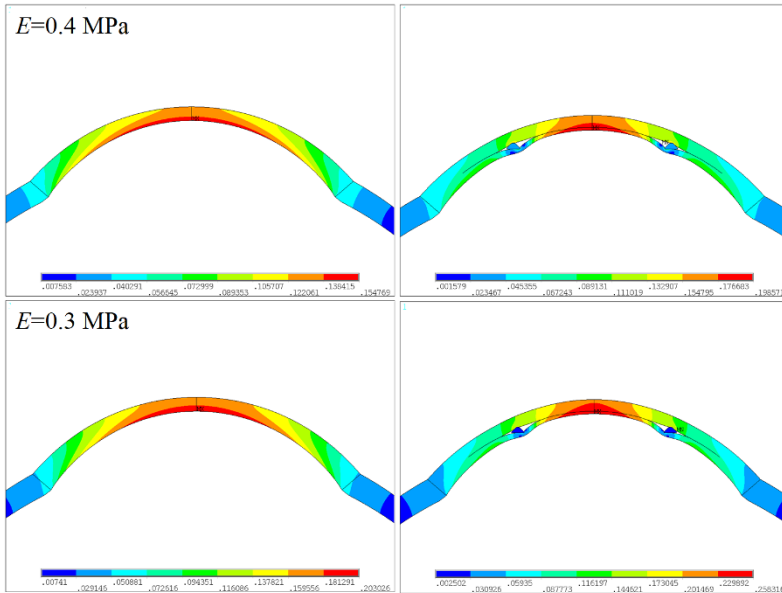
Fig. 6.7: Deformed state of cornea with elastic modulus of 0.4 MPa and 0.3 MPa before and after vision correction with 200 μm ring.

elastic properties of the cornea could affect refractive outcomes and should be taken into account.

To study the relationships between change in the apex radius of curvature (ΔR) before and after the surgery and the surgical parameters (ring thickness and implantation depths) we employed statistical analysis to analyse the clinical data (see Fig. 6.9). For linear regression models, the determination coefficients are equal to $R^2 = 0.864$ and $R^2 = 0.876$ for the relationships between change in the apex radius of curvature and a MyoRing thickness and the implantation depth, respectively. We see that each of the considered parameters explains more than 86% of the variability of the ΔR variable, which indicates a fairly good quality of the linear model. The difference in quality between the linear and quadratic models is insignificant and therefore we can restrict ourselves to the linear model only.

Due to its limitations, the presented model can only provide a qualitative assessment of the eyeball's behaviour as a result of the MyoRing implant surgery. One of the model limitations is the characterization of the eyeball tissue as linear elastic materials. It was reported, that the eyeballs' tissues (cornea, sclera) exhibit nonlinear elastic behaviour [9–11].

Several models (N-order Ogden model, modified Gasser-Holzapfel-Ogden model, Neo-Hookean hyperelastic model etc.) have been proposed and used in the literature to describe the mechanical properties of the cornea [3, 4, 12]. Determination of the assumed model parameters is a topical problem in computational biomechanics
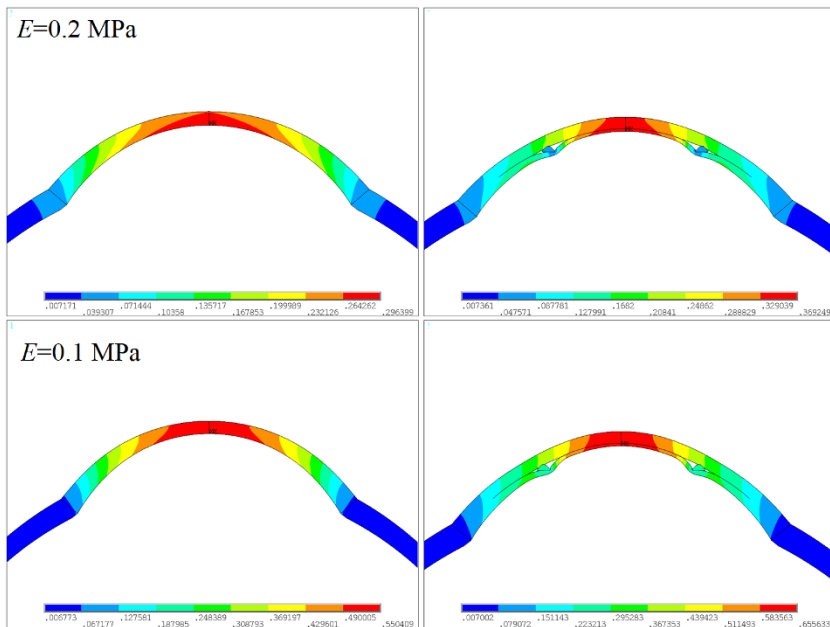
Fig. 6.8: Deformed state of cornea with elastic modulus of 0.2 MPa and 0.1 MPa before and after vision correction with 200 μm ring.
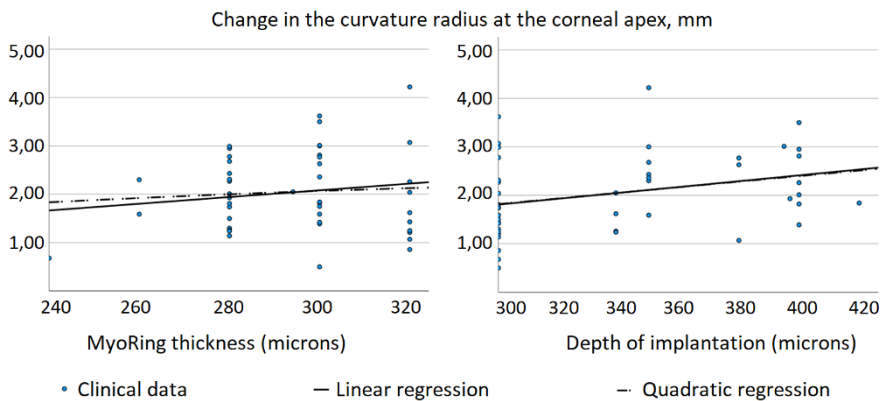
Fig. 6.9: Statistical analysis of the clinical data. Solid lines represent linear regression curves, Dash-Dotted lines correspond to quadratic regression curves.

nowadays, particularly when creating personalized patient models. According to [13], the problem of estimation of the eye material parameter can be fully solved only when all three main mechanical characteristics of the eye are determined in complex: two stiffnesses (corneal and scleral) and the true intraocular pressure.

One of the methods for selecting nonlinear material characteristics is presented in [14] and is based on the optimization method and finite element model. The Levenberg-Marquardt least-squares algorithm is used as an optimization approach to estimate corneal material properties.

Mathematical models together with clinical statistical data could be used for a better understanding of tissues biomechanics and for describing their mechanical behaviour. The data-driven approach (model-free) for the determination of constitutive relations is presented in [15]. Instead of assuming a certain parametric representation of the elastic potential, the authors obtain the material characteristics from experimental data.

6.4 Conclusion

Two segments eyeball model to estimate the mechanical behaviour of the cornea after the MyoRing implantation is presented. Numerical calculations show that MyoRing implants enable changing of corneal profile without surgical impact on its outer or inner layers, as in myopia correction by other methods. Deformations in the central corneal zone are mostly influenced by the ring diameter and its implantation depth. Analysis of the stress state showed that the greatest stresses occur in the MyoRing itself, thus the ring acts as an additional corneal framework.

References

[1] Daxer A (2008) Corneal intrastromal implantation surgery for the treatment of moderate and high myopia. Journal of Cataract & Refractive Surgery **34**(2):194–198

[2] Ertan A, Colin J (2007) Intracorneal rings for keratoconus and keratectasia. Journal of Cataract & Refractive Surgery **33**(7):1303–1314

[3] Bagheri N, Kadkhodaei M, Pirhadi S, Mosaddegh P (2021) Effects of intra-corneal ring segments implementation technique and design on corneal biomechanics and keratometry in a personalized computational analysis. Scientific Reports **11**(1), 14433

[4] Lago M, Rupérez M, Monserrat C, Martínez-Martínez F, Martínez-Sanchis S, Larra E, Díez-Ajenjo M, Peris-Martínez C (2015) Patient-specific simulation of the intrastromal ring segment implantation in corneas with keratoconus. Journal of the Mechanical Behavior of Biomedical Materials **51**:260–268

[5] Ariza-Gracia MA, Flecha-Lescún J, Büchler P, Calvo Bn (2020) Corneal Biomechanics After Intrastromal Ring Surgery: Optomechanical In Silico Assessment. Translational Vision Science & Technology **9**(11):26–26

[6] Bauer SM, Venatovskaya LA, Kachanov AB, Kornikov VV (2021) Mathematical models of laser correction of myopia by lasik, smile and prk methods. Russian Journal of Biomechanics **25**(4):317–322

[7] Bauer SM, Venatovskaya LA, Voronkova EB, Kachanov AB (2022) Modeling approaches for an eyeball deformation after intravitreal injection. In: Altenbach H, Eremeyev VA, Galybin A, Vasiliev A (eds) Advanced Materials Modelling for Mechanical, Medical and Biological Applications, Springer International Publishing, Cham, pp 77–85

[8] Iomdina E, Bauer S, Kotlyar KE (2015) Biomechanics of the Human: Theoretical Aspects and Clinical Applications (in Russ.). Real Time, Moscow

[9] Bryant MR, McDonnell PJ (1996) Constitutive Laws for Biomechanical Modeling of Refractive Surgery. Journal of Biomechanical Engineering **118**(4):473–481

[10] Elsheikh A, Alhasso D, Rama P (2008) Biomechanical properties of human and porcine corneas. Experimental Eye Research **86**(5):783–790

[11] Dyk DW, Miller KM (2018) Mechanical model of human eye compliance for volumetric occlusion break surge measurements. Journal of Cataract & Refractive Surgery **44**(2):231–236

[12] Pandolfi A, Holzapfel GA (2008) Three-dimensional modeling and computational analysis of the human cornea considering distributed collagen fibril orientations. Journal of Biomechanical Engineering **130**(6), p. 061006

[13] Moiseeva IN, Stein AA (2022) Differential tonometry with a Schiotz tonometer: Mathematical modeling with account for the nonlinearity of the elastic behavior of the cornea and comparison with clinical data. Russian Journal of Biomechanics **26**(4):10–18

[14] Jannesari M, Kadkhodaei M, Mosaddegh P, Kasprzak H, Behrouz M (2018) Assessment of corneal and fatty tissues biomechanical response in dynamic tonometry tests by using inverse models. Acta of bioengineering and biomechanics **20**(1):39–48

[15] Salamatova VY, Liogky AA (2020) Hyperelastic membrane modelling based on data-driven constitutive relations. Russian Journal of Numerical Analysis and Mathematical Modelling **35**(3):163–173

Chapter 7
Numerical Modeling the Stresses in Incompressible and Rigid Bodies

Nikolai M. Bessonov and Yaroslava I. Litvinova

Abstract Issues related to the calculation of stresses in an incompressible medium are considered. The problems of modeling the flow of a classical Newtonian viscous liquid and micropolar liquid are discussed. The problem of calculating stresses in incompressible elastomers (rubber-like) bodies is considered. The problem of determining stresses in a fully incompressible (rigid) body is considered also. Examples are given.

7.1 Introduction

The model of an absolutely or perfectly rigid (or rigid for the shortest) body is used in analytical mechanics when solving dynamic problems. But analytical mechanics does not allow looking inside a rigid body and solving the problem of finding stresses. On the other hand, the theory of elasticity studies the stresses in elastic bodies in detail, but rarely does anyone ask the question, is it possible to calculate the stresses in a rigid body from the standpoint of the theory of elasticity?

An absolutely solid body is a model concept of classical mechanics, denoting a set of material points, the distances between which are preserved in the process of any movements made by this body. In other words, an absolutely solid body not only does not change its shape but also keeps the distribution of mass inside unchanged.

Nikolai M. Bessonov
Institute of Problems of Mechanical Engineering, Russian Academy of Sciences, Bol'shoy, 61, V.O., 199178 St. Petersburg, Russian Federation,
e-mail: nickbessonov1@gmail.com

Yaroslava I. Litvinova
Peter the Great St. Petersburg Polytechnic University, Polytechnicheskaya, 29, 195251 St.Petersburg, Russian Federation,
e-mail: yailitvinova@gmail.com

It is a traditional opinion that for a rigid material, the stress is undetermined [1]. This idea arises also from the observation that no constitutive relation connecting the stress to the motion is necessary to determine the motion of a rigid body, unlike what happens for deformable continua.

We could find only a few articles devoted to the study of a rigid body from the point of view of the theory of elasticity. For example, the question of the limiting transition from an elastic to a rigid body was studied in articles [2], [3]. A brief review of this question in the literature is also given here.

An Internet search for an answer to a question: "Is there and if there is, is it possible to find stresses in an absolutely solid body?" gave two variants of answers. The first one is: "What you are asking is not physical", and the second one is: "If the stiffness is infinite and the strain is zero, then the stress is mathematically indeterminate".

In this article, we do not discuss the fundamental aspects of these problems in detail. Our goal is to consider this problem from the point of view of numerical modeling.

The model of an incompressible media can be considered the first approximation to the model of a perfectly rigid body. In the theory of elasticity, the incompressibility condition is used, for example, when modeling rubber-like bodies, for which the incompressibility condition determines the invariance of the volume, but shear deformations remain. The study of rubber-like bodies is of great practical interest; therefore, many different methods have been developed for finding stresses and strains in such bodies. Also, a large section of hydrodynamics deals with the description of the behavior of incompressible liquids.

In Sect. 7.2, examples of the numerical solution of problems in the hydrodynamics of incompressible classical and micropolar liquids are considered. In Sect. 7.3, the solution to the problem of deformation of an elastomer (an incompressible elastic body) is considered. In Sect. 7.4, the problem of calculating the stresses in a rigid body is considered and examples are given.

7.2 Numerical Modeling of the Flow of the Incompressible Micropolar Liquids

The classical model of Newtonian liquid is a well-known example of an incompressible medium. Methods for numerical simulation of the flow of an incompressible Newtonian viscous liquid are considered [4–6], among others. The restriction to incompressible flow introduces the computational difficulty that the continuity equation contains only velocity components, and there is no obvious link with the pressure as there is for compressible flow through the density ρ.

Two broad approaches to computing incompressible flow are available. First, the source (or elementary) variables, (u, v, p) in two dimensions, are used and special procedures are introduced to handle the continuity equation. The extension to three spatial dimensions creates no additional difficulty. Second, in two dimensions the explicit treatment of the continuity equation can be avoided by introducing the stream

function. In addition, the introduction of a transport equation for the vorticity leads to the stream function vorticity formulation. The extension of this formulation to three dimensions is not straightforward, since a three-dimensional stream function is not available [4].

An approach based on the use of source variables was applied in [7–10]. For the solution of the discretized equations the iterative alternative direction implicit method was used [5, 11–13].

There is a significant class of hydrodynamic problems in which the liquid flow cannot be correctly described using the classical Navier-Stokes equations. An example of such a model is the micropolar fluid model, which is based on the assumption of incompressibility also. The model of micropolar liquid is applied in the theory of lubrication, porous media, liquid crystals, thin films of polymers, the flow of suspensions, physiological liquids (blood), and soil mechanics as well as in several other areas.

Micropolar liquids are incompressible liquids with microstructure. They belong to a class of liquids with nonsymmetric stress tensors and include, as a special case, the Newtonian model of classical viscous liquids. The model of micropolar fluids was introduced by Eringen in 1966 [14] "micropolar" hydrodynamics, and independently by Aero, Buligin, and Kuvshinsky in 1965 [15] "asymmetrical" hydrodynamics. Here in addition to the usual tensor of force stresses $\boldsymbol{\sigma}$ the tensor of moment stresses $\boldsymbol{M}$ is introduced.

The equations of motion of micropolar liquid (in absence of external body forces and moments) have the next form [15, 16]:

$$\nabla \cdot \vec{v} = 0, \tag{7.1}$$

$$\rho \frac{d\vec{v}}{dt} = \nabla \cdot \boldsymbol{\sigma}, \tag{7.2}$$

$$\rho I \frac{d\vec{\omega}}{dt} = \vec{i}_1 \times \left(\vec{i}_1 \cdot \boldsymbol{\sigma} \right) + \vec{i}_2 \times \left(\vec{i}_2 \cdot \boldsymbol{\sigma} \right) + \vec{i}_3 \times \left(\vec{i}_3 \cdot \boldsymbol{\sigma} \right) + \underline{\nabla \cdot \boldsymbol{M}}, \tag{7.3}$$

where ρ is the density; $\vec{v}$ is the velocity; $\vec{\omega}$ is the microrotation velocity; I is the moment of microinertia per mass unit; t is the time; $\vec{i}_1, \vec{i}_2$ and $\vec{i}_3$ are the unit vectors along coordinate axes. In the classical model of the liquid microparticles are regarded to point. Therefore the terms underlined in Eq. (7.3) disappear. Then Eq. (7.3) gives the equalities for components of tensor $\boldsymbol{\sigma}$

$$\sigma_{23} = \sigma_{32}, \qquad \sigma_{31} = \sigma_{13}, \qquad \sigma_{12} = \sigma_{21}, \tag{7.4}$$

that point to its symmetry in classical ("symmetrical") hydrodynamics. In micropolar hydrodynamics the tensor $\boldsymbol{\sigma}$ is asymmetrical (hence the term "asymmetrical" hydrodynamics).

The connection between kinematic and dynamic characteristics of liquid movement is set here by the following linear rheological relations [15]

$$\sigma_{nk} = -p\delta_{nk} + \mu \left(\upsilon_{n,k} + \upsilon_{k,n} \right) + \underline{\mu_r \left(\upsilon_{k,n} - \upsilon_{n,k} - 2\omega_q \epsilon_{qnk} \right)}, \tag{7.5}$$

$$M_{nk} = \gamma\omega_{k,n} + \lambda\omega_{n,k} + \vartheta\delta_{nk}\omega_{q,q}, \qquad n, k, q = 1, 2, 3, \tag{7.6}$$

where μ_r is the coefficient of microrotation viscosity; p is the pressure; γ, λ and ϑ are the coefficients of dissipation in consequence of microrotation gradients; δ_{nk} and ϵ_{qnk} are Kroenecker's and permutation symbols correspondingly; $\upsilon_{n,k} = \partial\upsilon_n/\partial x_k$, etc., (doubly repeated subscripts imply summation over the range $1, 2, 3$).

The substitution of Eqs. (7.5) and (7.6) in Eqs. (7.2) and (7.3) give the full system of equations for incompressible micropolar liquid

$$\nabla \cdot \vec{v} = 0, \tag{7.7}$$

$$\rho\left(\frac{\partial\vec{v}}{\partial t} + \nabla \cdot \vec{v}\vec{v}\right) = -\nabla p + \mu\nabla^2\vec{v} + \mu_r\nabla \times (2\vec{\omega} - \nabla \times \vec{v}), \tag{7.8}$$

$$\rho I\left(\frac{\partial\vec{\omega}}{\partial t} + \nabla \cdot \vec{v}\vec{\omega}\right) = \gamma\nabla^2\vec{\omega} + (\lambda + \vartheta)\nabla(\nabla \cdot \vec{\omega}) - 2\mu_r(2\vec{\omega} - \nabla \times \vec{v}). \tag{7.9}$$

Let the scales of length, translation velocity, time, microrotation velocity, and pressure are taken to be h, U, h/U, U/h and ρU^2 correspondingly, where h is the transverse dimension of the flow region and U is the characteristic velocity of the flow. Then the Eqs. (7.7)–(7.9) take the following nondimensional form

$$\nabla \cdot \vec{v} = 0, \tag{7.10}$$

$$\frac{d\vec{v}}{dt} = -\nabla p + \frac{1}{\text{Re}}\nabla^2\vec{v} + \frac{1}{\text{Re}_r}\nabla \times (2\vec{\omega} - \nabla \times \vec{v}), \tag{7.11}$$

$$\left(\frac{L_1}{h}\right)^2\text{Re}\frac{d\omega}{dt} = \left(\frac{L_2}{h}\right)^2\nabla^2\omega + \left(\frac{L_3}{h}\right)^2\nabla(\nabla \cdot \omega) - \frac{2\text{Re}}{\text{Re}_r}(2\omega - \nabla \times v), \tag{7.12}$$

where $\text{Re} = \rho h U/\mu$; $\text{Re}_r = \rho h U/\mu_r$; $L_1 = I^{1/2}$; $L_2 = (\gamma/\mu)^{1/2}$; $L_3 = ((\lambda + \vartheta/\mu))^{1/2}$. All nondimensional values in Eqs. (7.10)–(7.12) keep the same notations as the correspondent dimensional ones in Eqs. (7.7)–(7.9). The complexes L_1, L_2, and L_3 have the dimensions of the length and play the role of inner linear scales of the liquid microstructure. The role of nonclassical terms in Eqs. (7.10)–(7.12) (in other words – the influence of fluid microstructure) grows with decreasing of the dimension h of the flow region. In contrast when h becomes much bigger than L_1, L_2 and L_3. Eq. (7.12) converts to the relation $\vec{\omega} = 1/2\nabla \times \vec{v}$ and Eq. (7.11) transforms into the classical Navier-Stokes equation as the partial case.

Parameter I characterizes the moment of rotation of fluid particles at a given point. As a rule, this value is negligible and can be considered equal to zero. for simplicity below we will consider the stationary two-dimensional equations in projection form:

$$\frac{\partial u}{\partial x} + \frac{\partial v}{\partial y} = 0, \tag{7.13}$$

$$-\frac{\partial uu}{\partial x} - \frac{\partial vu}{\partial y} + \frac{1}{\text{Re}}\left(\frac{\partial^2 u}{\partial x^2} + \frac{\partial^2 u}{\partial y^2}\right) - \frac{\partial p}{\partial x} + \frac{2}{\text{Re}_r}\left[\frac{\partial\omega}{\partial y} + \frac{1}{2}\left(\frac{\partial^2 u}{\partial x^2} + \frac{\partial^2 u}{\partial y^2}\right)\right] = 0, \tag{7.14}$$

$$-\frac{\partial uv}{\partial x} - \frac{\partial vv}{\partial y} + \frac{1}{Re}\left(\frac{\partial^2 v}{\partial x^2} + \frac{\partial^2 v}{\partial y^2}\right) - \frac{\partial p}{\partial y} + \frac{2}{Re_r}\left[-\frac{\partial \omega}{\partial x} + \frac{1}{2}\left(\frac{\partial^2 v}{\partial x^2} + \frac{\partial^2 v}{\partial y^2}\right)\right] = 0, \quad (7.15)$$

$$B\left(\frac{\partial^2 \omega}{\partial x^2} + \frac{\partial^2 \omega}{\partial y^2}\right) + \frac{\partial v}{\partial x} - \frac{\partial u}{\partial y} - 2\omega = 0, \quad (7.16)$$

where u, v are components of $\vec{v}$; $\omega = \vec{\omega}_z$; $B = 2L^2 Re_r/Re$ $L = L_2/h$.

In [17] a numerical method for solving the system of micropolar Eqs. (7.10)–(7.12) in a domain with complex boundaries was described. Let us rewrite the system (7.13)–(7.16) in the form

$$\Lambda f = 0, \quad (7.17)$$

where f is the column with components p, u, v, ω;

$$\Lambda = \begin{pmatrix} 0, & -\dfrac{\partial}{\partial x}, & -\dfrac{\partial}{\partial y}, & 0 \\[2mm] -\dfrac{\partial}{\partial x}, & -\nabla_{xy} + \left(\dfrac{1}{Re} + \dfrac{1}{Re_r}\right)\nabla^2, & 0, & \dfrac{2}{Re_r}\dfrac{\partial}{\partial y} \\[2mm] -\dfrac{\partial}{\partial y}, & 0, & -\nabla_{xy} + \left(\dfrac{1}{Re} + \dfrac{1}{Re_r}\right)\nabla^2, & \dfrac{2}{Re_r}\dfrac{\partial}{\partial y} \\[2mm] 0, & -\dfrac{\partial}{\partial y}, & \dfrac{\partial}{\partial x}, & B\nabla^2 - 2 \end{pmatrix}; \quad (7.18)$$

$\nabla_{xy}\varphi = \partial u\varphi/\partial x + \partial v\varphi/\partial y$; $\nabla^2\varphi = \partial^2\varphi/\partial x^2 + \partial^2\varphi/\partial y^2$ (φ is a any function).

Let us split the operator Λ into two parts:

$$\Lambda = \Lambda_1 + \Lambda_2, \quad (7.19)$$

where

$$\Lambda_1 = \begin{pmatrix} 0, & -\dfrac{\partial}{\partial x}, & 0, & 0 \\[2mm] -\dfrac{\partial}{\partial x}, & -\dfrac{\partial u}{\partial x} + \left(\dfrac{1}{Re} + \dfrac{1}{Re_r}\right)\dfrac{\partial^2}{\partial x^2}, & 0, & 0 \\[2mm] 0, & 0, & -\dfrac{\partial u}{\partial x} + \left(\dfrac{1}{Re} + \dfrac{1}{Re_r}\right)\dfrac{\partial^2}{\partial x^2}, & -\dfrac{2}{Re_r}\dfrac{\partial}{\partial x} \\[2mm] 0, & 0, & \dfrac{\partial}{\partial x}, & B\dfrac{\partial^2}{\partial x^2} - 2 \end{pmatrix}; \quad (7.20)$$

$$\Lambda_2 = \begin{pmatrix} 0, & 0, & -\dfrac{\partial}{\partial y}, & 0 \\[2mm] 0, & -\dfrac{\partial v}{\partial y} + \left(\dfrac{1}{Re} + \dfrac{1}{Re_r}\right)\dfrac{\partial^2}{\partial y^2}, & 0, & \dfrac{2}{Re_r}\dfrac{\partial}{\partial y} \\[2mm] -\dfrac{\partial}{\partial y}, & 0, & -\dfrac{\partial v}{\partial y} + \left(\dfrac{1}{Re} + \dfrac{1}{Re_r}\right)\dfrac{\partial^2}{\partial y^2}, & 0 \\[2mm] 0, & \dfrac{\partial}{\partial y}, & 0, & B\dfrac{\partial^2}{\partial y^2} - 2 \end{pmatrix}. \quad (7.21)$$

Let $f^1 = f$ is an initial estimate of f. The numerical method is based on the following iterative procedure:

Step 1:
$$\xi^n = \tau \Lambda f^n,$$

$$\max |\xi^n| < \varepsilon \to yes \to f^n \text{ is solution of (7.17)} \to STOP.$$

$$\downarrow$$

no

$$\downarrow$$

Step 2:
$$\frac{\xi^{n+1/2} - \xi^n}{\tau} = \Lambda_1 \xi^{n+1/2},$$

Step 3:
$$\frac{\xi^{n+1} - \xi^{n+1/2}}{\tau} = \Lambda_2 \xi^{n+1},$$

Step 4:
$$f^{n+1} = f^n + \xi^{n+1},$$

Go to Step 1.

Here ξ is residual of f; $n = 1, 2, 3, \ldots$ is number of iteration; $\max |\xi|$ is maximum of ξ overall mesh nodes; ε is small parameter; a parameter τ playing the role of the step of pseudo-time in the iterations,

$$f = \begin{pmatrix} p \\ u \\ v \\ \omega \end{pmatrix}, \quad \xi = \begin{pmatrix} \xi_p \\ \xi_u \\ \xi_v \\ \xi_\omega \end{pmatrix}.$$

The difference approximation of differential operators (7.18), (7.20), (7.21) are performed on the three-point stencil. Let us describe in detail the approximation in the example of Step 2:

$$\frac{\xi_p^{n+1/2} - \xi_p^n}{\tau} = -\frac{\partial \xi_u^{n+1/2}}{\partial x}, \tag{7.22}$$

$$\frac{\xi_u^{n+1/2} - \xi_u^n}{\tau} = -\frac{\partial (u^n \xi_u^{n+1/2})}{\partial x} + \left(\frac{1}{\text{Re}} + \frac{1}{\text{Re}_r} \right) \frac{\partial^2 \xi_u^{n+1/2}}{\partial x^2} - \frac{\partial \xi_p^{n+1/2}}{\partial x}, \tag{7.23}$$

$$\frac{\xi_v^{n+1/2} - \xi_v^n}{\tau} = -\frac{\partial (u^n \xi_v^{n+1/2})}{\partial x} + \left(\frac{1}{\text{Re}} + \frac{1}{\text{Re}_r} \right) \frac{\partial^2 \xi_v^{n+1/2}}{\partial x^2} - \frac{2}{\text{Re}_r} \frac{\partial \xi_\omega^{n+1/2}}{\partial x}, \tag{7.24}$$

$$\frac{\xi_\omega^{n+1/2} - \xi_\omega^n}{\tau} = B \frac{\partial^2 \xi_\omega^{n+1/2}}{\partial x^2} - 2\xi_\omega^{n+1/2} + \frac{\partial \xi_v^{n+1/2}}{\partial x}. \tag{7.25}$$

The Eqs. (7.22)–(7.25) are solved in the following sequence. The value of $\xi_p^{n+1/2}$ is determined from Eq. (7.22):

$$\xi_p^{n+1/2} = \xi_p^n - \tau \frac{\partial u^{n+1/2}}{\partial x}.$$

(7.26)

As a result of substituting Eq. (7.26) in (7.23) we get the Eq. (7.27) with respect to $\xi_u^{n+1/2}$:

$$\frac{\xi_u^{n+1/2} - \xi_u^n}{\tau} = -\frac{\partial (u^n \xi_u^{n+1/2})}{\partial x} + \left(\frac{1}{\mathrm{Re}} + \frac{1}{\mathrm{Re_r}} + \tau \right) \frac{\partial^2 \xi_u^{n+1/2}}{\partial x^2} - \frac{\partial \xi_p^n}{\partial x}.$$

(7.27)

For numerical simulations orthogonal mesh $I \times J$ $(i = 1, \ldots, I, \quad j = 1, \ldots, J)$ was introduced. The structure of the equations suggests defining the projections of translational velocity u, v, and rotational velocity ω at the nodes of the mesh (nodal variables) and the pressure p is defined inside the mesh cells (elements variable).

The finite-difference approximation of Eq. (7.26) in all grid cells and Eqs. (7.24), (7.25), (7.27) in all internal nodes has the next form:

$$\frac{\xi_{pi,j}^{n+1/2} - \xi_{pi,j}^n}{\tau} = -\frac{\xi_{ui,j}^{n+1/2} + \xi_{ui,j+1}^{n+1/2} - \xi_{ui+1,j+1}^{n+1/2} - \xi_{ui+1,j}^{n+1/2}}{2\Delta x_i},$$

(7.28)

$$\frac{\xi_{ui,j}^{n+1/2} - \xi_{ui,j}^n}{\tau} = K_u \xi_{ui,j}^{n+1/2} - \frac{\xi_{pi,j}^n + \xi_{pi,j-1}^n - \xi_{pi-1,j-1}^n - \xi_{pi-1,j}^n}{\Delta x_i + \Delta x_{i-1}}$$
$$+ \left(\frac{1}{\mathrm{Re}} + \frac{1}{\mathrm{Re_r}} + \tau \right) \left(\frac{\xi_{ui+1,j}^{n+1/2} - \xi_{ui,j}^{n+1/2}}{\Delta x_i} - \frac{\xi_{ui,j}^{n+1/2} - \xi_{ui-1,j}^{n+1/2}}{\Delta x_{i-1}} \right) \frac{2}{\Delta x_i + \Delta x_{i-1}},$$

(7.29)

$$\frac{\xi_{vi,j}^{n+1/2} - \xi_{vi,j}^n}{\tau} = K_u \xi_{vi,j}^{n+1/2} - \frac{2}{\mathrm{Re_r}} \frac{\xi_{\omega i+1,j}^{n+1/2} - \xi_{\omega i-1,j}^{n+1/2}}{\Delta x_i + \Delta x_{i-1}} +$$
$$\left(\frac{1}{\mathrm{Re}} + \frac{1}{\mathrm{Re_r}} \right) \left(\frac{\xi_{vi+1,j}^{n+1/2} - \xi_{vi,j}^{n+1/2}}{\Delta x_i} - \frac{\xi_{vi,j}^{n+1/2} - \xi_{vi-1,j}^{n+1/2}}{\Delta x_{i-1}} \right) \frac{2}{\Delta x_i + \Delta x_{i-1}},$$

(7.30)

$$\frac{\xi_{\omega i,j}^{n+1/2} - \xi_{\omega i,j}^n}{\tau} = \frac{\xi_{vi+1,j}^n - \xi_{vi-1,j}^n}{\Delta x_i + \Delta x_{i-1}} - \xi_{\omega i,j}^{n+1/2}$$
$$+ B \left(\frac{\xi_{\omega i+1,j}^{n+1/2} - \xi_{\omega i,j}^{n+1/2}}{\Delta x_i} - \frac{\xi_{\omega i,j}^{n+1/2} - \xi_{\omega i-1,j}^{n+1/2}}{\Delta x_{i-1}} \right) \frac{2}{\Delta x_i + \Delta x_{i-1}},$$

(7.31)

where $\Delta x_i = x_{i+1} - x_i$;

$$K_u \varphi_{i,j}^{n+1/2} = \frac{2}{\Delta x_i + \Delta x_{i-1}} \left(\frac{|u_L^n| + u_L^n}{2} \varphi_{i-1,j}^{n+1/2} + \left(\frac{|u_R^n| + u_R^n}{2} \right. \right.$$

$$\left. \left. + \frac{|u_L^n| - u_L^n}{2} \right) \varphi_{i,j}^{n+1/2} + \frac{|u_R^n| - u_R^n}{2} \varphi_{i+1,j}^{n+1/2} \right),$$

$u_L = (u_{i-1,j} + u_{i,j})/2$; $u_R = (u_{i,j} + u_{i+1,j})/2$; φ is the nodal variable (u, v or ω).

In the nodes beyond solid boundaries, the ξ_u, ξ_v, ξ_ω values are set to zero.

The solution of the finite-difference Eqs. (7.28)– (7.31) is carried out in the following sequence. By the method of tridiagonal matrix algorithm, the Eq. (7.29) is solved, and the values of the $\xi_{ui,j}^{n+1/2}$ in all nodes of the grid are determined. Then the values of $\xi_{pi,j}^{n+1/2}$ are determined (7.28). Equations (7.30), (7.31) is solved by the method of tridiagonal matrix algorithm also. The finite-difference approximation of steps 1 and 3 are done similarly.

The Fig. 7.1 shows the results of the numerical simulation of the flow of micropolar liquid in the 2D channel with a ledge. The height of the channel equals 1, its length equals 5. The following parameters for micropolar liquid have been set: Re = 500, Re_r = 500, B = 1. A unit velocity profile was set at the inlet, and the boundary conditions $\partial u/\partial x = \partial v/\partial x = \partial \omega/\partial x = 0$ were set at the outlet.

Figure 7.1a shows that one vortex flow is formed behind the barrier. Simulation shows that the flow of micropolar liquid is stationary here.

For comparison, the modeling of the flow of classical liquid in the same channel and for the same Reynolds number Re = 500 was done. For numerical modeling the non-stationary generalization of the method described above was used [18, 19] (see appendix also). Modeling shows that the flow of classical liquid becomes non-stationary. One frame of this flow is shown in Fig. 7.2a.
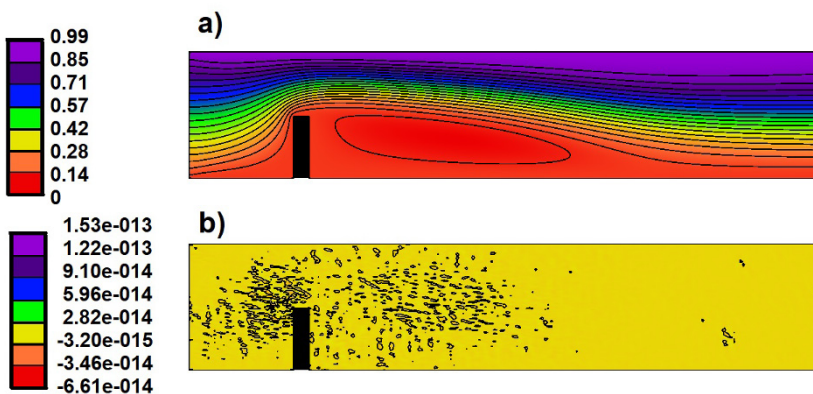
Fig. 7.1: Flow of micropolar fluid in a channel with the ledge. Re = 500, Re_r = 500, B = 1. a) streamline flow, b) distribution of $\nabla \cdot \vec{v}$.
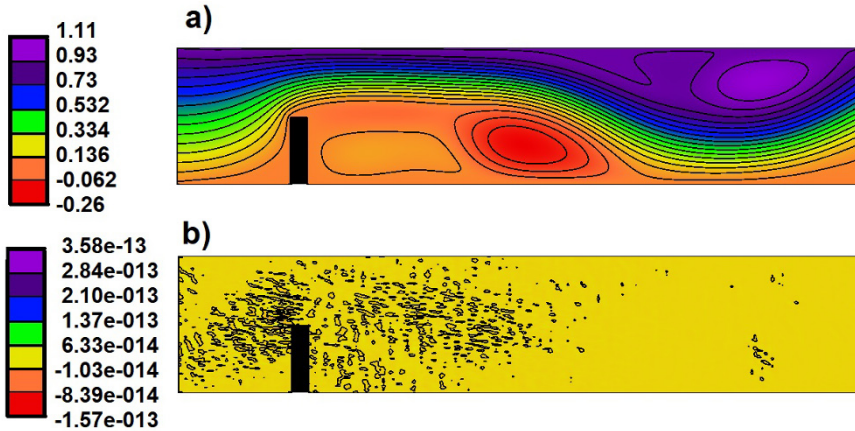
Fig. 7.2: The flow of classical fluid in a channel with the ledge. Re = 500. a streamline flow, b) distribution of $\nabla \cdot \vec{v}$.

The numerical simulation shows important differences in the flow of a micropolar liquid compare to a classical one. The transition of the flow from continuous to recirculation occurs in a micropolar liquid much later [17].

The main topic of this article is the numerical simulation of incompressible media. For a liquid, the incompressibility condition is given by (7.7). The measure of the accuracy of the fulfillment of the incompressibility condition in numerical simulation is the deviation of $\nabla \cdot \vec{v}$ from zero.

The distribution of $\nabla \cdot \vec{v}$ in the computational domain for micropolar liquid is shown in Fig. 7.1b. As can be seen from this figure, the maximum of $\nabla \cdot \vec{v}$ does not exceed the value of 10^{-13}. Which is almost close to the accuracy of computer calculations. The distribution of this value in the computational domain looks like white noise, which is vanishingly small in magnitude.

The results of the calculation of the distribution of $\nabla \cdot \vec{v}$ for a classical fluid are shown in Fig. 7.2b. Figure 7.2b shows the incompressibility condition (7.7) is satisfied with high accuracy.

7.3 Numerical Modeling of the Deformation of a Rubber-Like Incompressible Solid Body

This chapter deals with the problems of numerical modeling of an incompressible hyperelastic material. Elastomers or rubber-like materials are usually used in applications in which material must deform easily. That material exhibit a highly nonlinear behavior characterized by hyperelastic deformability and incompressibility. The study of rubber-like bodies is of great practical interest, so many different methods have

been developed for finding stresses and deformations in such bodies. Extensive literature is devoted to modeling the stationary and non-stationary behavior of elastomers [20–22] among others.

For example, in [23, 24] a computational technique for steady and unsteady deformations of elastomers as applied to seals in hydroelastic lubrication applications was developed. Consider the features of solving the problem of modeling the behavior of an incompressible elastomer. The general system includes conservation laws of mass, and momentum:

$$\nabla \cdot \vec{v} = 0, \tag{7.32}$$

$$\rho \frac{d\vec{v}}{dt} = \nabla \cdot \boldsymbol{\sigma} \tag{7.33}$$

and constitutive relationship for hyperelastic media [25]

$$\boldsymbol{\sigma} = -p\boldsymbol{I} + h_1 \boldsymbol{B} + h_2 \boldsymbol{B}^2, \tag{7.34}$$

where

$$\boldsymbol{B} = \boldsymbol{F} \cdot \boldsymbol{F}^T, \quad \boldsymbol{F} = d\vec{r}/d\vec{R} \equiv \vec{r}\nabla_{\vec{R}}, \tag{7.35}$$

t is the time; $\vec{v}$ is the velocity; ρ is the density; $\boldsymbol{\sigma}$ is the stress tensor; p is the pressure; $\boldsymbol{I}$ is a unit tensor; $\nabla_{\vec{R}} = \vec{i}_i \partial/\partial X_i$; $\vec{i}_i$ are the unit vectors ($i = 1, 2, 3$); $\vec{r} = \vec{e}_i x_i$ is the actual radius vector; $\vec{R} = \vec{e}_i X_i$ is the initial radius vector; h_1 and h_2 are the material properties that are functions of the invariants of $\boldsymbol{B}$ [21]; the summation convention from 1 to 3 over dummy subscripts is applied.

Let a 3D nonorthogonal Lagrangian mesh consists of linear tetrahedral elements (Fig. 7.3), unloaded at the initial moment and changing further under the action of an external load [24].

Let us find a finite-difference approximation of Eq. (7.34) for the tetrahedron (see Sect. 7.2 also for 2D case). We set a linear transformation of tetrahedron from the initial $\vec{R}$ to the actual $\vec{r}$ configuration [24]:

$$\vec{r} = \boldsymbol{A} \cdot \vec{R} + \vec{b}, \tag{7.36}$$

where $\boldsymbol{A}$ and $\vec{b}$ are 3D tensor and 3D vector which contain coefficients of linear transformation. Then substitution (7.36) to (7.35) we obtain

$$\boldsymbol{F} = \frac{d\vec{r}}{d\vec{R}} = \frac{d(\boldsymbol{A} \cdot \vec{R} + \vec{b})}{d\vec{R}} = \boldsymbol{A}. \tag{7.37}$$
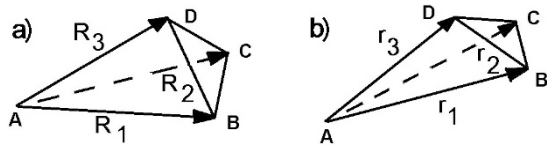
Fig. 7.3: Tetrahedral element. a) initial (unloaded) configuration, b) actual configuration.

We can write for the tetrahedron (Fig. 7.3) the next system

$$\begin{cases} \vec{r}_1 = \boldsymbol{A} \cdot \vec{R}_1 \\ \vec{r}_2 = \boldsymbol{A} \cdot \vec{R}_2 \\ \vec{r}_3 = \boldsymbol{A} \cdot \vec{R}_3 \end{cases}, \tag{7.38}$$

where $\vec{R}_1 = \vec{R}_B - \vec{R}_A$, $\vec{R}_2 = \vec{R}_C - \vec{R}_A$, $\vec{R}_3 = \vec{R}_C - \vec{R}_A$ and $\vec{r}_1 = \vec{r}_B - \vec{r}_A$, $\vec{r}_2 = \vec{r}_C - \vec{r}_A$, $\vec{r}_3 = \vec{r}_C - \vec{r}_A$ are the triples of vectors, that define the tetrahedron at the initial and actual moments (Fig. 7.3).

The system (7.38) has the solution:

$$\boldsymbol{A} = \vec{r}_i \vec{R}^i. \tag{7.39}$$

Here $\vec{R}^i$ and $\vec{R}_i$ $(i = 1, 2, 3)$ are the reciprocal set vectors, i.e.:

$$\vec{R}^1 = \frac{\vec{R}_2 \times \vec{R}_3}{\vec{R}_1 \cdot (\vec{R}_2 \times \vec{R}_3)}, \quad \vec{R}^2 = \frac{\vec{R}_3 \times \vec{R}_1}{\vec{R}_1 \cdot (\vec{R}_2 \times \vec{R}_3)}, \quad \vec{R}^3 = \frac{\vec{R}_1 \times \vec{R}_2}{\vec{R}_1 \cdot (\vec{R}_2 \times \vec{R}_3)}. \tag{7.40}$$

Then the finite-difference representation of the tensor $\boldsymbol{B}$ (7.35) becomes:

$$\boldsymbol{B} = \vec{r}_i \vec{i}_i \cdot \boldsymbol{G} \cdot \vec{i}_m \vec{r}_m, \tag{7.41}$$

or

$$\boldsymbol{B} = \vec{r}_i \vec{i}_i \cdot \boldsymbol{g}^{-1} \cdot \vec{i}_m \vec{r}_m,$$

where tensors $\boldsymbol{G}$ and $\boldsymbol{g}$ are expressed in components form:

$$\boldsymbol{G} = \begin{vmatrix} \vec{R}^1 \cdot \vec{R}^1 & \vec{R}^1 \cdot \vec{R}^2 & \vec{R}^1 \cdot \vec{R}^3 \\ \vec{R}^2 \cdot \vec{R}^1 & \vec{R}^2 \cdot \vec{R}^2 & \vec{R}^2 \cdot \vec{R}^3 \\ \vec{R}^3 \cdot \vec{R}^1 & \vec{R}^3 \cdot \vec{R}^2 & \vec{R}^3 \cdot \vec{R}^3 \end{vmatrix}, \quad \boldsymbol{g} = \begin{vmatrix} \vec{R}_1 \cdot \vec{R}_1 & \vec{R}_1 \cdot \vec{R}_2 & \vec{R}_1 \cdot \vec{R}_3 \\ \vec{R}_2 \cdot \vec{R}_1 & \vec{R}_2 \cdot \vec{R}_2 & \vec{R}_2 \cdot \vec{R}_3 \\ \vec{R}_3 \cdot \vec{R}_1 & \vec{R}_3 \cdot \vec{R}_2 & \vec{R}_3 \cdot \vec{R}_3 \end{vmatrix}, \quad \boldsymbol{G} = \boldsymbol{g}^{-1}. \tag{7.42}$$

Remark 7.1. From expression (7.42) follows that an arbitrary relative rotation of the initial (Fig. 7.3a) and actual (Fig. 7.3b) tetrahedrons does not affect the value of the tensor $\boldsymbol{B}$ and, therefore, does not require to correct the results of simulation from the rigid body rotation.

Remark 7.2. The 3D approximation of any differential relations $\nabla \Phi, \nabla \cdot \Phi, \nabla \times \Phi$, etc. for the tetrahedral element can be expressed symbolically in the following compact and universal form [24] (see Sect. 7.2, Eq. (7.22) for comparison)

$$\nabla \odot \Phi = \vec{r}^s \odot \Phi_s, \tag{7.43}$$

where Φ is scalar, vector, or tensor nodal variables; $\odot$ denotes distributive operation (dot, cross products, etc.) permissible for Φ; $\Phi_1 = \Phi_B - \Phi_A$, $\Phi_2 = \Phi_C - \Phi_A$, $\Phi_3 = \Phi_C - \Phi_A$. For example

$$\nabla \cdot \vec{v} = \vec{r}^s \cdot \vec{v}_s, \quad \nabla \vec{v} = \vec{r}^s \vec{v}_s, \quad \vec{v} \nabla = \vec{v}_s \vec{r}^s, \quad \nabla T = \vec{r}^s T_s.$$

Follow to the expression (7.41) the next finite-difference scheme for tetrahedral element

$$\boldsymbol{B} = h_1 \vec{r}_i \vec{i}_i \cdot \boldsymbol{G} \cdot \vec{i}_m \vec{r}_m + h_2 \vec{r}_j \vec{i}_j \cdot \boldsymbol{G} \cdot \vec{i}_n \vec{r}_n \cdot \vec{r}_p \vec{i}_p \cdot \boldsymbol{G} \cdot \vec{i}_q \vec{r}_q \qquad (7.44)$$

can be written for constitutive relationship (7.34). The finite difference-representation of the incompressibility condition (7.32) corresponds to the condition:

$$V = V_0, \qquad (7.45)$$

where $V_0 = \vec{R}_1 \cdot (\vec{R}_2 \times \vec{R}_3)/6$ is the initial volume of tetrahedron; $V = \vec{r}_1 \cdot (\vec{r}_2 \times \vec{r}_3)/6$ is the actual volume of the tetrahedron. For the numerical solution of the system (7.32)–(7.34) the implicit numerical method was used (see Appendix).

Figure 7.4 shows the results of the simulation of the bending of a hyperelastic thick-walled tube with the radius R=1cm and wall thickness R/4. Material properties h_1 and h_2 were taken similarly with natural rubber. The initial mesh and initial (unloaded) configuration is shown in Figs. 7.4a,b. The distribution of deformation is shown in Figs. 7.4e,f.

Numerical experiments have shown that, after bending, the hyperelastic tube can take various stationary shapes. The final shapes of the tube are greatly influenced by how the bending takes place during the simulation. Two such stable solutions and their cross-sections in the median plane of the tube are shown in Figs. 7.4c,d.

Figure 7.5 shows the results of the simulation of the rebounding of the hyperelastic ball from a rigid obstacle. The unloaded diameter of the ball equals to 6cm. The ball flies up to the obstacle with components of speed $V_x = V_y$ =50m/sec, V_z =-50m/sec. The coordinate axes x and y lie in the plane of the obstacle, and the z-axis is perpendicular to the obstacle. Rebound from the obstacle occurs without slipping.
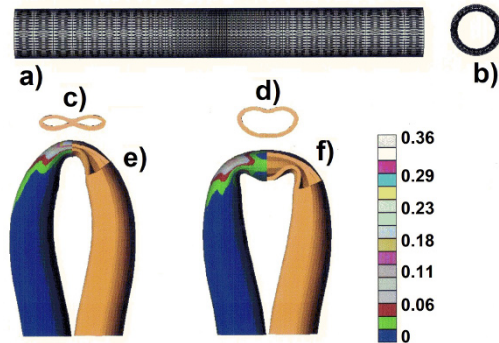
Fig. 7.4: The bending of hyperelastic incompressible thick-walled tube.

Fig. 7.5: Rebound of hyper-
elastic incompressible ball.
a) $t = 0$ s, b) $t = 2 \cdot 10^{-3}$ s.
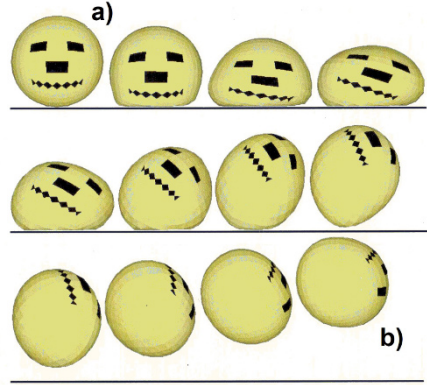
7.4 Numerical Modeling of Stresses in the Rigid Body

The question of finding stresses in the absolutely solid (rigid) body was discussed in literature [2, 3], and more. They relied on the idea that the concept of a rigid body, although different from the concept of an elastic body, it is possible to imagine the development of the former as the limit of the sequence of the latter. In this article, we will try to approach the solution to the problem from the point of view of numerical simulation and numerical experimentation.

The model of a rigid body is used in analytical mechanics when solving dynamic problems that do not include the problem of finding stresses. An absolutely solid body is an ideal structure obtained as the limit of deformable bodies. The determining relation between binding stresses and displacements is not necessary to determine the motion of a solid, unlike deformable continuous media.

In elastic body mechanics, the incompressible condition is used, for example, for the simulation of rubber-like bodies, for which the incompressible condition determines the immutability of the volume, but the shear deformations remain. A large section of hydrodynamics is engaged in describing the behavior of incompressible liquids.

Consider an equation of momentum and constitutive relation for the elastic body (Hooke's low):

$$\nabla \cdot \sigma = 0,$$
$$p = -K(\nabla \cdot \vec{u}),$$
$$S = G\left(\nabla \vec{u} + \vec{u}\nabla - 2/3\boldsymbol{I}(\nabla \cdot \vec{u})\right),$$

(7.46)

where $\sigma = -p\vec{I} + \vec{S}$; $\vec{u}$ is the displacement. Let stress be given on a part of the outer boundary of the body σ^*.

Let us write the system in dimensionless form. Introduce the scales as follow: $[L]$ is for length, $[U]$ is for displacement and $[|\sigma^*|]$ is for stress. Substituting the scales in (7.46), we obtain dimensionless equations:

$$\nabla \cdot \boldsymbol{\sigma} = 0,$$

$$p = -\frac{K[U]}{[L][|\sigma^*|]}(\nabla \cdot \vec{u}),$$

$$\boldsymbol{S} = \frac{G[U]}{[L][|\sigma^*|]}(\nabla \vec{u} + \vec{u}\nabla - 2/3\boldsymbol{I}(\nabla \cdot \vec{u})).$$

(7.47)

Here and below, the notation for dimensionless quantities (for simplicity) is retained. Let $[U] = [L][|\sigma^*|]/K$, then Eq. (7.47) are rewritten in the form:

$$\nabla \cdot \boldsymbol{\sigma} = 0,$$

$$p = -\nabla \cdot \vec{u},$$

$$\boldsymbol{S} = \frac{G}{K}(\nabla \vec{u} + \vec{u}\nabla - 2/3\boldsymbol{I}(\nabla \cdot \vec{u})).$$

(7.48)

In continuum mechanics, incompressibility is represented by the equation

$$\nabla \cdot \vec{v} = 0$$

(7.49)

for incompressible liquid and

$$\nabla \cdot \vec{u} = 0$$

(7.50)

for incompressible elastic media. Thus, the system (7.48) can be rewritten for an incompressible elastic media in the form:

$$\nabla \cdot \boldsymbol{\sigma} = 0,$$

$$\nabla \cdot \vec{u} = 0,$$

$$\boldsymbol{S} = \frac{G}{K}(\nabla \vec{u} + \vec{u}\nabla - 2/3\boldsymbol{I}(\nabla \cdot \vec{u})).$$

(7.51)

Here we propose to do the next step and define a rigid body as:

$$\nabla \cdot \vec{\sigma} = 0,$$

$$\nabla \cdot \vec{u} = 0,$$

$$\nabla \vec{u} + \vec{u}\nabla - 2/3\vec{I}(\nabla \cdot \vec{u}) = 0.$$

(7.52)

In other words, in addition to the incompressibility condition (7.51) second equation, the condition associated with the unchanged shape of a body is introduced (7.52) in the third equation.

Let us ask the question: does there exist a nontrivial solution of system (7.52) such that the conditions

$$\vec{u} = 0, \quad \vec{\sigma} \neq 0$$

(7.53)

are satisfied? To answer this question, we have done several numerical experiments.

The main purpose of this section is to show the possibility of numerical simulation of stresses in a perfectly rigid body. At this stage of research, we did not care about the development of effective numerical methods, leaving this for later. For the solution

of the system (7.52), we used the next simple explicit method. Let $\vec{u}^k$, p^k, $\vec{S}^k$, are an initial estimates of $\vec{u}$, p, $\vec{S}$ for $k = 0$, where k is a number of interaction.

Step 1:
$$\vec{\xi}_u^k = -\tau_u (\nabla \cdot \vec{\sigma}^k),$$
$$\xi_p^k = -\tau_p (\nabla \cdot \vec{u}^k),$$
$$\vec{\xi}_S^k = \tau_S \left(\nabla \vec{u}^k + \vec{u}^k \nabla - 2/3 \vec{I} (\nabla \cdot \vec{u}^k) \right),$$

$$\max \left(\frac{|\vec{\xi}_u^k|}{\tau_u}, \frac{|\xi_p^k|}{\tau_p}, \frac{|\vec{\xi}_S^k|}{\tau_S} \right) < \varepsilon \rightarrow yes \rightarrow \vec{u}^k, p^k, \vec{S}^k \text{ are the solution of } (7.52) \rightarrow STOP$$

$$\downarrow$$

no

$$\downarrow$$

Step 2:
$$\vec{u}^{k+1} = \vec{\xi}_u^k,$$
$$p^{k+1} = p^k + \xi_p^k,$$
$$\vec{S}^{k+1} = \vec{S}^k + \vec{\xi}_S^k,$$

Go to Step 1.

Here τ_u, τ_S and τ_p are an iteration parameters; ε is a small parameter. Numerical calculations were carried out with double precision. Consider the results of the numerical simulations.

7.4.1 First Example

2D square 1×1 under compressive external stress. The simulation was done in 2D Cartesian coordinates (x, y). The square is mounted on a rigid base with the possibility of slipping. An external normal stress equal to 1 is applied to a region with a length of 0.5 (Fig. 7.6).

A non-trivial solution (7.53) of system (7.52) was found numerically. The distribution of the pressure and the modulus of displacement $|\vec{u}|$ in the rigid body are shown in Figs. 7.6a,b reciprocally. As can be seen from the Fig. 7.6b, displacements in any point of the computational domain are vanishingly and small equal to or less than $\sim 5 \times 10^{-17}$, which indicates the complete fulfilment of the incompressibility conditions (7.52) (second and third equations). The value $\sim 5 \times 10^{-17}$ corresponds to zero for the range of numerical values of the quantities involved in the calculation and calculations with double precision.
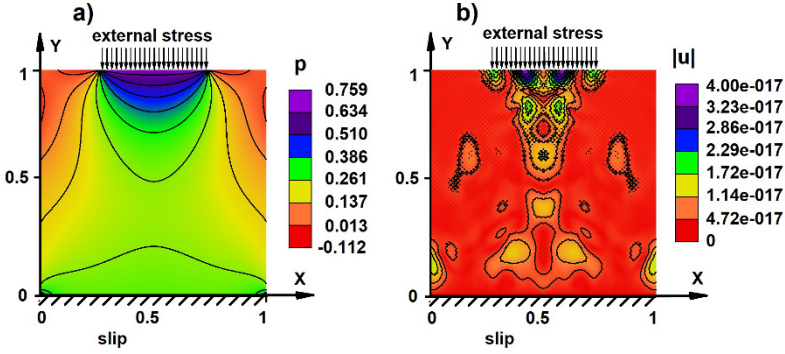
Fig. 7.6: Rigid square under external stress. $\tau_u = 10^{-6}$, $\tau_p = 2$, $\tau_S = 1$. a) distribution of the pressure p, b) distribution of the displacement modulus $|\vec{u}|$.

The numerical experiments show that the results of modeling do not depend on the values of τ_u and depend on the ratio τ_S/τ_p. Different values of this ratio lead to a different distribution of stresses in the body (the displacement values remained below the given small value ε always).

For comparison, a numerical simulation for the same body was done according to the system (7.48) (elastic body) using the next explicit numerical algorithm:

Step 1:
$$\vec{\xi}_u^k = -\tau(\nabla \cdot \vec{\sigma}^k),$$
$$\xi_p^k = -\nabla \cdot \vec{u}^k,$$
$$\vec{\xi}_S^k = \frac{G}{K}\left(\nabla \vec{u}^k + \vec{u}^k \nabla - 2/3\vec{I}(\nabla \cdot \vec{u}^k)\right),$$
$$\max(|\vec{\xi}_u^k|/\tau) < \varepsilon \to yes \to \vec{u}^k, p^k, \vec{S}^k \text{ are the solution of (7.48)} \to STOP$$

$$\downarrow$$

no

$$\downarrow$$

Step 2:
$$\vec{u}^{k+1} = \vec{u}^k + \vec{\xi}_u^k,$$
$$p^{k+1} = \xi_p^k,$$
$$\vec{S}^{k+1} = \vec{\xi}_S^k,$$

Go to Step 1.

Here τ is an iteration parameter.
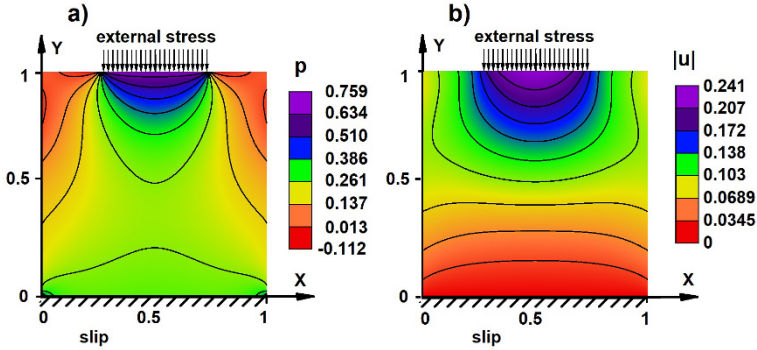
Fig. 7.7: Solid square under external stress. $\tau = 10^{-6}$, $K = 2$, $G = 1$. a) distribution of the pressure p, b) distribution of the displacement modulus $|\vec{u}|$.

Figure 7.7 illustrates a distribution of pressure (Fig. 7.7a) and modulus of displacement $|\vec{u}|$ (Fig. 7.7b) within the solid square for $G/K = 0.5$. We can see that the distributions of pressure in rigid (Fig. 7.6a) and solid (Fig. 7.7a) squares are identical. Calculations show that the values of other components of the stress tensor completely coincide. In contrast, as can be seen from the comparison of Fig. 7.6b and Fig. 7.7b, the distribution of displacement is completely different.

7.4.2 Second Example

The loading of the rectangular channel is considered. The height and width of the rectangular channel are both equal to 1. The width of the supports of the rectangular channel is equal to 0.2.

Two variants of the problem are considered: rigid rectangular channel Fig. 7.8 and solid rectangular channel Fig. 7.9. All parameters are the same as in the previous example. The base of the left support of the rectangular channel is fixed. The gap between the base and the unloaded right support of the rectangular channel equals 10^{-12}. The channel is loaded with the same external stress equal to 1 as shown in Figs. 7.8 and 7.9.

The distribution of a p for the rigid rectangular channel is shown in Fig. 7.8a. As can be seen from this figure, the gap between the right support and the base has not changed. As a result, the entire load fell on the left support. The distribution of a p for the solid rectangular channel is shown in Fig. 7.9a. Here the pattern is opposite compared to Fig. 7.8a. As a result of the external stress the gap between the rectangular channel and the base became equal to zero and the entire load fell on the right support. As can be seen from the Fig. 7.8b, displacements in any point of the rigid rectangular channel equal or less than $\sim 3 \times 10^{-5}$, which indicates the complete fulfilment of the incompressibility conditions (7.52) (second and third equations).
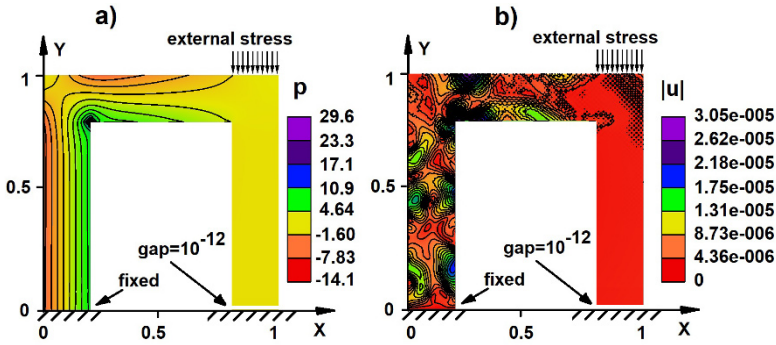
Fig. 7.8: Rigid rectangular channel. $\tau_u = 10^{-6}$, $\tau_p = 2$, $\tau_S = 1$. a) distribution of the pressure p, b) distribution of the displacement modulus $|\vec{u}|$.
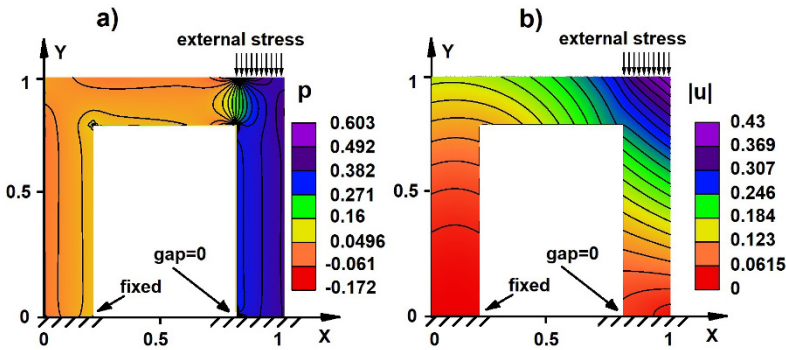
Fig. 7.9: Solid rectangular channel. $\tau_u = 10^{-6}$, $\tau_p = 2$, $\tau_S = 1$. a) distribution of the pressure p, b) distribution of the displacement modulus $|\vec{u}|$.

Further continuation of steps 1 and 2 of the algorithm allows for decreasing this quantity indefinitely. However, this accuracy of $10^{-3}...10^{-4}$ is already sufficient.

Appendix A: 3D Iterative Alternative Direction Implicit Method

Let us solve the 3D system of equations:

$$\Lambda f + af + b = 0, \tag{7.54}$$

where f is a unknown vector; Λ is a differences operator; a and b are coefficients. Let $f^1 = f$ is an initial estimate of f.

Step 1:
$$\xi^k = \tau(\Lambda f^k + a f^k + b),$$

$$\max |\xi^k| < \varepsilon \rightarrow yes \rightarrow f^k \text{ is solution} \rightarrow STOP.$$

$$\downarrow$$

no

$$\downarrow$$

Step 2:
$$\frac{\xi^{k+1/3} - \xi^k}{\tau} = \Lambda_1 \xi^{k+1/3} + a_1 \xi^{k+1/3},$$

Step 3:
$$\frac{\xi^{k+2/3} - \xi^{k+1/3}}{\tau} = \Lambda_1 \xi^{k+2/3} + a_1 \xi^{k+2/3},$$

Step 4:
$$\frac{\xi^{k+1} - \xi^{k+2/3}}{\tau} = \Lambda_1 \xi^{k+1} + a_1 \xi^{k+1},$$

Step 5:
$$f^{k+1} = f^k + \xi^{k+1},$$

Go to Step 1.

ξ is residual of f; $k = 1, 2, 3, \ldots$ is number of iteration; $\max |\xi|$ is maximum of ξ over all mesh nodes; ε is small parameter; Λ_1, , Λ_2 and Λ_3 are the differences operators; a_1, a_2 and a_3 are the coefficients; τ is an iteration parameters.

Let $\Lambda = \Lambda_1 + \Lambda_2 + \Lambda_3$ and $a = a_1 + a_2 + a_3$ then from steps 2–4 follows that

$$\begin{cases} (I - \tau\Lambda_1 - \tau a_1)\xi^{k+1/3} = \xi^k \\ (I - \tau\Lambda_2 - \tau a_2)\xi^{k+2/3} = \xi^{k+1/3} \\ (I - \tau\Lambda_3 - \tau a_3)\xi^{k+1} = \xi^{k+2/3} \end{cases}, \qquad (7.55)$$

where I is a unit operation, or

$$(I - \tau\Lambda_1 - \tau a_1)(E - \tau\Lambda_2 - \tau a_2)(I - \tau\Lambda_3 - \tau a_3)\xi^{k+1} = \xi^k,$$

or

$$\xi^{k+1} - \xi^k = \tau(\Lambda\xi^{k+1} + a\xi^{k+1}) + \tau^2(\Lambda_1\Lambda_2 + \ldots)\xi^{k+1}. \qquad (7.56)$$

Then

$$\xi^{k+1} = \tau(\Lambda\xi^{k+1} + a\xi^{k+1} + b) + \tau^2(\Lambda_1\Lambda_2 + \ldots)\xi^{k+1}. \qquad (7.57)$$

From (7.57) follows that this method correspond with the accuracy $O(\tau^2)$ to the completely implicit scheme

$$\frac{f^{k+1} - f^k}{\tau} = \Lambda \xi^{k+1} + a\xi^{k+1} + b. \tag{7.58}$$

Remark 7.3. Let $\Lambda \neq \Lambda_1 + \Lambda_2 + \Lambda_3$, or $a \neq a_1 + a_2 + a_3$. Nevertheless if $\xi^{k+1} \to 0$ then f^{k+1} is a solution of equation (7.54).

For example, in the simplest case when $\Lambda_1 = 0$, $\Lambda_2 = 0$ and $\Lambda_3 = 0$ then steps 2–4 are disappeared and the method is transformed to the simplest explicit method for solving Eq. (7.55).

Step 1:
$$\xi^k = \tau(\Lambda f^k + af^k + b),$$

$$\max|\xi^k| < \varepsilon \to yes \to f^k \text{ is solution} \to STOP.$$

$$\downarrow$$

$$no$$

$$\downarrow$$

Step 2:
$$f^{k+1} = f^k + \xi^{k+1},$$

Go to Step 1.

References

[1] Truesdell C, Noll W (1965) The Non-Linear Field Theories of Mechanics / Die Nicht-Linearen Feldtheorien der Mechanik. In: Flügge S (ed) Handbuch der Physik, Prinzipien der theoretischen Physik / Principles of Theoretical Physics, vol III/3, Springer, Berlin Heidelberg, pp 1–541

[2] Grioli G (1983) On the stress in rigid bodies. Meccanica **18**(1):3–7

[3] Fosdick R, Royer-Carfagni G (2004) Stress as a constraint reaction in rigid bodies. Journal of Elasticity **74**(3):265–276

[4] Fletcher CAJ (2006) Computational Techniques for Fluid Dynamics, Scientific Computation, vol 2 - Specific Techniques for Different Flow Categories. Springer, Berlin Heidelberg

[5] Hirsch C (2007) Numerical Computation of Internal and External Flows. John Wiley & Sons, New York

[6] Roache PJ (1998) Fundamentals of Computational Fluid Dynamics. Hermosa Publishers

[7] Bessonov NM, Koleshko SB (1988) Numerical simulation of stationary flow in artificial hearts valve on base of solution of Navier-Stokes equations on nonorthogonal grids (in Russ.). Simulation in Mechanics **22**(19)

[8] Bessonov N, Pojman JA, Volpert V (2004) Modelling of diffuse interfaces with temperature gradients. Journal of Engineering Mathematics **49**(4):321–338

[9] Bessonov, N, Pojman, J, Viner, G, Volpert, V, Zoltowski, B (2008) Instabilities of diffuse interfaces. Mathematical Modelling of Natural Phenomena **3**(1):108–125

[10] Pojman JA, Chekanov Y, Wyatt V, Bessonov N, Volpert V (2009) Numerical simulations of convection induced by Korteweg stresses in a miscible polymer-monomer system: Effects of variable transport coefficients, polymerization rate and volume changes. Microgravity Science and Technology **21**(3):225–237

[11] Douglas J, Gunn J (1964) A general formulation of alternating direction methods.Part I. Parabolic and hyperbolic problems. Numerische Mathematik **6**(1):428–453

[12] Kovenya VM, Yanenko NN (1981) The Method of Splitting in Gas Dynamics Problems (in Russ.). Izdatel'stvo Nauka, Novosibirsk

[13] Yanenko NN (1971) Method of Fractional Steps - The Solution of Problems of Mathematical Physics in Several Variables. Hermosa Publishers

[14] Eringen AC (1966) Theory of micropolar fluids. Journal of Mathematics and Mechanics **16**(1):1–18

[15] Aero EL, Bulygin AN, Kuvshinskii EV (1965) Asymmetric hydromechanics. Journal of Applied Mathematics and Mechanics **29**(2):333–346

[16] Bessonov NM, Frolova KP (2022) Application of micropolar theory to the description of ultrathin liquid layers. In: Polyanskiy VA, Belyaev AK (eds) Mechanics and Control of Solids and Structures, Springer Nature, Cham, Advanced Structured Materials, vol 164, pp 49–73

[17] Bessonov N, Aero E, Veretennikova T (1991) Numerical simulation of moment (micropolar) liquid flow in channels of complex shape (in Russ.). Preprint 56, IPME RAN

[18] Fomicheva M, Müller W, Vilchevskaya E, Bessonov N (2019) Funnel flow of a Navier-Stokes-fluid with potential applications to micropolar media. Facta Universitatis, Series: Mechanical Engineering **17**(2):255–267

[19] Fomicheva M, Vilchevskaya EN, Müller WH, Bessonov N (2019) Milling matter in a crusher: modeling based on extended micropolar theory. Continuum Mechanics and Thermodynamics **31**(5):1559–1570

[20] Mooney M (2004) A Theory of Large Elastic Deformation. Journal of Applied Physics **11**(9):582–592

[21] Morman Jr K (1994) A simple non-isothermal constitutive model for finite deformation rubber viscoelasticity. In: Voyiadjis GZ, Bank LC, Jacob LJ (eds) Mechanics of Materials and Structures, Studies in Applied Mechanics, vol 35, Elsevier, pp 297–318

[22] Rivlin RS (1956) Large elastic deformations. In: Eirich FR (ed) Rheology, Academic Press, New York

[23] Bessonov NM, Schultz WW (1997) Numerical simulation of 3D rubber-like solids with application to lubricated lip seals. Mechanical Engineering and Applied Mechanics, University of Michigan, Ford Motor Co, Detroit, USA

[24] Bessonov NM, Song DJ (2001) Application of vector calculus to numerical simulation of continuum mechanics problems. Journal of Computational Physics **167**(1):22–38

[25] Ciarlet PG (1993) Mathematical Elasticity, vol 1 - Three Dimensional Elasticity. North-Holland, Amsterdam

Chapter 8
Three-Dimensional Numerical Analysis of Natural Vibrations and Stability of Cylindrical Shells Interacting with Fluid

Sergey A. Bochkarev, Sergey V. Lekomtsev, Valerii P. Matveenko, and Alexander N. Senin

Abstract Natural vibrations and stability of cylindrical shells interacting with a quiescent and flowing ideal fluid are numerically investigated. A solution is implemented in a three-dimensional formulation using an algorithm that is based on the finite element method. In the numerical examples, shells with an elliptical cross section, coaxial shells, and shells with an eccentricity are considered. The influence of a fluid level inside these structures and axial misalignment on natural frequencies and vibration modes, and the critical velocities of instability are analyzed. Calculations has revealed the peculiarities of the dynamic characteristics of the shells under consideration in case of their partial filling with a fluid. It is shown that the stability of the system can be improved by selecting appropriate geometric parameters.

8.1 Introduction

Thin-walled cylindrical shells are the key structural elements, which are able to withstand considerable loads, strong vibrations or seismic effects. When they interact with fluids, resonance phenomena or loss of stability like flutter and divergence are possible. Dynamic processes that occur in this case can lead to large-amplitude vibrations, instantaneous or fatigue failure of the structure. In the context of the onset of an emergency, the greatest hazards are associated with storage tanks for technological and chemically aggressive fluids located in zones with increased seismic activity; pillars of river bridges; flexible tubes used in the oil-refining and aerospace industries; and different types of heat exchangers employed in power plants (assembly of parallel plates or group of circular cylindrical shells).

Sergey A. Bochkarev · Sergey V. Lekomtsev · Valerii P. Matveenko · Alexander N. Senin
Institute of Continuous Media Mechanics, Ural Branch of Russian Academy of Sciences, 1, Acad. Korolev str., 614068 Perm, Russian Federation,
e-mail: bochkarev@icmm.ru, lekomtsev@icmm.ru, mvp@icmm.ru, senin.a@icmm.ru

Distinguishing features in the interaction of shell structures with a quiescent or flowing fluid, as well as with a gaseous medium, have long been studied. An extensive bibliography of papers on this topic is presented in both parts of the well-known monograph [1, 2]. Literature reviews that expand this list of research sources and provide the reader with some pioneering works not mentioned yet can be found in recent articles by the authors [3–8]. Over the past few decades, analysis of the natural vibrations and hydroelastic stability of shells of revolution (cylindrical and conical, coaxial) has been carried out, as a rule, using a variety of numerical-analytical and numerical approaches implemented in an axisymmetric formulation or reduced to it. That is the reason why many significant factors remain unexplored, whose influence on the dynamic characteristics of the system can only be assessed when solving a 3D problem. The circumferential symmetry breaking of a cylindrical shell due to its partial filling with a fluid [9, 10], use of an open [11] or non-circular cross section [12–16], coaxial shells misalignment [7, 8, 17, 18], or due to the impact of spatial force factors, determines the specific behavior of natural vibration frequencies (mode shapes) and stability parameters, which is different from that of similar symmetrical configurations. Bearing in mind that the fluid flow has a destabilizing effect on the elastic shell and leads to significant changes in its dynamic behavior, the above-mentioned factors require careful analysis.

The main research tool used to solve the problems of hydroelasticity, including those of real practical interest, is a finite element method. In contrast to other numerous approaches, it is the most accurate and versatile method because it allows one to overcome the restrictions on the geometry of the structure and on the kinematic boundary conditions at its edges. The available commercial finite element analysis software helps researchers to solve transient, harmonic and modal problems via simulating the interaction of an arbitrary elastic structure and an acoustic environment [19]. However, there is no such possibility for stability problems in the case of a flowing fluid.

In this paper, the findings of studies on the hydroelastic interaction of shell structures asymmetric in the circumferential direction are generalized. The solution is found within the framework of a universal approach that is based on the developed three-dimensional mathematical formulation and its implementation by the finite element method.

8.2 Mathematical and Numerical Formulations

This section briefly describes the mathematical formulation and the corresponding finite element algorithm, which are designed to analyze natural vibrations and stability of three-dimensional thin-walled cylindrical shells in the general case with a non-circular cross section and interacting with an internal steady flow of an ideal compressible fluid. All basic relation are given for the configuration shown in Fig. 8.1, but they can be easily generalized to the case of coaxial [5, 6] and eccentric [8] cylindrical shells.

Fig. 8.1: Computational scheme of the elliptical cylindrical shell.
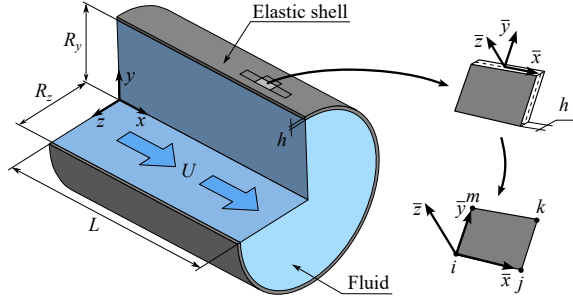
In the case of small perturbations the vortex-free dynamics of an ideal compressible fluid is described by wave equation [2, 20, 21], which is formulated in terms of the perturbation velocity potential ϕ in the global Cartesian coordinate system (x, y, z) and transformed to the weak form together with the impermeability and boundary conditions [21]. Finally, we get:

$$\int_{V_f} \nabla F_m \cdot \nabla \hat{\phi} \, dV + \int_{V_f} F_m \frac{1}{c^2} \frac{\partial^2 \hat{\phi}}{\partial t^2} dV + \int_{V_f} F_m \frac{2U}{c^2} \frac{\partial^2 \hat{\phi}}{\partial t \partial x} dV -$$

$$- \int_{V_f} F_m \frac{U^2}{c^2} \frac{\partial^2 \hat{\phi}}{\partial x^2} dV - \int_{S_\sigma} F_m \frac{\partial \hat{\bar{w}}}{\partial t} dS - \int_{S_\sigma} F_m U \frac{\partial \hat{\bar{w}}}{\partial x} dS = 0, \quad m = \overline{1, m_f}. \quad (8.1)$$

Here: $\hat{\phi}$ and $\hat{\bar{w}}$ are the trial solutions for the velocity potential ϕ and normal displacements of the thin-walled structure $\bar{w}$; V_f is the volume of fluid; S_σ is the fluid-structure interface; c is the speed of sound in a fluid; t is time; F_m and m_f are the basis functions and their number; U is the velocity of fluid in the direction of the x-axis.

The hydrodynamic pressure acting on the elastic structure wall is calculated using linearized Bernoulli's formula:

$$p = -\rho_f \left(\frac{\partial \phi}{\partial t} + U \frac{\partial \phi}{\partial x} \right), \quad (8.2)$$

where ρ_f is the density of a fluid. We use the following boundary conditions to solve Eq. (8.1):

$$x = 0 : \phi = 0, \quad x = L : \partial \phi / \partial x = 0, \quad (8.3)$$

where L is the length of the structure.

Modeling the shells partially filled with a fluid is based on the assumption that the free surface of the liquid S_{free} does not move and is not under the action of dynamic pressure and surface tension. An appropriate boundary condition is given by [10]:

$$\boldsymbol{x} \in S_{\text{free}} : \phi = 0. \quad (8.4)$$

A curvilinear surface of the structure is represented with sufficient accuracy as a set of flat rectangular segments (Fig. 8.1) [22]. Small strains in each of these segments are determined in the framework of the classical plate theory [23]:

$$\left\{\varepsilon_{\bar{x}\bar{x}}, \varepsilon_{\bar{y}\bar{y}}, \gamma_{\bar{x}\bar{y}}\right\}^{\mathrm{T}} = \left\{\varepsilon_{\bar{x}\bar{x}}^0, \varepsilon_{\bar{y}\bar{y}}^0, \gamma_{\bar{x}\bar{y}}^0\right\}^{\mathrm{T}} + \bar{z}\left\{\varepsilon_{\bar{x}\bar{x}}^1, \varepsilon_{\bar{y}\bar{y}}^1, \gamma_{\bar{x}\bar{y}}^1\right\}^{\mathrm{T}}, \tag{8.5}$$

$$\bar{\boldsymbol{\varepsilon}}^0 = \left\{\varepsilon_{\bar{x}\bar{x}}^0, \varepsilon_{\bar{y}\bar{y}}^0, \gamma_{\bar{x}\bar{y}}^0\right\}^{\mathrm{T}} = \left\{\frac{\partial \bar{u}}{\partial \bar{x}}, \frac{\partial \bar{v}}{\partial \bar{y}}, \frac{\partial \bar{u}}{\partial \bar{y}} + \frac{\partial \bar{v}}{\partial \bar{x}}\right\}^{\mathrm{T}},$$

$$\bar{\boldsymbol{\varepsilon}}^1 = \left\{\varepsilon_{\bar{x}\bar{x}}^1, \varepsilon_{\bar{y}\bar{y}}^1, \gamma_{\bar{x}\bar{y}}^1\right\}^{\mathrm{T}} = \left\{-\frac{\partial^2 \bar{w}}{\partial \bar{x}^2}, -\frac{\partial^2 \bar{w}}{\partial \bar{y}^2}, -2\frac{\partial^2 \bar{w}}{\partial \bar{x}\bar{y}}\right\}^{\mathrm{T}},$$

where $\bar{u}, \bar{v}, \bar{w}$ are the displacements of the points on the middle surface of the plane segment in the direction of the corresponding axes of the Cartesian coordinate system $(\bar{x}, \bar{y}, \bar{z})$ (Fig. 8.1).

The generalized vector $\bar{\boldsymbol{\varepsilon}}$, which contains the middle surface strains $\bar{\boldsymbol{\varepsilon}}^0$ and the curvatures $\bar{\boldsymbol{\varepsilon}}^1$, is written as:

$$\bar{\boldsymbol{\varepsilon}} = \begin{Bmatrix} \bar{\boldsymbol{\varepsilon}}^0 \\ \bar{\boldsymbol{\varepsilon}}^1 \end{Bmatrix} = \left\{\varepsilon_{\bar{x}\bar{x}}^0, \varepsilon_{\bar{y}\bar{y}}^0, \gamma_{\bar{x}\bar{y}}^0, \varepsilon_{\bar{x}\bar{x}}^1, \varepsilon_{\bar{y}\bar{y}}^1, \gamma_{\bar{x}\bar{y}}^1\right\}^{\mathrm{T}}. \tag{8.6}$$

The physical relations between the vector of forces and moments $\bar{t}$ and the vector of generalized strains $\bar{\boldsymbol{\varepsilon}}$ are formulated in the following form:

$$\bar{t} = \left\{N_{\bar{x}\bar{x}}, N_{\bar{y}\bar{y}}, N_{\bar{x}\bar{y}}, M_{\bar{x}\bar{x}}, M_{\bar{y}\bar{y}}, M_{\bar{x}\bar{y}}\right\}^{\mathrm{T}} = \boldsymbol{S}\bar{\boldsymbol{\varepsilon}}, \tag{8.7}$$

where the coefficients entering the matrix $\boldsymbol{S}$ are calculated for isotropic material using Young's modulus E and Poisson's ratio v by known way [23].

A mathematical formulation of the dynamics problem of thin-walled structure relies on the variational principle of virtual displacements, which takes into account the equation for hydrodynamic pressure (8.2) and the work done by inertial forces. In the absence of external loads it can be written in the matrix form as:

$$\int_{S_s} \delta\bar{\boldsymbol{\varepsilon}}^{\mathrm{T}}\boldsymbol{S}\bar{\boldsymbol{\varepsilon}}\mathrm{d}S + \int_{S_s} \delta\bar{\boldsymbol{d}}^{\mathrm{T}}\boldsymbol{J}\ddot{\bar{\boldsymbol{d}}}\mathrm{d}S + \int_{S_\sigma} \delta\bar{w}\,\rho_f\left(\frac{\partial \hat{\phi}}{\partial t} + U\frac{\partial \hat{\phi}}{\partial \bar{x}}\right)\mathrm{d}S = 0, \tag{8.8}$$

where $\bar{\boldsymbol{d}} = \{\bar{u}, \bar{v}, \bar{w}, \theta_{\bar{x}}, \theta_{\bar{y}}, \theta_{\bar{z}}\}^{\mathrm{T}}$ is the generalized vector of the thin-walled structure displacements, including rotation angles $\theta_{\bar{x}}, \theta_{\bar{y}}, \theta_{\bar{z}}$ with respect to the corresponding axes of the coordinate system $(\bar{x}, \bar{y}, \bar{z})$; S_s is the shell surface; $\boldsymbol{J} = \mathrm{diag}\,(J_0, J_0, J_0, J_2, J_2, J_2)$ is the inertia matrix, $J_0 = \rho_s h$, $J_2 = \rho_s h^3/12$ and ρ_s is the density of the elastic structure material.

The formulation of the natural vibrations problem is based on the representation

$$\boldsymbol{u}(\boldsymbol{x}, t) = \{\boldsymbol{d}(\boldsymbol{x}, t), \phi(\boldsymbol{x}, t)\}^{\mathrm{T}} = \tilde{\boldsymbol{u}}(\boldsymbol{x})\mathrm{e}^{\mathrm{i}\lambda t}, \tag{8.9}$$

where $\tilde{\boldsymbol{u}} = \left\{ \tilde{\boldsymbol{d}}(\boldsymbol{x}), \tilde{\phi}(\boldsymbol{x}) \right\}^{\mathrm{T}}$ is the vector function depending only on coordinates $\boldsymbol{x}$; i is the imaginary unit; $\lambda = \omega + \mathrm{i}\gamma$ is the characteristic index; ω is the natural frequency of vibrations; γ is the value, characterizing the damping of the system.

After substituting expression (8.9) into Eqs. (8.1) and (8.8), dividing by the exponent and implementing the known procedures of the finite element method, we obtain a coupled system of equations:

$$\left(-\lambda^2 \boldsymbol{M} + \mathrm{i}\lambda \boldsymbol{C} + \boldsymbol{K} + \boldsymbol{A} \right) \tilde{\boldsymbol{u}} = 0, \tag{8.10}$$

$$\boldsymbol{M} = \begin{bmatrix} \boldsymbol{M}_s & 0 \\ 0 & \boldsymbol{M}_f \end{bmatrix}, \quad \boldsymbol{C} = \begin{bmatrix} 0 & \boldsymbol{C}_{sf} \\ \boldsymbol{C}_{fs} & \boldsymbol{C}_f \end{bmatrix}, \quad \boldsymbol{K} = \begin{bmatrix} \boldsymbol{K}_s & 0 \\ 0 & \boldsymbol{K}_f \end{bmatrix}, \quad \boldsymbol{A} = \begin{bmatrix} 0 & \boldsymbol{A}_{sf} \\ \boldsymbol{A}_{fs} & \boldsymbol{A}_f \end{bmatrix},$$

where typical finite element matrices are determined in a well-known manner [6, 22]:

$$\boldsymbol{M}_f^e = \int\limits_{V_f} \frac{1}{c^2} \boldsymbol{F}^{\mathrm{T}} \boldsymbol{F} \mathrm{d}V, \quad \bar{\boldsymbol{M}}_s^e = \int\limits_{S_s} \boldsymbol{N}^{\mathrm{T}} \boldsymbol{J} \boldsymbol{N} \mathrm{d}S,$$

$$\boldsymbol{C}_f^e = \int\limits_{V_f} \frac{2U}{c^2} \frac{\partial \boldsymbol{F}^{\mathrm{T}}}{\partial x} \boldsymbol{F} \mathrm{d}V, \quad \bar{\boldsymbol{C}}_{fs}^e = -\int\limits_{S_\sigma} \boldsymbol{F}^{\mathrm{T}} \boldsymbol{N}_w \mathrm{d}S, \quad \bar{\boldsymbol{C}}_{sf}^e = \int\limits_{S_\sigma} \rho_f \boldsymbol{N}_w^{\mathrm{T}} \boldsymbol{F} \mathrm{d}S,$$

$$\boldsymbol{K}_f^e = \int\limits_{V_f} (\nabla \boldsymbol{F})^{\mathrm{T}} \nabla \boldsymbol{F} \mathrm{d}V, \quad \bar{\boldsymbol{K}}_s^e = \int\limits_{S_s} \boldsymbol{B}^{\mathrm{T}} \boldsymbol{S} \boldsymbol{B} \mathrm{d}S,$$

$$\boldsymbol{A}_f^e = -\int\limits_{V_f} \frac{U^2}{c^2} \frac{\partial \boldsymbol{F}^{\mathrm{T}}}{\partial x} \frac{\partial \boldsymbol{F}}{\partial x} \mathrm{d}V, \quad \bar{\boldsymbol{A}}_{fs}^e = -\int\limits_{S_\sigma} U \boldsymbol{F}^{\mathrm{T}} \frac{\partial \boldsymbol{N}_w}{\partial x} \mathrm{d}S, \quad \bar{\boldsymbol{A}}_{sf}^e = \int\limits_{S_\sigma} \rho_f U \boldsymbol{N}_w^{\mathrm{T}} \frac{\partial \boldsymbol{F}}{\partial x} \mathrm{d}S.$$

Here: $\boldsymbol{F}, \boldsymbol{N}, \boldsymbol{N}_w$ are the shape functions the trial solutions for the velocity potential of the fluid $\hat{\phi}$, the generalized vector of the nodal displacements of the thin-walled structure $\boldsymbol{d}$ and its normal component $\bar{w}$; $\boldsymbol{B}$ is the gradient matrix, which links the deformation vector with the vector of nodal displacements of the shell finite element. The constitutive relations defined in Eq. (8.5) do not contain the equation for rotation about the axis $\bar{z}$. To eliminate this problem, it is necessary to introduce zero rows and columns and a fictitious moment $M_{\bar{z}}$ into the stiffness matrix [22]. The matrices with overbar ($\bar{\boldsymbol{K}}_s^e, \bar{\boldsymbol{M}}_s^e, \bar{\boldsymbol{C}}_{sf}^e$, etc.) are formed in the coordinate system $(\bar{x}, \bar{y}, \bar{z})$. Their transformation to the global Cartesian coordinates (x, y, z) is performed for each element using the directional cosine matrix in a known way [6, 22].

In the finite element model, the perturbation velocity potential ϕ, the basis functions F_m, and the membrane displacements of the shell $\bar{u}$ and $\bar{v}$ are described using by Lagrange bi-linear shape functions. The bending displacement $\bar{w}$, the rotation angles $\theta_{\bar{x}}$ and $\theta_{\bar{y}}$ are approximated by the nonconforming cubic Hermite polynomials [22]. The discretization of the computational domains of the fluid and the thin-walled structure is carried out using the spatial 8-node prismatic and flat rectangular finite elements, respectively.

The system of equations (8.10) is converted into the generalized eigenvalue problem [24], which is solved by the implicitly restarted Arnoldi method [25]:

$$\left(\begin{bmatrix} C & K+A \\ -I & 0 \end{bmatrix} + i\lambda \begin{bmatrix} M & 0 \\ 0 & I \end{bmatrix} \right) \begin{Bmatrix} i\lambda\tilde{u} \\ \tilde{u} \end{Bmatrix} = 0. \tag{8.11}$$

The model described above and the finite element algorithm allow us to investigate a system of two coaxial or eccentric cylindrical shells with a fluid in the annular gap between them. In this case $\tilde{u} = \left\{ \tilde{d}^{(1)}, \tilde{d}^{(2)}, \phi \right\}^{\mathrm{T}}$ and the global matrices in equation (8.10) take the form:

$$M = \begin{bmatrix} M_s^{(1)} & 0 & 0 \\ 0 & M_s^{(2)} & 0 \\ 0 & 0 & M_f \end{bmatrix}, \quad K = \begin{bmatrix} K_s^{(1)} & 0 & 0 \\ 0 & K_s^{(2)} & 0 \\ 0 & 0 & K_f \end{bmatrix}, \tag{8.12}$$

$$C = \begin{bmatrix} 0 & 0 & -C_{sf}^{(1)} \\ 0 & 0 & C_{sf}^{(2)} \\ -C_{fs}^{(1)} & C_{fs}^{(2)} & C_f \end{bmatrix}, \quad A = \begin{bmatrix} 0 & 0 & -A_{sf}^{(1)} \\ 0 & 0 & A_{sf}^{(2)} \\ -A_{fs}^{(1)} & A_{fs}^{(2)} & A_f \end{bmatrix}.$$

where $\tilde{d}^{(1)}$ and $\tilde{d}^{(2)}$ are the generalized vectors of displacements of the inner and outer shells.

The numerical implementation of the finite element algorithm has been carried out in MATLAB software using the capabilities of the ANSYS package to create a mesh. The stability estimation is based on the analysis of complex eigenvalues of problem (8.11), which were obtained under the condition of gradually increasing fluid velocity. In our simulations we consider the shells with different kinematic boundary conditions at the edges and denote them as: F – free edge, S – simple support ($v = w = 0$) and C – rigid clamping ($u = v = w = 0$, $\theta_x = \theta_y = \theta_z = 0$).

8.3 Single Cylindrical Shells

The developed finite-element algorithm was applied to investigate the influence of the fluid level, the ratio of ellipse semi-axes and the linear dimensions on the natural frequencies and mode shapes of vibrations, and the boundary of the hydroelastic stability of circular and elliptical cylindrical shells interacting with quiescent and flowing fluid (Fig. 8.1). The analysis of the obtained results was carried out using the dimensionless quantities, such as the fluid level η, the ellipticity parameter β, the eigenvalue Λ, the natural frequency of vibrations Ω and the flow velocity Y:

$$\eta = \frac{V_f}{V_i}, \quad \beta = \frac{R_z}{R_y}, \quad \Lambda = \lambda R_y \psi, \quad \Omega = \omega R_y \psi, \quad \mathrm{Y} = U\psi, \quad \psi = \sqrt{\frac{\rho_s (1 - \nu^2)}{E}}, \quad (8.13)$$

where V_i is the volume of the shell interior, R_z and R_y are the ellipse semi-axes (Fig. 8.1). The parameters used in computations are listed in the Table 8.1.

Table 8.1: Computation parameters.

Case	E, GPa	ν	ρ_s, kg/m³	c, m/s	ρ_f, kg/m³	R_y, mm	h, mm	L/R_y
I	205	0.3	7800	1500	1000.0	77.25	1.5	2.99
II	206	0.3	7850	1500	1004.8	200	2.0	5.00

8.3.1 Circular Cylindrical Shells

It is known that the empty and fluid-filled vertical circular ($\beta = 1$) cylindrical shells are characterized by the multiple frequencies of the spectrum. They correspond to the symmetric and antisymmetric mode shapes with the same number of circumferential (j) and meridional (m) half-waves, which differ only by rotation in the circumferential direction. When horizontal shells are partially filled, mode shapes with one combination of the wave numbers (m, j) correspond to unequal natural frequencies (Fig. 8.2a, b). This difference varies and depends on the fluid level η of the structure (Fig. 8.3). The interesting thing about the lowest vibration modes is that, at any values of the parameter η, the displacements are always at a maximum in the fluid-structure interface (Fig. 8.2). A similar conclusion was made earlier in [10].

The change of the six lowest natural vibration frequencies of a horizontal circular cylindrical shells (Case I, $\beta = 1$) in response to the filling level η is shown in Fig. 8.3 for different variants of boundary conditions. It is seen that even a small amount of a fluid inside the structure causes a notable decrease in the vibration frequency, which most significantly affects the shell rigidly clamped at both edges (Fig. 8.3b).

Figure 8.4 illustrates the comparison of the natural vibration frequencies of the shells of different orientations depending on the amount of a fluid inside these structures (Case I, $\beta = 1$). In the case of horizontally located shells, we confine ourselves to considering the odd modes Ω_1, Ω_3, Ω_5, since the frequencies of even modes Ω_2, Ω_4, Ω_6 differ only slightly from them (Fig. 8.3). For the vertical configurations, the symmetric and antisymmetric mode shapes have multiple frequencies, and thus
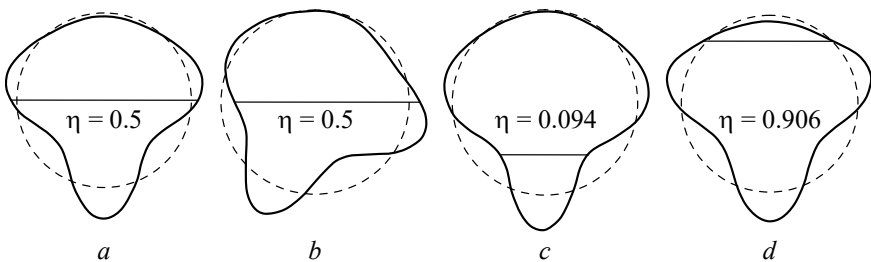
Fig. 8.2: Schematic view of mode shapes of a horizontal cylindrical shell (SS): $a - \omega_1 = 282$ Hz, $b - \omega_2 = 287$ Hz, $c - \omega_2 = 399$ Hz, $d - \omega_1 = 265$ Hz.
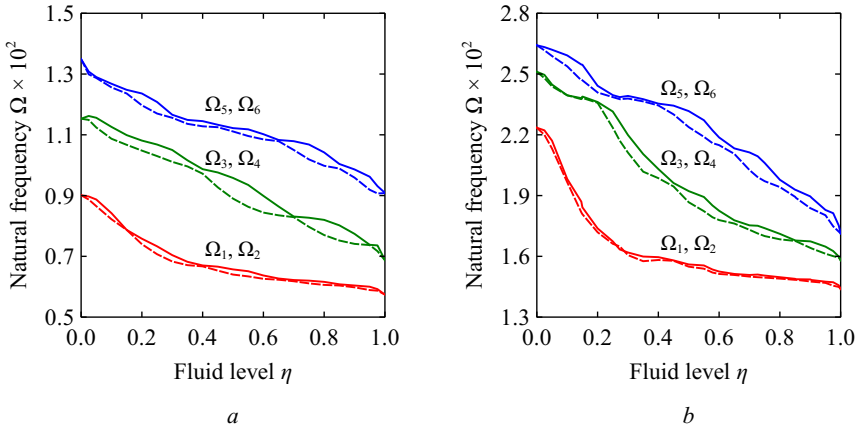
Fig. 8.3: Six lowest natural vibration frequencies of a horizontal cylindrical shell at different fluid level: a – CF, b – CC.

$\Omega_1 = \Omega_2$, $\Omega_3 = \Omega_4$ and $\Omega_5 = \Omega_6$. Analysis of the obtained dependencies showed that not only the added mass of a fluid but also the hydroelastic interaction on the wetted surface cause significant changes in the spectrum. This is reflected in the fact that, at the same amounts of the fluid, the natural vibration frequencies of the partially filled vertically and horizontally oriented shells fail to coincide in most cases. As seen in Fig. 8.4a, the frequencies of the horizontal structure clamped at one edge are lower compared to the vertical one. An exception is almost completely filled shells, for which the difference at $\eta > 0.9$ can be termed insignificant. A more complex dependence is observed under boundary conditions referring to rigid clamping at
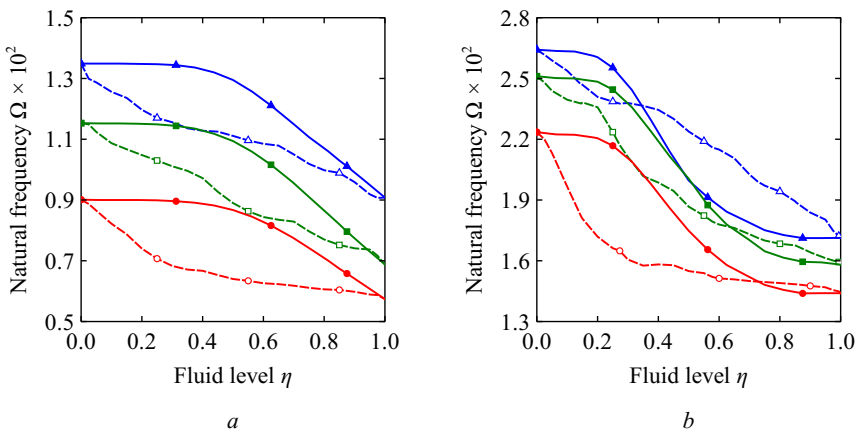
Fig. 8.4: Natural vibration frequencies Ω_1 ($\circ$, $\bullet$), Ω_3 ($\square$, $\blacksquare$), Ω_5 ($\triangle$, $\blacktriangle$) of a horizontal (dashed lines) and vertical (solid lines) cylindrical shell at different fluid level: a – CF, b – CC.

both edges (Fig. 8.4*b*). In this case, situations may arise where the natural vibration frequencies of the systems with different orientations coincide. As an example, we consider the modes Ω_1 and Ω_3 at $\eta \approx 0.72$ and $\eta \approx 0.35$ (the points of intersection of the dashed and solid lines), respectively.

The next example illustrates the problem of hydroelastic stability of a simply supported cylindrical shell (SS) interacting with an internal fluid flow (Case II, $\beta = 1$). The analytical solution of this problem at complete filling ($\eta = 1$) was derived in work [26]. It was found that, under such conditions for fixing the structure, the loss of stability occurs through divergence. With an increase in the flow velocity, the lowest natural frequency of the system decreases until it becomes equal to zero at $Y = Y_D$. At this moment, there appears a pair of imaginary parts of this mode, one of which is negative. Considering the results presented in Fig. 8.5, it follows that an increase in the length of the shell L leads to a noticeable decrease in the critical velocity of divergence Y_D. This dependence exhibits a non-monotonic character that can be attributed to the change in the vibration mode, according to which the loss of stability is implemented. As a result, the curve has a break, after which, instead of the local region of increase, the region of decrease appears. Fig. 8.5 shows that a decrease in the fluid level η leads to an increase in the critical velocities of instability. The calculation results demonstrate that the type of stability loss remains the same in this case. Dotted line in Fig. 8.5 corresponds to the results obtained in the framework of the two-dimensional formulation using the semi-analytical finite element method. The presented data illustrate the identity of the found critical velocities for different linear dimensions.

8.3.2 Elliptical Cylindrical Shells

In the numerical examples given in this section, horizontally located elliptical cylindrical shells (Case I) are considered. The study of the results revealed several
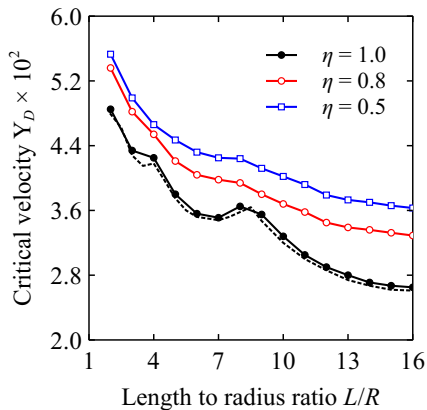
Fig. 8.5: Dimensionless critical velocities of divergence Y_D for circular cylindrical shells as a function of the ratio L/R.

distinguishing features in the behavior of the lowest natural frequencies of vibrations of these structures [3]. Analysis of the effect of the ellipticity parameter β was performed assuming that the size of the vertical semi-axis R_y is kept constant, unless otherwise specified. In this case a change in the value of β is associated with a monotonic change in the cross-sectional area of the shell and the fluid level in it at a fixed value of η.

Figure 8.6*a* shows that the presence of even a small amount of a fluid inside the horizontal circular and elliptical cylindrical shells promotes a significant decrease in their lowest natural frequency of vibrations. Moreover, at $\beta < 1$ it monotonically decreases over the entire range of the values of the parameter η and at $\beta > 1$ becomes an asymptotic dependence. It is seen that when a certain fluid level is reached, the frequency ceases to change from its further increase (Fig. 8.6*a*). The threshold value η, at which the asymptotic behavior occurs, is determined by the ellipticity parameter. This feature is clearly visible in Fig. 8.6*b*, where several curves begin to merge with each other at $\beta > 1.2$.

It should be noted that the dependence of the lowest natural frequency on the ellipticity parameter β exhibits the non-monotonic behavior (Fig. 8.6*b*) and reaches its maximum at $\beta < 1$. This feature is caused by a change in the vibration mode and is illustrated in more detail in Fig. 8.7 for the shells completely filled with a fluid. At $\beta = 1$, the frequencies corresponded to the symmetric and antisymmetric mode shapes with one combination of wave numbers (m, j) coincide. However, at $\beta \neq 1$, there may be more than two modes with the same number of half-waves in the longitudinal and circumferential directions. In this case, only the lowest frequency mode is taken into account. As can be seen from Fig. 8.7*a*, the lowest natural vibration frequency is determined by the frequencies which correspond to three mode shapes with different numbers of circumferential half-waves ($j = 2, 3, 4$). The deviation of the cross section of the shell from the circular profile due to a change in the ellipticity parameter leads
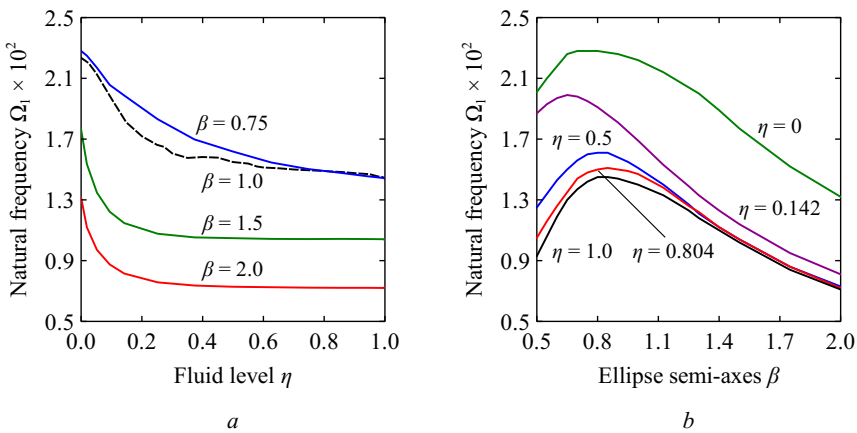
Fig. 8.6: The lowest natural vibration frequencies of an elliptical cylindrical shell (CC) at different fluid level (*a*) and ratio of ellipse semi-axes (*b*).
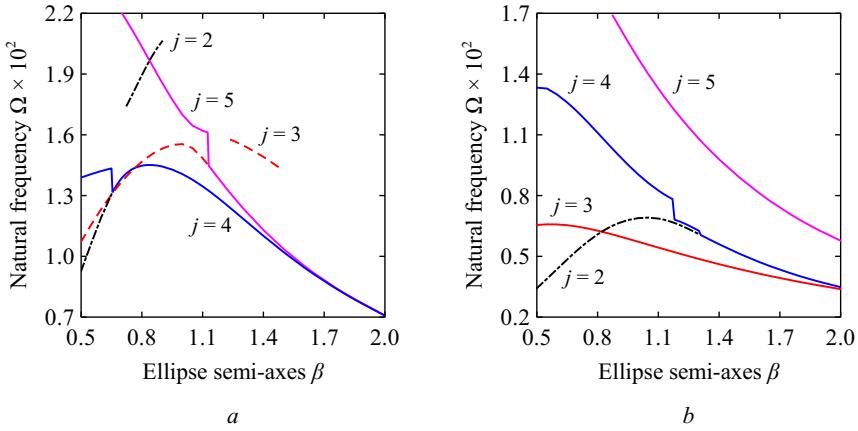
Fig. 8.7: Natural vibration frequencies of an elliptical cylindrical shells completely filled with a fluid ($m = 1$): a – CC, b – CF.

to a non-uniform rigidity of the structure along the circumferential coordinate. In turn, this contributes to the appearance of various vibration mode shapes. The jumps in frequency were driven by the degeneration of one of the vibration modes and its transformation to a new one. For example, at $\beta \approx 1.13$, mode $(1,3)$ converts into $(1,5)$. With a further increase in the parameter β, mode $(1,3)$ is not realized on the considered frequency spectrum, but it appears again, starting from $\beta \approx 1.24$. The features mentioned above continue to exist at another variant of the kinematic boundary conditions. The dependence of the lowest natural vibration frequency of the shell fixed at one edge on the ellipticity parameter is also nonmonotonic and has a pronounced extremum (at $\beta = 0.82$). As one can see in Fig. 8.7b, the number of circumferential half-waves changes at this point from $j = 2$ to $j = 3$.

It is also important to point out one more feature previously determined for the horizontal circular cylindrical shells and which is preserved for elliptical one. The maximum height of the half-waves in the circumferential direction of the lowest vibration mode is observed on the fluid-structure interface. For the vibration modes corresponding to the highest frequencies of the spectrum, this pattern does not always manifest itself.

The dependencies of the critical velocities of instability of the completely filled simply supported cylindrical shells with circular and elliptical cross-sections on the ratio L/R_y are shown in Fig. 8.8a. In both cases, the divergence boundary significantly depends on the linear dimensions of the structure. With an increase in the length of the shell L, the critical velocities Y_D decrease. The kinks of the curves are due to a change in the mode according to which the loss of stability occurs. For example, for the shell with $\beta = 1.5$ the number of circumferential half-waves j changes from $j = 4$ to $j = 3$ at $L/R_y > 5$.

In the next series of examples, the hydroelastic stability of the partially filled shells clamped at both edges is considered at different ratios of the ellipse semi-axes.
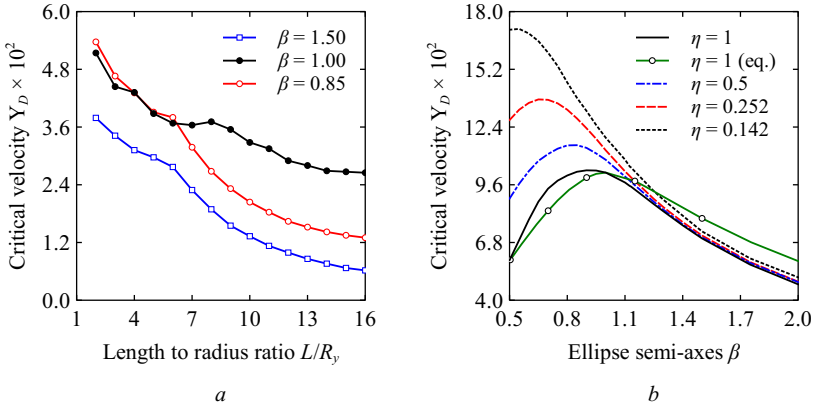
Fig. 8.8: Dimensionless critical velocity of instability Y_D for elliptical cylindrical shells depend on the ratio L/R_y (*a*) ($\eta = 1$, Case II, SS) and the ratio of the ellipse semi-axes (*b*) (Case I, CC).

Analysis of the results presented in Fig. 8.8*b* indicates that a decrease in the fluid level η leads to an increase in the critical flow velocities Y_D. However, there are such values of η and β, starting from which the value of Y_D changes insignificantly (at $\beta > 1.25$, the curves almost coincide). In the case of a quiescent fluid, the dependence of the lowest natural vibration frequency of such structures on the ellipticity parameter β has an extremum, which is observed at $\beta < 1$ and shifts depending on the fluid level (Fig. 8.6*b*). Figure 8.8*b* shows that this feature is also characteristic of the critical flow velocities. In both cases, everything is explained by the fact that the cross-sectional area of the cylindrical shell is not a constant value at a change in β (since $R_y = const$). Further, we will consider the situation where the ellipticity parameter changes and the cross-sectional area of the shell remains equal to a similar circular configuration. The results obtained are shown as line with circles in Fig. 8.8*b*. In this example, there is no difference between the critical velocities at $\beta > 1$ and $\beta < 1$, and the given dependence has a maximum at $\beta = 1$.

8.4 System of two Circular Cylindrical Shells

In this section we consider examples, which are concerned with two horizontally oriented circular cylindrical shells (Fig. 8.9), and use the following parameters: *isotropic shells*

$$L^{(1)} = L^{(2)} = L = 1 \text{ m}, \ R^{(2)} = 0.1 \text{ m}, \ h^{(1)} = h^{(2)} = h = 5 \times 10^{-4} \text{ m},$$
$$E^{(1)} = E^{(2)} = E = 200 \text{ GPa}, \ \nu^{(1)} = \nu^{(2)} = \nu = 0.3, \ \rho_s^{(1)} = \rho_s^{(2)} = \rho_s = 7800 \text{ kg/m}^3,$$

ideal fluid
$$\rho_f = 1000 \text{ kg/m}^3, \ c = 1500 \text{ m/s}.$$

Fig. 8.9 Section of eccentric cylindrical shells with the annular gap partially filled with a flowing fluid.
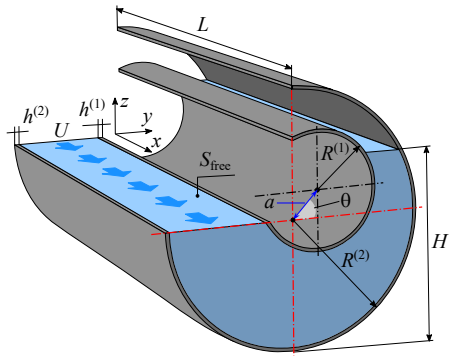
The computations were done for different values of the dimensionless annular gap between them, which is defined as $k = \left(R^{(2)} - R^{(1)} \right) / R^{(1)}$. In the analysis of the influence of the fluid level H, consideration is given only to such values of H at which both shells remain wetted. This yields to the following condition:

$$\left(R^{(2)} - R^{(1)} \right) \le H \le 2R^{(2)}. \tag{8.14}$$

Hereinafter, superscripts "(1)" and "(2)" denote the inner and outer shells, respectively. The obtained results are represented in terms of dimensionless quantities. Some of them are given in expressions (8.13) and new ones are defined below:

$$\eta = \frac{H}{2R^{(2)}}, \quad \Lambda = \lambda R^{(1)} \psi, \quad \Omega = \omega R^{(1)} \psi, \quad \xi = \frac{a}{\left(R^{(2)} - R^{(1)} \right)}, \tag{8.15}$$

where η is the fluid level, ξ is the eccentricity (Fig. 8.9), a is the distance between the rotation axes of the shell.

8.4.1 Coaxial Shells

As has been shown previously, the violation of circumferential symmetry of the horizontally oriented shells partially filled with a fluid causes the frequency spectrum to split. For this reason, the frequencies for the mode shapes with the same combination of wave numbers are different, which is shown in Fig. 8.10*a* for $k = 1/10$. In the calculations, it was assumed that the inner elastic shell is clamped at both edges (CC), and the outer shell is absolutely rigid. The natural frequencies of vibrations of such configuration, corresponding to symmetric and antisymmetric modes, coincide when the annular gap is completely filled ($\eta = 1$). When the fluid level decreases in this gap ($\eta < 1$), they begin to differ from each other, and their further change goes along different branches. Another limiting case corresponds to the configuration with ($\eta = 0$). Under such conditions, the frequency spectrum will be closest to the
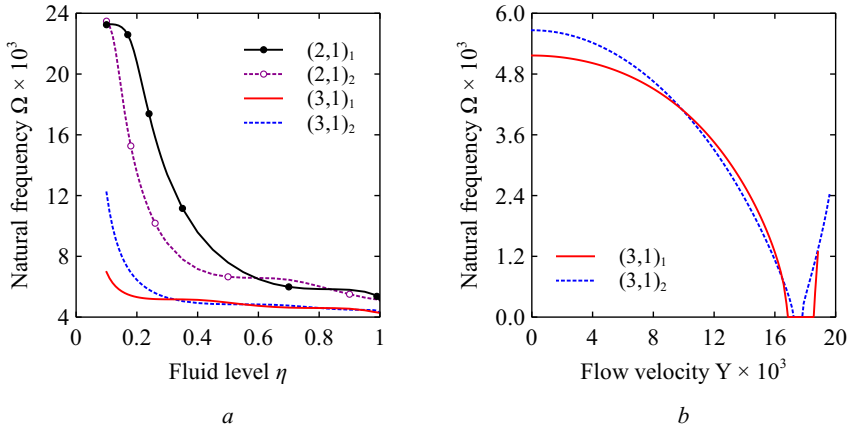
Fig. 8.10: Dependencies of the natural frequencies Ω on the fluid level η (*a*) and the flow velocity Y at $\eta = 0.25$ (*b*) for the outer rigid shell ($k = 1/10$, CC).

vibrations of shells with air in the annular gap, and different branches will coincide. By virtue of Eq. (8.14), this situation cannot arise at all frequencies. On the other hand, the dependencies presented in Fig. 8.10*a* for the same combination of wave numbers (j, m) clearly demonstrate that in some cases the coincidence between symmetric and antisymmetric components also takes place at the values ($\eta > 0$).

Figure 8.10*b* shows the variation of the natural frequencies with the same set of wave numbers (j, m) depend on the flow velocity Y. It follows from the graphs that, when the annular gap is only partially filled with fluid, there is no qualitative difference in the behavior of the presented curves. In particular, the imaginary parts of these two modes do not merge together due to their proximity, and the instability mode remains unchanged.

Figure 8.11 presents the dependencies of the lowest natural frequencies Ω_1 and the critical flow velocities Y_D on the dimensionless fluid level η in the annular channel at different values of k. This example illustrates the case when two elastic coaxial shells are rigidly clamped at their edges. The above graphs show that a decrease in the fluid level leads to an increase in both frequencies and critical velocities. This behavior occurs due to a decrease in the total area of wetted surfaces and is associated with diminishing the role of the added mass of a fluid. The wavy character of the curves in Fig. 8.11*a* is associated with the alternation of the minimum values corresponding to the vibration modes with the same combination of wave numbers. A rapid change in the quantities under study is observed at a low fluid level η for the gap $k = 1/100$. Similar results were obtained for the partial filling of single shells [3, 5]. This phenomenon occurs only at small values of k due to the need for the existence of a wetted surface of the inner shell, that may be absent when the amount of a fluid in a relatively wide annular channel is small (see condition (8.14)). As in the case of complete filling ($\eta = 1$), an increase in the annular gap (Fig. 8.11*b*) and in the rigidity of the outer shell causes the critical velocities to increase as well . Thus,
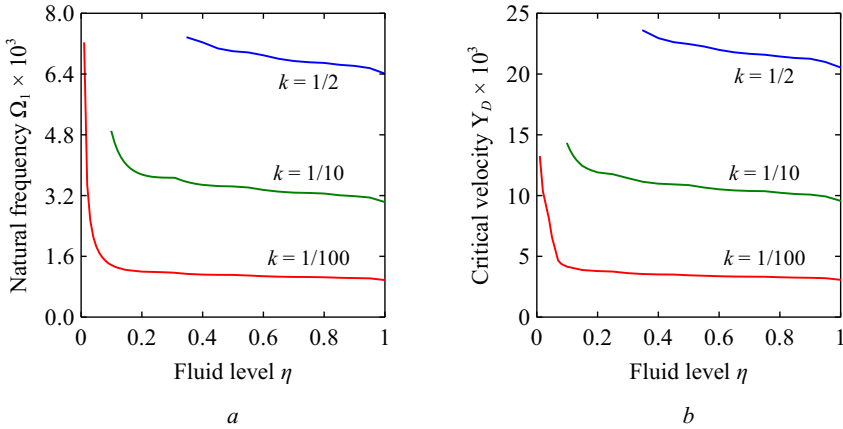
Fig. 8.11: Dependencies of the lowest natural frequencies Ω_1 (*a*) and critical velocities of instability Y_D (*b*) on the fluid level η at different values of the annular gap k.

the narrower is the annular channel (i.e., the smaller is k), the greater is the range within which the fluid level has little effect on the characteristics under consideration.

8.4.2 Eccentric shells

During operation or due to the imperfect shell manufacturing process, the alignment of coaxial shells can be broken. In [8] the influence of the eccentricity ξ and the angle θ, characterizing, respectively, the value and direction of axial deviation of the inner shell is described in detail. It was shown that, when the annular gap is completely filled with fluid and the body forces are absent, the angle θ does not affect the stability boundary, while the eccentricity (ξ increases in absolute value) reduces critical velocity.

In the case of partial filling, the picture becomes much more complicated. When the inner shell is displaced along the free surface, the added mass of the liquid is redistributed. This reduces the critical velocity, regardless of the direction of axial deviation ($\theta = 0°$ or $\theta = 180°$) and the fluid level η. The angle $\theta = 90°$ and the positive values of eccentricity ξ ($\xi > 0$) characterize the rise of the inner shell out of the fluid. In response to the changes in the wetted surface area and to the hydrodynamic pressure redistribution, the critical flow velocities increase or decrease, respectively. The size of the annular gap k has no qualitative effect on the dependence of the critical velocities Y_D on the inner shell eccentricity. A decrease in the value of k leads to a decrease in the stability boundary. This has been established previously for the coaxial cylindrical shells in case of full or partial filling of the annular channel [2, 6].

The results demonstrate that, as the filling level η increases, the influence of the angle θ on the stability boundary decreases until it ceases to have any effect in case of complete filling. The minimum critical velocity Y_D is always obtained at the same eccentricity ($\xi \approx -1$) regardless of the values of θ and η. As for the maximum value of Y_D, it can be achieved at different values of eccentricity on the half-interval $\xi \in [0; 1)$ through the selection of θ and η. As noted earlier, this is explained by changes in the inner shell wetted surface and in the fluid added mass. These statements are true when the values of the angle θ are positive, and the negative values of ξ match positive values, though in the direction of the negative angles θ. Furthermore, the data presented in Fig. 8.12 can be arguments for the existence of such configurations in which, subject to proper selection of all parameters, the higher hydroelastic stability threshold than obtained at the coaxial shells can be provided.

The dependencies of the critical velocity Y_D on the angle θ and the eccentricity of the inner shell ξ are presented in Fig. 8.12*b*. When the angle θ decreases, there is such a range of its values where the Y_D remains unchanged. The calculations showed in [8] that, as the fluid level increases, the size of this interval increases as well until the angle θ ceases to affect the stability boundary in the case of full filling (the straight line is parallel to the abscissa axis). At the same time, with an increase in the eccentricity ξ the critical velocity Y_D changes over a wide range (Fig. 8.12*b*), thus providing more opportunities to control dynamic behavior of such structures.

Figures 8.13 and 8.14 gives the mode shapes of the shells for $k = 1/10$ at different variants of annular gap filling, assuming that the value and direction of axial deviation of the inner shell are also different. For each configuration, the flow velocity was set close to the critical value Y_D. In the figures, the dotted lines denote the non-deformed shells, and the solid lines correspond to the deformed one; the fluid level is given in grey. In the spatial mode shapes, the displacements are scaled for clarity in presentation of the data on the relative maximum value of the given configuration.
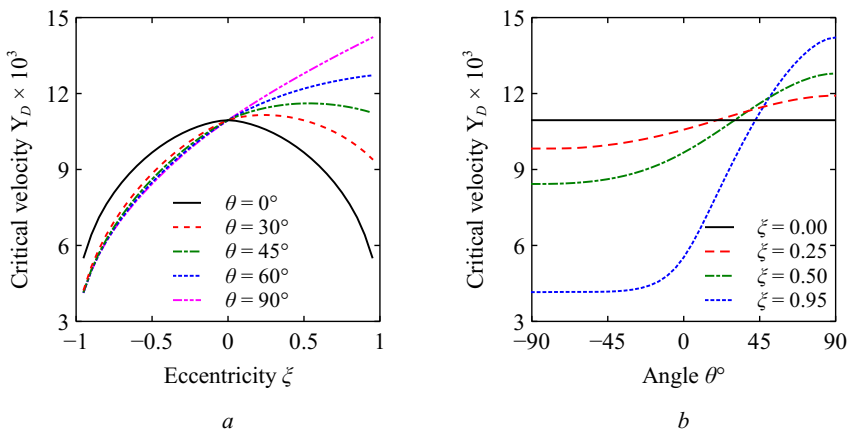
Fig. 8.12: Dependencies of the critical velocities Y_D for $k = 1/10$ at $\eta = 0.5$ on the excentricity ξ at different values of the angle θ (*a*) and the angle θ at different values of excentricity ξ (*b*).

Fig. 8.13: Mode shapes of eccentric shells interacting with the fluid (the cross section at $x = L/2$, the inner and outer shells) for $k = 1/10$ at $Y \approx Y_D$: $a - \eta = 1, \xi = 0$; $b - \eta = 1, \xi = 0.95, \theta = 90°$; $c - \eta = 0.5, \xi = 0$.
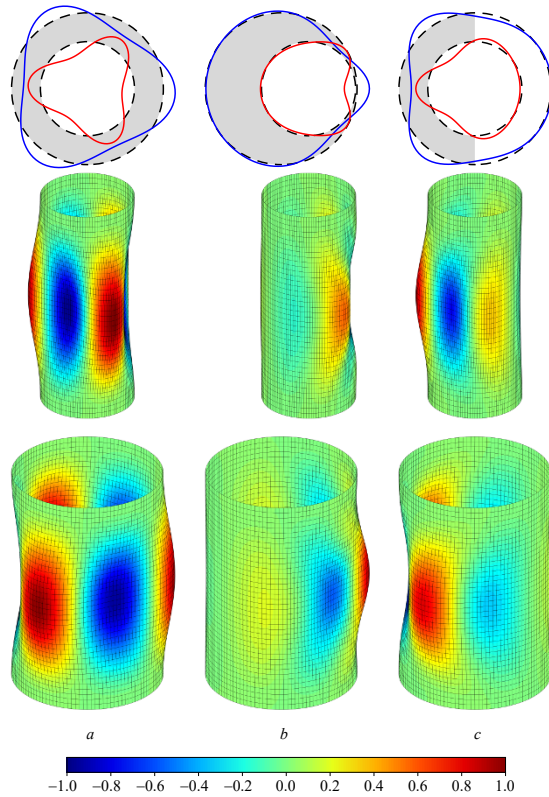
Red and blue on the color scale indicates the displacement in the direction of the outer normal to the shell surface and in the opposite them.

For the completely filled coaxial shells ($\eta = 1, \xi = 0$), the circumferential half-waves have the same height, the size of which is different for the inner and outer shells. In the presence of eccentricity ($\eta \neq 0$), their height within the same shell becomes different. The maximum displacements occur in the surface areas, which correspond to the minimum distance between the shells. With a decrease in the fluid level ($\eta < 1$), there appear half-waves of different heights, while the maximum displacements develop on those parts of the surfaces which interact with the fluid. For the partially filled eccentric structures, the largest half-wave size is observed on the wetted surfaces. Based on the data, we can come to a conclusion that the fluid level of the annular gap has a greater effect on the displacement of the shells subject to vibrations than the eccentricity.

Fig. 8.14: Mode shapes of eccentric shells interacting with the fluid (the cross section at $x = L/2$, the inner and outer shells) for $k = 1/10$ at $Y \approx Y_D$: $a - \eta = 0.50$, $\xi = 0.95, \theta = 0°$; $b - \eta = 0.50$, $\xi = 0.95, \theta = 90°$; $c - \eta = 0.5$, $\xi = 0, \theta = -90°$.
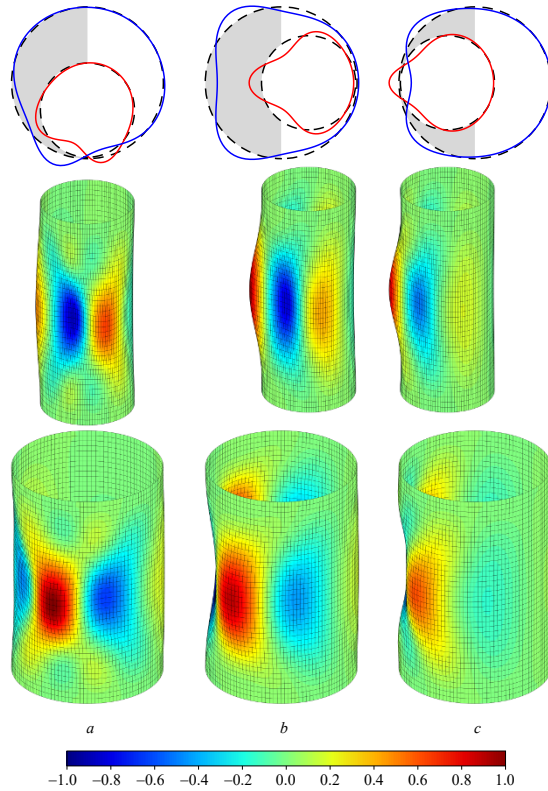
8.5 Conclusion

Natural vibrations and stability of cylindrical shells interacting with quiescent and flowing fluid has been investigated in a three-dimensional formulation based on the proposed mathematical model and developed finite element algorithm. In the first group of numerical examples single circular and elliptical cylindrical shells with different boundary conditions, linear dimensions and filling level were analyzed. In another part of the calculations, we studied a system of two coaxial and eccentric circular cylindrical shells. The influence of the fluid level, the annular gap size, the value and direction of axial deviation of the inner shell on the natural vibration frequencies and hydroelastic stability boundary were investigated. The obtained results can be summarized as follows:

- horizontal cylindrical shells partially filled with fluid can have more than two mode shapes with the same number of half-waves in the circumferential and the meridional directions, which correspond to different natural frequencies of vibrations;
- small amount of the fluid in horizontal circular, elliptical and coaxial cylindrical shells lead to an essential decrease in the lowest vibration frequency;

- the lowest natural vibration frequency of horizontal elliptical cylindrical shells has a local extremum, which depends on the fluid level and the ratio of ellipse semi-axes;
- a decrease in the fluid level leads to a growth of the critical flow velocities;
- an increase in the structure length decreases the critical flow velocities;
- for coaxial cylindrical shells with narrow annular gap there is a wide range of the fluid level in which it has little effect on the lowest natural frequency of vibrations and critical velocity of instability;
- hydroelastic stability threshold of the eccentric circular cylindrical shells can be improved by selecting appropriate value and direction of axial deviation of the inner shell.

References

[1] Païdoussis MP (2014) Fluid-structure Interactions: Slender Structures and Axial Flow, vol 1, 2nd edn. Elsevier Academic Press, London

[2] Païdoussis MP (2016) Fluid-structure Interactions: Slender Structures and Axial Flow, vol 2, 2nd edn. Elsevier Academic Press, London

[3] Bochkarev SA, Lekomtsev SV, Matveenko VP (2016) Natural vibrations and stability of elliptical cylindrical shells containing fluid. Int J Struct Stabil Dyn **16**(10), 1550076

[4] Bochkarev SA, Lekomtsev SV, Matveenko VP (2016) Dynamic analysis of partially filled non-circular cylindrical shells with liquid sloshing. Int J Appl Mech **8**(3), 1650027

[5] Bochkarev SA, Lekomtsev SV, Senin AN (2019) Analysis of the spatial vibrations of coaxial cylindrical shells partially filled with a fluid. J Appl Mech Tech Phy **60**(7):1249–1263

[6] Bochkarev SA, Lekomtsev SV, Matveenko VP, Senin AN (2019) Hydroelastic stability of partially filled coaxial cylindrical shells. Acta Mech **230**(11):3845–3860

[7] Bochkarev SA, Lekomtsev SV, Senin AN (2019) Analysis of spatial vibrations of piezoceramic eccentric cylindrical shells interacting with an annular fluid layer. Fract Struct Integr **13**(49):814–830

[8] Bochkarev SA, Lekomtsev SV, Senin AN (2020) Numerical modeling of eccentric cylindrical shells partially filled with a fluid (in Russ.). J Samara State Tech Univ, Ser Phys Math Sci **24**(1):95–115

[9] Ergin A, Price WG, Randall R, Temarel P (1992) Dynamic characteristics of a submerged, flexible cylinder vibrating in finite water depths. J Ship Res **36**(2):154–167

[10] Amabili M (1996) Free vibration of partially filled, horizontal cylindrical shells. J Sound Vib **191**(5):757–780

[11] Selmane A, Lakis AA (1997) Vibration analysis of anisotropic open cylindrical shells subjected to a flowing fluid. J Fluids Struct **11**(1):111–134

[12] Sewall JL, Pusey CG (1971) Vibration study of clamped-free elliptical cylindrical shells. AIAA J **9**(6):1004–1011

[13] Soldatos KP (1999) Mechanics of cylindrical shells with non-circular cross-section: A survey. Appl Mech Rev **52**(8):237–274

[14] Xiang Y, Huang Y (2005) A novel semi-analytical method for solving acoustic radiation from longitudinally stiffened infinite non-circular cylindrical shells in water. Acta Mech Solida Sin **18**(1):1–12

[15] Kumar A, Patel BP (2018) Nonlinear dynamic response of elliptical cylindrical shell under harmonic excitation. Int J Non-Lin Mech **98**:102–113

[16] Firouz-Abadi RD, Noorian MA, Haddadpour H (2010) A fluid–structure interaction model for stability analysis of shells conveying fluid. J Fluids Struct **26**(5):747–763

[17] Jeong KH (1999) Dynamics of a concentrically or eccentrically submerged circular cylindrical shell in a fluid-filled container. J Sound Vib **224**(4):709–732

[18] Jhung MJ, Jeong KH, Hwang WG (2002) Modal analysis of eccentric shells with fluid-filled annulus. Struct Eng Mech **14**(1):1–20

[19] ANSYS (2022) Release 2022 R1 Documentation. Canonsburg

[20] Il'gamov MA (1969) Vibrations of Elastic Shells Containing Liquid and Gas (in Russ.). Nauka, Moscow

[21] Bochkarev SA, Lekomtsev SV, Matveenko VP (2016) Hydroelastic stability of a rectangular plate interacting with a layer of ideal flowing fluid. Fluid Dynam **51**(6):821–833

[22] Zienkiewicz OC, Taylor RL (2000) The Finite Element Method, vol 1, 5th edn. Butterworth-Heinemann, Oxford

[23] Reddy JN (2015) An Introduction to Nonlinear Finite Element Analysis, 2nd edn. Oxford University Press, London

[24] Tisseur F, Meerbergen K (2001) The quadratic eigenvalue problem. SIAM Rev **43**(2):235–286

[25] Lehoucq RB, Sorensen DC (1996) Deflation techniques for an implicitly restarted Arnoldi iteration. SIAM J Matrix Anal Appl **17**(4):789–821

[26] Weaver DS, Unny TE (1973) On the dynamic stability of fluid-conveying pipes. J Appl Mech **40**(1):48–52

Chapter 9
On the Problem of Modeling the Influence of Ice Cover and Surface Waves of a Liquid on the Dynamics of a Floating Body

Anastasiia A. Chevrychkina, Nikolai M. Bessonov, and Andrei K. Abramian

Abstract An approach to numerical simulation of the evaluation of the influence of a semi-infinite ice cover on the dynamics of a floating body is proposed. The problem is solved numerically for 2D case. The ice cover is modeled as a semi-infinite beam with a bending stiffness equal to the cylindrical bending stiffness of the plate. Considered cases of action on a floating body (plate) are concentrated unsteady and stationary harmonic forces. Water was considered as an ideal incompressible homogeneous fluid, and its motion is irrotational. Nonlinear boundary conditions were assumed on the free surface of the fluid. Displacement values and angles of rotation of the floating body has been found. It is shown that under non-stationary load the maximum displacements and rotation angles of a floating body can exceed their values in stationary modes. Examples are found in which, for nonlinear conditions on the free surface, the values of displacements and angles of rotation exceed the values obtained for linear conditions. At the same time, for a wide range of parameters of the considered hydroelasticity system, considering nonlinear boundary conditions does not give a difference in the values of displacements and angles of rotation of the floating body from the case of using a linear boundary condition. The existence of low-frequency range of the acting harmonic force, in which the ice cover does not affect the angles of rotation of the floating body has been found. The calculations showed that for floating body parameters corresponding to the parameters of real offshore structures, it is not necessary to consider the bending rigidity of the floating body, and the motion of the body can be considered as the motion of a rigid body.

Anastasiia A. Chevrychkina · Nikolai M. Bessonov · Andrei K. Abramian
Institute for Problems in Mechanical Engineering of the Russian Academy of Sciences, Bolshoy prospekt 61, V.O., 199178 St. Petersburg, Russian Federation,
e-mail: Anastasiia.Che@gmail.com, nickbessonov1@gmail.com, andabr55@gmail.com

9.1 Introduction

The operation of floating-type structures in the presence of ice cover in various marine conditions and external loads acting on structures were studied in many works. Historically, the first studies were devoted to the behavior of ships near ice floes, which was caused by the need to ensure safe navigation [1–4]. Currently, floating oil platforms and nuclear power plants have increased the class of objects, ensuring the safety of navigation of which has become the subject of research [5–8]. When posing problems related to the above issue, the floating structure was modeled either as a rigid body [4–7] or as a plate (beam) [1–3, 8]. As an external influence on a floating object, harmonic force [2–7] or moment actions [8], as well as progressive waves [3–6], were considered. Water was considered as an ideal incompressible heavy liquid, and the ice cover as a plate floating on its surface. The paper [9] presents a solution to the linear hydroelasticity problem of steady-state forced vibrations of a semi-infinite ice cover under the action of a localized external load. The ice cover is modeled by a viscoelastic thin plate, the liquid layer thickness is assumed to be small, and the shallow water theory is used. The paper [10] considers the problem of determining the stationary field of forced joint gravitational motions of an incompressible fluid in a cylindrical reservoir and a round elastic plate covering its surface. To solve problems in [1–7], linear boundary conditions on the water surface were used. In [1–7, 9, 10], various analytical methods were used to obtain solutions, and in [8, 11, 12] numerical methods were used. A review of works devoted to various methods for solving problems on the interaction of an ice cover, a floating body, and water is presented in [13]. The result of solving problems was usually the dependence of displacements (including angular ones) of both the floating body and the ice cover on the frequencies of the external action and on the spatial coordinate. In this paper, we consider issues that have not been considered previously in other papers. One of these questions is, for example, the question of the behavior of a floating body and an ice cover in an unsteady regime. The results obtained in this work indicate that the maximum displacements of a floating body and ice cover in an unsteady regime can be significantly greater than in a steady regime. Another issue is the question of the influence of the elasticity of a floating body on the maximum displacements under the action of external forces applied to it. Although in [11] an assumption was made about the smallness of the influence of nonlinearity in the boundary conditions on the surface of a liquid on the displacements of a floating body and ice cover, in the present work, the values of the parameters of the considered system are found for which such an influence is significant. In this article, the authors from the very beginning abandoned the attempt to solve the problem analytically and used a numerical method. The reason for this is that a mathematically rigorous solution of the problem requires the construction of a solution that not only takes into account the singularity that occurs at the edge of the ice plate, but also obtains a solution that correctly describes waves that go to infinity. As far as the authors of this article know, researchers have not yet been able to overcome both difficulties and obtain a satisfactory analytical solution.

9.2 Statement of the Problem

Consider the problem of joint motion of the ice cover, body (floating structure) and water under them (Fig. 9.1). An ice cover floating on the water surface will be considered as an elastic plate lying on a base of an incompressible fluid [1]. The floating body is also represented as an elastic plate with its cylindrical rigidity much greater than that of ice. Elastic plates located on the water surface are separated by areas with a free surface. The problem will be considered in a two-dimensional setting. In this regard, instead of the equations of the plates, the equations of the beam type will be used, in which the cylindrical stiffness of the plate will be taken as the bending stiffness of the beam. The Cartesian coordinate system in the plane will be used.

Following the assumptions accepted in the literature, water is considered an ideal, incompressible fluid, and its flow is irrotational [1]. The potential of fluid motion velocities Φ satisfies the Laplace equation in the area occupied by the fluid:

$$\Delta \Phi = 0, \tag{9.1}$$

$$\frac{\partial \Phi}{\partial t} + \frac{|\nabla \Phi|^2}{2} = -\frac{1}{\rho} p - gy, \tag{9.2}$$

where p is a pressure, ρ is a water density, g is the acceleration of gravity.

Let us assume, for definiteness, that here and below the pressure p is measured from the atmospheric pressure.

In what follows, we confine ourselves to small flexural vibrations of the ice cover. We will simulate the movement of the ice cover, the free surface of the liquid and the floating body as the movement of a beam of variable stiffness. The equation of motion of such a beam can be written in the following form:

$$\rho_0 h \frac{\partial^2 w}{\partial t^2} = -\frac{\partial^2}{\partial x^2} \left(D \frac{\partial^2 w}{\partial x^2} \right) + p + q, \tag{9.3}$$

where $w(x,t)$ is a vertical movement of the beam from the equilibrium horizontal position; ρ_0 is a beam material density; p is a liquid side pressures; q is an external force applied to the body; $D = D(x)$ is a plate cylindrical stiffness
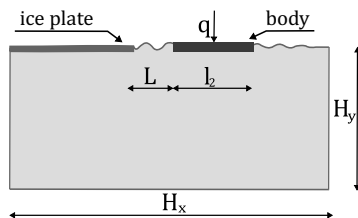
Fig. 9.1: Schematic arrangement of the ice cover and the body simulating the floating structure in the calculated area.

$$D = \frac{Eh^3}{12(1-v^2)},$$

where E, v are the modulus of elasticity and the Poisson's ratio, h is a plate thickness. The stiffness of the beam is given as a variable along its longitudinal axis and is equal to either the cylindrical stiffness of the ice part of the beam, or the stiffness of the floating body, or is taken on the free surface of the liquid to be small compared to the cylindrical stiffness of ice on the free water surface, so that the bending moment

$$M = D\frac{\partial^2 w}{\partial x^2}$$

in Eq. (9.3) is negligibly small. Similarly, the density ρ_0 is given as a variable and equals either the density of ice, or the reduced density of the floating body, or, on the free surface, a much lower density of ice. To test the proposed model of a beam with variable stiffness, the results obtained using this model were compared with the results obtained using analytical and numerical methods in [11]. In [11], the problem of the behavior of the same hydroelasticity system as in the present work was solved, but in a linear formulation. A comparison of the results obtained in this work with the results obtained in [11] is presented in Sect. 9.4. Also, as a test problem, we considered the problem of the dynamics of a single finite beam in contact with a basin of finite depth and infinite length along the coordinate x, which is affected by the harmonic force, attached to its center. The results of this test problem were compared with the results obtained in [6] and showed a qualitative agreement.

Thus, an approach is proposed that allows to describe an ice beam, a free surface, and a floating body by the general Eq. (9.3) and boundary conditions on the surface, bottom, and side surfaces of the calculated area.

9.3 Numerical Method

The equations describing the motions of the system have the form.

$$\Delta\Phi = 0, \tag{9.4}$$

$$\frac{\partial\Phi}{\partial x}\Big|_{x=0} = 0, \qquad \frac{\partial\Phi}{\partial x}\Big|_{x=H_x} = 0, \qquad \frac{\partial\Phi}{\partial y}\Big|_{y=-H_y} = 0, \qquad \frac{\partial\Phi}{\partial y}\Big|_{y=0} = \frac{dw}{dt}, \tag{9.5}$$

$$\rho_0 h\frac{\partial^2 w}{\partial t^2} = -\frac{\partial^2}{\partial x^2}\left(D\frac{\partial^2 w}{\partial x^2}\right) + q - \rho\left(\frac{\partial\Phi}{\partial t} + \alpha\frac{|\nabla\Phi|^2}{2}\right) - \rho g w - \mu\frac{\partial w}{\partial t}, \tag{9.6}$$

$$\frac{\partial w}{\partial x}\Big|_{x=0} = 0, \qquad w\big|_{x=0} = 0, \qquad \frac{\partial w}{\partial x}\Big|_{x=H_x} = 0, \qquad w\big|_{x=H_x} = 0, \tag{9.7}$$

where H_x, H_y are a width and a depth of the calculated area. The initial conditions are given as

$$\Phi|_{t=0} = 0, \qquad w|_{t=0} = 0, \qquad \frac{dw}{dt}\Big|_{t=0} = 0.$$

In the literature, usually, the case of small surface displacements is considered, when it is assumed

$$\frac{d\Phi}{dt} \approx \frac{\partial\Phi}{\partial t}. \tag{9.8}$$

In this paper, we consider a more general, non-linear case

$$\frac{d\Phi}{dt} = \frac{\partial\Phi}{\partial t} + \alpha\frac{|\nabla\Phi|^2}{2}. \tag{9.9}$$

Here the linear case corresponds to $\alpha = 0$ and the non-linear case corresponds to $\alpha = 1$.

The system of Eqs. (9.4)–(9.7) was solved numerically. A two-dimensional orthogonal non-uniform mesh $I \times J$ was introduced with steps Δx_i and Δy_i in x and y respectively ($i = 1, \ldots, I$, $j = 1, \ldots, J$). To improve the accuracy of calculations, the mesh was thickened along the axis in the vicinity of the ends of the body and the edges of the ice cover and expanded near the left and right sides of the computational domain. Vertically, the mesh thickened near the water surface.

The size of the region o extends to "infinity" in reality. However, in numerical simulation, one has to set these dimensions to be limited, although they are as far apart as possible. To move away the boundaries of the computational domain without increasing the number of mesh nodes, an uneven mesh was used with a gradually increasing step towards the boundaries of the domain. However, starting from the moment of time equal to the time of passage of surface waves to the boundaries of the computational domain and back, the solution begins to be affected by the waves reflected from the boundaries of the domain. To reduce the influence of the reflection effect, damping boundary conditions were introduced at the boundaries of the region, which damped the incoming waves. Such a numerical technique has proven itself well in practice and is often used to reduce the influence of reflection from boundaries [14, 15]. The term $-\mu\partial w/\partial t$ was added to the right side of Eq. (9.6) to introduce damping boundary conditions, where μ is the coefficient of external friction. The experience of test calculations to study the effect of μ on the degree of reflection of waves from the boundaries showed that the optimal solution, which reduces the influence of reflected waves by 85-95%, is to set on an area with a length of about 5% of the size of the entire area. In the rest (central) part of the computational domain, the value μ was set equal to zero. Test calculations also showed that a very sharp change in the value μ does not give the desired result, but, on the contrary, leads to the appearance of additional reflected waves at the boundary of a sharp change in the μ. In the rest (central) part of the computational domain, the value was set equal to zero. Test calculations also showed that a very sharp change in the value μ does not give the desired result, but, on the contrary, leads to the appearance of additional reflected waves at the boundary of a sharp change in the μ.

When calculating numerically, system (9.4)-(9.7) was divided into two subsystems (9.4), (9.5) and (9.6), (9.7), which were solved sequentially in two stages at each time step. At each time step, nodal values were calculated for the potential $\Phi_{i,j}^n$, where n is a time step number. At the mesh nodes corresponding to the liquid surface, the deviations of the surface from the equilibrium horizontal position were determined w_i^n.

The sequence of calculations was as follows. Let the potential values $\Phi_{i,1}^n$ at all nodes and vertical deviations at near-surface nodes w_i^n and w_i^{n-1} be known either from the previous time step Δt or taken from the initial conditions.

- Using the values w_i^n and w_i^{n-1} find the velocities

$$\left(\frac{dw}{dt}\right)^n \approx (w_i^n - w_i^{n-1})/\Delta t, i = 1, \ldots, I$$

  in all near-surface nodes.
- The found values $(dw/dt)^n$ are substituted into the boundary condition (9.5), then system (9.4), (9.5) is solved numerically and new values $\Phi_{i,j}^{n+1}$ are found at all mesh nodes.
- Using the obtained values $\Phi_{i,j}^{n+1}$ and the values $\Phi_{i,j}^n$, taken from the previous time step, the values $(d\Phi/dt)^{n+1}$ are calculated at all near-surface mesh nodes using difference approximations of relations (9.8) or (9.9).
- The obtained values $(d\Phi/dt)^{n+1}$ are substituted into Eq. (9.6), which is solved numerically, as a result of which the values w_i^{n+1} are found at all near-surface nodes. Then the process is repeated.

The iterative method [12] was used to numerically solve system (9.4) and (9.5). To solve Eq. (9.6), we used the substitution

$$M = D(x)\frac{\partial^2 w}{\partial x^2}.$$

This made it possible to replace the fourth-order Eq. (9.6) in x with a system of two second-order equations. This system was approximated by a three-point implicit difference scheme and solved using the matrix sweep method.

9.4 Results

The presence of ice makes the problem asymmetric with respect to the floating body. The waves reflected from the ice come only to the left of the floating body, which leads not only to the movement of the floating body, but also to its rotation, due to the presence of asymmetric water pressure. The tangent of the angle of rotation of the floating body was calculated as the ratio of the difference in the displacements of its ends to its length. This is true in the case of a large flexural rigidity of the body, for which the calculations were carried out. The displacement and rotation

angle of the floating body and ice were calculated for the case of the action of a force non-stationary harmonic action concentrated in the center of the body, given in the following form:

$$q = A\sin(\omega t)\delta(x - H_x/2)H(t),$$

where A is an impact amplitude, ω is a circular impact frequency, $\delta(x)$ is the delta function, the floating body is in the center of the calculated width pool H_x, $H(t)$ is the Heaviside function:

$$H(t) = \begin{cases} 0, t < 0 \\ 1, t \geqslant 0 \end{cases}$$

The load values were chosen the same as in [11] or close, which made it possible to compare the results obtained in it with the results of this article. The values of the main parameters are given in Table 9.1.

Figures 9.2 and 9.3 show typical dependencies of the maximum displacement of a floating body under the action of a force concentrated in the center of the body on its frequency at different ice thicknesses in unsteady and steady modes, respectively. The steady-state mode is the mode in which the maximum amplitude of oscillations practically does not change for at least 10 periods. All graphs show the maximum displacements or angles of rotation in steady or unsteady conditions.

Table 9.1: Values of physical parameters, geometry parameters of the pool and floating body. l_2 is a floating body length, $h_2\rho_2$ is a product of thickness and density of a body, ρ_1 is a ice density, h is a ice thickness.

H_y, m	H_x, m	h, m	ρ_1, kg/m^3	v_{ice}	E_{ice}, GPa	$h_2\rho_2$, kg/m^2	l_2, m
100	200	1	925	0.3	5	3218	30
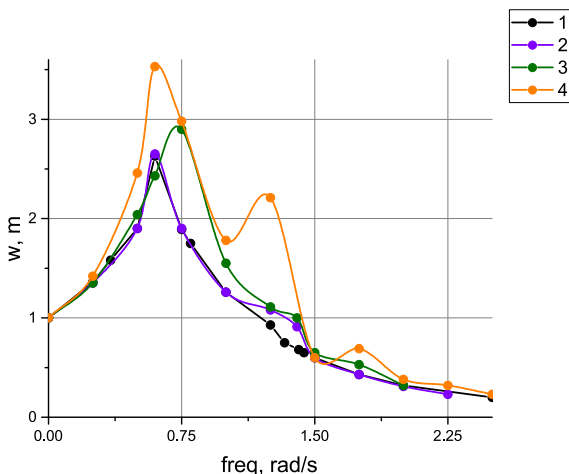
Fig. 9.2 Dependence of the displacement of the left edge of the body on the frequency of the force with an amplitude of 294300 N/m in an unsteady regime. Comparison for different ice thicknesses h. Line 1 - $h = 0$ - no ice; line 2 - $h = 0.1$ m; line 3 - $h = 1$ m; line 4 - $h = 10$ m.

Fig. 9.3 Dependence of the displacement of the left edge of the body on the frequency of the force with an amplitude of 294300 N/m in steady state. Comparison for different ice thicknesses h. Line 1 - $h = 0$ − no ice; line 2 - $h = 0.1$ m; line 3 - $h = 1$ m; line 4 - $h = 10$ m.
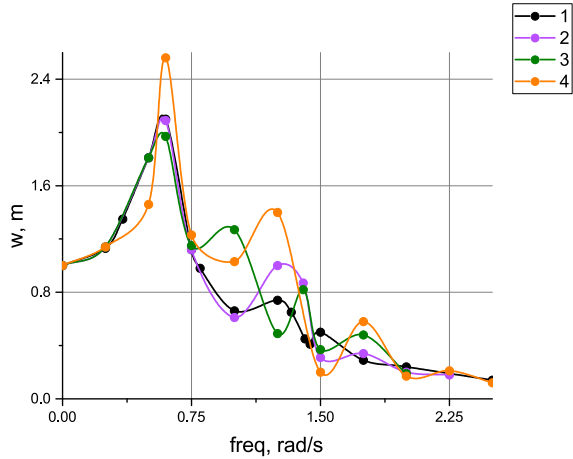
The dependencies are obtained for the distance from the ice edge to the floating body $L = 15$ m. The dependence of the movement of the left edge of the body on frequency shown in Fig. 9.3 shows that there are frequency ranges in which the influence of reflected waves on these movements is visible. When a body vibrates, it transfers energy into the liquid in the form of radiated waves. Part of this energy, which fell into the gap between the body and ice, is contained in the resulting quasi-standing wave [11]. In these frequency ranges, the surface wave length is proportional to the gap length. At the same time, there is an increase in the energy transmitted to this wave in the formed "trap" and an increase in the maximum displacements of the edge of the body. It should be noted that when the phases of the reflected waves and the floating body coincide, a resonance occurs, leading to an increase in the displacements of the body. In the case of antiphase motion, the reflected waves reduce the displacement of the body.

In addition, based on the graphs in Figs. 9.2 and 9.3, it can be concluded that it is important to consider the unsteady loading mode, since the maximum displacements in this mode exceed the maximum displacements in the steady state. It should be noted that with an increase in the thickness of the ice, the displacement of the floating body also increases. At the same time, as calculations showed, the displacements of the ice edge under the action of the same harmonic force decreased with increasing ice thickness as a result of an increase in the cylindrical rigidity of the plate. The results presented in Fig. 9.3 were compared with the results obtained in [11] with an ice thickness of 1 m. The comparison showed that the dependencies of displacements on the force frequency have a similar form. However, the resonance peaks obtained in this article are slightly shifted to the left towards lower frequencies compared to the peaks in [11]. At the same time, the values of displacements on the peaks of the curves in this article are slightly larger than those on the curves in [11]. This difference can be explained by the fact that the fluid pressure in the nonlinear setting is somewhat higher than in the linear one.

As can be seen from the graphs in Fig. 9.4, the number of resonant peaks increases with a decrease in the cylindrical stiffness of ice, which qualitatively coincides with the results obtained in [6] for the case of a free-floating beam.

Most of the calculations performed by the authors of this article confirm the conclusion made in [11] about the insignificant effect of nonlinear conditions on the liquid surface. The results of solving the linear problem performed by the authors of this article showed good agreement with the results given in [11] using the analytical method of expansion in terms of vertical eigenmodes in the steady state for a harmonic external disturbance. Due to the good agreement between the displacement values obtained from the solution of the problem by numerical and analytical methods, the solution by analytical formulas is not shown on the graphs. However, for some values of the parameters of the system under consideration, it turned out that considering the nonlinearity in the boundary conditions on the liquid surface leads to a difference from the case of a linear condition. The displacements of the edge of the floating body for linear and non-linear conditions on the water surface are shown in Fig. 9.5 for the values $L = 5$ m and the value of the amplitude of the applied force of 250000 N/m up to the frequency value corresponding to the first resonant peak. The limitation of the frequency range is due to the fact that the difference between the displacements between the nonlinear and linear cases is most noticeable at the first peak. At other peaks, the difference between the nonlinear and linear cases is not so noticeable. From the graphs in Fig. 9.5, it can be seen that at a frequency of the applied force equal to 0.5 rad/s, the magnitude of the displacement amplitude of the floating body in the non-linear case is greater than the linear one. Also, an increase in the displacement amplitude was observed for nonlinear boundary conditions for the values of the distance to the ice edge $L = 15$ m at the same frequency as for $L = 5$ m.

In addition, differences were found in the values of the maximum angle of rotation of the floating body in linear and non-linear cases in steady state for frequencies in the range of $0.6 - 1.3$ rad/s, as follows from the curves in Fig. 9.6.
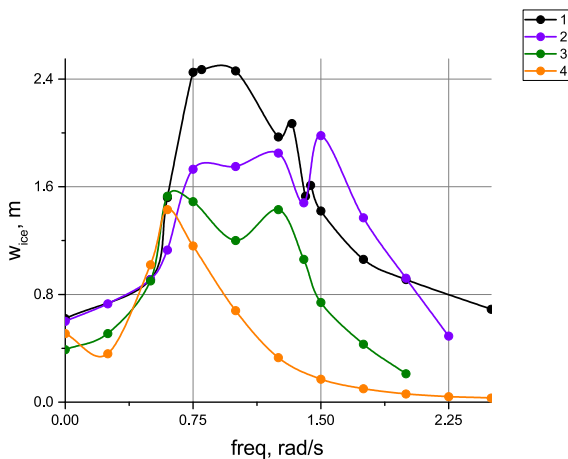
Fig. 9.4 Dependence of the ice edge displacement on the force frequency with an amplitude of 294300 N/m in steady state. Comparison for different ice thicknesses h. Line 1 - $h = 0 -$ no ice; line 2 - $h = 0.1$ m; line 3 - $h = 1$ m; line 4 - $h = 10$ m.

Fig. 9.5 Comparison of the linear and non-linear cases of the dependence of the displacement of the left edge of the body on the frequency of the force with an amplitude of 250000 N/m in the steady state at a distance between the ice and the body $L = 5$ m. Line 1 - $\alpha = 0$; line 2 - $\alpha = 1$.
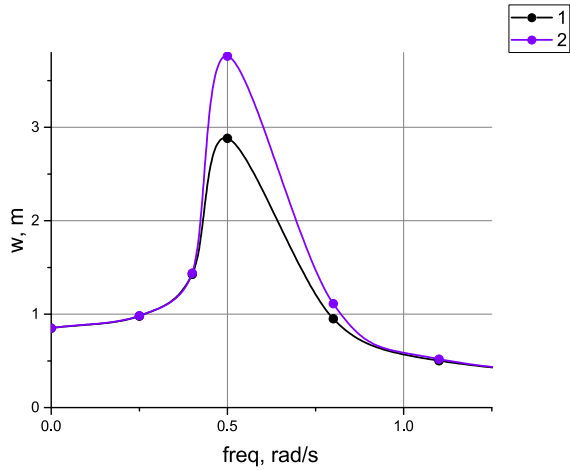
Fig. 9.6 Comparison of the dependence of the angle of rotation of the body on the frequency of the force with an amplitude of 294300 N/m at a distance between the ice and the body $L = 3$ m. Line 1 - $\alpha = 0$ steady state; line 2 - $\alpha = 1$ steady state; line 3 - $\alpha = 0$ unsteady state; line 4 - $\alpha = 1$ unsteady state.
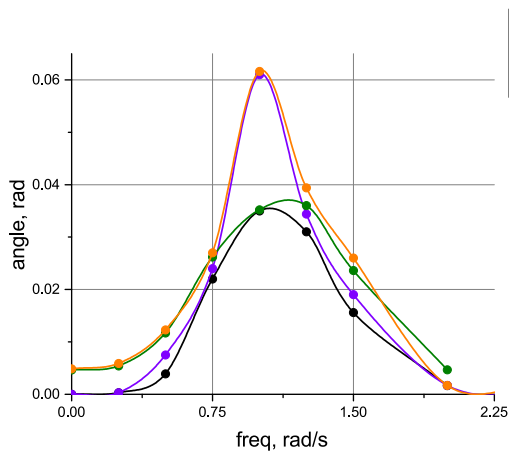
However, in a wide range of values of the system parameters, the difference between displacements and rotation angles of a floating body in a linear and non-linear setting is not observed. Figure 9.7 shows a typical dependence of the angles of rotation on the frequency of the acting force in a steady linear regime for various distances from the ice edge to the body.

To interpret the results shown in Fig. 9.7, it is necessary to note the following: due to the symmetry of the floating body itself, in the absence of ice, the angle of rotation of the body under force loading is zero. In addition, as can be seen from the graphs in Fig. 9.7, the presence of ice has little effect on the angle of rotation of the floating body up to a frequency of 0.55 rad/s acting force. At frequencies greater than 0.55 rad/s, the effect of the presence of ice is significant and manifests itself, among other things, in the presence of resonant peaks. The reason for the lack of influence of ice on the angle of rotation in a certain frequency range is due to the interaction of reflected and

Fig. 9.7: Dependence of the
angle of rotation of the body on
the frequency of the force with
an amplitude of 200000 N/m
in steady state. Comparison of
the influence of the distance
between the ice and the body
and nonlinearity. Line 1 -
$L = 15$ m, $\alpha = 0$; line 2 – $L =$
15 m, $\alpha = 1$; line 3 - $L = 10$
m, $\alpha = 0$; line 4 - $L = 10$ m,
$\alpha = 1$.
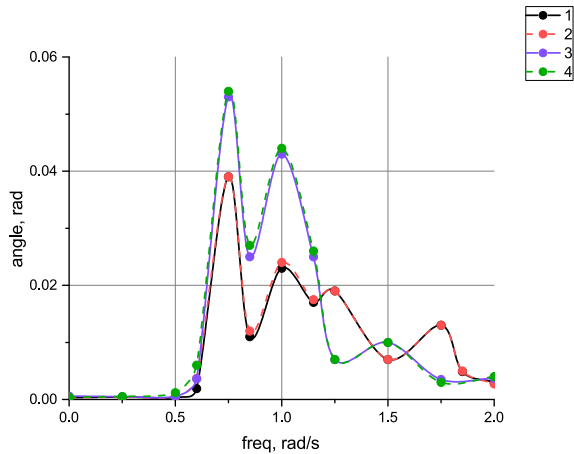
incident waves on the edge of the ice. It was shown in [12] that when a low-frequency wave is incident normal to the edge, its energy is transferred to a floating plate, while when a high-frequency wave is incident, its energy is completely reflected into the water. A similar behavior can be seen in Fig. 9.7, where at frequencies below 0.55 rad/s, the waves are almost not reflected. Non-propagating waves that can form in the space between the ice and the body quickly decay along the coordinate and do not affect the floating body. Therefore, propagating reflected surface waves are the main ones in the process. In Fig. 9.7 at $h = 1$ m results presented were compared with the results obtained in [11]. The comparison showed that the dependencies of the angle of rotation of the floating body on the force frequency have a similar form. The resonance peaks obtained in this article are slightly shifted to the left towards lower frequencies compared to the peaks presented in [11]. The values of the rotation angles obtained in this article are larger at resonant frequencies than the values of the rotation angles obtained in [11]. According to the authors, this difference in the values of these angles is a consequence of taking into account the nonlinearity, which leads to large values of the fluid pressure on the floating body. In addition, a comparison of the dependences in Figs. 9.6 and 9.7 allows us to conclude that the number of resonant peaks decreases with decreasing distance between the ice cover and the floating body.

The dependence of the displacements of a floating body on frequency as the distance between it and the ice edge was also studied. The dependencies of the maximum displacement of the left edge of the floating body on the frequency of the harmonic force with an amplitude of 200000 N/m for various distances to the ice edge are shown in Fig. 9.8. As can be seen from the graphs in Fig. 9.8, a decrease in the distance to the ice edge increases the maximum displacements of the floating body in the frequency range from 0.75 to 1.25 rad/s. However, other calculations for other parameters of the system do not show a clear dependence of the displacement amplitude on the distance to the ice edge. A similar result is associated with a complex wave pattern of waves reflected from the ice edge, which depends on the lengths

Fig. 9.8: Dependence of the ice edge displacement on the frequency of the force with an amplitude of 200,000 N/m in steady state. Comparison of the influence of the distance between the ice and the body and nonlinearity. Line 1 - $L = 15$ m, $\alpha = 0$; line 2 - $L = 15$ m, $\alpha = 1$; line 3 - $L = 1$ m, $\alpha = 0$; line 4 - $L = 1$ m, $\alpha = 1$.
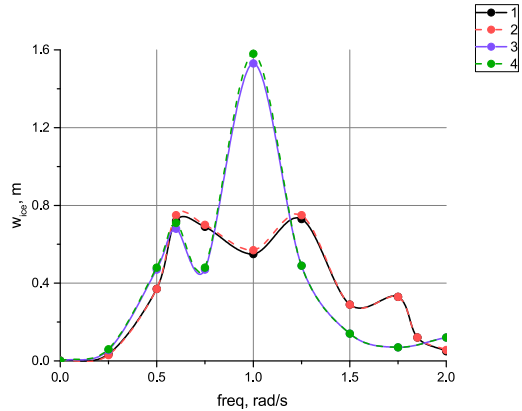
of the interacting waves. The lack of symmetry of the problem makes it difficult to interpret the result.

Another factor was considered that presumably affects the movement of ice and a floating body, namely its cylindrical rigidity. As the calculations showed, the cylindrical rigidity of the body begins to affect the maximum displacements of both ice and the floating body, only in the case of a significant decrease in its value, namely, by 1000 times compared with the parameters of offshore structures selected in [11]. Therefore, we can consider the behavior of a real offshore structure in the problem under consideration as the behavior of a rigid whole. As for the influence of the mass of the floating body, then, as in [11], an increase in the mass of the floating body led to a decrease in the magnitude of the resonance peaks, but the resonances themselves occurred at the same frequencies as at other masses.

9.5 Conclusion

In this paper, we propose an approach to the numerical solution of the problem of the effect of ice cover and surface waves of a liquid on the dynamics of a floating body. Based on the obtained numerical solution, the analysis of the behavior of displacements and angles of rotation of a floating body under the action of a harmonic concentrated force on the latter is carried out. It was shown that in an unsteady loading regime, the values of the maximum displacements and angles of rotation of a floating body can differ significantly from the values determined in the steady state. It was shown that the assumption made earlier in [11] about the possibility of using linear boundary conditions on the liquid surface can be used for most of the system parameters that are possible in practice. At the same time, for several parameters, and at certain impact frequencies, the nonlinear boundary conditions lead to larger values of the maximum displacements and rotation angles of the floating

body than in the linear setting. The flexural rigidity of a floating body begins to affect the displacements and angles of rotation of the body on the liquid surface at its values far from those that floating offshore structures can have. The influence of the distance from the ice edge to the floating body requires additional analysis. It should also be noted that such important factors as the influence of the three-dimensional formulation of the problem on the results obtained, the inhomogeneities of the ice cover (inclusions of old ice, cavities filled with brine, etc.), slush, momentary effects on the floating body, and its speed proximity to ice. All these factors are expected to be considered in the following works.

References

[1] Heisin DE (1967) Ice Cover Dynamics (in Russ.). Gidrometeorologicheskoye izd-vo, Leningrad

[2] Li ZF, Wu GX (2021) Hydrodynamic force on a ship floating on the water surface near a semi-infinite ice sheet. Physics of Fluids **33**(12)

[3] Li ZF, Wu GX, Ren K (2021) Interactions of waves with a body floating in an open water channel confined by two semi-infinite ice sheets. Journal of Fluid Mechanics **917**:A19

[4] Nelli F, Bennetts L, Skene D, Monty J, Lee J, Meylan M, Toffoli A (2017) Reflection and transmission of regular water waves by a thin, floating plate. Wave Motion **70**:209–221, Recent Advances on Wave Motion in Fluids and Solids

[5] Taylor RE, Ohkusu M (2000) Green functions for hydroelastic analysis of vibrating free–free beams and plates. Applied Ocean Research **22**(5):295–314

[6] Sturova IV (2002) The action of periodic surface pressures on a floating elastic platform. Journal of Applied Mathematics and Mechanics **66**(1):71–81

[7] Tkacheva LA (2005) Action of a periodic load on an elastic floating plate. Fluid Dynamics **40**(2):282–296

[8] Keijdener C (2019) The effect of hydrodynamics on the interaction between floating structures and flexible ice floes. Phd thesis, Delft University of Technology, Delft

[9] Sturova IV (2017) Action of periodic surface pressure on an ice cover in the vicinity of a vertical wall. Journal of Applied Mechanics and Technical Physics **58**(1):80–88

[10] Lavrov YA (2022) The response of a round plate and a cylindrical water-filled volume underneath to a point load moving periodically. St Petersburg State Polytechnical University Journal Physics and Mathematics **15**(2):140–147

[11] Keijdener C, de Oliveira Barbosa JM, Metrikine AV (2017) The influence of level ice on the frequency domain response of floaters. Cold Regions Science and Technology **143**:112–125

[12] Fox C, Squire VA (1990) Reflection and transmission characteristics at the edge of shore fast sea ice. Journal of Geophysical Research: Oceans **95**(C7):11,629–11,639

[13] Ni B, Han D, Di S, Xue Y (2020) On the development of ice-water-structure interaction. Journal of Hydrodynamics **32**(4):629–652

[14] Samarskiy AA, Nikolayev ES (1978) Methods for Solving Mesh Equations (in Russ.). Nauka, Moscow

[15] Ferziger JH, Peric M, Street RL (2020) Computational Methods for Fluid Dynamics, 4th edn. Springer Nature, Cham

Chapter 10
Nonlinear Stationary Waves in a Thin-Walled Bar Affected by Deplanation of Its Cross-Section in Torsion

Vladimir Erofeev, Boris Lampsi (Jr.), Anna Leonteva, and Nadezhda Semerikova

Abstract A mathematical model is herein considered which enables one to describe the propagation of a torsional wave in a thin-walled bar. The model includes geometric and physical elastic nonlinearities, as well as warping or deplanation, i.e. the withdrawal of the cross section from the initial plane state in the course of the bar deformation. It is determined based on the model analysis that warping, which causes the occurrence of dispersion in the phase velocity of a torsional wave also entails the emergence of the quadratic nonlinearity specific for intense longitudinal vibrations but having never been encountered before in mathematical models describing torsional vibrations. It is shown that a stationary torsional wave can be formed in a bar with quadratic nonlinearity. This is a periodic wave and it moves faster than any linear perturbation. The wave has a saw-tooth shape; the wavelength extends with the increase of its amplitude. Furthermore, it is shown that the joint action of cubic nonlinearity (generated by high vibration intensity) and dispersion (resulted from warping) in the bar can cause the formation of non-sinusoidal stationary waves propagating at a constant velocity without changing their shape.

Vladimir Erofeev · Anna Leonteva
Mechanical Engineering Research Institute of Russian Academy of Sciences, 85 Belinskogo str., 603024 Nizhny Novgorod, Russian Federation
e-mail: erof.vi@yandex.ru, aleonav@mail.ru

Boris Lampsi (Jr.)
Nizhny Novgorod State University of Architecture and Civil Engineering, 65 Ilinskaya str., 603950 Nizhny Novgorod, Russian Federation,
e-mail: boris-lampsi@yandex.ru

Nadezhda Semerikova
National Research Lobachevsky State University of Nizhny Novgorod, 23 Gagarina av., 603022 Nizhny Novgorod, Russian Federation,
e-mail: nadezhda.semerikova@yandex.ru

10.1 Introduction

Torsional waves on par with bending and longitudinal waves play a major role in the formation of vibration fields of engineering structures [1–3]. Mathematical models, which describe torsional waves propagating in homogeneous thin bars, are generally based on the engineering theory of torsion (Coulomb's theory) or on the theory of constrained torsion refining thereof.

Coulomb's engineering theory is based on assumptions of the nondeformity of the cross section in its plane (rigid contour) and the lack of warping (deplanation), i.e. the withdrawal of the cross section from the initial plane state. Under these hypotheses the bar cross-sections slide over each other rotating in their plane through a small angle like rigid platforms. Torsional waves are described by a wave equation and they propagate without dispersion at the shear wave velocity in an unbounded medium.

It is known that for circular and annular cross-section bars the effect of warping remains minor even at significant angles of torsion and it is usually neglected in calculations [1, 2]. For thin-walled bars of other cross sections the warping can be significant even at small angles of torsion.

It is assumed in the theory of constrained torsion that the bar torsion is composed of two interrelated motions: the rotation of cross sections in their plane (Coulomb torsion) and their warping. Such warping results from the not-uniform stretching of longitudinal fibers during torsion. According to the theories of Timoshenko and Vlasov the warping is proportional to the relative angle of torsion. Timoshenko equation and Vlasov equation in common with the "wave" operator (d'Alembert operator) contain terms describing the torsional wave dispersion, i.e. the dependence of wave velocity on frequency.

Slivker [4] proposed an improved theory wherein the relationship of the torsion angle $\theta(x,t)$ and warping measure $\beta(x,t)$ is not postulated as in the theories of Timoshenko and Vlasov but is determined when solving the problem. In [5] showed that the Slivker model states that the propagation of a torsional wave is characterized by two dispersion branches ("acoustic" and "optical").

10.2 Differential Equation for Torsional Vibrations of a Bar Taking into Account the Nonlinearity and Deplanation of the Bar Cross Section

In [6–8] Slivker model is generalized for the case of consideration to geometric and physical elastic nonlinearities. The expression for the kinetic deformation energy is as follows:

$$W_k = \frac{1}{2}\left[\rho I_r \left(\frac{\partial \theta}{\partial t}\right)^2 + \rho I_\omega \left(\frac{\partial \beta}{\partial t}\right)^2\right] \tag{10.1}$$

where ρ is the bar material density; I_r is a polar moment of inertia; I_ω is a sectorial moment of inertia.

To take into account the elastic nonlinearity in the expression for the potential energy density, there shall be retained not only quadratic terms but also terms in the fourth power:

$$W_p = \frac{1}{2}GI_x\left(\frac{\partial\theta}{\partial x}\right)^2 + \frac{1}{2}EI_\omega\left(\frac{\partial\beta}{\partial x}\right)^2 + \frac{1}{2}GI_g\left(\frac{\partial\theta}{\partial x}-\beta\right)^2 + \alpha_1\left(\frac{\partial\theta}{\partial x}\right)^4 +$$
$$+\alpha_2\left(\frac{\partial\beta}{\partial x}\right)^4 + \alpha_3\left(\frac{\partial\theta}{\partial x}-\beta\right)^4 \tag{10.2}$$

where $G = E/[2(1+\gamma)]$ is the shear modulus; E is Young's modulus; I_x is the torque of inertia; γ is Poisson's ratio; $I_g = I_x/(\psi - 1)$ is the warping moment of inertia; ψ is geometric parameter (see [4]); α_i are coefficients characterizing the geometric and physical non-linearity of the bar. If the bar is geometrically nonlinear, $\alpha_i > 0$, if it is physically nonlinear, $\alpha_i < 0$.

By compiling Lagrangian $L = W_k - W_p$ and applying the Hamilton-Ostrogradsky variational principle [2], we obtain the following system of equations for the bar dynamics:

$$\begin{cases} \dfrac{\partial}{\partial t}\left(\dfrac{\partial L}{\partial\theta_t}\right) + \dfrac{\partial}{\partial x}\left(\dfrac{\partial L}{\partial\theta_x}\right) - \dfrac{\partial L}{\partial\theta} = 0 \\[4mm] \dfrac{\partial}{\partial t}\left(\dfrac{\partial L}{\partial\beta_t}\right) + \dfrac{\partial}{\partial x}\left(\dfrac{\partial L}{\partial\beta_x}\right) - \dfrac{\partial L}{\partial\beta} = 0 \end{cases} \tag{10.3}$$

where the following notations are introduced:

$$\theta_t = \frac{\partial\theta}{\partial t}; \theta_x = \frac{\partial\theta}{\partial x}; \beta_t = \frac{\partial\beta}{\partial t}; \beta_x = \frac{\partial\beta}{\partial x}.$$

Upon the completion of necessary differentiations and transformations (10.3) will be written as follows:

$$\begin{cases} \rho I_r \dfrac{\partial^2\theta}{\partial t^2} - G(I_x+I_g)\dfrac{\partial^2\theta}{\partial x^2} + GI_g\dfrac{\partial\beta}{\partial x} + N_1 = 0 \\[4mm] \rho I_\omega \dfrac{\partial^2\beta}{\partial t^2} - EI_\omega\dfrac{\partial^2\beta}{\partial x^2} - GI_g\left(\dfrac{\partial\theta}{\partial x}-\beta\right) + N_2 = 0 \end{cases} \tag{10.4}$$

Here the non-linear terms are designated through $N_{1,2}$:

$$N_1 = -12(\alpha_1+\alpha_3)\left(\frac{\partial\theta}{\partial x}\right)^2\frac{\partial^2\theta}{\partial x^2} + 24\alpha_3\beta\frac{\partial\theta}{\partial x}\frac{\partial^2\theta}{\partial x^2} + 12\alpha_3\left(\frac{\partial\theta}{\partial x}\right)^2\frac{\partial\beta}{\partial x} -$$
$$-24\alpha_3\beta\frac{\partial\beta}{\partial x}\frac{\partial\theta}{\partial x} - 12\alpha_3\beta^2\frac{\partial^2\theta}{\partial x^2} + 12\alpha_3\beta^2\frac{\partial\beta}{\partial x} \tag{10.5}$$

$$N_2 = -12\alpha_3\frac{\partial\beta}{\partial x}\frac{\partial^2\beta}{\partial x^2} - 4\alpha_3\left(\frac{\partial\theta}{\partial x}\right)^3 + 12\alpha_3\beta\left(\frac{\partial\theta}{\partial x}\right)^2 - 12\alpha_3\frac{\partial\theta}{\partial x}\beta^2 + 4\alpha_3\beta^3 \tag{10.6}$$

System (10.4) - (10.6) is rather complicated for analysis. To simplify it, we will assume that deplanation $\beta(x,t)$ is quite small. Since non-linear effects are displayed at values of a higher order of smallness than linear ones, it enables us to consider the deplanation only in the linear part of equations and to approximately assume in non-linear terms that $\beta \approx \frac{\partial \theta}{\partial x}$. The nonlinear terms will thereat be as follows:

$$N_1 = -12\alpha_1 \left(\frac{\partial \theta}{\partial x}\right)^2 \frac{\partial^2 \theta}{\partial x^2}, \tag{10.7}$$

$$N_2 = -12\alpha_3 \frac{\partial \theta}{\partial x} \frac{\partial^2 \theta}{\partial x^2} \tag{10.8}$$

With the introduced assumptions the system of equations (10.4) is reduced to one equation for $\theta(x,t)$. In order to obtain it, from the first equation of the system we express

$$\frac{\partial \beta}{\partial x} = \frac{(I_x + I_g)}{I_g} \frac{\partial^2 \theta}{\partial x^2} - \frac{I_r \rho}{GI_g} \frac{\partial^2 \theta}{\partial t^2} + \frac{12\alpha_1}{GI_g} \left(\frac{\partial \theta}{\partial x}\right)^2 \frac{\partial^2 \theta}{\partial x^2}$$

and substitute thereof into the second equation pre-differentiated with respect to x. Thus, the nonlinear differential equation for torsional vibrations of the bar with consideration to the warping of its cross section will be as follows:

$$\frac{\partial^2 \theta}{\partial t^2} - c_s^2 \frac{\partial^2 \theta}{\partial x^2} + \frac{I_\omega}{c_\tau^2 I_g}\left(\frac{\partial^2}{\partial t^2} - \frac{(I_x + I_g)c_\tau^2}{I_g}\frac{\partial^2}{\partial x^2}\right)\left(\frac{\partial^2}{\partial t^2} - c_0^2 \frac{\partial^2}{\partial x^2}\right)\theta -$$

$$-\frac{12 I_\omega \alpha_1}{GI_g I_r}\frac{\partial^2}{\partial t^2}\left[\left(\frac{\partial \theta}{\partial x}\right)^2 \frac{\partial^2 \theta}{\partial x^2}\right] + \frac{12 I_\omega \alpha_1 EI_\omega}{\rho I_r GI_g}\frac{\partial^2}{\partial x^2}\left[\left(\frac{\partial \theta}{\partial x}\right)^2 \frac{\partial^2 \theta}{\partial x^2}\right] - \tag{10.9}$$

$$-\frac{12\alpha_1}{\rho I_r}\left(\frac{\partial \theta}{\partial x}\right)^2 \frac{\partial^2 \theta}{\partial x^2} + \frac{12\alpha_3}{\rho I_r}\frac{\partial}{\partial x}\left(\frac{\partial \theta}{\partial x}\frac{\partial^2 \theta}{\partial x^2}\right) = 0$$

Here $c_s = \sqrt{GI_x/\rho I_r}$ is the velocity of the torsional wave propagation in the bar.

Note that equation (10.9) contains in addition to the cubic nonlinearity typical of intense torsional vibrations of bars also the quadratic nonlinearity (the last term) typical of intense longitudinal vibrations and having not been encountered before in mathematical models describing torsional vibrations.

10.3 Wave Processes in a Thin-Walled Bar Taking into Account the Quadratic Nonlinearity

We will further consider wave processes taking into account the quadratic nonlinearity ($\alpha_3 \neq 0$) and neglecting the cubic nonlinearity ($\alpha_1 = 0$). Equation (10.9) in this case may be written as follows:

$$\frac{\partial^2 \theta}{\partial t^2} - c_s^2 \frac{\partial^2 \theta}{\partial x^2} + \frac{I_\omega}{c_\tau^2 I_g} \left(\frac{\partial^2}{\partial t^2} - \frac{(I_x + I_g)c_\tau^2}{I_g} \frac{\partial^2}{\partial x^2} \right) \left(\frac{\partial^2}{\partial t^2} - c_0^2 \frac{\partial^2}{\partial x^2} \right) \theta +$$

$$+ \frac{6\alpha_3}{\rho I_r} \frac{\partial^2}{\partial x^2} \left(\frac{\partial \theta}{\partial x} \right)^2 = 0 \tag{10.10}$$

Here $c_0 = \sqrt{E/\rho}$ is the longitudinal wave propagation velocity in the bar; $c_\tau = \sqrt{G/\rho}$ is the shear wave propagation velocity.

Linear torsional waves in the bar have the phase velocity dispersion [5]. Thus, the propagation of torsional waves described by Eq. (10.10) will be affected by the following two factors: dispersion and nonlinearity. The nonlinearity causes the generation of new harmonics in the wave spectrum, thus promoting the emergence of sharp spikes in the moving wave profile. But the dispersion, on the contrary, smooths out such spikes because of the difference in phase velocities of harmonic components of a wave. The joint action of these factors may cause the formation of stationary waves which propagate at a constant speed without changing their shape. [9] contains the review of the main results obtained in theoretical and experimental studies of nonlinear stationary waves in bars, plates and shells.

We will search for the solution of Eq. (10.10) in the form: $\theta(x,t) = \theta(\xi)$, where $\xi = x - Vt$, V is the stationary wave velocity (unknown before). Partial differential equation (10.10) for the bar cross-section torsion $\Theta = d\theta/d\xi$ will be reduced to an ordinary differential equation:

$$\frac{d^2 \Theta}{d\xi^2} + m_1 \Theta + m_2 \frac{d}{d\xi}(\Theta)^2 = 0 \tag{10.11}$$

where

$$m_1 = \frac{V^2 - \frac{c_\tau^2 I_x}{I_r}}{\frac{I_\omega}{c_\tau^2 I_g} \left(V^2 - \frac{(I_x + I_g)c_\tau^2}{I_g} \right)(V^2 - c_0^2)}, \qquad m_2 = \frac{6\alpha_3 c_\tau^2 I_g}{\rho I_r I_\omega \left(V^2 - \frac{(I_x + I_g)c_\tau^2}{I_g} \right)(V^2 - c_0^2)}.$$

The analysis of Eq. (10.11) on the phase plane $(\Theta, \frac{d\Theta}{d\xi})$ shows that closed phase trajectories, whereas only finite solutions of the equation correspond thereto, are possible, if $m_1 > 0$. Therefore, nonlinear torsional stationary waves can only exist when $m_1 > 0$. It is possible, if a non-linear wave is "fast", i.e. its velocity exceeds the velocities of all linear perturbations:

$$V > c_0 > c_\tau \sqrt{\frac{(I_x + I_g)}{I_g}} > c_s \tag{10.12}$$

or if a non-linear wave is "slow" and its velocity is within the interval:

$$c_s < V < c_\tau \sqrt{\frac{(I_x + I_g)}{I_g}} \tag{10.13}$$

A singular "center"-type point is available at the origin of coordinates on the phase plane. The straight line $\frac{d\Theta}{d\xi} = \varepsilon^*$ determines steady motions (closed phase trajectories):

$$\varepsilon^* = \frac{m_1}{2m_2} = \frac{\rho I_r c_s^2}{12\alpha_3}\left(\frac{V^2}{c_s^2} - 1\right)$$

(10.14)

This parameter increases with a growing relative value of the nonlinear stationary wave velocity, i.e. $|\varepsilon^*| \sim \left(\frac{V}{c_s}\right)^2$, and decreases with increasing $\alpha_3 : |\varepsilon^*| \sim \frac{1}{|\alpha_3|}$. The sign of m_2 is determined by the sign of α_3.

Figure 10.1 shows the phase portrait of Eq. (10.11) at $\alpha_3 < 0$ (10.1a) and the stationary wave profile at amplitudes close to ε^* (10.1b). Analytical constructions made for the case of $\alpha_3 > 0$ are shown in Fig. 10.2.

(a)   (b)
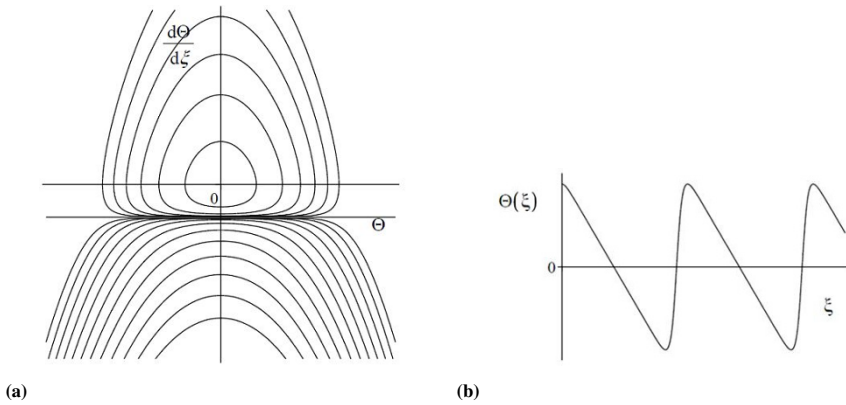
Fig. 10.1: Phase portrait of Eq. (10.11) for $\alpha_3 < 0$ (a) and stationary wave profile (b).

(a)   (b)
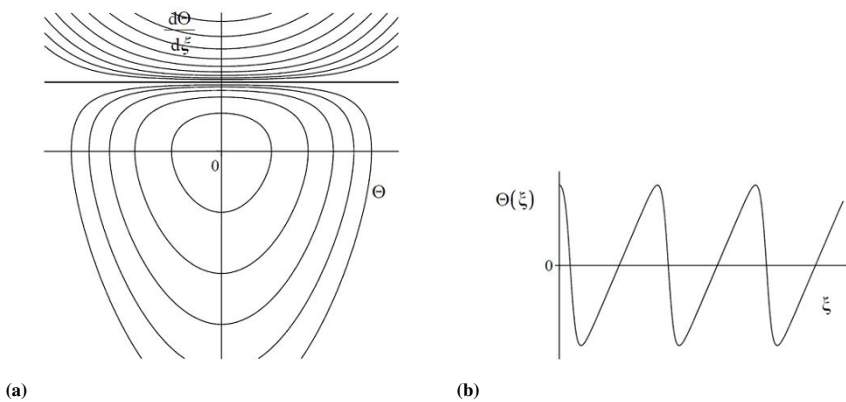
Fig. 10.2: Phase portrait of Eq. (10.11) for $\alpha_3 > 0$ (a) and stationary wave profile (b).

The phase portrait enables us to assess the dependence of the wavenumber of nonlinear wave (k) on its amplitude (a):

$$\frac{k}{k_0} = \frac{1}{\sqrt{1 + \left(\frac{a/a_0}{\pi \varepsilon^*}\right)^2}} \tag{10.15}$$

where k_0, a_0 are the wavenumber and amplitude of a harmonic (linear) wave.

With the increasing wave amplitude the relative value of the wavenumber decreases (the wavelength increases) (Fig. 10.3). The nonlinear wave profiles at the fixed amplitude ($a/a_0 = $ const) and various values of ε^* re shown in Fig. 10.4.

10.4 Wave Processes in a Thin-Walled Bar Taking into Account the Cubic Nonlinearity

We will further consider wave processes taking into account the cubic nonlinearity ($\alpha_3 = 0$) and neglecting the quadratic nonlinearity ($\alpha_1 \neq 0$). Equation (10.9) may be written in this case as follows:
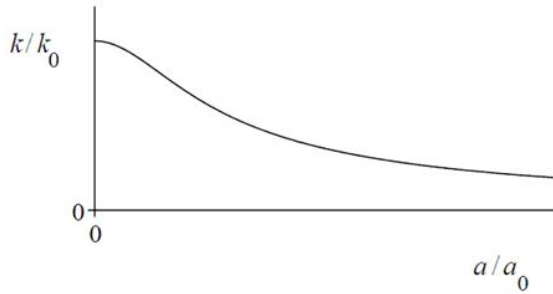
Fig. 10.3 Dependence of the wave number of a nonlinear periodic wave on its amplitude.

(a)

(b)
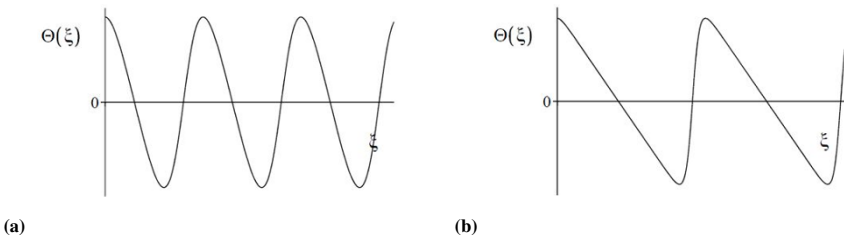
Fig. 10.4: Profiles of a nonlinear periodic wave at a fixed amplitude ($a/a_0 = $ const) and at various values of ε^* : $\varepsilon^* = \varepsilon_1^*$ (a), $\varepsilon^* = \varepsilon_2^*$ (b), where $\varepsilon_2^* > \varepsilon_1^*$.

$$\frac{\partial^2\theta}{\partial t^2} - c_s^2\frac{\partial^2\theta}{\partial x^2} + \frac{I_\omega}{c_\tau^2 I_g}\left[\frac{\partial^2}{\partial t^2} - \frac{I_x + I_g}{I_g}c_\tau^2\frac{\partial^2}{\partial x^2}\right]\left(\frac{\partial^2}{\partial t^2} - c_0^2\frac{\partial^2}{\partial x^2}\right)\theta -$$

$$-\frac{4\alpha_1}{\rho I_r}\frac{\partial}{\partial x}\left(\frac{\partial\theta}{\partial x}\right)^3 = 0 \tag{10.16}$$

The third term in equation (10.16) appeared because of available warping, which causes the emerging dispersion of the torsional wave phase velocity; the fourth term appeared in the equation because of the available nonlinearity. Coefficient α_1 characterizes the geometric and physical non-linearity of the bar. If the bar is geometrically nonlinear, $\alpha_1 > 0$, if it is physically nonlinear, $\alpha_1 < 0$.

Thus, the propagation of torsional waves described by equation (10.16) will be affected by the following two factors: dispersion and nonlinearity. The nonlinearity causes the generation of new harmonics in the wave spectrum, thus promoting the emergence of sharp spikes in the moving wave profile. But the dispersion, on the contrary, smooths out such spikes because of the difference in phase velocities of harmonic components of a wave. The joint action of these factors may cause the formation of stationary waves which propagate at a constant speed without changing their shape.

We will search for the solution of equation (10.16) in the form: $\theta(x,t) = \theta(\xi)$, where $\xi = x - Vt$, V is the stationary wave velocity (unknown before). Partial differential equation (10.16) for the relative angle of the cross section rotation of the bar $\Theta = d\theta/d\xi$ will be reduced to an ordinary differential equation (Duffing equation) [10]:

$$\frac{d^2\Theta}{d\xi^2} + m_1\Theta + m_2\Theta^3 = 0 \tag{10.17}$$

where

$$m_1 = \frac{(V^2 - c_s^2)c_\tau^2 I_g}{I_\omega[V^2 - ((I_x + I_g)/I_g)c_\tau^2](V^2 - c_0^2)}$$

$$\tag{10.18}$$

$$m_2 = \frac{-4\alpha_1 c_\tau^2 I_g^2}{\rho I_r I_\omega[V^2 - ((I_x + I_g)/I_g)c_\tau^2](V^2 - c_0^2)}$$

For linear perturbation velocities included in (10.18) the following inequality is valid:

$$c_0 > c_\tau\sqrt{\frac{I_x + I_g}{I_g}} > c_\tau > c_s$$

If the bar has the geometric nonlinearity ($\alpha_1 > 0$), there are no stationary torsional waves within the velocity range $V < c_s$. In all other ranges non-linear stationary waves can develop. However, depending on the value of the velocity V there are qualitatively different wave patterns, since the Duffing equation (10.17) has thereat various solutions.

Equation (10.17) has the first integral:

$$\frac{1}{2}\left(\frac{d\Theta}{d\xi}\right)^2 = E - \frac{m_1}{2}\Theta^2 - \frac{m_2}{4}\Theta^4 \tag{10.19}$$

which may be interpreted as the energy conservation law for an anharmonic oscillator. Here E – is the integration constant, which has the meaning of the initial energy of the system and the function

$$f(\Theta) = (m_1/2)\Theta^2 - (m_2/4)\Theta^4$$

has the meaning of potential energy.

Equation (10.19) allows the separation of variables:

$$\sqrt{2}d\xi = \frac{d\Theta}{\sqrt{E - f(\Theta)}} \tag{10.20}$$

and has bounded solutions in the region between any real roots of the polynomial $E - f(\Theta)$, where $E - f(\Theta) > 0$. Let $m_1 > 0$, $m_2 < 0$. It is possible, if the stationary wave velocity is within the range $c_s < V < c_\tau\sqrt{(I_x + I_g)/I_g}$ or $V > c_0$. In this case the potential energy function $f(\Theta) = (m_1/2)\Theta^2 - (m_2/4)\Theta^4$ has the local maximum $f_{max} = -m_1^2/4m_2$ at points $\Theta = \pm\sqrt{-m_1/m_2}$ and the local minimum $f_{min} = 0$ at $\Theta = 0$ (Fig. 10.5a). Therefore, the point $(0;0)$ on the phase plane $(\Theta; d\Theta/d\xi)$ is the stable "center"-type equilibrium position and points $(\pm\sqrt{m_1/m_2};0)$ are unstable "node"-type equilibrium positions. The phase portrait of the system is shown in Fig. 10.5b.

Bounded solutions of equation (10.20) in this case only exist at $0 \le E \le f_{max}$. The polynomial $E - f(\Theta)$ has thereat four real roots $\Theta_{1,2} = \pm\alpha$, $\Theta_{3,4} = \pm\beta$, where

$$\alpha^2 = \frac{m_1 - \sqrt{m_1^2 + 4m_2E}}{-m_2}, \quad \beta = \frac{m_1 + \sqrt{m_1^2 + 4m_2E}}{-m_2}, \quad (\alpha^2 > \beta^2) \tag{10.21}$$

(a)   (b)
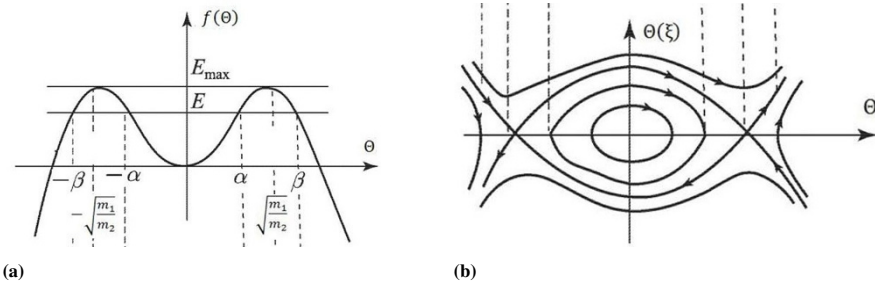
Fig. 10.5: Potential energy of the Duffing equation (10.17) for $m_1 > 0, m_2 < 0$ (a) and the phase portrait corresponding to this case (b).

and takes positive values at $-\alpha < \Theta < \alpha$. At $E = f_{max} = -m_1/4m_2$ the roots coincide in pairs $\Theta_1 = \Theta_3$, $\Theta_2 = \Theta_4$, it corresponds to the motion along the separatrix on the phase plane.

Equation (10.20) takes on the following form:

$$\alpha\beta\sqrt{-\frac{m_2}{2}}\,d\xi = \frac{d\Theta}{\sqrt{\left(1 - (\Theta^2/\alpha^2)\right)\left(1 - (\Theta^2/\beta^2)\right)}} \tag{10.22}$$

and with substituting

$$\frac{\Theta}{\alpha} = z \tag{10.23}$$

is reduced to an elliptic integral of the first kind

$$\sqrt{\frac{m_2}{2}}\,(\xi - \xi_0) = \frac{1}{\beta}\int_0^z \frac{dz}{\sqrt{(1 - z^2)(1 - s^2 z^2)}}, \tag{10.24}$$

where $s^2 = \alpha^2/\beta^2$.

By converting the elliptic integral in the right-hand side of (10.24) at $z = 0, \xi_0 = 0$ we obtain the solution describing nonlinear periodic vibrations as follows:

$$\Theta(\xi) = \alpha \operatorname{sn}\left(-\sqrt{\frac{1}{2}m_2\beta^2}\xi, s\right) \tag{10.25}$$

In expression (10.25) we introduce the following notations:

$$A = \alpha = \sqrt{\frac{(m_1 - \sqrt{m_1^2 + 4m_2 E})}{-m_2}},$$

$$k = \sqrt{-\frac{1}{2}m_2\beta^2} = \sqrt{\frac{1}{2}\left(m_1 + \sqrt{m_1^2 + 4m_2 E}\right)}, \tag{10.26}$$

$$s^2 = \frac{\alpha^2}{\beta^2} = \frac{m_1 - \sqrt{m_1^2 + 4m_2 E}}{m_1 + \sqrt{m_1^2 + 4m_2 E}}$$

where A is the stationary wave amplitude, k is the nonlinear analog of the wavenumber, s is the elliptic function modulus and the wavelength Λ is equal to

$$\Lambda = 4\frac{K(s)}{k}.$$

It follows from relations (10.26) that when changing E from 0 to $E_{max} = -m_1^2/4m_2$ the vibration frequency decreases from $k = \sqrt{m_1}$ to $\sqrt{m_1/2}$ and the vibration amplitude changes within the ranges

$$0 \le A \le A_c^1 = \sqrt{\frac{m_1}{m_2}},$$

where A_c^1 is the vibration amplitude corresponding to the motion along the separatrix on the phase plane. The elliptic function modulus (linear distortion factor) thereat changes within the range $0 \le s^2 \le 1$. Similarly, by excluding E from expressions (10.26), we obtain relationships of the parameters A, k, s in the solution (10.25):

$$s^2 = -\frac{m_1 A^2}{2m_1 + m_2 A^2}, \quad k = \sqrt{\frac{2m_1 + m_2 A^2}{2}}, \quad \Lambda = \frac{4K(s)}{\sqrt{m_1 + m_2 A^2/2}} \tag{10.27}$$

Another form of these expressions shall be:

$$A = \pm\sqrt{-\frac{2m_1}{m_2} \frac{s^2}{1 + s^2}}, \quad k = \sqrt{\frac{m_1}{1 + s^2}} \tag{10.28}$$

Taking into account the introduced notations the solution (10.25), which describes nonlinear periodic vibrations along closed phase trajectories near the separatrix, can be represented as an elliptic sine:

$$\Theta(\xi) = A \operatorname{sn}(k\xi, s) \tag{10.29}$$

The parameters of a torsional stationary wave are bound by correlation (10.29). When substituting expressions (10.18) into (10.29), we obtain:

$$A = \pm\sqrt{\frac{(V^2 - c_s^2)\rho I_r}{2\alpha_1} \frac{s^2}{(1 + s^2)}} \tag{10.30}$$

Hence, the wave amplitude grows in direct proportion to its increasing velocity and the angle of curve slope (10.30) increases as s grows from 0 to 1. At s which are close to unity, the shape of vibrations is shown in Fig. 10.6a.

A solitary wave is the limiting case of periodic wave (10.29). At $E = E_{max} = -m_1^2/4m_2$, $s^2 = 1$ the expression (10.25) describes the separatrix solution:

(a)   (b)
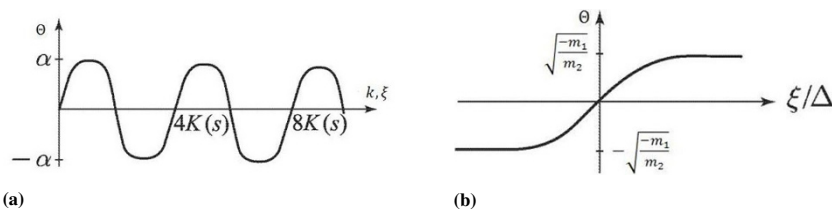
Fig. 10.6: Profiles of a nonlinear stationary wave: periodic, described by formula (10.29) (a) and solitary, described by formula (10.31) (b).

$$\Theta(\xi) = A \, \text{th}\left(\frac{\xi}{\Delta}\right), \tag{10.31}$$

where

$$A = \pm\sqrt{-\frac{m_1}{m_2}} = \pm\sqrt{\frac{(V^2 - c_s^2)\rho I_r}{4\alpha_1}} \tag{10.32}$$

$$\Delta = \frac{1}{k} = \sqrt{\frac{2}{m_2}} = \sqrt{\frac{2I_\omega\left[V^2 - ((I_x + I_g)/I_g)\,c_\tau^2\right](V^2 - c_0^2)}{(V^2 - c_s^2)c_\tau^2 I_g}} \tag{10.33}$$

V is the solitary wave velocity, A is the amplitude, Δ is the width. The separatrix solution has the form of overfall, its view is shown in Fig. 10.6b. The solitary wave amplitude increases with growing velocity but the graph thereof lies above the relevant dependence (10.30) for a periodic wave.

The width of the solitary wave (10.33) at $c_s < V < c_\tau\sqrt{(I_x + I_g)/I_g}$ decreases proportionally to $1/V$. At velocities $V > c_0$ an anomalous behaviour of a solitary wave is displayed, which is expressed in the extension of its width ($\Delta \sim V$) with its growing velocity and amplitude.

Let $m_1 < 0$, $m_2 > 0$. This case is valid for velocities within the interval $c_\tau\sqrt{(I_x + I_g)/i_g} < v < c_0$. In this case, the potential-energy function $f(\Theta) = (m_1/2)\Theta^2 - (m_2/4)\Theta^4$ has the local maximum $f_{max} = 0$ at $\Theta = 0$ and the local minimum $f_{min} = -m_1^2/4m_2$ at points $\Theta = \pm\sqrt{-m_1/m_2}$ (Fig. 10.7a). Points $(\pm\sqrt{-m_1/m_2}, 0)$ on the phase plane $(\Theta; d\Theta/d\xi)$ are the stable "center"-type equilibrium position and the point $(0,0)$ is the "saddle" (Fig. 10.7b). Bounded solutions of equation (10.20) are available, if the integration constant varies within the range $f_{min} \leq E < +\infty$, and qualitatively different motion modes correspond to different values of the initial energy E.

Let $f_{min} \leq E \leq 0$. The polynomial $E - f(\Theta)$ has thereat four real roots $\Theta_{1,2} = \pm\alpha$, $\Theta_{3,4} = \pm\beta$, where

(a)   (b)
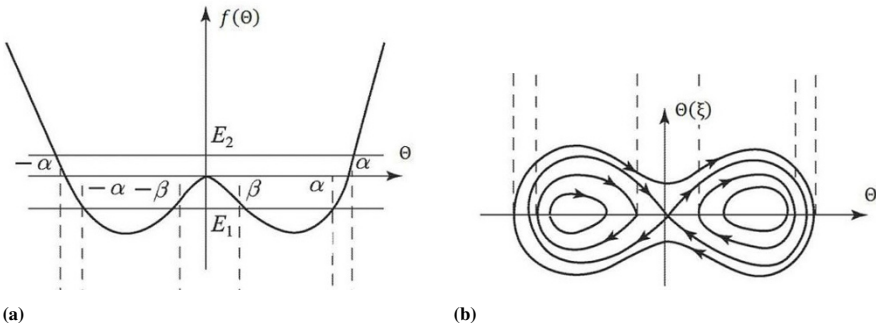
Fig. 10.7: Potential energy of the Duffing equation (10.17) for $m_1 < 0, m_2 > 0$ (a) and the phase portrait corresponding to this case (b).

$$\alpha^2 = \frac{-m_1 + \sqrt{m_1^2 + 4m_2E}}{m_2}, \quad \beta^2 = \frac{-m_1 - \sqrt{m_1^2 + 4m_2E}}{m_2}, \quad (\alpha^2 \geq \beta^2) \qquad (10.34)$$

and takes positive values in the regions $|\alpha| \leq \Theta \leq |\beta|$ (Fig. 10.7a). Closed trajectories lying inside the separatrix correspond thereto on the phase plane. Equation (10.20) takes the following form:

$$\alpha\beta\sqrt{\frac{m_2}{2}}\,d\xi = \frac{d\Theta}{\sqrt{-(1-(\Theta^2/\alpha^2))(1-(\Theta^2/\beta^2))}} \qquad (10.35)$$

and with substituting

$$\frac{\Theta}{\alpha} = \sqrt{1 - \frac{\alpha^2 - \beta^2}{\alpha^2}z^2} \qquad (10.36)$$

it is reduced to an elliptic integral of the first kind

$$\sqrt{\frac{m_2}{2}}(\xi - \xi_0) = \frac{1}{\alpha}\int_0^z \frac{dz}{\sqrt{(1-z^2)(1-s^2z^2)}}, \qquad (10.37)$$

where $s^2 = (\alpha^2 - \beta^2)/\alpha^2$. By converting the elliptic integral at $z = 0$, $\xi_0 = 0$, we obtain the solution which describes nonlinear periodic vibrations as follows:

$$\Theta(\xi) = \alpha\,dn\left(\sqrt{\frac{1}{2}m_2\alpha^2}\xi,\,s\right) \qquad (10.38)$$

In expression (10.38) we introduce the following notation:

$$A = \alpha = \sqrt{\frac{\left(-m_1 + \sqrt{m_1^2 + 4m_2E}\right)}{m_2}}$$

$$k = \sqrt{-\frac{1}{2}m_2\alpha^2} = \sqrt{\frac{1}{2}\left(-m_1 + \sqrt{m_1^2 + 4m_2E}\right)} \qquad (10.39)$$

$$s^2 = \frac{\alpha^2 - \beta^2}{\beta^2} = \frac{2\sqrt{m_1^2 + 4m_2E}}{-m_1 + \sqrt{m_1^2 + 4m_2E}}$$

where A is the stationary wave amplitude, k is the nonlinear analog of the wavenumber, s is the elliptic function modulus, $\Lambda = 4\boldsymbol{K}(s)/k$ is the wavelength. It follows from relations (10.39) that when E changes from $E_{min} = -m_1^2/4m_2$ to 0 the vibration frequency increases from $k = \sqrt{-m_1/2}$ to $k = \sqrt{-m_1}$, and the amplitude of periodic vibrations changes from $A = A_c^1 = \sqrt{-m_1/m_2}$ to $A = A_c^2 = \sqrt{-2m_1/m_2}$, where A_c^1, A_c^2 are amplitudes of vibrations corresponding to movements along separatrices

for phase portraits shown in Fig. 10.5 and 10.7, respectively. The elliptic function modulus varies within $0 \leq s^2 \leq 1$.

Eliminating the integration constant E from expressions (10.39) we obtain the relationship of parameters A, k, s in solution (10.38):

$$s^2 = 2\left(1 + \frac{m_1}{m_2 A^2}\right), \quad k = \sqrt{\frac{m_2 A^2}{2}}, \quad \Lambda = \frac{4\sqrt{2}\boldsymbol{K}(s)}{\sqrt{m_2 A^2}}, \tag{10.40}$$

which may be represented as:

$$A = \sqrt{-\frac{2m_1}{m_2}\frac{1}{2-s^2}} = \sqrt{\frac{(V^2 - c_s^2)\rho I_r}{2\alpha_1}\frac{1}{2-s^2}}, \quad k = \sqrt{-\frac{m_1}{2-s^2}}, \quad 0 \leq s^2 \leq 1 \tag{10.41}$$

i.e. $A \sim V$, but the periodic wave amplitude at any s is less than the solitary wave amplitude.

With the notations introduced, solution (10.38) describing nonlinear periodic vibrations along closed phase trajectories inside the separatrix may be represented as an elliptic function of the delta amplitude:

$$\Theta(\xi) = A\, dn(k\xi, s) \tag{10.42}$$

These vibrations do not have any linear degeneracy, since at $E \to E_{min} = -\frac{m_1^2}{4m_2}s \to 0$ and $dn(k\xi, s) = 1$. At $E = 0$, $s = 1$ from (10.38) we obtain degeneration into a separatrix solution (Fig. 10.8c):

$$\Theta(\xi) = A_c^2\, ch^{-1}(\xi/\Delta) \tag{10.43}$$

where:

$$\begin{aligned} A_c^2 &= \pm\sqrt{-\frac{2m_1}{m_2}} = \pm\sqrt{\frac{(V^2 - c_s^2)\rho I_r}{2\alpha_1}} \\ \Delta &= \frac{1}{k} = \sqrt{-\frac{1}{m_1}} = \sqrt{\frac{I_\omega\left[V^2 - ((I_x + I_g)/I_g)c_\tau^2\right](V^2 - c_0^2)}{(V^2 - c_s^2)c_\tau^2 I_g}} \end{aligned} \tag{10.44}$$

A_c^2 is the vibration amplitude, Δ is the solitary wave width. It is seen that within this range $A \sim V$ and $\Delta \sim \sqrt{1 - V^2/c_0^2}$. The qualitative type of nonlinear periodic motions described by the delta amplitude is shown in Fig. 10.8a and Fig. 10.8b shows a separatrix solution.

If $E = 0$, in this case the polynomial $E - f(\Theta)$ has two real roots $\Theta_{1,2} = \pm\alpha$, $\Theta_{3,4} = \pm i\beta$, where

$$\alpha^2 = \frac{-m_1 + \sqrt{m_1^2 + 2m_2 E}}{m_2}, \quad \beta^2 = \frac{m_1 + \sqrt{m_1^2 + 4m_2 E}}{m_2} \tag{10.45}$$

(a)

(b)

(c)
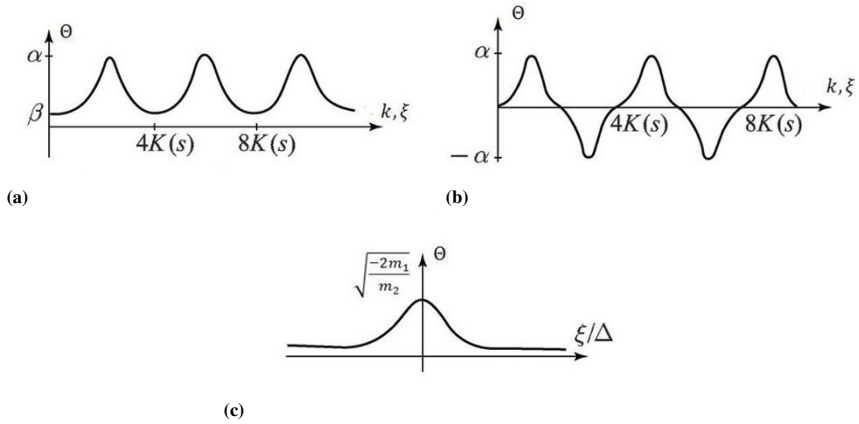
Fig. 10.8: Profiles of a nonlinear stationary wave: periodic, described by formulas (10.29) (a) and (10.53) (b), solitary, described by formula (10.43) (c).

and takes positive values within the regions $-\alpha < \Theta < \alpha$ (Fig. 10.7a). Closed phase trajectories lying outside the separatrix loop correspond to bounded solutions on the phase plane at such values of E (Fig. 10.7b).

Equation (10.20) takes the following form:

$$\alpha\beta\sqrt{\frac{m_2}{2}}\,d\xi = \frac{d\Theta}{\sqrt{(1-(\Theta^2/\alpha^2))(1-(\Theta^2/\beta^2))}} \qquad (10.46)$$

and with substituting

$$\frac{\Theta}{\alpha} = \sqrt{1-z^2} \qquad (10.47)$$

it is reduced to an elliptic integral of the first kind

$$\sqrt{\frac{m_2}{2}}(\xi-\xi_0) = -\frac{1}{\sqrt{\alpha^2+\beta^2}}\int_0^z \frac{dz}{\sqrt{(1-z^2)(1-s^2z^2)}}, \qquad (10.48)$$

where $s^2 = \alpha/(\alpha^2+\beta^2)$.

By converting the elliptic integral at $z = 0, \xi_0 = 0$, we obtain the solution describing nonlinear periodic vibrations as follows:

$$\Theta(\xi) = \alpha\,cn\left(\sqrt{\frac{m_1}{2}(m_1^2+\beta^2)}\xi, s\right) \qquad (10.49)$$

In expression (10.49) we introduce the following notations:

$$A = \alpha = \sqrt{\frac{\left(-m_1 + \sqrt{m_1^2 + 4m_2 E}\right)}{m_2}}$$

$$k = \sqrt{\frac{m_1}{2}(\alpha^2 + \beta^2)} = (m_1^2 + 4m_2 E)^{1/4} \qquad (10.50)$$

$$s^2 = \frac{\alpha^2}{\alpha^2 + \beta^2} = \frac{-m_1\sqrt{m_1^2 + 4m_2 E}}{2\sqrt{m_1^2 + 4m_2 E}}$$

where A is the stationary wave amplitude, k is the nonlinear analog of the wavenumber, s – is the elliptic function modulus, $\Lambda = 4\boldsymbol{K}(s)/k$ is the wavelength.

While analyzing relations (10.50), we find that when E varies from 0 to $+\infty$, the vibration frequency increases from $k = \sqrt{-m_1}$ to $+\infty$, the vibration amplitude also indefinitely increases from $A = A_c^1 = \sqrt{-2m_1/m_2}$ and the elliptic function modulus decreases within the range $0.5 \le s \le 1$. Eliminating the integration constant E from (10.50) we obtain the relationship of parameters A, k, s in the solution:

$$s^2 = \frac{m_2 A^2}{2(m_1 + m_2 A^2)},$$

$$k = \sqrt{2m_1 + m_2 A^2}, \qquad (10.51)$$

$$\Lambda = \frac{4\boldsymbol{K}(s)}{\sqrt{m_1 + m_2 A^2}}.$$

This relationship may be represented as follows:

$$A = \sqrt{-\frac{2m_1}{m_2}\frac{s^2}{2s^2 - 1}} = \sqrt{\frac{(V^2 - c_s^2)\rho I_r}{2\alpha_1}\frac{s^2}{2s^2 - 1}},$$

$$k = \sqrt{-\frac{m_1}{2s^2 - 1}}, \qquad (10.52)$$

$$1 > s^2 > \frac{1}{2}$$

With the notations introduced, solution (10.49) describing vibrations along closed phase trajectories outside the separatrix may be represented as follows:

$$\Theta(\xi) = A\,\mathrm{cn}(k\xi, s) \qquad (10.53)$$

This solution describes non-linear vibrations, which do not have any linear degeneracy. Their shape at s^2, which are close to unity, is shown in Fig. 10.8b. At $s = 1$ we obtain from (10.53) the separatrix solution (10.43). The amplitude of such periodic vibrations is always greater than the amplitude of solitary ones.

Based on the above reasoning the following conclusion may be drawn: if the bar has the geometric nonlinearity ($\alpha_1 > 0$), no stationary torsional waves are available

within the velocity range $V < c_s$. In all other ranges non-linear stationary waves can develop. But depending on the value of velocity V there are qualitatively different wave patterns, since Duffing equation (10.17) has thereat different solutions. If the stationary wave velocity is $c_s < V < c_\tau \sqrt{(I_x + I_g)/I_g}$ or $V > c_0$, Duffing equation (10.17) has two types of finite solutions - periodic solution (10.29) expressed through the elliptic sine and solitary solution (10.31), which is the limiting case of the periodic one.

For velocities within the interval $c_\tau \sqrt{(I_x + I_g)/I_g} < V < c_0$, the phase portrait of Eq. (10.17) contains two stable equilibrium positions, in the vicinity thereof phase trajectories have a near-ellipse shape. In this case, the following three types of finite solutions are available. One of them is the solitary stationary wave (10.43) linking two classes of periodic waves. This solution corresponds on the phase plane to separatrix passing through the origin of coordinates and separating one solution region from another. The second type of the finite solution corresponds to a closed-path motion near the equilibrium position and is described by the elliptic delta-amplitude function (10.42). Another type of the periodic motion is described by elliptic cosine (10.53).

If the bad has the physical nonlinearity ($\alpha_i < 0$), depending on the stationary wave velocity there are possible phase portraits of equation (10.17), which are shown in Fig. 10.9. Let $m_1 > 0$, $m_2 > 0$. It is valid, if the stationary wave velocity is within the range $c_s < V < c_\tau \sqrt{(I_x + I_g)/I_g}$ or $V > c_0$. In this case the potential energy function $f(\Theta) = (m_1/2)\Theta^2 - (m_2/4)\Theta^4$ has the local minimum $f_{min} = 0$ at $\Theta = 0$ (Fig. 10.10a). The point with coordinates $(0,0)$ on the phase plane $(\Theta; d\Theta/d\xi)$ is the stable "center"- type equilibrium position (Fig. 10.10b).

Bounded solutions of equation (10.20) are available at $0 < E < +\infty$. The polynomial $E - f(\Theta)$ has in this case two real roots $\Theta_{1,2} = \pm\alpha$ and two imaginary roots $\Theta_{3,4} = \pm i\beta$, where

$$\alpha^2 = \frac{-m_1 + \sqrt{m_1^2 + 4m_2 E}}{m_2}, \quad \beta^2 = \frac{m_1 + \sqrt{m_1^2 + 4m_2 E}}{m_2} \tag{10.54}$$
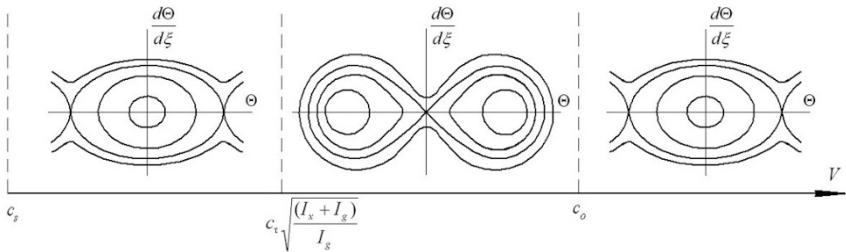
Fig. 10.9: Types of phase portraits of the Duffing equation (10.17) depending on the speed of a stationary wave for a rod with geometric nonlinearity ($\alpha_1 > 0$).

and takes positive values within the regions $-\alpha < \Theta < \alpha$ (Fig. 10.10a). Equation (10.20) will be written as follows:

$$\alpha\beta\sqrt{\frac{m_2}{2}}\,d\xi = \frac{d\Theta}{\sqrt{(1-(\Theta^2/\alpha^2))(1-(\Theta^2/\beta^2))}} \tag{10.55}$$

and with substituting

$$\frac{\Theta}{\alpha} = \sqrt{1-z^2} \tag{10.56}$$

it is reduced to an elliptic integral of the first kind

$$\sqrt{\frac{m_2}{2}}(\xi-\xi_0) = -\frac{1}{\sqrt{\alpha^2+\beta^2}}\int_0^z \frac{dz}{\sqrt{(1-z^2)(1-s^2z^2)}}, \tag{10.57}$$

where $s^2 = \alpha/(\alpha^2+\beta^2)$.

By converting the elliptic integral in the right-hand side of (10.57) at $z = 0, \xi_0 = 0$, we obtain the solution describing nonlinear periodic vibrations as follows:

$$\Theta(\xi) = \alpha\,\mathrm{cn}\left(\sqrt{\frac{m_1}{2}(\alpha^2+\beta^2)}\xi, s\right) \tag{10.58}$$

In expression (10.58) we introduce the following notations:

(a)   (b)
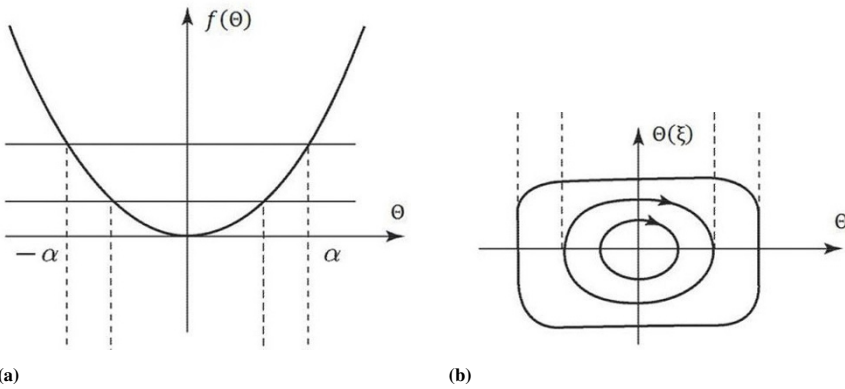
Fig. 10.10: Potential energy of the Duffing equation (10.17) for $m_1 > 0, m_2 > 0$ (a) and the phase portrait corresponding to this case (b).

$$A = \alpha = \sqrt{\frac{\left(-m_1 + \sqrt{m_1^2 + 4m_2 E}\right)}{m_2}}$$

$$k = \sqrt{\frac{m_1}{2}(\alpha^2 + \beta^2)} = (m_1^2 + 4m_2 E)^{1/4} \qquad (10.59)$$

$$s^2 = \frac{\alpha^2}{\alpha^2 + \beta^2} = \frac{-m_1 \sqrt{m_1^2 + 4m_2 E}}{2\sqrt{m_1^2 + 4m_2 E}}$$

where A is the stationary wave amplitude, k is the nonlinear analog of the wavenumber, s is the elliptic function modulus, which has the meaning of the coefficient of non-linear distortion of the waveform $\Theta(\xi)$. It can be seen from relations (10.59) that when E varies from 0 to $+\infty$, the vibration amplitude and frequency vary within the ranges $0 < A < +\infty$, $\sqrt{m_1} < k < \infty$, and the nonlinear distortion coefficient changes within the range $0,5 \leq s^2 \leq 1$.

By eliminating the integration constant E from (10.59) we obtain relations of parameters A, k, s in solution (10.58):

$$s^2 = \frac{m_2 A^2}{2(m_1 + m_2 A^2)}, \quad k = \sqrt{m_1 + m_2 A^2}, \quad \Lambda = \frac{4\boldsymbol{K}(s)}{\sqrt{m_1 + m_2 A^2}}. \qquad (10.60)$$

where Λ is the wavelength, $\boldsymbol{K}(s)$ is the complete elliptic integral of the first kind. From these relations we express the dependence of the amplitude and frequency of vibrations on the nonlinear distortion coefficient and the coefficients of Duffing equation:

$$A = \sqrt{\frac{2m_1}{m_2}\frac{s^2}{1 - 2s^2}} = \sqrt{\frac{(V^2 - c_s^2)\rho I_r}{-2\alpha_1}\frac{s^2}{1 - 2s^2}}, \quad k = \sqrt{\frac{m_1}{1 - 2s^2}} \qquad (10.61)$$

At $E \to +\infty$ ($s^2 \approx 0$ and $A \to 0$) the expression describes quasi-harmonic oscillations near the equilibrium position as follows:

$$\Theta = A\cos(k, \xi) \qquad (10.62)$$

At $E \to +\infty$, $s^2 \to 1/2$ and in this case (10.58) describe essentially non-linear vibrations,

$$\Theta = A\operatorname{cn}(k\xi, s), \qquad (10.63)$$

which have a saw-tooth shape (Fig. 10.11). The phase portrait of equation (10.17) contains within the velocity range $V < c_s$ two "center"- type equilibrium positions and the point $(0,0)$ is a saddle (see Fig. 10.7b). In this case, as for a geometrically nonlinear bar, three types of finite solutions will be available; periodic waves (10.48) and (10.53) will correspond to two of them and a solitary wave (10.43) to the third one.

The solitary wave velocity, amplitude and width are bound by correlations (10.44). The parameters of a periodic wave (10.42) are bound by correlation (10.41) and the parameters of a periodic wave (10.53) by correlation (10.52). If velocity V is within the range $c_\tau \sqrt{(I_x + I_g)/I_g} < V < c_0$ and it means that $m_1 < 0, m_2 > 0$, equation (10.17) does not have closed phase trajectories. Hence, non-linear stationary waves are not available within this range of velocities.

Types of phase portraits of Duffing equation depending on the stationary wave velocity for a bar with physical nonlinearity are shown in Fig. 10.12. It is shown based on the performed analysis that the joint action of the nonlinearity (caused by high vibration intensity) and dispersion (resulted from warping) non-sinusoidal stationary waves can develop in a bar which propagate at a constant speed without changing their shape.

10.5 Wave Processes in a Thin-Walled Bar with Simultaneous Consideration to the Quadratic and Cubic Nonlinearities

If in the analysis of stationary waves both the cubic and quadratic nonlinearities are taken into account in (10.9), the ordinary differential equation, thereto (10.9) is reduced, will be as follows:

$$\frac{d^2\Theta}{d\xi^2} + m_1\Theta + m_2\Theta\frac{d\Theta}{d\xi} + m_3\Theta^3 = 0 \qquad (10.64)$$

The following system is equivalent to this equation:
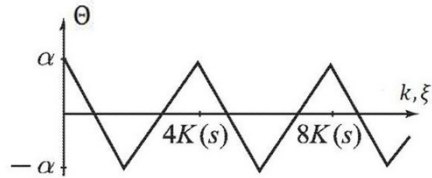
Fig. 10.11 Profile of a nonlinear periodic stationary wave described by formula (10.63)
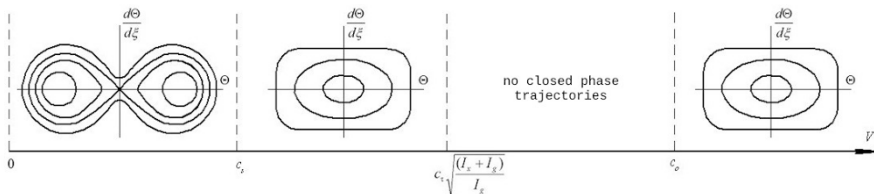
Fig. 10.12: Types of phase portraits of the Duffing equation (10.17)) depending on the speed of a stationary wave for a rod with physical nonlinearity ($\alpha_1 < 0$).

$$\begin{cases} \dfrac{d\Theta}{d\xi} = \varphi \\[2mm] \dfrac{d\varphi}{d\xi} = m_3\Theta^3 - m_1\Theta - m_2\Theta\varphi \end{cases} \tag{10.65}$$

The equilibrium position coordinates are sought on the phase plane (Θ, φ) from the conditions $(\Theta = 0, \varphi = 0)$. Thus, the ordinates of all equilibrium positions are equal to zero and the abscissas are the real roots of the algebraic equation of the third degree:

$$m_1\Theta - m_3\Theta^3 = 0 \tag{10.66}$$

At $m_1 m_3 < 0$ origin of coordinates, the point $(0,0)$ is the only equilibrium position; and in any case, at $m_1 < 0$ it is the "saddle" and at $m_1 > 0$ it is the "center". If there is the only "saddle" point in the system, there are no periodic motions, so, this case is of no interest for the search of stationary waves. If there is the only "center" in the system, all motions are periodic and the phase portrait is a set of non-intersecting closed curves. For a certain set of parameters, namely $m_1 > 0$, $m_1 = 3$ and $m_1 = -1$ it is possible to write the exact analytical solution:

$$\Theta(\xi) = \frac{\sqrt{m_1}(C_1\sin(\sqrt{m_1}\xi) + C_2\cos(\sqrt{m_1}\xi))}{C_1\sin(\sqrt{m_1}\xi) + C_2\cos(\sqrt{m_1}\xi) + C_3} \tag{10.67}$$

where C_1, C_2, C_3 - integration constants are to be found from the initial conditions.

At first sight it may seem strange that the equation is of the second order but there are three integration constants; that is not the case, since the numerator and denominator can be divided by any non-zero constant and there will be two unknowns. This form of the solution is here presented just for generality, assuming that any of the constants can become zero and vanish. The non-periodic solution at such parameter values and $m_1 < 0$ can also be written in terms of exponents with indices $\pm\sqrt{|m_1|}\xi$. With any other set of parameters m_2 and m_3 surely with the same signs, the system dynamics does not qualitatively change but no exact solutions can be found. A nonlinear term with coefficient m_2 is asymmetric; therefore, the phase portrait is asymmetric about the abscissa axis. When the sign of coefficient m_2 changes to the opposite one, the phase portrait (and in the case of a non-single equilibrium position) is symmetrically reflected with respect to $(0, \Theta)$ and the solution (10.67) just changes the sign. The movement along closed phase trajectories always occurs clockwise.

At $m_1 m_3 > 0$ three equilibrium positions are available with coordinate $(-\sqrt{m_1/m_3}, 0)$, $(0,0)$ and $(\sqrt{m_1/m_3}, 0)$, at $m_3 > 0,\ldots (\pm\sqrt{m_1/m_3}, 0)$ it is a "saddle", with $(0,0)$ it is the "center". In this case, all periodic motions are within the region bounded by a pair of separatrices emanating from the left "saddle" to the right and from the right to the left. Because of the asymmetric nonlinearity the separatrices are also asymmetrical and are differently described, though the value of the transition (amplitude) from one state to another is the same but the transition rate is different. So, at $m_1 > 0$ the separatrix from the left "saddle" to the right one has the following form:

$$\Theta(\xi) = -\sqrt{\frac{m_1}{m_3}}\,th\left(\frac{2m_1 m_3 \sqrt{\frac{m_1}{m_3}}}{m_1 m_2 - \sqrt{m_1^2 m_2^2 + 8m_1^2 m_3}}\xi\right) \tag{10.68}$$

and from the right "saddle" to the left one:

$$\Theta(\xi) = -\sqrt{\frac{m_1}{m_3}}\,th\left(\frac{2m_1 m_3 \sqrt{\frac{m_1}{m_3}}}{m_1 m_2 + \sqrt{m_1^2 m_2^2 + 8m_1^2 m_3}}\xi\right) \tag{10.69}$$

If the sign before m_2 is changed, the pattern is symmetrically reflected about the abscissa.

In the case of $m_1 < 0$ and $m_3 < 0$ the origin of coordinates is the "saddle" and points $(\pm\sqrt{m_1/m_3}, 0)$ are "foci" at $m_2 > 0$ the left "focus" is unstable, the right one is stable. When the sign before m_2 is changed, the stability of the foci is also changed to the opposite. With increasing the coefficient m_2 the domain of attraction of a stable "focus" increases, behind this domain there is a periodic movement domain corresponding to closed phase trajectories. Unfortunately, no exact analytical solutions are found for this case. All qualitatively different phase portraits are shown in the Table 10.1.

10.6 Conclusions

A mathematical model is herein discussed, which enables to describe the torsional wave propagation in a thin-walled bar. The model includes the geometric and physical elastic nonlinearities, as well as the warping (deplanation). The relationship of an angle of torsion of the bar and the degree of warping is not postulated in this model as in most known models, but is in the process of solving the problem. Based on the model analysis it is determined that warping, which causes the emergence of dispersion of the phase velocity of a torsional wave, also results in the occurrence of the quadratic nonlinearity specific to intense longitudinal vibrations, which has never been encountered before in mathematical models describing torsional vibrations. It is shown that non-sinusoidal strain waves localized in space can develop in a thin-walled bar, which performs intense torsional vibrations.

Table 10.1: Phase portraits.

m_1	m_3	$m_2 > 0$	$m_2 < 0$
< 0	< 0		
< 0	> 0	no periodic movements	no periodic movements
> 0	< 0		
> 0	> 0		

References

[1] Artobolevsky II, Bobrovnitsky YI, Genkin MD (1979) Introduction to the Acoustic Dynamics of Machines (in Russ). Nauka, Moscow

[2] Bolotin VV (ed) (1999) Vibrations in Technology (in Russ), vol 1. Mashinos-troenie, Moscow

[3] Beards CF (2003) Structural Vibration: Analysis and Damping. Oxford University Press, Oxford

[4] Slivker VI (2007) Mechanics of Structural Elements: Theory and Applications. Springer, Berlin - Heidelberg

[5] Dyakov SF, Lalin VV (2013) The dispersion of the torsion wave in the thin-walled bar. Internet Journal Naukovedenie (5)

[6] Erofeev VI, Lampsi BB (2014) Mathematical model of elastic thin-walled bar committing torsional oscillations in the presence of nonlinearity and warping.

Privolzhsky Scientific Journal **2**(30):14–17

[7] Erofeev VI, Lampsi BB (2015) The effect of the nonlinearity and warping on the parameters of the torsional wave propagating in the thin-walled rod. Problems of Strength and Plasticity **77**(7):191–197

[8] Erofeev VI, Yudnikov SG, Lampsi BB (2017) Stressed state in the wall of a composite beam subject to local torque and local load. Privolzhsky Scientific Journal **3**(43):15–25

[9] Erofeev VI, Klyueva NV (2002) Solitons and nonlinear periodic strain waves in rods, plates, and shells (a review). Acoustical Physics **48**(6):643–655

[10] Rabinovich MI, Trubetskov DI (1889) Oscillations and Waves in Linear and Nonlinear Systems. Kluwer Academic Publishers, Dordrecht, Boston, London

Chapter 11

Linear Reduced Elastic Isotropic Cosserat Medium Subjected to the External Follower Viscoelastic Torque as a Smart Acoustic Metamaterial

Elena F. Grekova and Sabina M. Isaeva

Abstract We consider a linear elastic isotropic reduced Cosserat medium under viscoelastic follower torque. Reduced Cosserat elastic medium is an elastic continuum whose body points possess both rotational and translational degrees of freedom, but the medium does not react on the gradient of micro-rotation. Such an isotropic medium has a bandgap for the shear–rotational wave, i.e. it is an acoustic single negative metamaterial in this frequency domain. Introducing a volume follower elastic torque, we change the bandgap parameters. A viscoelastic external torque changes qualitatively the wave propagation in the medium: there appears a running evanescent solution, in many cases having a decreasing part of the dispersion curve, thus demonstrating properties of a double negative acoustic metamaterial.

11.1 Introduction and Notation

After the seminal work by E. & F. Cosserat, which opened the new area in mechanics, namely, mechanics of 3D continua with rotational degrees of freedom, many investigations were performed on various Cosserat-type theories [1–3]. Foundations of this theory one can find in [4, 5]. Full basic equations of 3D elastic Cosserat media were firstly suggested in [1], but the universal method to obtain the equations of elastic complex media, based on the fundamental laws of balance and the material objectivity, was proposed in [6]. Thermoelastic Cosserat media are considered in [7, 8]. Space

Elena F. Grekova
Institute for Problems in Mechanical Engineering of the Russian Academy of Sciences, Bolshoy prospekt 61, V.O., 199178 St. Petersburg, Russian Federation,
e-mail: elgreco@pdmi.ras.ru

Sabina M. Isaeva
Scientific and Education center Gazpromneft-Politech, Polytechnicheskaya, 29AF, Tehnopolis Politeh A 2.24, 195251 St. Petersburg, Russian Federation,
e-mail: sabinca98@list.ru

(eulerian) approach to the Cosserat media is developed in [9] and successive works of these authors.

Rotational degrees of freedom influence wave propagation in minerals [10] and granular materials [11]. Reduced elastic isotropic linear Cosserat theory was firstly suggested for the description of dynamic behaviour of granular materials in [12]. Reduced Cosserat continuum is a medium where the strain energy depends on the micro-rotation but not on its gradient. Waves in such a medium are investigated in [13]. This continuum possesses a band gap, i.e. it is a single negative acoustic metamaterial. Adding a small viscosity to the elastic interactions, we transform it to a double negative acoustic metamaterial, i.e. a medium that has a decreasing part of the dispersion curve [14, 15].

Acoustic metamaterials demonstrate peculiar dynamic properties. Single negative acoustic metamaterials possess band gaps, and double negative acoustic metamaterials have frequency domains where group velocity and phase velocities have different signs. These materials are often designed to mask objects, control wave beams and reduce vibration [16, 17]. Reduced continua, where the stresses depend on a certain special generalised co-ordinate but not on its gradient, in the elastic case under certain symmetry conditions behave as single negative acoustic metamaterials [18], and in the viscoelastic case may occur to be double negative acoustic metamaterials [19]. They can be schematically represented as a bearing continuum enhanced by a distributed dynamic absorber (corresponding to the special generalised co-ordinate). This "dynamic absorber" may have different nature, e.g. mass-in-mass model is also an example of such an acoustic metamaterial [20].

This reminds a mixed continuum-discrete (structural) approach, where discrete elements are considered to be embedded into a whole structure, described as a continuum, and they have a coupled dynamics [21, 22]. However, in this work pseudo-"discrete" elements (dynamic absorbers) are distributed in a continuous way, they simply do not interact in a direct way, but only via the bearing continuum. Note that this important feature is present also in the discrete-continuum model considered in [22] and leads to the existence of resonant absorption at the partial eigen-frequency of the distributed dynamic absorbers.

We will consider a linear elastic medium consisting of infinitesimal body points. Denote by $\boldsymbol{u}$ the translational displacement, by $\boldsymbol{\theta}$ an infinitesimal micro-rotation vector (rotation tensor can be approximated as $\boldsymbol{E} + \boldsymbol{\theta} \times \boldsymbol{E}$, where $\boldsymbol{E}$ is the identity tensor), let $\nabla = \frac{d}{d\boldsymbol{r}}$ be the gradient operator, $\boldsymbol{r}$ the position vector.

11.2 Equations of the Reduced Elastic Linear Isotropic Cosserat Medium Subjected to a Viscoelastic Follower Body Torque. Spectral Problem

First here we recall some facts for the convenience of the reader that can be found in [12, 13].

- Constitutive equations for the linear reduced isotropic elastic Cosserat medium can be written in the following way:

$$\boldsymbol{\tau} = \lambda \nabla \cdot \boldsymbol{u}\, E + 2\mu (\nabla \boldsymbol{u})^S + 2\alpha (\nabla \boldsymbol{u} + \boldsymbol{\theta} \times E)^A, \qquad \boldsymbol{\mu} = \boldsymbol{0}.$$

  Here $\boldsymbol{\tau}$ is the stress tensor, $\boldsymbol{\mu}$ is the couple tensor, λ, μ are Lamé parameters, α the Cosserat couple modulus.
- Dynamic equations for the reduced Cosserat medium are: balance of force

$$\nabla \cdot \boldsymbol{\tau} + \rho \boldsymbol{F} = \rho \ddot{\boldsymbol{u}}, \tag{11.1}$$

  $\rho \boldsymbol{F}$ is the density of the external body force, and balance of moments

$$\boldsymbol{\tau}_\times + \rho \boldsymbol{L} = \rho I \ddot{\boldsymbol{\theta}}, \tag{11.2}$$

  where $\boldsymbol{\tau}_\times = \tau_{mn} \boldsymbol{i}_m \times \boldsymbol{i}_n$, $\rho \boldsymbol{F}$ is the density of the external body torque, $\rho I E$ is the density of tensor of inertia, considered as spherical for sake of simplicity.
- Equations in displacements take the form

$$(\lambda + 2\mu)\nabla\nabla \cdot \boldsymbol{u} - (\mu + \alpha)\nabla \times (\nabla \times \boldsymbol{u}) + 2\alpha \nabla \times \boldsymbol{\theta} = \rho \ddot{\boldsymbol{u}}$$

$$2\alpha \nabla \times \boldsymbol{u} - 4\alpha \boldsymbol{\theta} + \rho \boldsymbol{L} = \rho I \ddot{\boldsymbol{\theta}}$$

We will consider plane waves in this medium $\boldsymbol{u} = \boldsymbol{u}_0 e^{i(\omega t - \boldsymbol{k} \cdot \boldsymbol{r})}$, $\boldsymbol{\theta} = \boldsymbol{\theta}_0 e^{i(\omega t - \boldsymbol{k} \cdot \boldsymbol{r})}$, for zero external body forces and viscoelastic external body torque with density $\rho \boldsymbol{L} = -c\boldsymbol{\theta} - C\dot{\boldsymbol{\theta}}$. We will investigate plane waves in the same way as is was done in [13] but taking into account the body external moment.

Then we obtain the following spectral problem:

$$-k^2(\lambda + 2\mu)\hat{\boldsymbol{k}}\hat{\boldsymbol{k}} \cdot \boldsymbol{u} - k^2(\mu + \alpha)\hat{\boldsymbol{k}} \times (\hat{\boldsymbol{k}} \times \boldsymbol{u}) + 2\alpha i k \hat{\boldsymbol{k}} \times \boldsymbol{\theta} = -\rho\omega^2 \boldsymbol{u}, \tag{11.3}$$

$$2\alpha k \hat{\boldsymbol{k}} \times \boldsymbol{u} - 4\alpha \boldsymbol{\theta} - (c + i\omega C)\boldsymbol{\theta} = -\rho I \omega^2 \boldsymbol{\theta}. \tag{11.4}$$

We express $\boldsymbol{\theta}$ via $\boldsymbol{u}$ from the last equation (balance of moments):

$$\boldsymbol{\theta} = \frac{2\alpha k}{4\alpha + c + i\omega C - \rho I \omega^2}\hat{\boldsymbol{k}} \times \boldsymbol{u} \tag{11.5}$$

and substitute it into the balance of force, thus obtaining a reduced spectral problem:

$$(\rho\omega^2 - k^2(\lambda + 2\mu))\hat{\boldsymbol{k}}\hat{\boldsymbol{k}} \cdot \boldsymbol{u}$$

$$+ (\rho\omega^2 - k^2(\mu + \alpha - \frac{4\alpha^2}{4\alpha + c + i\omega C - \omega^2 \rho I}))(E - \hat{\boldsymbol{k}}\hat{\boldsymbol{k}}) \cdot \boldsymbol{u} = \boldsymbol{0}. \tag{11.6}$$

Due to isotropy we can separate the P-wave, whose dispersion equation is classical ($\omega = \sqrt{\frac{\lambda + 2\mu}{\rho}}k$). The spectral problem for the shear–rotational wave looks as follows

$$(\rho\omega^2 - k^2(\mu + \alpha - \frac{4\alpha^2}{4\alpha + c + i\omega C - \omega^2\rho I}))(E - \hat{k}\hat{k}) \cdot u = 0. \qquad (11.7)$$

11.3 Isotropic Linear Elastic Reduced Cosserat Medium Subjected to an Elastic Follower Torque

Let us consider $C = 0$, $\rho L = -c\theta$. Then we obtain from (11.7) the following dispersion relation:

$$k^2 = \frac{\omega^2}{c_{s\alpha}^2} \frac{(\omega^2 - \omega_{0e}^2)}{(\omega^2 - \omega_{1e}^2)},$$

where

$$c_{s\alpha}^2 = \frac{\mu + \alpha}{\rho}, \quad \omega_{0e}^2 = \frac{4\alpha + c}{\rho I},$$

$$\omega_{1e}^2 = \omega_{0e}^2 - \frac{4\alpha^2}{(\mu + \alpha)\rho I}.$$

Note that at low frequencies the wave velocity depends on the external elastic torque, and its square is equal to

$$c_0^2 = c_s^2 \frac{1 + \frac{c}{4\alpha\Omega_1^2}}{1 + \frac{c}{4\alpha}}, \qquad (11.8)$$

$$\Omega_1^2 = \frac{\omega_1^2}{\omega_0^2} = \frac{\mu}{\mu + \alpha}, \qquad (11.9)$$

$c_s^2 = \frac{\mu}{\rho}$ is a square of the shear–rotational velocity at low frequencies when there is no external torque,

$$\omega_0 = \sqrt{\frac{4\alpha}{\rho I}}, \qquad \omega_1 = \sqrt{\frac{\mu}{\mu + \alpha}}\omega_0 \qquad (11.10)$$

are the cut-off frequency and boundary frequency, respectively, in the medium without external torque. In the high-frequency limit the elastic torque does not influence the wave velocity, it is equal to $c_{s\alpha}$. An example of dispersion curves under action of an external moment and without it is shown in Fig. 11.1.

Let us see how the band gap changes under the action of the external follower body moment:

$$\frac{\omega_{0e} - \omega_{1e}}{\omega_0} = \sqrt{1 + \frac{c}{4\alpha}} - \sqrt{\Omega_1^2 + \frac{c}{4\alpha}}. \qquad (11.11)$$

Fig. 11.1 Dispersion curves for the shear–rotational wave, under (solid) / without (dashed) follower external elastic moment.
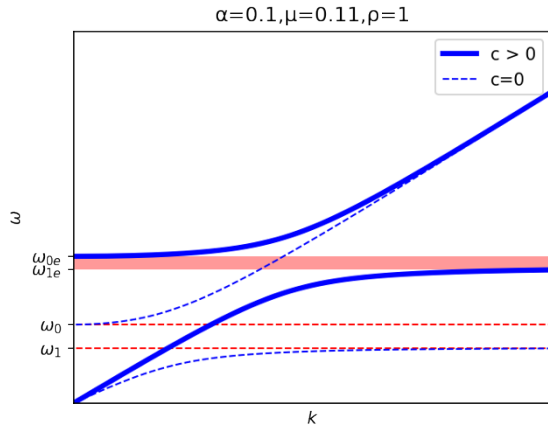
This is a monotonically decreasing (to zero at infinity) function of $\frac{c}{4\alpha}$ at fixed μ/α, it reaches the maximal value $\sqrt{1-\Omega_1^2} = 1/\sqrt{1+\mu/\alpha}$ at $\frac{c}{4\alpha} = -\Omega_1^2$. An example of this dependence is shown in Fig. 11.2.
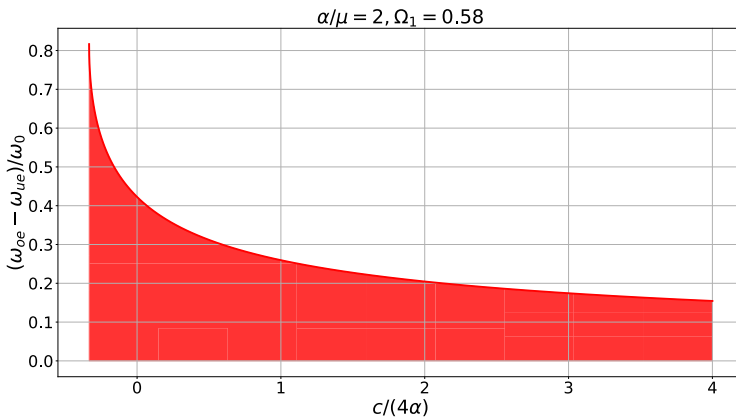
Fig. 11.2: Band gap $\omega_{0e} - \omega_{1e}$ vs follower elastic torque. Positive follower elastic moment reduces the band gap, but does not destroy it. Boundary and cut-off frequencies increase. Negative follower moment increases the size of the band gap and moves it downwards.

11.4 Isotropic Elastic Reduced Cosserat Medium Subjected to a Viscous or Viscoelastic Follower Torque

Considering $\rho L = -C\dot{\boldsymbol{\theta}}$, i.e. $c = 0$ in (11.7), we obtain the dispersion relation for the shear–rotational wave:

$$k^2 = \frac{\omega^2}{c_{s\alpha}^2}\left(\frac{\omega^2 - \omega_0^2 - \frac{i\omega C}{\rho I}}{\omega^2 - \omega_1^2 - \frac{i\omega C}{\rho I}}\right) \tag{11.12}$$

Analogy with polarization wave in non-polar dielectrics. The same dispersion relation characterizes wave propagation of polarization field in non-polar dielectrics, initially induced by an external field [23]. The external follower viscous body moment corresponds to the dissipation coefficient for polarization, $c_{s\alpha}$ to the light velocity, $\omega_0^2 = \omega_r^2 + \frac{2}{3}\omega_p^2$, where ω_r is the resonant frequency of electron oscillations in the molecule, ω_p the plasma frequency, $\omega_1^2 = \omega_r^2 - \frac{1}{3}\omega_p^2$. The case of purely elastic or zero external torque corresponds to the case of dielectric without dissipation.

Viscoelastic follower torque $-c\boldsymbol{\theta} - C\dot{\boldsymbol{\theta}}$ will give us the dispersion relation

$$k^2 = \frac{\omega^2}{c_{s\alpha}^2}\left(\frac{\omega^2 - \omega_0^2 - \frac{c+i\omega C}{\rho I}}{\omega^2 - \omega_1^2 - \frac{c+i\omega C}{\rho I}}\right) = \frac{\omega^2}{c_{s\alpha}^2}\left(\frac{\omega^2 - \omega_{0e}^2 - \frac{i\omega C}{\rho I}}{\omega^2 - \omega_{1e}^2 - \frac{i\omega C}{\rho I}}\right),$$

thus all the results for the viscous external body torque presented further in this section can be extrapolated to the case of the viscoelastic external body torque, substituting ω_0 for ω_{0e} and ω_1 for ω_{1e}. In what follows we consider $c = 0$.

11.4.1 Dispersion Relation for the Shear–Rotational Wave

We will introduce dimensionless wave number K, dimensionless frequency Ω and dimensionless parameter b, expressing in these terms dispersion relation (11.12):

$$K^2 = \frac{c_{s\alpha}^2}{\omega_0^2}k^2 = \Omega^2\frac{\Omega^2 - 1 - ib\Omega}{\Omega^2 - \Omega_1^2 - ib\Omega} \tag{11.13}$$

$$\Omega = \frac{\omega}{\omega_0}, \quad \Omega_1^2 = \frac{\mu}{\alpha + \mu}, \quad b = \frac{C}{\rho I \omega_0} = \frac{C\omega_0}{4\alpha} \tag{11.14}$$

We can transform dispersion relation (11.13) as follows

$$(\mathfrak{R}K)^2 - (\mathfrak{I}K)^2 + 2i\mathfrak{R}K\mathfrak{I}K$$
$$= \Omega^2\frac{(\Omega^2 - 1)(\Omega^2 - \Omega_1^2) + b^2\Omega^2 - ib\Omega(1 - \Omega_1^2)}{\left(\Omega^2 - \Omega_1^2\right)^2 + b^2\Omega^2} \tag{11.15}$$

Thus we obtain

$$2\mathfrak{R}K\mathfrak{I}K = -\frac{b(1-\Omega_1^2)\Omega^3}{\left(\Omega^2-\Omega_1^2\right)^2+b^2\Omega^2}, \tag{11.16}$$

$$(\mathfrak{R}K)^4 + \Omega^2\frac{(\Omega^2-1)(\Omega^2-\Omega_1^2)+b^2\Omega^2}{\left(\Omega^2-\Omega_1^2\right)^2+b^2\Omega^2}(\mathfrak{R}K)^2$$

$$-\frac{b^2(1-\Omega_1^2)^2\Omega^6}{4((\Omega^2-\Omega_1^2)^2+b^2\Omega^2)^2} = 0. \tag{11.17}$$

We solve this biquadratic equation:

$$(\mathfrak{R}K)^2 = \frac{1}{2}\left(\frac{\Omega^2}{z}\left((\Omega^2-1)(\Omega^2-\Omega_1^2)+b^2\Omega^2\right)\pm\sqrt{D}\right), \tag{11.18}$$

where

$$D = \left(\frac{\Omega^2}{z}\left((\Omega^2-1)(\Omega^2-\Omega_1^2)+b^2\Omega^2\right)\right)^2 + \frac{b^2\Omega^6(1-\Omega_1^2)^2}{z^2}, \tag{11.19}$$

$$z = (\Omega^2-\Omega_1^2)^2+b^2\Omega^2. \tag{11.20}$$

Imaginary part of the wave number can be obtained as

$$(\mathfrak{I}K)^2 = \frac{1}{2}\left(-\frac{\Omega^2}{z}\left((\Omega^2-1)(\Omega^2-\Omega_1^2)+b^2\Omega^2\right)\pm\sqrt{D}\right)$$

Denote

$$f(\Omega) = (\Omega^2-1)(\Omega^2-\Omega_1^2)+b^2\Omega^2. \tag{11.21}$$

Then

$$D^{1/2} = \frac{\Omega^2}{z}(f^2+b^2(1-\Omega_1^2)^2\Omega^2)^{1/2}, \tag{11.22}$$

$$2(\mathfrak{R}K)^2 = \frac{\Omega^2}{z}(f\pm(f^2+b^2(1-\Omega_1^2)^2\Omega^2)^{1/2}), \tag{11.23}$$

$$2(\mathfrak{I}K)^2 = \frac{\Omega^2}{z}(-f\pm(f^2+b^2(1-\Omega_1^2)^2\Omega^2)^{1/2}), \tag{11.24}$$

$$\left(\frac{\mathfrak{I}K}{\mathfrak{R}K}\right)^2 = \frac{-f\pm(f^2+b^2(1-\Omega_1^2)^2\Omega^2)^{1/2}}{f\pm(f^2+b^2(1-\Omega_1^2)^2\Omega^2)^{1/2}}$$

$$(\text{if } f\neq 0) = \frac{-\operatorname{sgn}f\pm(1+b^2(1-\Omega_1^2)^2\frac{\Omega^2}{f^2})^{1/2}}{\operatorname{sgn}f\pm(1+b^2(1-\Omega_1^2)^2\frac{\Omega^2}{f^2})^{1/2}}. \tag{11.25}$$

We see that we always have positive expression in the right side of (11.23)–(11.25), i.e. there exist a running evanescent plane wave solution at all frequencies. This is a

qualitative difference with the elastic case. We can see various numerical examples for the dispersion curves of the shear–rotational waves. Figures 11.3 and 11.4 present dispersion curves for $2\alpha = \mu = 10$, $b = 0.22$ and $b = 2.2$ respectively. In the first case, for a not very large dissipation parameter, we observe a decaying part of $\mathfrak{R}K(\omega)$, maximum of the logarithmic decrement inside the former bandgap and the maximal attenuation at a fixed distance just above the lower limit of the former band gap. In the second case, for larger b, attenuation in the former band gap is much less than for $b = 0.22$, the real part of the wave number is slightly dispersive and monotone.

In case $\alpha > \mu$ the tendencies are similar. Indeed, in Figs. 11.5, 11.6 and 11.7 dispersion curves are presented for large dissipation $b = 1.58$, and in Figs. 11.8, 11.9 and 11.10 for a relatively small dissipation $b = 0.158$. For a large viscous torque, there is no decreasing part of the dispersion curve. For a small dissipation parameter, we observe in numerical examples a decreasing part of the dispersion curve. The type of acoustic metamaterial changes. We will show it analytically further.
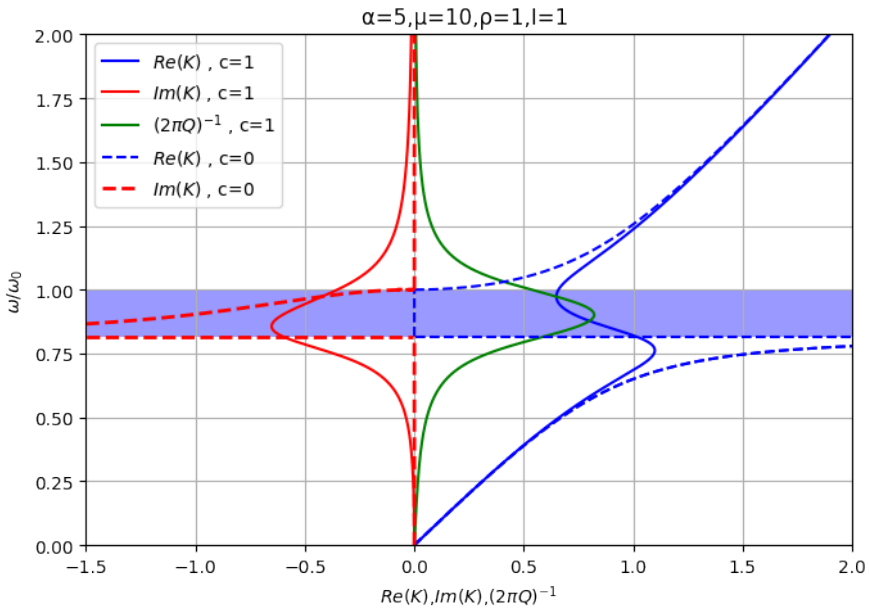
Fig. 11.3: Dispersion curves, $\Omega_1^2 = 0.816$, $\omega_0^2 = 20$, $b = 0.22$. Dashed lines: elastic case, solid lines: viscous external body torque. Left part of the graph: $\mathfrak{I}K$, right part of the graph: $|\mathfrak{I}K/\mathfrak{R}K| = (2\pi Q)^{-1}$, $\mathfrak{R}K$, K the dimensionless wave number. Running evanescent solution exists at all frequencies and has a decreasing part of dispersion curve in the lower part of the former band gap and somewhat below it.
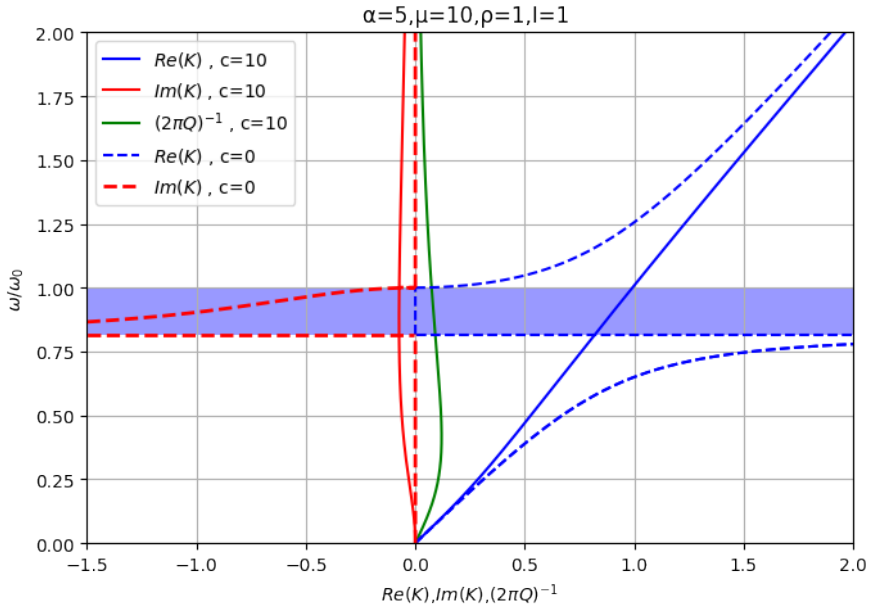
Fig. 11.4: Dispersion curves, $\Omega_1^2 = 0.816$, $\omega_0^2 = 20$, $b = 2.2$. Dashed lines: elastic case, solid lines: viscous external body torque. Left part of the graph: $\Im K$, right part of the graph: $|\Im K / \Re K| = (2\pi Q)^{-1}$, $\Re K$, K the dimensionless wave number. Running evanescent solution exists at all frequencies, it has no decreasing part of dispersion curve. It is slightly dispersive.

11.4.2 Small Dissipation far from Characteristic Frequencies $\Omega = \Omega_1$ and $\Omega = 1$

11.4.2.1 Real Part of the Wave Number

Consider a small dissipation parameter $b^2 = o(1)$. If we are near the elastic band gap limits $\Omega = \Omega_1$ and $\Omega = 1$, functions $z(\Omega)$ and $f(\Omega)$ take infinitesimal values, and this case requires a separate consideration. Let us consider in this section the case when $|\Omega - \Omega_1| \gg b$, $|\Omega - 1| \gg b$.

Then we may write down the following approximations of formulae (11.23)–(11.25):

$$
2(\Re K)^2 = \frac{\Omega^2 f}{\left(\Omega^2 - \Omega_1^2\right)^2 \left(1 + b^2 \frac{\Omega^2}{\left(\Omega^2 - \Omega_1^2\right)^2}\right)} \left(1 \pm \left(1 + b^2 \left(1 - \Omega_1^2\right)^2 \frac{\Omega^2}{f^2}\right)^{1/2}\right)
$$

$$
= \frac{\Omega^2 \left(\Omega^2 - \Omega_1^2\right)\left(\Omega^2 - 1\right)\left(1 + b^2 \frac{\Omega^2}{\left(\Omega^2 - \Omega_1^2\right)\left(\Omega^2 - 1\right)}\right)}{\left(\Omega^2 - \Omega_1^2\right)^2 \left(1 + b^2 \frac{\Omega^2}{\left(\Omega^2 - \Omega_1^2\right)^2}\right)}
$$
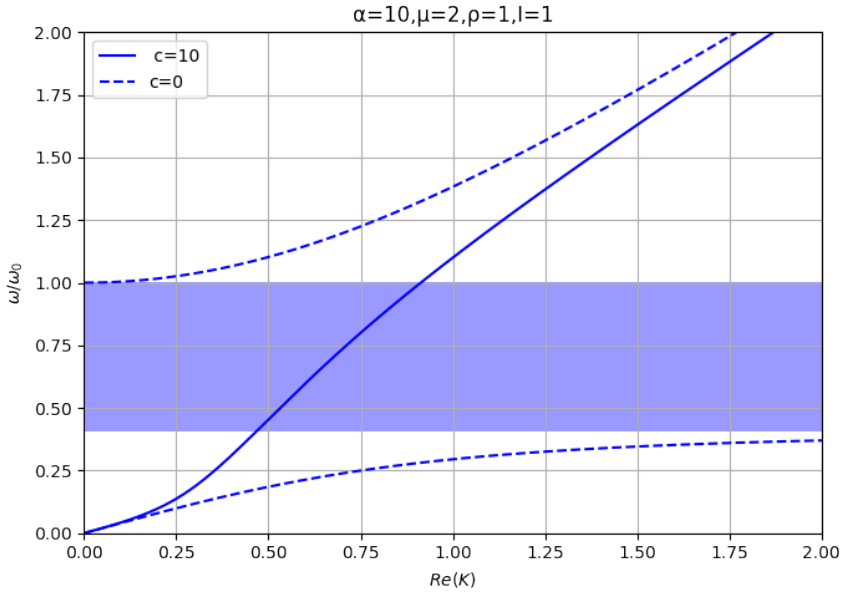
Fig. 11.5: Dispersion curves for the real part of dimensionless wave number, large dissipation parameter $b = 1.58$. There is no decreasing part of the dispersion curve.
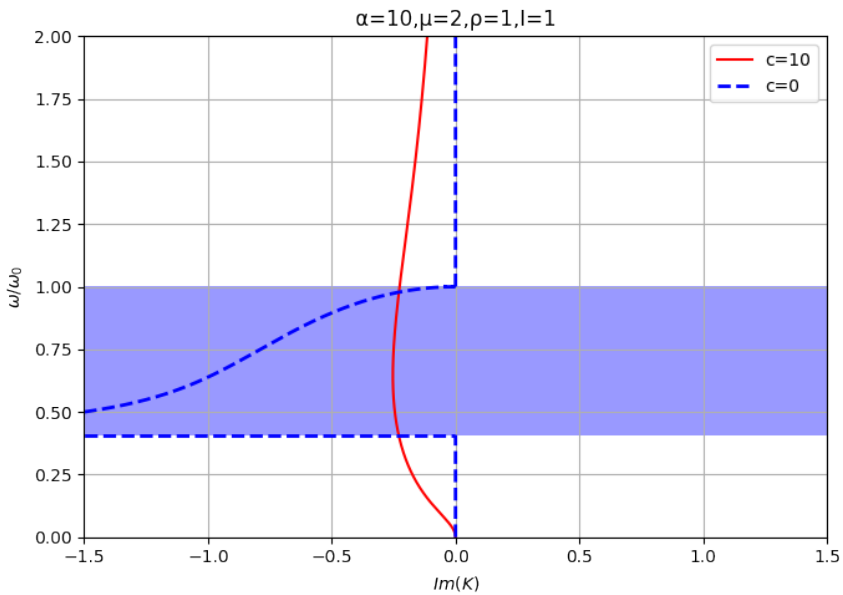
Fig. 11.6: Dispersion curves for the imaginary part of dimensionless wave number, large dissipation parameter $b = 1.58$. Attenuation decreases in comparison with the small dissipation inside the band gap and increases outside it.
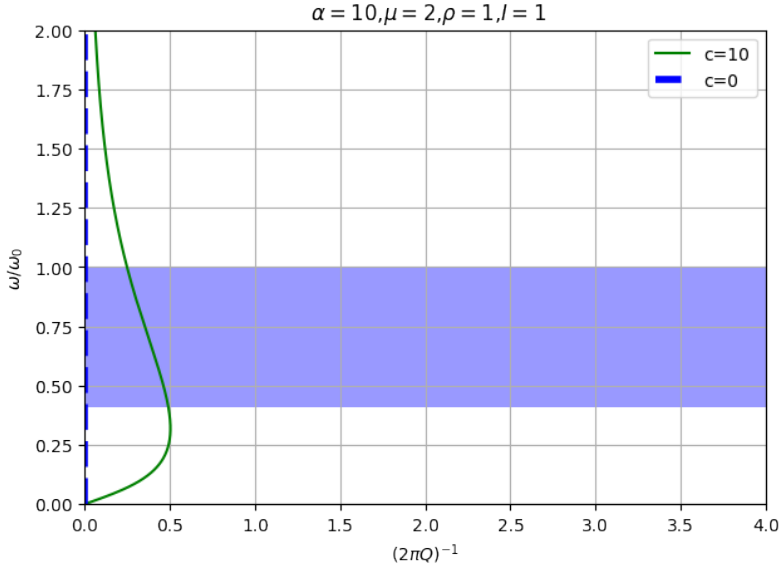
Fig. 11.7: Dispersion curves for $|\Im K/\Re K| = (2\pi Q)^{-1}$, where Q^{-1} is the logarithmic decrement, large dissipation parameter $b = 1.58$. Attenuation decreases in comparison with the small dissipation inside the band gap and increases outside it. Maximum of the logarithmic decrement is situated below the band gap.

$$\cdot (1 \pm (1 + b^2(1-\Omega_1^2)^2 \frac{\Omega^2}{(\Omega^2-\Omega_1^2)^2(\Omega^2-1)^2(1+b^2(1-\Omega_1^2)^2\frac{\Omega^2}{(\Omega^2-\Omega_1^2)^2(\Omega^2-1)^2})})^{1/2})$$

$$= \frac{\Omega^2(\Omega^2-1)(1+b^2\frac{\Omega^2}{(\Omega^2-\Omega_1^2)(\Omega^2-1)})}{(\Omega^2-\Omega_1^2)(1+b^2\frac{\Omega^2}{(\Omega^2-\Omega_1^2)^2})}$$

$$\cdot (1 \pm (1 + \frac{b^2(1-\Omega_1^2)^2}{2} \frac{\Omega^2(1+o(b^2))}{(\Omega^2-\Omega_1^2)^2(\Omega^2-1)^2(1+b^2(1-\Omega_1^2)^2\frac{\Omega^2}{(\Omega^2-\Omega_1^2)^2(\Omega^2-1)^2})}))$$

$$= \frac{\Omega^2(\Omega^2-1)(1+b^2\frac{\Omega^2}{\Omega^2-\Omega_1^2}(\frac{1}{\Omega^2-1}-\frac{1}{\Omega^2-\Omega_1^2}))}{\Omega^2-\Omega_1^2}$$

$$\cdot (1 \pm (1 + \frac{b^2(1-\Omega_1^2)^2(1+o(b^2))}{2} \frac{\Omega^2(1-b^2(1-\Omega_1^2)^2\frac{\Omega^2}{(\Omega^2-\Omega_1^2)^2(\Omega^2-1)^2})}{(\Omega^2-\Omega_1^2)^2(\Omega^2-1)^2})). \quad (11.26)$$

Now we have to consider two cases: the frequency is inside the band gap in the elastic case $(\Omega_1; 1)$ and it is outside it. Recall that we do not consider the vicinities of its limits.
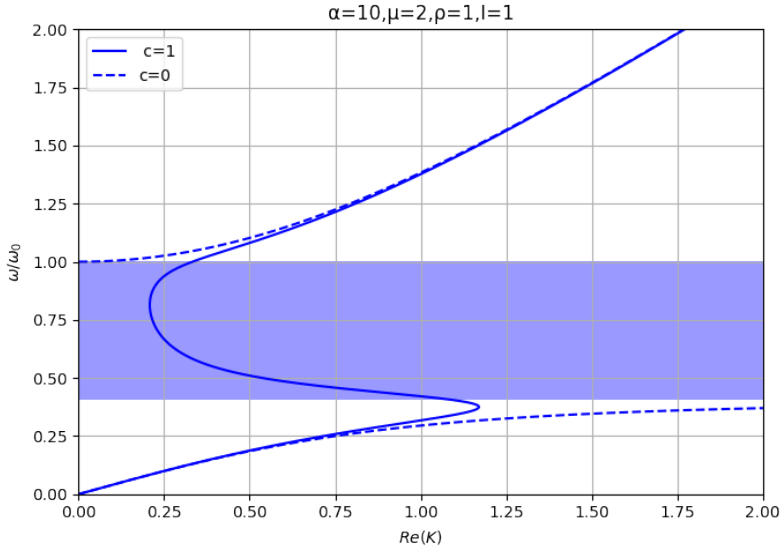
Fig. 11.8: Real part of the dimensionless wave number for the elastic case (dashed line) and under viscous follower torque $c = 1$ (solid line). Dissipation parameter $b = c/\rho I \omega_0 = 0.158$, $\Omega_1^2 = 1/6$. We observe a decreasing part of the dispersion curve approximately from $\omega/\omega_0 = 0.36$ to $\omega/\omega_0 = 0.82$.
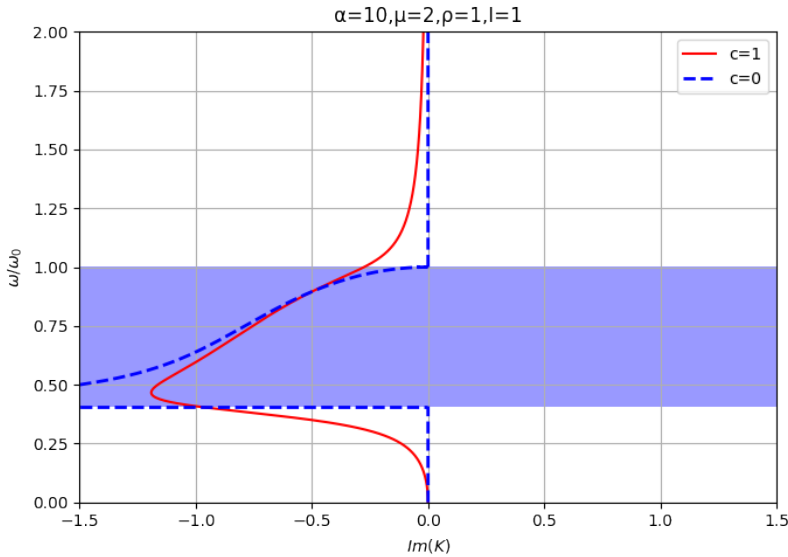
Fig. 11.9: Imaginary part of the dimensionless wave number for the elastic case (dashed line) and under viscous follower torque $c = 1$ (solid line). Dissipation parameter $b = c/\rho I \omega_0 = 0.158$, $\Omega_1^2 = 1/6$. We observe the maximal attenuation just above the lower limit of the band gap, at $\omega/\omega_0 \approx 0.45$.
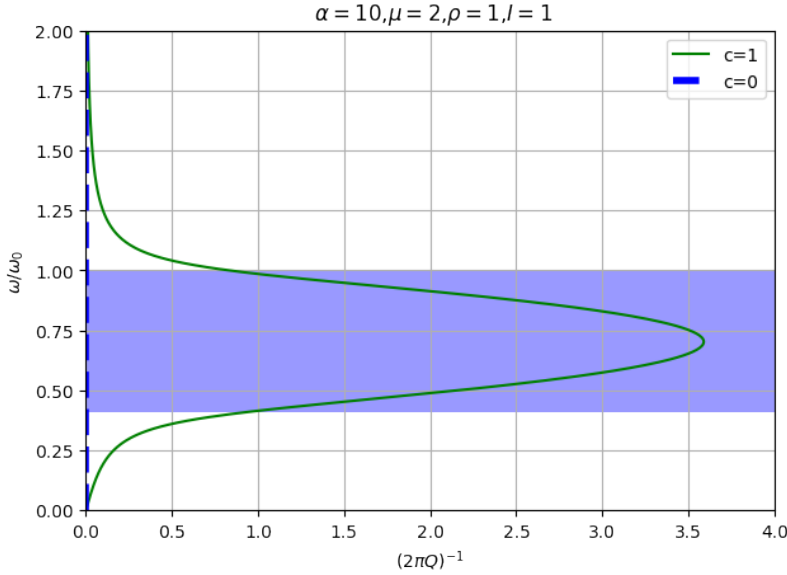
Fig. 11.10: Dispersion curves for $|\Im K/\Re K| = (2\pi Q)^{-1}$, where Q^{-1} is the logarithmic decrement, dissipation parameter $b = 0.158$. Attenuation is larger in comparison with the big dissipation inside the band gap and less outside it. Maximum of the logarithmic decrement is situated inside the band gap.

Outside the band gap $(\Omega_1; 1)$ the solution is given by the "+" sign, since $(\Re K)^2 \geqslant 0$, and the main term in this expression is finite. We obtain

$$\Re K = \frac{\Omega(\Omega^2 - 1)^{1/2}}{(\Omega^2 - \Omega_1^2)^{1/2}}\left(1 + \frac{b^2(1 - \Omega_1^2)\Omega^2}{2(\Omega^2 - \Omega_1^2)^2(\Omega^2 - 1)}\right) + o(b^2),$$

$$\Omega < \Omega_1 \text{ or } \Omega > 1. \tag{11.27}$$

In this domain $\Re K(\Omega)$ increases. It is slightly changed by the small dissipation in comparison with the elastic case.

Inside the band gap $(\Omega_1; 1)$ the solution is given by the "-" sign, the main term in (11.26) is of order $O(b^2)$. We have

$$(\Re K)^2 = -\frac{b^2(1 - \Omega_1^2)^2}{4}\frac{\Omega^4}{(\Omega^2 - \Omega_1^2)^3(\Omega^2 - 1)}$$

$$\cdot\left(1 + b^2(1 - \Omega_1^2)\frac{\Omega^2}{(\Omega^2 - \Omega_1^2)^2(\Omega^2 - 1)}(1 - \frac{1 - \Omega_1^2}{\Omega^2 - 1})\right)(1 + o(b^2)). \tag{11.28}$$

The main term is of the order of the dissipation parameter:

$$\Re K = \frac{b(1-\Omega_1^2)}{2} \frac{\Omega^2}{(\Omega^2 - \Omega_1^2)^{3/2}(1-\Omega^2)^{1/2}}, \qquad \Omega_1 < \Omega < 1 \qquad (11.29)$$

This expression is in accordance with [19], formula (6.47), case of viscoelastic foundation for the dynamic absorber, coupling between the dynamic absorber co-ordinate and the gradient of the bearing continuum co-ordinate, zero elastic foundation for the bearing continuum. We observe a decaying part of the dispersion curve above Ω_1.

Looking for the extremum of $\Re K(\Omega)$ inside the bandgap (function defined by eq. (11.29)), we find that at

$$\Omega_* = \frac{1}{2}(1 - \Omega_1^2 + (1 + 14\Omega_1^2 + \Omega_1^4)^{1/2})^{1/2} \qquad (11.30)$$

it reaches a minimal value. It can be easily proved that it takes minimum always inside the interval $(\Omega_1; 1)$ but we skip the proof since it is a simple technical exercise. This point is upper limit of the zone of anomalous refraction, where $\dfrac{d\omega}{d\Re K} < 0$. This limit does not depend on the small dissipation parameter in the first approximation, but only on Ω_1 determined by the parameter α/μ. For instance, if $\alpha = 10, \mu = 2$, then $\Omega_* = \sqrt{2/3} \approx 0.816$. The value, calculated using formula (11.29) at this point for $b = 0.158$, gives us the minimal value $\Re K \approx 0.216$. We see in Fig. 11.8 that this point indeed corresponds to the upper limit of the decreasing part of the dispersion curve, though the dissipation in this numerical example is not so small.

11.4.2.2 Imaginary Part of the Wave Number

Note that $(\Re K)_+^2 = -(\Im K)_-^2$, and $(\Re K)_-^2 = -(\Im K)_+^2$, where "+" and "-" correspond to the choice of the signs in Eqs. (11.23) and (11.24). Therefore the approximation (11.29) inside the band gap for $\Re K$, multiplied by $-i$, can serve as an approximation for $\Im K$ outside the band gap:

$$\Im K = -\frac{b(1-\Omega_1^2)}{2} \frac{\Omega^2}{(\Omega^2 - \Omega_1^2)^{3/2}(\Omega^2 - 1)^{1/2}}, \qquad \Omega < \Omega_1 \text{ or } \Omega > 1 \qquad (11.31)$$

Note that this function has no extremum outside the band gap: $|\Im(\Omega)|$ increases monotonically below the band gap ($\Omega < \Omega_1$) and decreases monotonically above the band gap ($\Omega > 1$). Thus, since $|\Im K|$ is continuous, it must have a maximum inside the band gap or close to its borders.

Vice versa, the approximation (11.27) for $\Re K$ outside the band gap, multilplied by $-i$, gives us the approximation for $\Im K$ inside the band gap, thus resulting in

$$\Im K = -\frac{\Omega(1-\Omega^2)^{1/2}}{(\Omega^2-\Omega_1^2)^{1/2}}\left(1-\frac{b^2(1-\Omega_1^2)\Omega^2}{2(\Omega^2-\Omega_1^2)^2(1-\Omega^2)}\right)+o(b^2),\tag{11.32}$$

$$\Omega_1 < \Omega < 1.$$

We see that inside the band gap small dissipation enhances the wave propagation: the wave decays less at a fixed distance. This effect is often, though not in all cases, observed in systems with small dissipation, added to a single negative elastic acoustic metamaterial [19]. We see that the main term for $\Im K$ has no extremum inside the band gap. Therefore, it must be in the vicinity of one of the characteristic frequencies. We will show it further.

11.4.2.3 Logarithmic Decrement

We calculate the logarithmic decrement multiplied by 2π. Outside the band gap

$$\left|\frac{\Im K}{\Re K}\right| = \frac{b(1-\Omega_1^2)}{2}\frac{\Omega}{(\Omega^2-\Omega_1^2)(\Omega^2-1)}+o(b^2)\tag{11.33}$$

It increases from zero below the band gap and decreases above it, tends to zero for large frequencies. It grows if we increase the viscous follower torque.

Inside the band gap the relation is inverse:

$$\left|\frac{\Im K}{\Re K}\right| = \frac{2}{b(1-\Omega_1^2)}\frac{(\Omega^2-\Omega_1^2)(1-\Omega^2)}{\Omega}+o(1)\tag{11.34}$$

It has a maximum at

$$\Omega_{\mathrm{D\,max}} = \frac{(\Omega_1^2+1+(\Omega_1^4+14\Omega_1^2+1)^{1/2})^{1/2}}{\sqrt{6}}\tag{11.35}$$

One can check that this frequency belongs to the band gap. It does not depend on the small dissipation in the first approximation, but the maximal value of the logarithmic decrement does. It decreases as the small dissipation increases. This apparently strange behaviour is observed due to the fact that attenuation is not related to the dissipation but to the existence of standing evanescent waves in the elastic medium (in this zone the logarithmic decrement was infinite in the elastic case). For the parameters corresponding to Fig. 11.10 we obtain $\Omega_{\mathrm{D\,max}} = \sqrt{2}/2$, $|\Im K/\Re K|_{\max} = 3.58$. We see that Fig. 11.10 confirms this result.

11.4.3 Small Dissipation near the Lower Characteristic Frequency Ω_1

Let us consider the case $b = o(1)$, $\Omega^2 = \Omega_1^2 - a_1 b$, where $a_1 = O(1)$ is a certain finite parameter. Then we obtain the following approximations:

$$z = b^2(a_1^2 + \Omega_1^2) + o(b^2), \tag{11.36}$$

$$f = ba_1(1 - \Omega_1^2) + o(b), \tag{11.37}$$

$$2(\Re K)^2 = \frac{\Omega_1^2(1 - \Omega_1^2)}{b} \frac{a_1 \pm (a_1^2 + \Omega_1^2)^{1/2}}{a_1^2 + \Omega_1^2} = \frac{\Omega_1(1 - \Omega_1^2)}{b} \frac{\xi + (\xi^2 + 1)^{1/2}}{1 + \xi^2}, \tag{11.38}$$

where $\xi = a_1/\Omega_1$. We have to choose the "+" root for this domain of frequencies since "-" gives a negative value for $(\Re K)^2$. Note that $\Omega = \Omega_1 - b\xi/2$. We see that in this domain $\Re K$ is large for small dissipation b.

It is easy to obtain that this function takes a maximal value at $\xi = 1/\sqrt{3}$, i.e. $\Re K(\Omega)$ reaches its maximal value

$$\Re K = \frac{3^{3/4}\Omega_1^{1/2}(1 - \Omega_1^2)^{1/2}}{2\sqrt{2b}} \quad \text{at} \quad \Omega = \Omega_1 - \frac{b}{2\sqrt{3}}. \tag{11.39}$$

Below this point we have a zone of normal refraction (positive $d\omega/d\Re k$), and above it a zone of negative refraction (negative $d\omega/d\Re k$). For the parameters corresponding to Fig. 11.5 the lower limit of the band gap equals $\Omega_1 - b/(2\sqrt{3}) \approx 0.363$.

In the same frequency domain

$$2(\Im K)^2 = \frac{\Omega_1^2(1 - \Omega_1^2)}{b} \frac{(a_1^2 + \Omega_1^2)^{1/2} - a_1}{a_1^2 + \Omega_1^2} = \frac{\Omega_1(1 - \Omega_1^2)}{b} \frac{(\xi^2 + 1)^{1/2} - \xi}{1 + \xi^2}, \tag{11.40}$$

Here we have chosen again the "+" branch for the same reason as above. In this domain attenuation is large for small dissipation b. It has its maximum at $\xi = -1/\sqrt{3}$, i.e. $|\Im K(\Omega)|$ reaches its maximal value

$$|\Im K| = \frac{3^{3/4}\Omega_1^{1/2}(1 - \Omega_1^2)^{1/2}}{2\sqrt{2b}} \quad \text{at} \quad \Omega = \Omega_1 + \frac{b}{2\sqrt{3}}. \tag{11.41}$$

At this frequency we have a maximal attenuation at a fixed distance. For parameters shown in Fig. 11.9 we obtain $\Omega = 0.454$, $|\Im K|_{\max} = 1.18$. We see that the graph confirms this prediction. At $\Omega_1^2 = 1/3$, i.e. $\alpha = 2\mu$ we have the maximal attenuation at a fixed distance in the former bandgap, reached at the frequency

$$\Omega_1 + \frac{b}{2\sqrt{3}},$$

corresponding to $|\Im K| = 1/(2\sqrt{b})$.

The logarithmic decrement can be obtained from the approximation

$$\left(\frac{\Im K}{\Re K}\right)^2 = \frac{-a_1(1-\Omega_1^2)b + (a_1^2+\Omega_1^2)^{1/2}(1-\Omega_1^2)b}{a_1(1-\Omega_1^2)b + (a_1^2+\Omega_1^2)^{1/2}(1-\Omega_1^2)b} = \frac{-\xi + (1+\xi^2)^{1/2}}{\xi + (1+\xi^2)^{1/2}} \qquad (11.42)$$

We see that the main term for the logarithmic decrement does not depend neither on the small dissipation b nor on the elastic constants in the vicinity of Ω_1, it is a monotonically increasing function of frequency in this domain, and $|\Im K/\Re K| = 1$ at Ω_1.

11.4.4 Small Dissipation near the Upper Characteristic Frequency $\Omega = 1$

Now consider the case $b = o(1)$, $\Omega^2 = 1 - a_0 b$, where $a_0 = O(1)$ is a certain finite parameter ($\Omega = 1 - a_0 b/2$). We proceed again with approximations:

$$z = (1 - \Omega_1)^2 + O(b^2) \qquad (11.43)$$

$$f = -ba_0(1 - \Omega_1^2) + o(b), \qquad (11.44)$$

$$2(\Re K)^2 = \frac{b}{1 - \Omega_1^2}((a_0^2+1)^{1/2} - a_0), \qquad (11.45)$$

it is a small in value, monotonically decreasing function of a_0, i.e. in this domain $\Re K(\Omega)$ increases. We have to choose the "+" root since the "-" root gives negative $(\Re K)^2$ and $(\Im K)^2$. For the imaginary part we have the following approximation

$$2(\Im K)^2 = \frac{b}{1 - \Omega_1^2}\left[(a_0^2+1)^{1/2} + a_0\right], \qquad (11.46)$$

it is a small in value, monotonically increasing function of a_0, i.e. in this domain $|\Im K|(\Omega)$ decreases.

The logarithmic decrement can be obtained from the approximation

$$\left(\frac{\Im K}{\Re K}\right)^2 = \frac{(1+a_0^2)^{1/2} - a_0}{(1+a_0^2)^{1/2} + a_0} \qquad (11.47)$$

We see that the main term for the logarithmic decrement does not depend on the small dissipation in the vicinity of $\Omega = 1$, it is a monotonically increasing function of frequency in this domain, and $|\Im K/\Re K| = 1$ at $\Omega = 1$.

11.5 Conclusions

Linear elastic reduced isotropic homogeneous Cosserat medium, subjected to a follower viscoelastic body torque, is a smart acoustic metamaterial.

1. Elastic follower torque controls properties of the single negative acoustic metamaterial.
   Positive elastic follower moment:

   - increases the shear–rotational wave velocity at low frequencies
   - moves the band gap upwards
   - reduces the width of band gap

   Negative elastic follower moment:

   - decreases the wave velocity at low frequencies
   - increases the width of band gap and moves it downwards

2. Viscous (not large) follower torque converts it into a double negative acoustic metamaterial. Positive viscous follower moment:

   - completely destroys the band gap for $\Re k$ (there is always a running evanescent solution, no standing waves)
   - makes to appear a decreasing part of the dispersion curve for enough small torque values
   - reduces the wave attenuation in the former band gap

We have obtained the expressions for the zone of anomalous refraction for the small dissipation. In the first approximation its upper limit does not depend on the dissipation parameter and is situated inside the band gap. The lower limit is just below the bandgap, its dimensionless frequency equals $\Omega_1 - 2b/\sqrt{3}$, b is the dimensionless dissipation parameter. The maximal attenuation for small dissipation at a fixed distance is reached inside the band gap, just above Ω_1, on the same distance from it. Attenuation inside the band gap far from the characteristic frequencies is inverse proportional to the dissipation b, and the local maximal value of $\Re K$ near the band gap is inverse proportional to $\sqrt{b}$, if b is small. Thus changing the external viscoelastic moment we can control the properties of the acoustic metamaterial and change its type. The same dispersion relation characterizes wave propagation of polarization field in non-polar dielectrics.

References

[1] Kafadar CB, Eringen AC (1971) Micropolar media — I the classical theory. International Journal of Engineering Science **9**(3):271–305

[2] Altenbach H, Eremeyev VA (2013) Cosserat media. In: Generalized Continua from the Theory to Engineering Applications, International Centre for Mechanical Sciences: Courses and Lectures, vol 541, Springer, Vienna, pp 65–130

[3] Altenbach H, Eremeyev VA (2014) Strain rate tensors and constitutive equations of inelastic micropolar materials. International Journal of Plasticity **63**:3–17

[4] Eremeyev VA, Lebedev LP, Altenbach H (2012) Foundations of Micropolar Mechanics. SpringerBriefs in Applied Sciences and Technology (SpringerBriefs in Continuum Mechanics), Springer Science & Business Media, Berlin, Heidelberg

[5] Eringen AC (2012) Microcontinuum Field Theories: I. Foundations and Solids. Springer Science & Business Media

[6] Altenbach H, Zhilin P (1988) A general theory of elastic simple shells (in Russ.). Uspekhi Mekhaniki **11**(4):107–148

[7] Marin M, Öchsner A, Vlase S (2022) A final boundary problem for modeling a thermoelastic Cosserat body. Continuum Mechanics and Thermodynamics **34**(2):627–636

[8] Erofeev VI, Leontieva AV, Malkhanov AO (2017) Stationary longitudinal thermoelastic waves and the waves of the rotation type in the non-linear micropolar medium. ZAMM-Journal of Applied Mathematics and Mechanics/Zeitschrift für Angewandte Mathematik und Mechanik **97**(9):1064–1071

[9] Ivanova EA, Vilchevskaya EN (2016) Micropolar continuum in spatial description. Continuum Mechanics and Thermodynamics **28**:1759–1780

[10] Abreu R, Thomas C, Durand S (2018) Effect of observed micropolar motions on wave propagation in deep earth minerals. Physics of the Earth and Planetary Interiors **276**:215–225

[11] Merkel A, Tournat V, Gusev V (2011) Experimental evidence of rotational elastic waves in granular phononic crystals. Physical Review Letters **107**(22):225,502

[12] Schwartz LM, Johnson DL, Feng S (1984) Vibrational modes in granular materials. Physical Review Letters **52**(10):831

[13] Grekova EF, Kulesh MA, Herman GC (2009) Waves in linear elastic media with microrotations, part 2: Isotropic reduced Cosserat model. Bulletin of the Seismological Society of America **99**(2B):1423–1428

[14] Grekova EF, Piatysheva AP (2020) Reduced linear viscoelastic isotropic cosserat medium with translational viscosity: a double negative acoustic metamaterial. In: Altenbach H, Eremeyev VA, Pavlov IS, Porubov AV (eds) Nonlinear Wave Dynamics of Materials and Structures, Advanced Structured Materials, vol 122, Springer, pp 153–167

[15] Piatysheva AP, Grekova EF (2021) Reduced linear viscoelastic isotropic cosserat medium with rotational viscosity: an acoustic metamaterial. Continuum Mechanics and Thermodynamics **33**(4):1765–1780

[16] Guenneau S, Movchan A, Pétursson G, Ramakrishna SA (2007) Acoustic metamaterials for sound focusing and confinement. New Journal of Physics **9**(11):399

[17] Kaina N, Lemoult F, Fink M, Lerosey G (2015) Negative refractive index and acoustic superlens from multiple scattering in single negative metamaterials. Nature **525**(7567):77–81

[18] Grekova EF (2019) Reduced enhanced elastic continua as acoustic metamaterials. Dynamical Processes in Generalized Continua and Structures pp 253–268

[19] Grekova EF (2022) Viscoelastic reduced enhanced isotropic continua as acoustic metamaterials. Philosophical Transactions of the Royal Society A **380**(2237), p. 20210371

[20] Porubov AV, Antonov ID (2021) On control of harmonic waves in an acoustic metamaterial. Mechanics Research Communications **116**, 103745

[21] Belyaev AK (1990) On the application of the locality principle in structural dynamics. Acta Mechanica **83**(3-4):213–222

[22] Belyaev AK (2004) High Frequency Dynamics of Engineering Structures. Springer

[23] Ostrovsky LA, Potapov AI (2003) Introduction into the Theory of Modulated Waves (in Russ.). Fizmatlit, Moscow

Chapter 12
Nonlinear Vibrations of Bimodular Continua by Means of Isogeometric Analysis

Rudolf Heuer and Galeb El Chabaan

Abstract The modeling and numerical analysis of the dynamic response of originally straight homogeneous Bernoulli-Euler beam rigid in shear with classical boundary conditions under time-varying excitation are studied. However, the beam is composed of a bimodular material, thus behaving differently in tension and compression. This implies that the neutral axis does not pass through the geometric centroid of the cross-section and depends not only on the elastic material properties but also on the curvature's sign and the geometry of the cross-section. Within this study, an isosceles triangular cross-section is analyzed, showing a difference in neutral axis position between positive and negative curvature with respect to the modular ratio. The governing equation for flexural oscillations of the bimodular beam is formulated based on the model with effective two-layer laminates and discontinuous natural beam axis with respect to the axis through the cross-section's geometric centroid, which is used as an independent reference axis of the bimodular beam structure. The numerical analysis of the dynamic response of the bimodular beam is investigated by means of isogeometric analysis (IGA). The fundamental idea behind isogeometric analysis is to use the same basis functions for constructing the exact original geometric model and for approximating the unknown solution fields. Finally, a numerical study is given to verify the effectiveness of the isogeometric approach on the dynamic analysis of the bimodular beam.

12.1 Introduction

The stress-strain curve of these so-called bimodular materials is usually approximated by two straight lines with a slope discontinuity at the origin, see e.g. [1]. A com-

Rudolf Heuer · Galeb El Chabaan
Institute of Structural Engineering
Research Unit of Mechanics and Structural Dynamics, TU Wien, Vienna, Austria
e-mail: rudolf.heuer@tuwien.ac.at, galeb.el.chabaan@tuwien.ac.at

prehensive study about the mechanical behavior of bimodular composite structures can be found in [2]. Publication [3] focuses on the nonlinear bending of laminated fibrous composite beams by incorporating a higher-order shear deformation beam theory. Bert and Tran [4] analyze the transient response of moderately thick bimodular beams using the transfer-matrix method. An analytical solution of tapered bimodular beams can be found in [5]. In [6], the authors considered the influence of the various cross-section geometry and material properties on the position of the neutral axis as well as on the dynamic response of the bimodular beam. A detailed introduction and review of the concept of isogeometric analysis and applications of this computational approach to structural vibration analysis are presented in [7] and [8]. Based on [6], the first section of this paper gives a brief overview of kinematic assumptions and governing equations. Beams of isosceles triangle cross-section are considered showing the nonlinear effect of the discontinuous natural axis on the dynamic response. The aim of this study is to introduce the central concept of isogeometric analysis and apply it to the dynamic analysis of the bimodular Bernoulli-Euler beam.

12.2 Mechanical Modeling

12.2.1 Kinematic Relations

According to Bernoulli-Euler beam theory, the plane of the cross-section remains plane and orthogonal to the beam axis during the deformation. In this case, the effect of transverse shear deformation can be neglected, which implies that the rotation of the cross-section $\psi(x;t)$ is equal to the negative slope of the beam axis

$$\psi(x;t) = -\frac{\partial w(x;t)}{\partial x} = -w(x;t)_{,x} \qquad (12.1)$$

where x denotes the axial beam coordinate and t is time. Based on these assumptions, the displacement field expressed by the axial displacement $u(x,\zeta;t)$, transverse displacement in the η-direction $v(x,\zeta;t)$ and transverse displacement in the ζ-direction $w(x,\zeta;t)$ can be written as

$$\begin{pmatrix} u(x,\zeta;t) \\ v(x,\zeta;t) \\ w(x,\zeta;t) \end{pmatrix} = \begin{pmatrix} u_0(x;t) + \left(\zeta_0(t) - \zeta\right)w(x;t)_{,x} \\ 0 \\ w(x;t) \end{pmatrix} \qquad (12.2)$$

The Cartesian (x,η,ζ) -coordinate system is located in the geometrical centroid of the cross-section S, as shown in Fig. 12.1 for the case of the triangle cross-section.
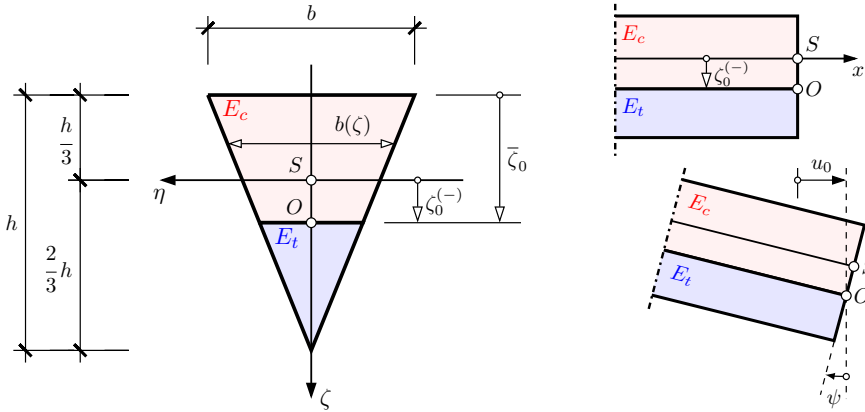
Fig. 12.1: Geometry and deformation of a bimodular beam in case of upward bending $(w_{,xx} < 0)$.

12.2.2 Governing Equations of Elastic Bimodular Beams

Based on the kinematic assumption made in Subsect. 12.2.1 and for the case when only transverse load $q(x;t)$ is considered, the equation of motion for the bimodular Bernoulli-Euler beam can be written as

$$\left(D - B\,\zeta_0\right) w(x;t)_{,xxxx} + \mu\,\ddot{w}(x;t) = q(x;t) \tag{12.3}$$

where D and B define bending and bending-extensional coupling stiffness expressed in terms of time-independet Young's modulus E, respectively, as

$$D = \int_A E\,\zeta^2\,\mathrm{d}A = \int_h E(\zeta)\,\zeta^2\,b(\zeta)\,\mathrm{d}\zeta \tag{12.4}$$

$$B = \int_A E\,\zeta\,\mathrm{d}A = \int_h E(\zeta)\,\zeta\,b(\zeta)\,\mathrm{d}\zeta \tag{12.5}$$

Furthermore, the position of the neutral axis ζ_0 can be found from nonlinear algebraic equation obtained from the following condition

$$\zeta_0 = \frac{B}{\bar{A}} = \frac{\displaystyle\int_A E\,\zeta\,\mathrm{d}A}{\displaystyle\int_A E\,\mathrm{d}A} = \frac{\displaystyle\sum_{i=1}^{2}\zeta_{S_i}E_i A_i}{\displaystyle\sum_{i=1}^{2}E_i A_i} \tag{12.6}$$

where $\bar{A}$ denotes the extensional stiffness defined as

$$\overline{A} = \int_A E\, dA = \int_h E(\zeta)\, b(\zeta)\, d\zeta \tag{12.7}$$

The mass per unit length μ is defined as integral of the mass density ρ over the cross-section area A

$$\mu = \int_A \rho\, dA = \int_h \rho(x,\zeta)\, b(\zeta)\, d\zeta \tag{12.8}$$

The detailed derivation of the kinematic relations (12.2.1) and governing equation (12.3) of the bimodular Bernoulli-Euler beam can be found in [6].

12.3 Considered Geometries - Isosceles Triangle Cross-Section

Considering beams with isosceles triangle cross-section (see Fig. 12.1), the width can be expressed by a linear function as

$$b(\zeta) = b\left(\frac{2}{3} - \frac{\zeta}{h}\right) \tag{12.9}$$

Determination of the stiffness parameters according to Eqs. (12.7), (12.5) and (12.4) renders in case of the configuration "upward bending", $w_{,xx} < 0$,

$$\overline{A}^{(-)} = E_c b\left[\frac{h}{18}\left(4\delta + 5\right) - \frac{2}{3}\left(\delta - 1\right)\zeta_0 + \frac{1}{2h}\left(\delta - 1\right)\zeta_0^2\right] \tag{12.10}$$

$$B^{(-)} = E_c b\left[\frac{4}{81}h^2\left(\delta - 1\right) - \frac{1}{3}\left(\delta - 1\right)\zeta_0^2 + \frac{1}{3h}\left(\delta - 1\right)\zeta_0^3\right] \tag{12.11}$$

$$D^{(-)} = E_c b\left[\frac{h^3}{972}\left(16\delta + 11\right) - \frac{2}{9}\left(\delta - 1\right)\zeta_0^3 + \frac{1}{4h}\left(\delta - 1\right)\zeta_0^4\right] \tag{12.12}$$

and for "downward bending", $w_{,xx} > 0$,

$$\overline{A}^{(+)} = E_c b\left[\frac{h}{18}\left(5\delta + 4\right) + \frac{2}{3}\left(\delta - 1\right)\zeta_0 - \frac{1}{2h}\left(\delta - 1\right)\zeta_0^2\right] \tag{12.13}$$

$$B^{(+)} = E_c b\left[-\frac{4}{81}h^2\left(\delta - 1\right) + \frac{1}{3}\left(\delta - 1\right)\zeta_0^2 - \frac{1}{3h}\left(\delta - 1\right)\zeta_0^3\right] \tag{12.14}$$

$$D^{(+)} = E_c b\left[\frac{h^3}{972}\left(11\delta + 16\right) + \frac{2}{9}\left(\delta - 1\right)\zeta_0^3 - \frac{1}{4h}\left(\delta - 1\right)\zeta_0^4\right] \tag{12.15}$$

where the modular ratio

$$\delta = \frac{E_t}{E_c} \tag{12.16}$$

contains both Young's modulus of tension, E_t, and of compression, E_c. The cross-section with the areas of compression and tension for both cases is presented in Fig. 12.1, where it is assumed that $E_t > E_c$. The position of the neutral axis can be obtained from the lowest root of an algebraic equation of fourth order, which follows from Eq. (12.6), giving for the configuration of negative curvature, $w_{,xx} < 0$,

$$\left(\delta - 1\right)\overline{\zeta}_0^4 - 5h\left(\delta - 1\right)\overline{\zeta}_0^3 + h^2\left(9\delta - 6\right)\overline{\zeta}_0^2 - 7h^3\delta\overline{\zeta}_0 + 2h^4\delta = 0 \tag{12.17}$$

and for configuration of positive curvature, $w_{,xx} > 0$,

$$\left(\delta - 1\right)\overline{\zeta}_0^4 - 5h\left(\delta - 1\right)\overline{\zeta}_0^3 + h^2\left(6\delta - 9\right)\overline{\zeta}_0^2 + 7h^3\overline{\zeta}_0 - 2h^4 = 0 \tag{12.18}$$

12.4 Application of Isogeometric Analysis to the Bimodular Beam

12.4.1 B-Splines

Starting from a knot vector in one dimension as a non-decreasing set of coordinates in the parameter space

$$\Xi = \{\xi_1, \xi_2, \ldots, \xi_{n+p+1}\} \tag{12.19}$$

where $\xi_i \in \mathbb{R}$ is the i-th knot, i is the knot index, n is the number of basis functions and p is the polynomial order. The B-spline basis functions are defined by the *Cox-de Bor recursion formula*. For $p = 0$ (piecewise constants)

$$N_{i,0}(\xi) = \begin{cases} 1 & \text{if } \xi_i \leq \xi < \xi_{i+1} \\ 0 & \text{otherwise} \end{cases} \tag{12.20}$$

and for $p \geq 1$

$$N_{i,p}(\xi) = \frac{\xi - \xi_i}{\xi_{i+p} - \xi_i} N_{i,p-1}(\xi) + \frac{\xi_{i+p+1} - \xi}{\xi_{i+p+1} - \xi_{i+1}} N_{i+1,p-1}(\xi) \tag{12.21}$$

The first derivative of a B-spline basis function with respect to the parametric coordinates is computed by the following recursive formula

$$\frac{d}{d\xi} N_{i,p}(\xi) = \frac{p}{\xi_{i+p} - \xi_i} N_{i,p-1}(\xi) - \frac{p}{\xi_{i+p+1} - \xi_{i+1}} N_{i+1,p-1}(\xi) \tag{12.22}$$

By differentiating both sides, this can be generalized to higher derivatives

$$\frac{d^k}{d\xi^k}N_{i,p}(\xi) = \frac{p}{\xi_{i+p} - \xi_i}\left(\frac{d^{k-1}}{d\xi^{k-1}}N_{i,p-1}(\xi)\right) - \frac{p}{\xi_{i+p+1} - \xi_{i+1}}\left(\frac{d^{k-1}}{d\xi^{k-1}}N_{i+1,p-1}(\xi)\right)$$

$$(12.23)$$

where k denotes the k-th derivative. A picewise-polynomial B-spline curve of the order p can be obtained by taking a linear combination of n B-spline basis functions and control points $\boldsymbol{P}_i$, which are points in the physical space

$$\boldsymbol{C}(\xi) = \sum_{i=1}^{n} N_{i,p}(\xi)\boldsymbol{P}_i \qquad (12.24)$$

12.4.2 Isogeometric Analysis of Bimodular Beam Vibration

The method of separation of variables can be applied to the homogeneous partial differential equation (12.3) with $q(x;t) = 0$ to transform the equation into two ordinary differential equations, one governing the time function and the other governing the following spatial function

$$\left(D - B\zeta_0\right)w(x)_{,xxxx} - \omega^2\mu w(x) = 0 \qquad (12.25)$$

The weak form of the differential equation (12.25) can be derived using the method of weighted residuals, namely multiplying the equation with a test function $v(x)$, taking the integral over the length of the beam L and applying twice integration by parts of the first term

$$\int_0^L \left(D - B\zeta_0\right)w(x)_{,xx}\,v(x)_{,xx}\,dx - \omega^2\int_0^L \mu w(x)\,v(x)\,dx$$

$$= \left(D - B\zeta_0\right)\left[w(x)_{,xx}\,v(x)_{,x} - w(x)_{,xxx}\,v(x)\right]_0^L \qquad (12.26)$$

Specifically, considering a simply supported bimodular beam with the following homogeneous boundary conditions

$$\begin{aligned} w(x = 0) &= 0 & w(x = 0) &= 0 \\ w(x = 0)_{,xx} &= 0 & w(x = L)_{,xx} &= 0 \end{aligned} \qquad (12.27)$$

the weak form (12.26) reduces to

$$\int_0^L \left(D - B\zeta_0\right)w(x)_{,xx}\,v(x)_{,xx}\,dx - \omega^2\int_0^L \mu w(x)\,v(x)\,dx = 0 \qquad (12.28)$$

The isogeometric analysis utilizes the isoparametric concept, which refers to the use of the same basis function for constructing the exact original geometric model and for approximating the unknown solution fields. Using a B-spline curve of order p with knot vector Ξ and control points $\boldsymbol{P}_i$, the parametrization of the x-coordinate is given by

$$x(\xi) = \boldsymbol{C}(\xi) = \sum_{i=1}^{n} N_{i,p}(\xi)\boldsymbol{P}_i \tag{12.29}$$

The bending displacement field $w(x)$ and the test function $v(x)$ can be approximated as

$$w^h(x) = \sum_{i=1}^{n} N_{i,p}(x)\,w_i = \boldsymbol{N}\boldsymbol{w} \qquad v^h(x) = \sum_{j=1}^{n} N_{j,p}(x)\,v_i = \boldsymbol{N}\boldsymbol{v} \tag{12.30}$$

where w_i and v_i are the control variables. Inserting the shape-function expansions for $w^h(x)$ and $v^h(x)$ into the weak form (12.28) gives the well-known discrete eigenvalue problem for the k-th natural circural frequency ω_k and the k-th natural mode $\boldsymbol{\phi}_k$

$$\left(\boldsymbol{K} - \omega_k^2 \boldsymbol{M}\right)\boldsymbol{\phi}_k = 0 \tag{12.31}$$

The global stiffness and mass matrices are obtained in a standard way by assembly of the element matrices

$$\boldsymbol{K} = \underset{e=1}{\overset{n_e}{\mathsf{A}}} \int_0^{l_e} \boldsymbol{N}_{,xx}^T \left(D - B\zeta_0\right)\boldsymbol{N}_{,xx}\,\mathrm{d}x \tag{12.32}$$

$$\boldsymbol{M} = \underset{e=1}{\overset{n_e}{\mathsf{A}}} \int_0^{l_e} \boldsymbol{N}^T \mu \boldsymbol{N}\,\mathrm{d}x \tag{12.33}$$

where A is the assembly operator, n_e is the number of elements and l_e is the length of element e.

12.5 Numerical Studies

In order to validate the isogeometric approach to the bimodular beam vibration analysis and compare the natural circular frequencies by isogeometric analysis using B-splines with the values from [6], a simply supported beam is considered with the same geometrical and material parameters as in [6], except the trapezoidal cross-section, for which an isosceles triangular cross-section is considered. The material of the beam is characterized by the following properties: Young's modulus of tension, $E_t = 12\,000$ kN/cm^2, Young's modulus of compression, $E_c = 3\,000$ kN/cm^2 and mass density, $\rho = 2\,500$ kg/m^3. The damping effects are included by the assumption of

a viscous damping with a modal damping ratio of $\zeta_n = 0.03$. As mentioned before, within this analysis, two cross-sections are considered, namely the isosceles triangle and rectangular cross-section, whose parameters are listed in Table 12.1 below. From Table 12.1 it is obvious that the dimensions of both cross-sections are chosen in such a way that they have approximately equal cross-sectional area as well as the approximately equal moment of inertia with respect to the η-axis. The initial beam geometry is straight and described by a 5-th order B-spline curve with the open knot vector $\Xi = \{0, 0, 0, 0, 0, 1, 2, 3, 4, 5, 6, 7, 8, 8, 8, 8, 8\}$ and corresponding control points. The number of elements is defined by the number of non-zero knot spans in the knot vector. In this case, the bimodular beam is represented by eight elements. Table 12.2 contains a comparison between the natural circular frequencies in the case of upward, $\omega_0^{(-)}$, and downward, $\omega_0^{(+)}$, bending motion for the first eight vibration modes. The last column of the Table 12.2 contains values from [6].

Within the second example forced vibrations are considered, where the following half-cycle sine pulse force is applied to the beam with the isosceles triangle cross-section

$$q(x;t) = \begin{cases} q_0 \sin \dfrac{\pi t}{t_d} & t \le t_d \\ 0 & t \ge t_d \end{cases} \tag{12.34}$$

where $q_0 = 5$ kN/m is the amplitude of uniformly distributed transverse dynamic load over the entire beam length of $l = 8$ m and $t_d = 0.3$ s is the half-cycle sine pulse duration. The corresponding initial conditions of displacement and velocity are assumed to be zero. The dynamic response of the bimodular beam strongly depends not only on the modular ratio δ but also on the geometry of the cross-section. Figure 12.2 indicate that, based on different bending stiffness, there are significant differences between the amplitudes of displacement response of unimodular and bimodular beams. The effect of the geometry of the cross-section on the amplitude

Table 12.1: Cross-section parameters.

			Triangle cross-section	Rectangular cross-section
Height	h	[cm]	36.74	30.00
Top width	b	[cm]	32.67	20.00
Cross-sectional area	A	[cm^2]	600.15	600.00
Moment of inertia about η-axis	I_η	[cm^4]	45 005.34	45 000.00
Neutral axis position ($w_{,xx} < 0$)	$\zeta_0^{(-)}$ [cm]		5.27	5.00
Neutral axis position ($w_{,xx} > 0$)	$\zeta_0^{(+)}$ [cm]		-4.53	-5.00

Table 12.2: Numerical comparison of natural circular frequencies ω_0 [rad/s].

	Triangle cross-section		Rectangular cross-section	
	$\omega_0^{(-)}$	$\omega_0^{(+)}$	$\omega_0^{(-)} = \omega_0^{(+)}$	$\omega_0^{(-)} = \omega_0^{(+)}$ [6]
n=1	66.15	58.37	61.68	61.68
n=2	264.61	233.49	246.74	246.74
n=3	595.41	525.38	555.20	555.16
n=4	1 059.08	934.51	987.55	986.96
n=5	1 659.98	1 464.74	1 547.87	1 542.13
n=6	2 425.16	2 139.92	2 261.37	2 220.66
n=7	3 441.16	3036.42	3 208.76	3 022.56
n=8	4 237.65	3 739.23	3 951.46	3 947.84
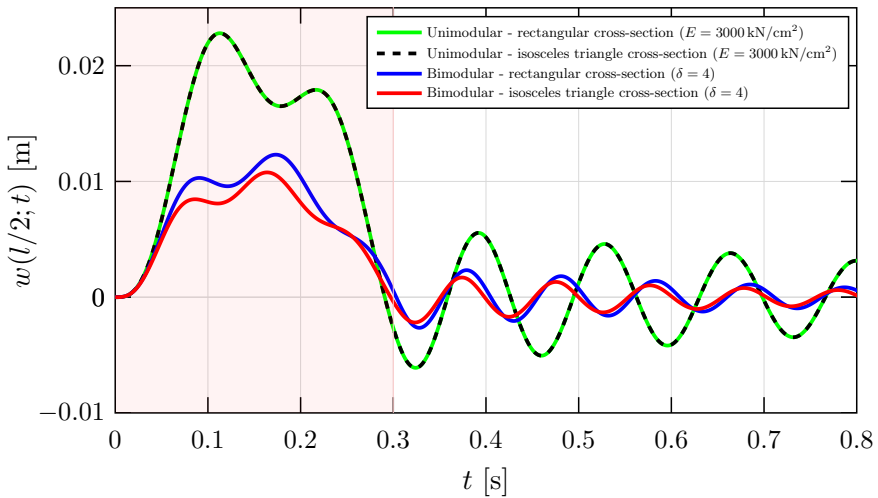
Fig. 12.2: Comparison of displacement response $w(l/2;t)$.

and period of the vibration is also graphically illustrated. The reason for that is the influence of the cross-section geometry on finding the neutral axis position (hence on determining the stiffness and frequency), whose absolute values are different for negative and positive curvature in the case of the isosceles triangle but equal in the case of the rectangular cross-section. Because of that, the period of vibration of the bimodular beam with the isosceles triangle cross-section is also affected by curvature-dependent frequency.

12.6 Conclusions

Composites exhibiting load-dependent elastic properties cannot be treated as structures with, e.g., effective isotropic parameters, which implies that the bimodular beams can be modeled as effective two-layer laminates. However, their neutral axis depends not only on the elastic material properties but also on the curvature's sign and the geometry of the cross-section. In the case of the isosceles triangle cross-section, the position of that natural axis follows from a nonlinear equation of fourth order depending on the cross-section's geometry and the elastic material properties. Thus, an independent reference axis must be used when formulating the equations of motion for flexural oscillations.

Within numerical studies, the dynamic response of simply supported beams with the isosceles triangle as well as rectangular cross-section are analyzed for half-cycle sine pulse excitation. Comparison to the response of unimodular beams shows a significant influence of the nonlinear bimodular effect. Computational application of the isogeometric finite element discretization with B-splines to the straight Bernoulli-Euler bimodular beam is presented as a powerful tool for the analysis of bimodular structural vibrations.

References

[1] Tseng YP, Lee CT (1995) Bending analysis of bimodular laminates using a higher-order finite strip method. Composite Structures **30**(3):341–350

[2] Bert CW, Reddy JN (1983) Mechanics of bimodular composite structures. In: Hashin Z, Herakovich CT (eds) Mechanics of Composite Materials, Pergamon, pp 323–337

[3] Ghazavi A, Gordaninejad F (1989) Nonlinear bending of thick beams laminated from bimodular composite materials. Composites Science and Technology **36**(4):289–298

[4] Bert CW, Tran AD (1982) Transient response of a thick beam of bimodular material. Earthquake Engineering & Structural Dynamics **10**(4):551–560

[5] K JD (2012) Analytical solution of tapered bimodular beams. Anbar Journal for Engineering Sciences pp 79–101

[6] Heuer R, El Chabaan G (2022) On nonlinear vibrations of bimodular beam structures. In: Irschik H, Krommer M, Matveenko VP, Belyaev AK (eds) Dynamics and Control of Advanced Structures and Machines, Advanced Structured Materials, vol 156, Springer, Cham, pp 61–71

[7] Cottrel JA, Hughes TJR, Bazilevs Y (2009) Isogeometric Analysis: Toward Integration of CAD and FEA. Wiley, New York

[8] Cottrell JA, Reali A, Bazilevs Y, Hughes TJR (2006) Isogeometric analysis of structural vibrations. Computer Methods in Applied Mechanics and Engineering **195**(41):5257–5296, John H. Argyris Memorial Issue. Part II

Chapter 13

On the Equivalence Between Singular Waves Propagating in Force Loaded Viscoelastic Bodies and in Elastic Bodies Additionally Loaded by Eigenstrains

Hans Irschik, Michael Krommer, and Astrid S. Pechstein

Abstract The present contribution is devoted to a special equivalence problem concerning the linear dynamic theories of elasticity and viscoelasticity. We seek for distributions of eigenstrain-induced actuation stresses acting upon a force loaded linear elastic body, such that the resulting displacements are equal to the displacements of a viscoelastic body that is loaded by the same set of forces, but in the absence of actuating stresses. Special emphasis is given to the presence of propagating singular waves. A three-dimensional solution for this equivalence problem is presented first. The presented special solution yields equivalence of stresses in both problems, so that a complete analogy is obtained. The solution then is exemplified for the one-dimensional case of a uni-axial shock wave propagating in a semi-infinite half-space made of a viscoelastic material of the Maxwell-type.

13.1 Introduction

It was Ernst Mach [1], who systematically proposed the advantages of searching for similarities and analogies that may exist between apparently different scientific problems. As pointed out by Mach, similarity can be understood as an identity in parts. In the present contribution, we deal with a special partial identity, namely with the equivalence that may exist between the displacement fields in elastic and inelastic bodies, but not necessarily for the corresponding stresses. Particularly, our present study refers to the linear theories of elasticity and viscoelasticity, see e.g. Lurie [2], Gurtin [3] and Leitman and Fisher [4] for comprehensive representations. We deal with a force loaded viscoelastic body as our original object, and we seek for eigenstrain loadings that, additionally to the given force loading, act upon an auxiliary

Hans Irschik · Michael Krommer · Astrid S. Pechstein
Institute of Technical Mechanics, Johannes Kepler University Linz, Altenberger Str. 69, 4040 Linz, Austria, e-mail: hans.irschik@jku.at, michael.krommer@jku.at, astrid.pechstein@jku.at

201

elastic body of the same shape, such that the displacements in both problems become equivalent, i.e. that they are identical. For this question we use the notion of a displacement equivalence problem. We particularly will treat this problem in the dynamic setting of singular wave propagation, referring to the presence of shock and acceleration waves. It is hoped that the subsequently developed solution of this problem will contribute to the completeness of the underlying theories of elasticity and viscoelasticity by adding respective eigenstrain analogies.

Hence, eigenstrains represent the source of possible similarity in the present displacement equivalence problem. The notion of eigenstrains refers to various physical effects; e.g., thermal actuation represents an important classical example for eigenstrains, see e.g. Parkus [5, 6] and Carlson [7] for thermally induced dynamic elastic displacements and stresses. Another example, being of particular importance in smart structures and intelligent material systems, are piezoelectric eigenstrains, see e.g. Fung et al. [8] and Haddad [9] for thermally and electrically induced eigenstrains in elastic and viscoelastic solids. In the linear theories under consideration, it usually can be assumed that the dependence of material parameters on the amount of eigenstrains can be disregarded; eigenstrains then do appear as isolated extra terms in the constitutive relations only. The latter terms are subsequently gathered as what we call actuation stresses: we seek for actuation stresses, such that our equivalence problem is solved. Our subsequent results thus hold whether or not eigenstrains are considered as being thermodynamically coupled to the time rate of displacement gradients. The problem of computing the necessary eigenstrains from the required actuation stresses, which is a comparatively straightforward task in the uncoupled case, is not treated in the subsequent contribution.

That certain similarities between displacements of elastic and inelastic bodies do exist in the form of eigenstrain analogies has long been known, and it has been used by the senior author of the present contribution, in cooperation with the late Professor Franz Ziegler and co-workers, to develop numerical computation methods, which utilize advances of linear schemes in an inelastic and non-linear context, see e.g. Refs. [10, 11] and the literature cited there. While vibrations were the main objects of these studies, also numerical schemes for wave propagation in inelastic bodies have been developed using the eigenstrain analogy, see e.g. Refs. [12, 13]. In the following, we particularly will refer to Ref. [14], to which important contributions were made by Professor Alexander K. Belyaev, who served as Guest-Professor at the Johannes Kepler University of Linz at that time, and to whom the present book is dedicated on the occasion of his 70th birthday.

A problem that is related to the present displacement equivalence context is represented by the problem of controlling the displacement of force loaded solids and structures by means of eigenstrains, [15] in the present book, and the literature cited there for displacement control in linear elastic structures. Seen from the present equivalence point of view, one could shortly interpret this displacement control problem as follows: one again seeks for similarities between an original and an auxiliary problem, where however both problems are governed by the same linear elastic constitutive relations, the original problem being loaded by forces only, while the auxiliary problem is loaded by actuation stresses only. Having found a distribution

of actuation stresses that guarantees that the displacements of the auxiliary problem are equivalent to the sum of the desired displacement field and the negative of the original displacements, then, applying the so found actuation stresses in addition to the forces will produce the desired displacement field to be controlled. Of course, it is more convenient to formulate displacement control in a more direct manner, cf. Ref. [15], where emphasis however is given to the more complex problem of strain control in subdomains.

As already mentioned, in the present contribution we seek for equivalence between the displacements in force loaded viscoelastic bodies and in linear elastic ones with an additional actuation stress loading, giving special emphasis to the presence of singular wave fronts. Our paper is organized as follows: In the next section, we formulate the three-dimensional (3D) basic relations for linear viscoelastic bodies loaded by forces and actuation stresses, including the relations of jump at the propagating wave fronts. Constitutive relations are presented in the Boltzmann hereditary integral form, considering a vanishing initial past history. The displacement based formulation of this initial-boundary value problem is given. In the latter formulation, a original viscoelastic problem is stated, in which actuation stresses are absent. Moreover, an auxiliary linear elastic problem is formulated by taking the tensorial relaxation function to be independent of time. The latter problem is loaded by the same forces as the original one, but has an additional actuation stress distribution. The actuation stresses necessary for equivalence of displacements in the two problems are derived from the uniqueness assumption that the homogeneous auxiliary problem, i.e. the linear elastic problem with zero input data, has vanishing displacements as the only solution. The resulting conditions for the actuation stresses allow non-unique solutions; however, a special solution for the actuation stresses is presented, for which not only the displacements, but also the stresses of the two problems turn out to be equivalent, so that a complete analogy is derived. The 3D results afterwards are applied to the one-dimensional (1D) problem of uni-axial wave propagation in a semi-infinite half-space (or, equivalently, in a semi-infinite rod) that is made of a Maxwell-type viscoelastic material. Using symbolic computations, the case of a half-space loaded by a tensile Heaviside-type normal surface traction, i.e. by a suddenly applied force normal to the surface, the intensity of which is maintained, is treated. Correctness of the results is analytically checked in the Laplace-domain, and the time-evolution of the 1D propagating displacements, stresses and actuation stresses is depicted. We note that the corresponding results accompany the 1D numerical results presented in the study [14] by providing analytic expressions for the necessary actuation stresses. It is also noted that the complementary problem of displacement tracking of 1D singular wave propagation in a linear elastic half-space loaded by a suddenly applied surface traction and in a Maxwell-type viscoelastic half-space under the action of additional actuation stresses has recently been established by Irschik and Krommer [16]. Before, displacement control of singular waves in linear elastic bodies by eigenstrains was treated by Irschik and Brandl [17] in a contribution dedicated to Professor Alexander K. Belyaev on the occasion of his 65th birthday.

13.2 Basic Relations

The set of field equations of the linear theory of viscoelasticity is written as

$$\text{div}\boldsymbol{S} + \boldsymbol{b} = \rho\ddot{\boldsymbol{u}} \,, \quad \boldsymbol{S} = \boldsymbol{S}^T, \tag{13.1}$$

$$\boldsymbol{S} = \mathbb{G}_0\left[\boldsymbol{E}(t)\right] + \int_0^t \dot{\mathbb{G}}(s)\left[\boldsymbol{E}(t-s)\right]ds - \boldsymbol{S}_A, \tag{13.2}$$

$$\boldsymbol{E} = \nabla\boldsymbol{u}^S, \tag{13.3}$$

see Leitman and Fisher [4] for details and mathematical notation, see also Gurtin [3] and Carlson [7]. In the present section, we consider three-dimensional (3D) solids or structures. The symmetric Cauchy stress tensor is denoted as $\boldsymbol{S}$, the linearized strain tensor is $\boldsymbol{E}$, and $\boldsymbol{u}$ stands for the displacement vector. Time is denoted as t, a superimposed dot stands for the time derivative, and ∇ is the Nabla-operator of the undeformed configuration. Mass density is written as ρ; it is taken as time-independent in the linear theory. Imposed body forces per unit volume are denoted by $\boldsymbol{b}$. In the viscoelastic constitutive relation, Eq. (13.2), the tensorial actuation stress $\boldsymbol{S}_A$ gathers the effect of eigenstrains, stemming e.g. from temperature, moisture, or similar physical fields. In smart structures, piezoelectric eigenstrains represent the most promising candidates for applications. The tensor of initial elasticity, $\mathbb{G}_0 = \mathbb{G}(t = 0)$, is taken as symmetric and positive definite, where $\mathbb{G}$ is the tensorial relaxation function, and $\dot{\mathbb{G}}(s) = \partial\mathbb{G}/\partial s$. The relaxation function remains constant for a purely elastic material, which thus is included as a special case. In the hereditary integral in Eq. (13.2) we have assumed the case of a vanishing initial past history, for which the strain vanishes up to time $t = 0$. In the present dynamic context, the motion is assumed to start from rest, adding homogeneous initial conditions to the field equations in Eqs. (13.1) – (13.3):

$$t = 0: \quad \boldsymbol{u} = \boldsymbol{0}, \, \dot{\boldsymbol{u}} = \boldsymbol{0}. \tag{13.4}$$

The field equations stated in Eqs. (13.1) – (13.3) are accompanied by mixed boundary conditions at the boundary $\partial B = \partial B_u \cup \partial B_S$ of the solid B under consideration:

$$\partial B_u: \quad \boldsymbol{u} = \hat{\boldsymbol{u}}, \tag{13.5}$$

$$\partial B_S: \quad \boldsymbol{Sn} = \hat{\boldsymbol{s}}, \tag{13.6}$$

where $\boldsymbol{n}$ denotes the unit outward normal vector of ∂B, and $\hat{\boldsymbol{s}}$ is the surface traction applied at ∂B_S The kinematic boundary condition in Eq. (13.5) must be consistent with the quiet initial conditions in Eq. (13.4). In the present contribution, we particularly

consider the presence of singular waves of order 1, so-called shock waves, and of singular waves of order 2, also denoted as acceleration waves, that propagate through B. The relations of jump at the fronts ∂B_1 and ∂B_2 of the shock and acceleration waves are

$$\partial B_1 : \quad [\![\boldsymbol{S}]\!]\boldsymbol{m} + \rho V [\![\dot{\boldsymbol{u}}]\!] = \boldsymbol{0}, \tag{13.7}$$

$$\partial B_2 : \quad [\![\dot{\boldsymbol{S}}]\!]\boldsymbol{m} + \rho V [\![\ddot{\boldsymbol{u}}]\!] - V[\![\boldsymbol{b}]\!] = \boldsymbol{0}. \tag{13.8}$$

The propagating fronts are assumed to be smooth and orientable surfaces, with the unit normal vector $\boldsymbol{m}$ pointing in the direction of propagation, and with the speed of propagation V. Double square brackets denote a jump across the fronts.

Eliminating the stress tensor $\boldsymbol{S}$ and the strain tensor $\boldsymbol{E}$ from the above relations gives the displacement based formulation of the considered dynamic linear viscoelastic problem to

$$\mathrm{div}\left(\mathbb{G}_0\left[\nabla\boldsymbol{u}(t)\right] + \int_0^t \dot{\mathbb{G}}(s)\left[\nabla\boldsymbol{u}(t-s)\right] ds\right) - \rho\ddot{\boldsymbol{u}} = \mathrm{div}\boldsymbol{S}_A - \boldsymbol{b}, \tag{13.9}$$

$$t = 0 : \quad \boldsymbol{u} = \boldsymbol{0}, \ \dot{\boldsymbol{u}} = \boldsymbol{0}, \tag{13.10}$$

$$\partial B_u : \quad \boldsymbol{u} = \hat{\boldsymbol{u}}, \tag{13.11}$$

$$\partial B_S : \quad \left(\mathbb{G}_0\left[\nabla\boldsymbol{u}(t)\right] + \int_0^t \dot{\mathbb{G}}(s)\left[\nabla\boldsymbol{u}(t-s)\right] ds\right)\boldsymbol{n} = \boldsymbol{S}_A\boldsymbol{n} + \hat{\boldsymbol{s}}, \tag{13.12}$$

$$\partial B_1 : \quad [\![\mathbb{G}_0\left[\nabla\boldsymbol{u}(t)\right] + \int_0^t \dot{\mathbb{G}}(s)\left[\nabla\boldsymbol{u}(t-s)\right] ds]\!]\boldsymbol{m} + \rho V[\![\dot{\boldsymbol{u}}]\!] = [\![\boldsymbol{S}_A]\!]\boldsymbol{m}, \tag{13.13}$$

$$\partial B_2 : \quad \left(\frac{d}{dt}[\![\mathbb{G}_0\left[\nabla\boldsymbol{u}(t)\right] + \int_0^t \dot{\mathbb{G}}(s)\left[\nabla\boldsymbol{u}(t-s)\right] ds]\!]\right)\boldsymbol{m} + \rho V[\![\ddot{\boldsymbol{u}}]\!]$$
$$= [\![\dot{\boldsymbol{S}}_A]\!]\boldsymbol{m} + V[\![\boldsymbol{b}]\!]. \tag{13.14}$$

In the present paper we consider a viscoelastic problem, in which the actuation stress is absent, $\boldsymbol{S}_A = \boldsymbol{0}$, as a reference problem. Using this assumption in the displacement based formulation of Eqs. (13.9) – (13.14), we will talk about the original viscoelastic problem in the following.

Secondly, we also consider an auxiliary problem in Eqs. (13.9) – (13.14), which will be indicated by an asterisk. In this auxiliary problem, a displacement field $\boldsymbol{u}^*$ due to an auxiliary actuation stress $\boldsymbol{S}_A^*$ is considered, assuming the same imposed body forces and imposed surface traction as in the original problem, $\boldsymbol{b}^* = \boldsymbol{b}$ in Eqs. (13.9) and (13.14), and $\hat{\boldsymbol{s}}^* = \hat{\boldsymbol{s}}$ in Eq. (13.12). The same kinematic boundary condition is used as in the original problem, $\hat{\boldsymbol{u}}^* = \hat{\boldsymbol{u}}$ in Eq. (13.11). Particularly, we assume that the auxiliary problem is purely elastic

$$\mathbb{G}^*(t) = \mathbb{G}_0 \,, \quad \dot{\mathbb{G}}^*(s) = \boldsymbol{0}. \tag{13.15}$$

Hence, the displacement based formulation for this auxiliary elastic problem reads

$$\operatorname{div}\left(\mathbb{G}_0\left[\nabla \boldsymbol{u}^*\right]\right) - \rho \ddot{\boldsymbol{u}}^* = \operatorname{div}\boldsymbol{S}_A^* - \boldsymbol{b}, \tag{13.16}$$

$$t = 0: \quad \boldsymbol{u}^* = \boldsymbol{0}, \ \dot{\boldsymbol{u}}^* = \boldsymbol{0}, \tag{13.17}$$

$$\partial B_u: \quad \boldsymbol{u}^* = \hat{\boldsymbol{u}}, \tag{13.18}$$

$$\partial B_S: \quad \left(\mathbb{G}_0\left[\nabla \boldsymbol{u}^*\right]\right)\boldsymbol{n} = \boldsymbol{S}_A^*\boldsymbol{n} + \hat{\boldsymbol{s}}, \tag{13.19}$$

$$\partial B_1: \quad \llbracket \mathbb{G}_0\left[\nabla \boldsymbol{u}^*\right]\rrbracket \boldsymbol{m} + \rho V \llbracket \dot{\boldsymbol{u}}^*\rrbracket = \llbracket \boldsymbol{S}_A^*\rrbracket \boldsymbol{m}, \tag{13.20}$$

$$\partial B_2: \quad \left(\frac{d}{dt}\llbracket \mathbb{G}_0\left[\nabla \boldsymbol{u}^*\right]\rrbracket\right)\boldsymbol{m} + \rho V \llbracket \ddot{\boldsymbol{u}}^*\rrbracket = \llbracket \dot{\boldsymbol{S}}_A^*\rrbracket \boldsymbol{m} + V \llbracket \boldsymbol{b}\rrbracket. \tag{13.21}$$

Note that homogeneous initial conditions are considered in Eq. (13.17), likewise to the original viscoelastic problem. We moreover assume that shock or acceleration fronts in the auxiliary elastic problem do occur at the same wave fronts ∂B_1 and ∂B_2 as in the original viscoelastic problem. This assumption is backed by the fact that the direction and the speed of propagation of wave fronts is dictated by the initial elasticity of the viscoelastic materials, see Herrera and Gurtin [18] and Fisher and Gurtin [19] for a corresponding elastic-viscoelastic correspondence principle, see also Leitman and Fisher [4].

For later use we note that under rather mild conditions, among them the symmetry and definiteness of the initial tensor of elasticity $\mathbb{G}_0$, it can be assumed that the completely homogeneous version of the elastic relations in Eqs. (13.16) – (13.21), namely

$$\operatorname{div}\left(\mathbb{G}_0\left[\nabla \boldsymbol{y}\right]\right) - \rho \ddot{\boldsymbol{y}} = \boldsymbol{0}, \tag{13.22}$$

$$t = 0: \quad \boldsymbol{y} = \boldsymbol{0}, \ \dot{\boldsymbol{y}} = \boldsymbol{0}, \tag{13.23}$$

$$\partial B_u : \quad \boldsymbol{y} = \boldsymbol{0}, \tag{13.24}$$

$$\partial B_S : \quad (\mathbb{G}_0\,[\nabla \boldsymbol{y}])\,\boldsymbol{n} = \boldsymbol{0}, \tag{13.25}$$

$$\partial B_1 : \quad [\![\mathbb{G}_0\,[\nabla \boldsymbol{y}]]\!]\,\boldsymbol{m} + \rho V[\![\dot{\boldsymbol{y}}]\!] = \boldsymbol{0}, \tag{13.26}$$

$$\partial B_2 : \quad \left(\frac{d}{dt}[\![\mathbb{G}_0\,[\nabla \boldsymbol{y}]]\!]\right)\boldsymbol{m} + \rho V[\![\ddot{\boldsymbol{y}}]\!] = \boldsymbol{0}, \tag{13.27}$$

has a vanishing displacement as its only solution,

$$\boldsymbol{y} = \boldsymbol{0}. \tag{13.28}$$

For a thorough discussion of the uniqueness of the mixed initial boundary value problem of the linear theory of elasticity, from which Eq. (13.28) follows, see e.g. Gurtin [3].

13.3 An Equivalence Problem and its Solution

We now seek for an actuation stress $\boldsymbol{S}_A^*$ acting upon the auxiliary elastic problem in Eqs. (13.16) – (13.21), such that the displacement fields $\boldsymbol{u}$ of the original viscoelastic problem and $\boldsymbol{u}^*$ of the auxiliary problem are equivalent:

$$\boldsymbol{u} = \boldsymbol{u}^*. \tag{13.29}$$

For a solution of this equivalence problem, we subtract the displacement based formulation of the original viscoelastic problem, Eqs. (13.9) – (13.14) with $\boldsymbol{S}_A = \boldsymbol{0}$, from the displacement based formulation of the auxiliary elastic problem, Eqs. (13.16) – (13.21). Setting $\boldsymbol{u} - \boldsymbol{u}^* = \boldsymbol{y}$, we eventually enforce the right hand sides of the resulting set of equations to vanish, such that $\boldsymbol{u} - \boldsymbol{u}^* = \boldsymbol{y} = \boldsymbol{0}$, according to the uniqueness formulation stated in Eqs. (13.22) – (13.28). This gives

$$\mathrm{div}\boldsymbol{S}_A^* = -\mathrm{div}\left(\int_0^t \dot{\mathbb{G}}(s)\,[\nabla \boldsymbol{u}(t-s)]\,ds\right), \tag{13.30}$$

$$\partial B_S : \quad \boldsymbol{S}_A^*\boldsymbol{n} = -\left(\int_0^t \dot{\mathbb{G}}(s)\,[\nabla \boldsymbol{u}(t-s)]\,ds\right)\boldsymbol{n}, \tag{13.31}$$

$$\partial B_1: \quad [\![\boldsymbol{S}_A^*]\!]\boldsymbol{m} = -[\![\int_0^t \dot{\mathbb{G}}(s)\,[\nabla\boldsymbol{u}(t-s)]\,ds]\!]\boldsymbol{m}, \qquad (13.32)$$

$$\partial B_2: \quad [\![\dot{\boldsymbol{S}}_A^*]\!]\boldsymbol{m} = -\left(\frac{d}{dt}[\![\int_0^t \dot{\mathbb{G}}(s)\,[\nabla\boldsymbol{u}(t-s)]\,ds]\!]\right)\boldsymbol{m}. \qquad (13.33)$$

Obviously, Eqs. (13.30) – (13.33) are satisfied when we set

$$\boldsymbol{S}_A^* = -\int_0^t \dot{\mathbb{G}}(s)\,[\nabla\boldsymbol{u}(t-s)]\,ds = \mathbb{G}_0\,[\nabla\boldsymbol{u}] - \boldsymbol{S}, \qquad (13.34)$$

cf. the constitutive relation in Eq. (13.2). The result given in Eq. (13.34) can be evaluated directly in case the displacement $\boldsymbol{u}$ and the stress $\boldsymbol{S}$ in the original viscoelastic problem are known. Then, the actuation stress $\boldsymbol{S}_A^*$ according to Eq. (13.34) enforces equivalence between the displacement $\boldsymbol{u}^*$ of the auxiliary elastic problem and the displacement $\boldsymbol{u}$ of the original viscoelastic problem. This coincidence will be exemplified in the subsequent one-dimensional (1D) example. Before, we note that the stress $\boldsymbol{S}$ in the original viscoelastic problem and the stress $\boldsymbol{S}^*$ in the auxiliary elastic problem are equal, too. This follows simply by applying the constitutive relation in Eq. (13.2) to the elastic problem, which gives $\boldsymbol{S}_A^* = \mathbb{G}_0\,[\nabla\boldsymbol{u}^*] - \boldsymbol{S}^*$. Comparing to Eq. (13.34), it follows that

$$\boldsymbol{S}^* = \boldsymbol{S}, \qquad (13.35)$$

when Eq. (13.29) holds. A complete analogy between the original viscoelastic and the auxiliary linear elastic problem has thus been obtained. Concerning the presence of singular waves, note that satisfaction of the relations of jump across the wave fronts, Eq. (13.32) and (13.33), is immediately guaranteed by Eq. (13.34).

13.4 1D Shock Wave Propagating in a Semi-Infinite Half-Space or Rod

The following one-dimensional (1D) example is considered: As the original problem, we study the uni-axial deformation of a viscoelastic half-space under the action of a suddenly applied tensile surface traction of the Heaviside type at $x = 0$, i.e. the stress intensity is maintained constant after its application at time $t = 0$. In its mathematical formulation, this problem coincides with the wave propagation in a slender viscoelastic semi-infinite rod under a suddenly applied tensile force at its end, see e.g. Kolsky [20]. A uni-axial shock wave propagates into the half-space (or semi-infinite rod) in this problem. Our goal is to find a spatial distribution of actuation

stresses such that the displacement of an auxiliary purely elastic half-space coincides with the shock wave produced in the viscoelastic half-space due to the suddenly applied surface traction. We particularly consider a half-space made of a viscoelastic Maxwell-type material. In a uni-axially deforming Maxwell-type material, the scalar 1D relaxation function, which replaces the tensorial relaxation function $\mathbb{G}(t)$ from above, see Eq. (13.2), can be formulated as

$$Y(t) = Y_0 e^{-\frac{t}{\tau}}, \tag{13.36}$$

where Y_0 denotes an (effective) Young's modulus, and the relaxation time of the Maxwell-type material is $\tau = (Y_0\mu)^{-1}$, see Leitman and Fisher [4], who used the parameter $\nu = \mu^{-1}$. The viscosity parameter μ vanishes for a purely elastic material. The Heaviside-type tensile surface traction suddenly applied in $t = 0$ is

$$x = 0: \ S_{xx} \equiv \sigma = \sigma_0 H(t), \tag{13.37}$$

where the axial normal stress component is shortly written as σ, and σ_0 is the intensity of the suddenly applied surface traction. The Heaviside function is abbreviated by $H(t)$. The original viscoelastic problem under consideration is complementary to the problem of a suddenly applied axial surface velocity, see Lee and Kanter [21], who obtained an analytic representation of the respective stress field by means of the Laplace transform technique, see e.g. Churchill [22]. The problem of the stress propagation in a Maxwell-type viscoelastic rod under the action of a box-type impulsive load at its end was solved by Irschik, Belyaev and Raschl [14], who utilized Green's function representation together with the Laplace transform technique. This analytic solution was considered in [14] for a successful comparison with the stress outcome of a numerical technique based on an eigenstrain analogy. Recently, the following analytic formulation for the axial displacement $u_x \equiv u$ of the viscoelastic shock wave due to the surface traction in Eq. (13.37) was presented by Irschik and Krommer [16], who for their derivation utilized symbolic computation using Maple[1] in the framework of the Laplace transform technique:

$$u = \frac{\sigma_0}{Y_0} c \int_0^t ((s-t)\mu Y_0 - 1) H\left(\frac{cs - x}{c}\right) e^{-\frac{s\mu Y_0}{2}} I_0\left(\frac{\sqrt{c^2 s^2 - x^2}\mu Y_0}{2c}\right) ds, \tag{13.38}$$

see [16] for details of computation. The shock wave front to be observed in Eq. (13.38) travels with the elastic speed of propagation

$$V = c = \sqrt{\frac{Y_0}{\rho}}.$$

No further singular fronts are present in the semi-infinite half-space under the action of the suddenly applied surface traction in Eq. (13.37). In Eq. (13.38), I_0 denotes

---

[1] Maple is a trademark of Waterloo Maple Inc.

the modified Bessel function of first kind. The viscoelastic displacement u is shown in Fig. 13.1 as a function of the axial coordinate x for three time instants, while Fig. 13.2 shows the stress distributions σ, see Irschik and Krommer [16] for the corresponding analytic expression, which also involves the modified Bessel function I_1. In Figs. 13.1 and 13.2, and in the subsequent figures, consistent dimensions are presumed, where the artificial input parameters $\sigma_0 = 1$, $Y_0 = 1.5$, $c = 1$ and $\mu = 2$ are considered; a different set was used for presentation in [16]. Results are depicted for three time-instants: $t = 0.5$ (dash-dotted line), $t = 1.5$ (dashed line) and $t = 2.5$ (solid line). Setting $\mu = 0$ gives the elastic counterparts to Figs. 13.1 and 13.2, where Fig. 13.3 shows the respective elastic displacements, which we denote as u_{tel}, the index t referring to the action of the surface traction σ_0, and the corresponding elastic stresses σ_{tel} are depicted in Fig. 13.4.

The equivalence problem formulated in the preceding section requires the total elastic displacement

$$u^* = u_{\mathrm{tel}} + u_{\mathrm{ael}} \tag{13.39}$$

to be equal to the viscoelastic displacement u in Eq. (13.38), see Eq. (13.29), where u_{ael} is the elastic displacement due to the actuation stress stated in Eq. (13.34) for the 3D case. In the present 1D example, the latter relation reduces to

$$S^*_{Axx} \equiv \sigma^*_A = Y_0 \frac{\partial u}{\partial x} - \sigma, \tag{13.40}$$
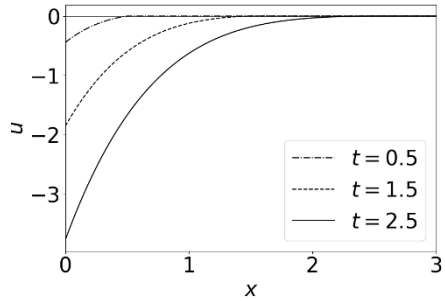
Fig. 13.1 Viscoelastic displacements u due to σ_0.
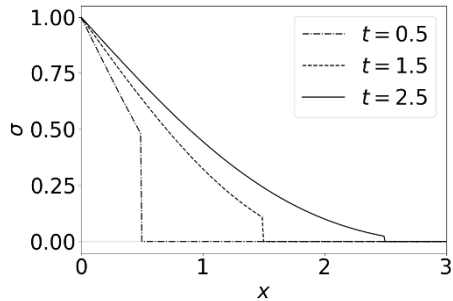
Fig. 13.2 Viscoelastic stresses σ due to σ_0.

Fig. 13.3 Elastic displacements u_{tel} due to σ_0.
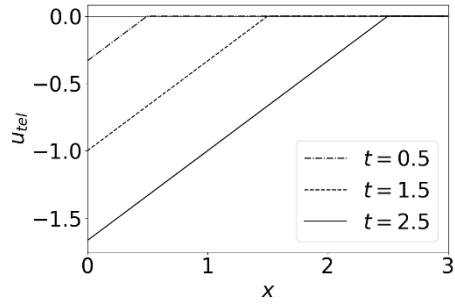
Fig. 13.4 Elastic stresses σ_{tel} due to σ_0.
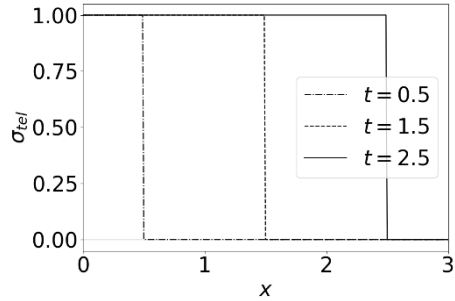
where σ_A^* denotes the axial actuation stress in the elastic half-space. For the sake of brevity, we here check the validity of Eq. (13.40) in the Laplace-domain. Using u from Eq. (13.38) and the corresponding formulation for σ stated in [16], the Laplace transform of σ_A^* according to Eq. (13.40) becomes

$$\mathcal{L}\left\{\sigma_A^*\right\} = \sigma_0 \frac{\mu Y_0}{p^2} e^{-\frac{x}{c}\sqrt{p}\sqrt{\mu Y_0 + p}}, \tag{13.41}$$

where p denotes the coordinate in the Laplace domain. For completeness, we note the Laplace transform of the viscoelastic stress σ:

$$\mathcal{L}\left\{\sigma\right\} = \sigma_0 \frac{1}{p} e^{-\frac{x}{c}\sqrt{p}\sqrt{\mu Y_0 + p}}. \tag{13.42}$$

The time-domain representation of σ_A^* is depicted in Fig. 13.5 for the set of parameters under consideration.

Setting $b = 0$ and $\hat{s} = 0$, the Laplace transform of the actuation stress σ_A^*, see Eq. (13.41) is introduced into the Laplace transform of the 1D version of the displacement-based elastic formulation in Eqs. (13.16) – (13.21), which yields the following expression for the Laplace transform of the elastic displacement u_{ael} due to σ_A^*:

$$\mathcal{L}\left\{u_{\text{ael}}\right\} = \frac{\sigma_0}{Y_0}\frac{c}{p^2}e^{-\frac{px}{c}} - \frac{\sigma_0}{Y_0}\left(e^{-\frac{x}{c}\sqrt{p}\sqrt{\mu Y_0 + p}}\right)\frac{c}{p^{5/2}}\sqrt{\mu Y_0 + p}. \tag{13.43}$$

Fig. 13.5 Actuation stress σ_A^*
necessary for equivalence.
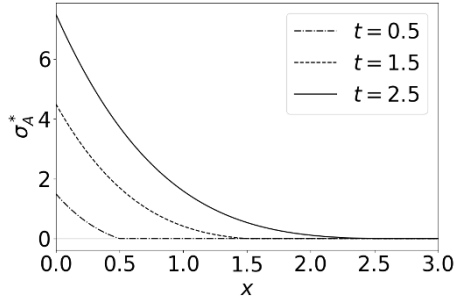
Now, the second part on the right hand side of Eq. (13.43) is the Laplace transform
of the relation for u stated in Eq. (13.38), and the first part is the Laplace transform
of $(-u_{\text{tel}})$, following from the second part by setting $\mu = 0$. Exemplarily, this proves
that there is

$$u^* = u_{\text{tel}} + u_{\text{ael}} = u.$$

The time domain representation of u_{ael} is shown in Fig. 13.6, compare also
Figs. 13.1 and 13.3. Again using symbolic computation by Maple, the Laplace
transform of the stress σ_{ael} due to σ_A^*, see Eq. (13.41), is obtained as

$$\mathcal{L}\{\sigma_{\text{ael}}\} = \sigma_0 \frac{1}{p} e^{-\frac{x}{c}\sqrt{p}\sqrt{\mu Y_0 + p}} - \sigma_0 \frac{1}{p} e^{-\frac{x}{c}p}. \qquad (13.44)$$

The first part on the right hand side of Eq. (13.44) is the Laplace transform of the
stress σ, see Eq. (13.42), and the second part is the Laplace transform of $(-\sigma_{\text{tel}})$,
following from the first part by setting $\mu = 0$. Hence, the total stress in the elastic
auxiliary problem is equal to the stress in the original viscoelastic one,

$$\sigma^* = \sigma_{\text{tel}} + \sigma_{\text{ael}} = \sigma,$$

as this should be according to Eq. (13.35). The time domain representation of σ_{ael} is
shown in Fig. 13.7, compare also Figs. 13.2 and 13.4. Satisfaction of the relations of
jump across the shock front is checked by using symbolic computation. The presented
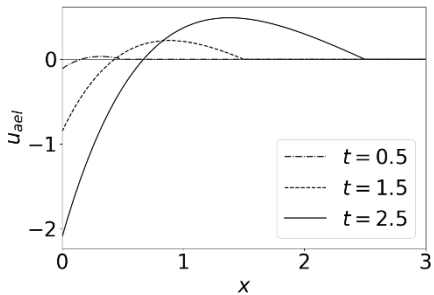
Fig. 13.6 Displacement u_{ael}
due to σ_A^*.

Fig. 13.7 Stress σ_{ael} due to σ_A^*.
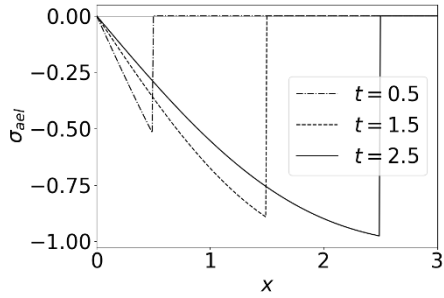
1D study gives evidence for the appropriateness of the 3D solution of the equivalence problem at hand, Eq. (13.34).

References

[1] Mach E (1902) Die Ähnlichkeit und die Analogie als Leitmotiv der Forschung. Annalen der Naturphilosophie **1**(1):5–14

[2] Lurie AI (2005) Theory of Elasticity (translated from Russian by A.K. Belyaev). Springer, Berlin-Heidelberg

[3] Gurtin ME (1972) The linear theory of elasticity. In: Flügge S (ed) Encyclopedia of Physics, vol VIa/2, Springer, Berlin, pp 1–296

[4] Leitman MJ, Fisher GMC (1973) The linear theory of viscoelasticity. In: Flügge S (ed) Encyclopedia of Physics, vol VIa/3, Springer, Berlin, pp 1–124

[5] Parkus H (1959) Instationäre Wärmespannungen. Springer, Vienna

[6] Parkus H (1976) Thermoelasticity, 2nd edn. Springer, Vienna

[7] Carlson DE (1972) Linear thermoelasticity. In: Flügge S (ed) Encyclopedia of Physics, vol VIa/2, Springer, Berlin, pp 297–345

[8] Fung YC, Tong P, Chen X (2017) Classical and Computational Solid Mechanics, 2nd edn. World Scientific, New Jersey

[9] Haddad YM (2000) Mechanical Behaviour of Engineering Materials, vol 2: Dynamic Loading and Intelligent Material Systems. Springer, Dordrecht

[10] Irschik H, Ziegler F (1988) Dynamics of linear elastic structures with selfstress: A unified treatment for linear and nonlinear problems. ZAMM - Journal of Applied Mathematics and Mechanics / Zeitschrift für Angewandte Mathematik und Mechanik **68**(6):199–205

[11] Irschik H, Ziegler F (1995) Dynamic Processes in Structural Thermo-Viscoplasticity. Applied Mechanics Reviews **48**(6):301–316

[12] Irschik H, Ziegler F (1994) Spherical elastic-viscoplastic waves. ZAMM - Journal of Applied Mathematics and Mechanics / Zeitschrift für Angewandte Mathematik und Mechanik **74**(4):T176–T179

[13] Ziegler F, Irschik H, Holl H (1995) Spherical elastic-plastic waves. Journal of Vibration and Control **1**(3):345–360

[14] Irschik H, Belyaev AK, Raschl P (1997) Eigenstrain-based algorithm for viscoelastic uniaxial wave propagation due to impact. In: Ravani B (ed) Proc. Design Engrg. Techn. Conf., Sacramento, ASME, paper No. DETC97/VIB-3927

[15] Krommer M, Pechstein A, Irschik H (2023) Computation of eigenstrains for static shape control of arbitrarily shaped sub-domains of force-loaded elastic bodies. In: Altenbach H, Irschik H, Porubov AV (eds) Progress in Continuum Mechanics, Advanced Structured Materials, Springer Nature, Cham

[16] Irschik H, Krommer M (Early Access) Dynamic displacement tracking in viscoelastic solids by actuation stresses: One-dimensional analytic example involving shock waves. Bulletin of the Polish Academy of Sciences: Technical Sciences **71**(3):e144,616

[17] Irschik H, Brandl A (2019) On control of structural displacements by eigenstrains in the presence of singular waves. In: Altenbach H, Irschik H, Matveenko VP (eds) Contributions to Advanced Dynamics and Continuum Mechanics, Advanced Structured Materials, Springer International Publishing, Cham, pp 95–109

[18] Herrera I, Gurtin ME (1965) A correspondence principle for viscoelastic wave propagation. Quarterly of Applied Mathematics **22**(4):360–364

[19] Fisher GMC, Gurtin ME (1965) Wave propagation in the linear theory of viscoelasticity. Quarterly of Applied Mathematics **23**(3):257–263

[20] Kolsky H (1953) Stress Waves in Solids. Clarendon Press, Oxford

[21] Lee EH, Kanter I (2004) Wave Propagation in Finite Rods of Viscoelastic Material. Journal of Applied Physics **24**(9):1115–1122

[22] Churchill RV (1972) Operational Mathematics, 3rd edn. McGraw-Hill, New York

Chapter 14

Influence Tensors for the Analytical Mechanics of Anisotropic Eigenstressed Composites with Inclusions of Various Shapes and Orientations

Nabor Jiménez Segura, Bernhard L.A. Pichler, and Christian Hellmich

Abstract The Mori-Tanaka-Benveniste scheme is very popular for the homogenization of the elastic stiffness of microheterogeneous composites consisting of one matrix phase and any number of inclusion phases. In addition, the scheme allows for homogenization of eigenstresses/eigenstrains, e.g. in the fields of poroelasticity, thermoelasticity, drying shrinkage, and elastoplasticity. Still, the Mori-Tanaka-Benveniste scheme cannot appropriately represent matrix-inclusion composites with non-aligned ellipsoidal inclusion phases, because

(i)   the respective homogenized stiffness estimate becomes non-symmetrical, and
(ii)   the eigenstrain influence tensors do not satisfy the elastic reciprocal theorem.

This problem has been recently solved by direct symmetrization of the homogenized Mori-Tanaka-Benveniste stiffness estimate, with corresponding modification of the matrix strains leading to improved macro-to-micro strain concentration tensor estimates. The present contribution extends these recent progress towards eigenstressed media, in terms of novel estimates for microscopic eigenstress-to-strain influence tensors which are

(i)   kinematically compatible, in the sense of satisfying the strain average rule,
(ii)   statistically admissible, in the sense that the stress average rule delivers the same macroscopic stress state as Levin's theorem, and
(iii)   energetically consistent, in the sense of satisfying the elastic reciprocal theorem.

Nabor Jiménez Segura · Bernhard L.A. Pichler · Christian Hellmich
Institute for Mechanics of Materials and Structures, TU Wien, Austria,
e-mail: nabor.segura@tuwien.ac.at,bernhard.pichler@tuwien.ac.at,
christian.hellmich@tuwien.ac.at

Notation: Mathematical Symbols, Abbreviations, and Operators

Variables:

$\mathbf{1}$ = second-order identity tensor

$\mathbb{A}_r$ = average strain concentration tensor of phase r

$\mathbb{A}_r^\infty$ = Eshelby-problem-related strain concentration tensor associated with phase r

$\mathbb{C}_{hom}$ = macroscopic homogenized stiffness tensor

$\mathbb{C}_r$ = microscopic stiffness tensor of phase r

$\mathbb{C}_I$ = stiffness of ellipsoidal inhomogeneity

$\mathbb{C}_M$ = matrix stiffness

$\boldsymbol{E}$ = macroscopic strain acting on the RVE

$\boldsymbol{E}_\infty$ = remote strain imposed on an infinite matrix

f_r = volume fraction of phase r $\left(\frac{V_r}{V_{\text{RVE}}}\right)$

$\boldsymbol{G}_M$ = Green's function of infinite elastic medium with stiffness $\mathbb{C}_M$

$\mathbb{I}$ = symmetric fourth-order identity tensor

$\mathbb{I}^{dev}$ = deviatoric part of $\mathbb{I}$

$\mathbb{I}^{vol}$ = volumetric part of $\mathbb{I}$

k_r = bulk modulus of phase r

$\mathbb{M}$ = fourth-order RVE-to-remote strain conversion tensor

n_I = number of inclusion phases $(n_p - 1)$

n_p = total number of phases

$\mathbb{P}_I^M$ = Hill tensor which accounts for shape and orientation of inclusion phase I

$\mathbb{Q}_{rs}$ = eigenstress-to-strain influence tensor quantifying the effect of eigenstresses in phase s on the strains in phase r

RVE = representative volume element

S_{RVE} = surface of the RVE

$\underline{u}$ = microscopic displacement field

V_r = volume of phase r

V_{RVE} = volume of the RVE

$\mathbb{W}_i$ = base vector of Walpole base

$\underline{x}$ = microscopic position vector

$\underline{y}$ = microscopic position vector in convolution integral formulation

δ_{ij} = Kronecker delta

$\boldsymbol{\varepsilon}$ = microscopic strain tensor field

$\boldsymbol{\varepsilon}_r$ = average microstrain in phase r

μ_r = shear modulus of phase r

$\boldsymbol{\sigma}_r$ = average microstress in phase r

$\boldsymbol{\sigma}_r^E$ = microscopic eigenstress in phase r

$\boldsymbol{\Sigma}$ = macroscopic stress acting on the RVE

$\boldsymbol{\Sigma}_{hom}^E$ = macroscopic homogenized eigenstress

ω = aspect ratio of prolate inclusion

Operators:

^{t} = transpose operator, acting on second-order tensor $\boldsymbol{X}$ as $X_{ij}^t = X_{ji}$ and on fourth-order tensor $\mathbb{X}$ as $X_{ijk\ell}^t = X_{k\ell ij}$; implying the following rules:

$$\boldsymbol{X}^t + \boldsymbol{Y}^t = (\boldsymbol{X} + \boldsymbol{Y})^t \qquad \mathbb{X}^t + \mathbb{Y}^t = (\mathbb{X} + \mathbb{Y})^t$$

$$(\boldsymbol{X} \cdot \boldsymbol{Y})^t = (\boldsymbol{Y}^t \cdot \boldsymbol{X})^t \qquad (\mathbb{X} : \mathbb{Y})^t = (\mathbb{Y}^t : \mathbb{X})^t$$

$$(\boldsymbol{X}^{-1})^t = (\boldsymbol{X}^t)^{-1} \qquad (\mathbb{X}^{-1})^t = (\mathbb{X}^t)^{-1}$$

$\sum_{r=1}^N$ = summation over variable r from 1 to N

$\underline{\nabla}_x^S$ = microscopic symmetric gradient with respect to variable $\underline{x}$

$\cdot$ = dot product or contraction product

$:$ = double contraction product

14.1 Introduction

The current megatrend of defossilizing human activities [1] calls for biologization of the traditional engineering fields, from the integration of plants into buildings [2], to the transformation of building materials towards biological role models [3–5]. Typically, the latter are hierarchically organized, fiber-reinforced materials with anisotropic constituents and a pronounced variability of fiber orientations, see Fig. 14.1a).

In order to integrate such materials into an engineering design process, efficient and reliable mathematical tools for their physical and mechanical behavior are required, and recent years have shown that the theoretical, analytical, and computational framework of continuum micromechanics [7] or composite material mechanics [8] is particularly suitable for the aforementioned design challenge. This field gains superior efficiency from the smart assembly of solutions of matrix-inclusions problems of the Eshelby-Laws type [9, 10]; and it is exactly this characteristic of the approach which calls for continuous theory refinement when it comes to more and more anisotropic and morphologically rich microstructural patterns.

The present contribution deals with an important aspect of the aforementioned refinement, namely the overcoming of certain limitations of one of the most popular, versatile, and successful methods in composite material mechanics: the Mori-Tanaka-Benveniste scheme [11, 12] for materials with matrix-inclusion morphologies. Namely, the Mori-Tanaka method delivers physically senseless, non-symmetrical elasticity tensor estimates whenever one or several of the following conditions are *not* met [13]
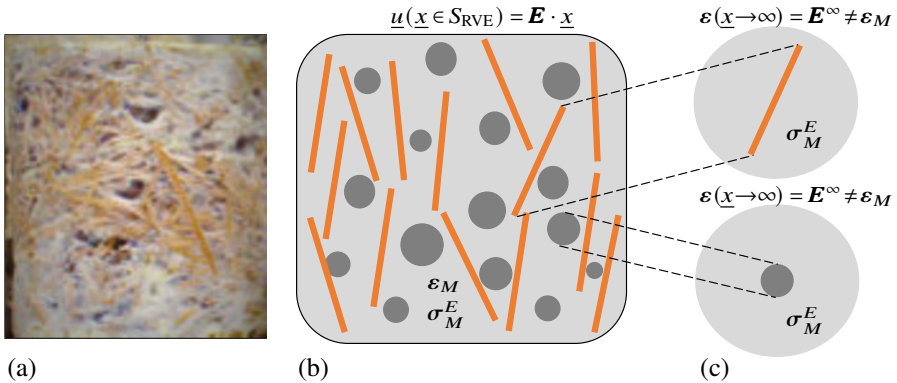
Fig. 14.1: Anisotropic multishape composites with anisotropic constituents undergoing total strains and eigenstresses: (a) photograph of biocomposite, edited from CoE BBE [6], (b) (2D sketch of a 3D) representative volume element (RVE) subjected to homogeneous boundary conditions (microscopic displacements $\underline{u}$ associated with macroscopic strains are imposed onto the RVE boundary denoted by S_{RVE}); the RVE being built up by (c) eigenstressed matrix-inhomogeneity problems with fictitious strains fulfilling stress and strain average rules, Levin's theorem, and the elastic reciprocal theorem.

1. all phases and the overall composite behave isotropically [14, 15];
2. all inclusion phases have the same stiffness [14, 16];
3. all inclusion phases have the same shape and the same orientation [14, 16, 17].

These limitations of the Mori-Tanaka method have been classically circumvented by turning towards the rich collection of tools available in the field of "computational homogenization" [18], requiring, however, much higher computational efforts in terms of CPU and data storage demands. It is only recently that the symmetry violation problem has been solved by a straightforward symmetrization step [14], and it has been even more recently that the implications of this symmetrization steps on the concentration tensors linking macroscopic and microscopic strains in an elastic composites have been understood and analytically represented [13]. We regard this as a major step forward in (semi-)analytical micromechanics, along with a significant widening of its practical application range, in particular so given the enormous technological challenges to be tackled nowadays.

Still, from the viewpoint of material design, not only elastic, but also strength properties are essential; and this motivates the present contribution which covers the interactions of inelastic (e.g. free) eigenstresses and eigenstrains throughout the material microstructure, through complementation of concentration tensors by influence tensors in the sense of the transformation field analyses pioneered by Dvorak and colleagues [19, 20], and later generalized towards more complex morphologies [21, 22]. In fact, the influence tensor concept has been an essential step towards the understanding of the dissipative deformations in hierarchically organized materials, governing their overall strength [23, 24].

Accordingly, this contribution is organized as follows: after a concise summary of theoretical pillars of continuum micromechanics, novel estimates for influence tensors are derived from eigenstressed Eshelby-type matrix-inclusion problems, considering recent results for concentration tensors associated with symmetrized Mori-Tanaka schemes [13]. The contribution is completed by illustrative numerical examples, followed by concluding comments.

14.2 Fundamentals of Continuum Micromechanics and Composite Mechanics

14.2.1 Representative Volume Element, Average Rules, and Scale Transition Relations

In classical continuum mechanics, a finite body is envisioned as the assembly of infinitely many, infinitesimally small material points to which stresses and strains, as well as (macroscopic) material properties are assigned. Physically speaking, these material points relate to small volumes of matter which are much smaller than the overall body or the characteristic length of its loading conditions. In continuum micromechanics or composite mechanics [7, 25], classical (macroscopic) material points are

indeed represented by (microscopically) finite volumes called representative volume elements (RVEs) which need to be much smaller than the scale of (macroscopic) structural loading and much larger than the microstructural features inside the RVE. The latter are represented by homogeneous subdomains called material phases, to which (microscopic) material properties, as well as (microscopic) stresses and strains are assigned.

Microscopically homogeneous geometric boundary conditions allow for derivation of the strain average rule [25]

$$\boldsymbol{E} = \sum_{r=1}^{n_p} f_r \, \boldsymbol{\varepsilon}_r \,, \tag{14.1}$$

with $\boldsymbol{E}$ standing for the macroscopic (linearized) strain tensor, while $\boldsymbol{\varepsilon}_r$ and f_r stand for the (average) microscopic strain tensor of phase r and the volume fraction of this phase; the total number of phases is given by n_p. Combination of the strain average rule with equilibrated forces and their virtual power duals allows for the derivation of the stress average rule [26]

$$\boldsymbol{\Sigma} = \sum_{r=1}^{n_p} f_r \, \boldsymbol{\sigma}_r \,, \tag{14.2}$$

with $\boldsymbol{\Sigma}$ standing for the macroscopic stress tensor, while $\boldsymbol{\sigma}_r$ stands for the (average) microscopic stress tensor of phase r. Stress average rule (14.2) may also be motivated from homogeneous stress boundary conditions [7] or macroscopic testing customs, i.e. tractions and displacements measured at surfaces of material samples in macroscopic material tests [27]. The phases exhibit elastic and inelastic behavior, according to the format

$$\boldsymbol{\sigma}_r = \mathbb{C}_r : \boldsymbol{\varepsilon}_r + \boldsymbol{\sigma}_r^E \,, \qquad \forall r \in \{1, 2, \dots, n_p\} \,, \tag{14.3}$$

with $\mathbb{C}_r$ as the symmetric stiffness tensor of phase r exhibiting eigenstresses $\boldsymbol{\sigma}_r^E$. (14.1) and (14.3) imply the existence of concentration-influence relations of the form [28]

$$\boldsymbol{\varepsilon}_r = \mathbb{A}_r : \boldsymbol{E} + \sum_{s=1}^{n_p} f_s \, \mathbb{Q}_{rs} : \boldsymbol{\sigma}_s^E \,, \qquad \forall r \in \{1, 2, \dots, n_p\} \,, \tag{14.4}$$

with $\mathbb{A}_r$ as the concentration tensor of phase r and $\mathbb{Q}_{rs}$ as influence tensor quantifying the effect of eigenstresses in phase s on the strains in phase r. Insertion of (14.4) into the phase behavior law (14.3) and averaging the resulting phase microstresses according to (14.2) yields the macroscopic stress-strain law

$$\boldsymbol{\Sigma} = \mathbb{C}_{hom} : \boldsymbol{E} + \boldsymbol{\Sigma}_{hom}^E \,, \tag{14.5}$$

whereby the macroscopic (homogenized) symmetric stiffness tensor, which characterizes the behavior of the RVE, and hence of the macroscopic material point, reads as

$$\mathbb{C}_{hom} = \sum_{r=1}^{n_p} f_r \, \mathbb{C}_r : \mathbb{A}_r \,, \tag{14.6}$$

while the macroscopic eigenstress reads as

$$\mathbf{\Sigma}_{hom}^E = \sum_{r=1}^{n_p} \left(f_r \, \boldsymbol{\sigma}_r^E + \sum_{s=1}^{n_p} f_r \, f_s \, \mathbb{C}_r : \mathbb{Q}_{rs} : \boldsymbol{\sigma}_s^E \right). \qquad (14.7)$$

Moreoever, eigenstress averaging is governed by Levin's theorem [7, 29]

$$\mathbf{\Sigma}_{hom}^E = \sum_{r=1}^{n_p} f_r \, \boldsymbol{\sigma}_r^E : \mathbb{A}_r . \qquad (14.8)$$

14.2.2 Characteristics of Strain Concentration and Microeigenstress-to-Microstrain Influence Tensors

Inserting the phase-specific concentration-influence relations according to (14.4) into the strain average rule (14.1) yields

$$\boldsymbol{E} = \sum_{r=1}^{n_p} f_r \left(\mathbb{A}_r : \boldsymbol{E} + \sum_{s=1}^{n_p} f_s \, \mathbb{Q}_{rs} : \boldsymbol{\sigma}_s^E \right). \qquad (14.9)$$

This relation has to hold for the case of vanishing phase eigenstresses, yielding

$$\mathbb{I} = \sum_{r=1}^{n_p} f_r \, \mathbb{A}_r , \qquad (14.10)$$

where $\mathbb{I}$ denotes the symmetric fourth-order identity tensor with components

$$I_{ijkl} = \frac{1}{2} \left[\delta_{ik} \, \delta_{jl} + \delta_{il} \, \delta_{jk} \right].$$

The Kronecker delta δ_{ik} is equal to 1 if $i = k$ and 0 otherwise. Furthermore, the condition (14.9) has to hold for the case of vanishing macroscopic strains and phase eigenstresses except for eigenstresses in a single phase, $\boldsymbol{\sigma}_s^E$, this yields

$$\sum_{r=1}^{n_p} f_r \, \mathbb{Q}_{rs} = 0, \qquad \forall s \in \{1, \dots, n_p\}. \qquad (14.11)$$

The two independent expressions for the homogenized eigenstress, namely Eqs. (14.7) and (14.8) can be identified, yielding

$$\sum_{r=1}^{n_p} \left(f_r \, \boldsymbol{\sigma}_r^E + \sum_{s=1}^{n_p} f_r \, f_s \, \mathbb{C}_r : \mathbb{Q}_{rs} : \boldsymbol{\sigma}_s^E \right) = \sum_{r=1}^{n_p} f_r \, \boldsymbol{\sigma}_r^E : \mathbb{A}_r . \qquad (14.12)$$

Considering RVEs in which only one single phase *s* exhibits an eigenstress and all other material phases are free of eigenstresses, Eq. (14.12) yields the condition

$$\mathbb{A}_s^t - \mathbb{I} = \sum_{r=1}^{n_p} f_r \, \mathbb{C}_r : \mathbb{Q}_{rs}, \qquad \forall s \in \{1, \ldots, n_p\}, \tag{14.13}$$

where $\mathbb{X}^t$ stands for the transpose operator

$$\mathbb{X}^t_{ijkl} = \mathbb{X}_{klij}.$$

Finally, the elastic reciprocal theorem implies an influence tensor transposition rule of the form [19, 22]

$$\mathbb{Q}_{rs} = \mathbb{Q}_{sr}^t \qquad \forall r, s \in \{1, 2, \ldots, n_p\}. \tag{14.14}$$

We will now employ an eigenstressed matrix-inclusion problem of the Eshelby-Laws type, in order to derive novel analytical expressions for the influence tensors – also referring to the concentration tensor expressions derived in [13].

14.3 Derivation of Influence Tensors for Inclusions in Anisotropic Multishape Composites, from Eigenstressed Matrix-Inclusion Problems

The dedicated use of matrix-inclusion problems of the Eshelby-Laws-type for the derivation of RVE-related properties has been one of the most successful strategies in the broad field of micromechanics or multiscale mechanics. We here provide a further extension of this strategy, by resorting to the problem of an eigenstressed inhomogeneity being embedded in an eigenstressed, infinite matrix, see Fig. 14.1 b), c). The homogeneous strains within an ellipsoidal inhomogeneity of stiffness $\mathbb{C}_I$ and eigenstress σ_I^E, being embedded into an infinite matrix with stiffness $\mathbb{C}_M$ and eigenstress σ_M^E can be given in the following analytical format [7, 22]

$$\varepsilon_I = \mathbb{A}_I^\infty : \left[\boldsymbol{E}^\infty - \mathbb{P}_I^M : (\sigma_I^E - \sigma_M^E) \right], \tag{14.15}$$

whereby the remote-to-inhomogeneity strain conversion tensor $\mathbb{A}_I^\infty$ reads as

$$\mathbb{A}_I^\infty = \left[\mathbb{I} + \mathbb{P}_I^M : (\mathbb{C}_I - \mathbb{C}_M) \right]^{-1} \tag{14.16}$$

and $\boldsymbol{E}^\infty$ is the (homogeneous) auxiliary strains imposed infinitely far from the inhomogeneity, see Fig. 14.2. In (14.15) and (14.16), $\mathbb{P}_I^M$ denotes the Hill or morphology tensor, which can be traced back to the Green's function $\boldsymbol{G}_M$ of an infinitely extended elastic medium with stiffness $\mathbb{C}_M$, through [10]

Fig. 14.2 Eshelby problem for the inclusion phase I: The properties of the inhomogeneity are equal to the properties of phase I. The stiffness of the infinite matrix is equal to the stiffness of the matrix phase. The eigenstress in the infinite matrix is equal to the eigenstress of the matrix phase. The auxiliary matrix is subjected to a remote strain $\boldsymbol{E}^\infty$, acting infinitely far from the inhomogeneity.

uniform strains at infinity:
$\varepsilon(\underline{x} \to \infty) = \mathbf{E}^\infty$

infinite 3D matrix:
stiffness: $\mathbb{C}_M$
eigenstress: $\boldsymbol{\sigma}_M^E$

ellipsoidal (3D) eigenstressed inhomogeneity:
stiffness: $\mathbb{C}_I$
eigenstress: $\boldsymbol{\sigma}_I^E$
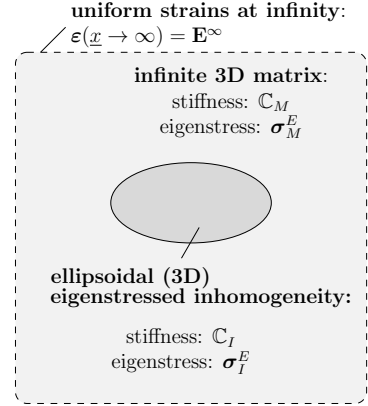
$$\mathbb{P}_I^M = -\int_{V_I} \nabla_x^S \nabla_x^S \boldsymbol{G}_M(\underline{x} - \underline{y}) \ dV(\underline{y}), \qquad (14.17)$$

with V_I standing for the volume of the inhomogeneity and ∇_x^S standing for the symmetrized nabla operator, i.e. the symmetrized gradient with respect to the microscopic location variable. The latter equation allows for the derviation of many different analytical formats of $\mathbb{P}_I^M$, related to different symmetry properties of both inhomogeneity shape and elasticity of the infinite matrix [30, 31].

The landmark works of Mori, Tanaka, and Benveniste [11, 12] have shown the extreme usefulness of deriving estimates for the concentrations tensors $\mathbb{A}_I$ of inclusion phases with an approximately ellipsoidal shape and stiffness $\mathbb{C}_I$ from the remote-to-inhomogeneity strain conversion tensors $\mathbb{A}_I^\infty$ of inhomogeneities with the same stiffness and the same shape; a corresponding general estimation scheme, which preserves symmetry of the overall stiffness tensor irrespective of anisotropy or shape properties of the material phases or the RVE, has been proposed in [13]. Mathematically, this scheme reads as

$$\mathbb{A}_I = \mathbb{A}_I^\infty : \mathbb{M}. \qquad (14.18)$$

with the RVE-to-remote strain conversion tensor $\mathbb{M}$ reading as [13]

$$\mathbb{M} = \left\{ f_M \mathbb{I} + \left(\sum_{I=1}^{n_I} f_I \mathbb{A}_I^\infty \right) - \frac{1}{2} \left[\left(\sum_{I=1}^{n_I} f_I \mathbb{A}_I^\infty \right) : \left(\sum_{I=1}^{n_I} f_I (\mathbb{C}_I - \mathbb{C}_M) : \mathbb{A}_I^\infty \right)^{-1} \right. \right.$$
$$\left. \left. - \left(\sum_{I=1}^{n_I} f_I (\mathbb{C}_I - \mathbb{C}_M) : \mathbb{A}_I^\infty \right)^{-1} : \left(\sum_{I=1}^{n_I} f_I \mathbb{A}_I^{\infty,t} \right) \right] : \left(\sum_{I=1}^{n_I} f_I (\mathbb{C}_I - \mathbb{C}_M) : \mathbb{A}_I^\infty \right) \right\}^{-1},$$
$$(14.19)$$

with $n_I = n_p - 1$ standing for the number of inclusion phases which are, in a composite material, embedded in a contiguous matrix phase.

With the concentration tensor of the inclusions being known, we are left with the determination of the concentration tensor of the matrix strains, which is determined from the concentration tensor average rule (14.10), yielding

$$
\mathbb{A}_M = \frac{1}{f_M}\Big(\mathbb{I} - \sum_{I=1}^{n_I} f_I \mathbb{A}_I\Big). \tag{14.20}
$$

We note that this is a fundamental difference to the Mori-Tanaka-Benveniste scheme where $\mathbb{A}_M$, by definition, is set equal to the symmetric identity tensor of fourth order.

Turning towards the estimation of influence tensors, i.e. the relation between phase eigenstresses and phase strains in the RVE, we identify eigenstresses and strains averaged over inclusion phases with the eigenstresses and strains occurring in an inhomogeneity of the same stiffness, being embedded in an infinite eigenstressed matrix, governed by Eq. (14.15). As regards the matrix phase, indicated by index "M", we specify (14.4) for $r = M$, yielding

$$
\boldsymbol{\varepsilon}_M = \mathbb{A}_M : \boldsymbol{E} + f_M \, \mathbb{Q}_{MM} : \boldsymbol{\sigma}_M^E + \sum_{I=1}^{n_I} f_I \, \mathbb{Q}_{MI} : \boldsymbol{\sigma}_I^E . \tag{14.21}
$$

A link between the auxiliary strain $\boldsymbol{E}^\infty$ and the quantities from the RVE (real macrostrain $\boldsymbol{E}$ and phase eigenstresses $\boldsymbol{\sigma}_j^E$) is established by specification of the strain average rule (14.1) for the considered matrix-inclusion composite,

$$
\boldsymbol{E} = f_M \boldsymbol{\varepsilon}_M + \sum_{I=1}^{n_I} f_I \boldsymbol{\varepsilon}_I, \tag{14.22}
$$

while applying the elastic reciprocal theorem (14.14) to $\mathbb{Q}_{MI}$,

$$
\mathbb{Q}_{MI} = \mathbb{Q}_{IM}^t. \tag{14.23}
$$

Mathematically speaking, insertion of the matrix microstrains $\boldsymbol{\varepsilon}_M$ according to (14.21) and the phase strains in the inclusion phases according to (14.15), into the strain average rule according to (14.22), while considering (14.23), yields

$$
\begin{aligned}
\boldsymbol{E}^\infty = \Big(\sum_{I=1}^{n_I} f_I \mathbb{A}_I^\infty \Big)^{-1} : & \Big[(\mathbb{I} - f_M \mathbb{A}_M) : \boldsymbol{E} - f_M f_M \mathbb{Q}_{MM} : \boldsymbol{\sigma}_M^E \\
& - \sum_{I=1}^{n_I} f_I f_M \mathbb{Q}_{IM}^t : \boldsymbol{\sigma}_I^E + \sum_{I=1}^{n_I} f_I \mathbb{A}_I^\infty : \mathbb{P}_I : (\boldsymbol{\sigma}_I^E - \boldsymbol{\sigma}_M^E) \Big].
\end{aligned} \tag{14.24}
$$

Insertion of (14.24) into (14.15) provides a multilinear form containing concentration and influence tensors associated with the inclusion phase I, namely

$$
\boldsymbol{\varepsilon}_I = \mathbb{A}_I : \boldsymbol{E} + f_M \mathbb{Q}_{IM} : \boldsymbol{\sigma}_M^E + \sum_{J=1}^{n_I} f_J \mathbb{Q}_{IJ} : \boldsymbol{\sigma}_J^E, \quad \forall I \in \{1, 2, \ldots, n_I\}, \tag{14.25}
$$

whereby the concentration and influence tensors are "abbreviations" for the following expressions

$$\forall I \in \{1, 2, \ldots, n_I\}: \qquad \mathbb{A}_I = \mathbb{A}_I^\infty : \big(\sum_{J=1}^{n_I} f_J \mathbb{A}_J^\infty\big)^{-1} : (\mathbb{I} - f_M \mathbb{A}_M), \quad (14.26)$$

$$\forall I \in \{1, 2, \ldots, n_I\}:$$

$$\mathbb{Q}_{IM} = \frac{1}{f_M} \mathbb{A}_I^\infty : \Big(\sum_{J=1}^{n_I} f_J \mathbb{A}_J^\infty\Big)^{-1} : \Big[-f_M^2 \mathbb{Q}_{MM} - \sum_{J=1}^{n_I} f_J \mathbb{A}_J^\infty : \mathbb{P}_J^M \Big]$$

$$+ \frac{1}{f_M} \mathbb{A}_I^\infty : \mathbb{P}_I^M, \qquad\qquad (14.27)$$

$$\forall I, J \in \{1, 2, \ldots, n_I\}, J \neq I:$$

$$\mathbb{Q}_{IJ} = \mathbb{A}_I^\infty : \Big(\sum_{K=1}^{n_I} f_K \mathbb{A}_K^\infty \Big)^{-1} : \Big(-f_M \mathbb{Q}_{JM}^t + \mathbb{A}_J^\infty : \mathbb{P}_J^M \Big), \qquad (14.28)$$

$$\forall I \in \{1, 2, \ldots, n_I\}:$$

$$\mathbb{Q}_{II} = \mathbb{A}_I^\infty : \Big(\sum_{J=1}^{n_I} f_J \mathbb{A}_J^\infty \Big)^{-1} : \Big(-f_M \mathbb{Q}_{IM}^t + \mathbb{A}_I^\infty : \mathbb{P}_I^M \Big) - \frac{1}{f_I} \mathbb{A}_I^\infty : \mathbb{P}_I^M . \;(14.29)$$

These concentration and influence tensor expressions deserve further discussion: Firstly, (14.26) is identical to (14.18), as can be seen from insertion of (14.18) into (14.20), solution of the corresponding result for $\mathbb{M}$, and insertion of the obtained expression for $\mathbb{M}$ back into (14.18). Secondly, all influence tensor expressions depend on the yet unknown influence tensor $\mathbb{Q}_{MM}^t$, which will be derived in the next section. Thirdly, all influence tensors fulfill the elastic reciprocal theorem, as is proved in the next but one subsection.

14.4 Determination of Matrix Influence Tensor $\mathbb{Q}_{MM}$

Specification of (14.13) for the matrix phase of a composite material, $s = M$, consisting of one matrix phase and $n_I = n_p - 1$ inclusion phases, yields

$$\mathbb{A}_M^t - \mathbb{I} = f_M \, \mathbb{C}_M : \mathbb{Q}_{MM} + \sum_{I=1}^{n_I} f_I \, \mathbb{C}_I : \mathbb{Q}_{IM}. \qquad (14.30)$$

Insertion of $\mathbb{Q}_{IM}$ according to Eq. (14.27) into (14.30) yields

$$\mathbb{A}_M^t - \mathbb{I} = f_M \, \mathbb{C}_M : \mathbb{Q}_{MM} + \frac{1}{f_M} \sum_{I=1}^{n_I} f_I \, \mathbb{C}_I : \mathbb{A}_I^\infty : \mathbb{P}_I^M -$$

$$- \Big(\sum_{I=1}^{n_I} f_I \, \mathbb{C}_I : \mathbb{A}_I^\infty \Big) : \Big(\sum_{I=1}^{n_I} f_I \, \mathbb{A}_I^\infty \Big)^{-1} : \Big[\Big(\sum_{i=I}^{n_I} f_I \, \mathbb{A}_I^\infty : \mathbb{P}_I^M \Big) - f_M^2 \, \mathbb{Q}_{MM} \Big].$$

(14.31)

Eventually, solving (14.31) for $\mathbb{Q}_{MM}$ yields the desired result as

$$\mathbb{Q}_{MM} = \frac{1}{f_M^2} \Big[\mathbb{C}_M - \Big(\sum_{I=1}^{n_I} f_I \, \mathbb{C}_I : \mathbb{A}_I^\infty \Big) : \Big(\sum_{I=1}^{n_I} f_I \, \mathbb{A}_I^\infty \Big)^{-1} \Big]^{-1} :$$

$$: \Big[f_M (\mathbb{A}_M^t - \mathbb{I}) - \Big(\sum_{I=1}^{n_I} f_I \, \mathbb{C}_I : \mathbb{A}_I^\infty : \mathbb{P}_I^M \Big) +$$

(14.32)

$$+ \Big(\sum_{I=1}^{n_I} f_I \, \mathbb{C}_I : \mathbb{A}_I^\infty \Big) : \Big(\sum_{I=1}^{n_I} f_I \, \mathbb{A}_I^\infty \Big)^{-1} : \Big(\sum_{I=1}^{n_I} f_I \mathbb{A}_I^\infty : \mathbb{P}_I^M \Big) \Big].$$

14.5 Check of Influence Tensor Expressions

14.5.1 Fulfillment of Influence Tensor Average Rule

In order to check the fulfillment of the influence tensor average rule (14.11), this condition is specified for one matrix phase and n_I inclusion phases. In this context, we start with $s = M$, yielding

$$f_M \mathbb{Q}_{MM} + \sum_{I=1}^{n_I} f_I \mathbb{Q}_{IM} = 0,$$

(14.33)

Insertion of $\mathbb{Q}_{IM}$ from (14.27) into (14.33) yields

$$f_M \mathbb{Q}_{MM} - \sum_{I=1}^{n_I} f_I \frac{1}{f_M} \mathbb{A}_I^\infty : \Big[\Big(\sum_{K=1}^{n_I} f_K \mathbb{A}_K^\infty \Big)^{-1} : \Big(f_M^2 \mathbb{Q}_{MM} - \sum_{K=1}^{n_I} f_K \mathbb{A}_K^\infty : \mathbb{P}_K \Big) + \mathbb{P}_I \Big] = 0.$$

(14.34)

Noting that

$$\Big(\sum_{I=1}^{n_I} f_I \mathbb{A}_I^\infty \Big) : \Big(\sum_{K=1}^{n_I} f_K \mathbb{A}_K^\infty \Big)^{-1} = \mathbb{I},$$

(14.35)

condition (14.34) can be simplified to

$$f_M \mathbb{Q}_{MM} - \Big(f_M \mathbb{Q}_{MM} - \frac{1}{f_M} \sum_{K=1}^{n_I} f_K \mathbb{A}_K^\infty : \mathbb{P}_K \Big) - \frac{1}{f_M} \sum_{I=1}^{n_I} f_I \mathbb{A}_I^\infty : \mathbb{P}_I = 0.$$

(14.36)

Because both K and I are silent indexes in (14.36), is readily seen that the condition (14.36) is fulfilled, which proves that the influence tensor expression (14.27) fulfills the influence tensor average rule (14.33).

Next, we specify (14.11) for a composite consisting of n_I inclusion phases being embedded in one matrix phase M, and choose $s = I$, yielding

$$f_M \mathbb{Q}_{MI} + \sum_{J=1}^{n_I} f_J \mathbb{Q}_{JI} = 0, \qquad \forall I \in \{1, 2, \ldots, n_I\}. \tag{14.37}$$

Insertion of $\mathbb{Q}_{MI}$ from (14.23), of $\mathbb{Q}_{JI}$ according to (14.28), and of $\mathbb{Q}_{II}$ from (14.29) into (14.37) yields

$$f_M \mathbb{Q}_{IM}^t + \sum_{J=1}^{n_J} \left[f_J \mathbb{A}_J^\infty : \left(\sum_{K=1}^{n_I} f_K \mathbb{A}_K^\infty \right)^{-1} : \left(-f_M \mathbb{Q}_{IM}^t + \mathbb{A}_I^\infty : \mathbb{P}_I \right) \right] - \mathbb{A}_I^\infty : \mathbb{P}_I = 0. \tag{14.38}$$

When considering the relation (14.35), it is readily seen that the condition (14.38) is fulfilled, which proves that the influence tensor expressions (14.27) and (14.28) fulfill the influence tensor average rule (14.37).

14.5.2 Consistency of Influence Tensor Expressions with Levin's Theorem

Equating the two alternative expressions for the macroscopic eigenstress, i.e.

(i)   the combination of stress average rule, microscopic material behavior, and concentration-influence relations, leading eventually to (14.7), and

(ii)   Levin' theorem (14.8),

has yielded the condition (14.13); specification of the latter has given access to the influence tensor $\mathbb{Q}_{MM}$.

We are left with checking whether the influence tensor expressions for $\mathbb{Q}_{IM}$ according to (14.27), $\mathbb{Q}_{IJ}$ according to (14.28), and $\mathbb{Q}_{II}$ according to (14.29) fulfill specification of (14.13) for the inclusion phases, namely the condition

$$\mathbb{A}_I^t = \mathbb{I} - f_M \mathbb{C}_M : \mathbb{Q}_{MI} - \sum_{J=1}^{n_I} f_J \mathbb{C}_J : \mathbb{Q}_{JI}, \qquad \forall I = 1, \ldots, n_I. \tag{14.39}$$

Insertion of $\mathbb{Q}_{MI}$ according to (14.23), of $\mathbb{Q}_{JI}$ according to (14.28), and of $\mathbb{Q}_{II}$ according to (14.29) into (14.39) yields

$$\begin{aligned}
\mathbb{A}_I^t = \mathbb{I} - f_m \mathbb{C}_m : \mathbb{Q}_{IM}^t &+ \left(\sum_{J=1}^{n_I} f_i \mathbb{C}_J : \mathbb{A}_J^\infty \right) : \left(\sum_{J=1}^{n_I} f_J \mathbb{A}_J^\infty \right)^{-1} : \\
&- \left(f_M \mathbb{Q}_{IM}^t + \mathbb{A}_I^\infty : \mathbb{P}_I^M \right) \mathbb{C}_I : \mathbb{A}_I^\infty : \mathbb{P}_I^M.
\end{aligned} \tag{14.40}$$

Transposing (14.28), inserting the corresponding result into (14.40), and considering

$$\mathbb{A}_I^\infty : \mathbb{P}_I^M = \mathbb{P}_I : (\mathbb{A}_I^\infty)^t \,, \tag{14.41}$$

yields, after a few simplification steps,

$$\mathbb{A}_I^t = \mathbb{I} - \left(\mathbb{C}_I - \mathbb{C}_M\right) : \mathbb{P}_I : (\mathbb{A}_I^\infty)^t + \left[\mathbb{C}_M - \left(\sum_{J=1}^{n_I} f_J\, \mathbb{C}_J : \mathbb{A}_J^\infty\right) : \left(\sum_{J=1}^{n_I} f_J\, \mathbb{A}_J^\infty\right)^{-1}\right] :$$
$$\left[f_M^2\, \mathbb{Q}_{MM}^t - \sum_{J=1}^{n_I} f_I\, \mathbb{P}_I^M : (\mathbb{A}_I^\infty)^t\right] : \left[\sum_{J=1}^{n_I} f_J\, (\mathbb{A}_J^\infty)^t\right]^{-1} : (\mathbb{A}_I^\infty)^t. \tag{14.42}$$

Solving (14.16) for the Hill tensor, yielding

$$\mathbb{P}_I^M = \left(\mathbb{C}_I - \mathbb{C}_M\right)^{-1} : \left[(\mathbb{A}_I^\infty)^{-T} - \mathbb{I}\right], \tag{14.43}$$

and insertion of this relation, as well as of (14.18) into (14.42), and solving the result for $\mathbb{M}^t$ yields

$$\mathbb{M}^t = \mathbb{I} + \left[\mathbb{C}_M - \left(\sum_{I=1}^{n_I} f_I\, \mathbb{C}_I : \mathbb{A}_I^\infty\right) : \left(\sum_{I=1}^{n_I} f_I\, \mathbb{A}_I^\infty\right)^{-1}\right] :$$
$$\left[f_M^2\, \mathbb{Q}_{MM}^t - \sum_{I=1}^{n_I} f_I\, \mathbb{P}_I : (\mathbb{A}_I^\infty)^t\right] : \left[\sum_{I=1}^{n_I} f_I\, (\mathbb{A}_I^\infty)^t\right]^{-1}. \tag{14.44}$$

Insertion of $\mathbb{M}$ according to (14.19) and of $\mathbb{Q}_{MM} = \mathbb{Q}_{MM}^t$ according to (14.32) into (14.44) yields

$$(1 - f_M)\,\mathbb{I} - \sum_{I=1}^{n_I} f_I\, (\mathbb{A}_I^\infty)^t = \sum_{I=1}^{n_I} f_I \left(\mathbb{C}_I - \mathbb{C}_M\right) : \mathbb{P}_I^M : (\mathbb{A}_I^\infty)^t \,, \tag{14.45}$$

Considering again (14.43) and the obvious rule for volume fractions, reading for the considered matrix-inclusion composites as

$$f_M + \sum_{I=1}^{n_I} f_I = 1 \,, \tag{14.46}$$

(14.45) turns out to be fulfilled. Consequently, the presented expressions for the influence tensors, together with the corresponding expression for the macroscopic eigenstress, are fully consistent with the macroscopic eigenstress expressions according to Levin's theorem.

14.5.3 Consistency of Influence Tensor Expressions with Elastic Reciprocal Theorem

The reciprocity of influence tensor associated with the matrix phase, given through Eq. (14.23), was explicitly used for the derivation of the influence tensors associated with the inclusion phases, given through (14.28) and (14.29). Hence, we are left with showing that the latter fulfill the elastic reciprocal theorem as well, i.e. with showing that

$$\mathbb{Q}_{IJ} = \mathbb{Q}_{JI}^{t}, \qquad \forall I, J \in \{1, \ldots, n_I\}, I \neq J. \tag{14.47}$$

Transposing expression (14.28) yields

$$\mathbb{Q}_{JI}^{t} = -\left[f_M \mathbb{Q}_{IM} + \mathbb{P}_I^M : (\mathbb{A}_I^{\infty})^t \right] : \left(\sum_{K=1}^{n_I} f_K \mathbb{A}_K^{\infty} \right)^{-t} : (\mathbb{A}_J^{\infty})^t. \tag{14.48}$$

Insertion of the expressions for $\mathbb{Q}_{IJ}$ according to (14.28) and for $\mathbb{Q}_{JI}^{t}$ according to (14.48) into (14.47), followed by insertion of the expressions for $\mathbb{Q}_{IM}$ and $\mathbb{Q}_{JM}^{t}$ according to (14.27), while considering (14.41), proves the validity of (14.47):

$$\mathbb{Q}_{IJ} = \mathbb{Q}_{JI}^{t} = \mathbb{A}_I^{\infty} : \left(\sum_{K=1}^{n_I} f_K \mathbb{A}_K^{\infty} \right)^{-1} : \left(f_M^2 \mathbb{Q}_{MM} - \sum_{K=1}^{n_I} f_K \mathbb{A}_K^{\infty} : \mathbb{P}_K^M \right) : \\ \left[\sum_{K=1}^{n_I} f_K (\mathbb{A}_K^{\infty})^t \right]^{-1} : (\mathbb{A}_J^{\infty})^t. \tag{14.49}$$

Similarly, in the case of $J = I$,

$$\mathbb{Q}_{II} = \mathbb{Q}_{II}^{t} = \mathbb{A}_I^{\infty} : \left(\sum_{K=1}^{n_I} f_K \mathbb{A}_K^{\infty} \right)^{-1} : \left(f_M^2 \mathbb{Q}_{MM} - \sum_{K=1}^{n_I} f_K \mathbb{A}_K^{\infty} : \mathbb{P}_K^M \right) : \\ \left[\sum_{K=1}^{n_I} f_K (\mathbb{A}_K^{\infty})^t \right]^{-1} : (\mathbb{A}_I^{\infty})^t - \frac{1}{f_I} \mathbb{A}_I^{\infty} : \mathbb{P}_I^M. \tag{14.50}$$

Finally, the elastic reciprocal theorem referring to the influence of the eigenstress in the matrix phase on its own strain will be treated, i.e.

$$\mathbb{Q}_{MM} = \mathbb{Q}_{MM}^{t}. \tag{14.51}$$

Transposing expression (14.32) yields

$$\mathbb{Q}_{MM}^t = \frac{1}{f_M^2} : \Big\{ f_M (\mathbb{A}_M - \mathbb{I}) - \Big[\sum_{I=1}^{n_I} f_I \, \mathbb{P}_I^M : (\mathbb{A}_I^\infty)^t : \mathbb{C}_I \Big]$$

$$+ \Big[\sum_{I=1}^{n_I} f_I \mathbb{P}_I^M : (\mathbb{A}_I^\infty)^t \Big] : \Big[\sum_{I=1}^{n_I} f_I \, (\mathbb{A}_I^\infty)^t \Big]^{-1} : \Big[\sum_{I=1}^{n_I} f_I \, (\mathbb{A}_I^\infty)^t : \mathbb{C}_I \Big] \Big\} : \quad (14.52)$$

$$: \Big\{ \mathbb{C}_M - \Big[\sum_{I=1}^{n_I} f_I \, (\mathbb{A}_I^\infty)^t \Big]^{-1} : \Big[\sum_{I=1}^{n_I} f_I \, (\mathbb{A}_I^\infty)^t : \mathbb{C}_I \Big] \Big\}^{-1}.$$

Insertion of the expressions for $\mathbb{Q}_{MM}$ according to (14.32) and for $\mathbb{Q}_{MM}^t$ according to (14.52) into (14.51), followed by multiplication of the corresponding result by

$$\Big[\mathbb{C}_M - (\sum_{I=1}^{n_I} f_I \, \mathbb{C}_I : \mathbb{A}_I^\infty) : (\sum_{I=1}^{n_I} f_I \, \mathbb{A}_I^\infty)^{-1} \Big]$$

from the left, and by

$$\Big\{ \mathbb{C}_M - \Big[\sum_{I=1}^{n_I} f_I \, (\mathbb{A}_I^\infty)^t \Big]^{-1} : \Big[\sum_{I=1}^{n_I} f_I \, (\mathbb{A}_I^\infty)^t : \mathbb{C}_I \Big] \Big\}$$

from the right, yields, after simplification,

$$\Big[f_M (\mathbb{A}_M^t - \mathbb{I}) - (\sum_{I=1}^{n_I} f_I \, \mathbb{C}_I : \mathbb{A}_I^\infty : \mathbb{P}_I^M) + (\sum_{I=1}^{n_I} f_I \, \mathbb{C}_I : \mathbb{A}_I^\infty) : (\sum_{I=1}^{n_I} f_I \, \mathbb{A}_I^\infty)^{-1} :$$

$$: (\sum_{I=1}^{n_I} f_I \mathbb{A}_I^\infty : \mathbb{P}_I^M) \Big] : \Big\{ \mathbb{C}_M - \Big[\sum_{I=1}^{n_I} f_I \, (\mathbb{A}_I^\infty)^t \Big]^{-1} : \Big[\sum_{I=1}^{n_I} f_I \, (\mathbb{A}_I^\infty)^t : \mathbb{C}_I \Big] \Big\} =$$

$$= \Big[\mathbb{C}_M - (\sum_{I=1}^{n_I} f_I \, \mathbb{C}_I : \mathbb{A}_I^\infty) : (\sum_{I=1}^{n_I} f_I \, \mathbb{A}_I^\infty)^{-1} \Big] : \qquad (14.53)$$

$$: \Big\{ f_M (\mathbb{A}_M - \mathbb{I}) - \Big[\sum_{I=1}^{n_I} f_I \, \mathbb{P}_I^M : (\mathbb{A}_I^\infty)^t : \mathbb{C}_I \Big] + \Big[\sum_{I=1}^{n_I} f_I \mathbb{P}_I^M : (\mathbb{A}_I^\infty)^t \Big] :$$

$$: \Big[\sum_{I=1}^{n_I} f_I \, (\mathbb{A}_I^\infty)^t \Big]^{-1} : \Big[\sum_{I=1}^{n_I} f_I \, (\mathbb{A}_I^\infty)^t : \mathbb{C}_I \Big] \Big\}.$$

Insertion of $\mathbb{A}_M$ and $\mathbb{A}_M^t$, according to (14.20) and its transpose, followed by adequate grouping of terms, yields

$$
(\sum_{I=1}^{n_I} f_I\, \mathbb{C}_I : \mathbb{A}_I^\infty : \mathbb{P}_I^M) : \mathbb{C}_M - [\sum_{I=1}^{n_I} f_I\,(\mathbb{C}_I - \mathbb{C}_M) : \mathbb{P}_I^M : (\mathbb{A}_I^\infty)^t] : [\sum_{I=1}^{n_I} f_I\,(\mathbb{A}_I^\infty)^t]^{-1} :
$$

$$
: [\sum_{I=1}^{n_I} f_I\,(\mathbb{A}_I^\infty)^t : \mathbb{C}_I] - \mathbb{M}^t : [\sum_{I=1}^{n_I} f_I\,(\mathbb{A}_I^\infty)^t : (\mathbb{C}_I - \mathbb{C}_M)] + (1 - f_M)[\sum_{I=1}^{n_I} f_I\,(\mathbb{A}_I^\infty)^t]^{-1} :
$$

$$
: [\sum_{I=1}^{n_I} f_I\,(\mathbb{A}_I^\infty)^t : \mathbb{C}_I] = \mathbb{C}_M : [\sum_{I=1}^{n_I} f_I\,\mathbb{P}_I^M : (\mathbb{A}_I^\infty)^t : \mathbb{C}_I] - (\sum_{I=1}^{n_I} f_I\,\mathbb{C}_I : \mathbb{A}_I^\infty) :
$$

$$
: (\sum_{I=1}^{n_I} f_I\,\mathbb{A}_I^\infty)^{-1} : [\sum_{I=1}^{n_I} f_I\,\mathbb{P}_I^M : (\mathbb{A}_I^\infty)^t : (\mathbb{C}_I - \mathbb{C}_M)] -
$$

$$
- [\sum_{I=1}^{n_I} f_I\,(\mathbb{C}_I - \mathbb{C}_M) : \mathbb{A}_I^\infty] : \mathbb{M} + (1 - f_M)(\sum_{I=1}^{n_I} f_I\,\mathbb{C}_I : \mathbb{A}_I^\infty) : (\sum_{I=1}^{n_I} f_I\,\mathbb{A}_I^\infty)^{-1}.
$$

$$(14.54)$$

Insertion of Eq. (14.43) into Eq. (14.54), and subsequent simplification of the corresponding result yields

$$
\mathbb{M}^t : [\sum_{I=1}^{n_I} f_I\,(\mathbb{A}_I^\infty)^t : (\mathbb{C}_I - \mathbb{C}_M)] = [\sum_{I=1}^{n_I} f_I\,(\mathbb{C}_I - \mathbb{C}_M) : \mathbb{A}_I^\infty] : \mathbb{M}. \qquad (14.55)
$$

Insertion of $\mathbb{M}$ and $\mathbb{M}^t$ according to (14.19) and its transposed, respectively, into Eq. (14.55) yields, under consideration of the tensor property $\mathbb{A} : \mathbb{B}^{-1} = (\mathbb{B} : \mathbb{A}^{-1})^{-1}$,

$$
\Big\{ \frac{1}{2}[\sum_{I=1}^{n_I} f_I\,(\mathbb{A}_I^\infty)^t : (\mathbb{C}_I - \mathbb{C}_M)]^{-1} : [\sum_{I=1}^{n_I} f_I\,(\mathbb{A}_I^\infty)^t] + \frac{1}{2}(\sum_{I=1}^{n_I} f_I\,\mathbb{A}_I^\infty) :
$$

$$
: [\sum_{I=1}^{n_I} f_I\,(\mathbb{A}_I^\infty)^t : (\mathbb{C}_I - \mathbb{C}_M)]^{-1} + f_M [\sum_{I=1}^{n_I} f_I\,(\mathbb{A}_I^\infty)^t : (\mathbb{C}_I - \mathbb{C}_M)]^{-1} \Big\}^{-1} =
$$

$$
= \Big\{ f_M [\sum_{I=1}^{n_I} f_I\,(\mathbb{C}_I - \mathbb{C}_M) : \mathbb{A}_I^\infty]^{-1} + \frac{1}{2}(\sum_{I=1}^{n_I} f_I\,\mathbb{A}_I^\infty) : [\sum_{I=1}^{n_I} f_I\,(\mathbb{C}_I - \mathbb{C}_M) : \mathbb{A}_I^\infty]^{-1} +
$$

$$
+ \frac{1}{2}[\sum_{I=1}^{n_I} f_I\,(\mathbb{C}_I - \mathbb{C}_M) : \mathbb{A}_I^\infty]^{-1} : [\sum_{I=1}^{n_I} f_I\,(\mathbb{A}_I^\infty)^t] \Big\}^{-1}.
$$

$$(14.56)$$

The validity of (14.56), and therefore (14.51), becomes trivial when noting, from (14.16), the following identity

$$
(\mathbb{C}_I - \mathbb{C}_M) : \mathbb{A}_I^\infty = (\mathbb{A}_I^\infty)^t : (\mathbb{C}_I - \mathbb{C}_M) = \left[(\mathbb{C}_I - \mathbb{C}_M)^{-1} + \mathbb{P}_I^M \right]^{-1}. \qquad (14.57)
$$

14.6 Benchmark Examples

The new scheme for influence tensor computations for anisotropic multishape-multiorientation composites, summarized in Table 14.1, is illustrated by two benchmark examples, which have already been used for illustrating concentration tensors preserving symmetry of the homogenized stiffness of anisotropic multishape composites [13]. Both benchmark examples refer to a matrix-inclusion composite with two types of inclusions, one spherical phase (index 1, aspect ratio $\omega_1 = 1$) and one prolate phase (index 2, aspect ratio $\omega_2 = 3$, major axis aligned with the z-direction), see Fig. 14.3 and Table 14.2 for the phase volume fractions.

The benchmark examples differ in terms of the elastic phase properties, being isotropic and transversely isotropic, respectively. Both benchmark examples are problematic from the viewpoint of the classical Mori-Tanaka-Benveniste scheme, because the homogenized composite is neither isotropic, nor do the inclusion phases have the same stiffness, nor do the inclusion phases have the same shape and orientation, see [14, 15, 17] and remarks made in the Introduction section; hence the use of the conversion tensor $\mathbb{M}$ according to (14.19), and of the novel expressions for

Table 14.1: Flowchart for computing influence tensors for matrix and inclusion phases in anisotropic multishape multiorientation composites..

1. Define matrix phase (in terms of elasticity tensor) and inclusion phases (in terms of shape, orientation, elasticity tensor, and volume fractions).

2. Compute the Hill tensors of the inclusion phases $\mathbb{P}_I^M$ and their auxiliary strain concentration tensor from the Eshelby problem $\mathbb{A}_I^\infty$ from Eq. (14.16).

3. Compute the RVE-to-remote strain conversion tensor $\mathbb{M}$ from Eq. (14.19).

4. Compute strain concentration tensors of the inclusion phases and of the matrix, $\mathbb{A}_I$ and $\mathbb{A}_M$, from Eqs. (14.18) and (14.20), respectively; followed by computation of the homogenized stiffness tensor $\mathbb{C}_{hom}$ from Eq. (14.6), and of the homogenized eigenstress Σ_{hom}^E from Eq. (14.8).

5. Compute the influence tensor relating matrix eigenstress to matrix strain, $\mathbb{Q}_{MM}$, from Eq. (14.32).

6. Compute the influence tensors relating matrix eigenstress and strains in inclusions I, $\mathbb{Q}_{IM}$ from Eq. (14.27).

7. Compute the influence tensor relating eigenstress in inclusion I to matrix strain, $\mathbb{Q}_{MI}$, from Eq. (14.23).

8. Compute influence tensor relating eigenstress in inclusion J to strains in inclusion I, $\mathbb{Q}_{IJ}$, with $I \neq J$, from Eq. (14.28).

9. Compute influence tensor relating eigenstress to strain in inclusion I, $\mathbb{Q}_{II}$, from Eq. (14.29).

Fig. 14.3 Benchmark material: matrix-inclusion composite with two types of inclusions, one spherical phase (index 1, aspect ratio $\omega_1 = 1$) and one prolate phase (index 2, aspect ratio $\omega_2 = 3$, major axis aligned with the z-direction), see Table 14.2 for the volume fractions and the isotropic elastic stiffness constants of the three material phases; two-dimensional representation showing qualitative properties of a three-dimensional RVE
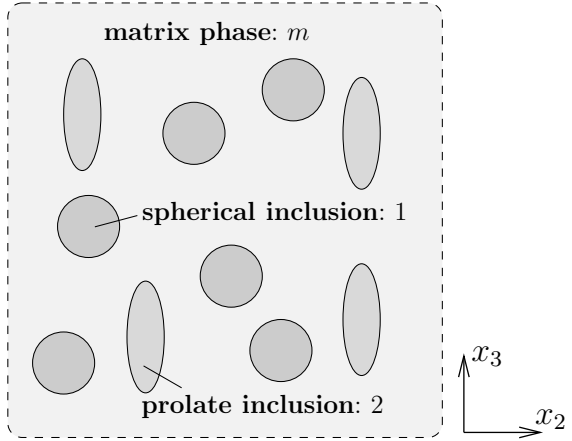
Table 14.2: Volume fractions and isotropic elastic stiffness constants of the three material phases of the composite illustrated in Fig. 14.3.

property	matrix phase	inclusion phase 1	inclusion phase 2
volume fraction	$f_M = 0.60$	$f_1 = 0.25$	$f_2 = 0.15$
bulk modulus	$k_M = 80.63\,\text{GPa}$	$k_1 = 19.29\,\text{GPa}$	$k_2 = 160.0\,\text{GPa}$
shear modulus	$\mu_M = 37.10\,\text{GPa}$	$\mu_1 = 14.30\,\text{GPa}$	$\mu_2 = 79.30\,\text{GPa}$
phase shape	–	spherical	prolate
aspect ratio	–	$\omega_1 = 1$	$\omega_2 = 3$

the influence tensors introduced through Eqs. (14.27), (14.28), (14.29), and (14.32) are mandatory.

14.6.1 Benchmark I: Multishape Composite with Isotropic Phase Properties

The isotropic phase properties in terms of bulk and shear moduli, see Table 14.2, enter the phase elasticity tensors according to

$$\mathbb{C}_j = 3k_j\, \mathbb{I}^{vol} + 2\mu_j\, \mathbb{I}^{dev}, \tag{14.58}$$

where $\mathbb{I}^{vol}$ and $\mathbb{I}^{dev}$ denote the volumetric and deviatoric part of the symmetric fourth-order identity tensor. Their components read as

$$I^{vol}_{ijkl} = \frac{1}{3}\,\delta_{ij}\,\delta_{kl}$$

and

$$I^{dev}_{ijkl} = \frac{1}{2}[\delta_{ik}\,\delta_{jl} + \delta_{il}\,\delta_{jk}] - \frac{1}{3}\,\delta_{ij}\,\delta_{kl};$$

whereby $\delta_{ij} = 1$ for $i = j$, and zero otherwise.

The components of a tensor X_{ijkl} with so-called minor symmetries $X_{ijkl} = X_{jikl}$ and $X_{ijkl} = X_{ijlk}$ can be represented in Kelvin-Mandel-Walpole notation [32–34] as a 6×6 matrix:

$$\mathbb{X} = \begin{pmatrix} X_{1111} & X_{1122} & X_{1133} & \sqrt{2}X_{1123} & \sqrt{2}X_{1131} & \sqrt{2}X_{1112} \\ X_{2211} & X_{2222} & X_{2233} & \sqrt{2}X_{2223} & \sqrt{2}X_{2231} & \sqrt{2}X_{2212} \\ X_{3311} & X_{3322} & X_{3333} & \sqrt{2}X_{3323} & \sqrt{2}X_{3331} & \sqrt{2}X_{3312} \\ \sqrt{2}X_{2311} & \sqrt{2}X_{2322} & \sqrt{2}X_{2333} & 2X_{2323} & 2X_{2331} & 2X_{2312} \\ \sqrt{2}X_{3111} & \sqrt{2}X_{3122} & \sqrt{2}X_{3133} & 2X_{3123} & 2X_{3131} & 2X_{3112} \\ \sqrt{2}X_{1211} & \sqrt{2}X_{1222} & \sqrt{2}X_{1233} & 2X_{1223} & 2X_{1231} & 2X_{1212} \end{pmatrix}. \tag{14.59}$$

As regards both the general derivation of the Hill or morphology tensor [10, 31, 35], and its specification for the spherical and prolate inclusion phases seen in Fig. 14.3, we refer to [13], and start here with directly giving the corresponding results

$$\mathbb{P}^M_1 = \begin{pmatrix} +5.1312 & -1.2845 & -1.2845 & 0 & 0 & 0 \\ -1.2845 & +5.1312 & -1.2845 & 0 & 0 & 0 \\ -1.2845 & -1.2845 & +5.1312 & 0 & 0 & 0 \\ 0 & 0 & 0 & +6.4157 & 0 & 0 \\ 0 & 0 & 0 & 0 & +6.4157 & 0 \\ 0 & 0 & 0 & 0 & 0 & +6.4157 \end{pmatrix} \times 10^{-12}\ \mathrm{Pa}^{-1}, \tag{14.60}$$

$$\mathbb{P}^M_2 = \begin{pmatrix} +6.0532 & -1.9863 & -0.6416 & 0 & 0 & 0 \\ -1.9863 & +6.0532 & -0.6416 & 0 & 0 & 0 \\ -0.6416 & -0.6416 & +2.1187 & 0 & 0 & 0 \\ 0 & 0 & 0 & +6.1880 & 0 & 0 \\ 0 & 0 & 0 & 0 & +6.1880 & 0 \\ 0 & 0 & 0 & 0 & 0 & +8.0395 \end{pmatrix} \times 10^{-12}\ \mathrm{Pa}^{-1}. \tag{14.61}$$

The Eshelby-problem-related strain concentration tensors of the inclusion phases are computed according to (14.16):

$$\mathbb{A}^\infty_1 = \begin{pmatrix} +1.5731 & +0.1596 & +0.1596 & 0 & 0 & 0 \\ +0.1596 & +1.5731 & +0.1596 & 0 & 0 & 0 \\ +0.1596 & +0.1596 & +1.5731 & 0 & 0 & 0 \\ 0 & 0 & 0 & +1.4135 & 0 & 0 \\ 0 & 0 & 0 & 0 & +1.4135 & 0 \\ 0 & 0 & 0 & 0 & 0 & +1.4135 \end{pmatrix}, \tag{14.62}$$

$$
\mathbb{A}_2^\infty =
\begin{pmatrix}
+5.9261 & -0.0315 & -0.5855 & 0 & 0 & 0 \\
-0.0315 & +5.9261 & -0.5855 & 0 & 0 & 0 \\
+0.0547 & +0.0547 & +8.1750 & 0 & 0 & 0 \\
0 & 0 & 0 & +6.5692 & 0 & 0 \\
0 & 0 & 0 & 0 & +6.5692 & 0 \\
0 & 0 & 0 & 0 & 0 & +5.9576
\end{pmatrix}
\times 10^{-1}. \quad (14.63)
$$

The RVE-to-remote strain conversion tensor is computed according to (14.19):

$$
\mathbb{M} =
\begin{pmatrix}
+9.3326 & -0.2574 & -0.1607 & 0 & 0 & 0 \\
-0.2574 & +9.3326 & -0.1607 & 0 & 0 & 0 \\
-0.4982 & -0.4982 & +8.8409 & 0 & 0 & 0 \\
0 & 0 & 0 & +9.5064 & 0 & 0 \\
0 & 0 & 0 & 0 & +9.5064 & 0 \\
0 & 0 & 0 & 0 & 0 & +9.5900
\end{pmatrix}
\times 10^{-1}. \quad (14.64)
$$

The strain concentration tensors of the inclusion and the matrix phases according to (14.18) and (14.20) , respectively:

$$
\mathbb{A}_1 =
\begin{pmatrix}
+1.4560 & +0.1005 & +0.1132 & 0 & 0 & 0 \\
+0.1005 & +1.4560 & +0.1132 & 0 & 0 & 0 \\
+0.0664 & +0.0664 & +1.3856 & 0 & 0 & 0 \\
0 & 0 & 0 & +1.3438 & 0 & 0 \\
0 & 0 & 0 & 0 & +1.3438 & 0 \\
0 & 0 & 0 & 0 & 0 & +1.3556
\end{pmatrix}, \quad (14.65)
$$

$$
\mathbb{A}_2 =
\begin{pmatrix}
+5.5605 & -0.1528 & -0.6123 & 0 & 0 & 0 \\
-0.1528 & +5.5605 & -0.6123 & 0 & 0 & 0 \\
-0.3576 & -0.3576 & +7.2257 & 0 & 0 & 0 \\
0 & 0 & 0 & +6.2449 & 0 & 0 \\
0 & 0 & 0 & 0 & +6.2449 & 0 \\
0 & 0 & 0 & 0 & 0 & +5.7134
\end{pmatrix}
\times 10^{-1}, \quad (14.66)
$$

$$
\mathbb{A}_M =
\begin{pmatrix}
+9.2097 & -0.3804 & -0.3187 & 0 & 0 & 0 \\
-0.3804 & +9.2097 & -0.3187 & 0 & 0 & 0 \\
-0.1874 & -0.1874 & +9.0868 & 0 & 0 & 0 \\
0 & 0 & 0 & +9.5064 & 0 & 0 \\
0 & 0 & 0 & 0 & +9.5064 & 0 \\
0 & 0 & 0 & 0 & 0 & +9.5900
\end{pmatrix}
\times 10^{-1}. \quad (14.67)
$$

The symmetric homogenized stiffness tensor is computed according to (14.6):

$$
\mathbb{C}_{hom} = \begin{pmatrix}
+1.0570 & +0.3972 & +0.3985 & 0 & 0 & 0 \\
+0.3972 & +1.0570 & +0.3985 & 0 & 0 & 0 \\
+0.3985 & +0.3985 & +1.0947 & 0 & 0 & 0 \\
0 & 0 & 0 & +0.6679 & 0 & 0 \\
0 & 0 & 0 & 0 & +0.6679 & 0 \\
0 & 0 & 0 & 0 & 0 & +0.6598
\end{pmatrix} \times 10^{11}\,\mathrm{Pa}.
$$

$$(14.68)$$

As key original contribution of the present chapter, the novel influence tensors are obtained from (14.32), (14.27), (14.28) and (14.23), as

$$
\mathbb{Q}_{MM} = \begin{pmatrix}
+4.2193 & -1.4600 & +0.0729 & 0 & 0 & 0 \\
-1.4600 & +4.2193 & +0.0729 & 0 & 0 & 0 \\
+0.0729 & +0.0729 & +0.0953 & 0 & 0 & 0 \\
0 & 0 & 0 & +4.4005 & 0 & 0 \\
0 & 0 & 0 & 0 & +4.4005 & 0 \\
0 & 0 & 0 & 0 & 0 & +5.6893
\end{pmatrix} \times 10^{-12}\,\mathrm{Pa}^{-1},
$$

$$(14.69)$$

$$
\mathbb{Q}_{1M} = \begin{pmatrix}
-0.7757 & +0.2370 & +0.0240 & 0 & 0 & 0 \\
+0.2370 & -0.7757 & +0.0240 & 0 & 0 & 0 \\
+0.0155 & +0.0155 & -0.2028 & 0 & 0 & 0 \\
0 & 0 & 0 & -0.8375 & 0 & 0 \\
0 & 0 & 0 & 0 & -0.8375 & 0 \\
0 & 0 & 0 & 0 & 0 & -1.0126
\end{pmatrix} \times 10^{-11}\,\mathrm{Pa}^{-1},
$$

$$(14.70)$$

$$
\mathbb{Q}_{2M} = \begin{pmatrix}
-3.9495 & +1.9307 & -0.6924 & 0 & 0 & 0 \\
+1.9307 & -3.9495 & -0.6924 & 0 & 0 & 0 \\
-0.5505 & -0.5505 & +2.9983 & 0 & 0 & 0 \\
0 & 0 & 0 & -3.6430 & 0 & 0 \\
0 & 0 & 0 & 0 & -3.6430 & 0 \\
0 & 0 & 0 & 0 & 0 & -5.8802
\end{pmatrix} \times 10^{-12}\,\mathrm{Pa}^{-1},
$$

$$(14.71)$$

$$
\mathbb{Q}_{11} = \begin{pmatrix}
+2.1014 & -0.5706 & -0.1995 & 0 & 0 & 0 \\
-0.5706 & +2.1014 & -0.1995 & 0 & 0 & 0 \\
-0.1995 & -0.1995 & +1.1228 & 0 & 0 & 0 \\
0 & 0 & 0 & +2.3628 & 0 & 0 \\
0 & 0 & 0 & 0 & +2.3628 & 0 \\
0 & 0 & 0 & 0 & 0 & +2.6719
\end{pmatrix} \times 10^{-11}\,\mathrm{Pa}^{-1},
$$

$$(14.72)$$

$$
\mathbb{Q}_{12} = \begin{pmatrix}
-0.3997 & +0.0031 & +0.2364 & 0 & 0 & 0 \\
+0.0031 & -0.3997 & +0.2364 & 0 & 0 & 0 \\
+0.2704 & +0.2704 & -1.0602 & 0 & 0 & 0 \\
0 & 0 & 0 & -0.5878 & 0 & 0 \\
0 & 0 & 0 & 0 & -0.5878 & 0 \\
0 & 0 & 0 & 0 & 0 & -0.4027
\end{pmatrix} \times 10^{-11}\,\mathrm{Pa}^{-1},
$$

$$(14.73)$$

$$
\mathbb{Q}_{21} = \begin{pmatrix}
-0.3997 & +0.0031 & +0.2704 & 0 & 0 & 0 \\
+0.0031 & -0.3997 & +0.2704 & 0 & 0 & 0 \\
+0.2364 & +0.2364 & -1.0602 & 0 & 0 & 0 \\
0 & 0 & 0 & -0.5878 & 0 & 0 \\
0 & 0 & 0 & 0 & -0.5878 & 0 \\
0 & 0 & 0 & 0 & 0 & -0.4027
\end{pmatrix} \times 10^{-11}\,\mathrm{Pa}^{-1},
$$

(14.74)

$$
\mathbb{Q}_{22} = \begin{pmatrix}
+2.2459 & -0.7774 & -0.1737 & 0 & 0 & 0 \\
-0.7774 & +2.2459 & -0.1737 & 0 & 0 & 0 \\
-0.1737 & -0.1737 & +0.5677 & 0 & 0 & 0 \\
0 & 0 & 0 & +2.4368 & 0 & 0 \\
0 & 0 & 0 & 0 & +2.4368 & 0 \\
0 & 0 & 0 & 0 & 0 & +3.0233
\end{pmatrix} \times 10^{-11}\,\mathrm{Pa}^{-1},
$$

(14.75)

$$
\mathbb{Q}_{M1} = \begin{pmatrix}
-0.7757 & +0.2370 & +0.0155 & 0 & 0 & 0 \\
+0.2370 & -0.7757 & +0.0155 & 0 & 0 & 0 \\
+0.0240 & +0.0240 & -0.2028 & 0 & 0 & 0 \\
0 & 0 & 0 & -0.8375 & 0 & 0 \\
0 & 0 & 0 & 0 & -0.8375 & 0 \\
0 & 0 & 0 & 0 & 0 & -1.0126
\end{pmatrix} \times 10^{-11}\,\mathrm{Pa}^{-1},
$$

(14.76)

$$
\mathbb{Q}_{M2} = \begin{pmatrix}
-3.9495 & +1.9307 & -0.5505 & 0 & 0 & 0 \\
+1.9307 & -3.9495 & -0.5505 & 0 & 0 & 0 \\
-0.6924 & -0.6924 & +2.9983 & 0 & 0 & 0 \\
0 & 0 & 0 & -3.6430 & 0 & 0 \\
0 & 0 & 0 & 0 & -3.6430 & 0 \\
0 & 0 & 0 & 0 & 0 & -5.8802
\end{pmatrix} \times 10^{-12}\,\mathrm{Pa}^{-1}.
$$

(14.77)

The concentration tensors (14.65)–(14.67) and the influence tensors (14.69)–(14.77) fulfill the conditions related to the strain average rule, see (14.10)–(14.11), the homogenized eigenstress, see (14.13), and the elastic reciprocal theorem, see (14.14).

14.6.2 Benchmark II: Multishape Composite with Transversely Isotropic Matrix Phase

In order to show that our method also holds for matrices which are not isotropic, we now consider the matrix to be transversely isotropic, with the anisotropic axis being aligned with the long axis of the prolate inclusion 2 shown in Fig. 14.3. In more detail, we adopt the transversely isotropic properties of zinc, which according to [36] are defined by the following independent component of the elasticity tensor

$$
C_{M,3333} = 73.4\,\mathrm{GPa},
$$
$$
C_{M,1111} = C_{M,2222} = 164.07\,\mathrm{GPa},
$$

$$C_{M,1133} = 33.43\,\text{GPa}, \tag{14.78}$$

$$C_{M,1122} = 49.99\,\text{GPa},$$

$$C_{M,1313} = C_{M,2323} = 38.15\,\text{GPa}.$$

Again referring to [13], the corresponding Hill tensors read as

$$\mathbb{P}_1^M = \begin{pmatrix} +3.7499 & -0.8497 & -1.0623 & 0 & 0 & 0 \\ -0.8497 & +3.7499 & -1.0623 & 0 & 0 & 0 \\ -1.0623 & -1.0623 & +7.5258 & 0 & 0 & 0 \\ 0 & 0 & 0 & +6.2742 & 0 & 0 \\ 0 & 0 & 0 & 0 & +6.2742 & 0 \\ 0 & 0 & 0 & 0 & 0 & +1.4501 \end{pmatrix} \times 10^{-3}\,\text{GPa}^{-1},$$

$$\tag{14.79}$$

$$\mathbb{P}_2^M = \begin{pmatrix} +4.3326 & -1.2311 & -0.4655 & 0 & 0 & 0 \\ -1.2311 & +4.3326 & -0.4655 & 0 & 0 & 0 \\ -0.4655 & -0.4655 & +2.5425 & 0 & 0 & 0 \\ 0 & 0 & 0 & +6.1766 & 0 & 0 \\ 0 & 0 & 0 & 0 & +6.1766 & 0 \\ 0 & 0 & 0 & 0 & 0 & +1.5508 \end{pmatrix} \times 10^{-3}\,\text{GPa}^{-1}.$$

$$\tag{14.80}$$

The RVE-to-remote strain conversion tensor, see (14.19), and the strain concentration tensors, see (14.18) and (14.20) read as

$$\mathbb{M} = \begin{pmatrix} +0.8783 & -0.0049 & -0.0071 & 0 & 0 & 0 \\ -0.0049 & +0.8783 & -0.0071 & 0 & 0 & 0 \\ -0.0022 & -0.0022 & +0.9742 & 0 & 0 & 0 \\ 0 & 0 & 0 & +1.0505 & 0 & 0 \\ 0 & 0 & 0 & 0 & +1.0505 & 0 \\ 0 & 0 & 0 & 0 & 0 & +1.0098 \end{pmatrix}, \tag{14.81}$$

$$\mathbb{A}_1 = \begin{pmatrix} +1.4953 & +0.0398 & +0.0560 & 0 & 0 & 0 \\ +0.0398 & +1.4953 & +0.0560 & 0 & 0 & 0 \\ +0.0008 & +0.0008 & +1.2383 & 0 & 0 & 0 \\ 0 & 0 & 0 & +1.1174 & 0 & 0 \\ 0 & 0 & 0 & 0 & +1.1174 & 0 \\ 0 & 0 & 0 & 0 & 0 & +1.0532 \end{pmatrix}, \tag{14.82}$$

$$\mathbb{A}_2 = \begin{pmatrix} +0.6656 & -0.0422 & -0.0731 & 0 & 0 & 0 \\ -0.0422 & +0.6656 & -0.0731 & 0 & 0 & 0 \\ -0.0514 & -0.0514 & +0.6975 & 0 & 0 & 0 \\ 0 & 0 & 0 & +0.6023 & 0 & 0 \\ 0 & 0 & 0 & 0 & +0.6023 & 0 \\ 0 & 0 & 0 & 0 & 0 & +0.8724 \end{pmatrix}, \tag{14.83}$$

$$
\mathbb{A}_M = \begin{pmatrix}
+0.8772 & -0.0060 & -0.0050 & 0 & 0 & 0 \\
-0.0060 & +0.8771 & -0.0050 & 0 & 0 & 0 \\
+0.0125 & +0.0125 & +0.9763 & 0 & 0 & 0 \\
0 & 0 & 0 & +1.0505 & 0 & 0 \\
0 & 0 & 0 & 0 & +1.0505 & 0 \\
0 & 0 & 0 & 0 & 0 & +1.0098
\end{pmatrix}.
\tag{14.84}
$$

The symmetric homogenized stiffness tensor, see (14.6), reads as

$$
\mathbb{C}_{hom} = \begin{pmatrix}
1.2589 & 0.3819 & 0.2975 & 0 & 0 & 0 \\
0.3819 & 1.2589 & 0.2975 & 0 & 0 & 0 \\
0.2975 & 0.2975 & 0.8037 & 0 & 0 & 0 \\
0 & 0 & 0 & 0.4636 & 0 & 0 \\
0 & 0 & 0 & 0 & 0.4636 & 0 \\
0 & 0 & 0 & 0 & 0 & 0.6284
\end{pmatrix} \times 10^2 \, \text{GPa}.
\tag{14.85}
$$

Finally, the novel influence tensors obtained from (14.32), (14.27), (14.28) and (14.23), as

$$
\mathbb{Q}_{MM} = \begin{pmatrix}
+3.3097 & -0.7358 & -1.2702 & 0 & 0 & 0 \\
-0.7358 & +3.3097 & -1.2702 & 0 & 0 & 0 \\
-1.2702 & -1.2702 & +9.0801 & 0 & 0 & 0 \\
0 & 0 & 0 & +3.8894 & 0 & 0 \\
0 & 0 & 0 & 0 & +3.8894 & 0 \\
0 & 0 & 0 & 0 & 0 & +0.8903
\end{pmatrix} \times 10^{-12} \, \text{Pa}^{-1},
\tag{14.86}
$$

$$
\mathbb{Q}_{1M} = \begin{pmatrix}
-0.5824 & +0.1094 & +0.2367 & 0 & 0 & 0 \\
+0.1094 & -5.8242 & +0.2367 & 0 & 0 & 0 \\
+0.2514 & +0.2514 & -1.8905 & 0 & 0 & 0 \\
0 & 0 & 0 & -0.7096 & 0 & 0 \\
0 & 0 & 0 & 0 & -0.7096 & 0 \\
0 & 0 & 0 & 0 & 0 & -0.1369
\end{pmatrix} \times 10^{-11} \, \text{Pa}^{-1},
\tag{14.87}
$$

$$
\mathbb{Q}_{2M} = \begin{pmatrix}
-3.5318 & +1.1206 & +1.1351 & 0 & 0 & 0 \\
+1.1206 & -3.5318 & +1.1351 & 0 & 0 & 0 \\
+0.8910 & +0.8910 & -4.8123 & 0 & 0 & 0 \\
0 & 0 & 0 & -3.7316 & 0 & 0 \\
0 & 0 & 0 & 0 & -3.7316 & 0 \\
0 & 0 & 0 & 0 & 0 & -1.2791
\end{pmatrix} \times 10^{-12} \, \text{Pa}^{-1},
\tag{14.88}
$$

$$
\mathbb{Q}_{11} = \begin{pmatrix}
+1.6342 & -0.3360 & -0.5701 & 0 & 0 & 0 \\
-0.3360 & +1.6342 & -0.5701 & 0 & 0 & 0 \\
-0.5701 & -0.5701 & +4.3551 & 0 & 0 & 0 \\
0 & 0 & 0 & +1.9391 & 0 & 0 \\
0 & 0 & 0 & 0 & +1.9391 & 0 \\
0 & 0 & 0 & 0 & 0 & +0.4204
\end{pmatrix} \times 10^{-11} \, \text{Pa}^{-1},
\tag{14.89}
$$

$$\mathbb{Q}_{12} = \begin{pmatrix} -3.9390 & +1.2251 & +0.0331 & 0 & 0 & 0 \\ +1.2251 & -3.9390 & +0.0331 & 0 & 0 & 0 \\ -0.5528 & -0.5528 & +3.0346 & 0 & 0 & 0 \\ 0 & 0 & 0 & -3.9371 & 0 & 0 \\ 0 & 0 & 0 & 0 & -3.9371 & 0 \\ 0 & 0 & 0 & 0 & 0 & -1.5293 \end{pmatrix} \times 10^{-12}\,\mathrm{Pa}^{-1},$$

(14.90)

$$\mathbb{Q}_{21} = \begin{pmatrix} -3.9390 & +1.2251 & -0.5528 & 0 & 0 & 0 \\ +1.2251 & -3.9390 & -0.5528 & 0 & 0 & 0 \\ +0.0331 & +0.0331 & +3.0346 & 0 & 0 & 0 \\ 0 & 0 & 0 & -3.9371 & 0 & 0 \\ 0 & 0 & 0 & 0 & -3.9371 & 0 \\ 0 & 0 & 0 & 0 & 0 & -1.5293 \end{pmatrix} \times 10^{-12}\,\mathrm{Pa}^{-1},$$

(14.91)

$$\mathbb{Q}_{22} = \begin{pmatrix} +2.0692 & -0.6524 & -0.3619 & 0 & 0 & 0 \\ -0.6524 & +2.0692 & -0.3619 & 0 & 0 & 0 \\ -0.3619 & -0.3619 & +1.4192 & 0 & 0 & 0 \\ 0 & 0 & 0 & +2.1488 & 0 & 0 \\ 0 & 0 & 0 & 0 & +2.1488 & 0 \\ 0 & 0 & 0 & 0 & 0 & +0.7665 \end{pmatrix} \times 10^{-11}\,\mathrm{Pa}^{-1},$$

(14.92)

$$\mathbb{Q}_{M1} = \begin{pmatrix} -0.5824 & +0.1094 & +0.2514 & 0 & 0 & 0 \\ +0.1094 & -0.5824 & +0.2514 & 0 & 0 & 0 \\ +0.2367 & +0.2367 & -1.8905 & 0 & 0 & 0 \\ 0 & 0 & 0 & -0.7096 & 0 & 0 \\ 0 & 0 & 0 & 0 & -0.7096 & 0 \\ 0 & 0 & 0 & 0 & 0 & -0.1369 \end{pmatrix} \times 10^{-11}\,\mathrm{Pa}^{-1},$$

(14.93)

$$\mathbb{Q}_{M2} = \begin{pmatrix} -3.5318 & +1.1206 & +0.8910 & 0 & 0 & 0 \\ +1.1206 & -3.5318 & +0.8910 & 0 & 0 & 0 \\ +1.1351 & +1.1351 & -4.8123 & 0 & 0 & 0 \\ 0 & 0 & 0 & -3.7316 & 0 & 0 \\ 0 & 0 & 0 & 0 & -3.7316 & 0 \\ 0 & 0 & 0 & 0 & 0 & -1.2791 \end{pmatrix} \times 10^{-12}\,\mathrm{Pa}^{-1}.$$

(14.94)

14.7 Conclusions

A new homogenization scheme for eigenstressed matrix-inclusion composites is proposed; which even holds for anisotropic composites comprising anisotropic inclusion phases of different shapes and orientations, and hence overcoming limitations arising from the traditional assumption of Mori and Tanaka, to assume the average matrix strain to be the average strain in the fictitious matrix of the auxiliary matrix-inhomogeneity problem of the Eshelby-Laws-type. In more detail, we adopt

the eigenstresses of different inhomogeneities as those of eigenstressed inclusion phases in the composite, and the eigenstresses of the fictitious infinite matrix as those of the matrix of composite, while we determine the matrix strains in such a way that key fundaments of continuum micromechanics, such as symmetry of the homogenized stiffness tensor, Levin's theorem, and the elastic reciprocal theorem are fulfilled. This widely extends the application range of eigenstressed Eshelby-problem-based homogenization theory for the realistic representation of anisotropic inelastic composites composed of anisotropic constituents, including the ever increasing set of biogenic and biological materials considered as key players in the ongoing Green Transformation.

References

[1] Schlögl R (2021) Chemical energy storage enables the transformation of fossil energy systems to sustainability. Green Chemistry **23**:251–256

[2] Tudiwer D, Korjenic A (2017) The effect of living wall systems on the thermal resistance of the façade. Energy and Buildings **135**:10–19

[3] Zelaya-Lainez L, Balduzzi G, Lahayne O, Ikeda KN, Raible F, Herzig C, Nischkauer W, Limbeck A, Hellmich C (2021) Jaws of platynereis dumerilii: miniature biogenic structures with hardness properties similar to those of crystalline metals. JOM **73**:2390–2402

[4] Bader TK, Dastoorian F, Ebrahimi G, Unger G, Lahayne O, Hellmich C, Pichler B (2016) Combined ultrasonic-mechanical characterization of orthotropic elastic properties of an unrefined bagasse fiber-polypropylene composite. Composites Part B: Engineering **95**:96–104

[5] McBee RM, Lucht M, Mukhitov N, Richardson M, Srinivasan T, Meng D, Chen H, Kaufman A, Reitman M, Munck C, Schaak D, Voigt C, Wang HH (2021) Engineering living and regenerative fungal–bacterial biocomposite structures. Nature Materials **21**:471–478

[6] Centre of Expertise Biobased Economy (2023) Building on Mycelium. downloaded at https://www.coebbe.nl/projecten/building-on-mycelium/, accessed 11 May 2023

[7] Zaoui A (2002) Continuum micromechanics: survey. Journal of Engineering Mechanics **128**(8):808–816

[8] Hill R (1965) A self-consistent mechanics of composite materials. Journal of the Mechanics and Physics of Solids **13**(4):213–222

[9] Eshelby JD (1957) The determination of the elastic field of an ellipsoidal inclusion, and related problems. Proceedings of the Royal Society of London Series A: Mathematical and Physical Sciences **241**(1226):376–396

[10] Laws N (1977) The determination of stress and strain concentrations at an ellipsoidal inclusion in an anisotropic material. Journal of Elasticity **7**(1):91–97

[11] Mori T, Tanaka K (1973) Average stress in matrix and average elastic energy of materials with misfitting inclusions. Acta Metallurgica **21**(5):571–574

[12] Benveniste Y (1987) A new approach to the application of Mori-Tanaka's theory in composite materials. Mechanics of Materials **6**(2):147–157

[13] Jiménez Segura N, Pichler BLA, Hellmich C (2023) Concentration tensors preserving elastic symmetry of multiphase composites. Mechanics of Materials **178**:104,555

[14] Sevostianov I, Kachanov M (2014) On some controversial issues in effective field approaches to the problem of the overall elastic properties. Mechanics of Materials **69**(1):93–105

[15] Ferrari M (1991) Asymmetry and the high concentration limit of the Mori-Tanaka effective medium theory. Mechanics of Materials **11**(3):251–256

[16] Benveniste Y, Dvorak GJ, Chen T (1991) On diagonal and elastic symmetry of the approximate effective stiffness tensor of heterogeneous media. Journal of the Mechanics and Physics of Solids **39**(7):927–946

[17] Benveniste Y, Dvorak GJ, Chen T (1989) Stress fields in composites with coated inclusions. Mechanics of Materials **7**(4):305–317

[18] Saeb S, Steinmann P, Javili A (2016) Aspects of Computational Homogenization at Finite Deformations: A Unifying Review From Reuss' to Voigt's Bound. Applied Mechanics Reviews **68**(5)

[19] Dvorak GJ, Benveniste Y (1992) On transformation strains and uniform fields in multiphase elastic media. Proceedings of the Royal Society of London Series A: Mathematical and Physical Sciences **437**(1900):291–310

[20] Dvorak GJ, Bahei-El-Din YA, Wafa AM (1994) The modeling of inelastic composite materials with the transformation field analysis. Modelling and Simulation in Materials Science and Engineering **2**(3A):571–586

[21] Michel JC, Suquet P (2003) Nonuniform transformation field analysis. International Journal of Solids and Structures **40**(25):6937–6955

[22] Pichler B, Hellmich C (2010) Estimation of influence tensors for eigenstressed multiphase elastic media with nonaligned inclusion phases of arbitrary ellipsoidal shape. Journal of Engineering Mechanics **136**(8):1043–1053

[23] Chaboche JL, Kanouté P, Roos A (2005) On the capabilities of mean-field approaches for the description of plasticity in metal matrix composites. International Journal of Plasticity **21**(7):1409–1434

[24] Morin C, Vass V, Hellmich C (2017) Micromechanics of elastoplastic porous polycrystals: Theory, algorithm, and application to osteonal bone. International Journal of Plasticity **91**:238–267

[25] Hashin Z (1983) Analysis of composite materials—A survey. Journal of Applied Mechanics **50**(3):481–505

[26] Jiménez Segura N, Pichler BL, Hellmich C (2022) Stress average rule derived through the principle of virtual power. ZAMM - Journal of Applied Mathematics and Mechanics / Zeitschrift für Angewandte Mathematik und Mechanik **102**(9):e202200,091

[27] Hori M, Nemat-Nasser S (1999) On two micromechanics theories for determining micro-macro relations in heterogeneous solids. Mechanics of Materials **31**(10):667–682

[28] Dvorak GJ (2012) Micromechanics of composite materials. Springer Science & Business Media

[29] Levin VM (1967) Thermal expansion coefficient of heterogeneous materials. Mekhanika Tverdogo Tela **2**(1):83–94

[30] Hellmich C, Barthélémy JF, Dormieux L (2004) Mineral-collagen interactions in elasticity of bone ultrastructure – a continuum micromechanics approach. European Journal of Mechanics - A/Solids **23**(5):783–810

[31] Barthélémy JF (2020) Simplified approach to the derivation of the relationship between Hill polarization tensors of transformed problems and applications. International Journal of Engineering Science **154**:103,326

[32] Mandel J (1965) Généralisation de la théorie de plasticité de W.T. Koiter. International Journal of Solids and Structures **1**(3):273–295

[33] Walpole LJ (1984) Fourth-rank tensors of the thirty-two crystal classes: multiplication tables. Proceedings of the Royal Society of London A Mathematical and Physical Sciences **391**(1800):149–179

[34] Helnwein P (2001) Some remarks on the compressed matrix representation of symmetric second-order and fourth-order tensors. Computer Methods in Applied Mechanics and Engineering **190**(22):2753–2770

[35] Parnell WJ (2016) The Eshelby, Hill, moment and concentration tensors for ellipsoidal inhomogeneities in the Newtonian potential problem and linear elastostatics. Journal of Elasticity **125**(2):231–294

[36] Pouya A, Zaoui A (2006) A transformation of elastic boundary value problems with application to anisotropic behavior. International Journal of Solids and Structures **43**(16):4937–4956

Chapter 15

Computation of Eigenstrains for Static Shape Control of Arbitrarily Shaped Sub-Domains of Force-Loaded Elastic Bodies

Michael Krommer, Astrid S. Pechstein, and Hans Irschik

Abstract The present paper is concerned with static shape control of sub-domains of material bodies. Eigenstrains or their corresponding actuation stresses are used as the actuation applied only in the sub-domain. Two problems are of particular interest, strain tracking and displacement tracking of the sub-domain. Exact solutions for the two tracking problems are derived and numerical results computed with the Finite Element method are presented for a plane stress problem for validation.

15.1 Introduction

The notion of shape control was introduced by Haftka and Adelman [1] for computing temperatures in control elements to minimize the overall distortion of large space structures from their original shape. In [1] static shape control refers to the situation, in which external disturbances are associated with fixed deformations or those that are slowly varying in time; in case, external disturbances are transient the problem is denoted as dynamic shape control. For reviews on both, static and dynamic shape control of structures we refer to Irschik [2], Irschik et al. [3] and Irschik and Krommer [4]. In the present paper only static shape control is studied.

In order to control the shape or deformation of a material body, which is under the action of external forces, a proper source of actuation must be available. Besides using forces in addition to the original external forces as the actuation, imposed eigenstrains or their corresponding actuation stresses can be used as well. In the present paper, we only consider the latter as the actuation for static shape control. Actuation stresses and eigenstrains are assumed to represent any possible source of self-stress. Sources of self-stress or *Eigenspannungsquellen* - as they are called in German - have been

Michael Krommer · Astrid S. Pechstein · Hans Irschik
Institute of Technical Mechanics, Johannes Kepler University Linz, Altenberger Str. 69, 4040 Linz, Austria,
e-mail: michael.krommer@jku.at, astrid.pechstein@jku.at, hans.irschik@jku.at

studied in the literature for about a century, see e.g. the original papers by Nemenyi [5] and Reissner [6] or the more recent one by Irschik and Ziegler [7]. The notion of eigenstrain was originally introduced by Mura [8] for inelastic strains resulting from e.g. thermal expansion, phase transformation, initial strains, plastic strains and misfit strains. In the context of shape control, Irschik and Pichler [9] used eigenstrains due to thermal expansion for dynamic shape control of solids and structures. Another example for eigenstrains are piezoelectric strains, which in the context of structural control are often considered as proper candidates for actuation stresses. Examples for both, static and dynamic shape control using piezoelectric actuation strains can be found in e.g. [10–14].

As already mentioned, Haftka and Adelman [1] introduced shape control in the sense of minimizing the deformation of a force loaded structure. However, in many problems one may not be interested in minimizing the deformation, but rather to assign a desired deformation or displacement to the structure. The latter problem has been introduced by Irschik and Krommer [15] using the notion of displacement tracking, and further contributions can be found in [16–19]. As with shape control static and dynamic displacement tracking is possible. The original notion of shape control is a particular case of displacement tracking, also called zero displacement tracking, as the displacement to be tracked is zero. In the present paper we study both, static displacement tracking and static zero displacement tracking referring to both problems as shape control.

There may also be situations, where either the actuation stress is not applicable throughout the whole material body, but only within a sub-domain, or where one seeks to control only the deformation of a sub-domain. Either way, the resulting problem is denoted as shape control of sub-domains. A very first contribution to shape control of sub-domains was presented by Krommer and Varadan [20], who studied the problem of controlling the sub-domain of a structure, to which a conformal antenna is attached. The method was further extended to problems of structural mechanics, such as moderately thick beams [21] and thin plates [22, 23]. Concerning shape control of sub-domains of three-dimensional material bodies, we refer to Krommer [24]. In the present paper we study static shape control of sub-domains with respect to tracking either the strain or the displacement, extending the methodology developed in [24].

Therefore, the present paper is concerned with static shape control of sub-domains of material bodies. Eigenstrains or their corresponding actuation stresses, which are used for control, are applied in the sub-domain only. Two problems are of particular interest, strain tracking and displacement tracking of the sub-domain. Besides the imposed eigenstrains, the material body itself is linear elastic and we remain with the geometrically linear regime. The paper is structured as follows. After a brief introduction into static shape control of whole material bodies is given in Sect. 15.2, we focus on the problem of static shape control of sub-domains of force-loaded material bodies by eigenstrains in Sect. 15.3. First, strain tracking is discussed as a problem, in which the eigenstrain acts only in the sub-domain to be controlled. Then, displacement tracking is studied. In the latter problem the controlled sub-domain is chosen slightly larger than the sub-domain, for which we track the displacement. In any case, exact solutions for the corresponding tracking problem are presented.

For each of the shape control problems discussed in Sects. 15.2 and 15.3 numerical results for a plane stress problem validate the proposed shape control methodologies. Standard finite elements are used to compute the numerical solutions.

15.2 Static Shape Control of Material Bodies - a Brief Introduction

Before we focus on the particular problem of static shape control of arbitrarily shaped sub-domains of a material body, we present a brief introduction to the problem of static shape control for a whole material body. In particular, quasi-static problems in a geometrically and physically linear regime are studied. We consider generic eigenstrains to provide the actuation needed for the control problem at hand without discussing their physical nature.

Hence, we study a material body of volume Ω with the boundary $\partial\Omega$. Kinematic boundary conditions are prescribed such that no rigid body motion can occur. $\boldsymbol{n}$ is the unit normal vector of the boundary pointing outwards. A sketch of the material body is shown in Fig. 15.1 with applied body forces $\boldsymbol{b}$ and surface tractions $\boldsymbol{t}$; these external forces are applied sufficiently slow, such that the solution at any time instant t can be approximately computed from equilibrium conditions. The body is assumed linear elastic with imposed eigenstrains $\boldsymbol{\varepsilon}^*$, to which so-called actuation stresses

$$\boldsymbol{\sigma}^* = -\mathbb{C} \cdot\cdot \boldsymbol{\varepsilon}^*$$

are assigned, see Mura [8] for the notion of eigenstrains and the original papers by Nemenyi [5] and Reissner [6] for the equivalent notion of sources of self-stress. With the elasticity tensor $\mathbb{C}$ the constitutive relations are

$$\boldsymbol{\sigma} = \mathbb{C} \cdot\cdot (\boldsymbol{\varepsilon} - \boldsymbol{\varepsilon}^*) = \mathbb{C} \cdot\cdot \boldsymbol{\varepsilon} + \boldsymbol{\sigma}^*, \tag{15.1}$$
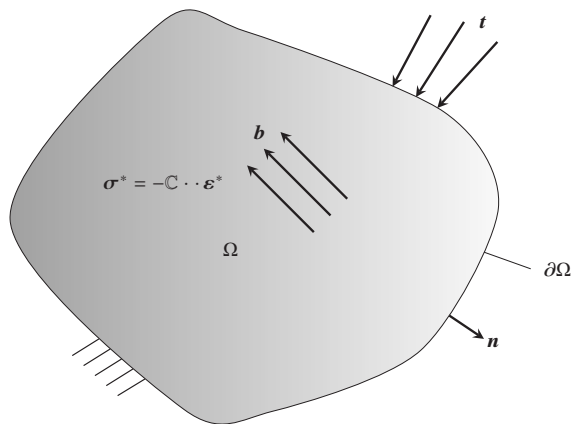
Fig. 15.1 Material body under the action of external forces and eigenstrains.

with the symmetric stress tensor $\boldsymbol{\sigma}$ and the symmetric linearized strain tensor $\boldsymbol{\varepsilon}$ defined as

$$\boldsymbol{\varepsilon} = \frac{1}{2}\left(\nabla\boldsymbol{u} + (\nabla\boldsymbol{u})^T\right) = \nabla\boldsymbol{u}^S; \tag{15.2}$$

$\boldsymbol{u}$ is the displacement vector. Now, we turn our attention to the actual static shape control problem, which we formulate as follows:

Problem 15.1 (Static shape control problem). Static shape control is concerned with the problem of computing an eigenstrain $\boldsymbol{\varepsilon}^*$, such that the displacement field of the material body under the action of quasi-static external forces $\boldsymbol{b}$ and $\boldsymbol{t}$ either vanishes or is prescribed. In the first problem we talk about *zero displacement tracking*, whereas we refer to the second problem as *displacement tracking*. Eigenstrains are assumed to be distributed freely within the body without any constraints.

Note, that the zero displacement tracking problem refers to the notion of shape control, as it has been originally introduced by Haftka and Adelman [1].

15.2.1 Displacement Tracking

To derive a solution of the static shape control problem we start with the equilibrium and boundary conditions, which are

$$\begin{aligned} \Omega: \quad & \nabla\cdot\boldsymbol{\sigma} + \boldsymbol{b} = \boldsymbol{0}, \\ \partial\Omega_\sigma: \quad \boldsymbol{\sigma}\cdot\boldsymbol{n} = \boldsymbol{t}, \quad & \partial\Omega_u: \quad \boldsymbol{u} = \boldsymbol{0}. \end{aligned} \tag{15.3}$$

Here, we have assumed the boundary to be rigidly supported at $\partial\Omega_u$ and tractions to be applied at $\partial\Omega_\sigma$. We now seek for the displacement field of the material body to be prescribed as $\boldsymbol{u} = \boldsymbol{z}$; note, that $\boldsymbol{z}$ must satisfy $\boldsymbol{z} = \boldsymbol{0}$ at $\partial\Omega_u$ and it must be kinematically admissible. Next, we insert the constitutive relation from Eq. (15.1) and the desired displacement field $\boldsymbol{u} = \boldsymbol{z}$ into the equilibrium conditions and the dynamic boundary conditions at $\partial\Omega_\sigma$. The result is

$$\begin{aligned} \Omega: \quad & \nabla\cdot\boldsymbol{\sigma}^* + \boldsymbol{b}^* = \boldsymbol{0}, \\ \partial\Omega_\sigma: \quad \boldsymbol{\sigma}^*\cdot\boldsymbol{n} = \boldsymbol{t}^*, \quad & \partial\Omega_u: \quad \boldsymbol{z} = \boldsymbol{0}, \end{aligned} \tag{15.4}$$

with effective body forces $\boldsymbol{b}^*$ and surface tractions $\boldsymbol{t}^*$ defined as

$$\boldsymbol{b}^* = \boldsymbol{b} + \nabla\cdot\left(\mathbb{C}\cdot\cdot\nabla\boldsymbol{z}^S\right), \quad \boldsymbol{t}^* = \boldsymbol{t} - \left(\mathbb{C}\cdot\cdot\nabla\boldsymbol{z}^S\right)\cdot\boldsymbol{n}. \tag{15.5}$$

The solution for the displacement tracking problem is:

Lemma 15.1. *The displacement field $\boldsymbol{u}$ of a material body under external force loadings $\boldsymbol{b}$ and $\boldsymbol{t}$ coincides with a desired displacement field $\boldsymbol{z}$, if the actuation stress $\boldsymbol{\sigma}^* = -\mathbb{C}\cdot\cdot\boldsymbol{\varepsilon}^*$ is any statically admissible stress for effective force loadings $\boldsymbol{b}^*$ and $\boldsymbol{t}^*$.*

The effective force loadings are defined in Eq. (15.5) and the notion statically admissible stress refers to the equilibrium conditions and the dynamic boundary conditions at $\partial\Omega_\sigma$ in Eq. (15.4). If $z = \mathbf{0}$, we have the solution for zero displacement tracking as a special case of the above solution. Concerning the proof of this solution we refer to Irschik and Pichler [25] in case of zero displacement tracking and to Irschik and Krommer [26] for displacement tracking in elastic and viscoelastic structures. It has been pointed out in the literature, that statically admissible stresses for given force loadings are in general non unique. Any stress tensor that satisfies

$$\Omega: \quad \nabla \cdot \boldsymbol{\sigma}^*_{\text{nil}} = \mathbf{0}, \quad \partial\Omega_\sigma: \quad \boldsymbol{\sigma}^*_{\text{nil}} \cdot \boldsymbol{n} = \mathbf{0}, \tag{15.6}$$

when used as an actuation stress produces no displacement in the material body. Such actuation stresses $\boldsymbol{\sigma}^*_{\text{nil}}$ and their corresponding eigenstrains

$$\boldsymbol{\varepsilon}^*_{\text{nil}} = -\mathbb{C}^{-1} \cdot\cdot\, \boldsymbol{\sigma}^*_{\text{nil}}$$

are denoted as *nilpotent actuation stresses / nilpotent eigenstrains*. They produce no displacement, but only stresses $\boldsymbol{\sigma} = \boldsymbol{\sigma}^*_{\text{nil}}$ in the material body under consideration. The notion of nilpotent eigenstrains has been introduced by Irschik and Ziegler [27] and further discussed by Irschik and Pichler [28]. The inappropriateness of nilpotent eigenstrains for shape control has been pointed out by Irschik et al. [29].

A simple and straightforward way to compute a particular $\boldsymbol{\varepsilon}^*$ for the displacement tracking problem is as follows. First, we compute a solution for the displacement $\boldsymbol{u}_{\text{f}}$ in the absence of eigenstrains from

$$\begin{aligned} \Omega: \quad &\nabla \cdot \boldsymbol{\sigma}_{\text{f}} + \boldsymbol{b} = \mathbf{0}, \\ \partial\Omega_\sigma: \quad \boldsymbol{\sigma}_{\text{f}} \cdot \boldsymbol{n} = \boldsymbol{t}, \quad &\partial\Omega_u: \quad \boldsymbol{u}_{\text{f}} = \mathbf{0}, \end{aligned} \tag{15.7}$$

with $\boldsymbol{\sigma}_{\text{f}} = \mathbb{C} \cdot\cdot\, \boldsymbol{\varepsilon}_{\text{f}} = \mathbb{C} \cdot\cdot\, \nabla \boldsymbol{u}_{\text{f}}^S$. Then the effective force loadings in Eq. (15.5) are

$$\boldsymbol{b}^* = \nabla \cdot (\mathbb{C} \cdot\cdot\, \nabla(\boldsymbol{z} - \boldsymbol{u}_{\text{f}})^S), \quad \boldsymbol{t}^* = -(\mathbb{C} \cdot\cdot\, \nabla(\boldsymbol{z} - \boldsymbol{u}_{\text{f}})^S) \cdot \boldsymbol{n}, \tag{15.8}$$

and the particular eigenstrain and actuation stress follow to

$$\boldsymbol{\varepsilon}^* = \nabla(\boldsymbol{z} - \boldsymbol{u}_{\text{f}})^S, \quad \boldsymbol{\sigma}^* = -\mathbb{C} \cdot\cdot\, \nabla(\boldsymbol{z} - \boldsymbol{u}_{\text{f}})^S. \tag{15.9}$$

If we insert this solution of the static shape control problem into the original equilibrium and dynamic boundary conditions, Eq. (15.3), we derive a homogenous boundary-value problem for the deviation of the displacement field $\boldsymbol{u}$ from the desired displacement field $\boldsymbol{z}$ as

$$\begin{aligned} \Omega: \quad &\nabla \cdot \left(\mathbb{C} \cdot\cdot\, \nabla(\boldsymbol{u} - \boldsymbol{z})^S \right) = \mathbf{0}, \\ \partial\Omega_\sigma: \quad \left(\mathbb{C} \cdot\cdot\, \nabla(\boldsymbol{u} - \boldsymbol{z})^S \right) \cdot \boldsymbol{n} = \mathbf{0}, \quad &\partial\Omega_u: \quad \boldsymbol{u} - \boldsymbol{z} = \mathbf{0}, \end{aligned} \tag{15.10}$$

the unique solution of which can be easily shown to be $\boldsymbol{u} = \boldsymbol{z}$, see e.g. Gurtin [30]. The stress tensor is

$$\boldsymbol{\sigma} = \mathbb{C} \cdot\cdot (\nabla \boldsymbol{u}^S - \nabla(\boldsymbol{z} - \boldsymbol{u}_{\mathrm{f}})^S) = \mathbb{C} \cdot\cdot \nabla \boldsymbol{u}_{\mathrm{f}}^S = \boldsymbol{\sigma}_{\mathrm{f}}, \qquad (15.11)$$

because $\boldsymbol{u} = \boldsymbol{z}$ holds. Hence, the stress tensor in the problem with external forces $\boldsymbol{b}$ and $\boldsymbol{t}$ and with the eigenstrain

$$\boldsymbol{\varepsilon}^* = \nabla(\boldsymbol{z} - \boldsymbol{u}_{\mathrm{f}})^S$$

is equal to the stress tensor in the problem without the eigenstrain. Indeed, as $\boldsymbol{z}$ is kinematically admissible and $\boldsymbol{u}_{\mathrm{f}}$ is an actual displacement, the eigenstrain $\boldsymbol{\varepsilon}^*$ is compatible, and it therefore does not produce any stress in the material body, but only a deformation, $\boldsymbol{\varepsilon} = \boldsymbol{\varepsilon}^*$, as long as a quasi-static problem is considered. Such compatible eigenstrains $\boldsymbol{\varepsilon}^* \equiv \boldsymbol{\varepsilon}_{\mathrm{imp}}^*$ and their corresponding actuation stress

$$\boldsymbol{\sigma}_{\mathrm{imp}}^* = -\mathbb{C} \cdot\cdot \boldsymbol{\varepsilon}_{\mathrm{imp}}^*$$

are denoted as stress-free or impotent eigenstrains and actuation stresses, see Irschik and Ziegler [27] and Mura [8], who introduced the notion of impotent eigenstrain. Concerning the unique decomposition of any eigenstrain

$$\boldsymbol{\varepsilon}^* = \boldsymbol{\varepsilon}_{\mathrm{imp}}^* + \boldsymbol{\varepsilon}_{\mathrm{nil}}^*$$

into an impotent eigenstrain and a nilpotent eigenstrain we refer to Nyashin et al. [31], where the orthogonality relation

$$\int_{\Omega} \boldsymbol{\varepsilon}_{\mathrm{imp}}^* \cdot\cdot \mathbb{C} \cdot\cdot \boldsymbol{\varepsilon}_{\mathrm{nil}}^* d\Omega = 0 \qquad (15.12)$$

of the two parts has been proven as well.

15.2.2 Numerical Example

Without any loss of generality, we compute numerical results for a plane stress problem only. As a particular problem, we consider the plane problem as shown in Fig. 15.2. The material is assumed isotropic, such that the plane stress constitutive relation is

$$\boldsymbol{\sigma} = Y\nu(\mathrm{tr}\boldsymbol{\varepsilon}_{\mathrm{e}})\boldsymbol{I} + Y(1-\nu)\boldsymbol{\varepsilon}_{\mathrm{e}}, \qquad (15.13)$$

with the elastic part of the strain tensor

$$\boldsymbol{\varepsilon}_{\mathrm{e}} = \boldsymbol{\varepsilon} - \boldsymbol{\varepsilon}^*.$$

Fig. 15.2 Plane stress problem.
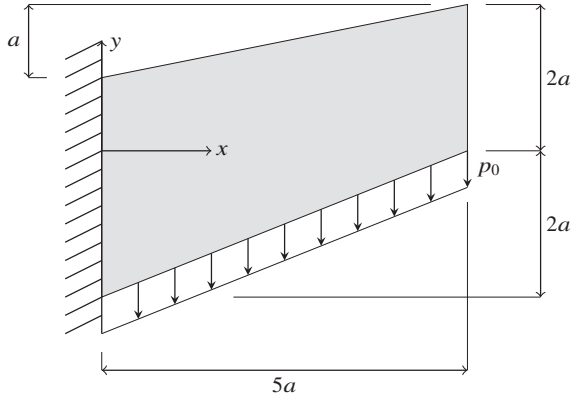
$$Y = \frac{E}{1 - \nu^2}$$

is the plane stress Young's modulus, with Young's modulus E and the Poisson ratio ν. Parameters for the numerical solution are given in Table 15.1.

First we solve the problem in the absence of any eigenstrain. Figure 15.3 shows the deformed configuration; in the left plot the norm of the strain tensor

$$\|\boldsymbol{\varepsilon}_f\| = \sqrt{\boldsymbol{\varepsilon}_f \cdot \cdot \boldsymbol{\varepsilon}_f}$$

is plotted, whereas the right plot presents the von Mises stress $\sigma_{v,f}$. Now, we set $z = \mathbf{0}$ for zero displacement tracking. With the solution $\boldsymbol{u}_f$ of the force problem at hand, we compute the impotent eigenstrain

Table 15.1: Parameters for example problem.

E/Nm^2	$\nu/1$	a/m	p_0/Nm^{-2}
210×10^9	0.3	1×10^{-2}	1×10^9
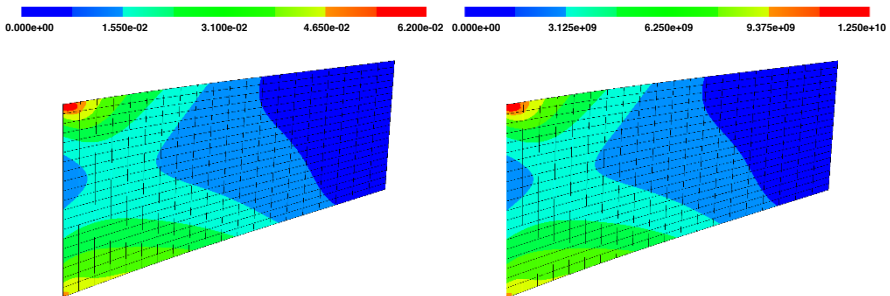
Fig. 15.3: Deformed configuration under pure force loading: Norm of strain tensor $\|\boldsymbol{\varepsilon}_f\|$ (left) and von Mises stress $\sigma_{v,f}$ (right).

$$\boldsymbol{\varepsilon}^*_{\text{imp}} = -\boldsymbol{\varepsilon}_{\text{f}} = -\nabla \boldsymbol{u}^S_{\text{f}},$$

which is applied to the material body together with the original force loading. As before, we show the deformed configuration in Fig. 15.4, with the norm of the strain tensor $\|\boldsymbol{\varepsilon}\|$ in the left plot, and the von Mises stress σ_{v} in the right plot. Obviously, no deformation occurs (note the color scheme in the left plot), as $\boldsymbol{\varepsilon}^*_{\text{imp}}$ produces a deformation, which is the negative of the force induced one. In contrast, as we use an impotent eigenstrain, the stress is identical to the one in the previous case without actuation. As the desired displacement $z = 0$ is zero, zero displacement tracking is exactly achieved within the context of a numerical finite element solution. Concerning the numerical solution, we used standard vector-valued third order displacement elements implemented in the open-source software package Netgen/NGSolve available at https://ngsolve.org.

Next, we introduce a non-zero displacement z as

$$z_x = 0, \quad z_y = -a\frac{4x - 15y}{15a - x} - y; \tag{15.14}$$

this particular displacement field maps our original domain from Fig. 15.2 into a rectangular domain with dimensions $5a \times 3a$. The Cartesian coordinates of the corresponding strain tensor ∇z^S are

$$\varepsilon_{xx} = \frac{\partial z_x}{\partial x} = 0, \quad \varepsilon_{yy} = \frac{\partial z_y}{\partial y} = \frac{15a}{15a - x} - 1,$$

$$\varepsilon_{xy} = \frac{1}{2}\left(\frac{\partial z_x}{\partial y} + \frac{\partial z_y}{\partial x}\right) = \frac{-4a(15a - x) - a(4x - 15y)}{2(15a - x)^2}. \tag{15.15}$$

Results for applying an impotentent eigenstrain

$$\boldsymbol{\varepsilon}^*_{\text{imp}} = \nabla(z - \boldsymbol{u}_{\text{f}})^S$$
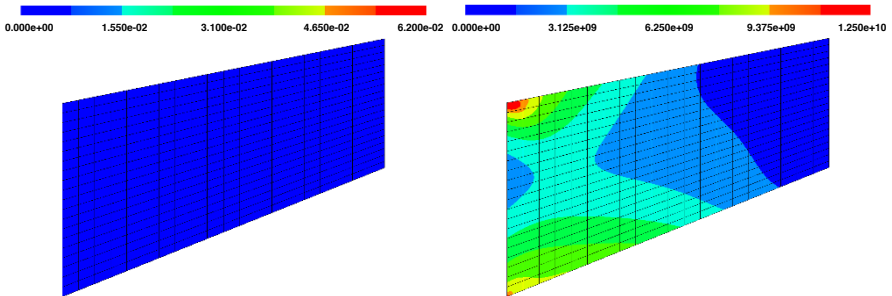
Fig. 15.4: Deformed configuration under combined force loading and eigenstrain for zero displacement tracking: Norm of strain tensor $\|\boldsymbol{\varepsilon}\|$ (left) and von Mises stress σ_{v} (right).

together with the original force loading are shown in Fig. 15.5. The deformed configuration corresponds to the prescribed displacement field z, the strain is $\varepsilon = \nabla z^S$ and the stress is again the original load stress. Hence, displacement tracking with $u = z$ is achieved without changing the stress distribution.

15.3 Static Shape Control of Sub-Domains

After our brief introduction into static shape control for a whole material body, we turn our attention to the actual topic of this paper - static shape control of sub-domains of material bodies. Based on our previous research on this topic, see [20–24], which was targeting systems of structural mechanics, such as beams and plates, we present an approach, which is applicable to arbitrarily shaped three-dimensional material bodies with arbitrarily shaped sub-domains, and compute numerical solutions for plane stress problems.

We introduce a sub-domain Ω_s within the material body, in which an eigenstrain or its corresponding actuation stress is applied. In the domain $\Omega_o = \Omega \setminus \Omega_s$ no eigenstrain is applied. Again, body forces b and surface tractions t are applied and kinematic boundary conditions prevent a rigid body motion of the material body. A sketch is presented in Fig. 15.6.

15.3.1 Strain Tracking

It is near at hand to ask, whether displacement tracking with an arbitrary prescribed z can be achieved within a sub-domain, if the eigenstrain is only applied to the sub-domain. As was already shown in our previous research, see the references on shape control of sub-domains above, this is not possible. Only the strain in the sub-domain
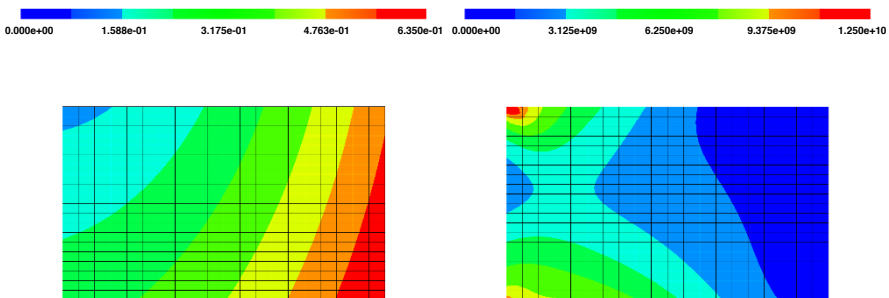
Fig. 15.5: Deformed configuration under combined force loading and eigenstrain for displacement tracking: Norm of strain tensor $\|\varepsilon\|$ (left) and von Mises stress σ_v (right).

Fig. 15.6 Material body under the action of external forces and eigenstrains applied in the sub-domain Ω_s only.
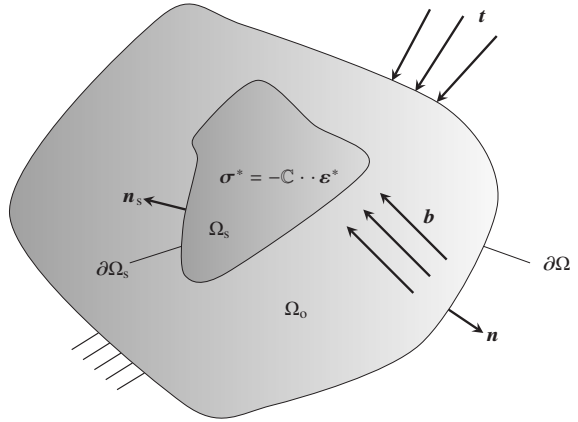
Ω_s can be controlled, if the eigenstrain is only applied in this sub-domain. Therefore, we discuss the following static shape control problem:

Problem 15.2 (Static shape control problem of sub-domains #1). Static shape control of sub-domains is concerned with the problem of computing an eigenstrain $\boldsymbol{\varepsilon}^*$ acting within the sub-domain Ω_s, such that the strain field of the material body under the action of external forces either vanishes or is prescribed within the sub-domain. In the first problem we talk about *zero strain tracking*, whereas we refer to the second problem as *strain tracking* of sub-domains. Eigenstrains are assumed to be distributed freely within the sub-domain without any constraints.

We denote the desired strain field in the sub-domain as $\boldsymbol{\zeta}$, which must be compatible $\nabla \times \boldsymbol{\zeta} \times \nabla = \mathbf{0}$. Therefore, we can compute the corresponding displacement field in the sub-domain as

$$z = z_0 + \boldsymbol{u}_A + \boldsymbol{\omega} \times \boldsymbol{r}_{PA}. \tag{15.16}$$

A is a given point in the sub-domain and $\boldsymbol{u}_A$ is its displacement vector. $\boldsymbol{r}_{PA}$ is a vector pointing from the point A to an arbitrary point of the sub-domain and $\boldsymbol{\omega}$ is the rigid body rotation of the sub-domain. z_0 is a displacement field with the desired strain tensor as its corresponding strain tensor $\boldsymbol{\zeta} = \nabla z_0^S$. To compute $\boldsymbol{\sigma}^* = -\mathbb{C} \cdot \cdot \boldsymbol{\varepsilon}^*$ acting within the sub-domain Ω_s, such that the strain tensor within Ω_s is $\boldsymbol{\varepsilon} = \boldsymbol{\zeta}$, we apply a two step procedure. In the first step, we only consider the outer domain Ω_o, which is not actuated. Forces $\boldsymbol{b}$ and $\boldsymbol{t}$ are acting, kinematic boundary conditions prevent a rigid body motion of the whole material body and the displacement at the inner surface $\partial\Omega_s$ is prescribed as $\boldsymbol{u}_o = z$; we denote the displacement vector in the outer domain as $\boldsymbol{u}_o$. The boundary value problem for $\boldsymbol{u}_o$ is

$$\begin{aligned} \Omega_o: \quad & \nabla \cdot \boldsymbol{\sigma}_o + \boldsymbol{b} = \mathbf{0}, \\ \partial\Omega_\sigma: \quad \boldsymbol{\sigma}_o \cdot \boldsymbol{n} = \boldsymbol{t}, \quad & \partial\Omega_u: \quad \boldsymbol{u}_o = \mathbf{0}, \quad \partial\Omega_s: \quad \boldsymbol{u}_o = z, \end{aligned} \tag{15.17}$$

with the constitutive relation $\sigma_o = \mathbb{C} \cdot \cdot \varepsilon_o$ and the strain tensor $\varepsilon_o = \nabla u_o^S$. As z depends on the unknown rigid body motion through the six rigid body degrees of freedom u_A and ω, six additional conditions are needed to compute the solution. These are

$$\boldsymbol{R} = \int_{\Omega_s} \boldsymbol{b} \, d\Omega + \int_{\partial\Omega_s} \sigma_o \cdot \boldsymbol{n}_s \, dS = \boldsymbol{0},$$

$$\boldsymbol{M}_{(A)} = \int_{\Omega_s} \boldsymbol{r}_{PA} \times \boldsymbol{b} \, d\Omega + \int_{\partial\Omega_s} \boldsymbol{r}_{PA} \times (\sigma_o \cdot \boldsymbol{n}_s) \, dS = \boldsymbol{0}; \qquad (15.18)$$

the resulting force $\boldsymbol{R}$ and moment $\boldsymbol{M}_{(A)}$ acting on the sub-domain Ω_s must be equilibrated. The result of the first step is the displacement field u_o, the corresponding strain tensor $\varepsilon_o = \nabla u_o^S$ and the stress tensor $\sigma_o = \mathbb{C} \cdot \cdot \varepsilon_o$. In the second step, we consider the actuated sub-domain only. At $\partial\Omega_s$ surface tractions $t_s = \sigma_o \cdot \boldsymbol{n}_s$ are applied, within the sub-domain $\boldsymbol{b}$ is acting together with an eigenstrain ε^*. The corresponding boundary value problem is

$$\begin{aligned} \Omega_s : & \quad \nabla \cdot \sigma_s + \boldsymbol{b} = \boldsymbol{0}, \\ \partial\Omega_s : & \quad \sigma_s \cdot \boldsymbol{n}_s = t_s, \end{aligned} \qquad (15.19)$$

with the constitutive relation $\sigma_s = \mathbb{C} \cdot \cdot (\varepsilon_s - \varepsilon^*)$ and the strain tensor $\varepsilon_s = \nabla u_s^S$. As we are discussing strain tracking within the sub-domain, the strain tensor in the sub-domain is actually known as $\varepsilon_s = \zeta = \nabla z_0^S$. Therefore, we have the problem

$$\begin{aligned} \Omega_s : & \quad \nabla \cdot \sigma^* + \boldsymbol{b}^* = \boldsymbol{0}, \\ \partial\Omega_s : & \quad \sigma^* \cdot \boldsymbol{n}_s = t^*, \end{aligned} \qquad (15.20)$$

with the actuation stress $\sigma^* = -\mathbb{C} \cdot \cdot \varepsilon^*$, and effective force loadings

$$\boldsymbol{b}^* = \boldsymbol{b} + \nabla \cdot (\mathbb{C} \cdot \cdot \nabla z_0^S), \quad t^* = t_s - (\mathbb{C} \cdot \cdot \nabla z_0^S) \cdot \boldsymbol{n}_s. \qquad (15.21)$$

Obviously, this is formally a displacement tracking problem, as we have introduced it in Eqs. (15.4) and (15.5). Therefore, the solution is

$$\varepsilon^* = \nabla(z_0 - \bar{u}_f)^S = \zeta - \nabla\bar{u}_f^S = -\mathbb{C}^{-1} \cdot \cdot \sigma^*, \qquad (15.22)$$

with $\bar{u}_f$ as the solution of the boundary value problem

$$\begin{aligned} \Omega_s : & \quad \nabla \cdot \bar{\sigma}_f + \boldsymbol{b} = \boldsymbol{0}, \\ \partial\Omega_s : & \quad \bar{\sigma}_f \cdot \boldsymbol{n}_s = t_s, \end{aligned} \qquad (15.23)$$

with $\bar{\sigma}_f = \mathbb{C} \cdot \cdot \nabla\bar{u}_f^S$. As $\boldsymbol{b}$ and t_s are equilibrated, we only need to prevent the sub-domain from any rigid motion for the numerical solution. Finally, the stress in the actuated sub-domain Ω_s is $\sigma_s = \mathbb{C} \cdot \cdot (\varepsilon_s - \varepsilon^*)$, and with $\varepsilon_s = \zeta$ and $\varepsilon^* = \zeta - \nabla\bar{u}_f^S$ we find

$$\boldsymbol{\sigma}_s = \mathbb{C} \cdot \cdot (\boldsymbol{\varepsilon}_s - \boldsymbol{\varepsilon}^*) = \mathbb{C} \cdot \cdot \nabla \bar{\boldsymbol{u}}_f^S = \bar{\boldsymbol{\sigma}}_f. \tag{15.24}$$

Therefore, $\boldsymbol{\varepsilon}^* = \boldsymbol{\zeta} - \nabla \bar{\boldsymbol{u}}_f^S$ does not produce any stress in addition to the stress $\bar{\boldsymbol{\sigma}}_f$ of the force problem for the sub-domain defined in Eq. (15.23).

15.3.1.1 Variational Formulation

Computing $\bar{\boldsymbol{u}}_f$ from Eq. (15.23) is straighforward; it respresents a standard static problem for a linear elastic body under the action of given external forces in a geometrically linear regime, which can be solved numerically with standard finite elements. In contrast, the computation of the solution for $\boldsymbol{u}_o$ in the outer domain Ω_o and the rigid body motion $\boldsymbol{u}_A$ and $\boldsymbol{\omega}$ is not straightforward. Therefore, we introduce the variational formulation of the problem as the basis for a numerical solution. We start with the principle of virtual work for the whole body in the form

$$\int_\Omega \boldsymbol{b} \cdot \delta \boldsymbol{u} d\Omega + \int_{\partial \Omega_\sigma} \boldsymbol{t} \cdot \delta \boldsymbol{u} dS - \int_\Omega \boldsymbol{\sigma} \cdot \cdot \delta \nabla \boldsymbol{u}^S d\Omega = 0. \tag{15.25}$$

Now, we split the volume integrals into two parts; one integrating over the outer domain and one integrating over the sub-domain. Moreover, we introduce the variation of the displacement vector $\delta \boldsymbol{u}_s$ in the sub-domain as

$$\delta \boldsymbol{u}_s = \delta \boldsymbol{z} = \delta (\boldsymbol{z}_0 + \boldsymbol{u}_A + \boldsymbol{\omega} \times \boldsymbol{r}_{PA}) = \delta \boldsymbol{u}_A + \delta \boldsymbol{\omega} \times \boldsymbol{r}_{PA}; \tag{15.26}$$

as $\boldsymbol{z}_0$ is prescribed, $\delta \boldsymbol{z}_0 = \boldsymbol{0}$ holds. Therefore, the virtual work of the internal forces in the sub-domain vanishes. Finally, the constraint that the displacement vector at $\partial \Omega_s$ must be continuous,

$$\boldsymbol{u}_o|_{\partial \Omega_s} = \boldsymbol{z}_0|_{\partial \Omega_s} + \boldsymbol{u}_A + \boldsymbol{\omega} \times \boldsymbol{r}_{PA}|_{\partial \Omega_s} \tag{15.27}$$

is accounted for by augmenting the principle of virtual work with

$$\delta C = \int_{\partial \Omega_s} \delta \left[\boldsymbol{\lambda} \cdot (\boldsymbol{z}_0 + \boldsymbol{u}_A + \boldsymbol{\omega} \times \boldsymbol{r}_{PA} - \boldsymbol{u}_o) \right] dS; \tag{15.28}$$

$\boldsymbol{\lambda}$ is a vector-valued Lagrange multiplier. The final form of the variational formulation is

$$0 = \int_{\Omega_o} \boldsymbol{b} \cdot \delta \boldsymbol{u}_o d\Omega + \int_{\partial \Omega_\sigma} \boldsymbol{t} \cdot \delta \boldsymbol{u}_o dS - \int_{\Omega_o} \boldsymbol{\sigma}_o \cdot \cdot \delta \nabla \boldsymbol{u}_o^S d\Omega - \int_{\partial \Omega_s} \delta \left[\boldsymbol{\lambda} \cdot \boldsymbol{u}_o \right] dS$$

$$+ \delta \boldsymbol{u}_A \cdot \int_{\Omega_s} \boldsymbol{b} d\Omega + \delta \boldsymbol{\omega} \cdot \int_{\Omega_s} \boldsymbol{r}_{PA} \times \boldsymbol{b} d\Omega + \int_{\partial \Omega_s} \delta \left[\boldsymbol{\lambda} \cdot (\boldsymbol{z}_0 + \boldsymbol{u}_A + \boldsymbol{\omega} \times \boldsymbol{r}_{PA}) \right] dS. \tag{15.29}$$

Introducing proper FE spaces for u_o and λ, the problem can be discretized and a numerical solution for u_o, λ, u_A and ω can be computed.

On the other hand, we can derive the strong form of the problem from the variational principle as well. From the variation $\delta\lambda$ of the Lagrange multiplier, we recover the continuity of the displacement vector at $\partial\Omega_s$

$$\partial\Omega_s : \ u_o = z_0 + u_A + \omega \times r_{PA} = z, \tag{15.30}$$

and the variation of the displacement vector in the outer domain δu_o results into

$$\Omega_o : \ \nabla \cdot \sigma_o + b = 0,$$
$$\partial\Omega_\sigma : \ \sigma_o \cdot n = t \quad \text{and} \quad \partial\Omega_s : \ \lambda = \sigma_o \cdot n_s; \tag{15.31}$$

the last relation identifies the Lagrange multiplier as the traction $t_s = \sigma_o \cdot n_s$ acting on the sub-domain. Finally, the variations of the rigid body degrees of freedom δu_A and $\delta\omega$ recover the equilibrium conditions for the sub-domain as

$$R = \int_{\Omega_s} b\,d\Omega + \int_{\partial\Omega_s} \lambda\,dS = 0,$$
$$M_A = \int_{\Omega_s} r_{PA} \times b\,d\Omega + \int_{\partial\Omega_s} r_{PA} \times \lambda\,dS = 0. \tag{15.32}$$

Therefore, the variational formulation is identical to our previous formulation in Eqs. (15.17) and (15.18).

15.3.1.2 Numerical Example

We consider the same example problem as before, but with the actuation applied only within a rectangular sub-domain, see Fig. 15.7. The center of the rectangle is located at $x = 1.2a$ and $y = 0$, and the dimension is $1.6a \times 1.5a$ in x and y directions. In the numerical scheme, it proves more efficient to enforce the kinematic constraint Eq. (15.27) directly through an appropriate choice of six displacement ansatz functions representing the six degrees of freedom of the rigid body motion of Ω_s. These functions are added to the set of nodal basis functions associated to nodes outside Ω_s. They are constructed as a linear combination of shape functions associated to nodes in Ω_s including its boundary nodes in such a way that a rigid body motion is achieved in Ω_s – this can be done exactly for any classical set of finite element shape functions. Note that in doing so, these additional functions are kinematically admissible, as they extend naturally to the outer domain Ω_o by using the according finite element shape functions of boundary nodes on $\partial\Omega_o$. In case of a prescribed strain different from zero, the displacement component z_0 has to be treated in a similar manner, and will contribute to the residual vector of the ensuing finite element problem. Once a finite element solution is computed, interface

Fig. 15.7 Plane stress problem with rectangular sub-domain Ω_s.
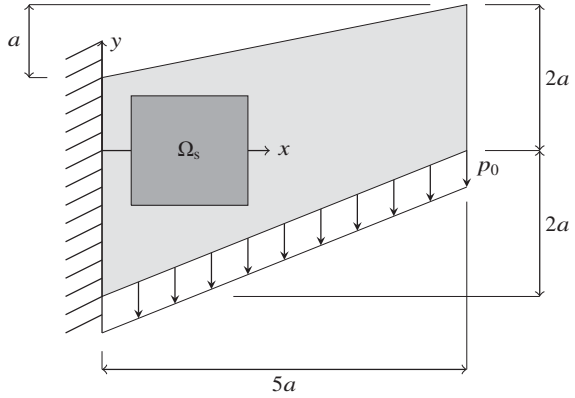
tractions $\lambda = t_s$ are computed as reaction forces that appear in the residual vector for the boundary nodes on $\partial\Omega_s$.

First, we show the solution without an actuation in Fig. 15.8, which is identical to the one before. The reason for re-presenting this solution is to show the deformation, the strain and the stress of the rectangular sub-domain, if no eigenstrain is applied. The only difference to the previous result for this force problem is the fact that we use an unstructured mesh with triangles in order to mesh the sub-domain and to use a fine mesh in the corners.

Now, we consider the case of zero strain tracking with $\zeta = 0$, for which we compute the eigenstrain as $\varepsilon^* = -\nabla \bar{u}_f^S$. Note that in the context of strain tracking of sub-domains $\bar{u}_f$ is not the displacement vector in the problem under pure force loading that is shown in Fig. 15.8, but $\bar{u}_f$ is the solution of Eq. (15.23). Numerical results are shown in Fig. 15.9. In the left plot the norm of the strain tensor $\|\varepsilon\|$ is presented; indeed, the strain is zero in the rectangular sub-domain $\varepsilon = \zeta = 0$, such that the goal of zero strain tracking is exactly reached. The von Mises stress is shown in the right plot. In contrast to zero displacement tracking with an eigenstrain applied in the whole domain Ω, the stress distribution changes compared to the case no eigenstrain is
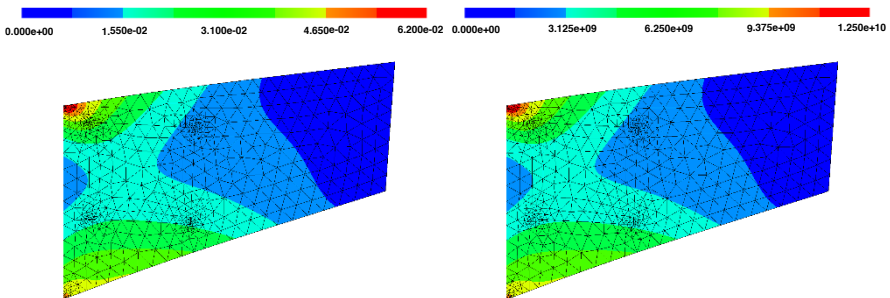
Fig. 15.8: Deformed configuration under pure force loading: Norm of strain tensor $\|\varepsilon_f\|$ (left) and von Mises stress $\sigma_{v,f}$ (right).
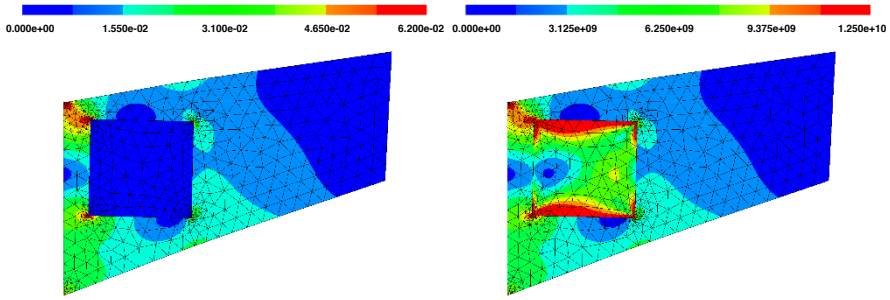
Fig. 15.9: Deformed configuration under combined force loading and eigenstrain for zero strain tracking with $\boldsymbol{\zeta} = \mathbf{0}$: Norm of strain tensor $\|\boldsymbol{\varepsilon}\|$ (left) and von Mises stress σ_v (right).

applied. The displacement in the sub-domain is not zero, but it represents a rigid body motion.

We proceed to the case of tracking a non-zero strain. In particular, we seek to deform the rectangular sub-domain such that the rectangle is transformed into a rhombus with side length $1.5a$ and angles $90° \pm \gamma$; the prescribed strain tensor is $\boldsymbol{\zeta} = \varepsilon_{xx} \boldsymbol{e}_x \boldsymbol{e}_x + \varepsilon_{xy} (\boldsymbol{e}_x \boldsymbol{e}_y + \boldsymbol{e}_y \boldsymbol{e}_x)$ with

$$\varepsilon_{xx} = -\frac{1}{16}, \quad \varepsilon_{xy} = \frac{\gamma}{2} = -\frac{1}{20}. \tag{15.33}$$

The eigenstrain is computed as $\boldsymbol{\varepsilon}^* = \boldsymbol{\zeta} - \nabla \bar{\boldsymbol{u}}_\mathrm{f}^S$, in which $\bar{\boldsymbol{u}}_\mathrm{f}$ is the solution of Eq. (15.23). We refer to this problem a shear strain tracking. Numerical results for $\|\boldsymbol{\varepsilon}\|$ and σ_v are shown in Fig. 15.10. In the left plot one can see the rhombus and the constant strain in the sub-domain. The von Mises stress in the right plot shows a significant increase compared to the case of zero strain tracking.

Finally, the norm of the eigenstrain $\|\boldsymbol{\varepsilon}^*\|$ for both problems, zero strain tracking and shear strain tracking is presented in Fig. 15.11. Likewise to the von Mises stress,
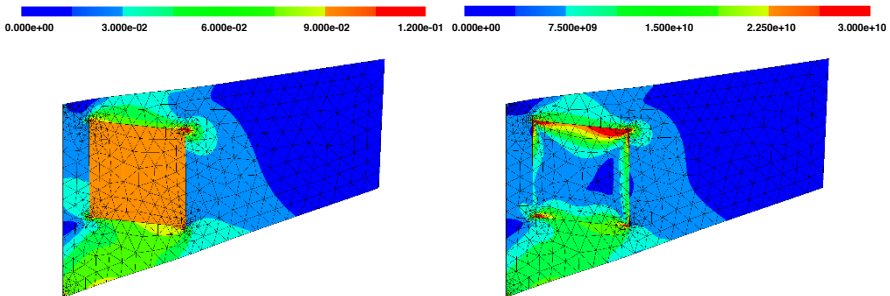
Fig. 15.10: Deformed configuration under combined force loading and eigenstrain for shear strain tracking with $\boldsymbol{\zeta} = \varepsilon_{xx} \boldsymbol{e}_x \boldsymbol{e}_x + \varepsilon_{xy} (\boldsymbol{e}_x \boldsymbol{e}_y + \boldsymbol{e}_y \boldsymbol{e}_x)$: Norm of strain tensor $\|\boldsymbol{\varepsilon}\|$ (left) and von Mises stress σ_v (right).
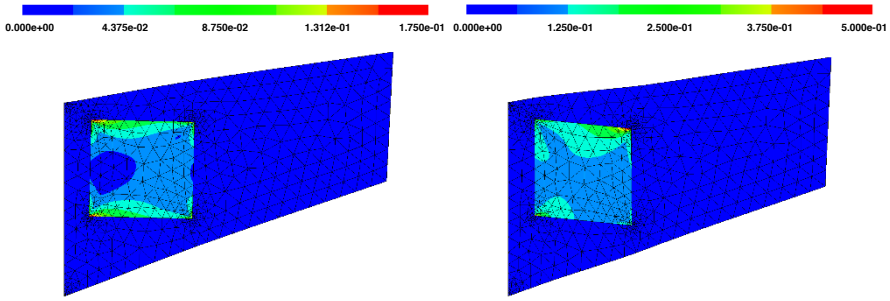
Fig. 15.11: Deformed configuration under combined force loading and eigenstrain: Norm of eigenstrain tensor $\|\boldsymbol{\varepsilon}^*\|$ for zero strain tracking (left) and for shear strain tracking (right).

the eigenstrain is significantly higher for shear strain tracking than for zero strain tracking.

15.3.2 Displacement Tracking

So far we have been discussing strain tracking within sub-domains only. Therefore, only the strain was prescribed in the sub-domain Ω_s, in which the eigenstrain was applied. As a result we were not able to control the rigid-body motion of the sub-domain. If for some reason, it is imperative to fully control the displacement of the sub-domain Ω_s, we must add a so-called interface domain Ω_i enclosing the sub-domain Ω_s, and apply the eigenstrain within $\Omega_i \cup \Omega_s$. A sketch of the problem is shown in Fig. 15.12. The resulting static shape control problem is stated as follows:
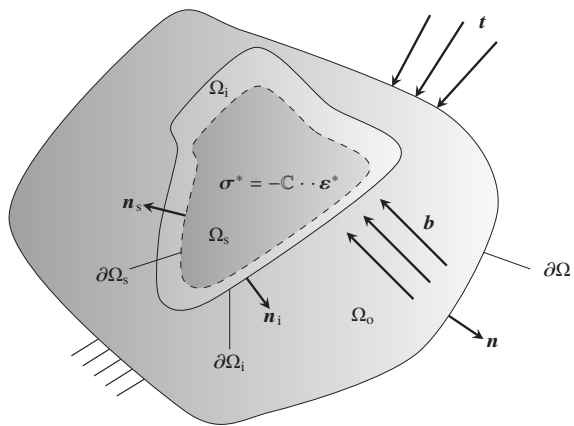
Fig. 15.12 Material body under the action of external forces and eigenstrains applied in the sub-domain Ω_s and in the interface domain Ω_i.

Problem 15.3 (Static shape control problem of sub-domains #2). Static shape control of sub-domains is concerned with the problem of computing eigenstrains $\boldsymbol{\varepsilon}^*$ acting within an extended sub-domain $\Omega_s \cup \Omega_i$, such that the displacement field of the material body under the action of external forces either vanishes or is prescribed within the sub-domain Ω_s. In the first problem we talk about *zero displacement tracking*, whereas we refer to the second problem as *displacement tracking* of sub-domains. Eigenstrains are assumed to be distributed freely within the extended sub-domain without any constraints.

The solution to this particular shape control problem is actually straightforward. First, we solve a purely elastic problem without any eigenstrain, but only with applied forces $\boldsymbol{b}$ and $\boldsymbol{t}$ in the whole domain of the material body $\Omega = \Omega_s \cup \Omega_i \cup \Omega_o$, from which we obtain the displacement field $\boldsymbol{u}_f$. Then, we recall the solution of displacement tracking for the whole material body. The desired displacement is chosen as $\boldsymbol{z} = \boldsymbol{u}_f$ in Ω_o and as an arbitrary displacement field within $\Omega_s \cup \Omega_i$, which satisfies $\boldsymbol{z}|_{\partial \Omega_i} = \boldsymbol{u}_f$. The solution of this displacement tracking problem for the whole material body is

$$\boldsymbol{\varepsilon}^* = \nabla (\boldsymbol{z} - \boldsymbol{u}_f)^S; \tag{15.34}$$

the corresponding proof was given in Sec. 2. No eigenstrain must be applied within Ω_o, because $\boldsymbol{u} = \boldsymbol{z} = \boldsymbol{u}_f$ holds in Ω_o. As the eigenstrain is impotent $\boldsymbol{\varepsilon}^* = \boldsymbol{\varepsilon}^*_{imp}$, the stress is equal to the stress in the purely elastic problem without any eigenstrain, $\boldsymbol{\sigma} = \boldsymbol{\sigma}_f = \mathbb{C} \cdot\cdot \nabla \boldsymbol{u}_f^S$.

15.3.2.1 Optimization

Finally, we discuss the choice of $\boldsymbol{z}$ in the actuated domain. We denote the desired displacement in the interface domain as $\boldsymbol{z} = \boldsymbol{z}_i$ and in the sub-domain as $\boldsymbol{z} = \boldsymbol{z}_s$. In the zero displacement tracking problem we have $\boldsymbol{z}_s = \boldsymbol{0}$ and in the displacement tracking problem $\boldsymbol{z}_s$ can be chosen sufficiently free as long as it is kinematically admissible. With $\boldsymbol{z}_s$ prescribed, $\boldsymbol{z}_i$ must satisfy the two conditions

$$\boldsymbol{z}_i|_{\partial \Omega_i} = \boldsymbol{u}_f|_{\partial \Omega_i} \quad \text{and} \quad \boldsymbol{z}_i|_{\partial \Omega_s} = \boldsymbol{z}_s|_{\partial \Omega_s}; \tag{15.35}$$

$\boldsymbol{u}_f$ still refers to the displacement vector in the force problem without eigenstrains. Within the interface domain Ω_i, we seek to find an eigenstrain of smallest maximal absolute value,

$$\sup_{\boldsymbol{x} \in \Omega_i} \|\boldsymbol{\varepsilon}^*(\boldsymbol{x})\| = \|\boldsymbol{\varepsilon}^*\|_{L_\infty} \to \min. \tag{15.36}$$

Above, $\|\boldsymbol{\varepsilon}^*(\boldsymbol{x})\| = \sqrt{\boldsymbol{\varepsilon}^*(\boldsymbol{x}) \cdot\cdot \boldsymbol{\varepsilon}^*(\boldsymbol{x})}$ denotes the *local* Frobenius norm of a tensor as introduced earlier, while $\|\boldsymbol{\varepsilon}^*\|_{L_\infty}$ is the Lebesgue norm for the function space $L_\infty(\Omega_i)$. As the condition in Eq. (15.36) is not differentiable, we resort to minimizing the L_p norm $\|\boldsymbol{\varepsilon}^*\|_{L_p}$ for large $p \gg 2$. This implies a choice of $\boldsymbol{\varepsilon}^* = \nabla \tilde{\boldsymbol{z}}^S$ such that $\tilde{\boldsymbol{z}} = \boldsymbol{z}_i - \boldsymbol{u}_f$ respects the boundary conditions $\tilde{\boldsymbol{z}}|_{\partial \Omega_i} = \boldsymbol{0}$ and $\tilde{\boldsymbol{z}}|_{\partial \Omega_s} = (\boldsymbol{z}_s - \boldsymbol{u}_f)|_{\partial \Omega_s}$, and further

$$\|\boldsymbol{\varepsilon}^*\|_{L_p}^P = \int\limits_{\Omega_i} \|\boldsymbol{\varepsilon}^*\|^P\, d\Omega = \int\limits_{\Omega_i} \|\nabla \tilde{z}^S\|^P\, d\Omega \to \min. \qquad (15.37)$$

For $p \neq 2$, the above optimization problem requires the numerical solution of a non-linear system of equations. Otherwise, the numerical solution for displacement tracking of sub-domains is straightforward, as it only requires the computation of the solution $\boldsymbol{u}_f$ of a linear elastic problem with external forces.

15.3.2.2 Numerical Example

We stick to our previous example. The sub-domain Ω_s is chosen as a slightly smaller rectangle with its center located at $x = 1.2a$ and $y = 0$ and with dimensions $1.2a \times 1.1a$ in x and y directions. The interface domain surrounds the sub-domain and its thickness is $h = 0.3a$. For a sketch see Fig. 15.13. We only consider the case of zero displacement tracking $z_s = \mathbf{0}$ within Ω_s. The stress tensor is identical to the one we computed for the force problem in Secs. 2 and 3, see the right plots in Figs. 15.3 and 15.8. The deformed configuration under applied forces and eigenstrains is shown in Fig. 15.14. The norm of the strain tensor is plotted; in the left plot for the case of minimizing $\|\boldsymbol{\varepsilon}^*\|_{L_2}$ and in the right plot for the case of minimizing $\|\boldsymbol{\varepsilon}^*\|_{L_{16}}$; $p = 16$ has been chosen, as for any $p > 16$ the computed solution did not improve any more, but convergence of the damped Newton iteration deteriorates for larger values of p. Due to the large strains in the interface domain, the strain in the outer domain appears to be close to zero; in reality, it is just much smaller than in the interface domain and therefore, its distribution is not resolved with the color scheme that was chosen to resolve the distribution in the interface domain. However, the strain in the outer domain is identical to the uncontrolled case, which has already been presented in Figs. 15.3 and 15.8. The corresponding eigenstrains are shown in Fig. 15.15. Obviously, the results for $p = 2$ and $p = 16$ are significantly different. To quantify this difference, we compute the mean value of the norm of the eigenstrain
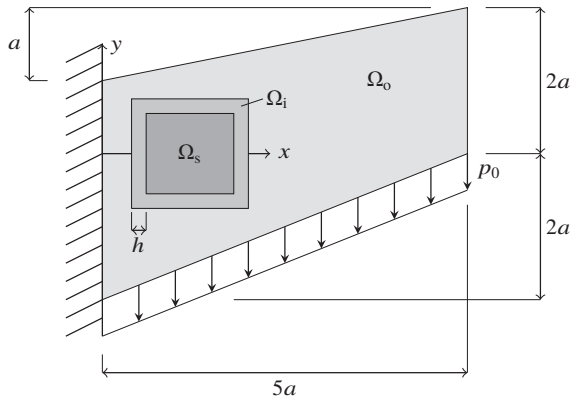
Fig. 15.13 Plane stress problem with rectangular sub-domain Ω_s, interface-domain Ω_i and outer domain Ω_o.
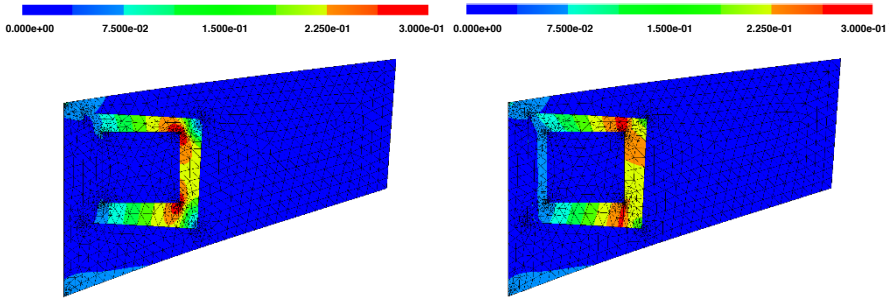
Fig. 15.14: Deformed configuration: Norm of strain tensor $\|\boldsymbol{\varepsilon}\|$ for minimizing $\|\boldsymbol{\varepsilon}^*\|_{L_2}$ (left) and for minimizing $\|\boldsymbol{\varepsilon}^*\|_{L_{16}}$ (right).
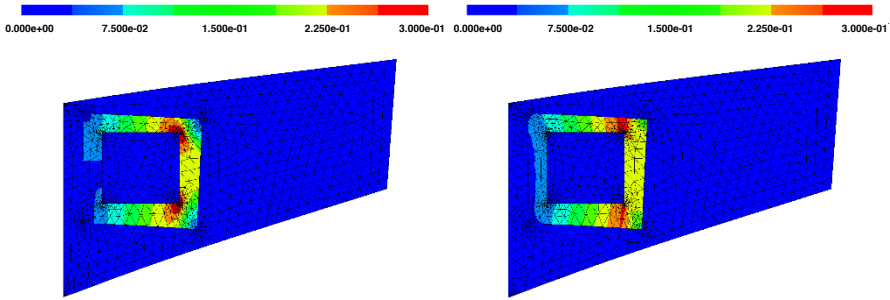
Fig. 15.15: Deformed configuration: Norm of eigenstrain $\|\boldsymbol{\varepsilon}^*\|$ for minimizing $\|\boldsymbol{\varepsilon}^*\|_{L_2}$ (left) and for minimizing $\|\boldsymbol{\varepsilon}^*\|_{L_{16}}$ (right).

in the interface domain; when using the mesh displayed in Fig. 15.15, a maximum of $\|\boldsymbol{\varepsilon}^*\| = 0.739$ is observed for $p = 2$, whereas for $p = 16$ we have the maximum $\|\boldsymbol{\varepsilon}^*\| = 0.301$. Finally, Fig. 15.16 shows the norm $\|\boldsymbol{u}\|$ of the displacement vector for the two cases $p = 2$ and $p = 16$. The displacement is zero in the sub-domain, in the
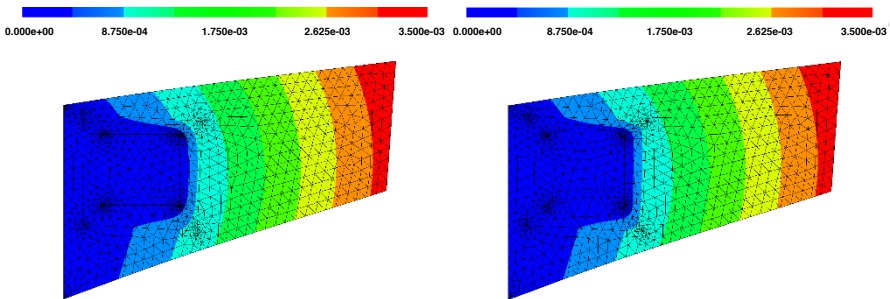
Fig. 15.16: Deformed configuration: Norm of displacement vector $\|\boldsymbol{u}\|$ for minimizing $\|\boldsymbol{\varepsilon}^*\|_{L_2}$ (left) and for minimizing $\|\boldsymbol{\varepsilon}^*\|_{L_{16}}$ (right)..

outer domain it is identical to the one in the problem without an eigenstrain and in the interface domain it smoothly transitions from the one in the outer domain to zero. The goal of zero displacement tracking of sub-domains is achieved exactly.

References

[1] Haftka RT, Adelman HM (1985) An analytical investigation of shape control of large space structures by applied temperatures. AIAA Journal **23**(3):450–457

[2] Irschik H (2002) A review on static and dynamic shape control of structures by piezoelectric actuation. Engineering Structures **24**(1):5–11

[3] Irschik H, Krommer M, Nader M, Schoeftner J, Zehetner C (2012) Active and passive shape control of structures. In: Grosso AD, Basso P (eds) CD-Rom Proc. of the 5th European Conference on Structural Control (EACS 2012), Genua, Italy

[4] Irschik H, Krommer M (2013) A review on static and dynamic shape control of structures: The period 2002-2012. In: Adam C, Heuer R, Lenhardt W, Schranz C (eds) Proc. of the Vienna Congress on Recent Advances in Earthquake Engineering and Structural Dynamics 2013 (VEESD 2013), Vienna, Austria

[5] Neményi P (1931) Selbstspannungen elastischer Gebilde. ZAMM - Journal of Applied Mathematics and Mechanics / Zeitschrift für Angewandte Mathematik und Mechanik **11**(1):59–70

[6] Reißner H (1931) Eigenspannungen und Eigenspannungsquellen. ZAMM - Journal of Applied Mathematics and Mechanics / Zeitschrift für Angewandte Mathematik und Mechanik **11**(1):1–8

[7] Irschik H, Ziegler F (1988) Dynamics of linear elastic structures with selfstress: A unified treatment for linear and nonlinear problems. ZAMM - Journal of Applied Mathematics and Mechanics / Zeitschrift für Angewandte Mathematik und Mechanik **68**(6):199–205

[8] Mura T (1991) Micromechanics of Defects in Solids, 2nd edn. Kluwer, Dordrecht, The Netherlands

[9] Irschik H, Pichler U (2001) Dynamic shape control of solids and structures by thermal expansion strains. Journal of Thermal Stresses **24**(6):565–576

[10] Irschik H, Krommer M, Pichler U (2000) Shaping distributed piezoelectric self-sensing layers for static shape control of smart structures. Journal of Structural Control **7**(2):173–189

[11] Irschik H, Krommer M, Nader M, Pichler U (2003) Dynamic piezoelectric shape control applied to shells of revolution with translatory support excitation. In: Faravelli L, Spencer, Jr BF (eds) Proc. of US - Europe Workshop on Sensors and Smart Structures Technology, Como and Somma Lombardo, Italy, John Wiley & Sons, Chichester, pp 139–148

[12] Irschik H, Krommer M, Pichler U (2003) Dynamic shape control of beam - type structures by piezoelectric actuation and sensing. International Journal of Applied Electromagnetics and Mechanics **17**(1-3):251–258

[13] Gattringer H, Nader M, Krommer M, Irschik H (2003) Collocative PD control of circular plates with shaped piezoelectric actuators/sensors. Journal of Vibration and Control **9**(8):965–982

[14] Nader M, Gattringer H, Krommer M, Irschik H (2003) Shape control of flexural vibrations of circular plates by shaped piezoelectric actuation. Journal of Vibration and Acoustics **125**(1):88–94

[15] Irschik H, Krommer M (2006) Tracking of transient displacements in solids and structures. In: CD-Rom Proc. of 4th World Conference on Structural Control and Monitoring (4WCSCM), San Diego, CA, U.S.A.

[16] Krommer M, Irschik H (2007) Sensor and actuator design for displacement control of continuous systems. Smart Structures and Systems **3**(2):147–172

[17] Krommer M, Irschik H, Zellhofer M (2008) Design of actuator networks for dynamic displacement tracking of beams. Mechanics of Advanced Materials and Structures **15**(3-4):235–249

[18] Huber D, Krommer M, Irschik H (2009) Dynamic displacement tracking of a one-storey frame structure using patch actuator networks: Analytical plate solution and FE validation. Smart Structures and Systems **5**(6):613–632

[19] Irschik H, Krommer M, Zehetner C (2016) Displacement tracking of pre-deformed smart structures. Smart Structures and Systems **18**(1):139–154

[20] Krommer M, Varadan VV (2003) Dynamic shape control of conformal antennas. In: Smith RC (ed) Smart Structures and Materials 2003: Modeling, Signal Processing, and Control, International Society for Optics and Photonics, SPIE, vol 5049, pp 622 – 630

[21] Krommer M (2005) Dynamic shape control of sub-sections of moderately thick beams. Computers & Structures **83**(15):1330–1339

[22] Krommer M, Varadan VV (2005) Control of bending vibrations within subdomains of thin plates — Part I: Theory and exact solution. Journal of Applied Mechanics **72**(3):432–444

[23] Krommer M, Varadan VV (2006) Control of Bending Vibrations Within Subdomains of Thin Plates — Part II: Piezoelectric Actuation and Approximate Solution. Journal of Applied Mechanics **73**(2):259–267

[24] Krommer M (2006) Dynamic shape control of subdomains of structures. Structural Control and Health Monitoring **13**(6):1080–1098

[25] Irschik H, Pichler U (2004) An extension of Neumann's method for shape control of force-induced elastic vibrations by eigenstrains. International Journal of Solids and Structures **41**(3):871–884

[26] Irschik H, Krommer M (2005) Dynamic Displacement Tracking of Force-Loaded Linear Elastic or Viscoelastic Bodies by Eigenstrain-Induced Actuation Stresses. In: Proceedings of the ASME 2005 International Design Engineering Technical Conferences and Computers and Information in Engineering Conference, vol Volume 1: 20th Biennial Conference on Mechanical Vibration and Noise, Parts A, B, and C, ASME, pp 681–688

[27] Irschik H, Ziegler F (2001) Eigenstrain without stress and static shape control of structures. AIAA Journal **39**(10):1985–1990

[28] Irschik H, Pichler U (2005) On eigenstrains without displacements. Acta Mechanica **178**:111–122

[29] Irschik H, Krommer M, Belyaev AK, Schlacher K (1998) Shaping of piezoelectric sensors/actuators for vibrations of slender beams: Coupled theory and inappropriate shape functions. Journal of Intelligent Material Systems and Structures **9**(7):546–554

[30] Gurtin ME (1972) The linear theory of elasticity. In: Flügge S (ed) Encyclopedia of Physics, vol VIa/2, Springer, Berlin, pp 1–296

[31] Nyashin Y, Lokhov V, Ziegler F (2005) Decomposition method in linear elastic problems with eigenstrain. ZAMM - Journal of Applied Mathematics and Mechanics / Zeitschrift für Angewandte Mathematik und Mechanik **85**(8):557–570

Chapter 16
Flexural Deformations and Vibrations of a Three-Layer Beam-Strip with a Stiff Core and Soft Skins

Gennadi Mikhasev, Marina Botogova, and Nguyen Le

Abstract The paper deals with the asymptotic derivation of governing equations predicting long-wave flexural response of a three-layer beam-strip with high-contrast mechanical properties. It is assumed that the material of each layer is isotropic, the core being stiff and the outer layers being soft. In the general case, the soft layers material can be considered as visco-elastic with the complex Young's and shear moduli. Three dimensionless parameters, the thickness-to-wavelength ratio, and ratios of the Young's moduli of soft and stiff layers are introduced as the small parameters with the first being assumed as the main parameter. The procedure of asymptotic step-by-step integration of the two-dimensional equations with respect to the transverse coordinate is proposed. Considering the first two approximations resulted in the novel one-dimensional Timoshenko-Reissner type differential equation taking into account shears in the stiff core and the deformations in the axial and transverse directions in the soft outer layers. The two examples on free low-frequency vibrations of three- and two-layer beam-strip with the simply supported edges are considered. In particular, the effect of a magnetorheological elastomer attached to an elastic strip on the natural frequencies and corresponding decrements under different intensity of the applied magnetic field is examined.

Gennadi Mikhasev
Belarusian State University, 4 Nezavisimosti Ave., 220030 Minsk, Belarus, & Harbin Institute of Technology, 92 West Dazhi Street, Nangang District, 150001 Harbin, P.R. China,
e-mail: mikhasev@bsu.by

Marina Botogova · Nguyen Le
Belarusian State University, 4 Nezavisimosti Ave., 220030 Minsk, Belarus,
e-mail: Batahova@bsu.by, dinhnguyen081017@gmail.com

16.1 Introduction

Thin-walled sandwich beams and plates assembled from laminae with contrasting mechanical and geometrical properties are intensively used as important elements in various engineering structures [1–4] as well as components of lightweight vehicles and building constructions [5, 6]. In particular, windscreens of up-to-date cars, windowpanes and photovoltaic panels are usually designed as three layer structures [3, 7–11]. Such sandwiches typically consists of a thin stiff and heavy facings as compared with the core. For instance, sandwich glasses have two stiff glass outer layers and relatively soft polymeric core [3, 12]. Another and rarer variant of a sandwich structure with high contrast properties is when the facing is much softer than the interlayer. An example of such laminate is a dust-covered precipitator plate being an important part of the gas filters [2].

There are not many papers considering bending sandwiches with contrast mechanical constants. All these studies can be conditionally subdivided into two main groups. Papers of the first group are based on engineering approaches and/or the introduction of kinematic hypotheses [8, 10, 12]. In particular, [12] considered a three-layer beam with the thick glass facings and the very thin thermoplastic (polyvinyl butyral) core; assuming the classical Bernoulli-Euler (BE) hypotheses for the outer stiff layers and introducing transverse shear only for the soft core, they derived three coupled differential equations with respect to the lateral and axial displacements. In paper by [8], the direct approach [13, 14] and the first order shear deformation plate theory were used for the analysis of bending of three-layer plates with both thin and thick soft core. The multiscale method with the finite element simulation has been utilized by [10] for the coupled global-local structural analysis of photovoltaic modules consisting of symmetric three-layered composite panels. Among many works, we mention also the papers by [15, 16], where the equivalent single-layer shell theory based on the generalised hypotheses of Timoshenko [17] was applied under studying free and forced vibrations of thin-walled structures consisting of stiff elastic layers and soft layers made of magneto- and electro-rheological composites.

Papers composing the second group are based on using the asymptotic approach which seems to be natural and very effective for analysing the dynamics of thin-walled layered structures with high contrast properties. The majority of these studies are devoted to the asymptotic analysis of the dispersion relations corresponding to the plane anti-symmetric [18, 19] and antiplane shear waves [20–22] in layered plates with contrast properties. Using the asymptotic procedure, [23] derived the dispersion equations corresponding to the wave motion of thin multi-layered structures composed of contrasting "strong" and "weak" layers. And in papers by [24] and [25], the Saint-Venant's principle in combination with the asymptotic approach taking into account the contrast in mechanical properties of the laminae were used to derive the asymptotically correct boundary conditions.

As for the derivation of asymptotically correct governing equations for layered structures with high-contrast properties, there are few works on the subject. Here, we mention the noticeable contribution by Tovstik and co-authors. Averaging the elastic moduli over the plate thickness, without focusing on their distribution in the

transverse direction, [26, 27] developed the procedure of asymptotic integration of 2D/3D equations of elasticity in the thickness direction and proposed the equivalent single layer model, which can be treated as the generalized Timoshenko-Reissner (TR) type model. Compared to the conventional BE, Kirchhoff-Love (KL) and TR models, the generalized TR model can be used for the prediction of bending deformations and vibrations of both functionally graded in the transverse direction and laminated beams/plates with the relatively large ratio between elastic moduli of layers [28–32]. In contrast to the above contributions, [33] and [34] introduced the ratios of moduli for soft and stiff layers as the additional small parameters. At that, [33] proposed a variational-asymptotic method that allows one to obtain various variational models of sandwiches depending on the assumed types of deformations of the soft core and hard facings, and [34] developed the asymptotic procedure [27, 35] for the step-by-step integration of the original 2D equations that makes it possible constructing hierarchical models for a two-layer beam strip with the high contrast mechanical properties.

In this paper, we generalize the approach developed in [34] for the three-layer beam-strip with a stiff core and soft skins. We restrict ourselves with the case of the high contrast mechanical constants of isotropic layers. In general, the material of outer soft layers may be viscoelastic. Considering the first two approximations, we derive the governing equation corresponding to the Timoshenko-Reissner model capturing the shear effects in the hard core and accounting for the transverse and longitudinal deformations in soft facings with their inertias. As examples, free low-frequency vibrations of three- and two-layered beam-strip assembled from high contrast material are considered. Particularly, the effect of viscoelastic magnetorheological elastomer attached to the hard ABS-plastic layer on the natural frequencies and decrement of free vibrations at different values of the applied magnetic field induction is analysed.

16.2 Statement of the Problem

We consider a three-layer strip consisting of an isotropic elastic stiff core and two isotropic relatively soft facings rigidly attached to the core. Let h_k be layer thickness, λ_k, μ_k be the Lamé constants, and ρ_k are material densities of layers, where subscripts $k = 1, 3$ and $k = 2$ correspond to the facings and core, respectively. In general, the material of outer layers may be considered as viscoelastic with the material constants λ_j, μ_j being complex for $j = 1, 3$. The peculiarity of the problem under consideration is that

$$|\lambda_j| \ll \lambda_2, |\mu_j| \ll \mu_2$$

for $j = 1, 3$.

The local coordinate systems $O_k x_k y_k$ are introduced as shown in Fig. 16.1 with $x_1 = x_2 = x_3 = x$ and $0 \leq y_k \leq h_k$. Let the beam-strip be under action of the body forces $\mathbf{F}_k = \left(f_1^{(k)}, f_2^{(k)} \right)$, where $f_\varsigma^{(k)}(x_k, y_k)$ are functions of the longitudinal and transverse coordinates x_k, y_k. Possible external forces acting at the soft facings are

assumed to be weak and ignored in our study. The 2D equations for each layer read

Fig. 16.1 Three-layer beam-strip under body forces. Coordinate systems.
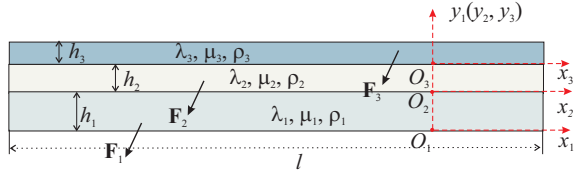
$$\frac{\partial s_{11}^{(k)}}{\partial x} + \frac{\partial s_{12}^{(k)}}{\partial y_k} - \rho_k \frac{\partial^2 u_1^{(k)}}{\partial t^2} + f_1^{(k)} = 0, \quad \frac{\partial s_{21}^{(k)}}{\partial x} + \frac{\partial s_{22}^{(k)}}{\partial y_k} - \rho_k \frac{\partial^2 u_2^{(k)}}{\partial t^2} + f_2^{(k)} = 0, \quad (16.1)$$

where $s_{ij}^{(k)}$ are components of the stress tensor in the kth layer under the plane stress state, and $u_1^{(k)}, u_2^{(k)}$ are the longitudinal and transverse displacements. The material for each layer is assumed to be isotropic and obeys the classical Hooke's law

$$s_{ij}^{(k)} = \lambda_k e_{ii}^{(k)} \delta_{ij} + 2\mu_k e_{ij}^{(k)}, \quad (16.2)$$

where $e_{ij}^{(k)}$ are linear components of the strain tensor.

Let $\varepsilon = h/l$ be a small parameter, where $h = h_1 + h_2 + h_3$ is the total thickness of the beam-strip, and l is either the characteristic size of bending deformation or the beam-strip length. We introduce the following assumption

$$\frac{E_m'}{E_2} = \varepsilon^2 \varsigma_m, \quad \varsigma_m \sim 1, \quad m = 1, 3 \quad (16.3)$$

where E_2 are the Young's modulus of the elastic stiff core, and $E_m' = \Re E_m$ is the real part of the complex Young's modulus for the mth soft layer.

We introduce the dimensionless variables,

$$x = l\xi, \quad y_k = h_k z_k, \quad \left\{ u_1^{(k)}, u_2^{(k)} \right\} = h \left\{ u^{(k)}, w^{(k)} \right\},$$

$$s_{ij}^{(k)} = E_k' \sigma_{ij}^{(k)}, \quad f_2^{(k)} = \frac{E_k'}{h_k} \hat{f}_2^{(k)}, \quad f_1^{(k)} = \frac{\varepsilon E_k'}{h_k} \hat{f}_1^{(k)}, \quad i, j, k = 1, 2. \quad (16.4)$$

where the dimensionless forces are values of the order $O(1)$ as $\varepsilon \to \infty$. In what follows, considering the kth layer, we omit the subscript in z_k.

Note that for low-frequency bending vibrations of beams and plates with a large characteristic strain size, the following asymptotic estimates are valid [34–36]:

$$w^{(k)} = \varepsilon^{-4} W^{(k)}, \quad u^{(k)} = \varepsilon^{-3} U^{(k)}, \quad \sigma_{12}^{(k)} = \varepsilon^{-1} \tau^{(k)}, \quad \sigma_{22}^{(k)} = \sigma^{(k)}, \quad (16.5)$$

where $W^{(k)}, U^{(k)}, \tau^{(k)}, \sigma^{(k)} \sim 1$. Taking into account relations (16.4) and (16.5), Eqs. (16.1) and (16.2) can be reduced to the following system of differential equations,

$$\frac{\partial W^{(k)}}{\partial z} = -\varepsilon^2 \kappa_k c_\nu^{(k)} \frac{\partial U^{(k)}}{\partial \xi} + \varepsilon^4 \kappa_k c_3^{(k)} \sigma^{(k)},$$

$$\frac{\partial U^{(k)}}{\partial z} = -\kappa_k \frac{\partial W^{(k)}}{\partial \xi} + \varepsilon^2 \kappa_k c_g^{(k)} \tau^{(k)},$$

$$\frac{\partial \tau^{(k)}}{\partial z} = -\kappa_k c_0^{(k)} \frac{\partial^2 U^{(k)}}{\partial \xi^2} - \varepsilon^2 \kappa_k c_\nu^{(k)} \frac{\partial \sigma^{(k)}}{\partial \xi} + \varepsilon^2 \eta_k \frac{\partial^2 U^{(k)}}{\partial t^2} - \varepsilon^2 \hat{f}_1^{(k)},$$

$$\frac{\partial \sigma^{(k)}}{\partial z} = -\kappa_k \frac{\partial \tau^{(k)}}{\partial \xi} + \eta_k \frac{\partial^2 W^{(k)}}{\partial t^2} - \hat{f}_2^{(k)}$$

(16.6)

with

$$\kappa_k = \frac{h_k}{h}, \quad c_3^{(k)} = \frac{E_k'}{\lambda_k + 2\mu_k}, \quad c_\nu^{(k)} = \frac{\lambda_k}{\lambda_k + 2\mu_k},$$

$$c_0^{(k)} = \frac{4\mu_k(\lambda_k + \mu_k)}{E_k'(\lambda_k + 2\mu_k)}, \quad c_g^{(k)} = \frac{E_k'}{\mu_k}, \quad \eta_k = \frac{\rho_k h_k h}{\varepsilon^4 E_k'}.$$

(16.7)

The boundary conditions at the face lines are assumed to be homogeneous:

$$\tau^{(1)}|_{z=0} = \sigma^{(1)}|_{z=0} = 0, \quad \tau^{(3)}|_{z=1} = \sigma^{(3)}|_{z=1} = 0.$$

(16.8)

At the interface lines, we consider the rigid contact conditions. When taking Eqs. (16.3)-(16.5) into account, these conditions become:

• for displacements,

$$W^{(1)}|_{z=1} = W^{(2)}|_{z=0}, \quad U^{(1)}|_{z=1} = U^{(2)}|_{z=0},$$

$$W^{(2)}|_{z=1} = W^{(3)}|_{z=0}, \quad U^{(2)}|_{z=1} = U^{(3)}|_{z=0},$$

(16.9)

• for stresses

$$\tau^{(2)}|_{z=0} = \varepsilon^2 \varsigma_1 \tau^{(1)}|_{z=1}, \quad \sigma^{(2)}|_{z=0} = \varepsilon^2 \varsigma_1 \sigma^{(1)}|_{z=1},$$

$$\tau^{(2)}|_{z=1} = \varepsilon^2 \varsigma_3 \tau^{(3)}|_{z=0}, \quad \sigma^{(2)}|_{z=1} = \varepsilon^2 \varsigma_3 \sigma^{(3)}|_{z=0}$$

(16.10)

We arrived at the boundary-value problem (16.6), (16.9), and (16.10).

16.3 Asymptotic Integration of Boundary-Value Problem

A solution of the boundary-value problem can be sought in the form of formal asymptotic series

$$W^{(k)} = w_0^{(k)} + \varepsilon^2 w_2^{(k)} + \dots, \quad U^{(k)} = u_0^{(k)} + \varepsilon^2 u_2^{(k)} + \dots,$$

$$\tau^{(k)} = \tau_0^{(k)} + \varepsilon^2 \tau_2^{(k)} + \dots, \quad \sigma^{(k)} = \sigma_0^{(k)} + \varepsilon^2 \sigma_2^{(k)} + \dots, \quad k = 1, 2, 3.$$

(16.11)

We substitute series (16.11) into Eqs. (16.6) and the boundary conditions (16.8)-(16.10) and consider arising boundary-value problems step-by-step.

16.3.1 Leading Approximation

In the leading approximation, one has the sequence of equations

$$
\frac{\partial w_0^{(k)}}{\partial z} = 0, \qquad \frac{\partial u_0^{(k)}}{\partial z} = -\kappa_k \frac{\partial w_0^{(k)}}{\partial \xi},
$$
$$
\frac{\partial \tau_0^{(k)}}{\partial z} = -\kappa_k c_0^{(k)} \frac{\partial^2 u_0^{(k)}}{\partial \xi^2}, \qquad \frac{\partial \sigma_0^{(k)}}{\partial z} = -\kappa_k \frac{\partial \tau_0^{(k)}}{\partial \xi} + \eta_k \frac{\partial^2 w_0^{(k)}}{\partial t^2} - \hat{f}_2^{(k)}
\tag{16.12}
$$

with the boundary conditions for displacements,

$$
\begin{aligned}
w_0^{(1)}|_{z=1} = w_0^{(2)}|_{z=0}, \quad & u_0^{(1)}|_{z=1} = u_0^{(2)}|_{z=0}, \\
w_0^{(2)}|_{z=1} = w_0^{(3)}|_{z=0}, \quad & u_0^{(2)}|_{z=1} = u_0^{(3)}|_{z=0},
\end{aligned}
\tag{16.13}
$$

and stresses,

$$
\begin{aligned}
\tau_0^{(1)}|_{z=0} = \sigma_0^{(1)}|_{z=0} = 0, \quad & \tau_0^{(3)}|_{z=1} = \sigma_0^{(3)}|_{z=1} = 0, \\
\tau_0^{(2)}|_{z=0} = \sigma_0^{(2)}|_{z=0} = 0, \quad & \tau_0^{(2)}|_{z=1} = \sigma_0^{(2)}|_{z=1} = 0,
\end{aligned}
\tag{16.14}
$$

respectively. We note that in the leading approximation the interface conditions (16.10) for the stresses $\tau_0^{(2)}, \sigma_0^{(2)}$ in the hard core degenerate into the homogeneous ones.

Sequential integration of Eqs. (16.12) over the segment $1 \leq z \leq 1$ with the boundary conditions (16.13), (16.14) taken into account leads to the formulas for displacements,

$$
w_0^{(k)} = w_0(\xi, t) \quad \text{for any} \quad k = 1, 2, 3,
$$
$$
u_0^{(1)} = -\frac{1}{2}[2\kappa_1(z-1) - \kappa_2] \frac{\partial w_0}{\partial \xi}, \quad u_0^{(2)} = -\frac{1}{2}\kappa_2(2z-1) \frac{\partial w_0}{\partial \xi},
\tag{16.15}
$$
$$
u_0^{(3)} = -\frac{1}{2}(2\kappa_3 z + \kappa_2) \frac{\partial w_0}{\partial \xi},
$$

and stresses,

$$\tau_0^{(1)} = \frac{1}{2}c_0^{(1)}\kappa_1[\kappa_1 z^2 - (2\kappa_1 + \kappa_2)z]\frac{\partial^3 w_0}{\partial \xi^3},$$

$$\tau_0^{(2)} = \frac{1}{2}c_0^{(2)}\kappa_2^2(z^2 - z)\frac{\partial^3 w_0}{\partial \xi^3},$$

$$\tau_0^{(3)} = \frac{1}{2}c_0^{(3)}\kappa_3[\kappa_3 z^2 + \kappa_2 z - \kappa_2 - \kappa_3]\frac{\partial^3 w_0}{\partial \xi^3},$$

$$\sigma_0^{(1)} = -\frac{1}{12}c_0^{(1)}\kappa_1^2[2\kappa_1 z^3 - 3(2\kappa_1 + \kappa_2)z^2]\frac{\partial^4 w_0}{\partial \xi^4} + \eta_1 z\frac{\partial^2 w_0}{\partial t^2} - F_2^{(1)}, \qquad (16.16)$$

$$\sigma_0^{(2)} = -\frac{1}{12}c_0^{(2)}\kappa_2^3(2z^3 - 3z^2)\frac{\partial^4 w_0}{\partial \xi^4} + \eta_2 z\frac{\partial^2 w_0}{\partial t^2} - F_2^{(2)},$$

$$\sigma_0^{(3)} = -\frac{1}{12}c_0^{(3)}\kappa_3^2[2\kappa_3 z^3 + 3\kappa_2 z^2 - 6(\kappa_2 + \kappa_3)z + 4\kappa_3 + 3\kappa_2]\frac{\partial^4 w_0}{\partial \xi^4}$$

$$\quad + \eta_3(z-1)\frac{\partial^2 w_0}{\partial t^2} + F_2^{(3)},$$

where

$$F_2^{(j)}(\xi,z) = \int_0^z \hat{f}_2^{(j)}(\xi,z)dz, \quad F_2^{(3)}(\xi,z) = \int_z^1 \hat{f}_2^{(3)}(\xi,z)dz, \quad j=1,2, \quad (16.17)$$

and the function $w_0(x,t)$ is determined from the classical differential equation,

$$\frac{1}{12}c_0^{(2)}\kappa_2^3\frac{\partial^4 w_0}{\partial \xi^4} + \eta_2\frac{\partial^2 w_0}{\partial t^2} = F_2^{(2)}(\xi,1), \qquad (16.18)$$

which is related to the Bernoulli-Euler type model.

16.3.2 First-Order Approximation

In the first-order approximation, we arrive at the following system of equations:

$$\frac{\partial w_2^{(k)}}{\partial z} = -\kappa_k c_v^{(k)}\frac{\partial u_0^{(k)}}{\partial \xi}, \quad \frac{\partial u_2^{(k)}}{\partial z} = -\kappa_k\frac{\partial w_2^{(k)}}{\partial \xi} + \kappa_k c_g^{(k)}\tau_0^{(k)},$$

$$\frac{\partial \tau_2^{(k)}}{\partial z} = -\kappa_k c_0^{(k)}\frac{\partial^2 u_2^{(k)}}{\partial \xi^2} - \kappa_k c_v^{(k)}\frac{\partial \sigma_0^{(k)}}{\partial \xi} + \eta_k\frac{\partial^2 u_0^{(k)}}{\partial t^2} - \hat{f}_1^{(k)}, \qquad (16.19)$$

$$\frac{\partial \sigma_2^{(k)}}{\partial z} = -\kappa_k\frac{\partial \tau_2^{(k)}}{\partial \xi} + \eta_k\frac{\partial^2 w_2^{(k)}}{\partial t^2}$$

with $k = 1,2,3$. The corresponding interface conditions (16.13) for displacements remain the same, and the boundary conditions (16.14)$_1$ for stresses at the outer layers are again homogeneous, with the replacement everywhere subscript 0 by 2. As for the interface conditions for stresses, they become inhomogeneous:

$$\tau_2^{(2)}|_{z=0} = \varsigma_1\tau_0^{(1)}|_{z=1}, \quad \sigma_2^{(2)}|_{z=0} = \varsigma_1\sigma_0^{(1)}|_{z=1},$$
$$\tau_2^{(2)}|_{z=1} = \varsigma_3\tau_0^{(3)}|_{z=0}, \quad \sigma_2^{(2)}|_{z=1} = \varsigma_3\sigma_0^{(3)}|_{z=0}. \tag{16.20}$$

Consider this approximation in more details. The integration of the first two equations from (16.19), with the boundary conditions taken into account, gives the corrections for displacements:

$$w_2^{(1)} = \frac{1}{2}c_\nu^{(1)}\kappa_1\left[\kappa_1 z^2 - (2\kappa_1+\kappa_2)z + \kappa_1 + \kappa_2\right]\frac{\partial^2 w_0}{\partial\xi^2} + w_{20}(\xi,t),$$

$$w_2^{(2)} = \frac{1}{2}c_\nu^{(2)}\kappa_2^2(z^2-z)\frac{\partial^2 w_0}{\partial\xi^2} + w_{20}(\xi,t),$$

$$w_2^{(3)} = \frac{1}{2}c_\nu^{(3)}\kappa_3(\kappa_3 z^2 + \kappa_2 z)\frac{\partial^2 w_0}{\partial\xi^2} + w_{20}(\xi,t),$$

$$u_2^{(1)} = \frac{1}{12}\kappa_1^2\left\{c_4^{(1)}\left[2\kappa_1 z^3 - 3(2\kappa_1+\kappa_2)z^2\right] - 6c_\nu^{(1)}(\kappa_1+\kappa_2)z\right.$$
$$\left. + c_4^{(1)}(4\kappa_1 + 3\kappa_2) + 6c_\nu^{(1)}(\kappa_1+\kappa_2)\right\}\frac{\partial^3 w_0}{\partial\xi^3} - \kappa_1(z-1)\frac{\partial w_{20}}{\partial\xi} + u_{20}(\xi,t),$$

$$u_2^{(2)} = \frac{1}{12}c_4^{(2)}\kappa_2^3(2z^3 - 3z^2)\frac{\partial^3 w_0}{\partial\xi^3} - \kappa_2 z\frac{\partial w_{20}}{\partial\xi} + u_{20}(\xi,t),$$

$$u_2^{(3)} = \frac{1}{12}\kappa_3^2\left\{c_4^{(3)}(2\kappa_3 z^3 + 3\kappa_2 z^2) - 6c_0^{(3)}c_g^{(3)}(\kappa_2+\kappa_3)z - c_4^{(2)}\right\}\frac{\partial^3 w_0}{\partial\xi^3}$$
$$- (\kappa_3 z + \kappa_2)\frac{\partial w_{20}}{\partial\xi} + u_{20}(\xi,t),$$

$$\tag{16.21}$$

where

$$c_4^{(k)} = \frac{3\lambda_k + 4\mu_k}{\lambda_k + 2\mu_k}, \tag{16.22}$$

and $w_{20}(\xi,t), u_{20}(\xi,t)$ are unknown functions to be determined below.

Consider the third equation from (16.19) for $k = 2$. Substituting corrections (16.21) for displacements into this equation and integrating it over the segment $0 \le z \le 1$ and satisfying the inhomogeneous boundary conditions (16.20) at the interfaces, we obtain the equation

$$c_0^{(2)}\kappa_2\frac{\partial^2 u_{20}}{\partial\xi^2} = \frac{1}{12}c_0^{(2)}\kappa_2^4\frac{\partial^4 w_0}{\partial\xi^4} + \frac{1}{2}\left[\varsigma_3 c_0^{(3)}\kappa_3(\kappa_2+\kappa_3)\right.$$
$$\left. - \varsigma_1 c_0^{(1)}\kappa_1(\kappa_1+\kappa_2)\right]\frac{\partial^3 w_0}{\partial\xi^3} - \frac{1}{2}\eta_2 c_\nu^{(2)}\kappa_2\frac{\partial^3 w_0}{\partial\xi^2\partial t}$$
$$+ \frac{1}{2}c_0^{(2)}\kappa_2^2\frac{\partial^3 w_{20}}{\partial\xi^3} + \int_0^1 G^{(2)}(\xi,z)dz, \tag{16.23}$$

with respect to the function u_{20} and the relation for correction of the shear stress in the stiff layer as well,

$$\tau_2^{(2)} = -\frac{1}{12}c_0^{(2)}\kappa_2^4(z^4 - 2z^3 + z)\frac{\partial^5 w_0}{\partial\xi^5} - \frac{1}{2}\left[\varsigma_1 c_0^{(1)}\kappa_1(\kappa_1 + \kappa_2)(1 - z)\right.$$

$$\left. + \varsigma_3 c_0^{(3)}\kappa_3(\kappa_2 + \kappa_3)z\right]\frac{\partial^3 w_0}{\partial\xi^3} - \frac{1}{4}\eta_2\kappa_2 c_0^{(2)}c_g^{(2)}(z^2 - z)\frac{\partial^3 w_0}{\partial\xi^2\partial t} \tag{16.24}$$

$$+ \frac{1}{2}c_0^{(2)}\kappa_2^2(z^2 - z)\frac{\partial^3 w_{20}}{\partial\xi^3} + \int_0^z G^{(2)}(\xi,z)dz - z\int_0^1 G^{(2)}(\xi,z)dz,$$

where the function $w_{20}(\xi,t)$ is not yet defined, and

$$G^{(2)}(\xi,z) = c_\nu^{(2)}\kappa_2\frac{\partial F_2^{(2)}}{\partial\xi} - \hat{f}_1^{(2)}. \tag{16.25}$$

The functions $\tau_2^{(1)}, \tau_2^{(3)}$ related to the soft layers can be determined in the same way by integrating the third equation from Eqs. (16.19) at $k = 1, 3$. We do not write down here the final relations, but note only that they are required to construct the next approximation and, particularly, to find the high-order correction $\varepsilon^4\tau_4^{(2)}$ for the stiff core.

Finally, consider the last equation from (16.19). Integrating it in the thickness direction with the functions $\tau_2^{(2)}, w_2^{(2)}$ taken into account, we arrive at the following formula for the correction to the normal stress:

$$\sigma_2^{(2)} = \frac{1}{120}c_0^{(2)}\kappa_2^5(2z^5 - 5z^4 + 5z^2)\frac{\partial^6 w_0}{\partial\xi^6}$$

$$+ \frac{1}{4}\kappa_2\left\{\left[c_0^{(3)}\varsigma_3\kappa_3(\kappa_2 + \kappa_3) - c_0^{(1)}\varsigma_1\kappa_1(\kappa_1 + \kappa_2)\right]z^2\right.$$

$$\left. + 2c_0^{(1)}\varsigma_1\kappa_1(\kappa_1 + \kappa_2)z\right\}\frac{\partial^4 w_0}{\partial\xi^4} + \frac{1}{12}\eta_2\kappa_2^2 c_6^{(2)}(2z^3 - 3z^2)\frac{\partial^4 w_0}{\partial\xi^2\partial t^2} \tag{16.26}$$

$$- \frac{1}{12}c_0^{(2)}\kappa_2^3(2z^3 - 3z^2)\frac{\partial^4 w_{20}}{\partial\xi^4} + \eta_2 z\frac{\partial^2 w_{20}}{\partial t^2}$$

$$- \kappa_2\int_0^z\int_0^z G^{(2)}(\xi,z)dz + \frac{1}{2}\kappa_2 z^2\int_0^1 G^{(2)}(\xi,z)dz + \sigma_{20}^{(2)}(\xi,t),$$

where

$$c_6^{(2)} = c_\nu^{(2)}c_4^{(2)} + c_0^{(2)}c_3^{(2)} = (1 + \nu_2)/(1 - \nu_2)$$

with the Poisson's ratio ν_2 for the stiff core, and $\sigma_{20}^{(2)}(\xi,t)$ is an unknown function.

Substituting Eq. (16.26) into the second condition (16.20) at the interface, we obtain the required function

$$\sigma_{20}^{(2)}(\xi,t) = \frac{1}{12}c_0^{(1)}\varsigma_1\kappa_1^2(4\kappa_1 + 3\kappa_2)\frac{\partial^4 w_0}{\partial\xi^4} + \varsigma_1\eta_1\frac{\partial^2 w_0}{\partial t^2} - \varsigma_1\int_0^1 \hat{f}_2^{(1)}dz. \tag{16.27}$$

Applying the forth inhomogeneous condition (16.20) to function (16.26) with relation (16.27) taken into account, we arrive at the following inhomogeneous differential equation

$$
\frac{1}{12}c_0^{(2)}\kappa_2^3\frac{\partial^4 w_{20}}{\partial\xi^4}+\eta_2\frac{\partial^2 w_{20}}{\partial t^2}=-\frac{1}{60}c_0^{(2)}\kappa_2^{(5)}\frac{\partial^6 w_0}{\partial\xi^6}
$$

$$
-\frac{1}{12}\left[\varsigma_1 c_0^{(1)}\kappa_1(4\kappa_1^2+6\kappa_1\kappa_2+3\kappa_2^2)+\varsigma_3 c_0^{(3)}\kappa_3(4\kappa_3^2+6\kappa_3\kappa_2+3\kappa_2^2)\right]\frac{\partial^4 w_0}{\partial\xi^4} \quad (16.28)
$$

$$
+\frac{1}{12}\eta_2 c_6^{(2)}\kappa_2^2\frac{\partial^4 w_0}{\partial\xi^2\partial t^2}-(\varsigma_1\eta_1+\varsigma_3\eta_3)\frac{\partial^2 w_0}{\partial t^2}+\mathcal{F}(\xi)
$$

with respect to the function w_{20}, where

$$
\mathcal{F}(\xi)=-\frac{\kappa_2}{2}\int_0^1\left[G^{(2)}(\xi,z)-2\int_0^z G^{(2)}(\xi,z)dz\right]dz+\varsigma_1 F_2^{(1)}(\xi,1)+\varsigma_3 F_2^{(3)}(\xi,0)
$$

$$
(16.29)
$$

is the given function depending on the volume forces.

Now, having determined the function w_{20}, one can calculate the corrections $\tau_2^{(2)}$ and $\sigma_2^{(2)}$ by formulas (16.24) and (16.26), respectively. The functions $\sigma_2^{(1)},\sigma_2^{(3)}$ are defined in the same way by integrating the last equation from (16.19) at $k=1,3$, but we do not give here the final relations because of their unhandiness.

We note that the maximum order of the derivative with respect to x on the right-hand side of Eq. (16.28) can be reduced to the forth order. Accounting for Eq. (16.18), we rewrite Eq. (16.28) as follows:

$$
\frac{1}{12}c_0^{(2)}\kappa_2^3\frac{\partial^4 w_{20}}{\partial\xi^4}+\eta_2\frac{\partial^2 w_{20}}{\partial t^2}=
$$

$$
-\frac{1}{12}\left[\varsigma_1 c_0^{(1)}\kappa_1(4\kappa_1^2+6\kappa_1\kappa_2+3\kappa_2^2)+\varsigma_3 c_0^{(3)}\kappa_3(4\kappa_3^2+6\kappa_3\kappa_2+3\kappa_2^2)\right]\frac{\partial^4 w_0}{\partial\xi^4}
$$

$$
+\eta_2\kappa_2^2\left(\frac{1}{5}+\frac{c_6^{(2)}}{12}\right)\frac{\partial^4 w_0}{\partial\xi^2\partial t^2}-(\varsigma_1\eta_1+\varsigma_3\eta_3)\frac{\partial^2 w_0}{\partial t^2}+\mathcal{F}(\xi)-\frac{1}{5}\kappa_2^2\frac{\partial^2 F_2^{(2)}(\xi,1)}{\partial\xi^2}.
$$

$$
(16.30)
$$

The process of integrating Eqs. (16.6) could be continued indefinitely, however, it involves complex transformations and leads to very cumbersome relations for corrections for displacements and stresses.

16.3.3 Governing Equation

We consider the transverse dimensionless displacements in the stiff core:

$$W^{(2)}(\xi, z, t) = w_0^{(2)}(\xi, t) + \varepsilon^2 w_2^{(2)}(\xi, z, t) + O\left(\varepsilon^4\right), \qquad (16.31)$$

where $w_2^{(2)}$ is determined by the second equation from (16.21). Note that

$$w_2^{(2)}(\xi, 0, t) = w_2^{(2)}(\xi, 1, t) = w_{20}(\xi, t),$$

where w_{20} is defined from Eq. (16.30). Then the displacement of points lying at the interface lines reads

$$w^\circ(\xi, t) = w_0^{(2)}(\xi, t) + \varepsilon^2 w_{20}(\xi, t) + O\left(\varepsilon^4\right). \qquad (16.32)$$

Summation of Eq. (16.18) and Eq. (16.30) multiplied by ε^2, taking into account Eq. (16.32), leads to the following differential equation for interface lines:

$$I\frac{\partial^4 w^\circ}{\partial \xi^4} + J\frac{\partial^4 w^\circ}{\partial t^2} = F(\xi), \qquad (16.33)$$

where

$$\begin{aligned}
I = \frac{1}{12} &\left\{ c_0^{(2)} \kappa_2^3 + \varepsilon^2 \left[\varsigma_1 c_0^{(1)} \kappa_1 \left(4\kappa_1^2 + 6\kappa_1 \kappa_2 + 3\kappa_2^2 \right) \right] \right. \\
&\left. + \varsigma_3 c_0^{(3)} \kappa_3 \left(4\kappa_3^2 + 6\kappa_3 \kappa_2 + 3\kappa_2^2 \right) \right\}
\end{aligned} \qquad (16.34)$$

is the reduced dimensionless flexural rigidity of the three-layer beam-strip,

$$J = \eta_2 + \varepsilon^2 \left[\varsigma_1 \eta_1 + \varsigma_3 \eta_3 - \eta_2 \kappa_2^2 \left(\frac{1}{5} + \frac{c_6^{(2)}}{12} \right) \frac{\partial^2}{\partial \xi^2} \right] \qquad (16.35)$$

is the operator of the so-called modified transverse inertia, and

$$F(\xi) = F_2^{(2)}(\xi, 1) + \varepsilon^2 \left[\mathcal{F}(\xi) - \frac{1}{5} \kappa_2^2 \frac{\partial^2 F_2^{(2)}(\xi, 1)}{\partial \xi^2} \right] \qquad (16.36)$$

is the dimensionless resultant of volume forces reduced to the reference surface (i.e., the interface surface between the upper layer and the core) with the functions $\mathcal{F}(\xi), F_2^{(2)}(\xi, z)$ defined by Eqs. (16.29), (16.25) and (16.17).

Equation (16.33) can be rewritten in the original dimensional variables:

$$I_r \frac{\partial^4 u_2^\circ}{\partial x^4} + J_r \frac{\partial^4 u_2^\circ}{\partial t^2} = E_2 F(x/l). \qquad (16.37)$$

In Eq. (16.37), u_2° is the transverse displacement of the core reference surface, and I_r and J_r are the dimensional flexural rigidity and the operator of the modified transverse inertia, respectively, calculated by the following formulas:

$$I_r = \frac{1}{12}\left[\frac{E_2 h_2^3}{1-v_2^2} + \frac{E_1 h_1}{1-v_1^2}\left(4h_1^2 + 6h_1 h_2 + 3h_2^2\right) + \frac{E_3 h_3}{1-v_3^2}\left(4h_3^2 + 6h_3 h_2 + 3h_2^2\right)\right],$$

$$J_r = \sum_{k=1}^{3}\rho_k h_k - \rho_2 h_2^3\left[\frac{1}{5} + \frac{1+v_2}{12(1-v_2)}\right]\frac{\partial^2}{\partial x^2}.$$

$$(16.38)$$

Equation (16.37) taking into account shears in the hard core is related to the Timoshenko-Reissner type model [37, 38]. The equation describes the flexural response of a single-layer beam-strip being equivalent to the considered three-layer beam-strip with the high contrast properties. When assuming $h_3 = 0$ in all aforementioned equations, then Eq. (16.37) together with relations (16.36), (16.38) degenerates into the governing equation for a two-layer beam-strip with contrast mechanical properties [34].

We note the presented above model is free of any kinematic hypotheses, it is asymptotically consistent for the long-wave vibrations and deformations, and under constructing more high approximations permits to obtain more correct distributions of displacements and stresses in the transverse direction when comparing it with the hypotheses based models.

We remind also that in the general case the moduli E_1 and E_3 can be complex values, so that Eq. (16.37) as well as other relations for calculating the strain-stress state can be used for the beam-strips with attached viscoelastic layers.

16.4 Free Vibrations

We apply our model for studying free low-frequency vibrations of the three-layer beam-strip of the length l with simply supported edges. Assume a small transverse displacement in the form of a function

$$u_2^\circ = A\sin\left(\frac{\pi n x_1}{l}\right)\exp\left(\mathrm{i}\omega t\right),$$

where A is an arbitrary constant, $\mathrm{i} = \sqrt{-1}$, ω is a natural frequency, and n is a number of semi-waves. Substituting this form into the homogeneous Eq. (16.37), we obtain the formula for natural frequencies:

$$\omega = \frac{(\pi n)^2 I_r^{1/2}}{l^2\sqrt{\sum_{k=1}^{3}\rho_k h_k + \rho_2 h_2^3\left[\frac{1}{5} + \frac{1+v_2}{12(1-v_2)}\right]\left(\frac{\pi n}{l}\right)^2}}, \quad n = 1,2,3,\ldots \quad (16.39)$$

As the first example, we consider the three-layer beam-strip of the length $l = 1$ m with the fixed total thickness $h = h_1 + h_2 + h_3 = 0.1$ m. The mechanical properties of the core and the outer layers correspond to steel and ABS-plastic SD-0170, respectively. The input mechanical parameters are the following:

$$E_2 = 200 \text{ GPa}, \quad \rho_2 = 7.8 \text{ g/cm}^3, \quad \nu_2 = 0.3,$$
$$E_1 = E_3 = 1.5 \text{ GPa}, \quad \rho_1 = \rho_3 = 1.4 \text{ g/cm}^3, \quad \nu_1 = \nu_3 = 0.4. \tag{16.40}$$

The calculations were performed for the beam-strip with the same thickness for the outer layers, $h_1 = h_3$, and the core thickness h_2 varying from 0 to 0.1 m. It can be seen from Fig. 16.2 that for the fixed total thickness the effect of soft outer layers on natural frequencies is qualitatively the same for both low-frequency and high-frequency modes. The attachment of soft layers and increase of their thickness first results in the decrease of all eigenfrequencies. However, there is a critical small value of the core thickness, h_2, at which an eigenfrequency ω has a minimum.

In the second example, we study free vibrations of the two-layer beam-strip (here, $h_3 = 0$) with mechanical properties of the magnetorheological elastomer (MRE) and ABS-plastic SD-0170 for the bottom and upper layers, respectively. As the MRE, we consider the rubber based MRE elaborated by [39] and containing 33% of iron practicals, 7% of carbon black and 60% of the rubber matrix. The principle characteristic of any MRE is the complex shear modulus $G_v = G'_v + iG''_v$, where $i = \sqrt{-1}$, and G'_v and G''_v are the storage and loss moduli, respectively. These quantities for the considered MRE, as functions of the magnetic field induction, are presented in Table 16.1. When assuming the MRE as an isotropic material, then the complex
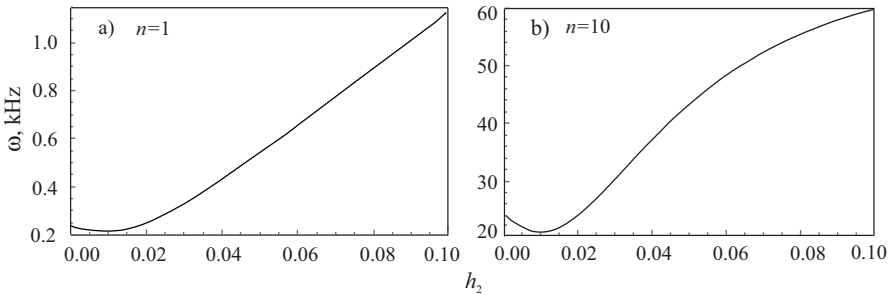
Fig. 16.2: Natural frequencies of the three-layer beam-strip with the mechanical properties of steel and ABS-plastic SD-0170 for the core and outer layers, respectively, vs. the core thickness h_2: a) number of semi-waves $n = 1$; b) number of semi-waves $n = 10$.

Table 16.1: Storage and loss moduli G'_v, G''_v vs. the magnetic induction B for the MRE [39] containing 33% of iron practicals and 7% of carbon black.

Magnetic induction B, mT	Storage modulus G'_v, kPa	Loss modulus G'_v, kPa
0	4050	567
200	4250	723
400	6000	960
600	7900	1185
800	8000	1120
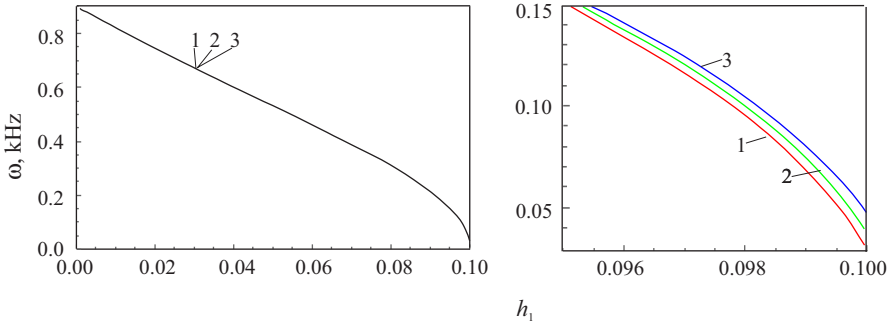
Fig. 16.3: The lowest ($n = 1$) natural frequencies of the two-layer beam-strip with the mechanical properties of MRE and ABS-plastic SD-0170 vs. the MRE layer thickness h_1 at different values of the magnetic field induction B: curve 1 (red line) - $B = 0$ mT, curve 2 (green) - $B = 400$ mT, curve 3 (blue) - $B = 700$ mT.

Young's modulus can be determined as $E_v = 2(1 + v_v)G_v$, where v_v is the Poison's ratio for the MRE. In our calculations, we assume $E_1 = E_v, v_v = 0.45$. The total thickness $h = h_1 + h_2 = 0.1$ m and the beam-strip length $l = 0.845$ m are fixed, while the MRE layer thickness h_1 is varied. Figure 16.3 displays the lowest natural frequencies versus the MRE layer thickness h_1 for different levels of the applied magnetic field, and Fig. 16.4 shows the corresponding logarithmic decrements

$$D_l = \frac{2\pi \Im \omega}{\sqrt{(\Re \omega)^2 - (\Im \omega)^2}}, \tag{16.41}$$

where $\Re Z$ and $\Im Z$ denote the real and imaginary parts of the complex quantity Z, respectively.

It can be seen that an increase in the thickness of the MRE layer leads to a decrease in natural frequencies and an increase in the corresponding decrements of free
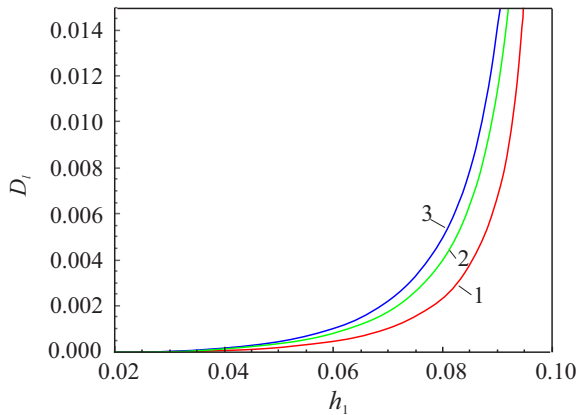
Fig. 16.4 The logarithmic decrement D_l for the first mode of the two-layer beam-strip with the mechanical properties of MRE and ABS-plastic SD-0170 vs. the MRE layer thickness h_1 at different values of the magnetic field induction B: curve 1 (red line) - $B = 0$ mT, curve 2 (green) - $B = 400$ mT, curve 3 (blue) - $B = 700$ mT.

oscillations. As for the influence of magnetic field, it affects the above characteristics only at large values of the thickness h_1, the higher the magnetic field induction, the greater the natural frequencies and the corresponding decrements.

16.5 Conclusions

We considered the three layer beam-strip with the isotropic hard core and soft skins. Introducing three small parameters, the strip width-to-length ratio and the ratios of moduli of soft facings and hard core, we performed asymptotic integrations of the 2D equations of elasticity with respect to the transverse coordinate. Considering only the leading and first-order approximations, we derived the one-dimensional differential equation predicting bending deformation and free low-frequency vibrations of the beam-strip corresponding to the Timoshenko-Reissner type model. The novel governing equation contains terms taking into account shears in the hard core as well as effects of the lateral and longitudinal displacements in the soft outer layers. As the first example, we considered free low-frequency vibrations of the three-layer "plastic-steel-plastic" beam-strip and analysed the influence of the quantity of the relatively soft plastic under the fixed total thickness on the natural frequency of the simply supported beam. In the second example, we studied the effect of the magnetorheological elastomer attached to the ABS-plastic on the natural frequencies and decrement of free vibrations of the two-layer beam under different intensity of the applied magnetic field.

References

[1] Vinson JR (1999) The behavior of sandwich structures of isotropic and composite materials. CRC Press
[2] Lee P, Chang N (1979) Harmonic waves in elastic sandwich plates. Journal of Elasticity **9**(1):51–69
[3] Schulze S, Pander M, Naumenko K, Altenbach H (2012) Analysis of laminated glass beams for photovoltaic applications. International Journal of Solids and Structures **49**(15):2027–2036
[4] Ivanov I (2006) Analysis, modelling, and optimization of laminated glasses as plane beam. International Journal of Solids and Structures **43**(22-23):6887–6907
[5] Njuguna J (2016) Lightweight Composite Structures in Transport: Design, Manufacturing, Analysis and Performance. Woodhead Publishing

[6] Davies J (2008) Lightweight Sandwich Construction. Wiley, New York

[7] Weps M, Naumenko K, Altenbach H (2013) Unsymmetric three-layer laminate with soft core for photovoltaic modules. Composite Structures **105**:332–339

[8] Altenbach H, Eremeyev VA, Naumenko K (2015) On the use of the first order shear deformation plate theory for the analysis of three-layer plates with thin soft core layer. ZAMM - Journal of Applied Mathematics and Mechanics / Zeitschrift für Angewandte Mathematik und Mechanik **95**(10):1004–1011

[9] Naumenko K, Eremeyev V (2014) A layer-wise theory for laminated glass and photovoltaic panels. Composite Structures **112**:283–291

[10] Aßmus M, Naumenko K, Altenbach H (2016) A multiscale projection approach for the coupled global–local structural analysis of photovoltaic modules. Composite Structures **158**:340–358

[11] Aßmus M, Nordmann J, Naumenko K, Altenbach H (2017) A homogeneous substitute material for the core layer of photovoltaic composite structures. Composites Part B **112**:353–372

[12] Aşik M, Tezcan S (2005) A mathematical model for the behavior of laminated glass beams. Computes & Structures **83**(21):1742–1753

[13] Altenbach H (2000) An alternative determination of transverse shear stiffnesses for sandwich and laminated plates. Intenational Journal of Solids and Structures **37**(25):3503–3520

[14] Altenbach H, Eremeyev V (2008) Direct approach based analysis of plates composed of fuctionally graded materials. Archives of Applied Mechanics **78**(10):775–794

[15] Mikhasev G, Altenbach H (2019) Equivalent single layer model for thin laminated cylindrical shells. In: Thin-walled Laminated Structures, Advanced Structured Materials, vol 106, Springer, Cham, pp 29–84

[16] Mikhasev G, Altenbach H (2019) Vibrations of laminated structures composed of smart materials. In: Thin-walled Laminated Structures, Advanced Structured Materials, vol 106, Springer, Cham, pp 199–272

[17] Grigoliuk E, Kulikov G (1988) Multilayered Reinforced Shells. Calculation of Pneumatic Tires (in Russ.). Mashinostroenie, Moscow

[18] Kaplunov J, Prikazchikov D, LA P (2017) Dispersion of elastic waves in a strongly inhomogeneous three-layered plate. International Journal of Solids and Structures **113-114**:169–179

[19] Kaplunov J, Prikazchikov D, Prikazchikova L (2017) Dispersion of elastic waves in laminated glass. Procedia Engineering **199**:1489–1494

[20] Prikazchikova L, Aydin Y, Erbas B, Kaplunov J (2020) Asymptotic analysis of an anti-plane dynamic problem for a three-layered strongly inhomogeneous laminate. Mathematics and Mechanics of Solids **25**(1):3–16

[21] Alkinidri M, Kaplunov J, Prikazchikova L (2020) A two mode non-uniform approximation for an elastic asymetric sandwich. In: Papadrakakis M, Fragiadakis M, Papadimitriou C (eds) EURODYN 2020 XI International Conference on Structural Dynamic, pp 528–536

[22] Alkinidri M, Kaplunov J, Prikazchikova L (2021) Two-mode long-wave low-frequency approximations for anti-plane shear deformation of a high-contrast

asymmetric laminate. In: Awrejcewicz J (ed) Perspectives in Dynamical Systems II: Mathematical and Numerical Approaches. DSTA 2019, Springer Proceedings in Mathematics and Statistics, vol 363, Springer, Cham, pp 275–285

[23] Kaplunov J, Prikazchikova L (2018) Low-frequency vibration modes of strongly inhomogeneous elastic laminates. Izvestiya Saratovskogo Universiteta (new seria), Ser Math Mech Inform **18**(4):447–457

[24] Kaplunov J, Prikazchikova L, Alkinidri M (2021) Antiplane shear of an asymmetric sandwich plate. Continuum Mechanics and Thermodynamics **33**:1247–1262

[25] Prikazchikova L (2022) Decay conditions for antiplane shear of a high-contrast multi-layered semi-infinite elastic strip. Symmetry **14**:1697–9

[26] Tovstik P, Tovstik T (2014) A thin-plate bending equation of second-order accuracy. Doklady Physics **59**(8):389–392

[27] Tovstik PE, Tovstik TP (2017) Generalized timoshenko-reissner models for beams and plates, strongly heterogeneous in the thickness direction. ZAMM - Journal of Applied Mathematics and Mechanics / Zeitschrift für Angewandte Mathematik und Mechanik **97**(3):296–308

[28] Morozov N, Tovstik P, Tovstik T (2016) Generalized timoshenko–reissner model for a multilayer plate. Mechanics of Solids **51**(5):527–537

[29] Morozov NF, Tovstik PE, Tovstik TP (2016) The timoshenko-reissner generalized model for a plate highly nonuniform in thickness (english transl.). Doklady Physics **61**(8):394–398

[30] Belyaev AK, Morozov NF, Tovstik PE, Tovstik TP (2020) Some two-dimensional non-classical models of anisotropic plates. In: Altenbach H, Chinchaladze N, Kienzler R, Müller WH (eds) Analysis of Shells, Plates, and Beams: A State of the Art Report, Advanced Structured Material, vol 134, Springer International Publishing, Cham, pp 75–94

[31] Mikhasev G, Botogova M, Mikhievich A (2020) Analysis of free vibrations of sandwich panel with electrorheological layer based on two models of laminated shells. Journal of the Belarusian State University: Mathematics and Informatics **3**:51–59

[32] Morozov N, Belyaev A, Tovstik P, Tovstik T (2021) Applicability ranges for four approaches to determination of bending stiffness of multilayer plates. Continuum Mechanics and Thermodynamics **33**:1659–1673

[33] Berdichesky V (2010) An asymptotic theory of sandwich plates. International Journal of Engineering Science **48**(3):383–404

[34] Mikhasev G, Le N (2023) Asymptotically correct analytical model for flexural response of a two-layer strip with contrast elastic constants. In: Altenbach H, Berezovski A, dell'Isola F, Porubov A (eds) Sixty Shades of Generalized Continua, Advanced Structured Materials, vol 555, Springer, Cham, pp 497–517

[35] Mikhasev G (2022) On governing equations for a nanoplate derived from the 3d gradient theory of elasticity. Mathematics and Mechanics of Solids **27**(9):1688–1702

[36] Tovstik P, Tovstik T (2007) On the 2D models of plates and shells including the transversal shear. ZAMM - Journal of Applied Mathematics and Mechanics / Zeitschrift für Angewandte Mathematik und Mechanik **87**(2):160–171

[37] Reissner E (1944) On the theory of bending of elastic plates. Journal of Mathematics and Physics **23**:184–191
[38] Reissner E (1945) The effect of transverse shear deformation on the bending of elastic plates. Journal of Applied Mechanics, Trans ASME **12**(2):A69–A67
[39] Chen L, Gong X, Li W (2008) Effect of carbon black on the mechanical peformances of magnetorheological elastomers. Polymer Testing **27**(3):340–345

Chapter 17
Maxwell's Equations Through the Ages

Wolfgang H. Müller and Elena N. Vilchevskaya

Abstract Ever since their appearance in Maxwell's famous Treatise the way of how to write His equations went through many changes. These changes were not just of cosmetic nature. Rather with every alteration new aspects of their meaning appeared. In this paper we shall pursue and comment on their development.

17.1 Introduction and Scope of the Paper

A first complete overview of what we call today *Maxwell equations* was given in Maxwell's famous Treatise [1] in Chapter IX, pp. 229. As we shall see below it was written in rather archaic notation, because the notion of vectors was just about to be developed. Based on this archaic form the equations were quickly adopted and investigated further by Maxwell's contemporaries, *e.g.*, by Boltzmann [2] and Hertz [3]. If we look at the titles Hertz choose for his presentation of the electromagnetic foundations, namely *Ueber die Grundgleichungen der Elektrodynamik für ruhende Körper* and *Ueber die Grundgleichungen der Elektrodynamik für bewegte Körper*[1] two important issues become immediately obvious. First, the question of how to formulate electrodynamics in matter and not just in vacuum is posed. Second, the problem of a change in observer is addressed, at least indirectly, because of the impact motion or velocity may have on the form of the equations. Consequently, one may ask such awkward questions as

Wolfgang H. Müller
Institute of Mechanics, Chair of Continuum Mechanics and Constitutive Theory, Technische Universität Berlin, Sekr. MS. 2, Einsteinufer 5, 10587 Berlin, Germany,
e-mail: wolfgang.h.mueller@tu-berlin.de

Elena N. Vilchevskaya
Flugsnapparegatan 6, Mölndal, Sweden,
e-mail: Vilchevska@gmail.com

[1] On the fundamental equations of electrodynamics for bodies at rest/in motion.

283

- "Are the electromagnetic fields transported with moving matter?"
- "How are the electromagnetic fields transported in vacuum, is there a carrier or an agent?"
- "Is electromagnetism a phenomenon of (instantaneous) action at a distance by particles or is it close range interaction through fields?"

It is fair to say that until today these points are still subject to scientific discussion although there exist also dogmatic tendencies to consider the case as closed.

The intention of this paper is to shed some light on this and to review the existing evidence. We will start by stating the two physical principles on which electromagnetism is based: the conservation of electromagnetic flux and the conservation of charge. We will formulate this in mathematical form, globally and locally, in 3D-space and time using contemporary vector formalism. Next we compare the results in the way they were written and stated by the pioneers, *i.e.*, Maxwell, Boltzmann, Hertz, *etc.*

Our next step is the 4D-spacetime formulation of electromagnetism. This will provide some answers regarding the impact of the choice of observer and movement on the Maxwell equations and it will lead us to the world of general frame indifference, *i.e.*, (general) relativity. It will also allow to introduce a special set of spacetime transformations, which guarantee a simple proportional relationship between the two sets of electromagnetic fields, the Lorentz transformations. We shall also see that the simple proportionality between the two sets of fields can be viewed as a constitutive equation for the vacuum or – if preferred – a constitutive relation for the material known as ether.

Finally we will present a metric free formulation of the Maxwell equations based on the so-called exterior differential calculus on manifolds, where the two electromagnetic world-tensors are reformulated as 1, 2, and 3-forms of exterior products and the Maxwell equations are reinterpreted in "geometric language". We will also see how this approach may connect the worlds of mechanics and electrodynamics.

17.2 Physical Principles of Electromagnetism

Wheeler states in [4] that "*Maxwell's synthesis of all the known laws of electricity and magnetism in 1865 can be condensed into either two or four equations, depending on whether one merges space and time into space-time or treats space and time separately.*" This is very true indeed, but no matter which form one prefers they are all based on two axioms for the conservation of two physical qualities, namely the electromagnetic flux and the electric charge. In this section we will state these axioms verbally and then recast them into mathematical form.

17.2.1 Conservation of Electromagnetic Flux

The *first axiom of electrodynamics* according to which the magnetic flux is conserved is based on Cavendish's and Faraday's experiments. It quantifies the belief that the *electric* and the *magnetic force fields*, $E(x,t)$ and $B(x,t)$, respectively, are responsible that resting and/or moving charges experience forces around condensers and magnets. In modern continuum balance notation it can be written like this:

$$\frac{\mathrm{d}}{\mathrm{d}t} \int_{a(t)} B \cdot n \, \mathrm{d}a = - \oint_{\partial a(t)} (E + v \times B) \cdot \tau \, \mathrm{d}l, \tag{17.1}$$

where $a(t)$ is an open, surface in 3D-space with outer normal n and peripheral tangent vector τ. The surface $a(t) \setminus \partial a(t)$ can be material or immaterial. v denotes the velocity of the material points constituting the noose of the wire $\partial a(t)$. Note that we need a material circumference $\partial a(t)$, *e.g.*, a noose made of metal to observe an induction effect. The description of the various fields can be material if there is (electrically charged) matter that moves. However, if a spatial description of fields is used, one is always on the safe side since both the electric and the magnetic field do not need matter. They can exist and propagate in vacuum as electromagnetic waves. Sometimes Eq. (17.1) is referred to as *Faraday's law of induction in global form* and

$$E + v \times B$$

is referred to as the *electromotive intensity*.

It is noteworthy that Eq. (17.1) is a flux balance for a *conserved* quantity, namely the magnetic flux on its left hand side. The right hand side is simply a line flux that in principle can be controlled by choosing a non-conducting and non-moving material for the periphery $\partial a(t)$. There is no volumetric supply of magnetic flux and, what is particularly important, there is no (volumetric) production of magnetic flux. Hence it can be considered as a conserved quantity.

If the surface is closed $a(t) \to \partial v(t)$ Eq. (17.1) obviously yields:

$$\oint_{\partial v(t)} B \cdot n \, \mathrm{d}a = 0, \tag{17.2}$$

which is also referred to as the law of non-existing magnetic monopoles according to which the magnetic field lines are always closed. $v(t)$ is the volume surrounded by the closed surface $\partial v(t)$, both of which do not necessarily need to be material. The application of Gauss' theorem and the usual localization procedures yield in regular points:

$$\nabla \cdot B = 0. \tag{17.3}$$

If now the transport theorem for open surfaces (see [5], Eqs. (1.12.12), (3.8.12) and its proof in the Appendix of [6]) is used for Eq. (17.1):

$$\frac{\mathrm{d}}{\mathrm{d}t} \int\limits_{a(t)} \boldsymbol{B} \cdot \boldsymbol{n} \, \mathrm{d}a = \int\limits_{a(t)} \left(\frac{\partial \boldsymbol{B}}{\partial t} + \boldsymbol{v} \nabla \cdot \boldsymbol{B} \right) \cdot \boldsymbol{n} \, \mathrm{d}a + \oint\limits_{\partial a(t)} \boldsymbol{B} \times \boldsymbol{v} \cdot \boldsymbol{\tau} \, \mathrm{d}l, \qquad (17.4)$$

and Eq. (17.3) is observed the usual localization procedure in regular points yields:

$$\frac{\partial \boldsymbol{B}}{\partial t} + \nabla \times \boldsymbol{E} = \boldsymbol{0}. \qquad (17.5)$$

Similarly one obtains for points on a *singular surface* with normal $\boldsymbol{n}$ moving with the velocity $\boldsymbol{w}^{\mathrm{I}}$ the following *jump* or *continuity conditions*:

$$[\![\boldsymbol{B}]\!] \cdot \boldsymbol{n} = 0 \,, \quad \boldsymbol{n} \times [\![\boldsymbol{E}]\!] - \boldsymbol{n} \cdot \boldsymbol{w}^{\mathrm{I}} [\![\boldsymbol{B}]\!] = \boldsymbol{0}. \qquad (17.6)$$

Note that Eq. (17.5) is also frequently referred to as *Faraday's law of induction in local form* and (17.2) or (17.3) are known as the *law of non-existing magnetic monopoles* in global and local form.

17.2.2 Conservation of Electric Charge

It is believed that electric charge cannot exists without matter carrying mass. For that reason it suffices to formulate the conservation of charge in material description by using material volumes $v(t)$. The generalization to open, matter containing volumes can be found in [6] . The *second axiom of electromagnetism* states that charge is a conserved volumetric quantity, such that:

$$\frac{\mathrm{d}}{\mathrm{d}t} \int\limits_{v(t)} q \, \mathrm{d}v = - \oint\limits_{\partial v(t)} \boldsymbol{j} \cdot \boldsymbol{n} \, \mathrm{d}a. \qquad (17.7)$$

It should be emphasized that q denotes the *total* charge density and $\boldsymbol{j}$ the *total* electric current of the system. This means that charge densities and currents due to a response of the matter are included and not only contributions through free charges or currents. For readers not familiar with electrodynamic notions but versed in continuum mechanics it might be helpful to point out that the electric current $\boldsymbol{j}$ is not a convective transport $q\boldsymbol{v}$ of electric charge. The latter is not missing but, as we shall see, appears immediately if we move to the local form of (17.7) (see the divergence term in Eq. $(17.8)_1$). In contrast to that $\boldsymbol{j}$ is a non-convective flux, similar in its continuum nature to the heat flux $\boldsymbol{q}$ of the energy balance. It is possible to relate $\boldsymbol{j}$ to the movement of elementary electric charges if a microscopic model and subsequent homogenization is used, which brings us to the continuum scale (see, *e.g.*, [5], Sects. 2.4 and 3.3).

As in the case of Eq. (17.1) the conservation character of this relation should be emphasized. This time the conserved physical quantity is the total charge on the left. The right hand side is simply a (non-convective) flux of charge through the surface

of the material volume. It can in principle be controlled, for example by insulating the surface. There is no volumetric supply of charge and, what is more, there is no volumetric production: Electric charge is a *conserved* quantity.

The localization of Eq. (17.7) is performed by using the volumetric transport theorem and pillbox arguments. We obtain in regular points:

$$\frac{\partial q}{\partial t} + \nabla \cdot (q\boldsymbol{v} + \boldsymbol{j}) = 0 \quad \Leftrightarrow \quad \frac{\delta q}{\delta t} + q\nabla \cdot \boldsymbol{v} + \nabla \cdot \boldsymbol{j} = 0, \tag{17.8}$$

where

$$\frac{\delta(.)}{\delta t}$$

refers to the material time derivative, and in singular points the jump condition:

$$\llbracket \boldsymbol{j} + q \left(\boldsymbol{v} - \boldsymbol{w}^{\mathrm{I}} \right) \rrbracket \cdot \boldsymbol{n} = 0. \tag{17.9}$$

(17.8) is a partial differential equation that bears a certain similarity to the mass balance

$$\frac{\partial \rho}{\partial t} + \nabla \cdot (\rho\boldsymbol{v}) = 0 \quad \Leftrightarrow \quad \frac{\delta \rho}{\delta t} + \rho\nabla \cdot \boldsymbol{v} = 0, \tag{17.10}$$

the purpose of which is to determine the field of mass density ρ. Consequently it is logical to think that the purpose of (17.8) is to determine the charge density field ρ. However, note the differences: First, ρ is a field of "its own right," whereas q bears an intrinsic *constitutive aspect*. Indeed, there is a part of the charge density that exists "by itself," like the mass density. We call it the free charge density q_{f} and an example for it are the charges spread over the plates of a condensor. However, charge densities can also be created by the presence of an external electric field $\boldsymbol{E}$ in certain types of materials, which we call dielectric materials. This charge density is called the polarization charge density q_{p}.

Second, unlike the mass balance the balance of charge contains the non-convective part $\boldsymbol{j}$. This is an additional vector field and, surely, the scalar equation (17.8) is insufficient for its determination. And, third, just like q the electric current density $\boldsymbol{j}$ also shows an intrinsic constitutive aspect. Indeed, there are free currents $\boldsymbol{j}_{\mathrm{f}}$, for example, realized on the atomic scale by the electron cloud drift in a conductor triggered by an external electric field $\boldsymbol{E}$. However, when polarized dielectric matter moves this macroscopic movement will lead to what we call polarization current $\boldsymbol{j}_{\mathrm{p}}$. Moreover, if the material is magnetizable, an external magnetic field $\boldsymbol{B}$ will induce magnetization currents $\boldsymbol{j}_{\mathrm{m}}$, which also need to be taken into account in a constitutive type of treatment.

In summary: Eq. (17.8) is not solved directly. It is solved formally by introducing two additional electromagnetic vector fields, called charge and current potentials $\boldsymbol{D}$ and $\boldsymbol{H}$, respectively. These are a.k.a. electric and magnetic excitation fields and they will address the constitutive aspects mentioned above: Matter and surrounding space are "excited" by external fields and, in turn, the space surrounding matter is "excited" by the presence of electric charges and electric currents. We proceed to introduce these fields.

The charge relation Eq. (17.7) is now formally solved by introducing the second set of electromagnetic fields $\boldsymbol{D}(\boldsymbol{x},t)$ and $\boldsymbol{H}(\boldsymbol{x},t)$. The first one is introduced by:

$$\oint_{\partial v(t)} \boldsymbol{D} \cdot \boldsymbol{n} \, \mathrm{d}a \equiv \int_{v(t)} q \, \mathrm{d}v, \qquad (17.11)$$

a.k.a. *Gauss' law*.

The pioneers of electrodynamics believed that the electric charge excites the surrounding space around it, may it be filled with matter or be a vacuum. Exactly this is expressed by this relation, and it is for this reason that $\boldsymbol{D}$ is also known as the *electric excitation*. Its presence is a consequence of the presence of electric charge. However, it is also called *electric charge potential*, and the reason for that will become obvious when we will move to its local form in regular points. To this end we use the Gauss-Ostrogradski theorem and perform the corresponding localization of Eq. (17.11) in regular points:

$$\nabla \cdot \boldsymbol{D} = q, \qquad (17.12)$$

which reveals the potential character of $\boldsymbol{D}$. Moreover, the localization on a singular surface carrying a surface charge density q^{I} yields

$$[\![\boldsymbol{D}]\!] \cdot \boldsymbol{n} = q^{\mathrm{I}}. \qquad (17.13)$$

Surely Eq. (17.11) does not solve by itself the balance of charge Eq. (17.7). To this end an extension is required, which introduces the last electromagnetic field $\boldsymbol{H}$ through:

$$\frac{\mathrm{d}}{\mathrm{d}t} \int_{a(t)} \boldsymbol{D} \cdot \boldsymbol{n} \, \mathrm{d}a = \oint_{\partial a(t)} (\boldsymbol{H} + \boldsymbol{D} \times \boldsymbol{v}) \cdot \boldsymbol{\tau} \, \mathrm{d}l - \int_{a(t)} \boldsymbol{j} \cdot \boldsymbol{n} \, \mathrm{d}a. \qquad (17.14)$$

This way we return to a flux balance for a *conserved* quantity, namely the flux of the electric excitation $\boldsymbol{D}$ (on the left) through an open (material or immaterial) surface $a(t)$: There is a supply through the periphery,

$$\boldsymbol{H} + \boldsymbol{D} \times \boldsymbol{v}$$

which, in view of what was said about the right hand side in Eq. (17.1), we are tempted to call magnetomotive intensity, although this is not customary. However, it contains the *magnetic excitation* $\boldsymbol{H}$, which is the field response of the surrounding to the presence of an electric current. It is a.k.a. *current potential*, a name that will become clearer if we move to the localization of in regular points further below. Indeed on the right hand side of Eq. (17.14) we have two controllable fluxes, one through the periphery $\partial a(t)$ and one through the open surface $a(t)$. There are no productions, which confirms the status of this relation as a conservation law. It is also known as the *Ampère-Øersted law*, because it was based on researches of these two scientists that involved electric currents and moving charges (which are convective currents so to speak).

If a surface transport theorem of the type shown in Eq. (17.4) is used on the left hand side of (17.14) the localization of Eq. (17.14) in regular points leads to:

$$-\frac{\partial \boldsymbol{D}}{\partial t} + \nabla \times \boldsymbol{H} = q\boldsymbol{v} + \boldsymbol{j}, \qquad (17.15)$$

and in singular points:

$$\boldsymbol{n} \times [\![\boldsymbol{H}]\!] + \boldsymbol{n} \cdot \boldsymbol{w}^{\mathrm{I}} [\![\boldsymbol{D}]\!] = \boldsymbol{j}^{\mathrm{I}} + q^{\mathrm{I}} \boldsymbol{w}^{\mathrm{I}}, \qquad (17.16)$$

$\boldsymbol{j}^{\mathrm{I}}$ being a possible line current on the singular surface.

We finally return to the quote by Wheeler at the beginning of this section. The following can be said: The relations (17.5), (17.12), and (17.15) are the four equations that were mentioned in the quote. As we shall see in Section 17.4 Eqns. (17.5)$_2$ and (17.12) are time components of a 4D world-tensor relation where space and time are merged, whereas (17.5)$_1$, (17.15) belong to spatial components in the 4D-formalism. However, before we turn to the 4-vector formalism, we will take a look how the pioneers of electromagnetism struggled with the concepts and their nomenclature, before the compact vector form used in this section resulted.

17.3 Early Forms of Maxwell's Equations

In this paper we restrict our review to four books of the early pioneers of electromagnetism: Maxwell himself in his Treatise on electromagnetism [1] and four ardent followers of his new lore, Boltzmann [2], Hertz [3], and Abraham & Föppl [7]. However, before we can start, a few remarks are in order:

- In an inertial frame of reference or (better) in a Lorentz system the two electric and the two magnetic fields are simply proportional, *i.e.*,

$$\boldsymbol{D} = \epsilon_0 \boldsymbol{E}$$

and

$$\boldsymbol{B} = \mu_0 \boldsymbol{H}$$

with the vacuum electric permittivity $\epsilon_0 = 8.854 \times 10^{-12} \frac{\mathrm{As}^2}{\mathrm{Nm}^2}$ and the vacuum magnetic permeability $\mu_0 = 4\pi \times 10^{-7} \frac{\mathrm{N}}{\mathrm{A}^2}$ in SI units. In Gaussian units they are numerically (but not conceptually) equal. Maxwell (and contemporaries) used Gaussian units, which he called electrostatic system. If one so wishes these are (linear) constitutive relations of the material we call "the ether", which have this simple form only in an inertial or Lorentz frame.[2]
- If we want to use and study the electromagnetic fields in matter, it is useful to decompose the total charge density q and the total current $\boldsymbol{j}$ additively into their

---

[2] More information on this cumbersome topic can be found in [6], Sects. 4.1 and 5.3 or [8], Sects. 1.6.2–1.6.5.

so-called "free" part (identified by an index f) and a response due to the material. In the case of the total charge density we write

$$q = q_{\mathrm{f}} - \nabla \cdot \boldsymbol{P},$$

where $\boldsymbol{P}$ is known as *polarization*. In the case of the electric current we have

$$\boldsymbol{j} = \boldsymbol{j}_{\mathrm{f}} + \boldsymbol{j}_{\mathrm{p}} + \nabla \times \boldsymbol{M},$$

where $\boldsymbol{M}$ is known as (the Minkowski) *magnetization*. Hence the second set of Maxwell equations in regular points now reads:[3]

$$-\frac{\partial (\boldsymbol{D} + \boldsymbol{P})}{\partial t} + \nabla \times (\boldsymbol{H} - \boldsymbol{M} - \boldsymbol{P} \times \boldsymbol{v}) = q_{\mathrm{f}} \boldsymbol{v} + \boldsymbol{j}_{\mathrm{f}}, \quad \nabla \cdot (\boldsymbol{D} + \boldsymbol{P}) = q_{\mathrm{f}}. \qquad (17.17)$$

- Just one remark on the side in order to touch upon the constitutive aspects of q and $\boldsymbol{j}$ once more: Let us assume that the dielectric responds linearly to the presence of an external electric field $\boldsymbol{E}$. Then we have in an inertial frame for the combination $\boldsymbol{D} + \boldsymbol{P}$ in the last expression

$$\boldsymbol{P} = \epsilon_0 \chi \boldsymbol{E} \quad \Rightarrow \quad \boldsymbol{D} + \boldsymbol{P} = \epsilon_0 \epsilon_{\mathrm{r}} \boldsymbol{E}, \quad \epsilon_{\mathrm{r}} = 1 + \chi. \qquad (17.18)$$

If one so wishes one can call the combination $\boldsymbol{D} + \boldsymbol{P}$ *electric excitation in matter* and frequently the symbol $\boldsymbol{D}$ is used for that, which clearly will give rise for confusion. χ is known as dielectric susceptibility and ϵ_{r} is the *relative dielectric permittivity* constant. Similar relations can be established for linearly magnetizable matter, *i.e.*, for the combination $\boldsymbol{H} - \boldsymbol{M}$.

17.3.1 Maxwell's Treatise on Electromagnetism

As with all historic literature Maxwell's treatise on electromagnetism in two volumes, [10] and [1] is difficult to read. The difficulties start with the notions and the corresponding mathematical symbols he uses. As a starting points we will use the compilation of his notation on pp. 238 and the *Table of Dimensions* on pp. 244.

Maxwell knew vectors, which, as he emphasizes, are identified by "*German letters*". He also decomposes them into (Cartesian) components. However, the corresponding components are not written in a manner customary to us. Rather he uses different letters for each of them, similarly as Love does for the stress vector in the early versions of his treatise of elasticity ([11], pg. 57). All of this shows that vector and tensor calculus were just in their infancy at that time.

Let us concentrate on the four electromagnetic fields first: We read of a *magnetic induction* $\mathfrak{B}$ with components (a, b, c). Next there is an *electromotive force* $\mathfrak{E}$ with components (P, Q, R). Then there is the *electric displacement* $\mathfrak{D}$, and its components

---

[3] The polarization current $\boldsymbol{j}_{\mathrm{p}}$ and the derivation are detailed in [9].

are (f, g, h). And, finally, we encounter a magnetic force $\mathfrak{H}$ or (α, β, γ) componentwise. Of course, one is tempted to identify them with "our" fields $\boldsymbol{B}, \boldsymbol{E}, \boldsymbol{D}$, and $\boldsymbol{H}$. However, care must be exercised, in view of the remarks above. To begin with, $\mathfrak{B}$ corresponds directly to the magnetic field $\boldsymbol{B}$. This is confirmed in Art. 405 of the treatise, where the vector potential $\boldsymbol{A}$ is introduced, such that

$$\boldsymbol{B} = \nabla \times \boldsymbol{A}.$$

Maxwell puts $\boldsymbol{A} \to \mathfrak{A} = (F, G, H)$ and later (in Art. 604) calls it also *electromagnetic momentum*. Not surprisingly the equation of non-existing magnetic monopoles Eq. $(17.5)_2$ is stated several times (*e.g.*, pg. 26 and 230) in the form:

$$\frac{da}{dx} + \frac{db}{dy} + \frac{dc}{dz} = 0. \tag{17.19}$$

In this context it should be noted that Maxwell uses straight d's instead of proper partials ∂. This was common in his days, *cf.*, [12], pg. xii.[4]

Gauss' law in the form Eq. 17.17_2 is stated in Art. 612 in the form

$$\rho = \frac{df}{dx} + \frac{dg}{dy} + \frac{dh}{dz}. \tag{17.20}$$

where Maxwell calls ρ the *volume-density of the free electricity*, what we called q_{f} and, unlike us, he puts it on the left hand side. Hence we must conclude that $\mathfrak{D} \to \boldsymbol{D} + \boldsymbol{P}$.

Another problem is to understand the various electric currents Maxwell introduces. There is the *total electric current* $\mathfrak{C} = (u, v, w)$ and the *current of conduction* $\mathfrak{K} = (p, q, r)$. However, the temporal change of $\mathfrak{D}$ is also a current for him. On pg. 235 he writes:

$$\mathfrak{C} = \mathfrak{K} + \dot{\mathfrak{D}}. \tag{17.21}$$

The dot could refer to a partial time derivative, which (indirectly[5]) is supported by the fact that when he switches to components he writes instead of (17.21):

$$u = p + \frac{df}{dt} \ , \quad v = q + \frac{dg}{dt} \ , \quad w = r + \frac{dh}{dt}. \tag{17.22}$$

Now, in order to retrieve the Ampère-Øersted law in a form similar to Eq. $(17.17)_1$ we have to combine this with Eq. (E) on pg. 233 of the Treatise:

---

[4] At this point a comment is in order: There is some belief in the St. Petersburg school of Rational Mechanics that Maxwell used d/dt to indicate a total (not to be confused with a substantial and also not (synonymously used) with a material time derivative), see *e.g.*, [13], pp. 312, or [14], Sect. 2.2. As it is shown in the reference time-dependent coordinate transformations (not to be confused with a change of observer) would then lead to internal contradictions. It is the belief of the first author that Maxwell never thought of that and conceived only non-moving coordinates spanning space and time. Unfortunately he cannot ask.

[5] Recall the belief of the first author that Maxwell's straight d's mean partials.

$$4\pi u = \frac{d\gamma}{dy} - \frac{d\beta}{dz}, \quad 4\pi v = \frac{d\alpha}{dz} - \frac{d\gamma}{dx}, \quad 4\pi w = \frac{d\beta}{dx} - \frac{d\alpha}{dy}. \tag{17.23}$$

The factor 4π appears because Maxwell uses Gaussian units. The right hand sides correspond to $\nabla \times \mathfrak{H}$ in modern notation. Hence in comparison with Eq. (17.17)$_1$ we conclude that $\mathfrak{H} \rightarrow \boldsymbol{H} - \boldsymbol{M} - \boldsymbol{P} \times \boldsymbol{v}$.

The meaning of Maxwell's $\mathfrak{E} = (P, Q, R)$ becomes clear if we look at his "Equations of Electromotoric force" on pg. 221 of the Treatise:

$$P = c\frac{dy}{dt} - b\frac{dz}{dt} - \frac{dF}{dt} - \frac{d\Psi}{dx},$$

$$Q = a\frac{dz}{dt} - c\frac{dx}{dt} - \frac{dG}{dt} - \frac{d\Psi}{dy}, \tag{17.24}$$

$$R = b\frac{dx}{dt} - a\frac{dy}{dt} - \frac{dH}{dt} - \frac{d\Psi}{dz}.$$

Recall that Maxwell uses (x, y, z) for the Cartesian components of the position vector, (F, G, H) for the vector potential of the magnetic field $\boldsymbol{A}$, and (a, b, c) for the magnetic field $\boldsymbol{B}$. Moreover, by Ψ he denotes the electric potential. Hence in modern notation we find $\mathfrak{E} \rightarrow \boldsymbol{v} \times \boldsymbol{B} + \boldsymbol{E}$, because we have

$$\boldsymbol{E} = -\frac{\partial \boldsymbol{A}}{\partial t} - \nabla \Psi.$$

In other words $\mathfrak{E}$ is not the electric field $\boldsymbol{E}$. Rather it is what was called electromotive intensity above.

But where in Maxwell's Treatise is Faraday's induction law, *i.e.*, Eq. (17.5)$_1$? Nowhere, at least not in that form. The closest we get to it is in a note by Maxwell from 1868, reprinted in his complete works [15], pp. 137, where we find

$$a\,(P - P_0) = -\frac{d}{dt}\int_0^z a\mu\beta dz. \tag{17.25}$$

According to Maxwell the meaning of the various (new) symbols is: a and z are the sides of a parallelogram (which embraces the lines of force, in other words, through which the magnetic field lines are streaming) along the axis of x and z, respectively, $a\,(P - P_0)$ is the total electromotive force per unit length in the direction of x, μ is the coefficient of magnetic induction and β is referred to as the magnetic intensity, a notion that is not used on the summary on pp. 238 of the Treatise.

In short, Eq. (17.25) seems to be a somewhat corrupted version of the integral form of the induction law Eq. (17.1). It clearly shows that the ongoing struggle of how to include the influence of matter (μ!) on the electromagnetic fields began early.

17.3.2 Maxwell's Disciples

A complete discussion of the electromagnetic literature of Maxwell's contemporaries is beyond the scope of this paper. May it suffice to comment on just a few.

The first edition Maxwell's Treatise was published in 1873. Boltzmann's series of lectures on electromagnetic theory were published twenty years later ([2], [16]) in 1891 and 1893, respectively. Boltzmann admires Maxwell, almost glorifies his findings and equations. This becomes obvious by the lyrical quotes of Goethe and reference to Schiller he uses at the beginning of both books: "*So soll ich denn mit saurem Schweiss Euch lehren, was ich selbst nicht weiss,*" "*Kein Wunder daher, dass sich zur Fortführung des Baues nun die Kärrner einfinden. Ein solcher Kärrner, dem die Aufgabe ward, den Weg zum Gebäude zu ebnen, die Façade zu putzen, vielleicht auch' dem Fundamente noch den einen oder anderen Stein einzufügen, will ich sein, und ich bin stolz darauf; denn gäbe es keine Kärrner, wie möchten wohl die Könige bauen?,*" and finally "*War es ein Gott, der diese Zeichen schrieb, Die mit geheimnisvoll verborg'nem Trieb Die Kräfte der Natur um mich enthüllen Und mir das Herz mit stiller Freude füllen.*" [6]

Hence it is not surprising that his summary of the Maxwell equations on pg. 87 in [2] basically coincides with Maxwell's summary in the Treatise and uses exactly the same symbols. Faraday's law of induction in the form of Eq. $(17.5)_1$ is also not presented. However, his book still needs to be mentioned, because, first, it certainly added to the dissemination of Maxwell's ideas on the Continent and particularly in Germany. Second, it supports the viewpoint of the first author of this article regarding the use of ∂ and d in the Maxwell equations. Note that Boltzmann constantly switches notation. For example, in his summary on pg. 84 of [2] he writes the law of non-existing monopoles in the form (17.19) Maxwell wrote it, whereas at the beginning of the very same lecture (pg. 81) we see:

$$\frac{\partial a}{\partial x} + \frac{\partial b}{\partial y} + \frac{\partial c}{\partial z} = 0. [7] \qquad (17.26)$$

Hertz is different. His two famous papers on the foundations of electrodynamics for bodies at rest and bodies in motion ([3], pp. 208) must be considered as a clarification, maybe even as a new beginning of electrodynamics. On pg. 214 of the first paper (bodies at rest) we find *two times two* sets of two equations each representing the electromagnetic effects for *the ether*, or we may simply want to say the vacuum viewed from a Lorentz system. Hertz uses (X, Y, Z) for what he calls

---

[6] "So I shall teach you with sour sweat what I do not know myself," "No wonder, therefore, that for the continuation of the construction now the carters come together. I want to be one of these carters, who has the task of paving the way to the building, cleaning the facade, and perhaps adding a stone or two to the foundation, and I am proud of it, because if there were no carters, how would the kings like to build?," and finally "Was it a God who wrote these symbols, Which with mysteriously hidden impulse The forces of nature around me reveal And fill my heart with quiet joy."

[7] The first author thinks this proves his point of view that neither Maxwell nor Boltzmann thought of time-dependent coordinate transformations. They were simply sloppy.

elektrische Kraft[8] and (L, M, N) for what he calls *magnetische Kraft*[9] and writes:

$$A\frac{dL}{dt} = \frac{dZ}{dy} - \frac{dY}{dz}, \quad A\frac{dX}{dt} = \frac{dM}{dz} - \frac{dN}{dy},$$
$$A\frac{dM}{dt} = \frac{dX}{dz} - \frac{dZ}{dz}, \quad A\frac{dY}{dt} = \frac{dN}{dx} - \frac{dL}{dz}, \tag{17.27}$$
$$A\frac{dN}{dt} = \frac{dY}{dx} - \frac{dX}{dy}; \quad A\frac{dZ}{dt} = \frac{dL}{dy} - \frac{dM}{dx};$$

and

$$\frac{dL}{dx} + \frac{dM}{dy} + \frac{dN}{dz} = 0,^{10} \quad \frac{dX}{dx} + \frac{dY}{dy} + \frac{dZ}{dz} = 0. \tag{17.28}$$

If we wish to link (17.27) to the Faraday law of induction in (17.5)$_1$ and to the Ampère-Øersted law from (17.15) we obviously have to assign a Minus to Hertz' *magnetische Kraft*. In this context several comments are in order:

• In a Lorentz system, where the ether is at rest so-to-speak, there is simple proportionality and no cross-linking within the pair $\boldsymbol{B}$ and $\boldsymbol{H}$ and within the pair $\boldsymbol{D}$ and $\boldsymbol{E}$, which explains the full symmetry of the equations in (17.27). In SI units we have
$$\boldsymbol{D} = \epsilon_0 \boldsymbol{E}, \quad \boldsymbol{B} = \mu_0 \boldsymbol{H}, \quad c = \frac{1}{\sqrt{\epsilon_0 \mu_0}}.$$

• The constant A, as Hertz remarks, is a property of the ether and is a reciprocal velocity, namely what we call vacuum speed of light, $c \equiv \frac{1}{A}$. In summary we write (17.27) in modern notation as follows:
$$\frac{\partial(-c\boldsymbol{B})}{\partial ct} = \nabla \times \boldsymbol{E}; \quad \frac{\partial(\boldsymbol{E})}{\partial ct} = \nabla \times (-c\boldsymbol{B}). \tag{17.29}$$

In a way this anticipates Minkowski's space-time notation, which we will discuss in Section 17.4 below.

After the discussion of the situation in vacuum Hertz extends the theory to isotropic and anisotropic non-conducting materials as well as to conductors obeying Ohm's law, in which the free current is proportional to the electric field, $\boldsymbol{j}_f = \sigma \boldsymbol{E}$, σ being the electric conductivity.

His second paper on electrodynamics of moving bodies addresses the question of how Maxwell's equations are affected if a change of observer is performed. This is a cumbersome topic and we shall not discuss it here. Rather we touch upon this issue in a slightly different way in the next section, which is dedicated to the space-time notation of Maxwell's equations. Finally, note that Minkowski already states in 1910 in [17] "*Über die Grundgleichungen der Elektrodynamik für bewegte Körper herrschen zur Zeit noch Meinungsverschiedenheiten. Die Ansätze*

---

[8] electric force

[9] magnetic force

[10] There is a typo in the last term, where Hertz writes $\frac{dN}{dx}$.

von Hertz ... (1890) mußten verlassen werden, weil sich herausgestellt hat, daß sie mit verschiedenen experimentellen Ergebnissen in Widerspruch geraten.[11] This led straight to the famous Abraham-Minkowski controversy that circles around the correct formulation of electrodynamic constitutive equations for (fast) moving bodies (see the literature, *e.g.*, compiled in [18]). And because Hertz is all but easy to read a detailed examination of what he knew and did not know is left to future work.

Finally in this section a few comments are due to the work of Abraham, which was co-authored by the Munich professor of technical mechanics, Föppl. The latter embraced enthusiastically the new electromagnetic theory and, what is more, the tensor calculus in the formulation of Heaviside. Indeed, in [7] he provides us with an introduction to this formerly new type of mathematics. He also compares the Heaviside version of tensor rules to the quaternion formalism established by Hamilton. This is extremely useful for understanding Maxwell's work, the mathematical formulation of which is somewhere in between so-to-speak. As it was emphasized above at least one of the authors of this work had a strong mechanical background. The work of the St. Petersburg school is a continuation of this unison of mechanics and electrodynamics so-to-speak.

Moreover, the Abraham book is the ancestor to the works of Becker and Sauter, *cf.*, [19–21], which are used until today as *the* reference to electromagnetism by the physics community throughout the world.

17.4 World-Tensor Form of Maxwell's Equations

We start our world-tensor formulation with the famous quote by Minkowski from [22]: *M. H.! Die Anschauungen über Raum und Zeit, die ich Ihnen entwickeln möchte, sind auf experimentell-physikalischem Boden erwachsen. Darin liegt ihre Stärke. Ihre Tendenz ist eine radikale. Von Stund an sollen Raum für sich und Zeit für sich völlig zu Schatten herabsinken und nur noch eine Art Union der beiden soll Selbstständigkeit bewahren.*[12]

Now we shall proceed as follows: First, we will give a somewhat naive explanation how Maxwell's equation can be written in spacetime coordinates. No absolute notation will be presented. Second, we will go through the modern literature and show how Maxwell's equation can be written in absolute coordinate and metric independent form, based on absolute world-tensors and exterior differential forms.

---

[11] "At present there are still differences of opinion about the basic equations of electrodynamics for moving bodies. The ansätze of Hertz ... (1890) had to be abandoned because they turned out to be in contradiction with various experimental results."

[12] Gentlemen! The views of space and time which I wish to lay before you have sprung from the soil of experimental physics, and therein lies their strength. Their tendency is a radical one. Henceforth space by itself, and time by itself, are doomed to fade away into mere shadows, and only a kind of union of the two shall preserve independence.

17.4.1 A Naive Introduction of the World-Tensors of Electrodynamics and Maxwell's Equation in Space-Time Formulation

By combining time and space we say that a change of the frame of reference of a world-event occurs when one observer – at rest in the frame S – locates the event at $x^A = (ct, x_a)$ and another observer – at rest in frame S' – locates it at $x^{A'} = (ct', x_a')$. The maps

$$x^{A'} = x^{A'}(x^B) \quad \Leftrightarrow \quad x^B = x^B(x^{A'}). \tag{17.30}$$

are called *spacetime transformation laws*. Following [23] the electric and magnetic fields, **E** and **B** will be combined in an absolute, covariant, completely antisymmetric tensor of rank 2, **F**, the *electromagnetic field tensor*, a.k.a. *Faraday* in [24],

$$F_{AB} = \left[\begin{array}{c|c} 0 & -E_b/c \\ \hline E_a/c & \varepsilon_{abc}B^c \end{array} \right], \tag{17.31}$$

which transforms according to:[13]

$$F_{A'B'} = \frac{\partial x^A}{\partial x^{A'}} \frac{\partial x^B}{\partial x^{B'}} F_{AB}. \tag{17.32}$$

If we introduce the 4D Levi-Civita tensor by:

$$\epsilon^{ABCD} = \begin{cases} +1 & \text{if } A, B, C, D = 0, 1, 2, 3 \text{ and even permutations} \\ -1 & \text{if } A, B, C, D = 1, 0, 2, 3 \text{ and even permutations} , \\ 0 & \text{otherwise} \end{cases} \tag{17.33}$$

which is a relative contravariant tensor of rank 4,

$$\varepsilon^{A'B'C'D'} = \left| \frac{\partial \boldsymbol{x'}}{\partial \boldsymbol{x}} \right|^{-1} \frac{\partial x^{A'}}{\partial x^A} \frac{\partial x^{B'}}{\partial x^B} \frac{\partial x^{C'}}{\partial x^C} \frac{\partial x^{D'}}{\partial x^D} \varepsilon^{ABCD}, \tag{17.34}$$

we can write the Maxwell equations for the electromagnetic flux (17.5), which were established in an inertial frame, in the following form,

$$\varepsilon^{ABCD} \frac{\partial F_{CD}}{\partial x^B} = 0. \tag{17.35}$$

Note that the spatial choice $A = (1, 2, 3)$ leads to Faraday's law of induction Eq. 17.5_1 (in Cartesian component form), and the temporal component $A = 0$ to the law of non-existing magnetic monopoles, Eq. 17.5_1. This explains in hindsight the quote by Wheeler at the beginning of Sect. 17.2.

---

[13] See [23] and [6] for more details on this and other transformation laws below. Some information reg. the useful distinction of co- and contravariant components in spatial Cartesian coordinates is provided in [6].

We now combine the charge density q and the total electric current $q\boldsymbol{v} + \boldsymbol{j}$ in a world object. In the nomenclature of [23] this charge-current vector $\boldsymbol{J}$ is a relative contravariant tensor of rank 1, which in the inertial system reads in Cartesian coordinates:

$$J^A = [cq, qv^a + j^a], \tag{17.36}$$

and which transforms according to:

$$J^{A'} = \left| \frac{\partial \boldsymbol{x}'}{\partial \boldsymbol{x}} \right|^{-1} \frac{\partial x^{A'}}{\partial x^A} J^A. \tag{17.37}$$

Then the conservation of charge (17.8) in the inertial system can be expressed by:

$$\frac{\partial J^A}{\partial x^A} = 0. \tag{17.38}$$

However, by means of (17.37) and the identity

$$\frac{\partial}{\partial x^A} \left(\left| \frac{\partial \boldsymbol{x}'}{\partial \boldsymbol{x}} \right| \frac{\partial x^A}{\partial x^{A'}} \right) = 0 \tag{17.39}$$

we can immediately transform this equation into an arbitrary other world frame (or better to arbitrary other world coordinates $x^{A'}$):

$$0 = \frac{\partial J^A}{\partial x^A} = \frac{\partial}{\partial x^A} \left(\left| \frac{\partial \boldsymbol{x}'}{\partial \boldsymbol{x}} \right| \frac{\partial x^A}{\partial x^{A'}} J^{A'} \right) = ... = \left| \frac{\partial \boldsymbol{x}'}{\partial \boldsymbol{x}} \right| \frac{\partial J^{A'}}{\partial x^{A'}} \implies \frac{\partial J^{A'}}{\partial x^{A'}} = 0. \tag{17.40}$$

This confirms form invariance of the conservation of charge when written in space-time notation. We may say it is valid in every frame and its concrete form can be specified if the space-time transformation (17.30) between an inertial frame and another completely arbitrarily moving one is detailed. Note that it was important that in (17.38) partial and not covariant differentiation is used. As mentioned above this is an inherent property of space-time conservation laws.

Eq. (17.38) is satisfied if the antisymmetric *charge current potential world tensor* $\boldsymbol{H}$, a.k.a. *electromagnetic excitation tensor* is used:

$$\frac{\partial H^{AB}}{\partial x^B} = J^A \quad \text{with} \quad H^{AB} = -H^{BA}. \tag{17.41}$$

In view of (17.37) and in order to fulfill the requirement that the tensorial properties on both sides of the tensor equation (17.41) are the same, it is required that H^{AB} transforms like a contravariant relative tensor:

$$H^{A'B'} = \left| \frac{\partial \boldsymbol{x}'}{\partial \boldsymbol{x}} \right|^{-1} \frac{\partial x^{A'}}{\partial x^A} \frac{\partial x^{B'}}{\partial x^B} H^{AB}. \tag{17.42}$$

If we now put in (17.41)

$$H^{AB} = \left[\begin{array}{c|c} 0 & cD^b \\ \hline -cD^a & \varepsilon^{abc}H_c \end{array}\right], \tag{17.43}$$

the second set of Maxwell equations (17.12) and (17.15) results in Cartesian coordinates. Note that Gauss' law (17.12) is hidden in the temporal component $A = 0$ and the Ampère-Øersted law (17.15) results component-wise from the spatial part $A = (1, 2, 3)$. Forminvariance under arbitrary transformations can be shown if we observe Eqs. (17.37), (17.39), and (17.42):

$$\frac{\partial H^{A'B'}}{\partial x^{B'}} = J^{A'}. \tag{17.44}$$

The connection between $\boldsymbol{H}$ and $\boldsymbol{F}$ is known as the *Maxwell-Lorentz ether relation* in [23] and as the *electromagnetic spacetime relation* in [25]. As detailed in [23] and [8] it becomes simple for the case of Lorentz transformations. Then is shows a direct proportionality between the vectors of the two pairs of the electromagnetic fields without coupling as mentioned above. The connection may be considered as constitutive equation of the ether (see [26]). This issue is also indirectly addressed by the Moscow school of mechanics in [27], Section 5.

It should be noted that making a distinction between F_{AB} and H^{AB} and not simply considering one to be the co- or contravariant version of the other, must not be taken for granted.[14] In [26] we find the following interesting statement: *In his [= Einstein's] "Meaning of Relativity" . . . , in the part on GR–often overlooked by aficionados of the two Poincaré covariant equations in (1)–he [= Einstein] picked the letter ϕ for the field strength apparently in order to stress the different nature of $\mathcal{F}$ and ϕ.* For [23] this distinction is imperative, and we kept this tradition from the very beginning on in our paper. In other words, *two* sets of *two* electromagnetic fields are required to describe electromagnetic phenomena. Moreover, the use of Maxwell ether relations between the fields of the two sets and emphasizing their simplicity for Lorentz transformations is also non-standard in textbooks on electrodynamics and was (maybe) clearly stated for the first time in [23].

17.4.2 Absolute Space-Time Notations

In [24] the coordinate form of Faraday F_{AB} is rewritten in absolute world-tensor form as follows:

$$\boldsymbol{F} = F_{AB}\boldsymbol{d}x^A \otimes \boldsymbol{d}x^B, \tag{17.45}$$

where $\boldsymbol{d}x^A$ are called *basis 1-forms*. With a grain of salt we may envisage them as not necessarily orthogonal, non-normalized tangent vectors to spacetime lines intersecting an event point, such that they form a basis, meaning they are linearly independent. Then the first set of Maxwell equations (17.35) can be written in coordinate- and metric-free form by using the so-called *exterior derivative* $\boldsymbol{d}$ ([24],

---

[14] See for example the opposite approach in [28] or [24].

[26], [29]):[15]

$$dF = 0. \tag{17.46}$$

Alternatively ([24], pg. 81) it is possible to write in absolute world-tensor notation:

$$\nabla \cdot {}^*F = 0, \tag{17.47}$$

where ∇ is a space-time Nabla operator and ${}^*F$ is the dual tensor to F.

The world-vector J^A from (17.36) is now redefined in a *dual 3-form* ${}^*J$ ([25], pg. 145, and [24], pg. 81), such that the conservation of charge and current (17.38) can be expressed by:

$$d{}^*J = 0. \tag{17.48}$$

Finally the second set of Maxwell equations is written in exterior differential forms as

$$d{}^*H = {}^*J, \tag{17.49}$$

where the excitation world-tensor ${}^*H$ is a *dual 2-form*. Alternatively, the duals to the duals, can be defined, called J and H ([24], pg. 83, §4.5), to write

$$\nabla \cdot H = J, \tag{17.50}$$

This way of writing is probably closest to (17.41). Then obviously ∇ is what one would call in traditional continuum mechanics tensor calculus a Nabla operation from the right side.

Summing up it should be mentioned that in [29], pg. 29 a nice table can be found to accompany our journey through time of writing the Maxwell equations.

17.5 Conclusions and Outlook

The following was achieved in this paper:

- Initially Maxwell's equations were stated in vector form of 3D-space based on the principles of conservation of electromagnetic flux and charge.
- The importance of two sets of two (independent) fields was emphasized. The Maxwell-Lorentz-ether relations connecting the fields were introduced.
- The origin of these equations in the works of Maxwell, Boltzmann, Hertz, Abraham and Föppl was explored.
- A spacetime notation was introduced, world-tensors were defined and the Maxwell equations were rewritten, first, in coordinate form and, second, in absolute notation following the mathematical principles of exterior differential forms.

What remains to be done? Maybe the following:

- A constitutive theory, *i.e.*, the material response of matter to the electrodynamic fields, is still not available in a rational way of presentation and subject of discussion.

---

[15] The mathematical definitions and details can be found in [24], [30] or [25].

Here the main problem is the clash between a 3D and a 4D formulation, small velocities of matter and velocities close to the speed of light.

- It needs to be clarified as to whether the world-tensor formalism is the key to what in classical continuum theory is known as change of observer. This should not ne confused with coordinate transformations, which seem to be meant in (17.30).
- What did the pioneers know about that? Is the theory by Hertz (and others) already an answer to the last two bullet points?
- How can electrodynamics and continuum mechanics be reconciled? Is electrodynamics possibly explainable by a refined mechanistic theory following up on Maxwell's vortices, maybe in the framework of micropolar theory (see [31–33])?

The future will tell!

References

[1] Maxwell JC (1873) A treatise on electricity and magnetism, vol 2. Clarendon press
[2] Boltzmann L (1891) Vorlesungen über Maxwells Theorie der Elektricität und des Lichtes, vol I. Theil. Johann Ambrosius Barth, Leipzig
[3] Hertz H (1894) Gesammelte Werke von Heinrich Hertz Band II Untersuchungen über die Ausbreitung der elektrischen Kraft. Barth, Leipzig
[4] Wheeler JA, Ford K (2000) Geons, black holes and quantum foam: a life in physics. W.W. Norton & Company, Inc.
[5] Eringen AC, Maugin GA (1990) Electrodynamics of continua I: Foundations and solid media. Springer Science & Business Media
[6] Müller WH, Vilchevskaya EN, Eremeyev VA (2022) Electrodynamics from the viewpoint of modern continuum theory—a review. ZAMM-Journal of Applied Mathematics and Mechanics/Zeitschrift für Angewandte Mathematik und Mechanik p e202200179
[7] Abraham M, Föppl A (1907) Theorie der Elektrizität, Erster Band: Einführung in die Maxwellsche Theorie der Elektrizität, mit einem einleitenden Abschnitte über das Rechnen mit Vektorgrössen in der Physik, 2nd edition. B.G. Teubner
[8] Müller I, Müller WH (2023) Electrodynamics and rational thermodynamics. ZAMM-Journal of Applied Mathematics and Mechanics/Zeitschrift für Angewandte Mathematik und Mechanik p e202300209
[9] Müller WH (2014) An Expedition to Continuum Theory. Solid Mechanics and its Applications Series, Springer, Berlin
[10] Maxwell JC (1873) A treatise on electricity and magnetism, vol 1. Clarendon press
[11] Love AEH (1892) A Treatise on the Mathematical Theory of Elasticity, Volume 1. Cambridge at the University Press, Cambridge

[12] Torrance TF (1996) Preface. In: Torrance TF (ed) A Dynamical Theory of the Electromagnetic Field, Wipf and Stock Publishers, Eugene, Oregon, pp ix–xiii

[13] Zhilin PA (2012) Rational Continuum Mechanics (in Russian). Publishing House of St. Petersburg University, St. Petersburg

[14] Ivanova EA (2022) A new approach to modeling of thermal and electrical conductivities by means of the Cosserat continuum. Continuum Mechanics and Thermodynamics **34**(5):1313–1342

[15] Niven W (2003) The Scientific Papers of James Clerk Maxwell, Volume Two. Dover Publications. Reprint of Cambridge University Press edition of 1890, New York

[16] Boltzmann L (1893) Vorlesungen über Maxwells Theorie der Elektricität und des Lichtes, vol II. Theil. Johann Ambrosius Barth, Leipzig

[17] Minkowski H (1910) Die Grundgleichungen für die elektromagnetischen Vorgänge in bewegten Körpern. Mathematische Annalen **68**(4):472–525

[18] Reich FA, Rickert W, Müller WH (2018) An investigation into electromagnetic force models: differences in global and local effects demonstrated by selected problems. Continuum Mechanics and Thermodynamics **30**:233–266

[19] Becker R (1957) Theorie der Elektrizität, Erster Band, Einführung in die Maxwellsche Theorie · Elektronentheorie · Relativitätstheorie. B.G. Teubner Verlagsgesellschaft, Stuttgart

[20] Sauter F, Becker R (1973) Theorie der Elektrizität. BG Teubner Stuttgart

[21] Becker R, Sauter F (1982) Electromagnetic fields and interactions. Dover Publications, Inc., Mineola, New York

[22] Minkowski H (1909) Raum und Zeit: Vortrag, gehalten auf der 80. Naturforscher-Versammlung zu Köln am 21. Sept. 1908. Teubner

[23] Truesdell C, Toupin RA (1960) The Classical Field Theories. Springer, Heidelberg

[24] Thorne KS, Misner CW, Wheeler JA (1973) Gravitation. Freeman San Francisco

[25] Hehl FW, Obukhov YN (2003) Foundations of classical electrodynamics: Charge, flux, and metric, vol 33. Springer Science & Business Media

[26] Hehl FW, Obukhov YN (2005) Dimensions and units in electrodynamics. General Relativity and Gravitation **37**(4):733–749

[27] Sedov LI, Tsypkin AG (1979) On the construction of models of continuous media interacting with an electromagnetic field. Journal of Applied Mathematics and Mechanics **43**(3):419–432

[28] Weinberg S (1972) Gravitation and Cosmology: Principles and Applications of the General Theory of Relativity. Wiley

[29] Thirring W (1990) Lehrbuch der Mathematischen Physik: Band 2: Klassische Feldtheorie. Springer-Verlag

[30] Von Westenholz C (1978) Differential forms in mathematical physics. North-Holland Publishing Company, Amsterdam New York Oxford

[31] Ivanova EA (2019) Towards micropolar continuum theory describing some problems of thermo-and electrodynamics. In: Contributions to Advanced Dynamics and Continuum Mechanics, Springer, pp 111–129

[32] Ivanova EA (2021) Modeling of electrodynamic processes by means of me-
     chanical analogies. ZAMM-Journal of Applied Mathematics and Mechan-
     ics/Zeitschrift für Angewandte Mathematik und Mechanik **101**(4):e202000,076
[33] Zhilin PA (2022) Modeling of the electromagnetic field based on rational
     mechanics approach. ZAMM-Journal of Applied Mathematics and Mechan-
     ics/Zeitschrift für Angewandte Mathematik und Mechanik **103**(4):e202302,004

Chapter 18
Multi-Objective Optimization of the Helix Shape of Cylindrical Milling Tools

Chigbogu Ozoegwu and Peter Eberhard

Abstract Milling flutes primarily often have helix shapes for dynamical and functional benefits like reducing impacts and easing chip evacuation. Traditionally, a milling flute is defined with a fixed helix angle and, much less frequently, with a varying helix angle. A segmented helix shape was proposed recently as a special case of generalized helix shape description of milling flutes with potential for significant cutting force reduction. Cutting force components in the feed and feed-normal directions are reported in some works to be competing criteria when tools with different fixed helix angles were compared. This work presents a multi-objective optimization for the force components that identifies the trade-off helix shapes from the space of feasible variable helix shapes (which includes also fixed and harmonic shapes) for cylindrical milling tools. The optimization is based on analytical expressions for cutting force components in terms of multiple helix angles describing the segmented flute and applying a genetic algorithm in determining the force-minimizing set of helix angles. Numerically computed illustrations are presented to show that significant reductions of the cutting force components can result from the optimization by choosing a preferred helix shape among the trade-off shapes.

18.1 Introduction

The dependence of cutting force on the helix shape of cutting tools during the milling process has received significant research interest. Cutting forces are known to reduce with increase of helix angle [1]. This is because larger helix angles elongate the

Chigbogu Ozoegwu

Department of Mechanical Engineering, University of Nigeria, Nsukka, Nigeria,
e-mail: chigbogug@yahoo.com

Peter Eberhard

Institute of Engineering and Computational Mechanics, University of Stuttgart, Germany,
e-mail: peter.eberhard@itm.uni-stuttgart.de

duration and geometric contact length of the tool with the workpiece thus reducing impact loads [2]. Experimental results show that the tangential and normal force components in milling processes decrease with increase of helix angle [3–5]. The axial force is found to increase with increase of helix angle [4, 5]. In [6], the helix angle is varied from 30 to 60 degrees and the finite element method is used to simulate the varying cutting force. The study shows that the resultant cutting force decreases for helix angle rise up to 45 degrees and increases thereafter. A similar trend is reported in [7] for the peak value of the feed-normal cutting force component that is modeled using the mechanistic approach. The optimal helix angle is dependent on the diameter, number of flutes, and axial depth of cut. Increase of the mean value of harmonically changing helix angles is seen in [8] to cause decrease of resultant cutting forces.

In the cited studies, the cutting tool is considered to have either fixed or harmonically varying helix angle. The thrust of the works is limited to modifying cutting forces by varying the fixed helix angle over very limited parametric ranges. On-flute harmonic variation of helix angle is typically used to reduce cutting forces in roughening operations [9]. The results in [6] show that the feed force increases while the feed-normal force decreases with increase of helix angle over the limited range 30 to 60 degrees. This contradicts the results in [1] that both the feed and feed-normal forces increase with decrease of helix angle when right-handed end-mills with helix angles 5, 25 and 45 degrees are compared. The contradiction could be a result of the different limited ranges studied in these works. Therefore, it can be said that the cutting force components constitute a pair of conflicting performance criteria in some portions of the set of helix shapes. The question of what helix shape minimizes cutting forces in a milling operation, and what range of trade-off helix shapes exist for the conflicting cutting force components has not been addressed sufficiently. Multi-objective optimization as carried out in this work is, therefore, advisable since the conflicting cutting force components correspond to conflicting objectives in milling operations. For example, increase of productivity, leads to unwanted increase in power demand and unwanted decrease of machining accuracy (as a result of form errors and chatter, see [10, 11]). These conflicting objectives are influenced by the cutting force components.

To address these research questions, the goal in this work is to establish an algorithm for systematic search of the trade-off helix shapes. This is done by formulating cutting force-based multi-objective functions using the geometric model for helix shape segmentation of a milling flute as introduced in [2], setting up the relevant optimization problem and solving the problem using an evolutionary algorithm. Evolutionary algorithms are typically applied in the optimization of the complex dynamics of different types of mechanical systems in manufacturing [12–14], multibody dynamics [15], automobile impact[16], and others.

An overview of the adopted force model of the milling process is presented in Sect. 18.2. A segmented-flute analytical model for determining the integrated cutting force is formulated in Sect. 18.3 to serve as the basis for the formulation of the objective functions. The multi-objective functions and the appropriate dynamical and geometric constraints are formulated in Sect. 18.4 to set up the optimization

problem. Results of the optimization based on a genetic algorithm are presented in Sect. 18.5. A conclusion is presented in Sect. 18.6.

18.2 Milling Flute Cutting Force

The cutting force is the primary performance indicator of the machining process since it is the driver of most of the other important metal cutting performance indicators. For example, higher cutting force translates to higher tool/workpiece deflection which causes higher form error, higher vibration amplitude which causes higher surface waviness, higher heat generation which causes more aggravated wear problems, and higher cutting energy demand. Cutting force components will serve as the building blocks of the objective functions for the intended optimization study. It is instructive at this point to first describe the applicable cutting force model.

The measurable cutting forces are usually integrated from the distributed or local forces (of interaction between the tool and the workpiece) for all the points on the cutting edge. Figure 18.1 shows a cutting edge element of a tool with diameter D. The element, which has the axial height dz and the helical length $dS = dz/\cos\beta(z)$ where $\beta(z)$ is the helix angle, is positioned at the axial location z. The cutting edge element rotates about the spindle axis (or axial direction) X_3 at the spindle speed Ω (given in revolutions per minute), translates along the feed direction X_1 at the velocity (feed rate) v, and, at the time instant t, is subjected to the local force vector $d\boldsymbol{F}_1(t,z)$ with the components

$$d\boldsymbol{F}_1(t,z) = [dF_\mathrm{t}(t,z)\ dF_\mathrm{n}(t,z)\ dF_\mathrm{a}(t,z)]^\mathrm{T} \tag{18.1}$$

in the tangential, radial and axial directions.
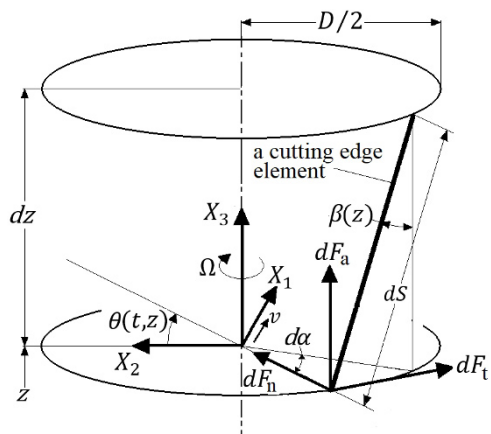
Fig. 18.1: Differential cutting edge element of a flute.

In machining operation, the local force components are usually captured using the dual-mechanism model [17] whereby each local force component is contributed from two sources. For the linear dual-mechanism model, the sources are the chip-forming force which is directly proportional to the undeformed chip cross-section (the product of the undeformed chip thickness and width or depth of cut) and the edge or ploughing force which is directly proportional to the contact length between the cutting edge flank and the machined surface. The constants of proportionality in the linear dual-mechanism model are called force coefficients in literature. In [18–21], the contact length S between the machined surface and the cutting edge which is needed for modeling the milling process edge force is considered to be helical in shape hence the local force components are given as

$$
\begin{aligned}
dF_t(t,z) &= g(t,z)(K_{ct}h(t,z)dz + K_{et}dS), \\
dF_n(t,z) &= g(t,z)(K_{cn}h(t,z)dz + K_{en}dS), \\
dF_a(t,z) &= g(t,z)(K_{ca}h(t,z)dz + K_{ea}dS).
\end{aligned}
\tag{18.2}
$$

The constants K_{ct}, K_{cn}, and K_{ca} are the chip-forming force coefficients in the tangential, radial and axial directions of the cutting edge and K_{et}, K_{en} and K_{ea} are the edge force coefficients in the corresponding directions. The screening function $g(t,z)$ guarantees the switching dynamics of the milling process by taking the value 1 if the cutting edge element is engaged with the workpiece at the time t and the value zero if not engaged. The chip thickness $h(t,z)$ is given as

$$
h(t,z) = v\tau \sin\theta(t,z)
\tag{18.3}
$$

with

$$
\theta(t,z) = \frac{\pi\Omega}{30}t + \theta(0,0) - \alpha(z), \quad \alpha(z) = \frac{2}{D}\int_0^z \tan\beta(\zeta)d\zeta,
\tag{18.4}
$$

where the parameter

$$
\tau = \frac{60}{N\Omega}
$$

is the rotational time lag between the flute and the preceding flute, N is the number of flutes of the tool, $\theta(t,z)$ is the rotational displacement of the local force component dF_n from the feed-normal direction X_2 (or the angular displacement of the cutting edge element from $-X_2$ direction), and $\alpha(z)$ is the lag angle of the cutting edge element at the axial position z which is integrated from the differential lag angles $d\alpha$ of the lower-positioned elements. The angle $\theta(0,0)$, which is the initial angular position of a flute at the tool tip ($z = 0$), is expressed in terms of the reference number j of the flute under consideration as

$$
\theta_j(0,0) = \frac{2\pi}{N}(j-1) \quad \text{for } j = 1, 2, 3, \ldots, N.
\tag{18.5}
$$

The cutting edge element enters the cutting zone at the angular position $\theta(t,z) = \theta_s$ and leaves at the angular position $\theta(t,z) = \theta_e$ which causes the earlier-mentioned

switching dynamic of milling. These boundary angles are given as

$$\theta_s = 0 \quad \text{and} \quad \theta_e = \arccos(1 - 2\rho) \qquad \text{for up-milling,}$$
$$\theta_s = \arccos(2\rho - 1) \quad \text{and} \quad \theta_e = \pi \qquad \text{for down-milling,}$$

(18.6)

where $\rho = B/D$ is the radial immersion and B is the radial depth of cut. In terms of $\theta(t,z)$, θ_s and θ_e, the screening function $g(t,z)$ is given in [22] as

$$g(t,z) = 0.5(1 + \text{sign}(G(t,z))),$$
$$G(t,z) = \sin(\theta(t,z) - \arctan\chi) - \sin(\theta_s - \arctan\chi),$$
$$\chi = \frac{\sin\theta_s - \sin\theta_e}{\cos\theta_s - \cos\theta_e}.$$

(18.7)

For the milling modes that combine up-milling and down-milling, the equations for the angles θ_s and θ_e, and the screening function $g(t,z)$ are given in [23].

The directions in that dynamical responses and operational motions are usually referred in milling operations are the feed (X_1), feed-normal (X_2), and axial (X_3) directions, see also Fig. 18.1. These are the directions that cutting forces are measured in the laboratory. Therefore, the local forces must be referred to these directions using an appropriate rotation matrix. For the purpose of the rotation, the local force vector is based on Eq. (18.2) written in the form

$$d\boldsymbol{F}_1(t,z) = g(t,z)\left(h(t,z)\boldsymbol{K}_c + \frac{1}{\cos\beta(z)}\boldsymbol{K}_e\right)dz,$$

(18.8)

where

$$\boldsymbol{K}_c = \{K_{ct}\ K_{cn}\ K_{ca}\}^T, \quad \boldsymbol{K}_e = \{K_{et}\ K_{en}\ K_{ea}\}^T.$$

(18.9)

The cutting force vector $\boldsymbol{F}(t)$ (with its components $F_1(t)$, $F_2(t)$ and $F_3(t)$ in the X_1, X_2, and X_3 directions) can now be integrated over an axial depth of cut w from the rotated local forces ($\boldsymbol{A}(t,z)d\boldsymbol{F}_1(t,z)$) to read

$$\boldsymbol{F}(t) = \int_0^w g(t,z)\boldsymbol{A}(t,z)\left(h(t,z)\boldsymbol{K}_c + \frac{1}{\cos\beta(z)}\boldsymbol{K}_e\right)dz,$$

(18.10)

where $\boldsymbol{A}(t,z)$ is the rotation matrix. Since the local force component dF_n is rotationally displaced clockwise from the X_2 axis by $\theta(t,z)$ as depicted in Fig. 18.1, the rotation matrix $\boldsymbol{A}(t,z)$ is given as

$$\boldsymbol{A}(t,z) = \begin{bmatrix} \cos\theta(t,z) & \sin\theta(t,z) & 0 \\ -\sin\theta(t,z) & \cos\theta(t,z) & 0 \\ 0 & 0 & 1 \end{bmatrix}.$$

(18.11)

As it is almost always the case that milling tools have multiple flutes, the foregoing analysis is repeated for each of the flutes noting that what differentiates one flute from

the other is Eq. (18.5) and the resulting force $\boldsymbol{F}(t)$ for such tools should be viewed as the summation from all the flutes.

To optimize the shape of a milling tool, the cutting forces must first be expressed in terms of an unknown distribution of the shape parameters of interest and an optimization algorithm is then used to determine the distribution of the parameters that optimizes the shape. The cutting force vector as given in Eq. (18.10) can only be used for formulating the objective functions for optimization analysis when the integration is evaluated symbolically so that the parameters of interest (helix angle distribution $\beta(z)$) can be retained as the optimization variable. Such a symbolic integration is not possible because $\beta(z)$ is assumed to be arbitrary and the lag angle $\alpha(z)$ can only be evaluated symbolically for very simple forms of $\beta(z)$ such as when fixed at a constant value. There is, therefore, the need to apply the discretization concept so that the distributed parameter $\beta(z)$ can be replaced with a set of symbolic parameters (helix angles β_p at heights z_p) such that each element of the set approximates the distribution between a pair of nodes. The discrete model can then be integrated symbolically. The geometric model for a segmented flute (a form of coarse discretization) as described in [2] is applied in the next section for this purpose.

18.3 An Analytical Cutting Force Model

The aim of the analysis that follows is to apply the segmented flute concept in formulating closed-form expressions for cutting forces in terms of the helix angles β_p which changes discretely from one segment of the flute to the next. This will enable the use of β_p as optimization variables when the cutting force components are used in the formulation of the objective functions such that the optimal set of β_p represents the optimal helix shape of the flute. The closed-form expressions for the cutting forces are derived in Subsection 18.3.1 while the dependence of the forces on β_p is explained in Subsection 18.3.2.

18.3.1 The Integrated Force Components

As hinted in the foregoing, the cutting force modeling idea in [2] of a milling tool with segmented (non-smooth) helix shape is built upon here to derive closed-form expressions for the cutting force components of any cylindrical helical milling tool. A segmented flute is made up of segments S_p of helix angles β_p for $p = 1, 2, 3, \ldots, P$. The segment S_p lies between the axial positions $z_{p-1} = (p-1)\Delta z$ and $z_p = p\Delta z$ where $\Delta z = w/P$ is the fixed height for all segments and w is the axial depth of cut. For the segmented flute, the cutting force $\boldsymbol{F}(t)$ is the summation of the segment forces

$$\boldsymbol{F}^{(p)}(t) = \left[F_1^{(p)}(t) \ F_2^{(p)}(t) \ F_3^{(p)}(t) \right]^{\mathrm{T}}$$

on the segments S_p. It follows from Eq. (18.10) that the force $\boldsymbol{F}^{(p)}(t)$ on the segment S_p is

$$\boldsymbol{F}^{(p)}(t) = \int_{z=z_{p-1}}^{z_p} g(t,z)\boldsymbol{A}(t,z)\left(h(t,z)\boldsymbol{K}_{\mathrm{c}} + \frac{1}{\cos\beta_p}\boldsymbol{K}_{\mathrm{e}}\right)dz. \tag{18.12}$$

In Eq. (18.12), $\cos\beta_p$ is used instead of $\cos\beta(z)$ because the helix angle has a fixed value β_p in the segment S_p. Though Eq. (18.12) is derived in view of a segmented tool, it also applies when Δz is small enough (fine segmentation). Fine segmentation allows further simplification of applying the screening function $g(t,z)$ at the center of the segment S_p. Hence under fine segmentation, the screening function is assigned a fixed value $g_p(t) = g(t,z_{p-0.5})$ where $z_{p-0.5} = (p-0.5)\Delta z$ over the segment S_p. Equation (18.12) becomes

$$\boldsymbol{F}^{(p)}(t) = g_p(t) \underbrace{\int_{z=z_{p-1}}^{z_p} \boldsymbol{A}(t,z)\left(h(t,z)\boldsymbol{K}_{\mathrm{c}} + \frac{1}{\cos\beta_p}\boldsymbol{K}_{\mathrm{e}}\right)dz}_{\boldsymbol{\Phi}^{(p)}(t)} = g_p(t)\boldsymbol{\Phi}^{(p)}(t). \tag{18.13}$$

There is then the need to evaluate the integral $\boldsymbol{\Phi}^{(p)}(t)$ in order to determine its close-form expression, and hence the close-form expressions for the cutting force components. By carrying out the matrix multiplications in the integrand using Eqs. (18.11) and (18.9), the components of $\boldsymbol{\Phi}^{(p)}(t)$ become

$$\Phi_1^{(p)}(t) = \int_{z=z_{p-1}}^{z_p} (K_{\mathrm{ct}}h\cos\theta + K_{\mathrm{cn}}h\sin\theta$$
$$+ \frac{1}{\cos\beta_p}K_{\mathrm{et}}\cos\theta + \frac{1}{\cos\beta_p}K_{\mathrm{en}}\sin\theta\bigg)dz,$$

$$\Phi_2^{(p)}(t) = \int_{z=z_{p-1}}^{z_p} (-K_{\mathrm{ct}}h\sin\theta + K_{\mathrm{cn}}h\cos\theta \tag{18.14}$$
$$- \frac{1}{\cos\beta_p}K_{\mathrm{et}}\sin\theta + \frac{1}{\cos\beta_p}K_{\mathrm{en}}\cos\theta\bigg)dz,$$

$$\Phi_3^{(p)}(t) = \int_{z=z_{p-1}}^{z_p} \left(K_{\mathrm{ca}}h + \frac{1}{\cos\beta_p}K_{\mathrm{ea}}\right)dz.$$

where $h \equiv h(t,z)$ and $\theta \equiv \theta(t,z)$ for brevity of the equations. In order to evaluate the integrals in Eqs. (18.14) effectively, it should be noted that $h(t,z)$ and $\theta(t,z)$ are the only functions of z (according to Eq. (18.3)) in the integrands.

The evaluation process is simplified by transforming the integration variable from z to θ as follows. It can be seen from Eq. (18.3) that

$$\frac{d\theta}{dz} = \frac{d\alpha}{dz}.$$

The rate of change of the lag angle at the axial position z is [2]

$$\frac{d\alpha}{dz} = \frac{2}{D}\tan\beta(z).$$

This can also be inferred from Fig. 18.1. Since $\beta(z)$ is fixed at β_p in the segment S_p, then

$$\frac{d\theta}{dz} = \frac{2}{D}\tan\beta_p$$

giving the transformation

$$d\theta = \frac{2}{D}\tan\beta_p\,dz.$$

The transformed integrals are evaluated between the corresponding limits

$$\theta_{p-1}(t) = \theta(t, z_{p-1}) \quad \text{and} \quad \theta_p(t) = \theta(t, z_p)$$

for S_p to give

$$\Phi_1^{(p)}(t) = K_{ct}v\tau\frac{D}{8}\frac{C_{2p}(t)}{\tan\beta_p} - K_{cn}v\tau\frac{D}{4}\frac{S_{2p}(t)}{\tan\beta_p} - K_{et}\frac{D}{2}\frac{S_{1p}(t)}{\sin\beta_p} + K_{en}\frac{D}{2}\frac{C_{1p}(t)}{\sin\beta_p},$$

$$\Phi_2^{(p)}(t) = K_{ct}v\tau\frac{D}{4}\frac{S_{2p}(t)}{\tan\beta_p} + K_{cn}v\tau\frac{D}{8}\frac{C_{2p}(t)}{\tan\beta_p} - K_{et}\frac{D}{2}\frac{C_{1p}(t)}{\sin\beta_p} - K_{en}\frac{D}{2}\frac{S_{1p}(t)}{\sin\beta_p},$$

$$\Phi_3^{(p)}(t) = K_{ca}v\tau\frac{D}{2}\frac{C_{1p}(t)}{\tan\beta_p} + K_{ea}\Delta z\frac{1}{\cos\beta_p}$$

$$(18.15)$$

with the time-varying abbreviation in Eqs. (18.15) being given as

$$\begin{aligned}
C_{1p}(t) &= \cos\theta_p(t) - \cos\theta_{p-1}(t),\\
C_{2p}(t) &= \cos(2\theta_p(t)) - \cos(2\theta_{p-1}(t)),\\
S_{1p}(t) &= \sin\theta_p(t) - \sin\theta_{p-1}(t),\\
S_{2p}(t) &= -\frac{2}{D}\Delta z\tan\beta_p - \frac{1}{2}(\sin(2\theta_p(t)) - \sin(2\theta_{p-1}(t))).
\end{aligned}$$

$$(18.16)$$

Equations (18.15) do not apply when $\beta_p = 0$. Under this case, none of the integrands in Eqs. (18.14) is a function of z, therefore, they can be evaluated to become

$$
\begin{aligned}
\Phi_1^{(p)}(t) =& K_{ct}h\Delta z\cos\theta_p(t) + K_{cn}h\Delta z\sin\theta_p(t) \\
& + K_{et}\Delta z\cos\theta_p(t) + K_{en}\Delta z\sin\theta_p(t), \\
\Phi_2^{(p)}(t) =& -K_{ct}h\Delta z\sin\theta_p(t) + K_{cn}h\Delta z\cos\theta_p(t) \\
& - K_{et}\Delta z\sin\theta_p(t) + K_{en}\Delta z\cos\theta_p(t), \\
\Phi_3^{(p)}(t) =& K_{ca}h\Delta z + K_{ea}\Delta z.
\end{aligned}
\tag{18.17}
$$

The components of the segment forces $\boldsymbol{F}^{(p)}(t)$ in Equation (18.13) can now be summed to give the needed closed-form expressions for the components of the cutting force $\boldsymbol{F}(t)$ in Equation (18.10), hence

$$
\boldsymbol{F}(t) = \sum_{p=1}^{P} \boldsymbol{F}^{(p)}(t) = \sum_{p=1}^{P} g_p(t)\boldsymbol{\Phi}^{(p)}(t).
\tag{18.18}
$$

It should be noted that this closed-form model in Eq. (18.18) is one of the special cases of the generalized closed-form model in [24]. These closed-form expressions for cutting force components can now be applied in the optimization of the helix shape of a cylindrical milling tool when the helix angles β_p are selected as independent optimization variables. Before that is done in Sect. 18.4, the dependence of the closed-form expressions for cutting force components, Eq. (18.18), on the changing helix angles β_p is first discussed in Subsect. 18.3.2.

18.3.2 Force Dependence on the Variable Helix Angle β_p

The dependence of the closed-form expressions for cutting force components on the changing helix angles β_p can be seen from the lag angle function $\alpha(z)$ of a segmented flute. The geometric definition of segmented helix shape in [2] in terms of the lag angle variation with axial coordinate z is

$$
\alpha(z) =
\begin{cases}
\dfrac{2}{D}z\tan\beta_1 & \text{for } S_1, \\[2ex]
\dfrac{2}{D}(z-z_{p-1})\tan\beta_p + \dfrac{2}{D}\Delta z\sum_{f=1}^{p-1}\tan\beta_f & \text{for } S_p \forall\, p > 1.
\end{cases}
\tag{18.19}
$$

It can be seen from Eqs. (18.19) and (18.3) that the nodal lag angles $\alpha_p = \alpha(z_p)$ and angular displacements $\theta_p(t) = \theta(t, z_p)$ are given as

$$
\alpha_p = \frac{2}{D}\Delta z\sum_{f=1}^{p}\tan\beta_f, \quad \theta_p(t) = \frac{\pi\Omega}{30}t + \theta(0,0) - \alpha_p.
\tag{18.20}
$$

It is visible in from Eqs. (18.20) that α_p and $\theta_p(t)$ are dependent on the set of parameters $\boldsymbol{\beta}_p = \{\beta_1\,\beta_2\,\ldots\,\beta_p\}$. This means that $\Phi_i^{(p)}(t)$ in Eqs. (18.15) can be

written as $\Phi_i^{(p)}(t, \boldsymbol{\beta}_p)$ since the terms in Eq. (18.16) are expressed in terms of $\theta_p(t)$ which in turn are dependent on α_p. This further implies that the integrated cutting force $\boldsymbol{F}(t)$ can be represented as $\boldsymbol{F}(t, \boldsymbol{\beta})$ where $\boldsymbol{\beta} = \{\beta_1 \beta_2 \ldots \beta_P\}$ to highlight the dependence on the changing helix angle. Note that $\boldsymbol{\beta}_p$ is a subset of $\boldsymbol{\beta}$ since the former is the set of the helix angles of the first p segments while the latter is the set of the helix angles of all the segments. When the cutting force is the performance consideration, the peak values of the forces can be used as the critical characteristic of interest. The time t_{peak} at which the cutting force on a flute peaks cannot the determined analytically for the arbitrary flute. A simpler alternative to t_{peak} is the mid-engagement time t_{mid} which is the time instant of coincidence of the cutting zone center (that is, the angular position $(\theta_e + \theta_s)/2$ where the angles θ_s and θ_e are as defined in Eq. (18.6) such that the flute enters the cutting zone at the angle θ_s and leaves at the angle θ_e) and the mid-axial depth of the cutting edge (that is, when $z = w/2$). The justification is that t_{mid} maximizes the contact between the tool and the workpiece which in addition to the chip thickness distribution $h(t, z)$ determines the peak force. Following this consideration, Eq. (18.20) gives

$$\theta_{P/2} = \frac{\pi \Omega}{30} t_{\text{mid}} + \theta(0,0) - \alpha_{P/2} = \frac{\theta_e + \theta_s}{2}$$

which yields

$$t_{\text{mid}} = \frac{30}{\pi \Omega} \left(\frac{\theta_e + \theta_s}{2} - \theta(0,0) + \alpha_{P/2} \right), \tag{18.21}$$

assuming that P is an even positive integer greater than 1. The dependence of t_{mid} on the set of parameters $\{\beta_1 \beta_2 \ldots \beta_{P/2}\} \subset \boldsymbol{\beta}$ is as a result of the dependence of $\alpha_{P/2}$ on the set of parameters $\{\beta_1 \beta_2 \ldots \beta_{P/2}\}$, see Eq. (18.20). Therefore, the mid-engagement cutting force $\overline{\boldsymbol{F}}(\boldsymbol{\beta})$ which is used as objective functions in the next section can be written as

$$\overline{\boldsymbol{F}}(\boldsymbol{\beta}) \equiv \boldsymbol{F}(t_{\text{mid}}(\beta_1, \beta_2, \ldots, \beta_{P/2}), \boldsymbol{\beta}) \tag{18.22}$$

since $\{\beta_1 \beta_2 \ldots \beta_{P/2}\} \subset \boldsymbol{\beta}$. Finally, the segmented force model, being a function of P helix angles in $\boldsymbol{\beta}$, can be optimized yielding the optimal helix shape. Note that $\boldsymbol{F}(t, \boldsymbol{\beta})$ is time dependent while $\overline{\boldsymbol{F}}(\boldsymbol{\beta})$ is for just one time instant.

18.4 Optimization

The aim of this section is to formulate the objective functions depending on the parameters $\boldsymbol{\beta} = \{\beta_1 \beta_2 \ldots \beta_P\}$ as presented in Subsect. 18.4.1, to set up the optimization problem as presented in Subsect. 18.4.2 and to describe how to select the preferred solution from the Edgeworth-Pareto front as presented also in Subsect. 18.4.2.

18.4.1 The Objective Functions

Here, the objective functions for the optimization are defined but the rationale behind the choice of the building blocks (the cutting force components in the feed and feed-normal directions) for the objective functions is first discussed. The relevance of the different cutting force components depends on the milling process under consideration. For example, when the tool-point feed power is of interest, the feed force $F_1(t)$ becomes the relevant component since the cutting power is estimated as $F_1(t)v$ where v is the feed rate, see [25]. A decision maker might be interested only on minimizing the cutting power for peculiar technical reasons, therefore, will seek the model parameters that minimize $F_1(t)$. When the machined-surface accuracy is of interest, the feed-normal force $F_2(t)$ becomes the relevant component, see [26]. The interest of another decision maker might be to minimize surface inaccuracy for peculiar technical reasons. This decision maker will seek for the model parameters that minimize $F_2(t)$. The interest of a decision maker might be on a trade-off which lies between the two extremes choices, for example the choice that minimizes the magnitude of the resultant force in the (1,2) plane $((F_1(t))^2 + (F_2(t))^2)^{1/2}$.

Through multi-objective optimization, the decision maker can be furnished with a range of solutions to choose from. Typical graphical representations of these two force components of interest for the constant helix angle shape defined by $\beta_p = \beta \forall p$ are shown in Fig. 18.2. The graphs are generated using $P = 20$ segments of $w = 10$ mm axial depth of cut and the values in Table 18.1. From the cutting speed V_t value in Table 18.1, the spindle speed Ω is calculated using the equation

$$V_t = \frac{\pi D \Omega}{60}.$$
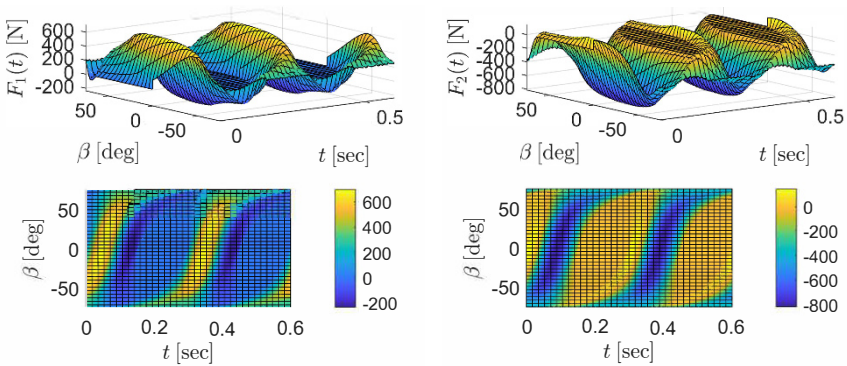
(a) feed direction.

(b) feed-normal direction.

Fig. 18.2: Cutting force components.

Table 18.1: Parameters for cutting force simulations taken from [4].

parameter	symbol	value			unit
tool diameter	D	12.7			mm
feed per tooth	f	0.1			mm
cutting speed	V_t	7.98			mmin^{-1}
radial immersion	ρ	1			
force coefficient	$\boldsymbol{K}_c$	{613.920	330.750	78.003}$^{\mathrm{T}}$	Nmm^{-2}
	$\boldsymbol{K}_e$	{12.7850	12.9020	1.3672}$^{\mathrm{T}}$	Nmm^{-1}

The flat surfaces (zero cutting force values) on the figures indicate the conditions under which no cutting edge element is engaged with the workpiece as a result of the switching dynamics of milling.

The axial force $F_3(t)$ is the important consideration regarding the issues of tool holding and workpiece clamping. Since the holding and clamping issues can be solved by proper practice, $F_3(t)$ is not seen here as an important consideration compared to $F_1(t)$ and $F_2(t)$.

The objective functions are here, therefore, according to Eq. (18.22) for a certain time instant t_{mid} formulated as

$$\boldsymbol{\Psi}(\boldsymbol{\beta}) = \begin{bmatrix} \overline{F}_1^2(\boldsymbol{\beta}) \\ \overline{F}_2^2(\boldsymbol{\beta}) \end{bmatrix}. \tag{18.23}$$

The objective functions emphasize that the absolute values of the force components are of interest.

18.4.2 The Optimization Problem

Based on the objective functions in Eq. (18.23) defined in Subsect. 18.4.1, a multi-objective optimization problem is formulated as

$$\begin{aligned} \underset{\boldsymbol{\beta} \in \mathcal{P}}{\text{minimize}} & \quad \begin{bmatrix} \overline{F}_1^2(\boldsymbol{\beta}) \\ \overline{F}_2^2(\boldsymbol{\beta}) \end{bmatrix}, \\ \text{with} & \quad \mathcal{P} := \{\boldsymbol{\beta} \in \mathbb{R}^P | \beta_{\mathrm{L}} \leqslant \beta_p \leqslant \beta_{\mathrm{U}}\}, \end{aligned} \tag{18.24}$$

where $\boldsymbol{\beta}$ is the vector of optimization parameters (the helix angles of all segments). The bounds satisfy $\beta_{\mathrm{L}} > -90^o$ and $\beta_{\mathrm{U}} < 90^o$.

The problem reduces to determining the Edgeworth-Pareto front, and then selecting a preferred solution from the Edgeworth-Pareto set $\boldsymbol{\beta}_{\mathrm{EP}}$. The traditional methods of selecting a preferred solution which is designated here as $\boldsymbol{\beta}^* \in \boldsymbol{\beta}_{\mathrm{EP}}$ include the pseudo-weight, the gain-to-loss and the $l_p - $norm methods [27]. In this work, the

Euclidean norm, that is the minimum geometric distance to the origin in the criteria space, is the selection criterion used. The preferred solution $\boldsymbol{\beta}^*$ is, therefore, defined as the solution that corresponds to the minimum value for the distance metric

$$d = \left((\overline{F}_1(\boldsymbol{\beta}) - \overline{F}_1(\boldsymbol{\beta}_{\text{utop}}))^2 + (\overline{F}_2(\boldsymbol{\beta}) - \overline{F}_2(\boldsymbol{\beta}_{\text{utop}}))^2 \right)^{1/2} \qquad \forall \boldsymbol{\beta} \in \boldsymbol{\beta}_{\text{EP}}, \quad (18.25)$$

where $\boldsymbol{\beta}_{\text{utop}}$ is the utopian solution. The utopian solution correspond to the objective vector

$$\boldsymbol{\Psi}(\boldsymbol{\beta}_{\text{utop}}) = [\overline{F}_1^2(\boldsymbol{\beta}_{\text{utop}}) \ \overline{F}_2^2(\boldsymbol{\beta}_{\text{utop}})]^{\text{T}}$$

resulting from single criterion optimization. The components of the objective vector $\boldsymbol{\Psi}(\boldsymbol{\beta}_{\text{utop}})$ satisfy

$$\begin{aligned} \overline{F}_1^2(\boldsymbol{\beta}_{\text{utop}}) &\leqslant \overline{F}_1^2(\boldsymbol{\beta}), \\ \overline{F}_2^2(\boldsymbol{\beta}_{\text{utop}}) &\leqslant \overline{F}_2^2(\boldsymbol{\beta}), \end{aligned} \qquad \forall \boldsymbol{\beta} \in \boldsymbol{\beta}_{\text{EP}}. \qquad (18.26)$$

This method is used in the next section for choosing a preferred solution from the Edgeworth-Pareto set.

18.5 Numerical Results

The goal in this section is to solve the optimization problem using the genetic algorithm solver `gamultiobj` that is provided in the Matlab optimization toolbox.

For a numerical solution of the optimization problem, the milling process parameters in Table 18.1 are used. Guided by the range of helix angles encountered in literature [4, 6, 7, 28], the lower bound β_{L} and the upper bound β_{U} for β_p are set at $0°$ and $70°$. Suppose the profile of a flute is to be optimized for a 10 mm axial depth of cut using $P = 20$ segments. This becomes a 20-parameter multi-objective optimization problem. The Edgeworth-Pareto front which results after 50000 iterations is given in Fig. 18.3a and the point corresponding to the preferred objective vector is marked on the front. Forty five minutes of computational time was needed for the 50000 iterations. The front represents the section of the objective front where the two objectives conflict. Figure 18.3b is a plot of all the 70 Edgeworth-Pareto solutions. The preferred solution is shown in Fig. 18.3c alongside the smoothed version which is generated by fitting the exponential function $\beta(z) = a_0 \exp(a_1 z)$ to the first four and the last four data points. The shapes corresponding to the preferred solution (PS) and the smoothed version are shown in Fig. 18.4. The two dimensional curves in Fig. 18.4 represent how the cutting edges would look when unwrapped on a two-dimensional plane. The inclination of the curves to the axial direction at any axial location represents the helix angles.

The optimization results in the foregoing arise from the exploitation of the derived analytical forces $F_1(t)$ and $F_2(t)$ in formulating the objective functions for the time instant $t = t_{\text{mid}}$ yielding $\overline{F}_1(\boldsymbol{\beta})$ and $\overline{F}_2(\boldsymbol{\beta})$. An important question to be addressed is how the preferred solution (helix shape) modifies the time-history of the cutting force
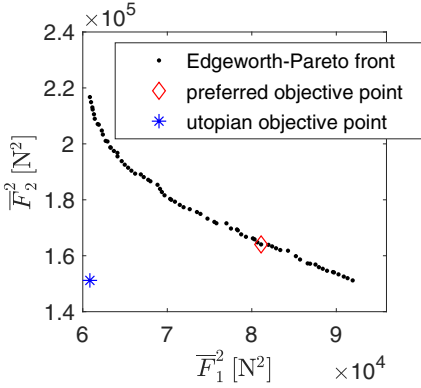
(a) Edgeworth-Pareto frontier indicating the preferred objective point and the utopian objective point.
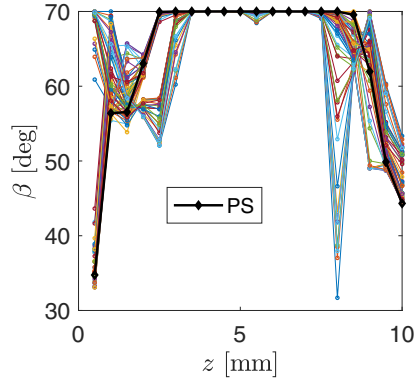
(b) Edgeworth-Pareto solutions and the preferred solution (PS).
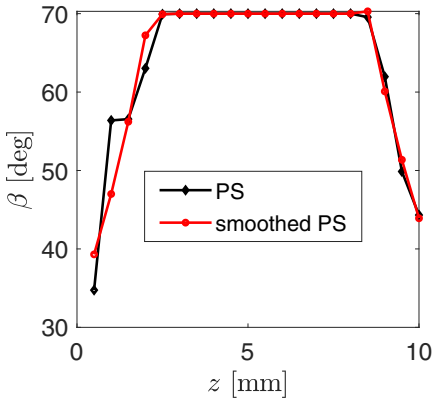
(c) the exponentially smoothed PS.

Fig. 18.3: Optimization results.

components when compared to the traditional tool helix shapes. This is investigated by substituting the preferred solution β^* and the conventional constant-helix shapes $\beta_p = \beta \, \forall \, p$ for the cases $\beta = 30°$, $45°$, and $60°$ into the milling model as given in Eq. (18.10) and solving by numerical means. The trapezoidal rule is the adopted numerical method in solving Eq. (18.10), see [2, 22, 29] for more details on computing helix-induced milling dynamics using numerical integration. The force components $\overline{F}_1(\beta)$ and $\overline{F}_2(\beta)$ for the compared helix shapes are marked with asterisks on the time histories in Fig. 18.5. It should be noted that the fact that t_{mid} differs for the compared shapes can be explained on the basis of the deduction in Subsect. 18.3.2 that t_{mid} depends on the first half of the elements of the helix shape β. As expected from an optimization (minimization) that is based on the components of $\Psi(\beta)$ as the objective functions, the marked points in Fig. 18.5 show that the preferred solution β^* leads to

(a) flute shape for the PS.

(b) flute shape for the smoothed PS.
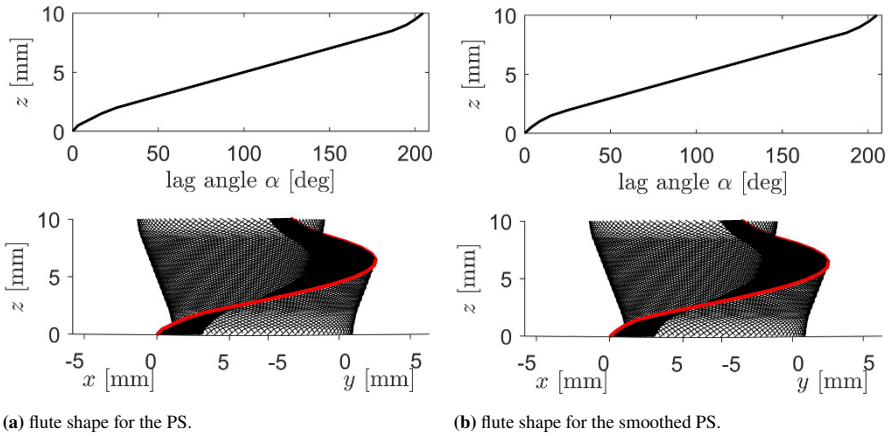
Fig. 18.4: Optimal helix shapes.

(a) feed direction.

(b) feed-normal direction.
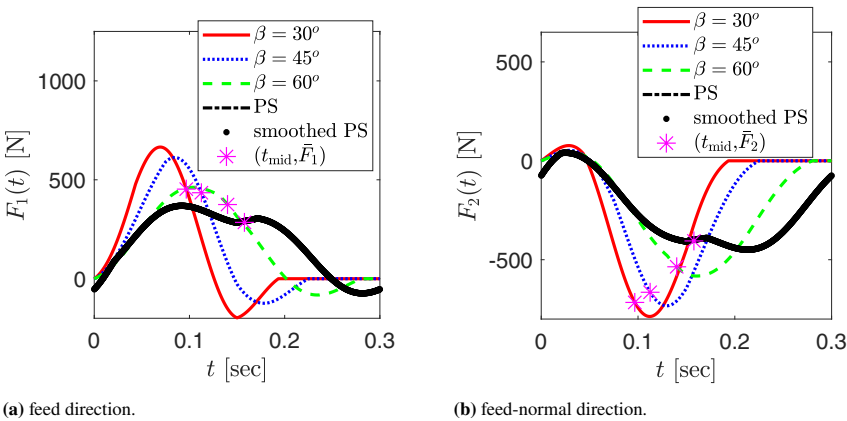
Fig. 18.5: Predicted cutting forces.

relative reduction of the cutting forces $\overline{F}_1(\boldsymbol{\beta})$ and $\overline{F}_2(\boldsymbol{\beta})$ which correspond to t_{mid}. As can be seen in Fig. 18.5, the preferred solution $\boldsymbol{\beta}^*$ also leads to relative reduction of the peak cutting forces justifying the choice of t_{mid} as an alternative to t_{peak} as made Subsect. 18.3.2 for constructing the objective functions. There is 48.67 % and 43.20 % reduction of cutting force variation range in the feed and feed-normal directions for the $\beta = 30°$ tool. The corresponding cutting force reductions are 39.84 % and 37.55 % for the $\beta = 45°$ tool and 18.60 % and 21.38 % for the $\beta = 60°$ tool. The results in Fig. 18.5 show that smoothing does not significantly affect the cutting forces of the preferred helix shape.

It is seen that although the peak forces and variation ranges of the cutting forces are suppressed, there is worsening of the cutting forces in some portions of the time-history. However, reduction of peak forces is of immense practical value since

that amounts to reduction of surface location error, and guarantees more that the machine tool power capacity is not exceeded. The results show that the proposed optimization method can be used in systematic search of trade-off helix shapes for the decision maker to choose from. It specifically demonstrates to be potentially useful in the milling of engineering parts for reducing cutting force components of interest (feed and feed-normal forces in this study) in comparison to the conventional constant-helix tools.

18.6 Conclusions

Milling cutting forces in the feed and feed-normal directions can serve different competing objectives. These force components are affected by the milling tool helix shape. Multi-objective optimization can be used to determine the trade-off shapes for the conflicting forces. To carry out the optimization, the cutting force components are first expressed in terms of unknown distribution of helix angle on the flute of a cylindrical milling tool. Analytical models for the forces are derived in terms of discretized approximation of the unknown distribution. Two objective functions that separately represent cutting forces in the feed and feed-normal directions for the time instant t_{mid} are defined. The Matlab genetic algorithm solver `gamultiobj` is used to solve the optimization problem to give the trade-off helix shapes. Though the optimization is formulated for the time instant t_{mid}, it is seen that the preferred trade-off helix shape can translate to reduction of the peaks and variation ranges of the cutting force components. In conclusion, the proposed optimization method provides a means of systematic search of non-conventional helix shapes for reducing the cutting force components in the milling of engineering parts, and for other purposes.

References

[1] Ema S, Davies R (1989) Cutting performance of end mills with different helix angles. International Journal of Machine Tools and Manufacture **29**(2):217–227
[2] Ozoegwu C, Eberhard P (2022) Geometric definition, rapid prototyping, and cutting force analysis of cylindrical milling tools with arbitrary helix angle variations. Proceedings of the Institution of Mechanical Engineers, Part B: Journal of Engineering Manufacture **236**(9):1232–1246
[3] Hosokawa A, Hirose N, Ueda T, Furumoto T (2014) High-quality machining of CFRP with high helix end mill. CIRP Annals **63**(1):89–92

[4] Adem KA, Fales R, El-Gizawy AS (2015) Identification of cutting force coefficients for the linear and nonlinear force models in end milling process using average forces and optimization technique methods. International Journal of Advanced Manufacturing Technology **79**(9-12):1671–1687

[5] Burek J, Żyłka Ł, Płodzień M, Sułkowicz P, Buk J (2017) The effect of the cutting edge helix angle of the cutter on the cutting force components and vibration acceleration amplitude. Mechanik **90**(11):971–973

[6] Li A, Zhao J, Pei Z, Zhu N (2014) Simulation-based solid carbide end mill design and geometry optimization. International Journal of Advanced Manufacturing Technology **71**(9-12):1889–1900

[7] Wan M, Feng J, Zhang WH, Yang Y, Ma YC (2017) Working mechanism of helix angle on peak cutting forces together with its design theory for peripheral milling tools. Journal of Materials Processing Technology **249**:570–580

[8] Sultan AA, Okafor AC (2016) Effects of geometric parameters of wavy-edge bull-nose helical end-mill on cutting force prediction in end-milling of inconel 718 under mql cooling strategy. Journal of Manufacturing Processes **23**:102–114

[9] Korovin GI, Petrushin SI, Gubaidulina RH (2018) Machining of titanium alloys with wave milling cutters. Materials Science Forum **927**:79–85

[10] Mann BP, Edes BT, Easley SJ, Young KA, Ma K (2008) Chatter vibration and surface location error prediction for helical end mills. International Journal of Machine Tools and Manufacture **48**(3):350–361

[11] Ozoegwu C, Eberhard P (2021) Automated upgraded generalized full-discretization method: Application to the stability study of a thin-walled milling process. In: Dixit US, Dwivedy SK (eds) Mechanical Sciences: The Way Forward, Springer Singapore, Singapore, pp 83–104

[12] Tehranizadeh F, Koca R, Budak E (2019) Investigating effects of serration geometry on milling forces and chatter stability for their optimal selection. International Journal of Machine Tools and Manufacture **144**:103,425

[13] Sabareeswaran M, Padmanaban KP, Sundararaman KA (2018) Comparison of evolutionary techniques for the optimization of machining fixture layout under dynamic conditions. Proceedings of the Institution of Mechanical Engineers, Part C: Journal of Mechanical Engineering Science **232**(12):2145–2158

[14] Deb K, Reddy AR, Singh G (2003) Optimal scheduling of casting sequence using genetic algorithms. Materials and Manufacturing Processes **18**(3):409–432

[15] Eberhard P, Dignath F, Kübler L (2003) Parallel evolutionary optimization of multibody systems with application to railway dynamics. Multibody System Dynamics **9**(2):143–164

[16] Ofochebe SM, Ozoegwu CG (2021) Monitoring the effects of vehicle components' size on optimum structural crashworthiness. Engineering Optimization **53**(7):1156–1172

[17] Endres WJ, DeVor RE, Kapoor SG (1995) A Dual-Mechanism Approach to the Prediction of Machining Forces, Part 1: Model Development. Journal of Engineering for Industry **117**(4):526–533

[18] Lee P, Altintaş Y (1996) Prediction of ball-end milling forces from orthogonal cutting data. International Journal of Machine Tools and Manufacture **36**(9):1059–1072

[19] Wang H, Qin X, Ren C, Wang Q (2012) Prediction of cutting forces in helical milling process. International Journal of Advanced Manufacturing Technology **58**(9):849–859

[20] Wang M, Gao L, Zheng Y (2014) An examination of the fundamental mechanics of cutting force coefficients. International Journal of Machine Tools and Manufacture **78**:1–7

[21] Song Q, Liu Z, Ju G, Wan Y (2019) A generalized cutting force model for five-axis milling processes. Proceedings of the Institution of Mechanical Engineers, Part B: Journal of Engineering Manufacture **233**(1):3–17

[22] Ozoegwu C, Eberhard P (2020) Stability analysis of multi-discrete delay milling with helix effects using a general order full-discretization method updated with a generalized integral quadrature. Mathematics **8**(6):1003

[23] Ozoegwu CG, Ofochebe SM, Omenyi SN (2016) A method of improving chatter-free conditions with combined-mode milling. Journal of Manufacturing Processes **21**:1–13

[24] Ozoegwu C, Eberhard P (2022) Closed-form models for the cutting forces of general-helix cylindrical milling tools. Proceedings of the Institution of Mechanical Engineers, Part B: Journal of Engineering Manufacture p 09544054221141130

[25] Liu N, Zhang Y, Lu W (2015) A hybrid approach to energy consumption modelling based on cutting power: a milling case. Journal of Cleaner Production **104**:264–272

[26] Kiss AK, Bachrathy D, Stepan G (2016) Cumulative surface location error for milling processes based on tool-tip frequency response function. Procedia CIRP **46**:323–326

[27] Deb K (2001) Multi-Objective Optimization Using Evolutionary Algorithms. John Wiley&Sons, West Sussex

[28] Ozturk E, Ozkirimli O, Gibbons T, Saibi M, Turner S (2016) Prediction of effect of helix angle on cutting force coefficients for design of new tools. CIRP Annals **65**(1):125–128

[29] Ozoegwu CG (2016) High order vector numerical integration schemes applied in state space milling stability analysis. Applied Mathematics and Computation **273**:1025–1040

Chapter 19
Experimental and Numerical Studies on the Tensile Strength of Lap Joints of PEEK Plates and CF Fabric Prepregs Formed by Ultrasonic Welding

Sergey V. Panin, Svetlana A. Bochkareva, Iliya L. Panov, Vladislav O. Alexenko, Anton V. Byakov, and Boris A. Lyukshin

Abstract Ultrasonic welding (USW) is a promising technology for permanent joint fabrication of thermoplastic based both particulate and laminated composites. One of the topical issues in this field is to improve their mechanical characteristics (including the interlayer shear strength/ISS). This paper presents the results of experimental and numerical studies aimed at increasing the tensile strength of USW lap joints of polyetheretherketone (PEEK) plates, which was achieved by placing a prepreg (a fabric based on high-modulus carbon fibers (CFs) impregnated with a high-temperature thermoplastic binder) in the fusion zone. The experimental studies of

Sergey V. Panin
Institute of Strength Physics and Materials Science, Siberian Branch of the Russian Academy of Sciences, 2/4, prospekt Akademicheskii, 634055 Tomsk & National Research Tomsk Polytechnic University, Lenin Ave 30, 634050 Tomsk, Russian Federation,
e-mail: svp@ispms.ru

Svetlana A. Bochkareva
Institute of Strength Physics and Materials Science, Siberian Branch of the Russian Academy of Sciences, 2/4, prospekt Akademicheskii, 634055 Tomsk & Tomsk State University of Control Systems and Radioelectronics, 40, prospect Lenina, 634050 Tomsk, Russian Federation,
e-mail: svetlanab7@yandex.ru

Iliya L. Panov
Institute of Strength Physics and Materials Science, Siberian Branch of the Russian Academy of Sciences, 2/4, prospekt Akademicheskii, 634055 Tomsk& National Research Tomsk State University, Lenin Ave 36, 634050 Tomsk, Russian Federation,
e-mail: panov.iliya@mail.ru

Vladislav O. Alexenko · Anton V. Byakov
Institute of Strength Physics and Materials Science, Siberian Branch of the Russian Academy of Sciences, 2/4, prospekt Akademicheskii, 634055 Tomsk, Russian Federation,
e-mail: vl.aleksenko@mail.ru, bjakov@ispms.ru

Boris A. Lyukshin
Institute of Strength Physics and Materials Science Siberian Branch of the Russian Academy of Sciences, 2/4, prospekt Akademicheskii, 634055 Tomsk, Tomsk State University of Control Systems and Radioelectronics, 40, prospekt Lenina, 634050 Tomsk & National Research Tomsk State University, Lenin Ave 36, 634050 Tomsk Russian Federation,
e-mail: lba2008@yandex.ru

the influence of the prepreg 'design' on the tensile strength of the USW joints of the PEEK plates showed that the prepreg thickness (related to the CF fabric-to-binder ratio) determined the ability of the thermoplastic to melt and subsequently spread in the USW process. This phenomenon governed the formation of the macro- and microstructure at the interface between the joined components via their mutual mixing. For a detailed analysis of the influence of the structure of the USW joints on the tensile strength and the fracture mechanisms, parametric investigations were performed based on both 2D and 3D numerical simulations. For doing so, software developed by the authors and the ABAQUS package, respectively were employed. The designed models of the USW lap joints considered:

i)   the prepreg orthotropic properties,
ii)   the non-linearity of the PEEK characteristics,
iii)   the presence of discontinuities at the interface, and
iv)   the interlayer adhesion strength.

The models implemented the fracture processes of the USW lap joints due to cracking of the joined materials as well as delamination at the interfaces. The significance of some factors was analyzed, including

i)   the adhesion level between the prepreg and the PEEK plates,
ii)   the shear strength of the prepreg in the reinforcement plane, and
iii)   the adhesion uniformity over the contact area of the USW joints.

The detailed investigations of stress–strain states of the USW lap joints enabled to conclude that macroscopic bending of the PEEK plates was one of the key factors determining their tensile strength, so its quantitative analysis was carried out.

19.1 Introduction

Ultrasonic welding of polymers is widely used in some industries. This process is performed in three main stages:

1. At the first stage, a gradual increase in the clamping force on the parts to be joined at the weld zone is implemented until a threshold level is reached.
2. Next, ultrasonic (US) vibrations of preset both frequency and amplitude are applied. In this case, US oscillations of a welding tool is converted into heat (due to frictional heating of the joined parts mutually moving relative to each other) during a certain period of time. As a rule, the clamping force is maintained constant at this stage.
3. At the third stage, the molten material is solidified without US vibrations but under the clamping force for a preset period. At the same time, polymer chains on the surfaces of the joined polymer plates should mutually penetrate.

When determining such parameters as the clamping force, as well as durations of both US vibrations and holding under pressure upon cooling, both glass transition

and melting temperatures of a polymer, its molecular structure (molecular weight and polarity of units) seem to be relevant. Due to the application of a compressive load at the interface of the parts to be joined, a diffusion rheological interaction of molecules should occur with a structural transition. Such mutual penetration is effectively implemented when the polymer is in a viscous state, and its molecules possess both maximum mobility and minimum packing density.

At present, there is an increased interest to application of the USW for joining laminated thermoplastic-based composites, while aspects of the process are actively discussed [1–3]. The relevance of this problem is caused by the possibility of manufacturing large-scale products. In this case, the use of energy directors (EDs) ensures formation of reliable permanent joints. In the USW process, the ED's melting occurs and a dense layer is formed that connects joined plates (made of similar materials, as a rule).

For manufacturing of EDs, in addition to films of the same materials as the laminates being joined, more fusible thermoplastics are used. Their thickness and porosity are varied, as well as reinforcing particles and fibers are additionally loaded [4, 5]. Some aspects of the USW fabricated laminates based on thermoplastic binders are actively studied nowadays [6, 7].

In addition to the mechanical characteristics of such USW joints, patterns of their structure formation are determined by the thermophysical properties of polymer binders, as well as the stacking sequence and orientation of fibers in the boundary layer facing the interface. Due to the anisotropic structure, carbon fibers (CFs) show high thermal conductivity along their direction, while it is extremely low perpendicular to them. It is obvious that the thermal conductivity inside each unidirectionally reinforced composite layer depends on the laying direction of CFs and their volume fraction [8, 9].

However, the interlayer shear strength (ISS) of USW joints is generally below the shear strength of a thermoplastic binder. Placing a prepreg (reinforcing fabric in a binder) into the fusion zone can improve their mechanical characteristics, but this issue has not been fully studied so far.

Most researchers emphasize that the bonding between the reinforcing synthetic fiber and PEEK is relatively weak because of i) the different polarity of the filler and the binder; ii) the absence of reactive functional groups in PEEK, and iii) the smooth fiber surfaces, as a rule [10–13]. Due to the low interfacial adhesion between the fiber and the polymer matrix, delamination occurs under mechanical loading, which limits the use of laminated PEEK-based composites.

Fiber surface modification is of relevance there, which is implemented, in particular, by (cold) plasma treatment [14–16]. It was shown that the strength characteristics can be improved by the formation of the C-O functional groups, which enhance the adhesion strength of the composites' components.

Common methods for the formation of functional oxygen-containing groups on the surface of fibers are chemical [17–21], thermal [22] and electrochemical oxidation [23], as well as treatment of CFs with low-temperature plasma [24]. All of them can be effectively applied over an industrial scale for functionalization of reinforcing fillers. Thus, the strength properties of laminated composites with a PEEK binder

cannot be improved without an increase in the interfacial adhesion, which depends on a number of parameters.

In this study, the influence of the macro- and microstructure on the tensile strength of USW lap joints was experimentally and numerically investigated. Two PEEK plates were joined with a prepreg from a solution-impregnated thermoplastic CF fabric at the interface. The influence of both properties and compositions of an ED and the prepreg, as well as USW parameters were analyzed in detail for improving the tensile strength of the USW lap joints.

19.2 Experimental Investigation of the Influence of the Prepreg 'Design' and its Properties on the Tensile Strength of the USW Lap Joints

As mentioned above, the prepreg properties could exert a significant effect on rising the interlaminar adhesion level (d) in the USW joints. An experimental study was performed on the influence of the (PEEK-CF) prepreg thickness (determined by the CF fabric–to–binder volume ratio) on the tensile strength of the USW lap joints of PEEK plates.

19.2.1 Samples' Fabrication

The USW lap joints included two PEEK plates (adherends), two EDs, and the PEEK-CF prepreg (Fig. 19.1). The 770PF powder (Zeepeek, China) was used as a feedstock for manufacturing the PEEK adherends with an 'RR/TSMP' injection molding machine (Ray-Ran Test Equipment Ltd., Nuneaton, UK). A temperature range for heating
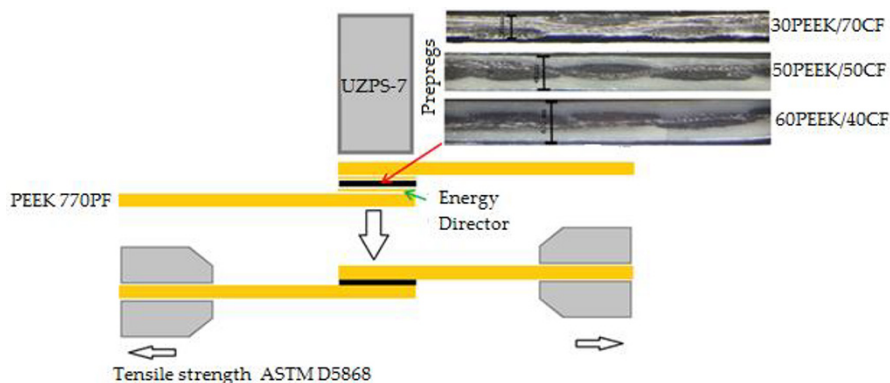
Fig. 19.1: A scheme of the formation of the USW joints.

a mold was 200–205°C; a hopper with the powder was heated up to a temperature of 395°C. As a result, rectangular shape adherends 100 mm×20 mm×2.2 mm in size were cast.

A PEEK film 250 μm thick (Victrex, Aptiv 2000) was used for ED fabrication. Square fragments 22 mm×22 mm in size was cut out from commercially availble film. Then, they were placed between the PEEK adherends and the prepreg at the center of the lap joints in the USW process (Fig. 19.1). The prepregs, in the form of square films 50 mm×50 mm in size, were made by pre-impregnating the 'ACM C285S' CF fabric (5/2 satin weave, UMATEX, Russia) with an alcohol suspension of the 'PEEK 770PF' powder, followed by evaporation of the liquid in a 'Memmert UF 55' oven (Memmert GmbH Co., Germany) at 150°C. Then, they were subjected to compression sintering in a mold at a temperature of 400°C and a pressure of 6 MPa. Thicknesses of the prepregs were varied by extruding a part of the melted PEEK binder. In this case, the CF fabric content also changed from 40 up to 70 wt.%. Table 19.1 presents the main parameters of the fabricated prepregs.

For the formation of the USW joints, an 'UZPS-7' ultrasonic welding machine (SpetsmashSonic, Russia) was employed. The overlap area of the joined adherends and the sonotrode size was 20 mm×20 mm. The PEEK plates to be welded were placed in a fixing clamp, which excluded their mutual movement during the USW process. Durations of US vibrations (t), hereinafter referred to as the 'USW durations', were 800 and 1400 ms. The clamping force was 3 atm (764 N). A time duration under the clamping upon cooling was 5000 ms. By varying the USW parameters, regimes were determined that made it possible to obtain a uniform interface structure (without visible damage to the CF fabric), as well as high mechanical properties.

19.2.2 Tensile Tests of the USW Joints

The tensile strength of the USW joints was evaluated according to ASTM D5868 (Russian state standard GOST R 57066). The tests were carried out with an 'Instron 5582' electro-mechanical machine at a cross head speed of 13 mm/min. Figure 19.2 shows the ultimate tensile strength (σ_U) levels for the USW joints with all three prepregs at both USW durations. With an increase in the t, the σ_U values increased in all studied cases. However, the tensile strength was lower at both USW durations of 800 and 1400 s for the prepreg with the maximum thickness of 620 μm.

Table 19.1: The prepreg parameters.

Designation	Thickness, μm	CF/PEEK, wt. %
30PEEK/70CF	280± 30	70/30
50PEEK/50CF	480±30	50/50
60PEEK/40CF	620±30	60/40
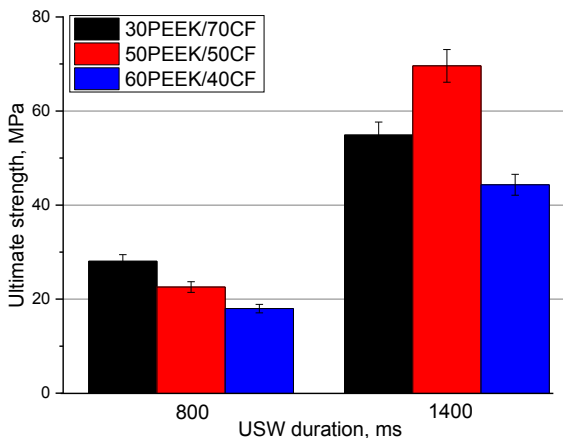
Figure 19.3 presents images of the fractured samples with the prepreg thickness of 280 μm. The fracture initiated at the 'PEEK adherends–USW joint' interface (a blue frame in Fig. 19.3, a). Then, a macrocrack propagated along the fusion boundary with a noticeable effect of macroscopic bending, which completed with the PEEK fracture at a stress of 28 MPa. In the fusion zone, the ED was predominantly melted (the color became milky-cloudy, in contrast to the transparent one for the initial ED). The CF fabric was not damaged and did not spread out from the fusion zone. According to the authors, this fact was caused by the low content of the PEEK binder in the prepreg.

At the USW duration of 1400 ms, the USW joint thickening was 400 μm, while it did not exceed 200 μm at $t = 800$ ms. Thus, in addition to the melting of the binder in the prepreg, the ED did intensively melt and extrude. As a result, the USW joint fractured by the CF fabric tearing mechanism (Fig. 19.3, b). Despite the fact that the USW joint showed the maximum tensile strength of 54.9 MPa, this USW mode had no prospects for any practical implementations due to the damaging of the CF fabric in the prepreg.
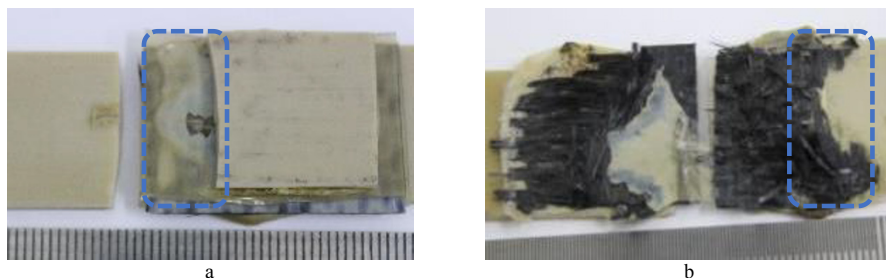
Fig. 19.3: The images of fractured USW lap joints. Prepreg thickness of 280 μm; the USW durations of 800 (a) and 1400 (b) ms.

Figure 19.4 shows images of the fractured USW joints at the prepreg thickness of 480 μm. At t = 800 ms, the USW joint components were melted slightly, the ED in the fusion zone was partially melted (its shade became dull), but not enough to ensure a high adhesion level. The USW joint thinning was 200 μm. A main crack initiated at the 'PEEK adherends–USW joint' interface (highlighted by a blue frame in Fig. 19.4, a), then it propagated approximately to the middle of the USW joint. The failure occurred due to macroscopic bending of the partially exfoliated PEEK adherends at a stress of 22 MPa (Fig. 19.2).

At t = 1400 ms, the maximum USW joint thinning of 500 μm was observed, which indicated complete melting of the components, besides adherends. This effect was not accompanied by a pronounced violation of the prepreg structural integrity. In the area circled by a red oval in Fig. 19.4, b, the polymer intensively squeezed out of the fusion zone, but the fractured fragments of the CF fabric were not found as part of a 'burr'. The fracture initiated at the 'PEEK adherends–USW joint' interface (a blue frame) and completed due to macroscopic bending at a stress of ~70 MPa (Fig. 19.2). According to the authors, the molten polymer squeezed out of the fusion zone at the prepreg thickness of 480 μm and the prolonged USW duration, strengthening the USW joint perimeter and preventing the initiation a main crack and its propagation to the interface. As a result, the maximum tensile strength value was registered.

Figure 19.5 presents images of the fractured USW lap joints at the prepreg thickness of 620 μm. At t = 800 ms, the USW joint thinning was 150 μm due to the low PEEK content in the prepreg and the short USW duration. Similar to the previous case, the 'excess' PEEK melted in the fusion zone squeezed out (marked with a red oval in Fig. 19.5, a). A crack initiated at the left edge of the USW joint, i.e. at the interface between the PEEK adherends and the ED (a blue frame in Figure 19.5, a). The fracture completed via macroscopic bending of the partially delaminated (upper) PEEK adherend.

At t = 1400 ms, the USW joint thinning was 300 μm, which was accompanied by intense extrusion of PEEK from the fusion zone (red ovals in Fig. 19.5, b). The main crack initiated at the right edge of the USW joint, i.e. at the 'PEEK adherend–ED' interface (a blue frame in Fig. 19.5, b). The fracture completed due to macroscopic bending of the partially delaminated (upper) PEEK adherend. Since local damage

a   b
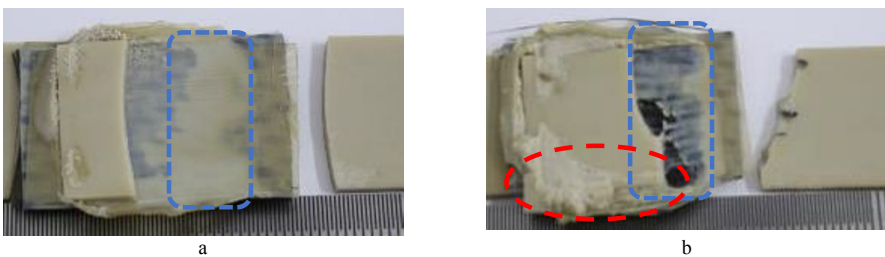
Fig. 19.4: The images of the fractured USW lap joints. The prepreg thickness of 480 μm; the USW durations of 800 (a) and 1400 (b) ms.
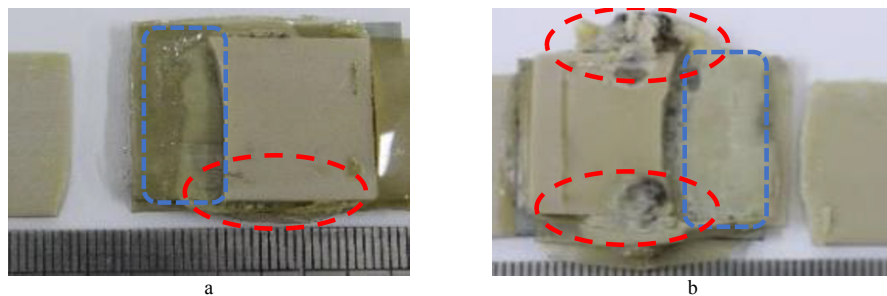
Fig. 19.5: The images of the fractured USW lap–joints. The prepreg thickness of 620 μm; the USW durations of 800 (a) and 1400 (b) ms.

of the PEEK plates was observed at $t = 1400$ ms, this mode is to be excluded for practical applications.

Figure 19.6 shows cross sections of the USW joints with the prepreg thickness of 280 μm for both USW durations. At $t = 800$ ms, the only CF fabric was clearly observed at the interface (a thickness of this "layer" was about 280 μm, corresponding to that of the prepreg), but no ED traces were found (despite the fact that the USW joint thinning was less than 250 μm). It could be concluded that the interface structure was homogeneous, the CF fabric showed no signs of damage, and no discontinuities (e.g., pores) were observed in the PEEK adherends.

At $t = 1400$ ms, traces of polymer both melting and flowing were found in the fusion zone (Fig. 19.6, b). Probably, the reason was local melting of the ED. To the left and right of the 'CF fabric layer', another layer was observed that differed in

Fig. 19.6: The images of the cross sections of the USW joints with the prepreg thickness of 280 μm; the USW durations of 800 (a) and 1400 (b) ms.

shade from the base PEEK material. In addition, individual pores were present. A thickness of the 'CF fabric layer' of 390 μm was noticeably greater than that of the prepreg. Intensive melting of the polymer components due to frictional heating, as well as the development of mass transfer (mixing) processes upon joining, caused partial local damage to the CF fabric as well.

Figure 19.7 presents cross sections of the USW joints with the prepreg thickness of 460 μm. At $t = 800$ ms, a well-pronounced interface between the ED/prepreg and the PEEK adherends was evident. In the prepreg, the CF fabric retained its integrity, while its thickness was 340 μm (in comparison with the initial value of 460 μm). The interface between the ED and the PEEK adherends was contrast, while it was hardly distinguishable between the ED and the prepreg. The reason was both melting and mixing of the thinner components compared to the PEEK adherends with the thickness of ~2.2 mm each. Due to both incomplete melting of the ED and low interlaminar adhesion, this composite showed the lower tensile strength than that of the 30PEEK/70CF prepreg (Fig. 19.2).

After rising the USW duration up to 1400 ms, melting of both the ED and the prepreg was observed (Fig. 19.7, b). The PEEK adherends had a low-contrast interface with the prepreg, and the distance between them could be estimated as ~1050 μm that was greater than the total thickness of both original prepreg and two EDs of ~960 μm. At the same time, a large number of pores were found at the fusion zone, while the CF fabric was noticeably damaged. Moreover, the thickness of the "layer" corresponding to the CF fabric could be estimated as ~610 μm, which was almost two times thicker than that of the original prepreg of ~340 μm (Fig. 19.7, a). This indicated damage of both the prepreg and the CF fabric. Note that the formation of the revealed macrostructure at the fusion zone was even accompanied by an increase in the tensile strength of the USW joint of 70 MPa (the maximum among all registered

a   b

Fig. 19.7: The images of the cross sections of the USW joints with the prepreg thickness of 460 μm; the USW durations of 800 (a) and 1400 (b) ms.

values according to Fig. 19.2). Thus, for structural reasons, this prepreg 'design' and the USW duration could not be recommended for further practical applications.

Figure 19.8 shows cross sections of the USW joints with the prepreg thickness of 620 μm at both USW durations. At $t = 800$ ms, a pronounced interface was observed between the 'prepreg–ED' and 'ED–PEEK adherend' boundaries. In this case, both surface layers of the prepreg was fused with the ED and the ED thickness changed little, while the CF fabric retained its structural integrity. The USW joint thinning was 100 μm according to Fig. 19.8, a.

At $t = 1400$ ms, a large number of large pores were found in the fusion zone, actually located between the CF fabric and the PEEK adherends (Fig. 19.8, b). A thickness of the CF fabric layer could be estimated as 440 μm, which was greater by about 100 μm than that of the original prepreg of 340 μm (Fig. 19.6, a). In the USW process, melting of the prepreg obviously accompanied by fracture of the CF fabric. Note that the formation of pores was more intense in the case of the binder content in the prepreg of 60% compared to other USW joints (Figs. 19.6 and 19.7). Similar to the above results, at the USW duration of 1400 ms and the prepreg thickness of 620 μm, the USW joint possessed the minimum tensile strength of 43 MPa. According to the authors, the reason for the high porosity was the excessive content of the PEEK binder, both melting and extrusion of which from the fusion zone was accompanied by active mixing of the polymer components during the USW process. Needless to note, this USW mode could not be relevant for any practical applications.

Thereby, based on the experimental data analysis, it was revealed that the structure of the USW lap joints was heterogeneous and their tensile strengths depended on several factors. The heterogeneity was caused by the composition and the properties of the EDs and the prepreg, as well as their total thickness (the CF fabric to binder ratio) and the USW parameters. It was rather difficult to differentiate the influence

a   b
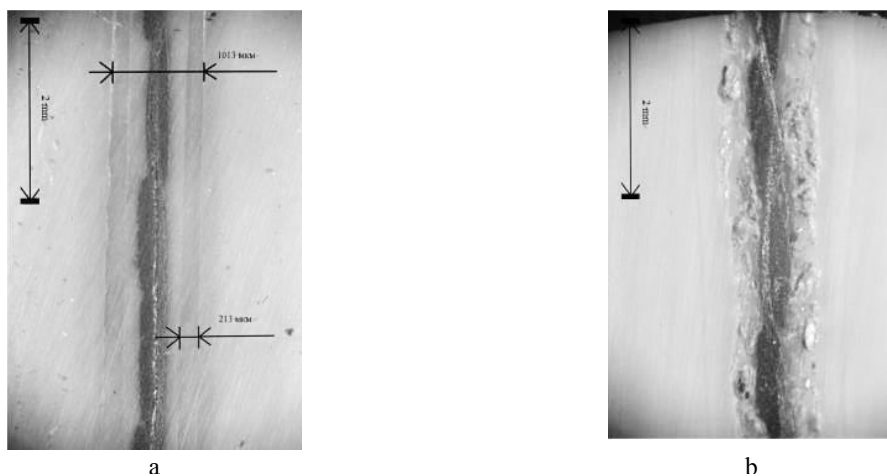
Fig. 19.8: The images of the cross sections of the USW joints with the prepreg thickness of 620 μm; the USW durations of 800 (a) and 1400 (b) ms.

of the identified factors on the tensile strength of the USW joints, but such estimates could be made by numerical simulation.

19.3 A Parametric Study of the Tensile Deformation Behavior of the USW Joints Based on Numerical Simulation

The properties of the USW lap joints were heterogeneous due to the fact that PEEK was melted and gradually extruded under the normal load from the center to the edges of the fusion zone. Inhomogeneity appeared because practically nothing prevented the material extrusion along the edges, while it was more difficult to extrude it in the center. This could be prevented by both PEEK and CFs, which could be moved, bent, or fractured due to both normal and shear loads in the USW process. On the other hand, pores could be formed in the fusion zone. In addition to affecting the USW lap joint properties, their presence at the interfaces between the prepreg and the PEEK adherends as well as between the layers in the prepreg could also affect the adhesion level at the contact areas and result in such inhomogeneities and discontinuities.

In this way, the factors identified in the experiment required numerical investigations for assessing the influence degree for each of them separately, including the interfacial adhesion level, the presence of discontinuities at the interface, as well as the thickness, composition and properties of the prepreg on the tensile strength of the USW lap joints. Numerical simulation enabled to study in detail the dynamics of stress–strain states (SSS) in the USW lap joints upon the tensile tests for evaluating the fracture development and tracking the influence of each of the factors on the failure mechanism separately.

19.3.1 The Problem Statement for the Parametric Studies on the Tensile Deformation Behavior of the USW Lap Joints

The SSS study in the USW lap joints upon the tensile tests was carried out via numerical simulations using both 2D software developed by the authors based on the finite element method (FEM) and the 3D Abaqus/CAE 2019 package. A scheme of the computational domain in the 3D formulation (Fig. 19.9) corresponded to the conditions of the tensile tests of lap joints according to ASTM D5868 (Russian state standard GOST R 57066). In the 2D formulation, the longitudinal section of the USW lap joints was taken as a computational domain (Fig. 19.10).

As in the experiment, the USW lap joints included two PEEK adherends with the dimensions of 45 mm×20 mm×2.2 mm, overlapped over the area of 20×20 mm. The model considered only the fused part of the USW lap joints without the areas clamped in the grips. In the center between the PEEK adherends, the prepreg layer was included, consisting of the CF fabric impregnated with PEEK. The prepreg thicknesses varied from 0.28 mm to 0.62 mm, depending on the PEEK contents,
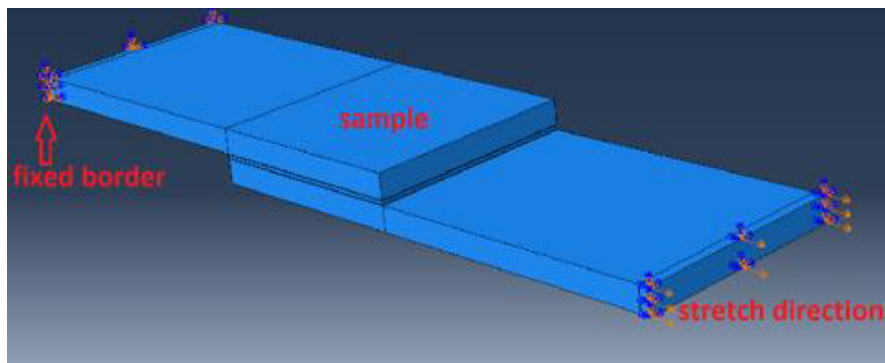
Fig. 19.9: The 3D scheme of the computational domain for the numerical simulation of tensile tests of the USW lap joints.
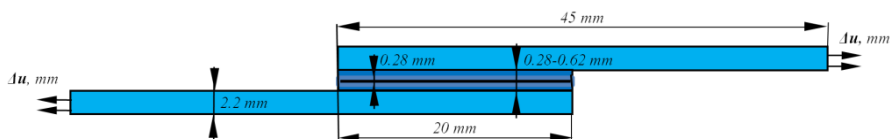
Fig. 19.10: The 2D scheme of the computational domain for the numerical simulation of the tensile tests of the USW lap joints.

which was mainly located on both sides of the middle layer with the CF fabric (the so-called 'facing' layers). In the experiment, the ED was placed between the prepreg and the PEEK adherends for improving the strength characteristics. Since the ED was completely melted in the USW process, its presence was taken into account by varying the adhesion level between the PEEK adherends and the prepreg.

For both models, the following boundary conditions were accepted:

• the left end of the USW lap joints was rigidly fixed, so no displacements were allowed in all directions;
• on the right end, displacements were set step-by-step in the direction of the Ox axis, so displacements were prohibited on along other axes (in the 2D formulation, displacements were set symmetrically on the left and right boundaries);
• all other boundaries remained free.

For PEEK, the non-linear pattern of the stress–strain diagram was considered, the elastic modulus was 2.4 GPa, the Poisson's ratio was 0.38, the ultimate strength values were assumed to be 109 MPa for normal stresses and 41 MPa for shear ones. The ED properties between the PEEK adherends and the prepreg were assumed to be the same. The CF fabric layer impregnated with PEEK (prepreg) was taken as a homogeneous material with the orthotropic properties obtained analytically [25–27].

The following designations were introduced: E_F, E_M and G_F, G_M, which were the elastic and shear modulus of CFs and the matrix, respectively; ϕ was the volumetric CF content. In the ideal adhesion case ($E_F \gg E_M$), the longitudinal elastic modulus

of the composite (in the reinforcement direction) was determined by that of CFs and their relative content in this direction according to the following expressions [26, 27]:

$$E_x = E_F \phi.$$

and similarly, for the strength values

$$\sigma_x = \sigma_F \phi.$$

The transverse both elastic modulus and strength can be estimated as follows

$$E_y = \frac{E_M}{1-\phi}; \quad \sigma_y = \frac{\sigma_M}{1-\phi}.$$

The shear modulus can be computed by

$$G = \frac{G_M G_F}{\phi G_M + (1-\phi) G_F}.$$

The strength of CFs was 4.9 GPa, while their elastic modulus was 240 GPa. The longitudinal elastic modulus of the CF fabric impregnated with PEEK, at the CF to PEEK ratio of 70/30 vol.% (with the prepreg thickness of 280 μm) was taken equal to 75 GPa in the direction along the Ox and Oy axes, but the transverse value along the Oz axis was 4.3 GPa. The ultimate strengths were 1.7 GPa along the reinforcement direction and 166 MPa across it, respectively.

When developing the 3D FEM model, the C3D8R volumetric hexahedral elements with a linear approximation of displacements were used. Between the layers, the 'Cohesive behavior' and 'Damage' contact conditions were considered, which did not enable mutual penetration of the layers, but allowed their delamination at the adhesion level (delamination stresses).

In the 2D formulation of the problem, triangular finite elements were used. A contact between surfaces was preset by linking displacements in the nodes of the dependent surface (layer) with sides of the main surface (plate). To ensure joining of the prepreg and the PEEK adherends, conditions of the equality of displacements were set in the contact nodes and the corresponding changes were made to the stiffness matrix, described in [28].

So, if the m and l nodes of one contacting surface (plate) were taken as the main ones, and the k node of another contacting surface (layer) was considered dependent, then its displacement was calculated through the movements of the main nodes:

$$u_k = u_l(1-h) + hu_m, \quad v_k = v_l(1-h) + hv_m,$$

where u and v were displacements along the x and y axes, respectively; h determined the normalized distance of the k point from the l node:

$$h = \sqrt{\frac{(y_k - y_l)^2 + (x_k - x_l)^2}{(y_m - y_l)^2 + (x_m - x_l)^2}}, \quad h \in [0, 1].$$

In both formulations, the problems were solved step by step. At each step in each finite element, the elastic modulus of the polymer was corrected according to the non-linear stress–strain dependence under tension and the fracture criteria were checked.

19.3.2 Criteria for the Damage Simulation

The Abaqus/Explicit software package enabled to simulate progressive damage and failure of connected elements, whose response was determined by the level of stresses at the contact interface (adhesion) and in the materials (cohesion). The general fracture scheme allowed to combine several damage mechanisms acting simultaneously on the same material. The fracture mechanism as a whole consisted of three components:

i)   the damage initiation criterion,
ii)   the damage evolution law, and
iii) the reaching of the completely damaged state.

The following criteria were used:

- The material fractured if the components of the stress tensor (normal and shear stresses) in the elements or the intensity of stresses and strains were greater than those corresponding to the yield and shear points in the corresponding directions. As a result, a crack initiated in the 3D formulation. In the 2D formulation, if the criterion was met in an element, then the elastic modulus in it decreased by a factor of 100 relative to the polymer level and the stresses were zeroed, which corresponded to fracture of the relevant element. If the element in which the criterion was fulfilled contained a contact node, then delamination between CFs and the PEEK binder was additionally implemented.
- Delamination was realized in nodes and surfaces at the contact boundaries, if both normal and shear stresses in the elements adjacent to the contact boundary were greater than the adhesion level (delamination stresses), the maximum values of which corresponded to the yield and shear points of PEEK in the corresponding directions. In the 3D formulation, the damage evolution was linear in the contact layer from the very beginning of the fracture process.

The tensile strength (at fracture) of the USW joints as a whole was estimated by the fact of a sharp drop in stresses on the stress–strain diagrams, as a result of the loss of their bearing capacity. Also, the initiation of a crack led to a termination in the calculation (equivalent to the fracture completing) when performing simulations in the Abaqus package.

In the 2D formulation, the step convergence was tested by varying its size (displacement) from 5 μm up to 50 μm. To achieve the convergence of the results, the step was 30 μm or less. The load step value was set automatically in the 3D formulation. The mesh convergence was refined at its different partitions in the contact areas, considering their uniformity (dimensions of the sides of adjacent elements differed by no more than 3 times, the angles in triangular elements were at least 30 degrees

in the 2D formulation). As a result, the minimum size of an element at the contact was 100 μm in the 3D formulation. The total number of elements was about 250 000. In the 2D formulation, the minimum element size was 30 μm, considering the convergence, and the number of elements was approximately 30 000.

19.3.3 A Study of the Tensile Strength of the USW Joints in the 3D Formulation

In order to evaluate the effect of the adhesion level (d) on the tensile strength of the USW joints, they were varied in the simulations: 1) between the prepreg and the PEEK adherends and 2) between the layers in the prepreg, i.e. between the CF fabric and the 'facing' PEEK layers, in the range from 30 up to 110 MPa (the maximum level of stresses corresponded to the PEEK yield point). As noted in the introduction, the adhesion level was not always the same at the interface between the prepreg and the PEEK adherends. There were regions with different adhesion, which affected the fracture mechanism and, ultimately, the strength characteristics of the USW lap joints in general. In this case, the adhesion heterogeneity was taken into account by simulating partial contacts between the prepreg and the PEEK adherends. The effect of the prepreg thicknesses (h) from 280 up to 620 μm on the tensile strength of the USW joints was evaluated at the adhesion levels of 30–110 MPa.

19.3.3.1 The Effect of the Prepreg Thickness on the Tensile Strength of the USW Lap Joints

In the experiment, the prepreg thickness varied from 0.28 to 0.62 mm by changing the PEEK contents, while it was located on both sides of the middle CF fabric layer (Figs. 19.7 and 19.8) and had different thicknesses depending on the USW mode. Therefore, the prepreg thickness (h) was varied from 280 to 620 μm at the adhesion levels of 30–110 MPa. Rising the prepreg thickness by increasing the PEEK content at the same adhesion level caused a slight decrease in the ultimate stresses (Fig. 19.11). The slope of the stress–strain curves and the tensile strength decreased slightly, since the prepreg thickness was several times lower than those of the PEEK adherends. Thus, the prepreg thickness did not significantly affect the tensile strength, but the adhesion level was the determining factor (Fig. 19.11).

Figure 19.12 shows distributions of the stress intensity at the prepreg thickness of 620 μm and the adhesion level of 60 MPa. In this case, the ultimate both stresses and strains were achieved due to macroscopic bending of the PEEK adherends at the beginning and at the end of the contact zone, causing fracture in these areas. The fracture proceeded symmetrically on both sides of the USW lap joints. Firstly, a slight delamination began (to the left of the USW lap joint in Fig. 19.11). Then, a crack initiated in the PEEK adherends (on the right) and propagated along the edge of the USW lap joint to its center. Due to delamination, stresses reduced in the prepreg at
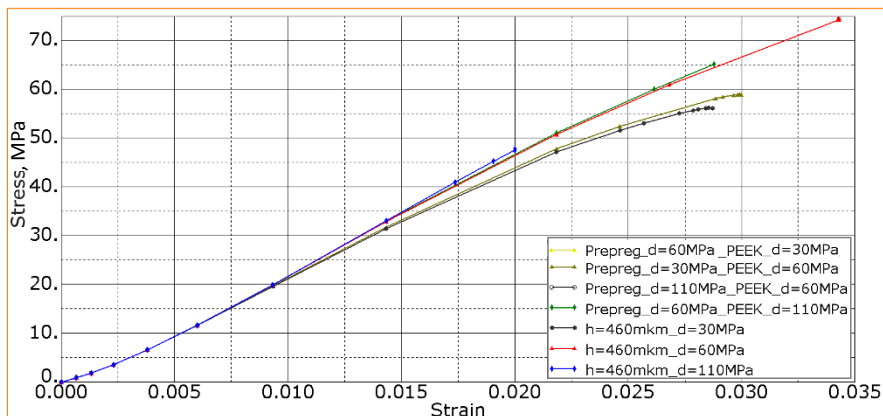
Fig. 19.11: The stress–strain diagrams for the USW lap joints with the prepreg thicknesses (h) from 280 to 620 μm and the adhesion levels (d) from 30 to 110 MPa.

the edges of the USW lap joints, but they remained high in the center, where there was no delamination. In this case, fracture of the USW lap joint completed in the PEEK adherends along the crack. On the whole, the process did not differ from those with the prepreg thicknesses of 280 and 460 μm at this adhesion level. The observed phenomenon also confirmed the fact that the prepreg thickness was not a significant factor for the strength characteristics of the USW lap joints.

19.3.3.2 The Effect of the Adhesion Level Between the Prepreg and the PEEK Adherends on the Tensile Strength of the USW Lap Joints

As shown above, the tensile strengths for all USW lap joints at the adhesion level of 60 MPa were much higher than those at 30 and 110 MPa (Fig. 19.11). At the highest adhesion level of 110 MPa, fracture occurred earlier than at the lower ones. To explain this feature, the SSS of the USW lap joints were analyzed at the prepreg thickness of 280 μm and different adhesion levels. Figure 19.13 presents the Mises stress distributions for the adhesion levels (delamination stresses) between the prepreg and the PEEK adherends of 110, 60 and 30 MPa.

At the considered dimensions of the USW lap joints and the material properties, macroscopic bending and interlaminar shear were observed in addition to tension. The PEEK adherends experienced the maximum bending near the edges of the USW joints, which led to fracture of these areas due to large plastic strains. The ultimate stresses were reached at the edges of the USW joints, then delamination began. As a result, stresses reduced in the bending region. At the highest adhesion level (Fig. 19.13, a), failure occurred via the crack propagation even in the absence of delamination. Therefore, the shear strength of the USW lap joint was the lowest
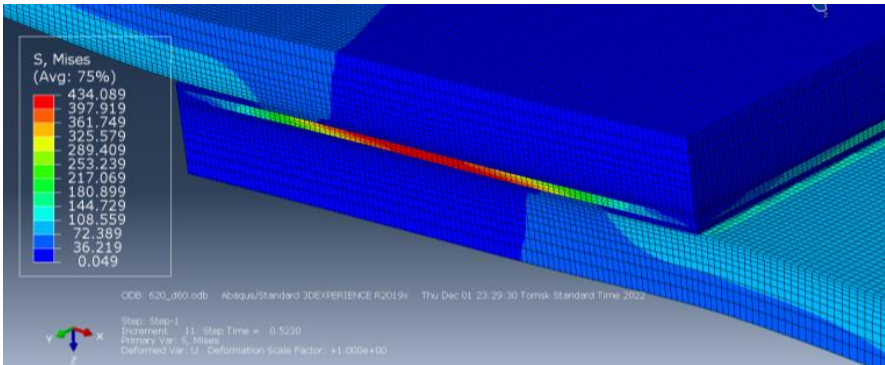
a
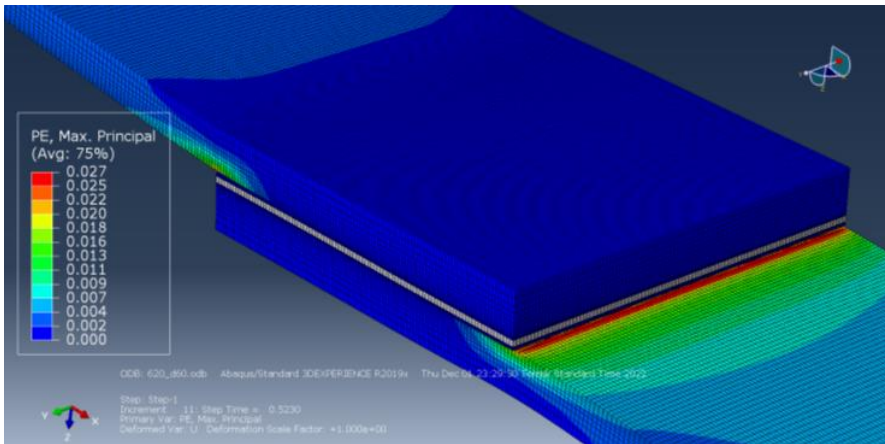
b

Fig. 19.12: The distributions of the intensity of stresses (a) and plastic strains (b) in the USW lap joint with the prepreg thickness of 620 μm and the adhesion level of 60 MPa.

because of fracture of the PEEK adherends in the bending areas at the maximum adhesion level.

Thus, the adhesion levels in combination with the specified properties of the PEEK adherends and the sizes of the USW joints determined the fracture mechanism:

1. At the high adhesion level, bending of the PEEK adherends increased upon loading; if delamination did not occur, then cracks initiated in the bending area on both sides of the USW joint due to large plastic strains (Fig. 19.13, a).
2. At the average adhesion level, bending of the PEEK adherends enhanced upon loading and delamination began. Stresses decreased in this region and did not lead to large plastic strains. With further loading, bending intensified and, despite the gradual delamination, caused the accumulation of plastic strains; in doing so, the initiation of cracks in the PEEK adherends on both sides of the USW joint (Fig. 19.13, b), completing fracture.
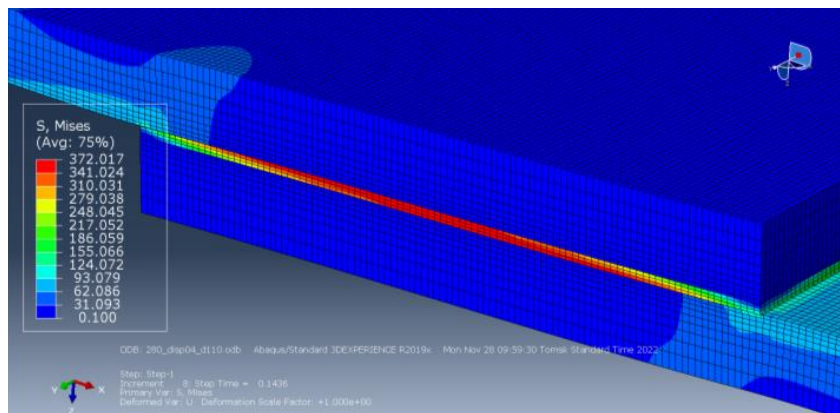
a
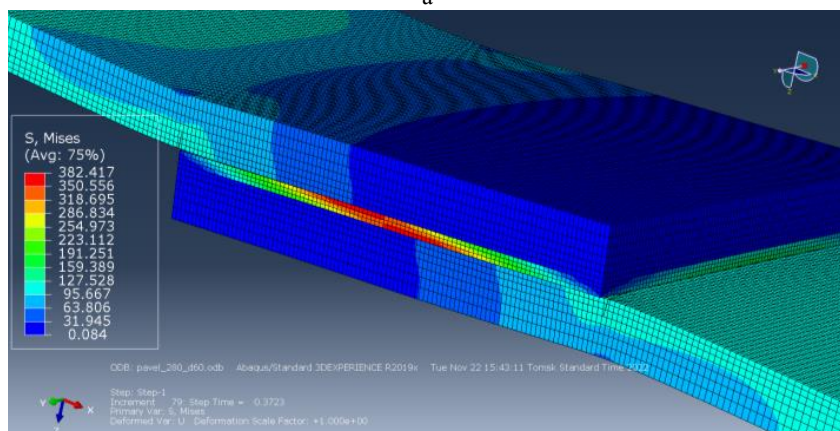
b
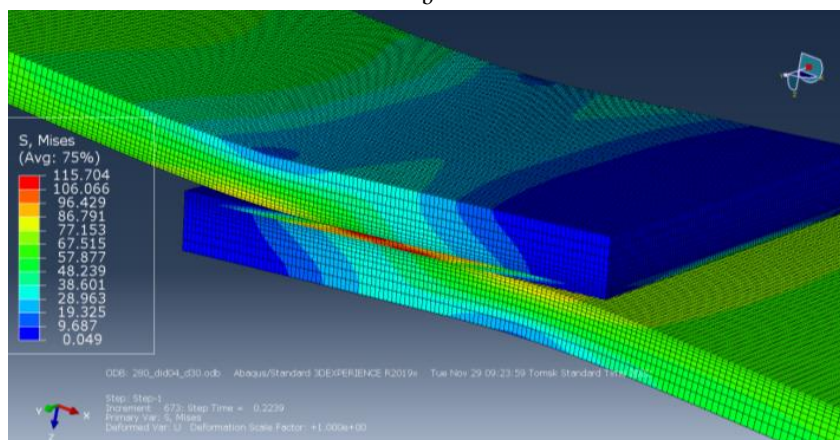
c

Fig. 19.13: The von Mises stress distributions in the USW lap joints in the tensile tests at the adhesion levels between the prepreg and the PEEK adherends of 110 (a), 60 (b) and 30 (c) MPa; the prepreg thickness of 280 μm.

3. At the low adhesion level, delamination occurred in the areas of the maximum stresses in the PEEK adherends at the contact edges. Then, stresses decreased in this region, so they did not give rise to the development of great plastic strains. Upon further loading, fracture was caused by completing delamination (at the low adhesion level), without the initiation of cracks in the PEEK adherends (Fig. 19.13, c).

19.3.3.3 The Effect of the Adhesion Level Between the CF Fabric and the PEEK 'Facing' Layer on the Tensile Strength of the USW Lap Joints

At the prepreg thicknesses of 460 and 620 μm, in addition to the impregnated CF fabric layer, a 'facing' PEEK one was formed, located between the PEEK adherends and the CF fabric (prepreg), according to Figs. 19.7 and 19.8. When varying the USW parameters, the adhesion level also changed both at the interface between the 'facing' PEEK layers and the CF fabric (prepreg), as well as between them and the PEEK adherends. Figure 19.14 shows examples with the prepreg thickness of 460 μm, when the adhesion levels of the 'facing' PEEK layers to the prepreg were lower than those to the PEEK adherends and vice versa, for comparison, other cases are presented when the adhesion levels were the same between all layers.

   When the adhesion levels were 60 and 30 MPa between the 'facing' layers and the prepreg and between them and the PEEK adherends, respectively, the strength and the fracture processes were the same as in the case of the similar adhesion levels of 30 MPa at these interfaces. At the same time, the corresponding curves coincided in Fig. 19.12 (Prepreg d = 60 MPa; PEEK d = 30 MPa and d = 30 MPa). When the adhesion level of the 'facing' layers to the prepreg was lower than that to the PEEK adherends (30 and 60 MPa, respectively), the tensile strength was almost the
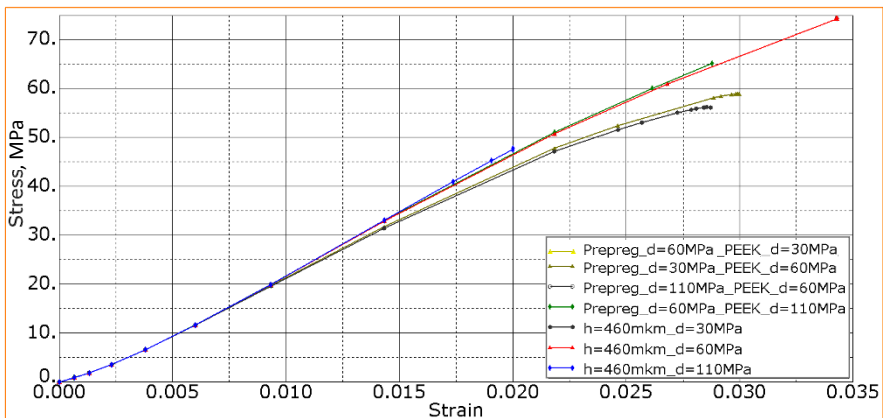
Fig. 19.14: The stress–strain diagrams of the USW lap joints with various locations of the contact areas and adhesion levels between the layers.

same as when the adhesion levels were 30 MPa at both interfaces. However, it was significantly lower than at both adhesion levels of 60 MPa. This fact showed that the decrease in the adhesion level at one of the interfaces reduced the tensile strength. In these cases, fracture occurred via delamination at the interface with the low adhesion level.

In the case of the adhesion levels between the 'facing' layers and the prepreg of 110 MPa and between them and the PEEK adherends of 60 MPa, the tensle strength and the fracture processes were the same as with the similar adhesion levels of 60 MPa at these interfaces. The corresponding curves match in Figure 14 (Prepreg d = 110 MPa; PEEK d = 60 MPa and d = 60 MPa). In the USW joint, the Mises stress distributions were also identical (Fig. 19.15, a). In this region, delamination was caused by the low adhesion level between the 'facing' layers and the PEEK adherends. Besides this, cracks initiated and propagated in the PEEK adherends on both sides of the USW joint (Fig. 19.15, a). The same fracture mechanism was observed with the same adhesion levels of 60 MPa (Figure 19.11).

If the opposite case was analyzed (Fig. 19.15, b), the adhesion level was lower at the interface between the 'facing' layers and the prepreg than that at the interface with the PEEK adherends (60 and 110 MPa, respectively). In this case, the tensile strength was higher compared to that with the same adhesion levels of 110 MPa at both interfaces. Nevertheless, it was lower than that with the same adhesion levels of 60 MPa. Figure 19.15, b indicates that delamination occurred at the interface of the prepreg with the 'facing' PEEK layer, and a crack initiated and propagated in the PEEK adherends as well (Fig. 19.15, b). This was similar to the case presented in
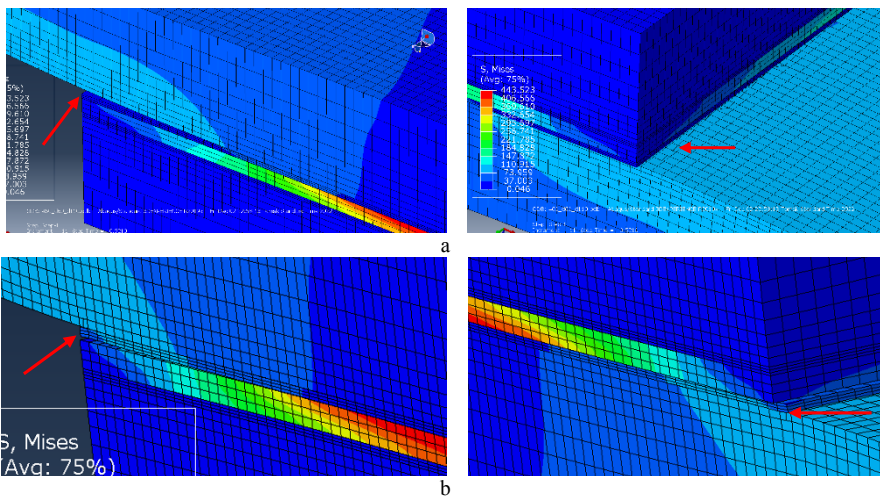
Fig. 19.15: The von Mises stress distributions in the USW joints at different adhesion levels between the layers: (a) Prepreg d = 110 MPa, PEEK d = 60 MPa; (b) Prepreg d = 60 MPa, PEEK d = 110 MPa.

Fig. 19.15, a, since the crack was caused by bending of the PEEK adherends at that region.

Note that the increase in the tensile strength in the last two cases with respect to that with the same adhesion levels of 110 MPa was caused by the delamination (which was absent at $d = 110$ MPa), stresses in the PEEK adherends were reduced at the edges of the USW joint. In turn, this decreased the intensity of plastic strains caused by stress concentrators (at the edges) upon bending.

Thus, if the change in the tensile strength at 110 MPa, caused by macroscopic bending, was excluded from the consideration, then delamination occurred at the weaker interface between the layers. At the same time, the adhesion levels between the 'facing' layers and the PEEK adherends and between them and the prepreg were almost equally significant. When varying the adhesion levels relative to the value of 110 MPa, its effect on the tensile strength was ambiguous, due to the development of macroscopic bending.

In practice, one of the ways to change the adhesion levels of the CF fabric to the 'facing' PEEK layer was treatment of CFs with low-temperature plasma [19], as well as the selection of technological parameters at which the adhesion level between the prepreg and the PEEK adherends was higher, with a reduced number of defects (pores, fractured CFs, etc.). The absence of a 'facing' layer between the prepreg and the PEEK adherends corresponded to obtaining a prepreg with a thickness equal to that of the used CF fabric (calculated as 280 μm), perfectly impregnated with PEEK. This eliminated the presence of 'facing' PEEK layers. Based on the above, the results below were based on the prepreg thickness of 280 μm, with no 'facing' PEEK layers between the prepreg and the PEEK adherends.

19.3.3.4 The Effect of the Adhesion Heterogeneity Between the Prepreg and the PEEK Adherends on the Tensile Strength of the USW Lap Joints

Investigations were carried out on the effect of imperfect contacts, when materials were joined not over the entire surface areas, but partially in several regions. Such a contact in 2D and 3D formulations was represented by identifying areas where adhesion was present or absent. Figure 19.16 shows examples of the location of the contact areas (shaded in red). For the v1 and v2 variants, the length of the sections
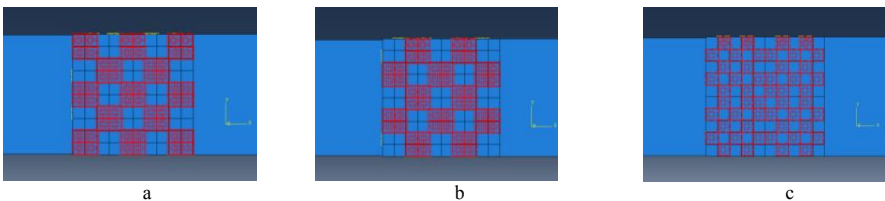
Fig. 19.16: The USW joints with the schematic arrangements of the contact areas for the following variants: (a) v1 (s=52%), (b) v2 (s=48%), (c) v3 (s=50%).

with adhesion was 4 mm each, and the contact area was about 50% of the entire joint. Fundamentally, the v1 and v2 variants differed in that a contact was at the corners of the joint in the first case (Fig. 19.16, a), while there was no contact in the second case. For the v3 variant, the length of the adhesion areas was 2 mm.

The contact between the prepreg layer and the PEEK adherends was taken into account due to a certain adhesion level at the interface, but there was no adhesion at the others. The ultimate stresses varied from 30 up to 110 MPa. Figure 19.17 presents stress–strain diagrams for the USW joints shown in Fig. 19.16 (v2 and v3) at the prepreg thickness of 280 μm, but with different adhesion levels and the one with the full contact area, for comparison.

At the adhesion level of 110 MPa, the tensile strength of the USW joints with both partial and full contact areas remained practically unchanged. Similar to the cases described above, fracture of the PEEK plates occurred at such an adhesion level. However, the strength decreased by about 30% at the adhesion levels of 60 and 30 MPa. Dependences were almost the same at the adhesion levels of 30 MPa (with the full contact area) and 60 MPa (with the v2 and v3 partial contact areas). Thus, the tensile strengths of the USW joints were the same at the high adhesion level of 60 MPa, but with the partial contact of 50% as at the low adhesion of 30% with the full contact.

Figures 19.18 and 19.19 show distributions of the intensity of strains (a) and stresses (b) in the USW lap joints with the v3 contact variant at the adhesion levels of 110 and 30 MPa. The uneven distributions of stresses and strains is observed in Fig. 19.18. In the case of the incomplete contact, the greatest plastic strains and stresses were found at the edges of the USW joints, but only at the contact points, contributing to the initiation and propagation of cracks.
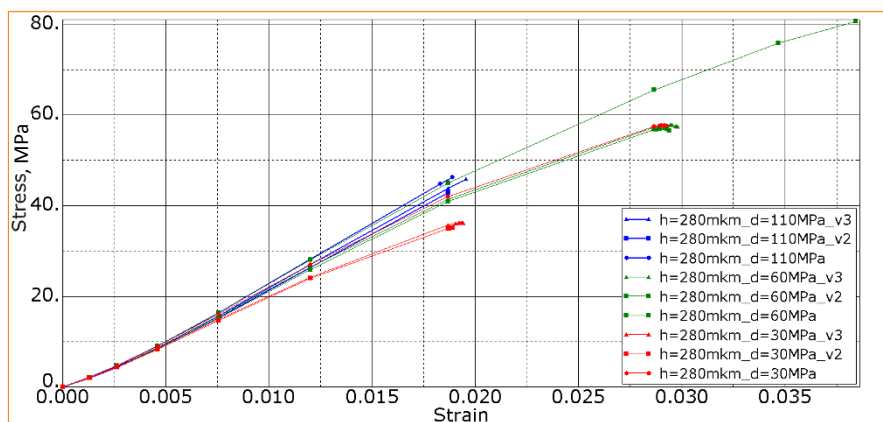
Fig. 19.17: The stress–strain diagrams for the USW lap joints in tensile tests at different locations of the contact areas for the v2 and v3 variants, according to Fig. 19.16; the full contacts at different adhesion levels.

a)

b)
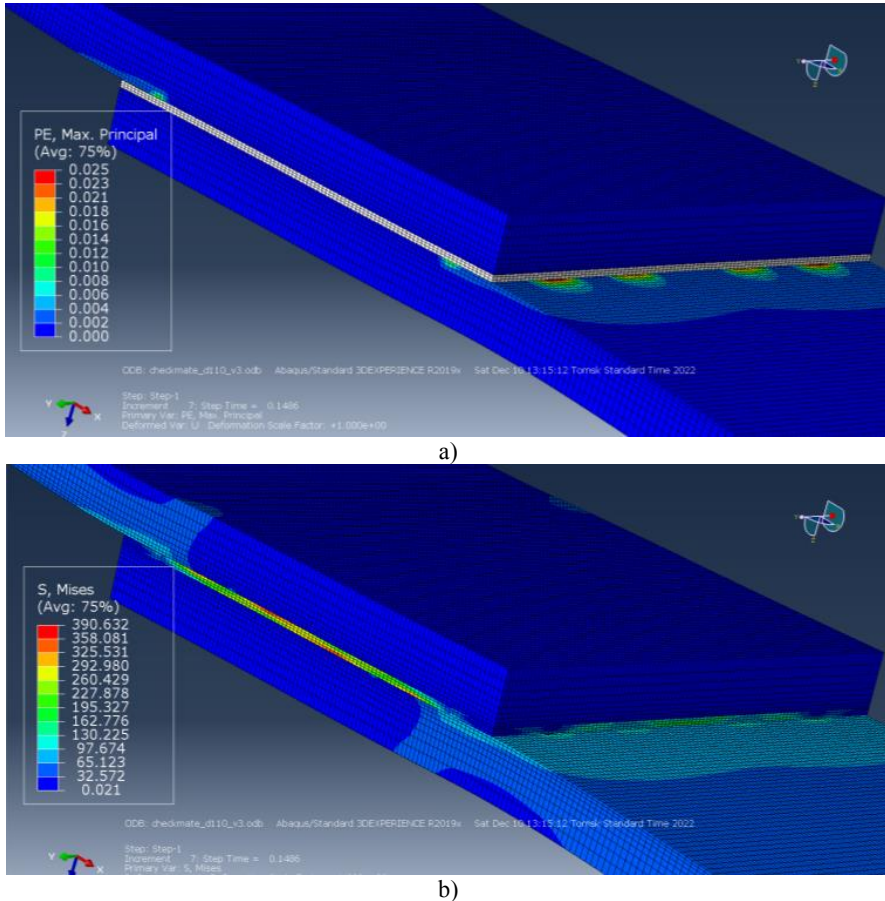
Fig. 19.18: The distributions of the intensity of plastic strains (a) and stresses (b) in the USW lap joint with the prepreg thickness of 280 μm and the adhesion level of 110 MPa; the v3 contact variant.

At the adhesion level of 30 MPa (Fig. 19.19), the uneven distribution of stresses and strains was also observed. However, plastic strains and stresses were much lower in magnitude than those at the high adhesion level (Fig. 19.18, a). Due to this reason, fracture of the PEEK adherends was not found, but delamination occurred. It was caused by the fact that stresses reached the adhesion level at the contact points, and since they occupied 50% of the joined region, delamination proceeded faster. So, it was illustrated how the adhesion inhomogeneity in the fusion zone significantly reduced the tensile strength of the USW joints.

At the high adhesion level of 110 MPa, the effect of the contact inhomogeneity was insignificant. As noted above, this was due not only to the concentration of stresses, but also the SSS of the USW lap joint. The latter was caused by misalignment of the
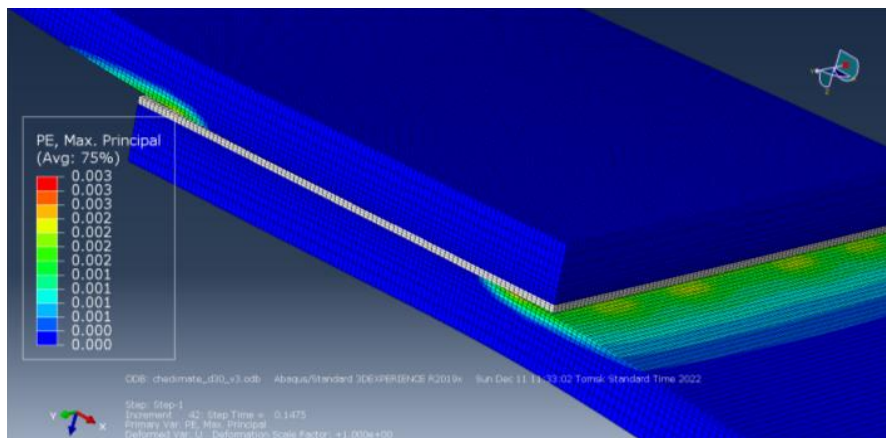
a
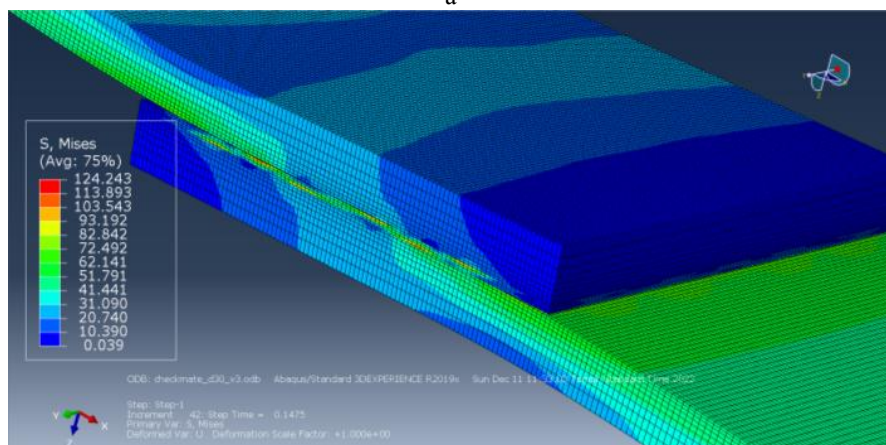
b

Fig. 19.19: The distributions of the intensity of plastic strains (a) and the stresses (b) in the USW lap joint with the prepreg thickness of 280 μm and the adhesion level of 30 MPa; the v3 contact variant.

PEEK adherends, resulting in macroscopic bending. This intensified the development of plastic strains and led to fracture of the PEEK adherends. Nevertheless, the USW joint was not failed completely, because the stiffness of the PEEK adherends was not high enough at this adhesion level.

19.3.4 The Effect of the Dimensions of the PEEK Adherends, Their Properties and the Loading Type on the Tensile Strength of the USW Lap Joints (2D Formulation)

As repeatedly shown above, macroscopic bending was characteristic of the USW lap joints because of the development of a torque moment under the uniaxial tension. As a result, several SSS types simultaneously arose in different regions, including tension, compression and shear stresses. The macroscopic bending degree depended on the dimensions of the PEEK adherends, the properties of the materials, and the adhesion level in the USW lap joints. With the maximum adhesion levels at the edges of the USW joints, macroscopic bending led to accelerated achievement of the ultimate stresses and strains in the PEEK adherends and their earlier fracture (compared to the case of the low adhesion level, as discussed above). Therefore, the tensile strength was lower at the maximum adhesion level of 110 MPa, although the USW lap joint was not failed completely. To avoid this and correctly assess the tensile strength of the USW lap joints, it was necessary to exclude the macroscopic bending. In order to reduce its contribution to the fracture process, the authors analyzed the effect of the dimensions and the properties of the PEEK adherends on macroscopic bending in the tensile tests of the USW lap joints.

Figure 19.20 presents the USW lap joints with the FEM mesh, where the joint rotation angle is clearly shown. Thicknesses of the PEEK plates were 2.2 and 1.1 mm. The rotation angle remained quite large as the thickness decreased. In addition, changing the thickness of the PEEK adherends had to cause significant variation of the USW lap joint properties, so the thinner one was not considered further.

Then, a case for the length of the PEEK adherends of 45 mm was consider, but with limited displacement of the USW lap joint in the vertical direction (by varying the adhesion level between the layers). Figure 19.21 shows its stress–strain diagrams. At the adhesion level of 110 MPa, the tensile strength was much higher than that at 60 MPa.

It was found on distributions of strains and stresses in the USW lap joints (Fig. 19.22) that no macroscopic bending occurred when the vertical displacements were restricted. Because of the high adhesion level, the PEEK adherends fractured due to the development of plastic strains. In the direction perpendicular to the surface of the PEEK adherends, necking was observed on both sides of the USW lap joints.

a   b
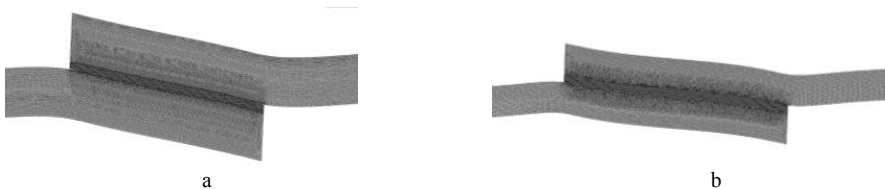
Fig. 19.20: Enlarged areas of the USW joints with the FEM mesh at the adhesion level of 110 MPa and the thicknesses of the PEEK plates 2.2 (a) and 1.1 (b) mm.

Fig. 19.21 The strain–stress
diagrams in the tensile tests
of the USW lap joints with
the limitation of their displace-
ments in the vertical direction
for various adhesion levels
between the layers.
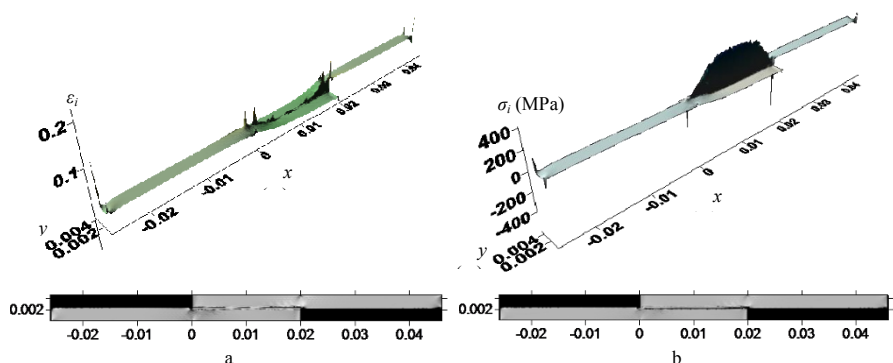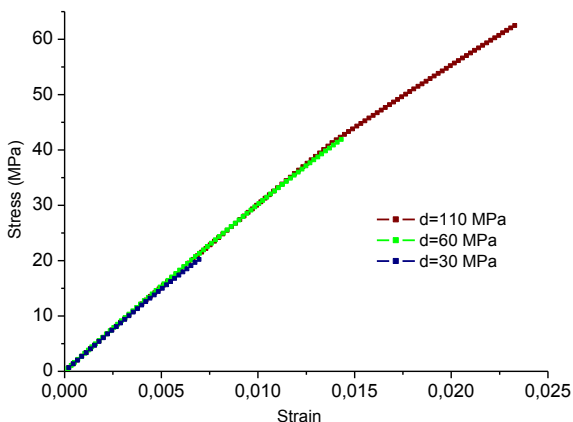
Fig. 19.22: The distributions of the intensity of strains (a) and stresses (b) in the USW lap joint and the corresponding gray scale images at the adhesion level of 110 MPa with the limited vertical displacements.

Since it was not always possible to limit the vertical displacements of the PEEK adherends in the experiment, the effect of the length of the plates on the tensile strength of the USW joints was investigated. Figure 19.23 shows parts of the computational domains with the FEM mesh at failure when varying the length of the PEEK adherends from 45.0 mm down to 22.5 mm.
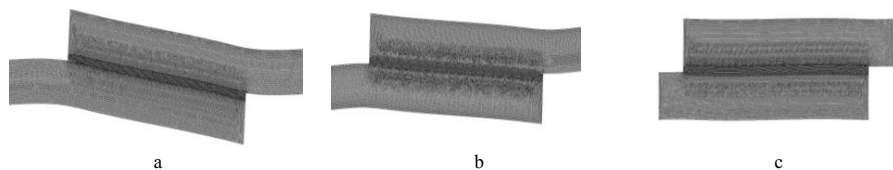
Fig. 19.23: Enlarged areas of the USW lap joints with the FEM mesh at the maximum adhesion level and the lengths of the PEEK adherends of 45 (a), 30 (b) and 22.5 (c) mm.

With a decrease in the length of the PEEK adherends, other things being equal, the rotation angle reduced significantly. At the length of the PEEK adherends of 22.5 mm, the SSS was close to that for 'pure shear'. At the maximum adhesion level, failure began via the formation of a neck in the PEEK adherends at the edges of the USW lap joints. However, delamination developed then under the action of shear stresses. Thus, to exclude the neck development, the length of the PEEK adherends was not taken less than 22.5 mm. Nevertheless, the effect of macroscopic bending increased with rising their length.

Figure 19.24 presents enlarged areas of the USW lap joints with the FEM mesh for the PEEK adherends 22.5 mm long and different adhesion levels, at which macroscopic bending was not observed.

For comparison, Fig. 19.25 shows stress–strain diagrams for the USW lap joints with the PEEK adherends 45.0 mm and 22.5 mm long and various adhesion levels between the layers. For the shortest PEEK adherends, the tensile strength at the adhesion levels of 110 MPa was much greater than that at 60 MPa (Fig. 19.25, b), in contrast to the case of the longest PEEK adherends, possessing the tensile strength lower at 110 MPa than at 60 MPa (Fig. 19.25, a).

Figure 19.26 presents distributions of the intensity of strains and stresses. Levels of the maximum stresses and strains enabled to conclude that fracture of the PEEK adherends occurred along the edges of the USW joints. However, due to the absence of macroscopic bending at the greater adhesion levels, it proceeded later (see the diagram in Fig. 19.25, b).Thus, lengths of the PEEK adherends less than 22.5 mm
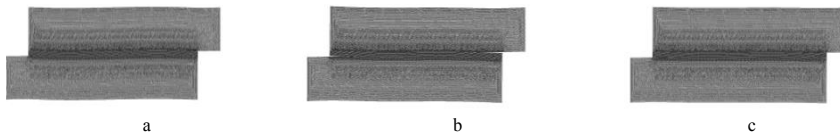
Fig. 19.24: The enlarged areas of the USW lap joints with the FEM mesh at the maximum adhesion level and the length of the PEEK adherends of 22.5 mm for the adhesion levels of 110 (a), 60 (b) and 30 (c) MPa.
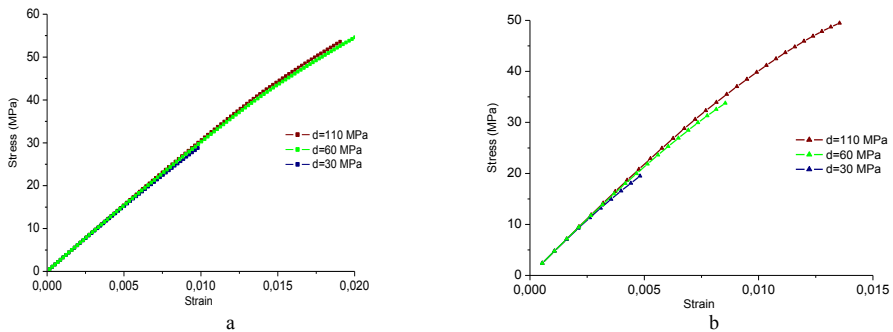
Fig. 19.25: The strain–stress diagrams for various adhesion levels between the layers at the lengths of the PEEK adherends of 45.0 mm (a) and 22.5 mm (b).
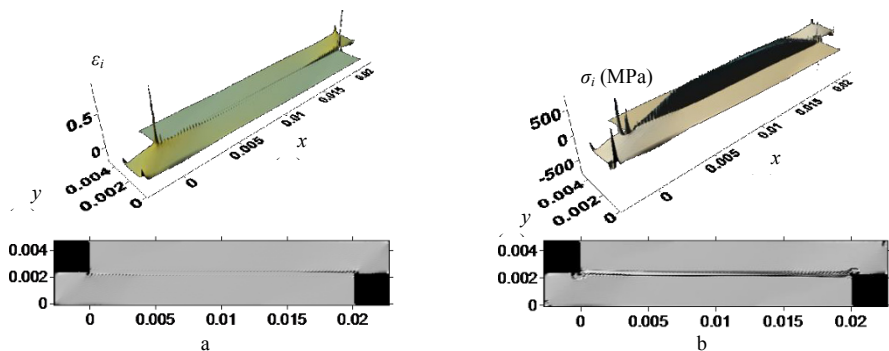
Fig. 19.26: The distributions of the intensity of strains (a) and stresses (b) in the USW lap joint at the length of the PEEK adherends of 22.5 mm and the adhesion level of 110 MPa.

made it possible to estimate more reliably the shear strength for the USW lap joints under the uniaxial tension.

Figure 19.27 shows the calculated areas of the USW lap joints at the elastic modulus of the PEEK plates of 30 GPa (for the length of 45 mm) and both adhesion levels of 550 and 110 MPa. The rotation angle was greater at the adhesion level of 550 MPa, while macroscopic bending was not observed at 110 MPa. Thereby, it was important to provide a certain combination of the elastic modulus and the adhesion level in the USW lap joints to obtain correct results at the length of the PEEK adherends of 45 mm. This fact had to be considered when testing the tensile strength of the USW lap joints at the high adhesion levels between the layers.

19.3.4.1 The Effect of the Prepreg's Elastic Modulus on the Tensile Strength of the USW Lap Joints

The CF fabric with the 5/2 satin weave was used for fabricating the prepreg (Fig. 19.28). Changing the rotation angle when laying the fabric in the prepreg, primarily varied its elastic tensile and shear modulus and the tensile strength [19].

Treatment of CFs with low-temperature plasma, as a rule, led to a decrease in both elastic and shear moduli of prepregs, and also reduced their strength due to
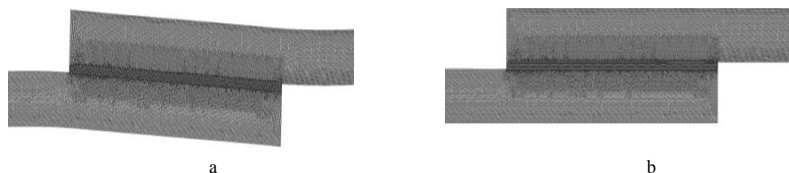
Fig. 19.27: The enlarged areas of the USW lap joints with the FEM mesh at the elastic modulus of the PEEK adherends of 30 GPa and the adhesion levels of 550 (a) and 110 (b) MPa.

a   b

Fig. 19.28: A sample of the CF fabric with the 5/2 satin weave for manufacturing the prepreg (a); a laying pattern for the prepreg (b).

the appearance of stress risers and damage (weakening) of CFs upon processing. At the same time, this treatment increased adhesion levels of CFs to polymers [24], which contributed to rising the adhesion level between the prepreg and the PEEK adherends.

In order to evaluate the dependence of the tensile strength of the USW lap joints on the variation in both elastic modulus and the adhesion level of the prepreg, numerical studies were performed in the 2D formulation. The prepreg thickness was 280 μm. The length of the PEEK adherends was assumed to be 22.5 mm.

The elastic (tensile) modulus of the prepreg in the reinforcement plane was varied in a range from 25 MPa up to 75 MPa. Since the layer properties were orthotropic, the transverse elastic modulus changed in proportion to the longitudinal component in tension along the y axis, thus varying the ultimate both normal and shear stresses. The obtained results are presented in Fig. 19.29. At the same adhesion level, the tensile strength changed slightly due to lowering the elastic modulus from 75 MPa down to 50 MPa.

At the lowest elastic modulus of 25 MPa, the slope of the curves and the tensile strength were was lower at both adhesion levels of 110 MPa and 60 MPa than those for other cases (Fig. 19.29). Additional calculations showed that the decrease in the
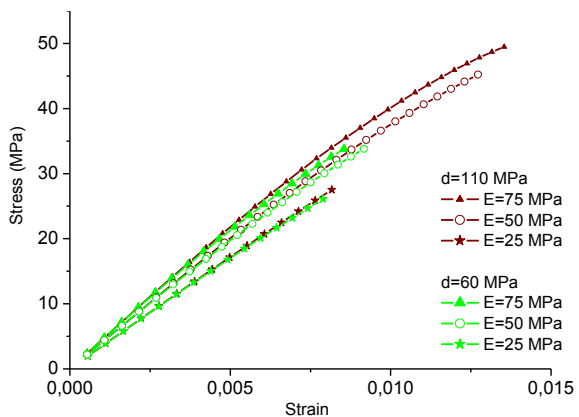
Fig. 19.29 The strain–stress diagrams in the tensile tests of the USW lap joint for various both elastic modulus and adhesion levels between the layers.

tensile strength at the same adhesion level was mainly caused by reducing the shear stiffness of the prepreg in the reinforcement plane (this was caused by the decrease in the elastic moduli proportionally in all directions in the above calculation). For the considered example, the shear strength was significantly higher at the adhesion level of 110 MPa than that at 60 MPa, in contrast to the results presented above, which were caused by the change in the length of the PEEK adherends.

19.3.4.2 The Effect of the Partial Interlayer Contact on the Tensile Strength of the USW Lap Joints in the Case of the Short PEEK Adherends

Below, the estimated results are reported on the tensile strength of the USW joints in the case of the partial contact at the adhesion level of 110 MPa and the length of the PEEK adherends of 22.5 mm (in the 2D formulation). Figure 19.30 shows distributions of the intensity of strains and stresses in the USW lap joint at the adhesion level of 60 MPa and the contact area of 50% of the entire USW lap joint. The length of the joined areas was 1.6 mm. At the boundaries and in the contact nodes, large strains and stresses were observed.

For comparison, Fig. 19.31 presents the calculated stress–strain diagrams at the contact areas of 100% and 50% (with partial adhesion at the contact lengths of 4.0 and 1.6 mm) when varying the adhesion levels between layers. In the case of the contact length of 4.0 mm (Fig. 19.31, a), the tensile strength decreased with lowering the adhesion level: the smaller the contact area and the adhesion levels were, the lower was the tensile strength. With the shortest contact length of 1.6 mm (Fig. 19.31, b), the tensile strength decreased equally for different contact areas with reducing the adhesion levels. This testified in favor of the important role of the adhesive contact homogeneity.
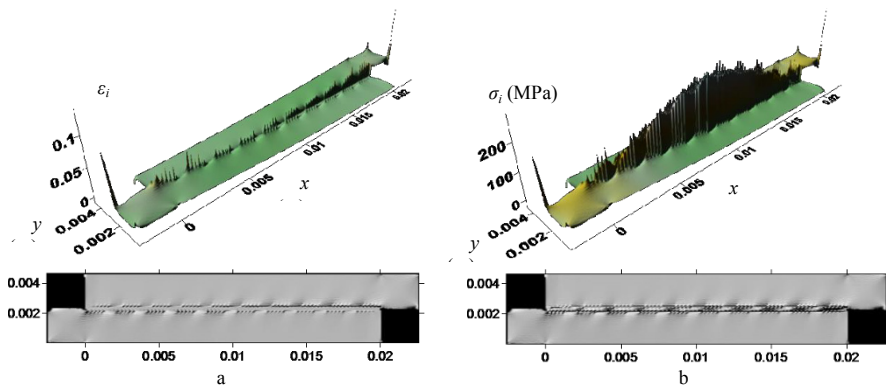
Fig. 19.30: The distributions of the intensity of strains (a) and stresses (b) in the USW joint at the length of the PEEK adherends of 22.5 mm and the adhesion level of 60 MPa ($l = 1.6$ mm).
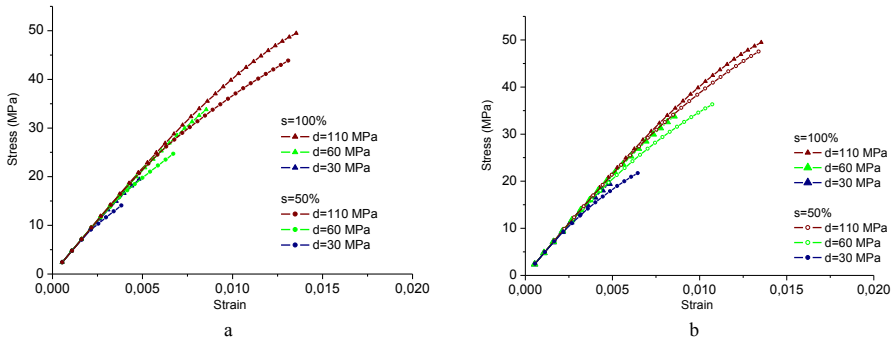
Fig. 19.31: The strain–stress diagrams in the tensile tests of the USW lap joint at the contact areas (*s*) of 100% and 50% for various adhesion levels (d) between the layers; the contact lengths (*l*) of 4.0 (a) and 1.6 (b) mm.

So, it was shown that the dimensions of the PEEK plates, their elastic modulus, and the adhesion level of the USW joints determined their fracture process. The combination of the low elastic modulus of the PEEK adherends and the high adhesion levels in the USW joints caused great macroscopic bending in the PEEK adherends, and could not always correctly reflect the tensile strength of the USW joints as a whole. Some methods were proposed to solve the issue for these cases, such as reducing the length of the PEEK adherends to avoid macroscopic bending, or limiting the vertical displacements of the USW joints. It was justified that for certain combinations of the elastic modulus values of the PEEK adherends and the adhesion levels, their macroscopic bending was negligible or absent at all.

19.4 Conclusions

The experimental studies of the effect of the PEEK-CF prepreg on the tensile strength of the USW lap joints of the PEEK adhrends showed that the prepreg thickness/binder content determined its ability to melt and subsequently form the macro- and microstructure, including maintaining the structural integrity of the CF fabric.

The developed and implemented numerical models of the USW lap joints in the 2D and 3D formulations enabled to analyze the effect of individual parameters on the fracture mechanism and the tensile strength of the USW lap joints, as well as to identify the most significant factors.

The numerical study of the influence of the prepreg thickness (determined by the binder content inside) on the tensile strength showed that the thickness of the prepreg layers was not a determining factor. With different prepreg thicknesses at the same adhesion level, the fracture mechanisms did not differ, the tensile strength decreased slightly with increasing the thickness. On the other hand, it was presented that delamination occurred at the interface between the 'facing' layers and the PEEK

adherends with the same adhesion levels of the 'facing' layers to the prepreg and to the 'PEEK' adherends. Nevertheless, it was not observed at the weaker interface with different adhesion levels to the PEEK adherends and to the prepreg. Thus, the adhesion levels of the 'facing' layers to the CF fabric should not be less than those to the PEEK adherends, or this interface should be excluded by minimizing the 'facing' layer in the USW lap joints. In the experiment, the absence of the 'facing' layer between the prepreg and the PEEK adherends corresponded to the decrease in the prepreg thickness almost to that of the CF fabric. However, the CF fabric should be perfectly impregnated with PEEK to obtain high adhesion levels.

A significant effect on the tensile strength of the USW lap joints had the decrease in that of the shear strength prepreg in the reinforcement plane. In the experiment, this could take place upon fracture of the CF fabric in the USW process.

The analysis of the obtained results by varying the adhesion levels between the prepreg and the PEEK adherends under the uniaxial tension enabled to conclude that the tensile strength of the USW lap joints increased with its rising, but its maximum values led to lowering the tensile strength due to bending stresses in the PEEK adherends at the edges of the USW lap joints.

Under the uniaxial tension, macroscopic bending of the USW lap joints played a great role in their failure. Its appearance was typical for a certain combination of the PEEK adherends stiffness (the elastic modulus) and the adhesion level. At the great stiffness combined with a certain adhesion level, macroscopic bending was not observed. Some corrected versions of the test models were proposed to avoid the development of macroscopic bending or to minimize it via combining the optimal length of the PEEK adherends, their stiffness and the adhesion levels. The selection was made on the basis of some preliminary estimations in the framework of the simulation.

The study of the effect of the adhesion levels in the USW lap joints between the prepreg and the PEEK adherends on the tensile strength showed that the decrease in the contact area led to its non-linear reducing. The lower the adhesion level was, the more the partial contact strength decreased. It was justified that the low adhesion level at the full contact provided the same tensile strength as with the twofold increase in the adhesion level (although the contact area was two times smaller). Obviously, it is necessary to strive for a uniform adhesion distribution over the entire contact area and its high levels in the case of the contact inhomogeneity.

References

[1] Khatri B, Roth MF, Balle F (2023) Ultrasonic welding of additively manufactured peek and carbon-fiber-reinforced peek with integrated energy directors.

Journal of Manufacturing and Materials Processing **7**(1)

[2] Fu X, Yuan X, Li G, Wu Y, Tong H, Kang S, Luo J, Pan Z, Lu W (2022) A study on ultrasonic welding of thermoplastics with significant differences in physical properties under different process parameters. Materials Today Communications **33**, 105009

[3] Zhang G, Qiu J (2022) Ultrasonic thermal welding of immiscible thermoplastics via the third phase. Journal of Materials Processing Technology **299**:117,330

[4] Fernandez Villegas I, Valle Grande B, Bersee HEN, Benedictus R (2015) A comparative evaluation between flat and traditional energy directors for ultrasonic welding of cf/pps thermoplastic composites. Composite Interfaces **22**(8):717–729

[5] Qiu J, Zhang G, Sakai E, Liu W, Zang L (2020) Thermal welding by the third phase between polymers: A review for ultrasonic weld technology developments. Polymers **12**(4):759

[6] Fernandez Villegas I (2019) Ultrasonic welding of thermoplastic composites. Frontiers in Materials **6**

[7] Köhler F, Fernandez Villegas I, Dransfeld C, Herrmann A (2021) Static ultrasonic welding of carbon fibre unidirectional thermoplastic materials and the influence of heat generation and heat transfer. Journal of Composite Materials **55**(15):2087–2102

[8] Hao M, Hu Z, Huang Y, Qian X, Wen Z, Wang X, Liu L, Lu F, Zhang Y (2022) Enhanced both in-plane and through-thickness thermal conductivity of carbon fiber/epoxy composites by fabricating high thermal conductive coaxial pan/pbo carbon fibers. Composites Part B: Engineering **229**:109,468

[9] Torokhov VG, Chukov DI, Tcherdyntsev VV, Sherif G, Zadorozhnyy MY, Stepashkin AA, Larin II, Medvedeva EV (2022) Mechanical and thermophysical properties of carbon fiber-reinforced polyethersulfone. Polymers **14**(14), 2956

[10] Yuan Y, Liu C, Huang M (2019) The structure and performance of short glass fiber/high-density polyethylene/polypropylene composite pipes extruded using a shearing–drawing compound stress field. Materials **12**(8), 1323

[11] Zhao X, Xiong D, Wu X (2017) Effects of surface oxidation treatment of carbon fibers on biotribological properties of cf/peek materials. Journal of Bionic Engineering **14**(4):640–647

[12] Zhu S, Qian Y, Hassan EA, Shi R, Yang L, Cao H, Zhou J, Ge D, Yu M (2020) Enhanced interfacial interactions by peek-grafting and coupling of acylated cnt for gf/peek composites. Composites Communications **18**:43–48

[13] Cole DP, Henry TC, Gardea F, Haynes RA (2017) Interphase mechanical behavior of carbon fiber reinforced polymer exposed to cyclic loading. Composites Science and Technology **151**:202–210

[14] Wu H, Li S, Zhang J, Tong L (2019) Electrical resistivity response of unidirectional thin-ply carbon fiber reinforced polymers. Composite Structures **228**:111,342

[15] Zhang S, Awaja F, James N, McKenzie DR, Ruys AJ (2011) Autohesion of plasma treated semi-crystalline peek: Comparative study of argon, nitrogen and

oxygen treatments. Colloids and Surfaces A: Physicochemical and Engineering Aspects **374**(1):88–95

[16] Gulyás J, Földes E, Lázár A, Pukánszky B (2001) Electrochemical oxidation of carbon fibres: surface chemistry and adhesion. Composites Part A: Applied Science and Manufacturing **32**(3):353–360

[17] Zhang S, Awaja F, James N, McKenzie DR, Ruys AJ (2011) Autohesion of plasma treated semi-crystalline PEEK: Comparative study of argon, nitrogen and oxygen treatments. Colloids and Surfaces A: Physicochemical and Engineering Aspects **374**(1):88–95

[18] Sun C, Min J, Lin J, Wan H (2019) Effect of atmospheric pressure plasma treatment on adhesive bonding of carbon fiber reinforced polymer. Polymers **11**(1):139

[19] Hassan EA, Ge D, Zhu S, Yang L, Zhou J, Yu M (2019) Enhancing CF/PEEK composites by CF decoration with polyimide and loosely-packed CNT arrays. Composites Part A: Applied Science and Manufacturing **127**:105,613

[20] Wang X, Huang Z, Lai M, Jiang L, Zhang Y, Zhou H (2020) Highly enhancing the interfacial strength of CF/PEEK composites by introducing PAIK onto diazonium functionalized carbon fibers. Applied Surface Science **510**:145,400

[21] Manikandan V, Winowlin Jappes J, Suresh Kumar S, Amuthakkannan P (2012) Investigation of the effect of surface modifications on the mechanical properties of basalt fibre reinforced polymer composites. Composites Part B: Engineering **43**(2):812–818

[22] Jha S, Bhowmik S, Bhatnagar N, Bhattacharya NK, Deka U, Iqbal HMS, Benedictus R (2010) Experimental investigation into the effect of adhesion properties of PEEK modified by atmospheric pressure plasma and low pressure plasma. Journal of Applied Polymer Science **118**(1):173–179

[23] Hassan EA, Yang L, Elagib TH, Ge D, Lv X, Zhou J, Yu M, Zhu S (2019) Synergistic effect of hydrogen bonding and π-π stacking in interface of CF/PEEK composites. Composites Part B: Engineering **171**:70–77

[24] Kosmachev PV, Panin SV, Panov IL, Bochkareva SA (2022) Surface modification of carbon fibers by low-temperature plasma with runaway electrons for manufacturing PEEK-based laminates. Materials **15**(21):7625

[25] Vanin G (1971) Konstruktsii povyshennoy plastichnosti (Reinforced plastic structures). Tekhnika, Kiyev

[26] Gunyaev GM (1981) Struktura i svoystva voloknistykh polimernykh kompozitov (Structure and properties of polymeric fibrous composites). Khimiya, Moscow

[27] Altenbach H, Altenbach J, Kissing W (2018) Mechanics of Composite Structural Elements, 2nd edn. Springer

[28] Bochkareva S, Panin S (2022) Investigation of fracture of 'peek-cf-prepreg' us-consolidated lap joints. Procedia Structural Integrity **40**:61–69, 15th International Conference on Mechanics, Resource and Diagnostics of Materials and Structures (MRDMS 2021)

Chapter 20

On two Approaches for Determination of the Effective Conductivity of a Polycrystalline Material by Homogenization Methods

Dmitry Pashkovsky, Ksenia Frolova, and Elena Vilchevskaya

Abstract This paper considers two approaches to calculating the effective conductivity tensor of a polycrystalline material with parallel orientation of spheroidal grains. The polycrystal models are based on consideration of a two-phase material consisting of an isotropic matrix and an isolated inhomogeneities. In the first approach the grains are modeled by inhomogeneities and grain boundaries are modeled by a matrix. In the second approach the grain boundaries are modeled by inhomogeneities and the grains are modeled by matrix. The Mori-Tanaka scheme is used to take into account the interaction between the inhomogeneities. The models are compared to each other. The paper is focused on the question about what model is better for polycrystalline material with parallel spheroidal grains.

20.1 Introduction

The problem of calculation of the effective conductivity coefficients of polycrystalline material is relevant to industrial and construction areas. Polycrystal consists of grains and grain boundaries and can be considered as inhomogeneous material. The problem of calculating the effective conductivity of microheterogeneous materials, in turn, has been addressed by many authors [1–13]. Fricke [1] calculated the coefficients

Dmitry Pashkovsky
Peter the Great St. Petersburg Polytechnic University, Polytechnicheskaya, 29, 195251 St.Petersburg, Russian Federation,
e-mail: mr.vivivilka@icloud.com

Ksenia Frolova
Institute for Problems in Mechanical Engineering of the Russian Academy of Sciences, Bolshoy prospekt 61, V.O., 199178 St. Petersburg, Russian Federation,
e-mail: kspfrolova@gmail.com

Elena Vilchevskaya
Flugsnapparegatan 6, Mölndal, Sweden,
e-mail: vilchevska@gmail.com

of effective electrical conductivity of a suspension of spheroids in the case of isotropic orientation distribution of spheroidal particles. Zimmerman [2, 3] estimated effective conductivity in the case of arbitrarily oriented two-dimensional elliptical inhomogeneties of finite conductivity embedded in an isotropic matrix and in the case of three-dimensional spheroids. Next, Hoenig in [4, 5] derived expression for effective conductivity of a three-dimensional solid with elliptical crack-like inhomogeneties with finite conductivity. Willis [6] obtained constraints of Hashin-Shtrikman type and estimated the effective conductivity of a solid with ellipsoidal inhomogeneities of finite conductivity. Next, Hatta and Taya [7, 8] considered a similar problem and applied results to the case when all inhomogeneities have the same shape. Chen and Wang [9] calculated the effective conductivity of a three-dimensional solid with randomly oriented short fibers in the framework of the Mori-Tanaka scheme [10]. Chen and Wang's results were generalized by Shafiro and Kachanov [11] in the case of ellipsoidal inhomogeneities.

In [1–13] the effective properties are found on the base of solution of the homogenization problem for an inhomogeneous material consisting of a matrix and isolated inhomogeneities. This approach can be applied to determination of the effective properties of a polycrystalline material. At the same time, the question arises what to choose as a matrix, and what as inhomogeneities (grains or grain boundaries). It is a common practice to choose the grain boundaries as the material matrix and grains as the inhomogeneities [14]. However, in principle, grain boundaries could be chosen as inhomogeneities and grains as a matrix. Both approaches have their shortcomings. In the polycrystal, the grains are located close to each other. And if the grains are chosen as inhomogeneities, then the isolation of inhomogeneities may be violated in the approach. In the second approach, where the inhomogeneities are chosen as grain boundaries, there is a small volume fraction of the inhomogeneities and they can be considered as isolated. However, the inhomogeneities have non-trivial geometric shape. Thus, it is necessary to compare the two approaches with each other in order to determine how big the difference is between them. If there is a difference, then a comparison with experimental data is required to answer the question of which approach is better.

The discussed approaches were compared in our previous work [13]. The most simple geometry of polycrystal was considered. In the first approach, the grains were chosen as spherical inhomogeneities and the grain boundaries as the material matrix. In the second approach, vice versa, grain boundaries were chosen spheroidal inhomogeneities with random distribution over orientation, and the grain boundaries were chosen as matrix. A considerable difference between the first and second approaches was found. The first approach was found to approximate the experimental data from work [15] better than the second one. To our opinion, the problem of second approach may be the incorrect choice of geometry for the shape of the inhomogeneities.

This paper considers a more complex geometry of polycrystal, which contains spheroidal grains of parallel orientation. As in [13], two approaches are constructed. In the first approach, the grains are modeled by the spheroidal inhomogeneities, and in the second approach grain boundaries are modeled by two groups of ellipsoidal

inhomogeneities. The aim of the this work is to compare these two approaches to estimation as the polycrystal conductivity properties. It is necessary to determine which of the approaches is better for estimating the properties of polycrystalline material and what differences exist between these approaches.

20.2 Problem Statement

Two models of polycrystalline material are considered. In the first model (M1) the grains are chosen as the inhomogeneities and the grain boundaries as matrix. In the second model (M2), the grain boundaries are chosen as the inhomogeneities and the grains boundary are chosen as the matrix. The visualisations of approaches is shown on Fig. 20.1. Figure 20.1 shows representative volume of polycrystal. This polycrystal is associated with two model M1 and M2. In the first line of Fig. 20.1 shows two projections of representative volume for the model M1 to planes based on vectors e_1, e_3 and e_1, e_2. These are spheroidal grains. The second and the third line are projections of representative volume for the model M2. The View 2 in the second
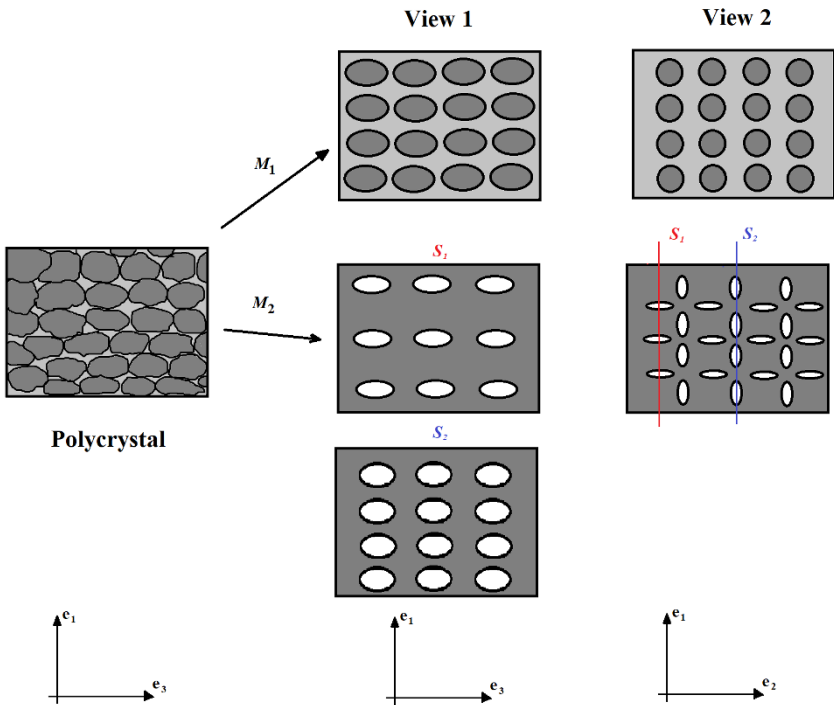
Fig. 20.1: General scheme.

line for the model M2 have two cross sections of representative volume (S1 and S2). Cross sections S1 and S2 of representative volume are shown on the View 1. These are two groups of ellipsoidal grain boundaries and each of them is oriented parallel.

In order to compare M1 and M2 it is necessary to construct an effective conductivity tensor in the form of a tensor function depending on the microstructural parameters.

$$\boldsymbol{K}_{\text{eff}} = \boldsymbol{F}(\text{microstructural parameters}) \tag{20.1}$$

The following parameters are used as microstructural ones: volume fraction of inhomogeneities; conductivity coefficients of the matrix and inhomogeneities; shape parameters of inhomogeneities.

The materials of grains and grain boundaries are isotropic. Hence, the conductivity tensor of grain boundaries has the form $\boldsymbol{K}_{GB} = K_{GB}\boldsymbol{E}$ and the conductivity tensor of grains has the form $\boldsymbol{K}_G = K_G\boldsymbol{E}$; K_{GB} is conductivity coefficient of the grain boundaries, K_G is conductivity coefficient of the grains.

The M1 model is based on consideration of a two-phase material with isolated spheroidal inhomogeneities. The parameters of the M1 model are given in Table 20.1, where φ_G is volume fraction of grains, $a_1 = a_2 = a$ are semiaxes along $\boldsymbol{e}_1$ and $\boldsymbol{e}_2$, a_3 is semiaxis along $\boldsymbol{e}_3$. We will vary the semiaxis a_3.

The M2 model is based on consideration of a two-phase material with two groups parallel inhomogenities: GB1 and GB2 (Fig. 20.1). The inhomogeneities in groups GB1 and GB2 are oriented in parallel. Groups GP1 and GB2 have the same volume fraction which is equal to $\varphi_{GB} = 0.5 \cdot (1 - \varphi_G)$. Parameters of the M2 model are shown in Table 20.2.

Two models can be compared if they describe a material with the same type of symmetry. The above models describe a transversally isotropic material with a symmetry axis along $\boldsymbol{e}_3$. Note that the proposed models can, in principle, also describe a material with spherical grains. In this case, $\gamma = 1$ in the first model and the material is isotropic at the macro level. In the second model, grain boundaries

Table 20.1: The model M1 parameters.

Conductivity of matrix, K_{GB}	Conductivity of inhomogeneities, K_G	Volume fraction, φ	Spheroid shape factor, $\gamma = a_3/a$	Spheroid axis of symmetry, $\boldsymbol{n}$
0.01	0.1	φ_G	a_3/a	$\boldsymbol{e}_3$

Table 20.2: The model M2 parameters.

Conductivity of matrix, K_G	Conductivity of inhomogeneities, K_{GB}	Volume fraction of GB1, φ_{GB1}	Volume fraction of GB2, φ_{GB2}	GB1: ellipsoid's semiaxes along directions $\boldsymbol{e}_1, \boldsymbol{e}_2, \boldsymbol{e}_3$	GB2: ellipsoid's semiaxes along directions $\boldsymbol{e}_1, \boldsymbol{e}_2, \boldsymbol{e}_3$
0.1	0.01	$0.5(1 - \varphi_G)$	$0.5(1 - \varphi_G)$	$(a, 0.1a, a_3)$	$(0.1a, a, a_3)$

are modeled by spheroidal inhomogeneities. In this case, the model M2 describes a transversally isotropic material. In order for the material to be isotropic in the M2 model, three groups of spheroids must be considered [13].

The homogenization problem must be solved to obtain the expression for transversely isotropic tensor $\boldsymbol{K}_{\text{eff}}$ of effective conductivity. The interaction of inhomogeneities is taken into account by using energy schemes. This paper uses the Mori-Tanaka scheme [10] because this scheme gives correct results for large volume fractions. The effective conductivity tensor is a solution of the homogenization problem [16–18], when the inhomogeneous material is replaced by homogeneous one which, in general, has anisotropic properties.

The temperature field is set on the boundary Γ_V of the representative volume V:

$$T(\boldsymbol{x})\big|_{\Gamma_V} = \boldsymbol{G}^0 \cdot \boldsymbol{x} \tag{20.2}$$

where $\boldsymbol{G}^0$ is the temperature gradient for the representative volume boundary. The effective conductivity tensor $\boldsymbol{K}_{\text{eff}}$ relates averaged heat flux $\langle \boldsymbol{q} \rangle_V$ and averaged temperature gradient $\langle \nabla T \rangle_V$ by Fourier's Law:

$$\langle \boldsymbol{q} \rangle_V = -\boldsymbol{K}_{\text{eff}} \cdot \langle \nabla T \rangle_V \tag{20.3}$$

where $\langle \dots \rangle = \int_V \dots dV / V$. The temperature gradient averaged over the representative volume V is written as follows:

$$\boldsymbol{G}^0 = \langle \nabla T \rangle_V = \frac{1}{V} \sum_{i=1}^{n} V_i \langle \nabla T \rangle_{in}^i + (1 - \varphi) \langle \nabla T \rangle_m \tag{20.4}$$

where $\langle \nabla T \rangle_{in}^i$ is average temperature gradient over i-th inhomogeneity, $\langle \nabla T \rangle_m$ is the average temperature gradient over matrix, V_i is volume of i-th inhomogeneity, φ is volume fraction of inhomogeneities. The averaged heat flux over the representative volume $\langle \boldsymbol{q} \rangle_V$ is represented as follows:

$$\langle \boldsymbol{q} \rangle_V = \frac{1}{V} \sum_{i=1}^{n} V_i \langle \boldsymbol{q} \rangle_{in}^i + (1 - \varphi) \langle \boldsymbol{q} \rangle_m \tag{20.5}$$

where $\langle \boldsymbol{q} \rangle_{in}^i$ is averaged heat flux for inhomogeneity, $\langle \boldsymbol{q} \rangle_m$ is averaged heat flux for matrix.

We have to take into account the interaction between the inhomogeneities. We use for this the Mori-Tanaka scheme [10]. In this scheme, each of the isolated inhomogeneities is placed in a uniform field of a temperature gradient equal to the average over the matrix:

$$\langle \nabla T \rangle_{in}^i = \boldsymbol{\Lambda}_c^{(i)} \cdot \langle \nabla T \rangle_m \tag{20.6}$$

where $\boldsymbol{\Lambda}_c^i$ is a concentration tensor:

$$\mathbf{\Lambda}_c^{(i)} = \left[\mathbf{E} + \mathbf{P}_i \cdot (\mathbf{K}_i - \mathbf{K}_0) \right]^{-1} \tag{20.7}$$

where $\mathbf{P}_i$ is Hill's tensor, which depends on the shape of inhomogeneities, $\mathbf{K}_i$ is the conductivity tensor of i-th inhomogenity, $\mathbf{K}_0$ is the conductivity tensor of matrix, $\mathbf{E}$ is the identity tensor.

In accordance with [18], the general expression for the tensor $\mathbf{K}_{\text{eff}}$ is as follows:

$$\mathbf{K}_{\text{eff}} = \mathbf{K}_0 + \frac{1}{V} \sum_{i=1}^{n} V_i (\mathbf{K}_i - \mathbf{K}_0) \cdot \mathbf{\Lambda}_c^i \cdot \left[\frac{1}{V} \sum_{i=1}^{n} V_i \mathbf{\Lambda}_c^i + (1-\varphi)\mathbf{E} \right]^{-1} \tag{20.8}$$

The difference between models M1 and M2 is that they are determined by a different sets of microstructural parameters, whereas the general form of the expression is the same. Next, we apply the general formula (20.8) to models M1 and M2.

Let us first consider the M1 model. For spheroidal inhomogeneities ($a_1 = a_2 = a$, $\gamma = a_3 / a$), the Hill's tensor takes the form [18]:

$$\mathbf{P} = \frac{1}{K_{GB}} \left(f_0(\gamma)(\mathbf{e}_1 \mathbf{e}_1 + \mathbf{e}_2 \mathbf{e}_2) + (1 - 2f_0(\gamma))\mathbf{e}_3 \mathbf{e}_3 \right) \tag{20.9}$$

where the function $f_0(\gamma)$ has form:

$$f_0(\gamma) = \frac{(1 - g(\gamma))\gamma^2}{2(\gamma^2 - 1)}, \quad g(\gamma) = \begin{cases} \dfrac{1}{\gamma\sqrt{1-\gamma^2}} \arctan\left(\dfrac{\sqrt{1-\gamma^2}}{\gamma}\right), & \gamma < 1 \\ \dfrac{1}{2\gamma\sqrt{1-\gamma^2}} \log\left(\dfrac{\gamma + \sqrt{\gamma^2-1}}{\gamma - \sqrt{\gamma^2-1}}\right), & \gamma > 1 \end{cases} \tag{20.10}$$

And the expression $\mathbf{\Lambda}_c$ for spheroidal inhomogeneities has the following form:

$$\mathbf{\Lambda}_c = A_1 \mathbf{E} + A_2 \mathbf{e}_3 \mathbf{e}_3 \tag{20.11}$$

$$A_1 = \left(1 + \frac{f_0(\gamma)(K_G - K_{GB})}{K_{GB}} \right)^{-1}$$

$$A_2 = \frac{K_{GB}(3f_0(\gamma) - 1)(K_G - K_{GB})}{(K_G - 2K_G f_0(\gamma) + 2K_{GB} f_0(\gamma))(K_G f_0(\gamma) + K_{GB} - K_{GB} f_0(\gamma))}$$

The Eq. (20.8) for the model M1 is reduced to this form:

$$\mathbf{K}_{\text{eff}} = K_{GB}\mathbf{E} + (K_G - K_{GB})\varphi_G \mathbf{\Lambda}_c \cdot \left[\varphi_G \mathbf{\Lambda}_c + (1 - \varphi_G)\mathbf{E} \right]^{-1} \tag{20.12}$$

where $\varphi = \varphi_G$ is volume fraction of grains, $\mathbf{\Lambda}_c$ is concentration tensor of the spheroidal inhomogeneities (20.11).

Next, the M2 model is considered. For ellipsoidal inhomogeneities, the Hill's tensor takes the form [18]:

$$\boldsymbol{P} = \frac{1}{2\pi K_G}\left(I_1\boldsymbol{e}_1\boldsymbol{e}_1 + I_2\boldsymbol{e}_2\boldsymbol{e}_2 + I_3\boldsymbol{e}_3\boldsymbol{e}_3\right) \tag{20.13}$$

where I_j, $j = 1,2,3$ is the elliptic integrals in Carlson's form [19]:

$$I_j = I(a_1, a_2, a_3, a_j) = \pi a_1 a_2 a_3 \int\limits_0^{+\infty} \frac{dp}{(a_j^2 + p)\sqrt{(a_1^2 + p)(a_2^2 + p)(a_3^2 + p)}}$$

The expression $\boldsymbol{\Lambda}_c$ for ellipsoidal inhomogeneities has the following form:

$$\boldsymbol{\Lambda}_c = B_1\boldsymbol{e}_1\boldsymbol{e}_1 + B_2\boldsymbol{e}_2\boldsymbol{e}_2 + B_3\boldsymbol{e}_3\boldsymbol{e}_3 \tag{20.14}$$

where $B_j = \left[1 + I_j(K_{GB} - K_G)\right]^{-1}$ for $j = 1,2,3$.

The Eq. (20.8) for the model M2 is reduced to the next form:

$$\begin{aligned}\boldsymbol{K}_{\text{eff}} = K_G\boldsymbol{E} &+ (K_{GB} - K_G)\left[\varphi_{GB}\boldsymbol{\Lambda}_c^{(1)} + \varphi_{GB}\boldsymbol{\Lambda}_c^{(2)}\right]\cdot \\ &\cdot\left[\varphi_{GB}\boldsymbol{\Lambda}_c^{(1)} + \varphi_{GB}\boldsymbol{\Lambda}_c^{(2)} + (1 - 2\varphi_{GB})\boldsymbol{E}\right]^{-1}\end{aligned} \tag{20.15}$$

where $\varphi_{GB1} + \varphi_{GB2} = 2\varphi_{GB} = 1 - \varphi_G$ are volume fractions of first and second group inhomogeneities, $\boldsymbol{\Lambda}_c^{(1)}$ and $\boldsymbol{\Lambda}_c^{(2)}$ are concentration tensors (20.14) of the first and the second group of ellipsoids (GB1 and GB2).

20.3 Results

The tensor $\boldsymbol{K}_{\text{eff}}$ (20.12) is used to calculate the effective conductivity in the M1 model. The parameters for M1 are given in Table 20.1. The tensor $\boldsymbol{K}_{\text{eff}}$ for M2 is calculated by using the Eq. (20.15). The parameters for M2 are given in Table 20.2. In this case, the parameter $a_3 = 5$ ($\gamma = 5$) for models M1 and M2.

Figure 20.2 shows the dependencies of the tensor components $K_{ii}^{\text{eff}}/K_{GB}$ on grain volume fraction φ_G, here $K_{11}^{\text{eff}} = K_{22}^{\text{eff}}$. According to Fig. 20.2 the models M1 and M2 are similar at small and large values of the volume fraction of grains. In a polycrystal, the volume fraction of grains should be at least 90% of the total volume. The models give almost the same result in the case of large volume fractions of grains (Fig. 20.2). Therefore, the models can be used to simulate polycrystals. But there are cases where this difference can be significant for modeling. Next, let us explore how the difference between the models is changed when considering more or less elongated grains. The parameter a_3 changes in models M1 and M2 (see Table 20.1 and 20.2).

The Fig. 20.3 shows the dependence of the tensor components $K_{ii}^{\text{eff}}/K_{GB}$ as a function of the grain volume fraction φ_G for M1 and M2 for different grain size $a_3 = 2, 10$. The minimum and maximum values of the spheroidal grain size from
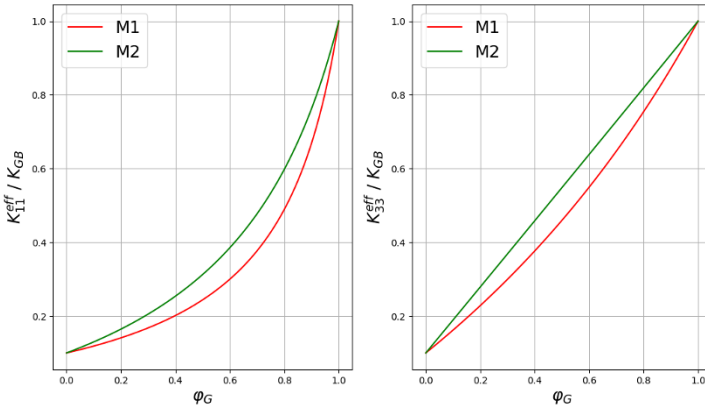
Fig. 20.2: The components $K_{ii}^{\text{eff}}/K_{GB}$ as a function of φ_G for the models M1 and M2 ($a_3 = 5$, $a = 1$).
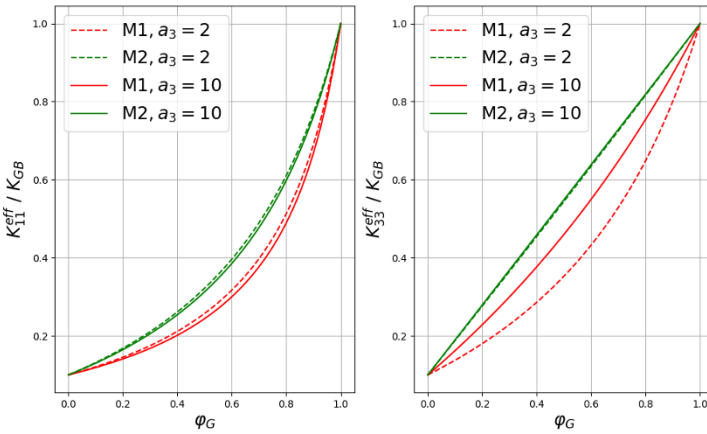
Fig. 20.3: The components $K_{ii}^{\text{eff}}/K_{GB}$ as a function φ_G for different $a_3 = 2$, 5, 10.

the considered range are taken on Fig. 20.3. The red curves are the components of the effective conductivity tensor of the M1 model, and the green curves are the components of the effective conductivity tensor of the M2 model. Solid lines and dashed lines correspond to different values of parameter a_3. Figure 20.3 shows that the difference between third components of $\boldsymbol{K}_{\text{eff}}$ for models M1 and M2 decreases with increasing parameter a_3. It is also seen that the tensor components $K_{11}^{\text{eff}} = K_{22}^{\text{eff}}$ are almost unchanged for different a_3. The $K_{33}^{\text{eff}}/K_{GB}$ components of the M2 model

Table 20.3: The maximum difference between the tensor $\boldsymbol{K}_{\mathrm{eff}}$ components for the models M1 and M2, $a_3 = 2,\ 5,\ 10$.

Difference	$a_3 = 2$	$a_3 = 5$	$a_3 = 10$
$\lvert (K_{11}^{\mathrm{eff}})_{M1} - (K_{11}^{\mathrm{eff}})_{M2} \rvert\ /\ K_{GB}$	0.0859	0.1086	0.112
$\lvert (K_{33}^{\mathrm{eff}})_{M1} - (K_{33}^{\mathrm{eff}})_{M2} \rvert\ /\ K_{GB}$	0.2767	0.0897	0.0372

for different a_3 are almost equal to each other. This is due to the choice of the ellipsoid parameters in Table 20.2.

Table 20.3 shows the difference of the tensor components when the parameter a_3 is changed. Let us calculate maximum deviation between curves for parameters $a_3 = 2,\ 5,\ 10$ and $a = 1$ ($\gamma = 2, 5, 10$). The difference between the conductivity along $\boldsymbol{e}_3$ for models M1 and M2 decreases with increasing parameter a_3 (Table 20.3). Also the first component of the $\boldsymbol{K}_{\mathrm{eff}}$ tensor practically does not change with increasing parameter a_3.

The differences between models M1 and M2 for parallel grains orientation are not a big for large a_3. If we want to estimate this difference, the models M1 and M2 must be compared with experimental data. In some cases, even this difference can be significant. For more correct modeling, it is necessary to take into account more complex geometry in the second model.

20.4 Conclusion

This paper compares two approaches to calculating the effective conductive properties of polycrystals. In the first approach, the grains were chosen as spherical inhomogeneities and the grain boundaries as the material matrix. In the second approach, vice versa, grain boundaries were chosen as the spheroidal inhomogeneities and the grain boundaries were chosen as matrix. In the second model, there were two groups of the grain boundaries that have ellipsoidal shape and the grains are chosen as matrix. The models M1 and M2 are similar at small and large values of the volume fraction of grains. In real polycrystals, the volume fraction of grains is on the range of 90% to 95% of the total volume. Hence, the both approaches can be used to simulate real polycrystalline material. But there are cases when the difference between models can be critical. Also note that the difference between the conductivity along $\boldsymbol{e}_3$ for models M1 and M2 decreases with increasing grain size along $\boldsymbol{e}_3$. But the components along $\boldsymbol{e}_1$ and $\boldsymbol{e}_2$ stay stable with increasing grain size along $\boldsymbol{e}_3$. Further analysis of the approaches and evaluation of the influence of the difference between the models requires comparison with experimental data or numerical simulation.

References

[1] Fricke H (1924) A mathematical treatment of the electric conductivity and capacity of disperse systems i. the electric conductivity of a suspension of homogeneous spheroids. Physical Review **24**:575–587

[2] Zimmerman RW, Yeo I (2000) Fluid Flow in Rock Fractures: From the Navier-Stokes Equations to the Cubic Law, American Geophysical Union (AGU), pp 213–224

[3] Zimmerman RW (1989) Thermal conductivity of fluid-saturated rocks. Journal of Petroleum Science and Engineering **3**(3):219–227

[4] Hoenig A (1978) Electric conductivities of a cracked solid. Pure and Applied Geophysics **117**(4):690–710

[5] Hoenig A (1983) Thermal conductivities of a cracked solid. Journal of Composite Materials **17**(3):231–237

[6] Willis J (1977) Bounds and self-consistent estimates for the overall properties of anisotropic composites. Journal of the Mechanics and Physics of Solids **25**(3):185–202

[7] Hatta H, Taya M (1985) Effective thermal conductivity of a misoriented short fiber composite. Journal of Applied Physics **58**(7):2478–2486

[8] Dunn ML, Taya M (1993) The effective thermal conductivity of composites with coated reinforcement and the application to imperfect interfaces. Journal of Applied Physics **73**(4):1711–1722

[9] Chen C, Wang Y (1996) Effective thermal conductivity of misoriented short-fiber reinforced thermoplastics. Mechanics of Materials **23**(3):217–228

[10] Mori T, Tanaka K (1973) Average stress in matrix and average elastic energy of materials with misfitting inclusions. Acta Metallurgica **21**(5):571–574

[11] Shafiro B, Kachanov M (2000) Anisotropic effective conductivity of materials with nonrandomly oriented inclusions of diverse ellipsoidal shapes. Journal of Applied Physics **87**(12):8561–8569

[12] Sevostianov I, Kachanov M (2009) Connections between elastic and conductive properties of heterogeneous materials. Advances in Applied Mechanics, vol 42, Elsevier, pp 69–252

[13] Pashkovsky DM, Frolova KP, Vilchevskaya EN (2022) Effective diffusion properties of a polycrystal (in Russ.). St Petersburg Polytechnical State University Journal Physics and Mathematics **15**(3):154–168

[14] Knyazeva AG, Grabovetskaya GP, Mishin IP, Sevostianov I (2015) On the micromechanical modelling of the effective diffusion coefficient of a polycrystalline material. Philosophical Magazine **95**(19):2046–2066

[15] Oudriss A, Creus J, Bouhattate J, Conforto E, Berziou C, Savall C, Feaugas X (2012) Grain size and grain-boundary effects on diffusion and trapping of hydrogen in pure nickel. Acta Materialia **60**(19):6814–6828

[16] Markov KZ (2000) Elementary micromechanics of heterogeneous media. In: Markov K, Preziosi L (eds) Heterogeneous Media: Micromechanics Modeling Methods and Simulations, Birkhäuser, Boston, MA, pp 1–162

[17] Sevostianov I, Mishuris G (2014) Effective thermal conductivity of a composite with thermo-sensitive constituents and related problems. International Journal of Engineering Science **80**:124–135, special issue on Nonlinear and Nonlocal Problems. In occasion of 70th birthday of Prof. Leonid Zubov

[18] Kachanov M, Sevostianov I (2018) Micromechanics of Materials, with Applications. Solid Mechanics and Its Applications, Springer, Cham

[19] Carlson BC (1995) Numerical computation of real or complex elliptic integrals. Numerical Algorithms **10**(1):13–26

Chapter 21
The Functionally Invariant Solutions and Nonlinear Wave Equations

Yuri V. Pavlov

Abstract An overview of the application of the functionally invariant solutions method for the nonlinear wave equation is given. A generalization of this method is presented to the case of the presence of the first derivatives and non-linearity of different types on the right side of the equation. The possibility of construction of the exact analytical solutions is discussed.

21.1 Introduction

The nonlinear sine-Gordon wave equation and its generalizations often appear in physics and mechanics. The sine-Gordon equation describes dislocations in solids [1, 2], deformation of a crystal media with complex lattice [3, 4], nonlinear wave processes [5]. It is used in field theory models and in elementary particle physics [6].

The efficient methods have been developed for solving nonlinear differential equations, including the sine-Gordon equation. These are the Lamb method [7] for the two-dimensional sine-Gordon equation, the Bäcklund transformation, the inverse scattering method [8, 9], etc. However, the needs of the development of the theory of nonlinear equations and problems of practical modeling of numerous physical phenomena necessitate finding new methods for the solution of nonlinear wave equations.

Here we consider the application of the functionally invariant solutions method to the search for a solution to the nonlinear wave equation

Yuri V. Pavlov
Institute for Problems in Mechanical Engineering of Russian Academy of Sciences, 61 Bol'shoy, V.O., 199178 St. Petersburg, Russian Federation,
e-mail: yuri.pavlov@mail.ru

H. Altenbach et al. (eds.), *Progress in Continuum Mechanics*,

$$\Box U + \sum_{i=1}^{n} \lambda_i \frac{\partial U}{\partial x_i} + \gamma \frac{\partial U}{\partial t} = V'(U), \tag{21.1}$$

where

$$\Box U = \sum_{i=1}^{n} \frac{\partial^2 U}{\partial x_i^2} - \frac{1}{v^2} \frac{\partial^2 U}{\partial t^2} \tag{21.2}$$

is the d'Alembert operator in n-dimensional space, λ_i $(i = 1, \ldots, n)$, γ, v are constants, $V(U)$ is some differentiable function.

In the absence of the first derivatives and with $V'(U) = \sin U$, the Eq. (21.1) is the sine-Gordon equation, for the case $V'(U) = p_1 \sin U + p_2 \sin 2U$ — the double sine-Gordon equation, for $V'(U) = p_1 \sin U + p_2 \sin 2U + p_3 \sin 3U$ — the triple sine-Gordon equation $(p_1, p_2, p_3 = \text{const})$, for $V'(U) = \exp U$ — the Liouville equation, for $V'(U) = \sinh U$ — the sinh-Gordon equation etc. In the field theory models [10] the Eq. (21.1) with $V'(U) = p_1 U^3 - p_2 U$ is widely applied.

21.2 Functionally Invariant Solutions

Let's consider the wave equation

$$\Box U = 0. \tag{21.3}$$

The solution $u(x_1, \ldots x_n, t)$ of the equation (21.3) is called functionally invariant if for arbitrary twice differentiable function f, the function $f[u(x_1, \ldots x_n, t)]$ will also be the solution. D'Alembert's solution of string oscillation equations in the form of traveling waves is obviously functionally invariant. It was found in the XVIII-th century (1749). In the middle of the XIX-th century, Jacobi obtained [11] the functional invariant solutions for the 3-dimensional Laplace equation. For the n-dimensional Poisson equation and the 3-dimensional wave equation, such solutions were obtained for the first time by Forsyth [12]. A number of functionally invariant solutions of the wave equation and electromagnetic field equations were obtained in [13]. Smirnov and Sobolev applied the functionally invariant solutions of wave equation for solving specific problems of mathematical physics [14].

Functionally invariant solutions of the wave equation can be found as solutions of the system of equations

$$\sum_{i=1}^{n} \left(\frac{\partial \Omega}{\partial x_i} \right)^2 - \left(\frac{\partial \Omega}{v \partial t} \right)^2 = 0, \tag{21.4}$$

$$\Box \Omega = 0. \tag{21.5}$$

In the three-dimensional case, all real and some part of complex functionally invariant solutions of the wave equation can be obtained from the expression [15]

$$\sum_{i=1}^{n} x_i \, l_i(\Omega) - tv^2 p(\Omega) + q(\Omega) = 0, \tag{21.6}$$

where $l_1(\Omega), \ldots, l_n(\Omega)$, $p(\Omega)$, $q(\Omega)$ are the arbitrary twice differentiable functions satisfying the condition

$$\sum_{i=1}^{n} l_i^2(\Omega) = v^2 p^2(\Omega). \tag{21.7}$$

In the two-dimensional case ($n = 2$), such formulas give all functionally invariant solutions of the wave equation [16].

From the relation (21.6) one obtains

$$\frac{\partial \Omega}{\partial x_i} = \frac{-l_i}{\lambda}, \quad \frac{\partial \Omega}{\partial t} = v^2 \frac{p}{\lambda}, \quad \lambda = \sum_{i=1}^{n} x_i \frac{dl_i}{d\Omega} - v^2 t \frac{dp}{d\Omega} + \frac{dq}{d\Omega}, \tag{21.8}$$

$$\frac{\partial^2 \Omega}{\partial x_i^2} = \frac{1}{\lambda^2}\left(2l_i \frac{dl_i}{d\Omega} - l_i^2 \frac{\mu}{\lambda}\right), \quad \frac{\partial^2 \Omega}{\partial t^2} = \frac{v^4}{\lambda^2}\left(2p \frac{dp}{d\Omega} - p^2 \frac{\mu}{\lambda}\right), \tag{21.9}$$

where the duplicate indexes do not imply summation and

$$\mu = \sum_{i=1}^{n} x_i \frac{d^2 l_i}{d\Omega^2} - v^2 t \frac{d^2 p}{d\Omega^2} + \frac{d^2 q}{d\Omega^2}. \tag{21.10}$$

Obviously, the nonlinear equations, in particular (21.1), cannot have functionally invariant solutions. Also, not every linear equation can have a functionally invariant solution. For example, the equation for spherical waves in three-dimensional space

$$\frac{\partial^2 U}{\partial r^2} + \frac{2}{r} \frac{\partial U}{\partial r} - \frac{1}{v^2} \frac{\partial^2 U}{\partial t^2} = 0 \tag{21.11}$$

has the general solution

$$U = \frac{1}{r}\left(F(r+vt) + G(r-vt)\right) \tag{21.12}$$

with arbitrary twice differentiable functions F, G. Due to the presence of the factor $1/r$ on the right side of (21.12), the functions $r - vt$ and $r + vt$ cannot be functionally invariant solutions to the wave equation (21.11).

Courant ([17], Chapt. 6, Sect. 18) introduced the concept of "relatively undistorted waves", generalizing the concept of spherical waves in three-dimensional space, namely, the solutions of the form

$$U(\mathbf{x}, t) = g(\mathbf{x}, t) F(\Omega(\mathbf{x}, t)), \quad \mathbf{x} = (x, y, z), \tag{21.13}$$

where $F(\Omega)$ is an arbitrary twice differentiable function, $g(\mathbf{x}, t)$, $\Omega(\mathbf{x}, t)$ are some function. For an arbitrary equation, the functions of the form (21.13), which are its

solutions with arbitrary $F(\Omega)$ and a special type functions $g(\boldsymbol{x}, t)$ and $\Omega(\boldsymbol{x}, t)$, are called generalized functional invariant solutions [18].

The functionally invariant solutions to equation (21.1) cannot exist if there is a nonlinear function $V(U)$ on the right side. However, after the series of transformations the search for some solutions to the sine-Gordon equation and its generalizations has been reduced in [19–21] to solving the auxiliary system of partial differential equations, which corresponds to the system of equations for functionally invariant solutions of the wave equation.

21.3 Solving the Nonlinear Equation

If you transform the Eq. (21.1) in a standard way by excluding the first derivatives, then on the right side we get a function that depends explicitly on the variables (x_i, t). This will not allow to use of known methods for solving the nonlinear partial differential equations. So let us find for a solution to Eq. (21.1) in the form $U = F[\Omega(x, y, z, t)]$. Then from (21.1) we get

$$F''(\Omega)\left[\sum_{i=1}^{n}\left(\frac{\partial \Omega}{\partial x_i}\right)^2 - \left(\frac{\partial \Omega}{v\partial t}\right)^2\right] + F'(\Omega)\left[\square\Omega + \sum_{i=1}^{n}\lambda_i\frac{\partial \Omega}{\partial x_i} + \gamma\frac{\partial \Omega}{\partial t}\right] = V'[F(\Omega)].$$
(21.14)

Equation (21.14) will be solved if

$$F''(\Omega)\,P(\Omega) + F'(\Omega)\,Q(\Omega) = V'[F(\Omega)],$$
(21.15)

$$\sum_{i=1}^{n}\left(\frac{\partial \Omega}{\partial x_i}\right)^2 - \left(\frac{\partial \Omega}{v\partial t}\right)^2 = P(\Omega),$$
(21.16)

$$\square\Omega + \sum_{i=1}^{n}\lambda_i\frac{\partial \Omega}{\partial x_i} + \gamma\frac{\partial \Omega}{\partial t} = Q(\Omega),$$
(21.17)

where $P(\Omega), Q(\Omega)$ are some arbitrary functions.

In the case $\sum_{i=1}^{n}\lambda_i^2 \neq 0$, let us choose $P(\Omega) = \Omega^2$, $Q(\Omega) = \Omega$ and enter the substitution

$$\Omega = e^{\phi}\omega, \quad \phi = \sum_{i=1}^{n}a_i x_i - \sigma v^2 t,$$
(21.18)

Equation (21.14) will be solved if

$$F''(\Omega)\,\Omega^2 + F'(\Omega)\,\Omega = V'[F(\Omega)],$$
(21.19)

$$\sum_{i=1}^{n}a_i^2 = 1 + \sigma^2 v^2,$$
(21.20)

$$\sum_{i=1}^{n} a_i \lambda_i = \gamma \sigma v^2, \tag{21.21}$$

$$\sum_{i=1}^{n} \lambda_i \frac{\partial \omega}{\partial x_i} + \gamma \frac{\partial \omega}{\partial t} = 0, \tag{21.22}$$

$$\sum_{i=1}^{n} a_i \frac{\partial \omega}{\partial x_i} + \sigma \frac{\partial \omega}{\partial t} = 0, \tag{21.23}$$

$$\Box \omega = 0, \tag{21.24}$$

$$\sum_{i=1}^{n} \left(\frac{\partial \omega}{\partial x_i} \right)^2 - \left(\frac{\partial \omega}{v \partial t} \right)^2 = 0. \tag{21.25}$$

Note that the arbitrary twice differentiable function $\tilde{\omega} = f(\omega)$ of ansa.tz $\omega(x_1, \ldots, x_n, t)$ will satisfy the same Eqs (21.22)–(21.25) if it is satisfied with the ansatz ω.

After replacing the variable $\zeta = \ln \Omega$, Eq. (21.19) will take the form

$$\frac{d^2 F}{d\zeta^2} = \frac{dV}{dF}. \tag{21.26}$$

Therefore, the solution to the equation (21.19) is the function $F(\Omega)$, implicitly defined from the expression

$$\int \frac{dF}{\sqrt{V(F) + E}} = \pm \sqrt{2} \ln \Omega + C, \tag{21.27}$$

where E and C are constants. For the generalized sine-Gordon equation under the choosing $V(F) = -\cos F$, $E = 1$, $C = 0$ (and sign plus in right side of (21.27)), we will receive

$$V'(F) = \sin F \quad \Rightarrow \quad F = 4 \arctan \Omega. \tag{21.28}$$

Other values of constants lead to need the inversion of the corresponding elliptic integral. For the generalized sinh-Gordon equation under the choosing $V(F) = \cosh F$, $E = 1$, $C = 0$, one has

$$V'(F) = \sinh F \quad \Rightarrow \quad F = 4 \operatorname{artanh} \Omega. \tag{21.29}$$

The function $U = F(e^\phi \omega)$ will solve the initial problem (21.1). The conditions for the solvability of the system of equations (21.20)–(21.25) in the three-dimensional case ($n = 3$) are analyzed in [20]. Note that not all solutions of (21.1) can be found in this way. However, the variety of solutions thus obtained is large due to the functional invariance of the set of valid functions ω. The number of different types of such solutions grows with the increase in the number of spatial dimensions n.

The proposed replacement $\Omega = e^\phi \omega$ does not allow to find real solutions depending on time, if in Eq. (21.1) there is only the first derivative with respect to time, i.e.

$\lambda_1 = \ldots = \lambda_n = 0$. In this case, from (21.22), (21.25) it would follow that $\omega = \mathrm{const}$ and $\sigma = 0$.

If you have only the first time derivative, let's choose $P(\Omega) = 0$, $Q(\Omega) = \Omega$. Then Eq. (21.15) can be integrated into the form

$$\int \frac{dF}{V'(F)} = \ln |\Omega|. \tag{21.30}$$

For the generalized sine-Gordon equation

$$V'(F) = \sin F \quad \Rightarrow \quad F = 2\arctan\Omega \tag{21.31}$$

one gets (with the appropriate selection of the integration constant). For the generalized sinh-Gordon equation one has

$$V'(F) = \sinh F \quad \Rightarrow \quad F = 2\,\mathrm{artanh}\,\Omega. \tag{21.32}$$

In accordance to (21.14), Eq. (21.1) will be solved if the following equations are fulfilled together with (21.15)

$$\sum_{i=1}^{n} \left(\frac{\partial\Omega}{\partial x_i}\right)^2 - \left(\frac{\partial\Omega}{v\partial t}\right)^2 = 0, \tag{21.33}$$

$$\Box\,\Omega + \gamma\frac{\partial\Omega}{\partial t} = \Omega. \tag{21.34}$$

To solve this system of equations, one can use the same approach as when finding the functionally invariant solutions of the wave equation. An example of such a solution of the system (21.33), (21.34) is given in [20]. A simple solution can be found in the form

$$G = A\exp\left(\sum_{i=1}^{n} a_i x_i + a_0 t\right), \tag{21.35}$$

where A, $a_0, a_1, \ldots a_n$ are some constants. From (21.33), (21.34) it follows that

$$a_0 = \frac{1}{\gamma}, \quad \sum_{i=1}^{n} a_i^2 = \frac{1}{\gamma^2 v^2}. \tag{21.36}$$

For the sinh-Gordon equation with the first time derivative the solution will be

$$U = 2\,\mathrm{artanh}\,A\exp\left(\sum_{i=1}^{n} a_i x_i + \frac{t}{\gamma}\right). \tag{21.37}$$

For the case of $n = 1$ for example, the solution is

$$U = 2\,\mathrm{artanh}\,A\exp\frac{tv \pm x}{\gamma v}. \tag{21.38}$$

Note that Eq. (21.15) for the arbitrary right side $V(F)$ can be integrated in quadratures in the case

$$Q(\Omega) = P'(\Omega)/2. \qquad (21.39)$$

The solution for $P(\Omega) > 0$ (see 2.9.2.34 in [22]) is

$$\int \frac{dF}{\sqrt{E + V(F)}} = \pm\sqrt{2} \int \frac{d\Omega}{\sqrt{P(\Omega)}}. \qquad (21.40)$$

If $P(\Omega) = 0$, then the solution of (21.15) is determined from

$$\int \frac{dF}{V'(F)} = \int \frac{d\Omega}{Q(\Omega)}. \qquad (21.41)$$

To find $F(\Omega)$ we need to inverse the integrals on the left side of (21.40), (21.41). For the sine-Gordon and double sine-Gordon equations, this reduced to the inversion of the elliptic integrals. For the triple sine-Gordon equation, the complex problem arises of the inversion of ultra-elliptic integrals [23].

Let us consider separately the case when the first derivatives are absent,

$$\square U = V'(U). \qquad (21.42)$$

According to (21.14), the function $U = F(\Omega)$ will be the solution if, together with (21.15), the relations

$$\sum_{i=1}^{n} \left(\frac{\partial\Omega}{\partial x_i}\right)^2 - \left(\frac{\partial\Omega}{v\partial t}\right)^2 = P(\Omega), \qquad (21.43)$$

$$\square\Omega = Q(\Omega) \qquad (21.44)$$

are performed.

Under the limit $v \to \infty$, the system of equations (21.43), (21.44) passes into the system

$$\sum_{i=1}^{n} \left(\frac{\partial\Omega}{\partial x_i}\right)^2 = P(\Omega), \qquad (21.45)$$

$$\Delta\Omega = Q(\Omega), \quad \Delta = \sum_{i=1}^{n} \frac{\partial^2}{\partial x_i^2}. \qquad (21.46)$$

In the three-dimensional case ($n = 3$), all real solutions of the system (21.45), (21.46) were found in [24]. The compatibility of the system of Hamilton-Jacobi equations (21.43) and the nonlinear Klein-Fock-Gordon equation (21.44) was investigated in [25, 26]. It was found that in addition to the case $P(\Omega) = Q(\Omega) = 0$, the system of equations (21.43), (21.44) with $P \neq 0$ and $n = 3$, is also compatibility under conditions

$$\frac{1}{\sqrt{P(\Omega)}}\left(Q(\Omega) - \frac{P'(\Omega)}{2}\right) = \frac{N}{\alpha + C}, \quad N = 0, 1, 2, 3, \quad \frac{d\alpha}{d\Omega} = \frac{1}{\sqrt{P(\Omega)}}, \qquad (21.47)$$

where C is an arbitrary constant. To obtain exact analytical solutions of Eq. (21.42), it is necessary to find an exact solution of Eq. (21.15). Therefore, at $P \neq 0$, we consider only the case $Q(\Omega) = P'(\Omega)/2$, i.e. the value $N = 0$ in the conditions (21.47).

For the function α by the relation on the right side of (21.47), we get instead of (21.43), (21.44)

$$\sum_{i=1}^{n}\left(\frac{\partial\alpha}{\partial x_i}\right)^2 - \left(\frac{\partial\alpha}{v\partial t}\right)^2 = 1, \tag{21.48}$$

$$\Box\,\alpha = 0. \tag{21.49}$$

Let us make the substitution

$$\alpha = \phi + \omega \tag{21.50}$$

with ϕ defined in (21.18) and satisfying the conditions (21.20). For ω we get Eqs. (21.23)–(21.25), which can be solved by the method of functionally invariant solutions of the wave equation with help the expression (21.6). The integral on the right side of (21.40) gives the expression of α from Ω. Thus, solving Eq. (21.42) without the first derivatives under the condition $Q(\Omega) = P'(\Omega)/2$, $P \neq 0$, regardless of the choice $P(\Omega)$ has the form

$$U = F(\phi + f(\omega)) \tag{21.51}$$

with an arbitrary twice differentiable function f and with the functions F and ϕ, ω defined by Eqs. (21.18), (21.20), (21.23)–(21.25). Note that the method of functionally invariant solutions can be used also for the case of a non-autonomous wave equation (in particular, the sine-Gordon equation with variable amplitude (see, for examples, [27, 28]).

21.4 Conclusion

The presented method of solving the nonlinear wave equation (21.1) with arbitrary nonlinearity on the right side of $V'(U)$ does not allow to find a general solution to such equation. However, the obtaining of some set of exact solutions to the nonlinear partial differential equation is of undeniable interest. The solutions obtained by this method have been used in nonlinear models of deformation of solids (see, for example, [29]). The set of types of solutions obtained in this way increase with the growth of the dimension of space, since the number of arbitrary functions in the system of equations for the ansatz Ω increases.

This work provides an overview of functionally invariant methods for solving the nonlinear wave equation and a generalization of the previously proposed [20] method for the case of first-order partial derivatives and arbitrary nonlinearity $V'(U)$ is obtained.

References

[1] Frenkel J, Kontorova T (1939) On the theory of plastic deformation and twinning (in Russ.). Izv Akad Nauk, Ser Fiz **1**:137–149

[2] Braun OM, Kivshar YS (2004) The Frenkel-Kontorova Model. Concepts, Methods, and Applications. Springer, Berlin

[3] Aero EL (2006) Micromechanics of a double continuum in a model of a medium with variable periodic structure. Journal of Engineering Mathematics **55**(1):81–95

[4] Aero EL, Bulygin AN (2002) Strongly nonlinear theory of nanostructure formation owing to elastic and nonelastic strains in crystalline solids. Mechanics of Solids **42**(5):807–822

[5] Lonngren K, Scott A (eds) (1978) Solitons in Action. Academic Press, New York

[6] Faddeev LD, Takhtajan LA (1974) Essentially nonlinear one-dimensional model of the classical field theory. Theoretical and Mathematical Physics **21**(2):1046–1057

[7] Lamb Jr GL (1971) Analytical descriptions of ultrashort optical pulse propagation in a resonant medium. Rev Mod Phys **43**:99–124

[8] Miura RM (ed) (1976) Bäcklund Transformations, the Inverse Scattering Method, Solitons, and Their Applications, Lecture Notes in Mathematics, vol 515. Springer, Berlin

[9] Takhtajan LA, Faddeev LD (1987) Hamiltonian Methods in the Theory of Solitons. Springer, New York

[10] Bogoliubov NN, Shirkov DV (1983) Quantum Fields. Benjamin Cammings

[11] Jacobi CGJ (1848) Über eine particuläre Lösung der partiellen Differentialgleichung $\frac{\partial^2 V}{\partial x^2} + \frac{\partial^2 V}{\partial y^2} + \frac{\partial^2 V}{\partial z^2} = 0$. Crelle Journal für die reine und angewandte Mathematik **36**:113–134

[12] Forsyth AR (1898) New solutions of some of the partial differential equations of mathematical physics. Messenger of Mathematics **27**:99–118

[13] Bateman H (1915) The Mathematical Analysis of Electrical and Optical Wave-Motion on the Basis of Maxwell's Equations. Cambridge Univ. Press, Cambridge

[14] Smirnoff V, Soboleff S (2006) Sur une méthode nouvelle dans le problème plan des vibrations élastiques (on a new method in the plane problem on elastic vibrations). In: Demidenko GV, Vaskevich VL (eds) Selected Works of S.L. Sobolev, vol I: Mathematical Physics, Computational Mathematics, and Cubature Formulas, Springer, New York, pp 45–80

[15] Erugin NP (1948) On functionally-invariant solutions (in Russ.). Uch Zap Leningrad Univ, Seriya Matematika **15**(96):101–134

[16] Sobolev S (1934) Functionally-invariant solutions of wave equation (in Russ.). Tr Fiz-Mat Inst Steklova **5**:259–264

[17] Courant R, Hilbert D (1962) Methods of Mathematical Physics, vol II. Partial Differential Equations. Interscience Publ., New York

[18] Erugin NP, Smirnov MM (1981) Functionally invariant solutions of differential equations. (in Russ.). Differ Uravn **17**:853–865

[19] Aero E, Bulygin A, Pavlov Y (2009) Solutions of the three-dimensional sine-gordon equation. Theoretical and Mathematical Physics **158**(3):313–319

[20] Aero EL, Bulygin AN, Pavlov YV (2011) New approach to the solution of the classical sine-Gordon equation and its generalizations. Differential Equations **47**(10):1442–1452

[21] Aero EL, Bulygin AN, Pavlov YV (2013) Functionally invariant solutions of nonlinear Klein–Fock–Gordon equation. Applied Mathematics and Computation **223**:160–166

[22] Polyanin AD, Zaitsev VF (2003) Handbook of Exact Solutions for Ordinary Differential Equations, 2nd edn. Chapmen & Hall/CRC, New York

[23] Aero EL, Bulygin AN, Pavlov YV (2013) Nonlinear Klein-Fock-Gordon equation and Abelian functions. In: Proceedings of the International Conference "Days on Diffraction" 2013, pp 5–10

[24] Collins CB (1976) Complex potential equations I. A technique for solution. Mathematical Proceedings of the Cambridge Philosophical Society **80**(1):165–187

[25] Fushchich WI, Zhdanov RZ (1989) On some new exact solutions of the nonlinear D'Alembert-Hamilton system. Physics Letters A **141**(3):113–115

[26] Zhdanov RZ (1995) Compatibility criteria and general solution of the nonlinear d'Alembert-Eikonal system. Reports on Mathematical Physics **36**(2):483–488, proceedings of the XXVI Symposium on Mathematical Physics

[27] Aero EL, Bulygin AN, Pavlov YV (2015) Solutions of the sine-Gordon equation with a variable amplitude. Theoretical and Mathematical Physics **184**(1):961–972

[28] Bulygin AN, Pavlov YV (2019) Methods of finding of exact analytical solutions of nonautonomous nonlinear Klein-Fock-Gordon equation. In: Altenbach H, Belyaev A, Eremeyev VA, Krivtsov A, Porubov AV (eds) Dynamical Processes in Generalized Continua and Structures, Advanced Structured Materials, vol 103, Springer International Publishing, Cham, pp 147–161

[29] Aero EL, Bulygin AN, Pavlov YV (2016) Nonlinear model of deformation of crystal media with complex lattice: Mathematical methods of model implementation. Mathematics and Mechanics of Solids **21**(1):19–36

Chapter 22
Hydrogen Skin Effect vs. Hydrogen Diffusion

Vladimir A. Polyanskiy, Dmitry G. Arseniev, Anastasiia A. Chevrychkina, and Yuri A. Yakovlev

Abstract Finite element simulation of hydrogen diffusion from charged samples during TDS measurement was carried out. Several variants of models were considered within the framework of the hydrogen diffusion model with traps of various nature McNabb and Foster. The simulation took into account the skin effect observed when charging the metal samples with hydrogen. It was found that the experimentally observed additional low-temperature peak of hydrogen on the TDS was observed only in the case of a hundredfold increase in the density of hydrogen sites in the surface layer. It was concluded that in some cases, after charging the samples, the diffusion fluxes of hydrogen in the skin layer change to gas fluxes of molecular hydrogen through the system of micropores formed during charging.

22.1 Introduction

The problems of metal hydrogen-induced cracking, hydrogen embrittlement, hydrogen brittleness and hydrogen-induced fracture have been very important for practice for more than 100 years. This is due to the fact that hydrogen and hydrogen-containing compounds such as water and hydrocarbons are found everywhere.

In the oil and gas industry, for example, hydrogen-induced destruction occurs during corrosion of the walls of pipelines, vessels and metal parts of machines [1]. The strengthening of the destructive influence of hydrogen occurs in the presence of H_2S sf. [2–5], at high mechanical stresses sf. [4, 6, 7] and in case of Stress Oriented Hydrogen Induced Cracking (SOHIC) sf. [8–10], in the presence of sulfur oxides Sulfide Stress Corrosion cracking (SSC) [2, 4].

Vladimir A. Polyanskiy · Dmitry G. Arseniev · Anastasiia A. Chevrychkina · Yuri A. Yakovlev
Institute for Problems in Mechanical Engineering RAS, V.O., Bolshoy prospekt, 61, 1999178 St.Petersburg, Russian Federation,
e-mail: vapol@mail.ru, adg@ipme.ru, anastasiia.che@gmail.com, yura.yakovlev@gmail.com

The use of high-strength metals enhances the influence of hydrogen significantly. Hydrogen brittleness and hydrogen cracking occur at significantly lower concentrations of hydrogen in the metal. Decrease in the maximum permissible concentration of hydrogen leads to the fact that not only metallurgical hydrogen, but also hydrogen accumulated during production and operation of metal begins to play a significant role even in cases where there is no pure hydrogen in the metal surrounding environment. Simultaneously with natural metallurgical hydrogen, hydrogen accumulated from the external environment begins to affect significantly the mechanical properties of metals and alloys which are: strength, ductility, impact viscosity, crack resistance [11].

A special role of hydrogen is worth mentioning if it is used as an energy source in various hydrogen energy projects. Transportation of a natural gas with hydrogen sf. [12–16] leads to a decrease in ductility, impact strength and crack resistance of pipe steels [17–20] even without mentioning transportation of pure hydrogen gas [20, 21].

To study the effect of hydrogen on the properties of metals and for industrial testing of metals for resistance to hydrogen brittleness, chemical and electrochemical methods of saturation of metals with hydrogen are widely used. The main methods are standardized: the saturation of metals by hydrogen using acid solution due to corrosion or stress corrosion [22–24]. The saturation of metals by hydrogen using cathodic hydrogen charging [22, 25]. The saturation of metals by hydrogen using in electrolyte associated with near-neutral pH SCC, simulating sea or groundwater or transported natural gas [26–30]. For instance, see Ref. [26] for standard set of test conditions for consistent evaluation of pipeline and pressure vessel steels and compares test results from different laboratories pertaining to the results of the absorption of hydrogen generated by corrosion of steel in wet H_2S.

There are many experimental works in which show that charging with hydrogen can lead to a strong inhomogeneity of the distribution of hydrogen concentrations, see [31–34]. We proposed to call the observed effect "the hydrogen skin effect" because of its similarity to the electric skin effect. The observed skin effect is reported in [33, 34]. Due to this effect, the hydrogen concentration in the surface layer with a thickness of the order of one metal grain size (60-100 micron) can exceed the concentration inside the sample by tens of times.

Numerous test results of hydrogen-charged samples show that, despite the shallow depth of the skin effect, it affects the strength and ductility of the metal significantly. The mechanism of such influence is discussed and modeled in the works, see [35, 36]. The test results show that, due to the skin effect, destruction occurs with a variable nature of the fracture of the samples. One part of the main crack grows according to brittle mechanism, another part grows according to viscous one. That was the reason for the development of new models of hydrogen embrittlement HELP+HEDE [37–39], combining the well-known models of hydrogen-enhanced decohesia HEDE [40, 41] and hydrogen-enhanced local plasticity HELP [42].

The nature of the hydrogen skin effect itself remains not fully investigated. In a number of papers, it is explained by the slow diffusion of hydrogen [43, 44]. This view allows many experimenters to use long-term charging of samples [45–47]

and exposure of samples to air after charging, as a method of homogenizing the concentration of hydrogen [48].

At the same time, there is an evidence that the additional concentration of hydrogen evaporates quickly after holding the samples in atmosphere, and even more so in vacuum, which should not be the case with slow diffusion [34]. Thus, the question of the nature of the skin effect is of direct importance for the technologies of preparation and industrial testing of metals for resistance to hydrogen brittleness.

22.2 The Theoretical Observation

The most popular method for researching the hydrogen diffusion and for determining the hydrogen binding in solid samples is the method based on thermal desorption spectra (TDS). There is an extensive literature, see for example, [48–59, 59–63]. After experimental measurement of several TDS with different heating rates of the identical samples, the Choo-Lee graph is plotted. The binding energies are determined from the results of linearization of Choo-Lee plot. The method is based on chemical kinetics, see [64].

A paradoxical but generally accepted approach is that for the case of hydrogen TDS, the emission of hydrogen from traps during heating of the samples is considered as a first-order chemical reaction. Diffusion of hydrogen which removes hydrogen from the sample is considered to be a significantly faster process. This allows one to neglect the account of diffusion while calculating the hydrogen binding energy, at least it was not taken into account by Kissinger who is the author of the method for determining the binding energy, [64].

Numerous studies carried out by means of mathematical modeling, see, for example, [65–69], have shown that the process of hydrogen diffusion does not significantly distort the thermal desorption spectra. The binding energies determined by the Kissinger [64] formula using the Choo-Lee plot correspond to the binding energies of the traps. There are some contradictions here, since some authors consider the diffusion activation energy as an addition to the binding energy of traps, while other authors do not take into account this "diffusion addition". But the binding energy in traps, as a rule, significantly exceeds the diffusion activation energy assumed by the authors. Therefore, these contradictions fit into the 15% range which can be recognized as the accuracy of the used methodology. In some standards for the measurement of diffusion-mobile hydrogen, it is even defined as hydrogen dissolved in a metal that does not have an activation or binding energy, see [70].

It is important to note that the simulation assumes, as a rule, a uniform or almost uniform initial distribution of hydrogen in the metal sample, see [71, 72]. Cases of uneven distribution have been considered in a relatively small number of papers, see [73–77].

In most articles the distribution of hydrogen concentration is specified as the initial condition for integrating the diffusion equations. It can also be calculated by simulating the saturation of a sample with zero initial concentration from a hydrogen-

containing medium such as in [74, 75]. When modeling the saturation process, the same equations of hydrogen diffusion and its capture in traps are used as in the simulation of degassing during the TDS measurement. The distribution of traps over the sample volume is assumed to be uniform.

At the same time, there is a problem of the sensitivity of the equipment used to measure the TDS. The hydrogen flux from a slowly heated sample must be accurately measured against the background of hydrogen fluxes both in the environment surrounding the sample and from the heated parts of the experimental setup. The water adsorbed on the sample surface can also affect the results of hydrogen flux measurements. Its volume concentration even in a specially dried gas is much higher than the concentration of hydrogen extracted gradually from the sample. The most popular solution to these measurement problems is to artificially saturate (or charge) the samples with hydrogen before taking the TDS measurements. Very often, first, the heat treatment and mechanical tests are carried out, and then, immediately before measuring the TDS, the samples are charged with hydrogen, see for example [78–83]. This approach makes it possible to minimize the effect of background hydrogen fluxes on the measurement results, since the hydrogen flux from the sample significantly exceeds the background one.

As experimentally found in [34, 84], the hydrogen charging of metal samples in an electrolyte or neutral solution leads to a strong unevenness in the distribution of hydrogen or the "skin effect" of hydrogen charging. In the articles [85, 86] we have already reported how the "skin effect" affects TDS. We performed simulations using diffusion equations. This approach was based on the assumption by Oriani [87] that the sites in the crystal lattice are weakly filled with hydrogen dissolved in the sample. That is, the limited capacity of the crystal lattice has practically no effect on diffusion. We have shown the "pure effect" of the uneven distribution of diffusely mobile hydrogen in the sample by comparing the model and experimental TDS [86]. We found that the skin effect of hydrogen charging can greatly distort the TDS curves. Additional peaks of the spectrum with fictitious binding energies appear. We noticed that such peaks are quite often observed in experimental TDS, their main feature is a low maximum temperature (less than 200°C) and, on the contrary, a high binding energy corresponding to the peak, see [88–92]. This energy is usually referred to as the binding energy of hydrogen traps.

At the same time, we did not discuss the physical origin of the skin effect. In an experimental study, it is extremely difficult to separate quantitatively the hydrogen located in the sites of the crystal lattice and that in the sites of traps, since the hydrogen is distributed inside the sample in microscopic traps of a very small volume. Therefore, mathematical modeling of the transport of hydrogen inside the sample and its extraction from the sample is the most accessible method, which does not require cutting the samples into pieces or other significant mechanical effects that can greatly change the initial distribution of hydrogen.

22.2.1 Hydrogen Transport Model

The Fick equation (22.1) is the simple one used to model the transport of hydrogen inside a solid [93]:

$$\frac{\partial C}{\partial t} = \nabla \cdot [D(T,r)\nabla C]. \tag{22.1}$$

Here C is the hydrogen concentration, t is the time, r is the polar coordinate, D is the diffusion coefficient, and T is the absolute temperature. The diffusion coefficient depends on the temperature according to the Arrhenius law [94]:

$$D(T) = D_0 e^{-\frac{u}{RT}}, \tag{22.2}$$

where u is the activation energy of diffusion, D_o is the diffusion constant, R is the universal gas constant.

Experimental studies have shown that the use of the Fick equation in the approximation of experimental data does not allow describing the dependence of the hydrogen flux on time, and the fitting of the parameters gives a large scatter of the diffusion coefficients and activation energies for the same materials. Darken and Smith [95] explained this variation by the fact that when metals are saturated with hydrogen, there is a limit value for the concentration of hydrogen, which depends on the way the sample is processed. That is, the laws of diffusion work only if the hydrogen concentration is less than the limiting values. Therefore, the concept of binding hydrogen and hydrogen traps distributed in the material was introduced into the description of the transport of hydrogen in a solid. The trap model of hydrogen transport by Mac Nabb and Foster [96] in the one-dimensional form proposed by the authors [96] is written as

$$\begin{cases} \dfrac{\partial C_L}{\partial t} + N_x \dfrac{\partial \theta_x}{\partial t} = D_L \dfrac{\partial^2 C_L}{\partial x^2}, \\ \dfrac{\partial \theta_x}{\partial t} = k_x C_L (1 - \theta_x) - k_L \theta_x. \end{cases} \tag{22.3}$$

Here C_L is the hydrogen concentration in the "normal" crystal lattice, D_L is the diffusion coefficient in the "normal" crystal lattice, N_x is the volume density of hydrogen traps, θ_x is the fraction of occupied sites in the traps ($0 \le \theta_x \le 1$), $N_x \theta_x = C_x$ is the volume concentration of hydrogen concentrated in traps, k_x represents the probability of jumping from a normal lattice to a trap, on the contrary k_L describes the probability from a trap to a normal lattice. The first equation describes diffusion, while the second one can be interpreted as "trap".
Here

$$\begin{cases} k_x(T) = k_{x0} e^{-\frac{u_t}{RT}}, \\ k_L(T) = k_{L0} e^{-\frac{u_d}{RT}} = k_{L0} e^{-\frac{u_b + u_t}{RT}}, \end{cases} \tag{22.4}$$

where u_b is the binding energy of hydrogen in traps, u_t is the energy of hydrogen capture by traps. Traps are understood as the bindingaries of single-crystal grains, foreign inclusions, internal defects, dislocations, vacancies, microcracks etc., see [97–100].

Another mathematical model was proposed by Oriani [87]. This model takes into account the bulk density of distribution of sites not only of trap-defect, but also of the "normal crystal lattice". Thus, the concentration of mobile hydrogen is written as the product

$$C_L = N_L \theta_L, \tag{22.5}$$

where N_L is the density of the distribution of the sites of the traps of the normal crystal lattice, which does not depend on the external pressure of hydrogen in the atmosphere above the metal, Hydrogen concentration inside the metal and the temperature, θ_L is the fraction of occupied sites in the normal crystal lattice ($0 \le \theta_L \le 1$). At low hydrogen concentrations and a constant density of sites in the crystal lattice, the MacNabb and Foster equations can be obtained from the Oriani model, but when the traps of the crystal lattice are occupied, additional nonlinearity appears, associated with restrictions on the coefficient . Thus, in the Oriani model, a number of additional parameters appear to describe the process of hydrogen transport. If we assume the presence in the material simultaneously of several types of traps with different binding energies, then there are even more "trap equations" and parameters for fitting to experimental data. This allows interpretation of almost any experiment [71, 72]. An important addition that Oriani introduced into his model is the thermodynamic dependence between the fraction of occupied sites in the crystal lattice θ_L (diffusion) and distributed traps θ_x.

$$K = e^{-\frac{\Delta u}{RT}} = \frac{\theta_x}{1 - \theta_x} \cdot \frac{1 - \theta_L}{\theta_L}, \tag{22.6}$$

here Δu is the difference between the activation energy of diffusion (diffusion sites) and the binding energy of traps (trap's sites).

Dependence (22.6) was obtained by means of the McLean equations [101], that is, under conditions of static thermodynamic equilibrium. The existence of this equilibrium in the case of nonstationary diffusion of hydrogen can, with some error, be assumed only with a very slow change in the distribution of the hydrogen concentration. Otherwise, the temperature change leads to an instantaneous change in the values of the occupation levels of the traps θ_x, θ_L. This is possible if we neglect the diffusion time constant and, as Oriani points out, under the assumption that the hydrogen concentration in the crystal lattice C_L satisfies the condition $\theta_L \ll 1$. In this case

$$K = \frac{\theta_x}{1 - \theta_x} \cdot \frac{1}{\theta_L} \tag{22.7}$$

and we can express the diffusion flux of hydrogen J in terms of the total concentration of hydrogen $C = C_L + C_x$

$$J = -D_{eff} \frac{dC}{dx}.$$

Here we used the effective diffusion coefficient D_{eff}. Using relation (22.6), we obtain the formula:

$$D_{eff} = D_L \frac{dC_L}{dC_T} = D_L \frac{C_L}{C_L + C_x (1 - \theta_x)}. \tag{22.8}$$

The relations (22.6) also allow us to describe the multichannel diffusion of hydrogen through traps [102–104], which is a further development of the Oriani model. Now we can list the significant limitations of the Oriani model:

- small parameter $\theta_L \ll 1$,
- artificial restrictions on the ratio between the values C_L and C_x due to the assignment of the density of sites,
- quasi-static character of the Oriani approach, see (22.6).

Such restrictions may not correspond to the experimental conditions for measuring the TDS, both in the case of a sufficiently rapid heating of the sample, and in the case of strong hydrogen saturation of the crystal lattice. These considerations allow us to consider the McNabb and Foster model (see [96] and Eqs. (22.3)) as more general.

22.2.2 Model Description

We consider the case of measuring the thermal desorption spectra of a hydrogen flux from cylindrical samples of radius R and height $2Z$ in the presence of the skin effect of their preliminary charging with hydrogen. In cylindrical coordinates with axial symmetry, the McNabb and Foster model is, see [96],

$$\begin{cases} \frac{1}{D(t)} \frac{\partial C_L}{\partial t} = \frac{1}{r} \frac{\partial}{\partial r} \left(r \frac{\partial C_L(r,z,t)}{\partial r} \right) + \frac{\partial^2 C_L(r,z,t)}{\partial^2 z} - \frac{N_{tr}}{D_L(t)} \frac{\partial \theta_{\text{tr}}}{\partial t}, \\ \frac{\partial \theta_{tr}}{\partial t} = \kappa \theta_L (1 - \theta_{tr}) - p \theta_{tr}, \\ C_L(R,z,t) = C_L(r,Z,t) = 0, \quad \text{sample boundary condition} \\ \frac{\partial C_L}{\partial r}(0,z,t) = \frac{\partial C_L}{\partial z}(r,0,t) = 0, \quad \text{symmetry condition} \\ C_L(r,z,0) + C_{tr}(r,z,0) = C_0(r,z). \quad \text{initial condition} \end{cases} \tag{22.9}$$

where C_L is the volume concentration of hydrogen in the crystal lattice, N_{tr} is the volume concentration of hydrogen in the trap sites, N_L is the volume concentration of hydrogen sites in the crystal lattice, θ_L is the fraction of occupied sites in the lattice, θ_{tr} is the fraction of occupied sites in the traps, κ is the trap capture rate, p is the trap release rate, D is the diffusion coefficient in the crystal lattice of the metal

$$C_L(r,z,t) = \theta_L(r,z,t) N_L(r,z,t),$$
$$C_{tr}(r,z,t) = \theta_{tr}(r,z,t) N_{tr}(r,z,t),$$

$$D = D_0 \exp\left(-\frac{U}{kT}\right),$$

$$\kappa = \kappa_0 \exp\left(-\frac{U_t}{kT}\right),$$

$$p = p_0 \exp\left(-\frac{U_d}{kT}\right).$$

Here T is the absolute temperature. U is the diffusion activation energy, U_t is the activation energy of hydrogen capture into traps, U_d is activation energy of hydrogen liberation from traps, D_0, κ_0, p_0 are the constants adjusted according to experimental data, k is the Boltzmann constant.

We assume is a uniform heating of the samples at a constant rate v, that is, the dependence of the absolute temperature T on time has the form:

$$T(t) = T_0 + vt.$$

According to experimental data on the skin effect [34, 84], the initial distribution of hydrogen in the sample (Fig. 22.1) is

$$C_0(r,z) = \theta_L(r,z,0) N_L(r,z) + \theta_{tr}(r,z,0) N_{tr}(r,z)$$

is non-uniform, namely, a jump in the hydrogen concentration at the boundary of the sample is observed. The initial distribution of the total hydrogen concentration $C_0(r,z)$ can be decomposed in different ways into the hydrogen concentration in the traps C_{tr} and the concentration of diffuse hydrogen in the C_L lattice. To analyze the effect of traps on TDS, we will consider four cases of hydrogen distribution, when the skin effect of hydrogen concentration is described only in $\theta_L, \theta_{tr}, N_L$ or N_{tr}, and the rest of the components corresponds to a uniform distribution of hydrogen. In general, the initial distribution, e.g. $\theta_L(r,z,0)$, can be given by the following function:
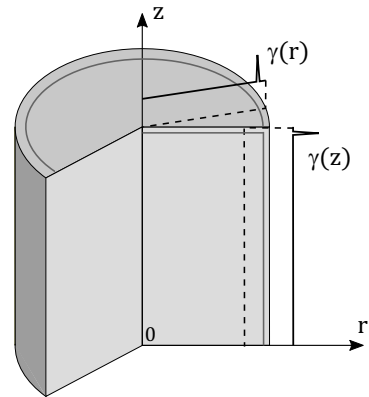
Fig. 22.1 The initial distribution of hydrogen concentration in a cylindrical sample according to Eq. (22.10).

$$\theta_L(r,z,0) = \begin{cases} \gamma(r), & z \le Z_1 - w \quad \text{or} \quad r \ge z + (R_1 - Z_1) \\ \gamma(z), & z > Z_1 - w \quad \text{and} \quad r < z + (R_1 - Z_1) \end{cases}, \qquad (22.10)$$

where the function γ is a piecewise linear function (here x means one of the coordinates r or z):

$$\gamma(x) = \begin{cases} \theta_L^1, & x \le X_1 - w \\ \theta_L^1 + \dfrac{\theta_L^2 - \theta_L^1}{w}(x - (X_1 - w)), & X_1 - w < x \le X_1 \\ \theta_L^1 - \dfrac{\theta_L^2 - \theta_L^1}{w}(x - (X_1 + w)), & X_1 < x \le X_1 + w \\ \dfrac{\theta_L^1}{X - (X_1 + w)}(X - x), & X_1 + w < x \le X \end{cases}$$

Here, if $\theta_L^2 = \theta_L^1$, then we obtain a uniform distribution of hydrogen in the sample; in the case $\theta_L^2 > \theta_L^1$, the hydrogen distribution will be piecewise linear, which in our case corresponds to the presence of a skin layer in the sample.

22.2.3 Computational Algorithm of the Model

To solve system (22.9), a two-stage explicit difference scheme is used. Solution at an intermediate time step $t + \Delta t/2$ is as follows:

$$\frac{r_i}{D^{n+1/2}} \frac{C_{Li}^{n+1/2} - C_{Li}^n}{\Delta t/2} = \frac{r_{i+1/2}\left(C_{Li+1,j}^{n+1/2} - C_{Li,j}^{n+1/2}\right) + r_{i-1/2}\left(C_{Li-1,j}^{n+1/2} - C_{Li,j}^{n+1/2}\right)}{\Delta r^2} +$$
$$+ r_i \frac{C_{Li,j+1}^n - 2C_{Li,j}^n + C_{Li,\,j-1}^n}{\Delta z^2} - \frac{r_i}{D^{n+\frac{1}{2}}} N_{tr}\left(\frac{\kappa_0 \theta_{Li,j}^{n+\frac{1}{2}}}{N_L}\left(1 - \theta_{tr,ij}^n\right) - p_0 \theta_{tr,ij}^n\right).$$
$$(22.11)$$

Here the superscript n, $n + 1/2$, denotes the time step, the subscripts are the number of the finite element. Using the solution to Eq. (22.11), we find the value of the fraction of the trap occupancy at the intermediate step $t + \Delta t/2$:

$$\theta_{tr}^{n+1/2} = \theta_{tr}^n + \frac{\Delta t}{2}\left(\frac{\kappa_0 C_{i,j}^{n+\frac{1}{2}}}{N_L}\left(1 - \theta_{tr}^n\right) - p_0 \theta_{tr}^n\right). \qquad (22.12)$$

At the second stage, the value of the hydrogen concentration in the lattice at the full step $t + \Delta t$ is determined by the difference equation:

$$\frac{r_i}{D^{n+1}} \frac{C_i^{n+1} - C_i^{n+1/2}}{\Delta t/2} = \frac{r_{i+1/2}\left(C_{i+1,j}^{n+1/2} - C_{i,j}^{n+1/2}\right) + r_{i-1/2}\left(C_{i-1,j}^{n+1/2} - C_{i,j}^{n+1/2}\right)}{\Delta r^2} +$$
$$+ r_i \frac{C_{i,j+1}^{n+1} - 2C_{i,j}^{n+1} + C_{i,\,j-1}^{n+1}}{\Delta z^2} - \frac{r_i}{D^{n+1}} N_{tr}\left(\frac{\kappa_0 C_{i,j}^{n+1}}{N_L}\left(1 - \theta_{tr,ij}^{n+\frac{1}{2}}\right) - p_0 \theta_{tr,ij}^{n+\frac{1}{2}}\right).$$

$$(22.13)$$

Using the solution to Eq. (22.13), we find the value of the fraction of the trap occupancy at the step $t + \Delta t$:

$$\theta_{tr}^{n+1} = \theta_{tr}^{n+1/2} + \frac{dt}{2}\left(\frac{\kappa_0 C_{i,j}^{n+1}}{N_L}\left(1 - \theta_{tr}^{n+\frac{1}{2}}\right) - p_0 \theta_{tr}^{n+\frac{1}{2}}\right). \qquad (22.14)$$

Successive solution of Eqs. (22.11) - (22.14) makes it possible to find the hydrogen concentrations C_L, C_{tr} and the hydrogen desorption flux.

22.3 Simulation Results

Consider four limiting cases of the non-uniform distribution of each of the hydrogen distribution parameters: $\theta_L, \theta_{tr}, N_L, N_{tr}$. In the case of the presence of a skin layer in θ_L or θ_{tr} we assume that the skin effect arises due to the non-uniform occupancy of sites in the crystal lattice or in traps, respectively. In the case of N_L or N_{tr}, it is assumed that the site occupancy is uniform, but their bulk density in the crystal lattice or in trap defects has an unevenness corresponding to the skin effect. We compare the result with the case of uniform distribution $\theta_L, \theta_{tr}, N_L, N_{tr}$, that is, without the skin effect.

The numerical solution of Eq. (22.9) obtained by means of Eqs. (22.11) - (22.14) is in Figs. 22.2–22.4. The curves of plots 22.2–22.4 are normalized to the maximum value of flux in the case of a uniform hydrogen distribution in the lattice and traps. The values of the mechanical parameters are given in Table 22.1 and correspond to the parameter estimates made in [105]. The parameters of the initial hydrogen distribution are adjusted in such a way as to provide the distribution of the total hydrogen concentration observed in the experiment when studying the results of charging samples from various steels [74, 75, 85]. The data are shown in Tables 22.2 and 22.3.

Table 22.1: Diffusion and trap parameters.

D_0, mm^2/s	U, eV	κ_0, 1/s	p_0, 1/s	U_t, eV	U_d, eV
0.05	0.2	5000	10	0.3	0.6
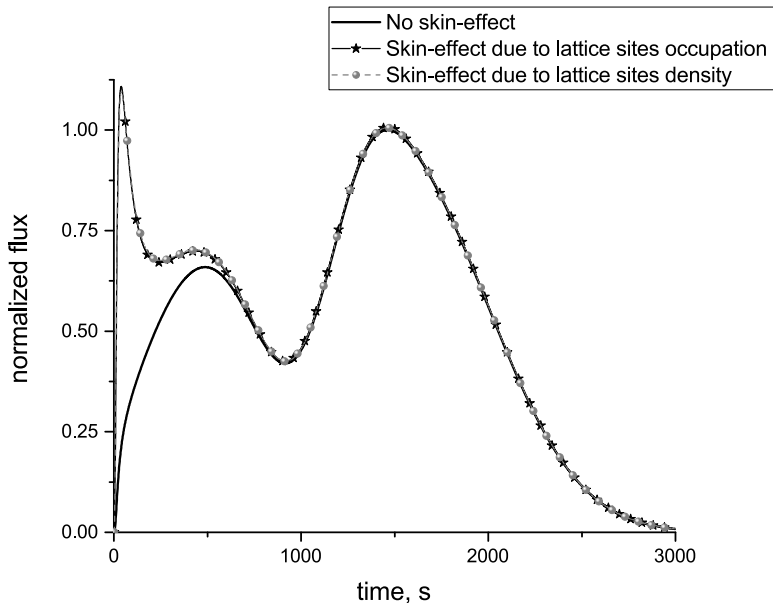
Fig. 22.2: Influence of the skin layer in the initial distribution of hydrogen in the lattice on the solution of system (22.9) at the heating rate $v = 0.5$ K/s and the parameters from Tables 22.1 – 22.3, taking into account $\theta_{tr}^2 = \theta_{tr}^1$ and $N_{tr}^2 = N_{tr}^1$. No skin-effect $\theta_L^2 = \theta_L^1$ and $N_L^2 = N_L^1$; skin-effect due to lattice sites occupation $\theta_L^2 = 10\theta_L^1$ and $N_L^2 = N_L^1$; skin-effect due to lattice sites density $\theta_L^2 = \theta_L^1$ and $N_L^2 = 10N_L^1$.

Table 22.2: Sample geometry parameters.

R,mm	R_1, mm	w, mm	Z, mm	Z_1, mm
3	2.94	0.02	10	9.84

Table 22.3: Initial condition parameters.

N_L^1, sites/mm^3	N_L^2, sites/mm^3	θ_L^1	θ_L^2	N_{tr}^1, sites/mm^3	N_{tr}^2, sites/mm^3	θ_{tr}^1	θ_{tr}^2
10^{20}	$10N_L^1$	$2 \cdot 10^{-6}$	$10\theta_L^1$	10^{16}	$10N_{tr}^1$	0.01	$10\theta_{tr}^1$
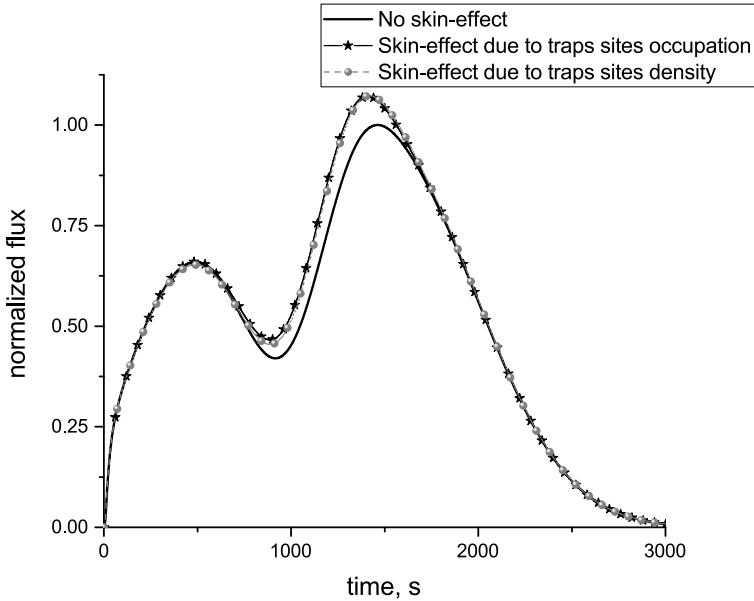
Fig. 22.3: Influence of the skin layer in the initial distribution of hydrogen in traps on the solution of system (22.9) at the heating rate and the parameters from Tables 22.1 – 22.3, taking into account $\theta_L^2 = \theta_L^1$ and $N_L^2 = N_L^1$. No skin-effect $\theta_{tr}^2 = \theta_{tr}^1$ and $N_{tr}^2 = N_{tr}^1$; skin-effect due to traps sites occupation $\theta_{tr}^2 = 10\theta_{tr}^1$ and $N_{tr}^2 = N_{tr}^1$; skin-effect due to traps sites density $\theta_{tr}^2 = \theta_{tr}^1$ and $N_{tr}^2 = 10N_{tr}^1$.

Figure 22.2 shows the effect of the skin layer in the crystal lattice on the thermal desorption spectrum. Three curves are displayed: (i) the skin layer in N_L and the uniform distribution θ_L, (ii) the skin layer in θ_L and the uniform distribution N_L, and (iii) the case of uniform distribution of hydrogen in the lattice $\theta_L^2 = \theta_L^1$ and $N_L^2 = N_L^1$ is also given for comparison. The skin layer in both cases demonstrates similar effects. The thermal desorption spectrum contains an additional low-temperature peak corresponding to the extraction of hydrogen from the near-surface part of the sample.

On the contrary, the skin layer in the distribution of sites and the occupancy of sites in the traps θ_{tr}, N_{tr} does not affect the thermal desorption curve, see Fig. 22.3. An additional peak associated with the skin layer in θ_{tr}, N_{tr} is absent on the TDS. From a mathematical point of view, this is due to the fact that the equation for θ_{tr} does not contain spatial derivatives. From a physical point of view, this is due to the absence of a separate channel for hydrogen diffusion through traps. There is a slight change in comparison with the uniform distribution of the position of the peak corresponding to the extraction of hydrogen from the traps. Skin layer in θ_{tr} and N_{tr} gives the same effect on TDS.
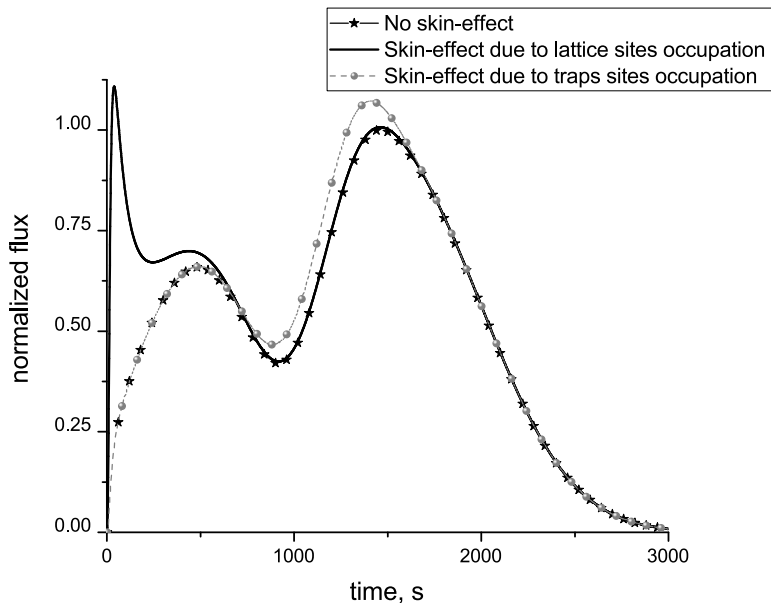
Fig. 22.4: Influence of the skin layer the lattice sites occupancy and traps sites occupancy on the solution of system (22.9) at the heating rate $v = 0.5$ K/s and the parameters from Tables 22.1 – 22.3, taking into account $N_L^2 = N_L^1$ and $N_{tr}^2 = N_{tr}^1$. No skin-effect $\theta_L^2 = \theta_L^1, \theta_{tr}^2 = \theta_{tr}^1$; skin-effect due to lattice sites occupation $\theta_L^2 = 10\theta_L^1, \theta_{tr}^2 = \theta_{tr}^1$; skin-effect due to traps sites occupation $\theta_L^2 = \theta_L^1, \theta_{tr}^2 = 10\theta_{tr}^1$.

For greater clarity, Fig. 22.4 displays the comparison of TDS with the non-uniform distribution of the trap occupancy in the crystal lattice θ_L, defects θ_{tr} with the uniform distribution of hydrogen in the sample. Modeling the skin layer in the crystal lattice shows that the second peak of the TDS curve is shifted relative to the other two peaks, see Fig. 22.4. As shown in our previous work [86] the second peak corresponds to the release of hydrogen from the inner part of the sample due to the skin effect. Fig. 22.4 shows that, in the case of a cylindrical sample, the position of the maximum of the second peak is displaced, and from a formal point of view, this is due to the features that arise when using a cylindrical coordinate system.

Simulation results are also presented for various values of the skin depth R_1 and Z_1. The results in Fig. 22.5 show that skin depth strongly influences the position of the first TDS peak. A decrease in depth leads to the shift to the low-temperature region of an additional peak. In this case, it is more difficult to detect it experimentally.
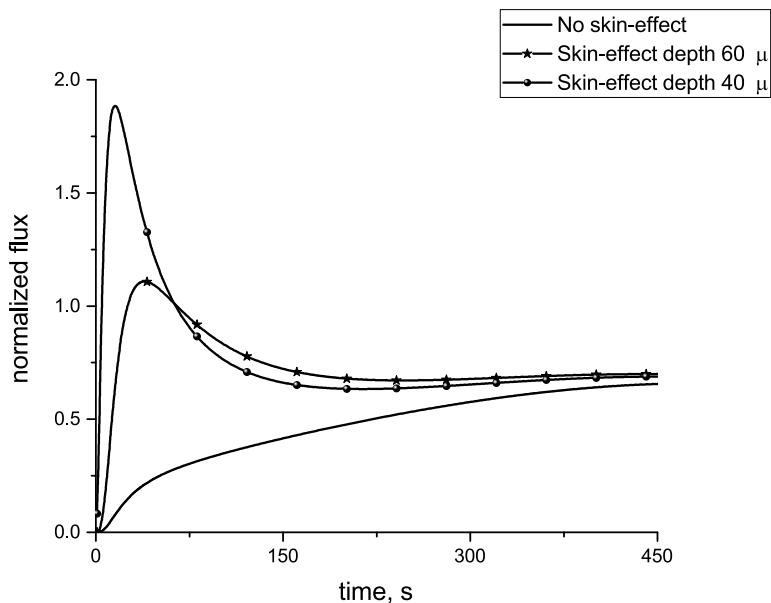
Fig. 22.5: Change in the low-temperature peak with a change in the depth of the skin layer at the heating rate of 0.5 K/s. Solution of system (22.9) with the parameters from Tables 22.1 – 22.3, taking into account $\theta_{tr}^2 = \theta_{tr}^1$, $N_L^2 = N_L^1$ and $N_{tr}^2 = N_{tr}^1$.

22.4 The Discussion of the Results

Consideration of various possible options for the formation of the skin effect, see Figs. 22.2–22.4, shows that it is formed due to diffuse hydrogen accumulated in the crystal lattice. Consequently, the additional low-temperature peak of TDS is often observed in real measurements of spectra, see, for example, experimental work with a concave peak at low temperatures [106–112] associated with the hydrogen traps outside the normal crystal lattice.

The study of samples charged with hydrogen after prolonged exposure to air shows that hydrogen is completely extracted from the skin layer by itself after about a month of exposure at room temperature [85]. This indirectly proves that the skin layer is formed due to diffuse hydrogen located in the sites of the normal crystal lattice.

With the skin effect, there is an uneven distribution of hydrogen in the sample. Excess hydrogen appears at the border of the sample, the concentration of which is hundreds of times higher than the average values inside the sample. We have shown by modeling that experimental manifestations of this effect are observed only in the case when excess hydrogen is in traps or in sites with their own dedicated diffusion channel. That is, the possibility of equalizing the hydrogen concentration in isolation of the other diffusion flows.

If this is a common diffusion channel operating throughout the metal, an inexplicable kinetic paradox appears. It lies in the fact that huge gradients of hydrogen concentrations, of the order of 1 ppm/micron, are formed in a few hours and remain stable for several hundred hours [31–34].

The stability of the skin effect is preserved when saturated with hydrogen. After the samples are extracted from the electrolyte, hydrogen is extracted into the external environment. Despite the huge gradients at the inner boundary of the skin layer, this extraction is not accompanied by significant diffusion into the metal [34].

When the samples are placed in a vacuum at room temperature, the additional hydrogen is extracted about a hundred times faster than when kept in the atmosphere [34]. This effect is also inexplicable from the point of view of ordinary diffusion, since diffusion depends on the difference in hydrogen concentrations, but there is practically no hydrogen in the atmosphere, nor in vacuum.

Thus, theoretical consideration shows that the nature of the skin effect cannot be explained simply by hydrogen diffusion. In fact, it turns out that different diffusion channels work inside the skin layer and in other internal areas of the metal, and there is a fundamentally larger number of hydrogen sites inside the crystal lattice.

This conclusion is confirmed by the results of microscopic studies. The paper [113] describes the formation of blisters, bubbles and microcracks in the surface layer of iron samples after hydrogen saturation. The paper [114] describes the formation of micropores and microcracks in the surface layer of nickel-based superalloy samples after cathodic charging. The paper [115] describes the formation of a whole system of subsurface micropores at the top of the incision on the sample surface after saturation of low-alloy steel after electrochemical saturation. A similar result is described in [116] for dual-phase steel. In [32] the formation of a system of nanosize hollowness in the surface layer of copper during cathodic charging is described. In [117] a similar result is presented for aluminum alloys.

Comparing these results with the theoretical description of various variants of hydrogen diffusion in metals after electrochemical or chemical charging of metal samples allows us to draw the main conclusion that the diffusion of hydrogen into the metal with all standardized methods of hydrogen charging leads to the destruction of the internal microstructure of the metal in the skin layer. This helps to stabilize the distribution of hydrogen concentrations in the metal. At the same time, such destruction makes the diffusion of hydrogen from charged samples fundamentally different from the diffusion inside the metal, up to the formation of ordinary gas flows of hydrogen through a system of near-surface micropores and microcracks in which it accumulated when charging.

22.5 Conclusions

The modeling of the effect of the skin effect on the TDS is carried out taking into account the hydrogen traps. The simulation results show that the skin effect is formed

due to diffuse hydrogen located in the sites of the normal crystal lattice. This is confirmed indirectly by some experimental data.

A comparison of mathematical modeling data with the features of the skin effect shows that, when hydrogen is charged, the main mechanism or channel of hydrogen diffusion in the crystal lattice of the metal surface layer with a thickness of about 50 microns changes and about a hundred times more sites for hydrogen retention appear. This explains the stability of the skin effect over time and the absence of hydrogen diffusion into the samples when exposed to air, despite the huge gradients of hydrogen concentrations of the order of 1 ppm/micron.

References

[1] Askari M, Aliofkhazraei M, Afroukhteh S (2019) A comprehensive review on internal corrosion and cracking of oil and gas pipelines. Journal of Natural Gas Science and Engineering **71**:102,971

[2] Kane RD, Cayard MS (1999) NACE Committee Report 8X294: Review of Published Literature on Wet H2S Cracking. In: CORROSION 99, NACE Corrosion, pp NACE–99,420, paper presented at the CORROSION 99, San Antonio, Texas, April 1999

[3] Heidersbach R (2018) Metallurgy and corrosion control in oil and gas production. John Wiley & Sons

[4] Ossai CI, Boswell B, Davies IJ (2015) Pipeline failures in corrosive environments – a conceptual analysis of trends and effects. Engineering Failure Analysis **53**:36–58

[5] Safadoost A, Davoodi M, Mansoori SAA (2014) Preventing corrosion and tube failure in sulfur condenser during normal operation, startup, and shutdown of the south pars gas processing plant (case study). Journal of Natural Gas Science and Engineering **19**:105–115

[6] Venegas V, Caleyo F, Baudin T, Espina-Hernández J, Hallen J (2011) On the role of crystallographic texture in mitigating hydrogen-induced cracking in pipeline steels. Corrosion Science **53**(12):4204–4212

[7] Elboujdaini M, Revie R (2009) Metallurgical factors in stress corrosion cracking (scc) and hydrogen-induced cracking (hic). Journal of solid state electrochemistry **13**(7):1091–1099

[8] Albarran J, Aguilar A, Martinez L, Lopez H (2002) Corrosion and cracking behavior in an api x-80 steel exposed to sour gas environments. Corrosion **58**(9):783–792

[9] Kobayashi K, Dent P, Fowler CM (2014) Effects of Stress Conditions and Microstructure on SOHIC Susceptibility. In: CORROSION 2014, NACE Corrosion, pp NACE–2014–3883, paper presented at the CORROSION 2014, San Antonio, Texas, March 2014

[10] Al-Shamari AR, Al-Sulaiman S, Amer J, Prakash S (2014) Cracking of a spiral weld pipeline in sour service. In: CORROSION 2014, NACE Corrosion, pp

NACE–2014–3835, paper presented at the CORROSION 2014, San Antonio, Texas, March 2014

[11] Maruschak P, Panin S, Chausov M, Bishchak R, Polyvana U (2017) Effect of long-term operation on steels of main gas pipeline. reduction of static fracture toughness. Journal of Natural Gas Science and Engineering **38**:182–186

[12] Ishaq H, Dincer I (2020) A comprehensive study on using new hydrogen-natural gas and ammonia-natural gas blends for better performance. Journal of Natural Gas Science and Engineering **81**:103,362

[13] Peng DD, Fowler M, Elkamel A, Almansoori A, Walker SB (2016) Enabling utility-scale electrical energy storage by a power-to-gas energy hub and underground storage of hydrogen and natural gas. Journal of Natural Gas Science and Engineering **35**:1180–1199

[14] Hafsi Z, Elaoud S, Mishra M (2019) A computational modelling of natural gas flow in looped network: Effect of upstream hydrogen injection on the structural integrity of gas pipelines. Journal of Natural Gas Science and Engineering **64**:107–117

[15] Ishaq H, Dincer I (2020) Performance investigation of adding clean hydrogen to natural gas for better sustainability. Journal of Natural Gas Science and Engineering **78**:103,236

[16] Ozturk M, Dincer I (2020) Development of renewable energy system integrated with hydrogen and natural gas subsystems for cleaner combustion. Journal of Natural Gas Science and Engineering **83**:103,583

[17] Meng B, Gu C, Zhang L, Zhou C, Li X, Zhao Y, Zheng J, Chen X, Han Y (2017) Hydrogen effects on x80 pipeline steel in high-pressure natural gas/hydrogen mixtures. International Journal of Hydrogen Energy **42**(11):7404–7412, special issue on The 6th International Conference on Hydrogen Safety (ICHS 2015), 19-21 October 2015, Yokohama, Japan

[18] Nguyen TT, Tak N, Park J, Nahm SH, Beak UB (2020) Hydrogen embrittlement susceptibility of x70 pipeline steel weld under a low partial hydrogen environment. International Journal of Hydrogen Energy **45**(43):23,739–23,753

[19] Shang J, Zheng J, Hua Z, Li Y, Gu C, Cui T, Meng B (2020) Effects of stress concentration on the mechanical properties of x70 in high-pressure hydrogen-containing gas mixtures. International Journal of Hydrogen Energy **45**(52):28,204–28,215, the 18th Conference of China Association for Hydrogen Energy (CAHE2019), 15 - 18 November 2019, Guangzhou, China

[20] Nguyen TT, Park J, Kim WS, Nahm SH, Beak UB (2020) Effect of low partial hydrogen in a mixture with methane on the mechanical properties of x70 pipeline steel. International Journal of Hydrogen Energy **45**(3):2368–2381

[21] Nguyen TT, Park JS, Kim WS, Nahm SH, Beak UB (2020) Environment hydrogen embrittlement of pipeline steel x70 under various gas mixture conditions with in situ small punch tests. Materials Science and Engineering: A **781**:139,114

[22] ISO16573 (2015) Steel - measurement method for the evaluation of hydrogen embrittlement resistance of high strength steels. ISO 16573:2015 International Organization for Standardization

[23] Johnson WH (1874) On some remarkable changes produced in iron and steel by the action of hydrogen and acids. Proceedings of the Royal Society of London **23**(156–163):168–179

[24] Kuduzovic A, Poletti M, Sommitsch C, Domankova M, Mitsche S, Kienreich R (2014) Investigations into the delayed fracture susceptibility of 34crnimo6 steel, and the opportunities for its application in ultra-high-strength bolts and fasteners. Materials Science and Engineering: A **590**(0):66 – 73

[25] ISO17081 (2014) Method of measurement of hydrogen permeation and determination of hydrogen uptake and transport in metals by an electrochemical technique. ISO 17081:2014 International Organization for Standardization

[26] TM0284 (2016) Evaluation of pipeline and pressure vessel steels for resistance to hydrogen-induced cracking. TM0284-2016 ANSI/NACE Standard, NACE International, Houston, TX

[27] Niu L, Cheng Y (2007) Corrosion behavior of X-70 pipe steel in near-neutral pH solution. Applied Surface Science **253**(21):8626 – 8631

[28] Cheng Y (2007) Fundamentals of hydrogen evolution reaction and its implications on near-neutral pH stress corrosion cracking of pipelines. Electrochimica Acta **52**(7):2661 – 2667

[29] Capelle J, Gilgert J, Dmytrakh I, Pluvinage G (2008) Sensitivity of pipelines with steel api X52 to hydrogen embrittlement. International Journal of Hydrogen Energy **33**(24):7630 – 7641

[30] Dmytrakh I, Leshchak R, Syrotyuk A, Barna R (2017) Effect of hydrogen concentration on fatigue crack growth behaviour in pipeline steel. International Journal of Hydrogen Energy **42**(9):6401 – 6408

[31] Wu TI, Wu JC (2008) Effects of cathodic charging and subsequent solution treating parameters on the hydrogen redistribution and surface hardening of ti–6al–4v alloy. Journal of Alloys and Compounds **466**(1):153–159

[32] Martinsson Å, Sandström R (2012) Hydrogen depth profile in phosphorus-doped, oxygen – free copper after cathodic charging. Journal of Materials Science **47**(19):6768–6776

[33] Alekseeva E, Belyaev A, Zegzhda A, Polyanskiy A, Polyanskiy V, Frolova K, Yakovlev YA (2018) Boundary layer influence on the distribution of hydrogen concentrations during hydrogen-induced cracking test of steels. Diagnostics, Resource and Mechanics of materials and structures (3):43

[34] Polyanskiy V, Belyaev A, Alekseeva E, Polyanskiy A, Tretyakov D, Yakovlev YA (2019) Phenomenon of skin effect in metals due to hydrogen absorption. Continuum Mechanics and Thermodynamics **31**(6):1961–1975

[35] Frolova KP, Vilchevskaya EN, Polyanskiy VA, Yakovlev YA (2021) Modeling the skin effect associated with hydrogen accumulation by means of the micropolar continuum. Continuum Mechanics and Thermodynamics **33**(3):697–711

[36] Frolova KP, Vilchevskaya EN, Bessonov NM (2022) On modeling of stress-induced diffusion within micropolar and classical approaches

[37] Gerberich W, Stauffer D, Sofronis P (2009) A coexistent view of hydrogen effects on mechanical behavior of crystals: Help and hede. Effects of hydrogen on materials Materials Park, OH: ASM international pp 38–45

[38] Djukic MB, Bakic GM, Zeravcic VS, Sedmak A, Rajicic B (2016) Hydrogen embrittlement of industrial components: prediction, prevention, and models. Corrosion **72**(7):943–961

[39] Djukic M, Zeravcic VS, Bakic G, Sedmak A, Rajicic B (2014) Hydrogen embrittlement of low carbon structural steel. Procedia Materials Science **3**:1167–1172, 20th European Conference on Fracture

[40] Birnbaum H, Sofronis P (1994) Hydrogen-enhanced localized plasticity-a mechanism for hydrogen-related fracture. Materials Science and Engineering: A **176**(1):191–202

[41] Oriani R (1972) A mechanistic theory of hydrogen embrittlement of steels. Berichte der Bunsengesellschaft für physikalische Chemie **76**(8):848–857

[42] Sofronis P, Birnbaum H (1995) Mechanics of the hydrogendashdislocation-dashimpurity interactions-i. increasing shear modulus. Journal of the Mechanics and Physics of Solids **43**(1):49–90

[43] Drexler A, Galler M, Elsayed H, Vallant R, Sommitsch C (2023) Critical verification of the effective diffusion concept. International Journal of Hydrogen Energy **48**(20):7499–7514

[44] Cauwels M, Claeys L, Depover T, Verbeken K (2019) The hydrogen embrittlement sensitivity of duplex stainless steel with different phase fractions evaluated by in-situ mechanical testing. Frattura ed Integrit? Strutturale **14**(51):449–458

[45] Drexler A, Helic B, Silvayeh Z, Sommitsch C, Mraczek K, Domitner J (2022) Influence of plastic deformation on the hydrogen embrittlement susceptibility of dual phase steels. Key Engineering Materials **926**:2077–2091

[46] Drexler A, Helic B, Silvayeh Z, Mraczek K, Sommitsch C, Domitner J (2022) The role of hydrogen diffusion, trapping and desorption in dual phase steels. Journal of Materials Science **57**(7):4789–4805

[47] Li X, Feng Z, Song X, Wang Y, Zhang Y (2022) Effect of hydrogen charging time on hydrogen embrittlement of cocrfemnni high-entropy alloy. Corrosion Science **198**:110,073

[48] Jin X, Xu L, Yu W, Yao K, Shi J, Wang M (2020) The effect of undissolved and temper-induced (Ti,Mo)C precipitates on hydrogen embrittlement of quenched and tempered Cr-Mo steel. Corrosion Science **166**:108,421

[49] Yang X, Yu H, Song C, Li L (2019) Hydrogen trapping behavior in vanadium microalloyed TRIP-assisted annealed martensitic steel. Metals **9**(7):741

[50] Depover T, Wan D, Wang D, Barnoush A, Verbeken K (2020) The effect of hydrogen on the crack initiation site of TRIP-assisted steels during in-situ hydrogen plasma micro-tensile testing: Leading to an improved ductility? Materials Characterization **167**:110,493

[51] Saito K, Hirade T, Takai K (2019) Hydrogen desorption spectra from excess vacancy-type defects enhanced by hydrogen in tempered martensitic steel showing quasi-cleavage fracture. Metallurgical and Materials Transactions A **50**(11):5091–5102

[52] Bellemare J, Laliberté-Riverin S, Ménard D, Brochu M, Sirois F (2020) Subtleties behind hydrogen embrittlement of cadmium-plated 4340 steel revealed

by thermal desorption spectroscopy and sustained-load tests. Metallurgical and Materials Transactions A pp 1–12

[53] Fangnon E, Malitckii E, Yagodzinskyy Y, Vilaça P (2020) Improved accuracy of thermal desorption spectroscopy by specimen cooling during measurement of hydrogen concentration in a high-strength steel. Materials **13**(5):1252

[54] Chen YS, Lu H, Liang J, Rosenthal A, Liu H, Sneddon G, McCarroll I, Zhao Z, Li W, Guo A, Cairney JM (2020) Observation of hydrogen trapping at dislocations, grain boundaries, and precipitates. Science **367**(6474):171–175

[55] Yousefi A, Itoh G, Ghorani Z, Kuramoto S (2019) Cracking process related to hydrogen behavior in a duplex stainless steel. ISIJ International **59**(12):2319–2326

[56] Rahimi N, Pax RA, MacA Gray E (2020) Mechanism of hydrogen modification of titanium-dioxide. Journal of Alloys and Compounds **815**:152,249

[57] Wang Y, Hu S, Li Y, Cheng G (2019) Improved hydrogen embrittlement resistance after quenching-tempering treatment for a Cr-Mo-V high strength steel. International Journal of Hydrogen Energy **44**(54):29,017 – 29,026

[58] Chen L, Xiong X, Tao X, Su Y, Qiao L (2020) Effect of dislocation cell walls on hydrogen adsorption, hydrogen trapping and hydrogen embrittlement resistance. Corrosion Science **166**:108,428

[59] Depover T, Monbaliu O, Wallaert E, Verbeken K (2015) Effect of Ti, Mo and Cr based precipitates on the hydrogen trapping and embrittlement of Fe-C-X Q&T alloys. International Journal of Hydrogen Energy **40**(47):16,977 – 16,984, special issue on 1st International Conference on Hydrogen Storage, Embrittlement and Applications (Hy-SEA 2014), 26-30 October 2014, Rio de Janeiro, Brazil

[60] Depover T, Verbeken K (2018) Thermal desorption spectroscopy study of the hydrogen trapping ability of W based precipitates in a Q&Tmatrix. International Journal of Hydrogen Energy **43**(11):5760 – 5769

[61] Cardenas A, Silva R, Eckstein C, dos Santos D (2018) Hydrogen effect on 2.25Cr–1Mo–0.25V bainitic steel under aging heat treatment. International Journal of Hydrogen Energy **43**(33):16,400 – 16,410

[62] Zhang Y, Hui W, Zhao X, Wang C, Cao W, Dong H (2019) Effect of reverted austenite fraction on hydrogen embrittlement of TRIP-aided medium Mn steel (0.1C-5Mn). Engineering Failure Analysis **97**:605 – 616

[63] Chatzidouros E, Traidia A, Devarapalli R, Pantelis D, Steriotis T, Jouiad M (2018) Effect of hydrogen on fracture toughness properties of a pipeline steel under simulated sour service conditions. International Journal of Hydrogen Energy **43**(11):5747 – 5759

[64] Kissinger HE (1957) Reaction kinetics in differential thermal analysis. Analytical chemistry **29**(11):1702–1706

[65] Claeys L, Cnockaert V, Depover T, De Graeve I, Verbeken K (2020) Critical assessment of the evaluation of thermal desorption spectroscopy data for duplex stainless steels: A combined experimental and numerical approach. Acta Materialia **186**:190–198

[66] Enomoto M, Hirakami D, Tarui T (2006) Modeling thermal desorption analysis of hydrogen in steel. ISIJ International **46**(9):1381–1387

[67] Hurley C, Martin F, Marchetti L, Chêne J, Blanc C, Andrieu E (2015) Numerical modeling of thermal desorption mass spectroscopy (TDS) for the study of hydrogen diffusion and trapping interactions in metals. International Journal of Hydrogen Energy **40**(8):3402–3414

[68] Diaz A, Cuesta I, Martínez-Pañeda E, Alegre J (2020) Influence of charging conditions on simulated temperature-programmed desorption for hydrogen in metals. International Journal of Hydrogen Energy **45**(43):23,704–23,720

[69] Wei FG, Enomoto M, Tsuzaki K (2012) Applicability of the kissinger's formula and comparison with the McNabb-Foster model in simulation of thermal desorption spectrum. Computational Materials Science **51**(1):322–330

[70] of Welding II (2018) Welding and allied processes – determination of hydrogen content in arc weld metal. ISO **3690:2018**:23

[71] Zaika YV, Sidorov NI, Fomkina OV (2020) Identification of hydrogen permeability parameters of membrane materials in an aggregated experiment. International Journal of Hydrogen Energy **45**(12):7433 – 7443, hydrogen separation/purification via membrane technology

[72] Zaika YV, Kostikova EK (2017) Computer simulation of hydrogen thermal desorption by ODE-approximation. International Journal of Hydrogen Energy **42**(1):405 – 415

[73] Mavrikakis M, Schwank J, Gland J (1996) Temperature programmed desorption spectra of systems with concentration gradients in the solid lattice. The Journal of Physical Chemistry **100**(27):11,389–11,395

[74] Yagodzinskyy Y, Todoshchenko O, Papula S, Hänninen H (2011) Hydrogen solubility and diffusion in austenitic stainless steels studied with thermal desorption spectroscopy. Steel Research International **82**(1):20–25

[75] Hurley C, Martin F, Marchetti L, Chêne J, Blanc C, Andrieu E (2015) Numerical modeling of thermal desorption mass spectroscopy (TDS) for the study of hydrogen diffusion and trapping interactions in metals. International Journal of Hydrogen Energy **40**(8):3402–3414

[76] Claeys L, Cnockaert V, Depover T, De Graeve I, Verbeken K (2020) Critical assessment of the evaluation of thermal desorption spectroscopy data for duplex stainless steels: A combined experimental and numerical approach. Acta Materialia **186**:190–198

[77] Castro FJ, Meyer G (2002) Thermal desorption spectroscopy (TDS) method for hydrogen desorption characterization (I): theoretical aspects. Journal of Alloys and Compounds **330-332**:59 – 63, proceedings of the International Symposium on Metal-Hydrogen Systems, Fundamentals and Applications (MH2000)

[78] Ronevich J, De Cooman B, Speer J, De Moor E, Matlock D (2012) Hydrogen effects in prestrained transformation induced plasticity steel. Metallurgical and Materials Transactions A **43**(7):2293–2301

[79] Koyama M, Bashir A, Rohwerder M, Merzlikin SV, Akiyama E, Tsuzaki K, Raabe D (2015) Spatially and kinetically resolved mapping of hydrogen in

a twinning-induced plasticity steel by use of scanning kelvin probe force microscopy. Journal of The Electrochemical Society **162**(12):C638–C647

[80] Chun YS, Park KT, Lee CS (2012) Delayed static failure of twinning-induced plasticity steels. Scripta Materialia **66**(12):960–965, viewpoint Set no. 50: Twinning Induced PlasticitySteels

[81] Guedes D, Cupertino Malheiros L, Oudriss A, Cohendoz S, Bouhattate J, Creus J, Thébault F, Piette M, Feaugas X (2020) The role of plasticity and hydrogen flux in the fracture of a tempered martensitic steel: A new design of mechanical test until fracture to separate the influence of mobile from deeply trapped hydrogen. Acta Materialia **186**:133–148

[82] Park IJ, Jo SY, Kang M, Lee SM, Lee YK (2014) The effect of ti precipitates on hydrogen embrittlement of Fe-18Mn-0.6C-2Al-xTi twinning-induced plasticity steel. Corrosion Science **89**:38–45

[83] Li L, Song B, Cai Z, Liu Z, Cui X (2019) Effect of vanadium content on hydrogen diffusion behaviors and hydrogen induced ductility loss of X80 pipeline steel. Materials Science and Engineering: A **742**:712–721

[84] Wu R, Ahlström J, Magnusson H, Frisk K, Martinsson A (2015) Charging, degassing and distribution of hydrogen in cast iron. Swerea KIMAB pp 1–41

[85] Alekseeva EL, Belyaev AK, Polyanskiy AM, Polyanskiy VA, Varshavchik EA, Yakovlev YA (2019) Surface vs diffusion in TDS of hydrogen. In: E3S Web of Conferences, EDP Sciences, vol 121, p 01012

[86] Polyanskiy V, Belyaev A, Chevrychkina A, Varshavchik E, Yakovlev Y (2021) Impact of skin effect of hydrogen charging on the Choo-Lee plot for cylindrical samples. International Journal of Hydrogen Energy **46**(9):6979–6991

[87] Oriani R (1970) The diffusion and trapping of hydrogen in steel. Acta Metallurgica **18**(1):147–157

[88] Ma M, Liang L, Wang L, Wang Y, Cheng Y, Tang B, Xiang W, Tan X (2015) Phase transformations of titanium hydride in thermal desorption process with different heating rates. International Journal of Hydrogen Energy **40**(29):8926–8934

[89] Liu Y, Wang M, Liu G (2013) Hydrogen trapping in high strength martensitic steel after austenitized at different temperatures. International journal of hydrogen energy **38**(33):14,364–14,368

[90] Takashima K, Han R, Yokoyama K, Funakawa Y (2019) Hydrogen embrittlement induced by hydrogen charging during deformation of ultra-high strength steel sheet consisting of ferrite and nanometer-sized precipitates. ISIJ International **59**(12):2327–2333

[91] Fernandez J, Cuevas F, Sanchez C (2000) Simultaneous differential scanning calorimetry and thermal desorption spectroscopy measurements for the study of the decomposition of metal hydrides. Journal of alloys and compounds **298**(1-2):244–253

[92] Liu Y, Wang M, Liu G (2013) Hydrogen trapping in high strength martensitic steel after austenitized at different temperatures. International journal of hydrogen energy **38**(33):14,364–14,368

[93] Fick A (1855) Ueber Diffusion. Annalen der Physik **170**(1):59–86

[94] Arrhenius S (1889) Uber die dissociationswarme und den einfluss der temperatur auf den dissociationsgrad der elektrolyte. Zeitschrift fur Physikalische Chemie **4U**(1):96–116

[95] Darken LS, Smith RP (1949) Behavior of hydrogen in steel during and after immersion in acid. Corrosion **5**(1):1–16

[96] McNabb A, Foster PK (1963) A new analysis of the diffusion of hydrogen in iron and ferrite. Trans of the metallic Soc **227**:618–627

[97] Pressouyre G (1979) A classification of hydrogen traps in steel. Metallurgical Transactions A **10**(10):1571–1573

[98] Pressouyre G (1983) Hydrogen traps, repellers, and obstacles in steel; consequences on hydrogen diffusion, solubility, and embrittlement. Metallurgical transactions A **14**(10):2189–2193

[99] Lecoester F, Chêne J, Noel D (1999) Hydrogen embrittlement of the Ni-base Alloy 600 correlated with hydrogen transport by dislocations. Materials Science and Engineering: A **262**(1):173–183

[100] Hirth JP (1980) Effects of hydrogen on the properties of iron and steel. Metallurgical Transactions A **11**(6):861–890

[101] McLean D, Maradudin A (1958) Grain boundaries in metals. Physics Today **11**(7):35

[102] Polyanskiy A, Polyanskiy V, Yakovlev YA (2014) Experimental determination of parameters of multichannel hydrogen diffusion in solid probe. International Journal of Hydrogen Energy **39**(30):17,381–17,390

[103] Belyaev A, Polyanskiy A, Polyanskiy V, Sommitsch C, Yakovlev YA (2016) Multichannel diffusion vs tds model on example of energy spectra of bound hydrogen in 34CrNiMo6 steel after a typical heat treatment. International Journal of Hydrogen Energy **41**(20):8627–8634

[104] Andronov D, Arseniev D, Polyanskiy A, Polyanskiy V, Yakovlev Y (2017) Application of multichannel diffusion model to analysis of hydrogen measurements in solid. International Journal of Hydrogen Energy **42**(1):699–710

[105] Turnbull A, Carroll M, Ferriss D (1989) Analysis of hydrogen diffusion and trapping in a 13% chromium martensitic stainless steel. Acta Metallurgica **37**(7):2039–2046

[106] Enomoto M, Hirakami D (2015) Influence of specimen thickness on thermal desorption spectrum of hydrogen in high strength SCM435 steel. ISIJ International **55**(11):2492–2498

[107] Liu Y, Wang M, Liu G (2013) Hydrogen trapping in high strength martensitic steel after austenitized at different temperatures. International journal of hydrogen energy **38**(33):14,364–14,368

[108] Takashima K, Han R, Yokoyama K, Funakawa Y (2019) Hydrogen embrittlement induced by hydrogen charging during deformation of ultra-high strength steel sheet consisting of ferrite and nanometer-sized precipitates. ISIJ International **59**(12):2327–2333

[109] Claeys L, Cnockaert V, Depover T, De Graeve I, Verbeken K (2020) Critical assessment of the evaluation of thermal desorption spectroscopy data for

duplex stainless steels: A combined experimental and numerical approach. Acta Materialia **186**:190–198

[110] Rhode M, Mente T, Steppan E, Steger J, Kannengiesser T (2018) Hydrogen trapping in T24 Cr-Mo-V steel weld joints-microstructure effect vs. experimental influence on activation energy for diffusion. Welding in the World **62**(2):277–287

[111] Laureys A, Claeys L, Pinson M, Depover T, Verbeken K (2020) Thermal desorption spectroscopy evaluation of hydrogen-induced damage and deformation-induced defects. Materials Science and Technology **36**(13):1389–1397

[112] Nagumo M, Takai K, Okuda N (1999) Nature of hydrogen trapping sites in steels induced by plastic deformation. Journal of alloys and compounds **293**:310–316

[113] Depover T, Laureys A, Pérez Escobar D, Van den Eeckhout E, Wallaert E, Verbeken K (2018) Understanding the interaction between a steel microstructure and hydrogen. Materials **11**(5):698

[114] Zhang Z, Obasi G, Morana R, Preuss M (2016) Hydrogen assisted crack initiation and propagation in a nickel-based superalloy. Acta Materialia **113**:272–283

[115] Lee AC, Parakh A, Sleugh A, Tertuliano OA, Lam S, Weker JN, Hosemann P, Gu XW (2023) Detection of voids in hydrogen embrittled iron using transmission x-ray microscopy. International Journal of Hydrogen Energy **48**(5):1968–1978

[116] Kumamoto T, Koyama M, Sato K, Tsuzaki K (2019) Strain-rate sensitivity of hydrogen-assisted damage evolution and failure in dual-phase steel: From vacancy to micrometer-scale void growth. Engineering Fracture Mechanics **216**:106,513

[117] Diehl D, Schneider EL, Clarke TGR (2021) Formation of hydrogen blisters during the solution treatment for aluminum alloys. Tecnologia em metalurgia, materiais e mineração São Paulo, SP **18**:e2374

Chapter 23
Bending Waves in Mass-in-Mass Metamaterial

Alexey V. Porubov and Yuting Zhao

Abstract Bending waves are studied for the mass-in -mass metamaterial model. The discrete equations of motion are derived from the variational principle. The long wavelength continuum limits of the equations are obtained in the form of the coupled partial differential equations. Dispersion relation analysis of the continuum equations demonstrates dependence of the band gap on the order of continualization. Also, no band gap of the constant width is obtained for the phase velocity as the order of continualization growths. Dispersion analysis of the discrete equations confirms this finding.

23.1 Introduction

Complex structure of the crystalline lattices provides effective modelling of new mechanical processes in solids [1–4]. Considerable attention is paid to the acoustic metamaterials [5–7], in particular, metamaterial mass-in-mass lattice model [5–14]. Propagation or non-propagation of acoustic waves in an acoustic metamaterial is caused by the presence of a band gap in the dispersion relation. Experimental realization of the metamaterial model with the internal resonators can be found in [15–18].

Longitudinal and shear strain waves are mainly studied in solids. Much less papers are devoted to consideration of bending waves [19, 20]. Usually bending waves are modelled in the continuum approach, however, there are papers where discrete

Alexey V.Porubov
Institute for Problems in Mechanical Engineering, Bolshoy prospekt 61, V.O., 1999178 St. Petersburg, Russian Federation,
e-mail: alexey.porubov@gmail.com

Yuting Zhao
Peter the Great St. Petersburg Polytechnic University, Polytechnicheskaya, 29, 195251 St.Petersburg, Russian Federation,
e-mail: chzhao13.yu@edu.spbstu.ru

consideration of the lattices is used [21]. Discrete modeling based on the study of the difference governing equations is a most favorable method for finding the solution of the metamaterial problems. The continuum modelling is used much less frequently [11–14]. The usual transfer from discrete to continuum approach is based on the long wavelength continuum limit giving rise to the partial differential governing equations [1–4]. It restricts the study by the long strain waves, however, continuum equations for the mass-in-mass metamaterial chain predict the same features of the band gap for longitudinal waves as the original lattice models even outside the long wavelengths [14].

The present paper concerns continuum modelling of the bending waves in the mass-in-mass metamaterial chain. In Sect. 23.2 the model of bending waves in the linearly elastic mass-in-mass metamaterial system is developed. The discrete equations of motion are obtained as well as their long wavelength continuum limit. The dispersion analysis is performed in Sect. 23.3 for the continuum equations of the basic and higher-order continuum limits. Next Section 23.4 is devoted to a comparison of the dispersion curves of the continuum equations with those obtained for the discrete equations.

23.2 Bending in Mass-in-Mass Chain

Consider the lattice model shown in Fig 23.1. The attached masses m are located inside the main masses M being attached to them by the springs with the stiffness κ. The masses M are connected each other by the springs with the stiffness C. We consider the bending motion of the main chain, and C accounts for the bending stiffness. The displacements of the masses of the main chain are denoted by Y_n while those of the attached masses by y_n.
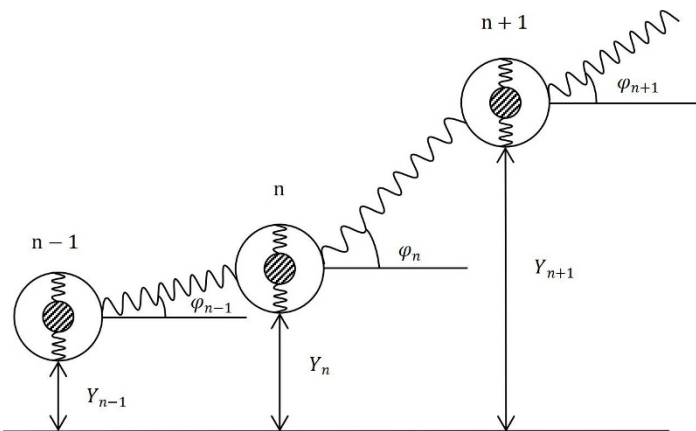
Fig. 23.1: Bending mass-in-mass metamterial chain.

The motion is described by the angular variations. We introduce φ_n to account for the angles realtive to the horizontal direction as shown in Fig. 23.1. Then

$$\varphi_n = \arcsin\left(\frac{Y_{n+1} - Y_n}{h}\right), \qquad (23.1)$$

where h is the distance between masses M. Then the angular variation of the mass with the number n is described by the angle θ_n,

$$\theta_n = \varphi_n - \varphi_{n-1} \qquad (23.2)$$

We consider only neighbouring interactions of the mass with the number n taking into account an influence of the masses with the numbers $n-1$ and $n+1$. Then we use

$$\theta_{n+1} = \varphi_{n+1} - \varphi_n, \qquad \theta_{n-1} = \varphi_{n-1} - \varphi_{n-2} \qquad (23.3)$$

We consider the case of infinitesimal small variations of the displacements that corresponds to the linearized problem. In this case Eq.(23.1) becomes

$$\varphi_n = \frac{Y_{n+1} - Y_n}{h}, \qquad (23.4)$$

and the functions θs are

$$\theta_n = \frac{Y_{n+1} - 2Y_n + Y_{n-1}}{h}, \quad \theta_{n+1} = \frac{Y_{n+2} - 2Y_{n+1} + Y_n}{h}, \quad \theta_{n-1} = \frac{Y_n - Y_{n-1} + Y_{n-2}}{h} \qquad (23.5)$$

Then the potential energy Π_n includes terms responsible for interactions between the masses M in the main chain and those of between the masses M and the attached masses m,

$$\Pi_n = \frac{C}{2}\left(\theta_{n-1}^2 + \theta_n^2 + \theta_{n+1}^2\right) + \frac{\kappa}{2}(Y_n - y_n)^2, \qquad (23.6)$$

The kinetic energy, K_n is

$$K_n = \frac{M}{2}\dot{Y}_n^2 + \frac{m}{2}\dot{y}_n^2 + \frac{J}{2}\dot{\theta}_n^2 \qquad (23.7)$$

where J is the inertia.

We use the variational Hamilton- Ostrogradsky principle or the Lagrange equations to obtain the equations of motion. The Lagrange equations in our case are

$$\frac{d}{dt}\frac{\partial\,(K_n - \Pi_n)}{\partial\dot{Y}_n} - \frac{\partial\,(K_n - \Pi_n)}{\partial\,Y_n} = 0, \quad \frac{d}{dt}\frac{\partial\,(K_n - \Pi_n)}{\partial\dot{y}_n} - \frac{\partial\,(K_n - \Pi_n)}{\partial\,y_n} = 0 \quad (23.8)$$

These equations allow us to obtain coupled differential-difference equations of motion

$$M\ddot{Y}_n - 2J(\ddot{Y}_{n-1} - 2\ddot{Y}_n + \ddot{Y}_{n+1}) + C(Y_{n-2} - 4Y_{n-1} + 6Y_n - 4Y_{n+1} + Y_{n+2}) + \kappa(Y_n - y_n) = 0,$$
$$m\ddot{y}_n + \kappa(y_n - Y_n) = 0. \qquad (23.9)$$

These equations can be solved directly. Another method of the study is obtaining of the long wavelength continuum limit of Eqs. (23.9). In this case the continuum functions $V(x,t)$, $v(x,t)$ are introduced for description of the displacements Y_n, y_n of the masses M, m. The continuum displacements of the neighboring masses are sought using the long wavelength approximation [1], based on the Taylor series,

$$Y_{n\pm1} = V \pm h\,V_x + \frac{h^2}{2}V_{xx} \pm \frac{h^3}{6}V_{xxx} + \frac{h^4}{24}V_{xxxx} + ...,$$

Substituting these series into Eqs. (23.9) and retaining there only the first nonzero terms, we obtain the basic-order continuum limit in the form of coupled partial differential equations,

$$M\,V_{tt} - 2\,J\,h^2 V_{xxtt} + C\,h^4 V_{xxxx} + \kappa(V - v) = 0, \qquad m\,v_{tt} + \kappa(v - V) = 0. \quad (23.10)$$

The particular case $\kappa = 0$, $m = 0$, $v = 0$ corresponds to the equation for the bending waves in an elastic wave guide obtained previously in [19, 22].

Retaining more non-zero terms in the continuum equations, we obtain a higher-order continuum model instead of Eqs. (23.10),

$$M\,V_{tt} - 2J\,h^2 V_{xxtt} + C\,h^4 V_{xxxx} - \frac{J\,h^4}{6}V_{xxxxtt} + \frac{C\,h^6 V_{xxxxxx}}{6} + \kappa(V - v) = 0,$$
$$(23.11)$$
$$m\,v_{tt} + \kappa(v - V) = 0. \qquad\qquad (23.12)$$

where higher-order dispersion of the main chain is taken into account.

23.3 Dispersion Analysis

The solution to Eqs. (23.10) is sought in the form

$$V = A\exp\!\big(\iota\,(k\,x - \omega t - x_0)\big), \qquad v = B\exp\!\big(\iota\,(k\,x - \omega t - x_0)\big), \qquad (23.13)$$

where x_0 accounts for an initial position of the wave, A and B are the wave amplitudes, k is the wave number, ω is the wave frequency, ι is the imaginary unit. Substitution of Eq. (23.13) into Eqs. (23.10) gives rise to

$$A = \frac{B(\kappa - \omega^2\,m)}{\kappa}, \qquad\qquad (23.14)$$

and the dispersion relation,

$$m\,(M + 2J\,h^2\,k^2)\,\omega^4 - (\kappa(M + m) + 2\kappa J\,h^2\,k^2 + mC\,h^4 k^4)\,\omega^2 + C\,h^4 k^4 \kappa = 0,$$
$$(23.15)$$

whose solutions are $\omega = \omega_a$, $\omega = \omega_o$, where

$$\omega_a^2 = \frac{\kappa(M+m)2\kappa + 2J\ h^2\ k^2 + mC\ h^4 k^4)}{2m\ (M+2J\ h^2\ k^2)} -$$

$$\frac{\sqrt{(\kappa(M+m)+2\kappa J\ h^2\ k^2 + mC\ h^4 k^4))^2 - 4C\ h^4 k^4 m\ \kappa(M+2J\ h^2\ k^2)}}{2m\ (M+2J\ h^2\ k^2)}. \quad (23.16)$$

$$\omega_o^2 = \frac{\kappa(M+m)+2\kappa J\ h^2\ k^2 + mC\ h^4 k^4)}{2m\ (M+2J\ h^2\ k^2)} +$$

$$\frac{\sqrt{(\kappa(M+m)+2\kappa J\ h^2\ k^2 + mC\ h^4 k^4))^2 - 4C\ h^4 k^4 m\ \kappa(M+2J\ h^2\ k^2)}}{2m\ (M+2J\ h^2\ k^2)}. \quad (23.17)$$

The acoustic branch of the frequency ω_a varies from 0 to $\sqrt{\kappa/m}$, while the optic one, ω_o, lies in the interval $(\sqrt{\kappa(m+M)/(m\ M)}, \infty)$. Therefore, there is a band gap $\sqrt{\kappa/m} < \omega < \sqrt{\kappa(m+M)/(m\ M)}$ where no harmonic traveling wave propagates. It has the same width as that known for longitudinal waves. Typical curves for ω_a and ω_o are shown in Fig. 23.2. Despite the long wavelength limit is considered, the band gap is observed at semi-infinite interval of the values of k.

We proceed with consideration of the phase velocities, V_p, where $V_{pa} = \omega_a/k$, $V_{po} = \omega_o/k$. Shown in Fig. 23.3 are the curves of the phase velocities. We see non-monotonic tendency to the asymptotic values at $k \to \infty$ for both velocities, curves 1 and 5 in 23.3. As a result, the band gap lies between the maximum and the minimum of the curves, lines 3 and 4. this is different from the case of longitudinal waves, where the dependence for the phase velocity demonstrates the band gap between the asymptotes like for the frequency [14].

We continue with the study of the higher-order continuum limit. The solution of Eqs. (23.11), (23.12) is sought in the form of (23.13). The dispersion relation is

$$m\left(6M + J\ h^2\ k^2(12 - h^2 k^2)\right)\omega^4 + C\ h^4 k^4 \kappa(6 - h^2 k^2) -$$

$$\left(6\kappa(M+m) + J\ \kappa\ h^2\ k^2(12 - h^2 k^2) + C\ m\ h^4 k^4(6 - h^2 k^2)\right)\omega^2 = 0, \quad (23.18)$$

whose solutions are

Fig. 23.2 Dispersion curves for the frequency. 1. Optic branch ω_o (23.17). 2. Horizontal dashed line corresponding to ω_o at $k = 0$. 3. Horizontal dashed line corresponding to acoustic branch ω_a (23.16) at $k \to \infty$. 4. Acoustic acoustic branch ω_a (23.16)
.
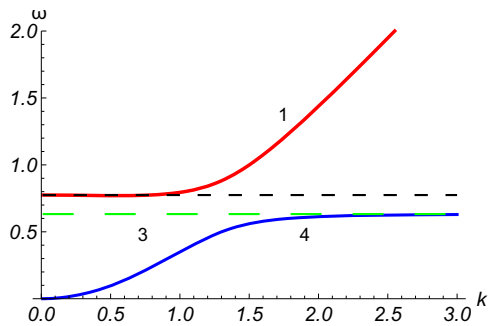
Fig. 23.3 Dispersion curves for the phase velocity. 1. Optic branch ω_o/k. 2. Horizontal dashed line corresponding to ω_o/k at $k \to \infty$. 3. Horizontal dashed line corresponding to the minimum of the optic branch. 4. Horizontal dashed line corresponding to the maximum of the acoustic branch ω_a/k (23.16). 5. Acoustic branch ω_a/k (23.16)

.
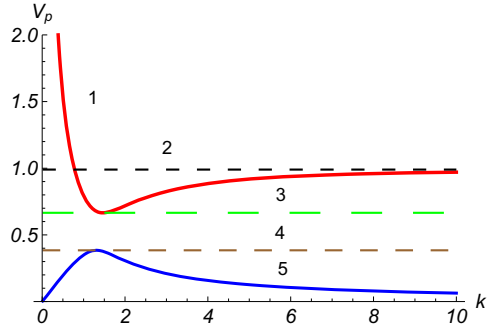
$$\omega_a^2 = \frac{6\kappa(M+m) + J\,\kappa\,h^2\,k^2(12 - h^2k^2) + C\,m\,h^4k^4(6 - h^2k^2)}{2m\,(6M + J\,\kappa\,h^2\,k^2(12 - h^2k^2))} -$$

$$\frac{1}{2m\,(6M + J\,h^2\,k^2(12 - h^2k^2))}\left(\,[6\kappa(M+m) + J\,\kappa\,h^2\,k^2(12 - h^2k^2) + \right.$$

$$\left. C\,m\,h^4k^4(6 - h^2k^2)]^2 - 4C\,h^4k^4\kappa(6 - h^2k^2)m\,(6M + J\,h^2\,k^2(12 - h^2k^2))\right)^{\frac{1}{2}}.$$

$$(23.19)$$

$$\omega_o^2 = \frac{6\kappa(M+m) + J\,\kappa\,h^2\,k^2(12 - h^2k^2) + C\,m\,h^4k^4(6 - h^2k^2)}{2m\,(6M + J\,h^2\,k^2(12 - h^2k^2))} +$$

$$\frac{1}{2m\,(6M + J\,h^2\,k^2(12 - h^2k^2))}\left(\,[6\kappa(M+m) + J\,\kappa\,h^2\,k^2(12 - h^2k^2) + \right.$$

$$\left. C\,m\,h^4k^4(6 - h^2k^2)]^2 - 4C\,h^4k^4\kappa(6 - h^2k^2)m\,(6M + J\,h^2\,k^2(12 - h^2k^2))\right)^{\frac{1}{2}}.$$

$$(23.20)$$

We see that the denominator of the solutions becomes zero as the wave number growths. The solutions becomes unbounded, that is why we can visualize the solutions for the frequency and the phase velocity only for small values of k as shown in Figs. 23.4 and 23.5. It does not contradict long wavelength continuum limit used on obtaining continuum equations from original discrete equations (23.9).

We see the band gap between lines 3 and 4 in Fig. 23.4 in the interval of small values of k, the width and the position of the band gap is the same as for basic model shown in Fig. 23.2 with the exception of small variations of the curve 3 around upper band 2. However, increase in the value of k results in the fatal variations in ω and breaking of the tendency to the asymptotes.

The phase velocities in Fig. 23.5 demonstrate variation in the width of the area between the acoustic, curve 2, and optic curve 1, velocities. The width decreases as the value of k increases. It seems this area between the velocities can't be considered as the band gap.
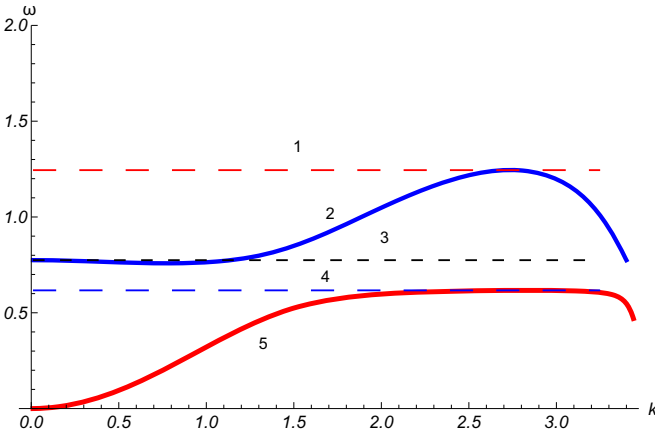
Fig. 23.4: Dispersion curves for the frequencies for the higher-order model. 1. Maximum of the optic frequency 2. Optic frequency 3. Line corresponding to the value of ω_o of the basic -order model at $k = 0$. 4. Line corresponding to the value of ω_a of the basic -order model at $k \to \infty$. 5. Acoustic frequency ω_a.

Fig. 23.5 Dispersion curves for the phase velocities for the higher-order model. 1. Optic branch. 2. Acoustic branch.
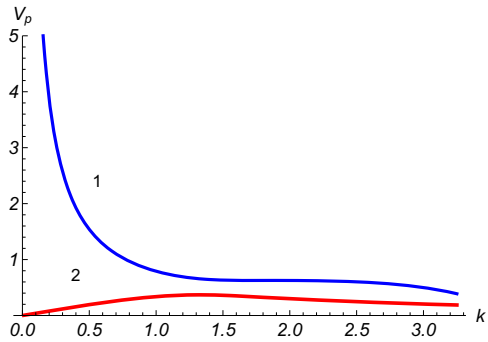
23.4 Discussion

The analysis of the dispersion relations of the continuum models of different order reveals variation in the description of the band gap area. Since continuum models are the long wavelength approximations of the discrete model (23.9), we study now the dispersion relation of the original equations. The solution of Eqs. (23.9) is sought in the form

$$Y_n = A \, \exp\Big(\iota\,(k\,h\,n - \omega\,t)\Big), \qquad y_n = B \, \exp\Big(\iota\,(k\,h\,n - \omega\,t)\Big). \tag{23.21}$$

Substitution of Eqs. (23.21) into Eqs. (23.9) gives rise to the dispersion relation,

$$m\Big(M + 8J\sin^2\Big(\frac{k\,h}{2}\Big)\Big)\,\omega^4 - \Big[\kappa(m+M) - 8J\kappa\sin^2\Big(\frac{k\,h}{2}\Big)$$

$$+16m\,C\,\sin^4\left(\frac{k\,h}{2}\right)\right]\,\omega^2+16\,C\,\sin^4\left(\frac{k\,h}{2}\right)=0. \qquad (23.22)$$

The solution to Eq. (23.22) consists of two branches, acoustic and optic,

$$\omega_a^2 = \frac{\kappa(m+M)-8J\kappa\sin^2\left(\frac{k\,h}{2}\right)+16m\,C\,\sin^4\left(\frac{k\,h}{2}\right)}{2m\left(\left[M+8J\sin^2\left(\frac{k\,h}{2}\right)\right]\right)} -$$

$$\frac{1}{2m\left[M+8J\sin^2\left(\frac{k\,h}{2}\right)\right]}\left(\left(\kappa(m+M)-8J\kappa\sin^2\left(\frac{k\,h}{2}\right)+16m\,C\,\sin^4\left(\frac{k\,h}{2}\right)\right)^2 - \right.$$

$$\left. 64mC\,\sin^4\left(\frac{k\,h}{2}\right)\left[M+8J\sin^2\left(\frac{k\,h}{2}\right)\right]\right)^{\frac{1}{2}} \qquad (23.23)$$

$$\omega_o^2 = \frac{\kappa(m+M)-8J\kappa\sin^2\left(\frac{k\,h}{2}\right)+16m\,C\,\sin^4\left(\frac{k\,h}{2}\right)}{2m\left(\left[M+8J\sin^2\left(\frac{k\,h}{2}\right)\right]\right)} +$$

$$\frac{1}{2m\left[M+8J\sin^2\left(\frac{k\,h}{2}\right)\right]}\left(\left(\kappa(m+M)-8J\kappa\sin^2\left(\frac{k\,h}{2}\right)+16m\,C\,\sin^4\left(\frac{k\,h}{2}\right)\right)^2 - \right.$$

$$\left. 64mC\,\sin^4\left(\frac{k\,h}{2}\right)\left[M+8J\sin^2\left(\frac{k\,h}{2}\right)\right]\right)^{\frac{1}{2}} \qquad (23.24)$$

The shapes of the solution are shown in Fig. 23.6. The band gap is seen, and it the same as in the continuum limit. We can observe small oscillations near the upper border of the band gap. As for the phase velocity. we see in Fig. 23.7 a decrease in the width of the area between the velocity curves similar to that shown for the higher-order continuum model.

Therefore, higher-order continuum limit predicts the dispersion properties better than the basic-order one. However, dispersion curves are obtained on the basis of the periodic solution, and further numerical study is needed to see how the band gap is

Fig. 23.6 Dispersion curves for the frequencies for the discrete model. 1. Optic frequency. 2. Line corresponding to the upper boundary of the basic-order continuum model. 4. Line corresponding to the lower boundary of the basic-order continuum model. 5. Acoustic frequency ω_a.
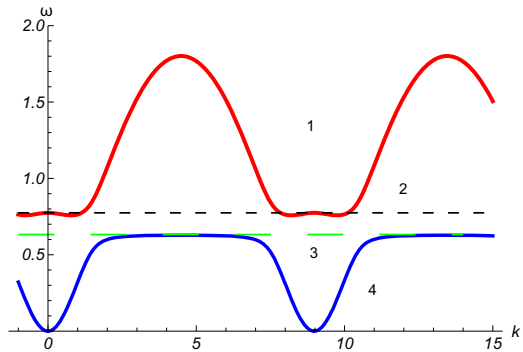
Fig. 23.7 Dispersion curves for the phase velocities for the discrete model. 1 Optic branch. 2 - Acoustic branch.
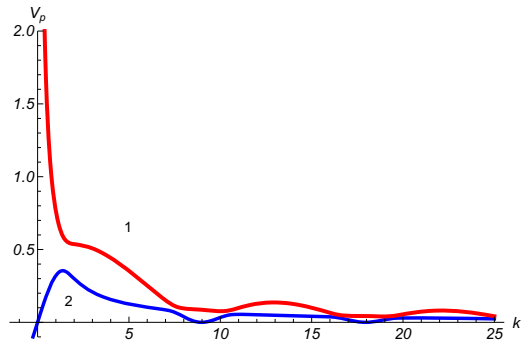
realized in an unsteady process. One possibility is the periodic boundary excitation. Of special interest are the localized bending waves. Recently no band gap has been found in the study of localized longitudinal wave dynamics for the mass-in-mass model [14]. Similar study should be performed for the bending waves. Of course non-linear consideration of the bending wave mass-in-mass model deserves special study both analytical and numerical like it was already done for longitudinal waves.

References

[1] Born M, Huang K (1954) Dynamical Theory of Crystal Lattices. Clarendon Press, Oxford

[2] Andrianov IV, Awrejcewicz J, Weichert D (2010) Improved continuous models for discrete media. Mathematical Problems in Engineering **2010**:986,242

[3] Askar A (1985) Lattice Dynamical Foundations of Continuum Theories. World Scientific, Singapore

[4] Ostoja-Starzewski M (2002) Lattice models in micromechanics. Applied Mechanics Reviews **55**(1):35–60

[5] Huang HH, Sun CT, Huang GL (2009) On the negative effective mass density in acoustic metamaterials. International Journal of Engineering Science **47**(4):610–617

[6] Ma G, Sheng P (2016) Acoustic metamaterials: From local resonances to broad horizons. Science Advances **2**(2):e1501,595

[7] Eremeyev VA, Turco E (2020) Enriched buckling for beam-lattice metamaterials. Mechanics Research Communications **103**:103,458

[8] Lazarov BS, Jensen JS (2007) Low-frequency band gaps in chains with attached non-linear oscillators. International Journal of Non-Linear Mechanics **42**(10):1186–1193

[9] Cveticanin L, Cveticanin D (2018) Acoustic metamaterials: Theory and application. In: Herisanu N, Marinca V (eds) Acoustics and Vibration of Mechanical Structures—AVMS-2017, Springer International Publishing, Cham, pp 21–32

[10] Fang X, Wen J, Bonello B, Yin J, Yu D (2017) Wave propagation in one-dimensional nonlinear acoustic metamaterials. New Journal of Physics **19**(5):053,007

[11] Erofeev V, Kolesov D, Malkhanov A (2020) Nonlinear strain waves in a metamaterial defined a mass-to-mass chain. IOP Conference Series: Materials Science and Engineering **709**(3):033,037

[12] Porubov AV, Antonov ID (2021) On control of harmonic waves in an acoustic metamaterial. Mechanics Research Communications **116**:103,745

[13] Porubov AV (2021) Wave modulation in a nonlinear acoustic metamaterial. International Journal of Non-Linear Mechanics **137**:103,788

[14] Porubov AV, Krivtsov AM (2022) Dispersive propagation of localized waves in a mass-in-mass metamaterial lattice. Continuum Mechanics and Thermodynamics **34**(6):1475–1483

[15] Yao S, Zhou X, Hu G (2008) Experimental study on negative effective mass in a 1d mass–spring system. New Journal of Physics **10**(4):043,020

[16] Zhou J, Cheng Y, Zhang H, Huang G, Hu G (2015) Experimental study on interaction between a positive mass and a negative effective mass through a mass–spring system. Theoretical and Applied Mechanics Letters **5**(5):196–199

[17] Yang T, Song ZG, Clerkin E, Zhang YW, Sun JH, Su YS, Chen LQ, Hagedorn P (2017) A programmable nonlinear acoustic metamaterial. AIP Advances **7**(9):095,323

[18] Zhou X, Liu X, Hu G (2012) Elastic metamaterials with local resonances: an overview. Theoretical and Applied Mechanics Letters **2**(4):041,001

[19] Erofeev VI (1991) Three-dimensional vibrations of a flexible rod. Soviet Applied Mechanics **27**:911–916

[20] Zemlyanukhin AI, Bochkarev AV, Mogilevich LI, Tindova EG (2016) Axisymmetric longitudinal-bending waves in a cylindrical shell interacting with a nonlinear elastic medium. Modelling and Simulation in Engineering **2016**:6596,231

[21] Wu H, Kuang Y (2022) Propagation characteristics of flexural wave in one-dimensional phononic crystals based on lattice dynamics model. Journal of Applied Mathematics and Physics **10**:1416–1431

[22] Erofeev VI, Leontieva AV (2021) Dispersion and Spatial Localization of Bending Waves Propagating in a Timoshenko Beam Laying on a Nonlinear Elastic Base. Mechanics of Solids **56**(4):443–454

Chapter 24
Numerical Investigations of Large Amplitude Oscillations of Planar Parametrically Excited Beams

Alois Steindl, Roman Buchta, Michael Ruttmann, and Yury Vetyukov

Abstract We consider a straight slender visco-elastic beam under periodic axial excitation. In order to determine the stability boundary of the undeformed configuration and the parameter domain for periodic solutions we apply different analytical and numerical methods, like simulation of a FE-model and path-following packages for different versions of reduced order models.

24.1 Introduction and Model Description

Periodic excitations of mechanical devices are a frequently investigated research topic with a lot of practical results [1, 2]. In this article we focus on parametric excitations, which act indirectly by causing variations of parameters. A very simple and well known example is the pendulum with vertically oscillating support; if the excitation frequency is close to twice the eigenfrequency of the pendulum, large oscillations may occur. Elaborate investigations of the Mathieu equation, which governs this type of oscillations, can be found in [3, 4].

Equations for the oscillations of a beam under periodic axial forcing are derived in [5], these equations will be used for the analytical treatment; the author also considers a periodic motion of the fixed support and an additional mass at the free end. It turns out, that the additional mass can change the branching behaviour of the bifurcating

Alois Steindl · Yury Vetyukov
Institute for Mechanics and Mechatronics, TU Wien, Getreidemarkt 9, 1060 Wien, Austria
e-mail: Alois.Steindl@tuwien.ac.at, Yury.Vetyukov@tuwien.ac.at

Roman Buchta
Institute of Energy Systems and Thermodynamics, TU Wien, Getreidemarkt 9, 1060 Wien, Austria
e-mail: roman.buchta@tuwien.ac.at

Michael Ruttmann
TU Wien, Getreidemarkt 9, 1060 Wien, Austria,
e-mail: e11909827@student.tuwien.ac.at

periodic solutions. In [5] numerical and experimental results are compared showing good agreement.

In our treatment of the problem we investigate numerical methods to determine the stability limit of the straight state of the beam and to obtain the range and stability of the excited periodic oscillations. Even for moderate excitation forces the oscillation amplitudes become quite large.

24.1.1 Model of a Parametrically Excited Beam

We consider a straight slender beam of length L, bending stiffness EJ, mass per unit length ϱA, and tensional stiffness EA, which is simply supported at its endpoints, where the left support is fixed and the right roller support can slide freely, as shown in Fig. 24.1. At the right end an axial periodic compressive force $P(t) = P_0 + P_t \sin(\vartheta t)$ is applied.

Explicit nonlinear differential equations for an inextensible beam were derived in [5]. The equations of planar motion (Fig. 24.2) for a relaxed beam are

$$\varrho A \boldsymbol{r}_{tt}(s,t) = \boldsymbol{n}_s(s,t), \tag{24.1a}$$

$$\varrho J \theta_{tt}(s,t) = \boldsymbol{m}_s(s,t) + \boldsymbol{\tau}(s,t) \times \boldsymbol{n}(s,t), \tag{24.1b}$$

where $\boldsymbol{\tau}(s,t) = \boldsymbol{r}_s(s,t), \boldsymbol{n}(s,t) = N(s,t)\boldsymbol{b}_1(s,t) + Q(s,t)\boldsymbol{b}_2(s,t), \boldsymbol{m}(s,t) = M(s,t)\boldsymbol{e}_3$, respectively, denote internal force and internal moment, transmitted in cross-section with the material length coordinate s at time t. Subscripts denote partial derivatives and the unit vectors $(\boldsymbol{b}_1, \boldsymbol{b}_2)$ are collinear with the normal and transverse directions of the deformed beam cross section. The position vector is given by

$$\boldsymbol{r}(s,t) = (s + u(s,t))\boldsymbol{e}_1 + v(s,t)\boldsymbol{e}_2, \tag{24.2}$$
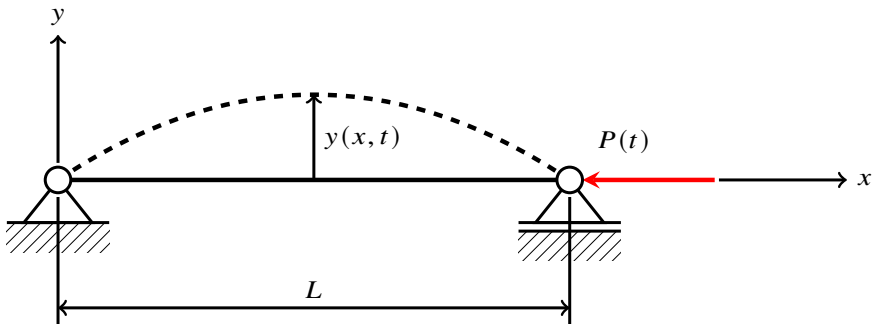
Fig. 24.1: Simply supported beam under axial excitation.
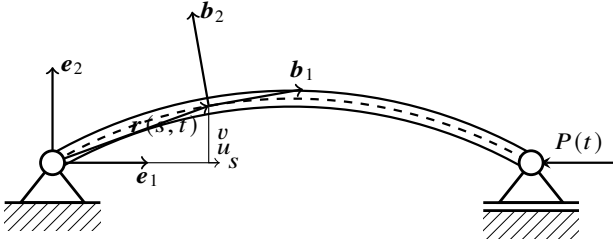
Fig. 24.2: Deformed planar configuration of the beam. The orientation of the cross section is described by the orthogonal tripod $(\boldsymbol{b}_1, \boldsymbol{b}_2, \boldsymbol{b}_3 = \boldsymbol{e}_3)$. For an Euler-Bernoulli beam the tangent vector to the centerline $\boldsymbol{r}(s,t)$ coincides with $\boldsymbol{b}_1$.

where u and v denote the horizontal and vertical deflections of the beam from the undeformed position $s\boldsymbol{e}_1$.

The boundary conditions are

$$u(0,t) = 0, \qquad v(0,t) = 0, \qquad v(L,t) = 0,$$
$$M(0,t) = 0, \qquad M(L,t) = 0, \qquad \boldsymbol{n}(L,t) \cdot \boldsymbol{e}_1 = -P(t). \qquad (24.3)$$

Assuming that the beam is inextensible and unshearable as per the kinematic constraint $\boldsymbol{\tau} = \boldsymbol{b}_1$ (which also implies that s remains the arc length coordinate in the deformed state), neglecting the rotatory inertia and using the variables

$$\theta = \arcsin(v_s), \quad \kappa = \theta_s = v_{ss}/\cos\theta = v_{ss}/\sqrt{1 - v_s^2},$$

where θ denotes the inclination angle of the centerline, κ is the curvature and taking the inner product of (24.1a) with $\boldsymbol{b}_1$ we obtain the equation

$$N_s = \kappa Q + \varrho A \boldsymbol{r}_{tt} \cdot \boldsymbol{b}_1, \qquad (24.4)$$

which together with the boundary condition $N(L)\cos(\theta(L)) - Q(L)\sin(\theta(L)) = -P$ yields the integral expression

$$N(s,t) = \frac{-P(t)}{\cos(\theta(L,t))} + Q(L,t)\tan(\theta(L,t)) - \int_s^L \kappa Q + \varrho A(u_{tt}\cos\theta + v_{tt}\sin\theta)d\xi. \qquad (24.5)$$

Assuming a visco-elastic material law

$$M = EJ(\kappa + \alpha\kappa_t) \qquad (24.6)$$

we obtain with $Q = -M_s$, which follows from (24.1b),

$$\varrho A(-u_{tt}\sin\theta + v_{tt}\cos\theta) = -M_{ss} + \kappa N \qquad (24.7)$$

by projecting (24.1a) into the direction of b_2.

The horizontal motion $u(s,t)$ is obtained by integrating the inextensibility constraint $r_s^2 = 1$

$$u(s,t) = \int_0^s \sqrt{1 - v_s^2(\xi,t)}\,d\xi - s. \tag{24.8}$$

It should be noted, that this formula is valid, as long as the beam has no vertical segment. For large deflections different variables must be used.

In order to obtain the linearized equations for small deformations $|v_s| \ll 1$ we set

$$\theta = v_s, \quad \kappa = v_{ss}, \quad M = EJ(v_{ss} + \alpha v_{sst}), \quad N = -P$$

and observe, that (24.8) does not contribute linear terms. That gives the linear PDE

$$\varrho A v_{tt} = -EJ(v_{ssss} + \alpha v_{sssst}) - P v_{ss}. \tag{24.9}$$

24.1.2 Finite Element Formulation

In order to treat the model with an FE code, the centerline of the beam in both directions is approximated by cubic Hermite polynomials on an equidistant grid with N intervals, which guarantees the necessary C^1 smoothness [6]. Because the inextensibility condition cannot be fulfilled exactly with this type of approximation, we introduce a large tension stiffness EA and also a small amount of material damping in the longitudinal direction to avoid high frequency vibrations. The strain energy is an integral of the quadratic form of the tensional deformation ϵ and curvature κ,

$$U = \frac{1}{2} \int_0^L \left(EA\epsilon^2 + EJ\kappa^2 \right) ds, \tag{24.10}$$

where

$$\epsilon = \frac{r_s^2 - 1}{2},$$
$$\kappa = \frac{r_{1,s}r_{2,ss} - r_{2,s}r_{1,ss}}{r_s^2}.$$

The potential of the excitation force $P(t)$ is given by

$$V_P = r_1(L,t)P(t), \tag{24.11}$$

and the kinetic energy by

$$T = \frac{\varrho A}{2} \int_0^L r_t^2 ds. \tag{24.12}$$

The influence of the damping forces is modelled by Rayleighs dissipation function

$$R = \int_0^L \frac{1}{2} \left(EA\alpha_1 \epsilon_t^2 + EJ\alpha_2 \kappa_t^2 \right) ds. \tag{24.13}$$

The integrals are evaluated by a 3-point Gauss-Legendre quadrature and the equations of motion are obtained as Lagrangian equations

$$\frac{d}{dt} \frac{\partial T}{\partial q_{i,t}} - \frac{\partial T}{\partial q_i} + \frac{\partial V}{\partial q_i} = -\frac{\partial R}{\partial q_{i,t}}, \tag{24.14}$$

where $V = U + V_P$ and the unknowns q_i are the coefficients of the Hermite polynomials. The equations (24.14) are evaluated within Mathematica ([7]) and can be used for simulations.

In order to use these equations for finding periodic solutions using the multiple shooting algorithm Boundsco ([8]), the equations were exported to Fortran. Due to the severe stiffness of the equations (for $N = 12$ there occur stable eigenvalues of magnitude $-O(10^9)$ in the axial direction), we had to use the implicit solver Radau ([9]) for integrating the initial value problems. The calculation of the periodic solution is numerically still very expensive, but it is more efficient than to carry out simulations and wait, until the solution becomes approximately periodic. For finding the periodic solutions for varying excitation frequencies the continuation algorithm Hom ([10]) with tangential updating and a remarkable simple and efficient step size control was used.

24.1.3 Parameter Values and Non-Dimensionalization

By using non-dimensional quantities the number of parameters can be reduced and the expressions can be simplified. As usual we introduce new length, time and force scales.

$$\omega_b = \sqrt{\frac{EJ}{\varrho AL^4}}, \qquad\qquad t^\star = t/\omega_b,$$

$$\nu = \vartheta/\omega_b, \qquad\qquad \alpha^\star = \omega_b \alpha,$$

$$s^\star = s/L, \qquad\qquad r = r^\star/L,$$

$$p = PL^2/EJ, \qquad\qquad a = L^2 EA/EJ.$$

After carrying out the rescalings, the star superscript is dropped for simplicity. We also use dots and primes to denote derivatives w.r.t. $t^\star$ and $s^\star$, respectively. For our investigations we consider a beam with the parameters shown in Table 24.1.

Table 24.1: Parameter values for the beam model.

Parameter	Value	Parameter	Value
L	1 m	EJ	500/3 Nm^2
ϱA	0.79 kg/m	EA	20 MN
P_0	50 N	P_t	120 – 1200 N
α_1	0.0005 s	$\alpha = \alpha_2$	0.0001 – 0.001 s
ω_b	$\sqrt{500/(3*0.79)}$	p_0	0.3
p_t	0.72 – 7.2		

24.2 Stability of the Trivial Solution

Using nondimensional equations (24.9) takes the form

$$\ddot{v} = -v'''' - \alpha \dot{v}'''' - (p_0 + p_t \sin \nu t)v''. \tag{24.15}$$

with the boundary conditions

$$v(0,t) = v''(0,t) = v(1,t) = v''(1,t) = 0.$$

24.2.1 Analytical Approximation of the Stability Limit (Bolotin's Method)

Our first goal is to find the stability limits of the straight beam in the (ν, p_t) parameter plane, keeping α and p_0 fixed. Assuming small excitation forces and sinusoidal mode shapes, we set

$$v(s,t) = \sum_{k=1}^{\infty} q_k(t) \sin(k\pi s)$$

and obtain the family of oscillation equations

$$\ddot{q}_k = -k^2\pi^2 [k^2\pi^2 - p(t)]q_k - \alpha k^4 \pi^4 \dot{q}_k, \quad k \in \mathbb{N}. \tag{24.16}$$

In order to transform these equations into the usual form of the damped Mathieu's equation

$$\ddot{q}_k + \delta_k \dot{q}_k + [a_k - 2\varepsilon_k \cos(2\tau)]q_k = 0, \tag{24.17}$$

we rescale and shift the time $t \mapsto (\pi/2 + \nu t)/2$ to get

$$\delta_k = 2\alpha k^4 \pi^4 / \nu, \quad a_k = 4k^2 \pi^2 (k^2/\pi^2 - p_0)/\nu^2, \quad \varepsilon_k = 2k^2 \pi^2 p_t / \nu^2.$$

These equations can be rewritten in a more convenient form

$$\ddot{q} + \delta \dot{q} + \frac{4\Omega^2}{\nu^2}[1 - 2\mu \cos(2\tau)]q, \tag{24.18}$$

where δ denotes the damping coefficient and the index k has been left out for simplicity and

$$\Omega^2 = a_k, \qquad \mu = \varepsilon_k / a_k.$$

The stability limits of the undamped Mathieu equation (24.17) are already available as library functions in programs like Mathematica ([7]). For practical purposes there are also simpler approximations available for sufficiently small values of ε. The leading power series expansions for the low order resonances for (24.17) with $\delta = 0$ are given by

$$l = 1: \qquad a = 1 \pm \varepsilon + O(\varepsilon^2), \tag{24.19a}$$

$$l = 2: \qquad a = 4 + \frac{1}{6}\varepsilon^2 \pm \frac{1}{4}\varepsilon^2 + O(\varepsilon^3), \tag{24.19b}$$

$$l = 3: \qquad a = 9 + \frac{1}{16}\varepsilon^2 \pm \frac{1}{64}\varepsilon^3 + O(\varepsilon^4). \tag{24.19c}$$

For the resonances close to $a = l^2$ for $l \in \{1, 2, 3\}$ Bolotin [11] derived the formulas for the critical frequencies $\nu_\star$

$$l = 1: \qquad \nu_\star = 2\Omega\sqrt{1 \pm \mu}, \tag{24.20a}$$

$$l = 2: \qquad \nu_\star = \Omega\left\{\sqrt{1 - 2\mu^2}, \sqrt{1 + \mu^2/3}\right\}, \tag{24.20b}$$

$$l = 3: \qquad \nu_\star = \frac{2\Omega}{3}\sqrt{1 - \frac{9\mu^2}{8 \pm 9\mu}}. \tag{24.20c}$$

In order to find the critical excitation frequencies $\nu_\star$ for given values of Ω and μ, we have to solve the equations

$$4\frac{\Omega^2}{\nu_\star^2} = a(\varepsilon) = a\left(\mu\frac{\Omega^2}{\nu_\star^2}\right)$$

for $\nu_\star$.

For $l > 1$ we can avoid to solve polynomial equations by simply performing a power series expansion: With

$$\psi = 4\frac{\Omega^2}{v_\star^2}$$

we have to solve $\psi = a(\mu\psi/4)$ up to the order of the given expansion in (24.19). For $l = 1$ we obtain from (24.19a)

$$\psi = 4(1 \pm \mu\psi/4) \Rightarrow \psi = 4(1 \pm \mu) + O(\mu^2). \tag{24.21}$$

Now we can solve $\psi = 4\Omega^2/v^2$ for v to obtain

$$v_\star = 2\Omega/\sqrt{\psi} = 2\Omega\sqrt{1 \mp \mu} + O(\mu^2), \tag{24.22}$$

which agrees well with (24.20).

Similarly we obtain from (24.19b) for $l = 2$

$$\psi = 4 + \left(\frac{1}{6} \pm \frac{1}{4}\right)\mu^2\psi^2 \Rightarrow \psi \approx 4 + 16\left(\frac{1}{6} \pm \frac{1}{4}\right)\mu^2, \tag{24.23}$$

giving

$$v_\star = \frac{2\Omega}{\sqrt{\psi}} \approx \Omega\sqrt{1 - 4\left(\frac{1}{6} \pm \frac{1}{4}\right)\mu^2}, \tag{24.24}$$

which differs slightly from (24.20). Finally we obtain from (24.19c) for $l = 3$

$$\psi = 9 + \frac{9^2}{16}\mu^2 \pm \frac{9^3}{64}\mu^3. \tag{24.25}$$

The leading power series of $1/\psi$ is

$$1/\psi \approx \frac{1}{9}\left(1 - \frac{9\mu^2}{16} \mp \frac{81}{64}\mu^3\right),$$

yielding

$$v_\star = \frac{2\Omega}{3}\sqrt{1 - \frac{9\mu^2}{32} \mp \frac{81}{64}\mu^3} \approx \frac{2\Omega}{3}\left(1 - \frac{9\mu^2}{64} \mp \frac{81}{128}\mu^3\right). \tag{24.26}$$

A comparison of the different approximations is shown in Fig. 24.3

In the preceding calculations we neglected the influence of the damping; as it is shown below in Subsubsect. 24.3.3, damping usually decreases the linearly unstable domain. Using Normal Form theory it is possible to improve the given expansions to include the influence of damping.

24.2.2 Numerical Determination of the Stability Boundaries

In order to verify the approximate stability boundaries (24.20) numerically, we applied different numerical methods.

Fig. 24.3 Comparison of the expansion formulas for the critical excitation frequency $v_\star$ for the undamped Mathieu equation (24.18). Black (red) [blue] curves indicate exact solutions (approximations by Bolotin) and [approximations by (24.22,24.24,24.26)], respectively.
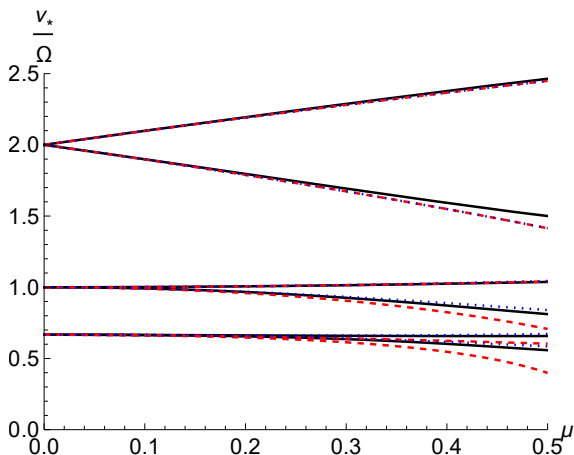
24.2.2.1 Simulation with Fixed Values of Frequency v

The simplest method to check the stability boundaries was to simulate the equations obtained by the FE formulation in Subsect. 24.1.2 for a number of fixed values of v, starting from a small steady deflection $y(s,0) = y_0 \sin(k\pi s)$ with $y_0 \ll 1$ over a fixed time interval. By monitoring the amplitude of the oscillation, we could approximately determine the unstable values of v. The method also provides a good guess about the stationary oscillation of the nonlinear system.

This method is of course not very efficient: Close to the stability limits it is numerically difficult to precisely detect increasing amplitudes. Due to the stiffness of the equations the simulations take quite long and admit only a rather coarse grid.

The method can be somewhat improved by starting the individual simulations from the previously obtained solutions. The time intervals can be chosen smaller and by varying v into the proper direction, we can also find stable oscillations outside the unstable interval of the trivial solution. Figure 24.4 displays results obtained by this method: The blue points were obtained for decreasing excitation frequencies.

The stability boundaries could also be obtained numerically by calculating the monodromy matrix of the linearized system over two excitation periods and calculating its eigenvalues, the Floquet multipliers. If one of these eigenvalues leaves the unit circle, the trivial solution becomes unstable. To calculate the stability for a specific value of v, one has to integrate the system for approximately $8N$ different initial conditions, which is comparable to the simple simulation method, but the results are quite accurate. The disadvantage of this method is, that it gives no information about the stationary solutions.
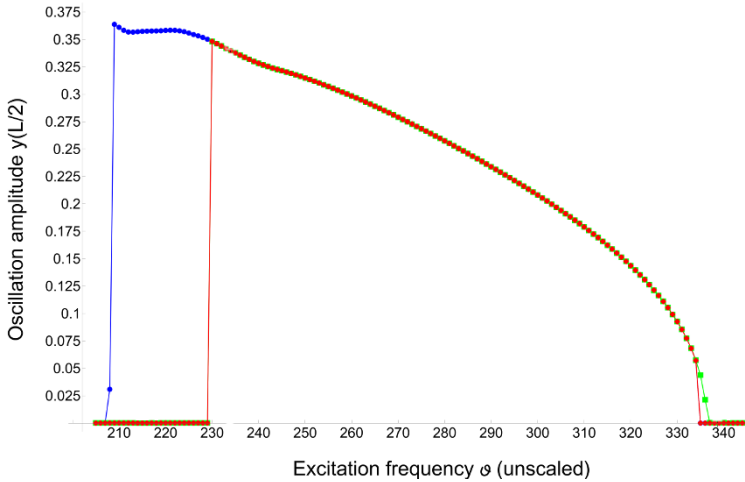
Fig. 24.4: Stationary oscillation amplitude at midspan for varying excitation frequencies ϑ (unscaled). The green (blue) dots are obtained for increasing (decreasing) values of ϑ, taking the last point of the previous solution as initial value. The red dots indicate the linear stability boundary.

24.2.2.2 Simulation of the FE Equations with Slowly Varying Frequency

Instead of carrying out many simulations with fixed values of v, we also performed simulations with slowly varying frequency

$$v(t) = v_0 + \lambda t, \qquad \text{with } |\lambda| \ll 1.$$

The excitation force takes the form

$$p(t) = p_0 + p_t \sin(v_0 t + \lambda t^2 / 2).$$

For sufficiently small values of λ the trajectory follows closely a branch of stable periodic solutions, as can be seen in Fig. 24.5, where the simulations for different values of λ are displayed. This method can also be used to monitor solution branches in the linear stable parameter range.

24.3 Calculation of Periodic Solutions Bifurcating from the Primary Resonance

In the simulation results for calculating the stability boundaries one could observe, that the branches of periodic oscillations continue across the lower stability boundary. So we tried to find out, how far the branches extend into the linearly stable domain and what happens at the endpoints. In the simplest analytical treatment of the nonlinear
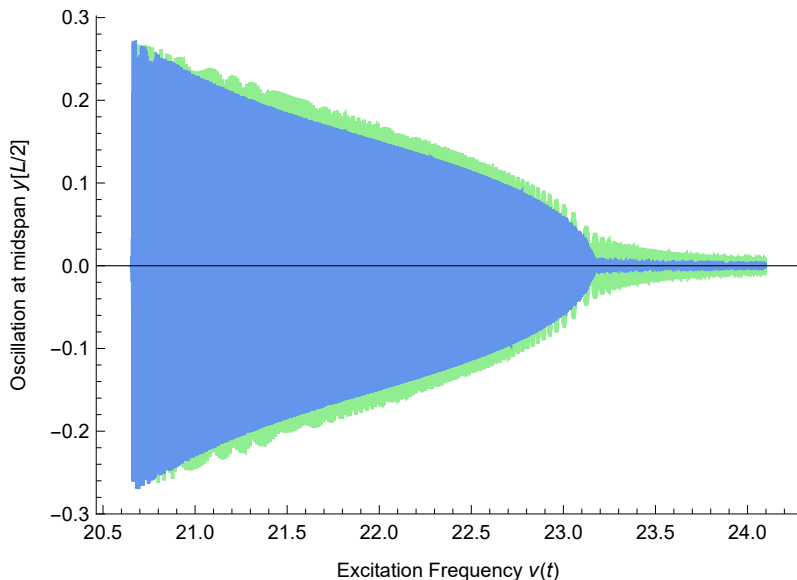
Fig. 24.5: Simulation of oscillations with $p_0 = 0.3$, $p_t = 7.2$, and slowly varying excitation frequency $v(t)$. Green: $\lambda = 0.07$, blue: $\lambda = 0.035$. Close to the stability boundary the oscillation amplitude decreases strongly.

Mathieu equation using only cubic terms one can see, that a branch of periodic solutions bifurcates from both stability boundaries, one of which is stable. These branches either continue infinitely, if the nonlinear damping term vanishes, or they connect in a limit point cycle. The behaviour for stronger nonlinearities might be considerably more complicated. In order to study the behaviour of our model for large amplitudes, we applied different numerical methods.

24.3.1 FE Simulations and Use of a Boundary Value Problem Solver

In order to directly obtain the periodic solutions bifurcatiing from the periodic solutions at the stability boundaries, we used the multiple shooting procedure Boundsco [8] for the equations generated in Mathematica [7]. To follow branches of periodic solutions, the continuation method Hom [10] was used, which is able to efficiently follow solution branches of nonlinear equations with tangential updating and automatic stepsize control. It is also able to follow the branches around turning points. The calculations were carried out for $N = 8$ and $N = 12$ intervals. Due to the severe stiffness of the equations the calculations needed several days for some branches, but one could obtain quite precise information about the periodic solutions.

Fig. 24.6 Periodic solution branches bifurcating from the stability boundaries of the primary resonance.
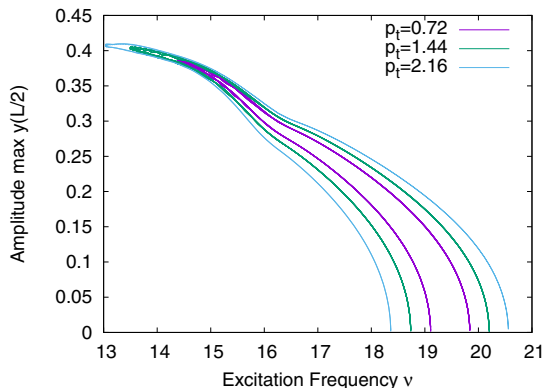
The excitation amplitude p_t turned out to be an important parameter: For $p_t <$ 2.5 we observe closed solution branches. At $p_t \approx 2.5$ there occurs a transcritical bifurcation and the lower and upper branch become disconnected. Figure 24.6 displays periodic solution branches obtained from the FE equations with $N = 8$. For $N = 12$ only for $p_t \leq 0.3$ closed branches could be obtained due to the strong stiffness of the problem and the intricate behaviour of the large amplitude periodic solutions. A typical phase portrait of the midpoint position for large oscillations is displayed in Fig. 24.7.

Fig. 24.7 Phase plane plot of the midpoint's vertical position $y(L/2)$ and velocity $\dot{y}(L/2)$ close to the turning point for $p_t = 2.16$.
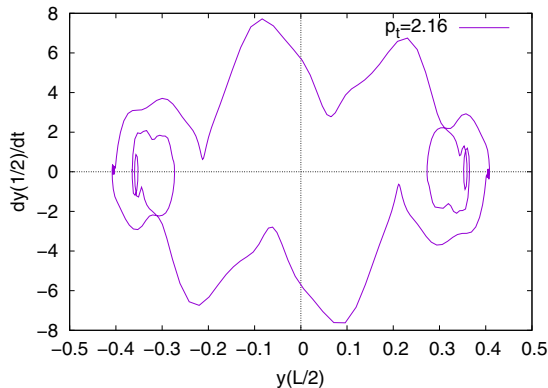
24.3.2 Application of the Galerkin Method

Equation (24.7) looks well suited for treatment by a Galerkin method. As first step we use an ansatz with one mode

$$v(s,t) = q(t)\sin(\pi s), \tag{24.27}$$

which satisfies all boundary conditions, and expand the equations up to third order in q. For $u(s,t)$ and $\ddot{u}(s,t)$ we obtain from (24.8) the second order expansion in q:

$$u(s,t) = -\frac{q^2\pi^2}{4}\left(s + \frac{\sin(2\pi s)}{2\pi}\right), \tag{24.28}$$

$$\ddot{u}(s,t) = -\frac{(q\ddot{q}+\dot{q}^2)\pi^2}{2}\left(s + \frac{\sin(2\pi s)}{2\pi}\right). \tag{24.29}$$

Further we obtain up to third order

$$\theta = \pi q\cos(\pi s) + (\pi q\cos(\pi s))^3/6, \tag{24.30a}$$

$$\cos(\theta) = 1 - (\pi q\cos(\pi s))^2/2, \tag{24.30b}$$

$$\tan(\theta) = \pi q\cos(\pi s) + (\pi q\cos(\pi s))^3/2, \tag{24.30c}$$

$$\kappa = \theta' = -\pi^2 q\sin(\pi s) - \pi^4 q^3\cos^2(\pi s)\sin(\pi s)/2, \tag{24.30d}$$

$$M = (1+\alpha\partial_t)\kappa, \tag{24.30e}$$

$$Q = (1+\alpha\partial_t)\left(\pi^3 q\cos(\pi s) + \pi^5 q^3(\cos^3(\pi s) - 2\cos(\pi s)\sin^2(\pi s))\right), \tag{24.30f}$$

$$\begin{aligned}
N = & -P(1+\pi^2 q^2/2) - \pi^4 q(q+\alpha\dot{q}) \\
& - \int_s^L \pi^6 q(q+\alpha\dot{q})\sin^2(\pi s)d\xi \\
& - \int_s^L \pi\ddot{q}q\sin(\pi s)\cos(\pi s) - \pi(2\pi\xi + \sin(2\pi\xi)))(\dot{q}^2 + q\ddot{q})/4d\xi \\
= & -P(1+\pi^2 q^2/2) - \pi^4 q(q+\alpha\dot{q}) \\
& - \pi^5 q(2\pi(s-1) + \sin(2\pi s))(q+\alpha\dot{q})/4 \\
& - \left((\pi^2(s^2-1) + \sin^2(\pi s))\dot{q}^2 + (\pi^2(s^2-1) - \sin^2(\pi s))q\ddot{q}\right)/4. \tag{24.30g}
\end{aligned}$$

Inserting these terms into (24.7) and taking the inner product with $\sin(\pi s)$, we arrive at the scalar oscillation equation

$$\begin{aligned}
\left(1 + \frac{(3+8\pi^2)q^2}{48}\right)\ddot{q} = & -(\pi^4 - p\pi^2)q - \pi^4\alpha(1+\pi^2 q^2)\dot{q} \\
& - \frac{(6\pi^4 - 5\pi^2 P)q^3}{8} + \frac{(9-8\pi^2)q\dot{q}^2}{48}. \tag{24.31}
\end{aligned}$$

24.3.3 Local Analytical Investigation of the Oscillation Equation Close to the 2 : 1-Resonance

First we approximate (24.31) by its cubic expansion

$$\ddot{q} = -(\omega_0^2 - p)q - \alpha_1\dot{q} + \beta q^3 + \gamma q\dot{q}^2 + \alpha_2 q^2\dot{q}, \tag{24.32}$$

where we neglect terms of order $O(Pq^3, |(q,\dot{q})|^5)$ and

$$\begin{aligned}
\omega_0^2 &= \pi^4 - \pi^2 p_0, & p &= p_t\sin(vt), \\
\alpha_1 &= \alpha\pi^4, & \alpha_2 &= \alpha\pi^6(45 - 8\pi^2)/48, \\
\beta &= -\pi^6(33 - 8\pi^2)/48, & \gamma &= \pi^2(9 - 8\pi^2)/48.
\end{aligned}$$

The linear approximation of (24.32)

$$\ddot{q} = -(\omega_0^2 - p)q - \alpha_1\dot{q} \tag{24.33}$$

is the well known damped Mathieu equation with main resonance close to $v_c = 2\omega_0$. Using the ansatz

$$q(t) = r(t)\cos(\varphi(t)), \quad \dot{q} = -\omega r(t)\sin(\varphi(t))$$

with $\omega = \omega_0 + \sigma/2$ and $\varphi(t) = 2\omega t + \psi(t)$, where $\sigma = v - 2\omega_0$ is the detuning parameter and $\psi(t)$ is a slowly varying variable, the averaging method yields the bifurcation equations

$$\dot{r} = -\frac{\alpha_1}{2}r + \frac{\alpha_2}{8}r^3 - \frac{p_t}{4}r\sin(2\psi), \tag{24.34}$$

$$r\dot{\psi} = -\frac{\sigma}{2}r - \frac{3\tilde{\beta}}{8}r^3 - \frac{p_t}{4}r\cos(2\psi) \tag{24.35}$$

with $\tilde{\beta} = \beta + 3\omega_0\gamma$. Nontrivial stationary solutions are obtained from the equation

$$\left(\frac{\alpha_1}{2} - \frac{\alpha_2}{8}r^2\right)^2 + \left(\frac{\sigma}{2} + \frac{3\tilde{\beta}}{8}r^2\right)^2 = \frac{p_t^2}{16}. \tag{24.36}$$

For fixed values of r (24.36) describes a circle in the (α_1, σ) parameter plane with radius $p_t/4$ and center at $(\alpha_2 r^2/4, -3\tilde{\beta}r^2/4)$. The stability boundary of the trivial solution is obtained for $r = 0$:

$$\alpha_1^2 + \sigma^2 = p_t^2/4. \tag{24.37}$$

The interior of this circle corresponds to unstable trivial solutions. For fixed values of the damping α_1 one obtains the well known hyperbolic stability boundaries in the (σ, p_t)-plane.

Fig. 24.8 Periodic solution branches obtained for the FE-model with $N = 8$ and for the Galerkin approximation with different numbers N of modes and approximation orders O. For $N = 1$ and $O = 3$ Eqn. (24.31) was used.
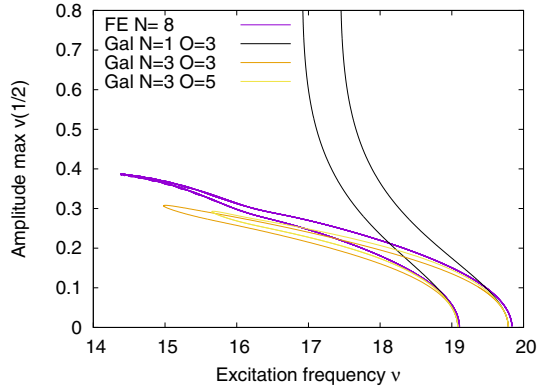
In order to explore the behaviour of the bifurcating solution branches, we used the continuation package MatCont [12], which is able to trace bifurcation branches and find critical points, like secondary bifurcations. The obtained solution branches close to the primary resonance at $v \approx 2\pi^2$ are displayed in Fig. 24.8: For quite small values of $p_0 = 0.3$ and $p_t = 0.72$ the bifurcation points from the straight configuration are detected precisely, but the large amplitude solutions do not make sense: Due to the boundary conditions the maximum amplitude can never exceed the value $q_{\max} = 0.5$. In the derivation of the differential equations the lowest order expansion for $u' = \sqrt{1 - v'^2}$ was used, which becomes inaccurate for large deflections of the centerline.

In order to improve the accuracy, we can increase the number N of ansatz functions

$$v(s,t) = \sum_{k=1}^{N} q_k(t) \sin(k\pi s)$$

or the order O of the terms considered in the expansion. Since the complexity of the expressions increases very rapidly with N and O, a symbolic Algebra system [7] was used to obtain the equations for the Galerkin reduction. As can be seen in Fig. 24.8, the results from the Galerkin method become considerably better, if more modes or higher orders are used. But for larger values of the excitation coefficient p_t the approximation deteriorates at large amplitudes, because the deflection angle θ becomes larger than $\pi/2$.

24.3.4 Approximation by the Ritz Method

In order to avoid the difficulties due to the large deflection, we used an ansatz

$$\theta(s,t) = \varepsilon \sum_{k=1}^{N} q_k(t) \cos(k\pi s)$$

for the angle $\theta(s,t)$, where ε is a book-keeping variable for the involved power series expansions, which is then set to 1. The deformations u and v are given up to order $O(\varepsilon^O)$ by

$$u(s,t) = \int_0^s \cos(\theta(\xi,t))d\xi - s, \qquad (24.38)$$

$$v(s,t) = \int_0^s \sin(\theta(\xi,t))d\xi. \qquad (24.39)$$

Since the ansatz functions enter the kinetic energy quadratically, it is sufficient to expand the velocities up to order $O/2$ to obtain terms of order O in the Lagrangian. For the damping terms the virtual variations

$$\delta\theta(s,t) = \varepsilon \sum_{k=1}^{N} \delta q_k(t) \cos(k\pi s) \qquad (24.40)$$

are required. The virtual work of the damping forces is given by

$$\delta A = -\alpha \int_0^1 \dot{\theta}'(s,t)\delta\dot{\theta}'(s,t)ds = -\frac{\varepsilon^2 \alpha \pi^2}{2} \sum_{k=1}^{N} k^2 \dot{q}_k(t)\delta q_k(t), \qquad (24.41)$$

leading to the generalized linear damping forces

$$Q_k = -\frac{\varepsilon^2 \alpha \pi^2 k^2}{2} \dot{q}_k(t). \qquad (24.42)$$

Also the elastic energy takes a nice form with these ansatz functions

$$U_E = \int_0^1 \frac{\theta'^2(s,t)}{2} ds = \frac{\varepsilon^2 \pi^2}{4} \sum_{k=1}^{N} k^2 q_k^2(t). \qquad (24.43)$$

For $N > 1$ the ansatz functions violate the boundary condition $v(1,t) = 0$; for $N = 3$ we obtain at leading order

$$v(1,t) = \frac{-\varepsilon^3 q_1(t)q_2(t)(q_1(t) + 2q_3(t))}{8}.$$

Therefore we add the penalty term

Fig. 24.9 Periodic solution branches obtained for the FE-model with $N = 8$ and for the Ritz approximation with different numbers N of modes and approximation orders O.
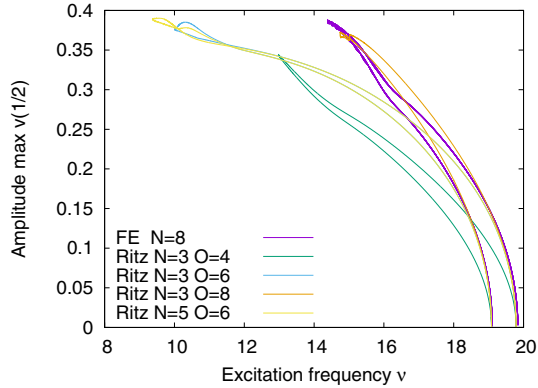
$$V_p = \frac{P_p v^2(1,t)}{2} \tag{24.44}$$

with some large parameter P_p to the potential energy; for our calculations we use the value $P_p = 50$, which is significantly larger than the considered excitation force. It would also be possible to regard the condition $v(1,t) = 0$ as isoperimetric constraint, but that would lead to a differential-algebraic system of index 3, which would have to be converted into an explicit system in order to treat it with MatCont.

In the simplest case $N = 1$, $O = 4$ we obtain the oscillation equation with cubic terms

$$\left(1 + \frac{8\pi^2 - 9}{48} q_1^2\right)\ddot{q}_1 = -(\pi^4 - \pi^2 p)q_1 - \alpha\pi^4\dot{q}_1 - \frac{\pi^2 p q_1^3}{8} - \frac{(8\pi^2 - 9)q_1\dot{q}_1^2}{48}, \tag{24.45}$$

which differs sligthly from (24.32). We observe, that (24.45) contains no nonlinear damping term and the coefficients of $q_1\dot{q}_1^2$ and $q_1^2\ddot{q}_1$ agree. For larger values of N and O the equations become very lengthy and are again obtained using a CAS ([7]).

A comparison between the periodic branches obtained by the FE equations and the Ritz method for different orders of approximation is displayed in Fig. 24.9. As expected, the agreement between the branches improves with increasing order O, but the range of existence for the different orders varies significantly. For $O = 6$ there is almost no difference between the branches for $N = 3$ and $N = 5$, respectively.

24.4 Conclusions and Further Research Goals

Using the applied methods it was possible to precisely determine the stability boundary of an axially excited beam. Also the initial behaviour of the periodic solutions branching off the stability boundaries can be computed sufficiently well. Problems arise for the determination of the endpoints of the branches, especially for large am-

plitude solutions. For these cases also the approaches using FE methods work quite poorly. Approximation methods would require a large number of ansatz functions, leading to overly complicated and untractable equations.

Since the problem turns out to be extremely stiff and the obtained numerical solutions display a quite regular spatial structure, this model would be an excellent benchmark example for advanced dimension reduction methods, like Nonlinear Galerkin methods.

References

[1] Thomsen JJ (2021) Vibrations and Stability - Advanced Theory, Analysis, and Tools. Springer
[2] Thompson JMT, Rainey RCT, Soliman MS, Thompson JMT, Gray P (1990) Ship stability criteria based on chaotic transients from incursive fractals. Philosophical Transactions of the Royal Society of London Series A: Physical and Engineering Sciences **332**(1624):149–167
[3] Rand RH (2012) Lecture notes on nonlinear vibrations, (online)
[4] Kovacic I, Rand R, Sah SM (2018) Mathieu's equation and its generalizations: Overview of stability charts and their features. Applied Mechanics Reviews **70**(2), 020802
[5] Lacarbonara W (2013) Nonlinear Structural Mechanics - Theory, Dynamical Phenomena and Modeling. Springer
[6] Vetyukov Y (2012) Hybrid asymptotic-direct approach to the problem of finite vibrations of a curved layered strip. Acta Mechanica **223**(2):371–385
[7] Wolfram Research, Inc (2022) Mathematica, Version 13.1. Champaign, IL, 2022
[8] Oberle HJ, Grimm W, Berger E (1985) BNDSCO, Rechenprogramm zur Lösung beschränkter optimaler Steuerungsprobleme. Benutzeranleitung M 8509, Techn. Univ. München
[9] Hairer E, Wanner G (1996) Solving Ordinary Differential Equations II - Stiff and Differential-Algebraic Problems. Springer Series in Computational Mathematics, Springer, Berlin, Heidelberg
[10] Seydel R (1984) A continuation algorithm with step control. In: Numerical methods for bifurcation problems. ISNM 70, Birkhäuser
[11] Bolotin WW (1961) Kinetische Stabilität elastischer Systeme. Mathematik für Naturwissenschaft und Technik, Band 2, VEB Deutscher Verlag der Wissenschaften, Berlin
[12] Dhooge A, Govaerts W, Kuznetsov YA, Meijer HGE, Sautois B (2008) New features of the software MatCont for bifurcation analysis of dynamical systems. MCMDS **14**(2):147–175

Chapter 25
Continuum Mechanics Applied for Studying Instabilities in Nanoparticles

Melanie Todt, Markus A. Hartmann, and Franz G. Rammerstorfer

Abstract Nanoparticles quite often consist of single or multiple layers of 2D materials, like graphene. For instance, carbon nanotubes, carbon crystallites forming the meso structure of high strength carbon fibers, as well as carbon onions can be treated as structures consisting of multiple layers of graphene, bond together by van der Waals forces and covalent inter-layer bonds. Despite the fact, that these carbon nanoparticles can hardly be considered as continuous systems, their mechanical response can – under certain limitations – be investigated using continuum mechanics. This chapter presents a review over published work related to models and methods which can be used to study the stability behaviour of nanoparticles by applying continuum mechanics. The determination of effective mechanical properties as well as the limitations of the continuum mechanics approaches are discussed. Some specific applications, in which peculiar phenomena such as the limited size of carbon onions or the shift in neutral axis of bent carbon fibers are clarified by computational simulations, are described in more detail.

25.1 Introduction

Within the wide variety of nanoparticles, the most investigated and promising ones are those consisting of two-dimensional carbon layers. Hence, in the present review layered carbon nonoparticles, such as graphene [1–5], carbon crystallites [6, 7], carbon

Melanie Todt · Franz G. Rammerstorfer
Institute of Lightweight Design and Structural Biomechanics, TU Wien, Vienna, Austria,
e-mail: melanie.todt@tuwien.ac.at, franz.rammerstorfer@tuwien.ac.at

Markus A. Hartmann
Ludwig Boltzmann Institute of Osteology at Hanusch Hospital of OEGK and AUVA Trauma Centre Meidling, Vienna, Austria,
e-mail: markus.hartmann@osteologie.lbg.ac.at

nanotubes [8–11], fullerenes [12, 13], and carbon onions [14–17], are considered. Bulk graphite and pyrolytic carbon are note considered in the present review.

Graphene is the main building block of all the carbon nanoparticles considered here and the strongest and thinnest material ever discovered [2]. Thus, all carbon nanoparticles should inherit the exceptional properties of graphene, making them promising candidates as fillers in nanocomposites especially for electronics applications [8, 18–20] and sensing devices [21, 22]. More potential applications can be found, e.g., in [8, 23, 24]. However, for an expedient application of carbon nanoparticles their properties, including their mechanical response, should be well understood. For this reason, a lot of experimental work has already been done to study the structure and properties such nanoparticles, see [12, 14, 25] and computational techniques have also shown to be powerful tools for this purpose, see e.g. [11, 26, 27] and references therein.

There exist a number of modelling methods of different accuracy and length-scale applicability to study the mechanical behavior of nanoparticles. Most accurate for atomistic modelling are *ab initio* methods that solve Schrödinger equation more or less directly. Atomistic classical molecular dynamics and Monte Carlo methods rely on the use of force fields whose parameters can be determined by *ab initio* methods. Lastly, continuum mechanical methods which disregard the atomistic nature of matter using macroscopic, i.e., effective material parameters. The descriptions of the models and their applications as provided in the present review paper are presented in more detail in [28].

Continuum mechanics approaches for studying the mechanical behaviour of layered nanoparticles quite often use shell models. Thus, the knowledge of properties like Young's modulus E, Poisson's ratio v, and shell thickness h, is required. Surprisingly, as will be shown in the following sections, published values for these parameters differ by orders of magnitude! Some of them are useful for describing the membrane behaviour of nanolayers but not for bending. The problem lies in the fact that one layer of atoms, as is found in graphene, does not have a clearly defined "physical thickness", h, in the sense of structural mechanics. However, graphene exhibits a measurable membrane and bending stiffness, both being structural characteristics of plates or shells that depend on the three mentioned parameters as long as linear elasticity and isotropy can be assumed. Certainly, E, h, and v must be seen as "effective" properties characterizing atomic layers in terms of continuum mechanical structures, such as plates or shells.

Nanoparticles can be considered as structures in the sense of mechanics. Thus, like structures in engineering constructions, they can lose their stability of equilibrium under certain circumstances, and bifurcation or snap-through buckling can be observed. In this review paper, instability is to be understood in the above mentioned sense. The focus is on the analytical and computational treatment of instabilities in carbon nanoparticles, especially carbon crystallites and carbon onions. Here, we refer to [29].

This review has two main goals: first, to provide a way for the determination of effective elastic constants in terms of continuum mechanics; second, to explain some peculiar experimental observations. Regarding determination of effective properties,

one should bear in mind that the buckling behaviour of layered carbon nanoparticles depends on both the membrane as well as the bending stiffness. It will be shown that this can be utilized in clarifying the unclear situation regarding the values of E, h, and ν. For this purpose stability analyses on well defined nanoparticles will be performed using atomistic simulations in conjunction with continuum mechanics approaches. Regarding clarification of the peculiar experimental observations, this review focuses on the buckling of (i) carbon crystallites and (ii) carbon onions.

It is well known that in carbon fibres built by carbon nanocrystallites the longitudinal Young's modulus in compression is smaller than in tension. Directly measuring the compression modulus is very difficult. Thus, bending experiments are performed in which a shift of the neutral axis towards the compressed portion of the fibre's cross section can be observed indicating a lower stiffness under compression than under tension. It has been argued that buckling of the nanocrystallites could be the reason for this stiffness reduction [7]. Computational simulations on the nano level [30] confirm this argument and allow determining the nonlinear elastic behaviour of carbon fibres by evaluating the post-buckling deformation of the nanocrystallites.

Carbon onions are special carbon nanoparticles with promising prospects of revolutionizing such diverse fields as electronic devices, photovoltaic applications, light weight materials, or lubricants. The number of layers in carbon onions can become very large, still it seems to be limited. Thus, the question arises what might cause such a growth limit. As shown in [31], loss of stability could be the reason for this. Interestingly, carbon onions buckle even without external loading. Another example for buckling of carbon nanostructures in the absence of external loads is the buckling of patches of graphene sheets as discussed in [32] and papers cited therein.

In the present review article instability of nanoparticles is mainly treated under the above mentioned aspects rather than in a fully general way. This is the reason why buckling of nanotubes, widely studied in the literature see, e.g., [8, 33, 34], is not considered here.

25.2 Methods and Models

The simulation of the mechanical behaviour and, thus, in particular the simulation of instabilities in layered nanoparticles involves different aspects, which are the correct representation of the layers, the van der Waals (vdW) interactions and for curved nanoparticles also the description of the excess surface energy. The input parameters required and the simplifications to be made depend strongly on the simulation technique used. Which methods and models should be applied, depends on the size of the investigated layered nanoparticles and on the specific goals of the investigations. In general a distinction is made between atomistic and continuum mechanics approaches.

25.2.1 Atomistic Approaches

Ab initio simulations, due to their complexity and, hence, high computational costs, are usually not used to investigate complex mechanical behaviours in single or multi-layer nanoparticles. Furthermore, in *ab initio* simulations the treatment of vdW interactions is a complicated task due to their non-local long-range nature. Nevertheless some concepts are proposed in [35, 36]. In the context of investigating instability phenomena in large nanoparticles *ab initio* methods are mainly used for determining input parameters required in Monte Carlo (MC), molecular dynamics (MD) or continuum mechanics (CM) simulations and also for gaining information about the excess surface energy in curved carbon nanoparticles.

In the quantum mechanical framework, addressing the solution of Schroedinger equation for many-body problems, the inter-atomic forces governing structural relaxations as well system dynamics, are obtained from the electronic structure via Hellman-Feynmann theorem. Using the Born-Oppenheimer approximation (called also the adiabatic approximation), the many-body eigenvalue problem can be decoupled into a separate many-body problem for electrons and ions. Since the ions are several orders of magnitude heavier and their motion is several orders of magnitude slower than electrons, their motion is well described by classical Newtonian equations of motion. The electronic part, however, has to be treated fully quantum mechanically. The most common approach in material science is the density functional theory (DFT) [37, 38] in which the search for many-body wave-function is replaced with the search for charge density distribution. The biggest advantage of *ab initio* techniques is that only information on the atoms making up a the structure (i.e., the type of elements) and their approximate structure is needed. Subsequently, scenarios including bond breaking and bond formation can also be considered which is not possible in other simulations. However, solving the underlying equations is a computationally expensive task, and therefore only applicable for small structures.

Monte Carlo (MC) simulation is a tool used in statistical physics to determine the static, i.e. time-independent, equilibrium properties of many particle systems [39]. The basic input of MC simulation is an expression for the potential (configurational) energy of the system, which is nothing more than the force field in MD.

In MC simulations the atoms forming the layers are explicitly modelled where the interactions between the individual atoms are described via potentials. Potentials are either found empirically or by *ab initio* calculations. Thus, most important for a reliable simulation is the knowledge of the underlying potential. One of the most famous potentials used for modelling of carbon is the Tersoff-Brenner potential [40–42].

The covered length scales of MC (and MD) simulations lie in between *ab initio* and continuum mechanical methods. Still atomistic in nature MC methods can deal with system sizes ranging from several thousands to millions of atoms.

25.2.2 Continnuum Mechanics Approaches

Continuum mechanical methods do not (explicitly) take into account the atomistic nature of matter but use macroscopic constitutive laws. When studying the mechanical behaviour of complex layered nanoparticles, the arising boundary value problem is typically solved by discretisation methods, such as the finite element (FE) method.

In comparison with *ab initio* and MC (and MD) simulations, continuum mechanics approaches have rather low computational costs and have shown to be appropriate for studying the mechanical properties of nanoparticles [10, 11, 43, 44]. Within the continuum approach the layers of nanoparticles can be modelled either as a space frame structure using beam and/or spring elements [45, 46] or as continuum shells [10, 11], where only continuum shell models are considered in this review.

Using continuum shells for modelling carbon layers was first proposed by Yakobson et al. [11]. It is assumed that the layers can be modelled as thin, linear elastic, isotropic shells possessing a membrane stiffness $C = \frac{Eh}{1-\nu^2}$ and a bending stiffness $D = \frac{Eh^3}{12(1-\nu^2)}$, where E is the Young's modulus, ν the Poisson's ratio, and h the layer thickness. It should be noted that E, ν, and h should be treated as "effective" properties; they must always be considered in combination, leading at the same time to proper values for the membrane and the bending stiffness.

25.3 Mechanical Properties Used in Continuum Shell Models

Continuum shell models require the knowledge of the values of the effective elastic properties, such as - at least - E, ν, and h. More advanced shell models are proposed, e.g. in [47–50] allowing to capture some features like the anisotropy of carbon layers due to chirality, but increase also the complexity of the models. However, the effect of anisotropy vanishes fast with increasing size of the nanoparticles, see [49] and needs not to be considered as long as strains are small [51]. When curved nanoparticles, such as fullerenes, carbon onions or carbon nanotubes, are considered, the intrinsic curvature induced excess surface energy must be considered, too, and in case of a multi-layer structure a proper continuum mechanics modelling of the vdW interaction is required.

25.3.1 Effective Elastic Properties and Thickness

As mentioned, the first who used continuum shell models were Yakobson et al. [11]. There, the elastic constants were obtained by MD simulations leading to $E = 5500\,\text{GPa}$, $\nu = 0.19$, and $h = 0.066\,\text{nm}$. The consistency of this approach has been confirmed in [52] by investigating the strain energy of carbon nanotubes. Isotropic thin shell models were successfully applied, e.g., in [10] to study buckling of multi-walled

carbon nanotubes. The small strain assumption holds for the carbon nanoparticles being investigated in the following, so the shell model proposed in [11] could be used.

Nanoindentation experiments revealed that graphene behaves elastic [53] almost until breaking. Therefore, the layer properties can be described using three independent parameters: the elastic modulus E, Poisson's ratio ν, and the layer thickness h. However, the choice of appropriate values for these parameters is far from obvious. Since the first attempts to determine these parameters made in [11] a lot of experimental and theoretical work has been carried out to estimate the elastic properties of a single carbon layer. Nevertheless, the values of the parameters given span an extremely wide range. The values reported for the membrane stiffness range from 159 to 480 N/m [1, 50, 53, 54] (and references therein). An even broader range of different values spanning one order of magnitude is reported for the effective thickness of graphene, ranging from $h = 0.617$ to $6.9\,\text{Å}$ [55]. This peculiar behaviour of the thickness was given the name "Yakobson Parodox" [56]. Among the different suggestions proposed to resolve this paradox is the observation that the thickness of nanotubes is not constant, but may depend on its size, chirality and loading situation [55] or that plate theory breaks down for a monolayer of graphene [5].

In [28] the membrane and bending stiffness as well as the Poisson's ratio of graphene is determined by stretching and bending graphene ribbons in MC simulations, There, the classical potentials for *sp2* bonded carbon derived in [57] from *ab initio* calculations are used. The reliability of these potentials was tested using MC simulations. The bonded interaction between carbon atoms is described by 2-atom bond-stretching E_S, 3-atom bond-bending E_B and 4-atom bond-torsion E_T energy contributions:

$$E_S(r_{ij}) = E_0\{[1 - \exp(-\beta(r_{ij} - r_0))]^2 - 1\} \qquad (25.1)$$

$$E_B(\theta_{ijk}) = \frac{1}{2}k_\theta(\cos\theta_{ijk} - \cos\theta_0)^2 \qquad (25.2)$$

$$E_T(\phi_{ijkl}) = \frac{1}{2}k_\phi(1 - \cos 2\phi_{ijkl}) \qquad (25.3)$$

In the stretching potential, E_0 denotes the binding energy of two carbon atoms, r_0 the equilibrium carbon-carbon bond length, β^{-1} the width of the potential and r_{ij} the actual distance between atoms i and j. The bending contribution is characterized by the bond angle θ_{ijk} between three carbon atoms, the equilibrium bond angle θ_0 and the bending force constant k_θ, the torsion contribution by the dihedral angle ϕ_{ijkl} between four atoms and the torsion force constant k_ϕ.

These potentials were used in MC simulations in the (NPT) ensemble using the classical algorithm of McDonald [58] to perform computational mechanical tests on graphene.

Figure 25.1 shows the model used in these MC simulations. The test length L_x was varied in a wide range in order to determine the size-limit of the structure up to which the computed effective properties can be used. In addition to the atoms forming
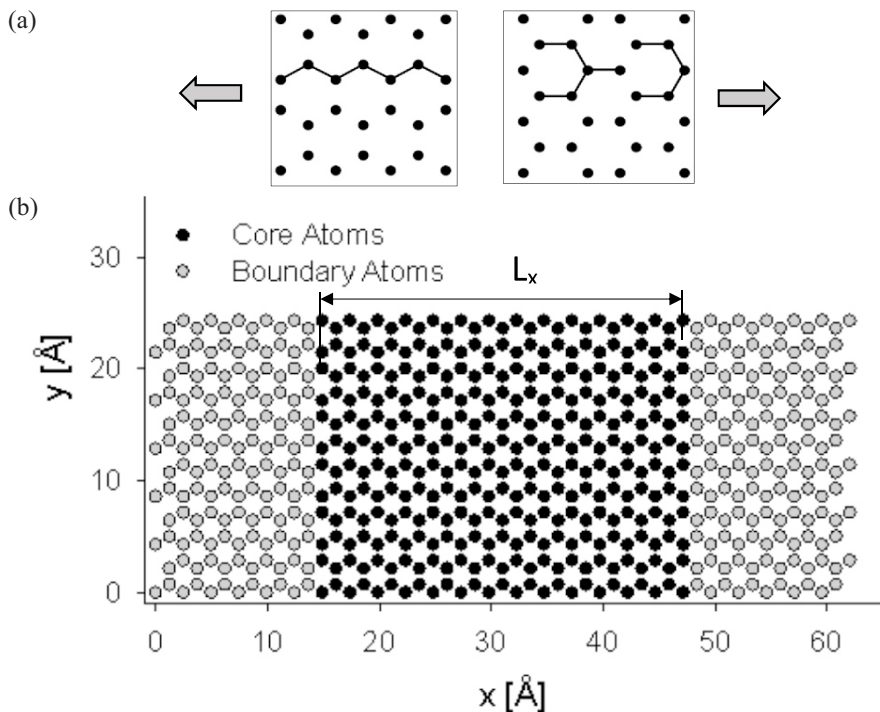
Fig. 25.1: MC Models: (a) schematic presentation of zig-zag and arm chair models for tension tests, L_x denotes the actual test length; (b) model for bending and buckling tests; the atoms forming the left boundary (gray) are held fixed, while the atoms on the right boundary (gray) can move collectively in x-direction allowing for a change of length of the stripe. In y-direction periodic boundary conditions are used. Figure adapted and reproduced with permission from [28].

the area for evaluation (i.e., within L_x), twelve rows of atoms were added on either side of the graphene ribbon. While the additional atoms on the left side of the ribbon were held fixed during the simulation, the corresponding atoms on the right side were allowed to move collectively in x-direction. These boundary conditions allow for a deformation of a finite sized graphene ribbon without the effect of dangling bonds, because the atoms of the last rows do not contribute to the total energy of the system. Both zig-zag and arm-chair configurations were considered.

Being interested in the ground state only, in the simulations the temperature was set to the small value of $k_B T = 25\ \mu$eV. More details as well as the values of the used parameters in the potentials can be found in [28].

Figure 25.2 shows the results from uniaxial tension tests on graphene in terms of a load-displacement (in fact strain) diagram, i.e. the value of the applied distributed line load q_x versus the corresponding strain ε_x. The load was gradually increased until failure, i.e. until no stable elongation was found but the system steadily increased its length. The strength and ultimate strain of graphene are found to be $q_S = 46 \pm 0.4$ N/m and $\varepsilon_S = 0.28$. The quantity $Y = Eh = (313.2 \pm 0.17)$ N/m was obtained by a linear

Fig. 25.2 Uni-axial stretching of graphene until failure. Y and ν were obtained by evaluation of the linear part of the curve ($\varepsilon_x < 0.005$). For large strains the deviation from the straight line is visible. Figure adapted and reproduced with permission from [28].
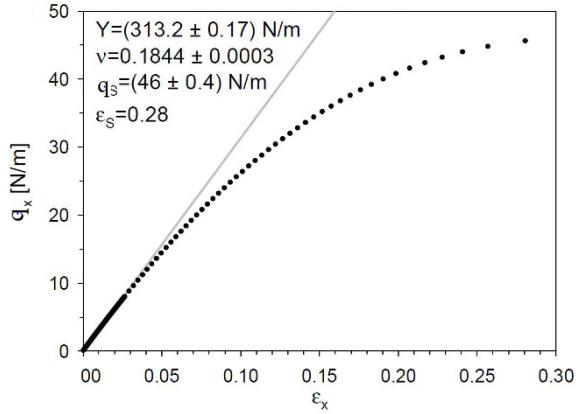
regression of the first, linear part of the curve ($\varepsilon_x < 0.005$), and the Poisson's ratio $\nu = 0.1844 \pm 0.0003$ was obtained by averaging the corresponding values of $-\varepsilon_y/\varepsilon_x$. Zig-zag and arm chair configurations yielded almost the same values for Y and ν confirming the in-plane isotropy of graphene. Accordingly the membrane stiffness is given by $C = Y/(1-\nu^2) = 324$ N/m. The values obtained are in good agreement with the measurements by Lee *et al.* [53] who report $Y = 340 \pm 50$ N/m and $q_S = 42 \pm 4$ N/m and the simulation results by Kalosakas *et al.* [59] who report $Y = 320$ N/m, a slightly higher Poisson's ratio of 0.22 and a strength of $39 - 45$ N/m. A further compilation of experimental and theoretical elastic constants of graphene can be found in [1] and references therein.

The effective thickness of monolayer graphene was determined by buckling tests. In these tests the distributed line load, applied as compression in x-direction, was gradually increased until buckling of the layer set in. The buckling load of in-plane loaded thin plates is (according to structural continuum mechanics) given by [60]

$$q_c = \sigma_c h = kEh\left(\frac{h}{L_x}\right)^2 \tag{25.4}$$

The buckling factor k depends on the boundary conditions, the ratio L_x/L_y and on the Poisson's ratio of the material the plate is made of. For the given boundary conditions and for L_y approaching infinity (see Fig. 25.1) its value can be taken from [60] as $k_{0.3} = 3.62$. This value is valid for $\nu = 0.3$.

In order to take into account the influence of the different Poisson's ratio for graphene on the bending stiffness and, thus, on the buckling load, the value of k must be adopted as: $k_{0.1844} = k_{0.3}(1-0.3^2)/(1-0.1844^2) = 3.41$. Thus, one gets

$$q_c = 3.41Y\left(\frac{h}{L_x}\right)^2 \tag{25.5}$$

Using the values of the buckling load q_c, determined by MC simulations in dependence of L_x, the corresponding effective thickness can be calculated as a

function of L_x by comparing with Eq. (25.5) and using the value of Y derived from the tensile test. The results are shown in Fig. 25.3.

For short ribbons (shorter than 50 Å) the calculated thickness decreases, which can be attributed to the breakdown of the continuum approximation for structures composed of too few atoms. For increasing length the effective thickness of graphene levels off approaching approximately $h = 1.32$ Å, resulting in a bending stiffness $K = 0.47$ nN.nm = 2.94 eV being in good agreement with the results from [61] obtained from molecular dynamics.

For cross checking these results, MC simulations of 3-point and 4-point bending tests, i.e. applying transversely acting loads in the middle or one third from the left and from the right end of the evaluation length L_x, were performed. Comparing the computed out-of-plane displacements at the load application lines with the analytical solutions of the accordingly loaded plates also resulted in values of the effective thickness. These values are shown in Fig. 25.3 by triangles.

It has been argued that the effective mechanical properties are not intrinsic properties of graphene, but depend on the topology of the carbon nanoparticle and on the loading situation [55, 62]. For checking the dependence of the effective properties on the loading situation, the above described cross checks by bending tests have not given any indication that there is a substantial difference between values for stretching and those for bending. However, for simulating the behaviour of curved nanostructures like carbon onions, it is essential to know whether curved layers can be described with the effective elastic properties found for planar graphene, too.

To answer this question additional mechanical tests were performed on fullerenes. Hydrostatic loading was applied to fullerenes of different size. The results for the reduction of the radius ΔR as a function of applied hydrostatic radial pressure p was compared to the corresponding analytical solution for thin spherical continuum shells modelled with the effective mechanical parameters found for planar monolayer graphene. This analytical solution can be expressed in the following form:
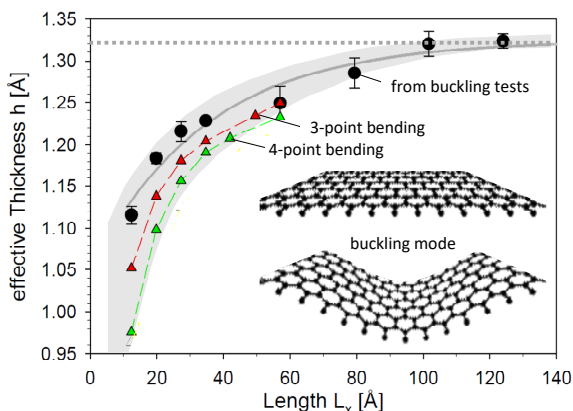
Fig. 25.3 Effective thickness of mono layer graphene determined from models with different length of the evaluation area L_x. Results derived from buckling tests are presented by black circles. For cross checking, results from 3-point and 4-point bending tests are shown, too. Figure adapted and reproduced with permission from [28].

$$F = \kappa \Delta R = \frac{8\pi E h}{1 - \nu} \Delta R = \frac{8\pi Y}{1 - \nu} \Delta R \tag{25.6}$$

There, the applied load intensity is expressed by

$$F = \int_S p \, dS$$

where the integration is carried out over the surface of the sphere. For thin spherical shells, the value of $\kappa = F/\Delta R$ is independent of the size of the shell. Using Y and ν as obtained from the MC simulation of the tensile test leads to a constant theoretical value $\kappa = 9651$ N/m.

The values of κ obtained in the MC simulations for pressure loaded spherical carbon nanostructures of different size in combination with Eq. (25.6) are presented in Fig. 25.4. These values should be constant and close to the theoretical value.

In Fig. 25.4 a slight decrease in κ with fullerene size can be observed. The smallest investigated fullerene (C_{60}) shows $\kappa = 10021$ N/m, the largest fullerene (C_{8820}) $\kappa = 9297$ N/m, which is a decrease of $\approx 7\%$ while the radius of the fullerenes changed more than a factor of 10. Thus, the requirement of constant values for κ can be seen as sufficiently fulfilled. Furthermore, because κ as derived from the MC simulations of fullerenes corresponds well with the theoretical value, these effective properties appear to be useful also for curved carbon nanoparticles, at least for spherical ones.

In conclusion, the results of the MC simulations show that graphene and fullerenes (and presumably also nanotubes) as well as corresponding multi-layer nanoparticles larger than 50 Å can be described as thin, isotropic shells with effective parameters $E = 2.4$ TPa, $\nu = 0.1844$ and $h = 1.32$ Å, independently of loading and deformation conditions. Care has to be taken for structures smaller than 50 Å, because the continuum approximation breaks down and no consistent bending stiffness can be deduced.
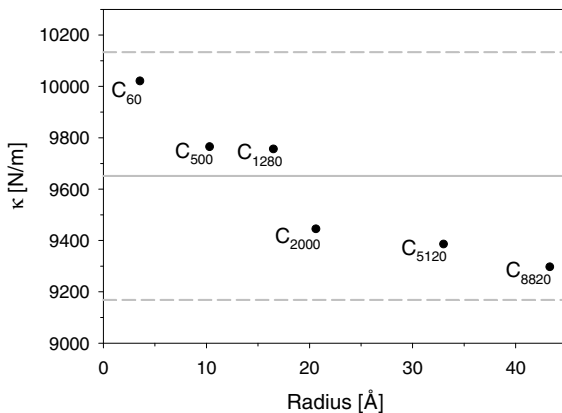
Fig. 25.4 Values of κ for fullerenes of different sizes. The theoretical value is shown by the gray line, the dashed lines indicate 5 % deviations. Figure adapted and reproduced with permission from [28]

25.3.2 Continuum Mechanics Models for van der Waals Interaction and the Intrinsic Curvature Induced Excess Surface Energy

In multi-layer carbon nanoparticles the vdW interactions in terms of interaction forces between the individual layers must be considered in addition to the layer behaviour. VdW interactions are non-local induced dipole interactions between uncharged atoms or molecules and are relatively weak compared to covalent bonds between the atoms forming a layer. The non-local interactions between two atoms can be described using a pair potential of the interaction forces, where usually the Lennard-Jones (LJ) potential [63]

$$U_{12} = 4\epsilon \left[\left(\frac{\sigma}{r}\right)^{12} - \left(\frac{\sigma}{r}\right)^{6} \right], \tag{25.7}$$

is used with r being the current atom-atom distance. The parameters σ and ϵ describe the atom-atom distance at $U_{12} = 0$ and the depth of the potential well, respectively, see Fig. 25.5. These parameters are usually referred to as Lennard-Jones parameters, and values can be found in [64, 65]. The pair potential consists of an attractive part $U_{atr} = \left(\frac{\sigma}{r}\right)^6$ and a repulsive part $U_{rep} = \left(\frac{\sigma}{r}\right)^{12}$. The 6th power in the attractive part follows from the London equation [66], whereas the 12th power in the repulsive part is used only for practical reasons and has no specific physical meaning.

In atomistic description the vdW interactions between two layers result from vdW interactions between the discrete atoms forming the layers. In MD or MC simulations the vdW interactions are included via an additional energy term $E_{nonbond}$ where for $E_{nonbond}$ the LJ-potential given in Eqn. (25.7) can be used. The atom-atom interactions, however, are not applicable in continuum mechanical shell models where pressure-distance relations are more feasible.

Appropriate pressure-distance relations can be derived by integrating over the vdW interactions between the individual atoms in adjacent layers, where the number
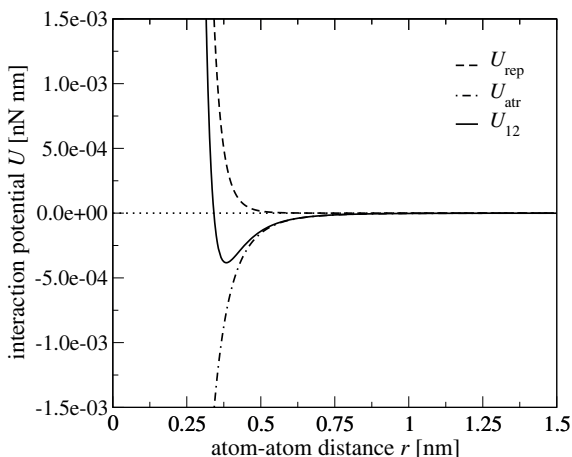
Fig. 25.5 Van der Waals interaction potential U of two interacting carbon atoms for Lennard-Jones parameters $\sigma = 0.3415$ nm $\epsilon = 0.00239$ eV. Values of the Lennard-Jones parameters are taken from [64]

of atoms within each layer is represented by an atom area density [64, 67, 68]. This allows to take different numbers of atoms in adjacent layers of curved nanoparticles into account. For the different multi-layer nanoparticles the pressure-distance relations are found as

$$p(\alpha) = \frac{C_{33}}{6} \left[\left(\frac{\sigma}{\alpha} \right)^{10} - \left(\frac{\sigma}{\alpha} \right)^4 \right] \tag{25.8}$$

for graphite [63] with $C_{33} = 36.5\,\text{GPa}$ and

$$p(\alpha) = \underbrace{8\,\epsilon\,(\rho_\infty)^2\,\sigma\,\pi}_{C_0} \left[\left(\frac{\sigma}{\alpha} \right)^{11} - \left(\frac{\sigma}{\alpha} \right)^5 \right] \tag{25.9}$$

for planar carbon nanoparticles such as multi-layer graphene [68],

$$p_1 = C_0 \frac{R_2}{R_1} \left[231 \left(\frac{\sigma}{R_1 + R_2} \right)^{11} \left(\frac{R_2 - R_1}{R_2 + R_1} E_{13} - E_{11} \right) \right.$$
$$\left. - 160 \left(\frac{\sigma}{R_1 + R_2} \right)^5 \left(\frac{R_2 - R_1}{R_2 + R_1} E_7 - E_5 \right) \right], \tag{25.10}$$

$$p_2 = C_0 \frac{R_1}{R_2} \left[231 \left(\frac{\sigma}{R_1 + R_2} \right)^{11} \left(\frac{R_2 - R_1}{R_2 + R_1} E_{13} + E_{11} \right) \right.$$
$$\left. - 160 \left(\frac{\sigma}{R_1 + R_2} \right)^5 \left(\frac{R_2 - R_1}{R_2 + R_1} E_7 + E_5 \right) \right], \tag{25.11}$$

with $C_0 = \frac{3\pi}{32} \epsilon \sigma \rho_\infty^2$ for multi-walled carbon nanotubes [64] and

$$p_1 = \frac{1}{R_1} C_0 \left[\frac{2\,\hat{E}_{11}\,\sigma^{11}}{(R_2^2 - R_1^2)^{11}} - \frac{5\,\hat{E}_{12}\,\sigma^5}{(R_2^2 - R_1^2)^5} \right], \tag{25.12}$$

$$p_2 = \frac{1}{R_2} C_0 \left[\frac{5\,\hat{E}_{21}\,\sigma^5}{(R_2^2 - R_1^2)^5} - \frac{2\,\hat{E}_{22}\,\sigma^{11}}{(R_2^2 - R_1^2)^{11}} \right], \tag{25.13}$$

with $C_0 = \frac{32}{5} (R_1^{(0)} R_2^{(0)} \rho_\infty)^2 \epsilon \pi \sigma$ for carbon onions [68] where $R_1^{(0)}$ and $R_2^{(0)}$ denote the radii of the inner and outer layer before the vdW interactions become active, respectively. In Eqs. (25.8) to (25.13) the parameter α denotes the current interlayer distance. In Eqs. (25.10) to (25.13) R_1 and R_2 refer to the current deformed radii of the inner (smaller) and outer (larger) layers involved in the vdW interactions, respectively. The parameters E_{13}, E_{11}, E_7, E_5 (Eqs. (25.10) and (25.11)) as well as the parameters $\hat{E}_11$, $\hat{E}_12$, $\hat{E}_21$, $\hat{E}_22$ in (Eqs. (25.12) and (25.13)) depend on R_1 and R_2. For more details see [64] and [68], respectively.

All pressure distance relations given here account only for vdW interactions between adjacent layers. This is admissible as the vdW interactions vanish fast with increasing atom-atom distance. It should be noted that for curved nanoparticles the vdW pressure experienced by the inner layer is different than the pressure experienced by the outer layer. This is a consequence of the different numbers of atoms within adjacent layers. Accounting for the different number of atoms in adjacent layers within the vDW model is especially crucial if the displacements and the subsequent stresses in the layers are of importance [64, 68], e.g., if the mechanical stability of a structure is considered. However, the analytical vdW models stated in Eqs. (25.10) to 25.13 have the drawback that they can hardly be incorporated into standard commercial FE codes. Thus, for finite element simulations usually the pressure distance relations derived for planar carbon nanoparticles, see Eqs. (25.8) and (25.9), are used [10, 31, 44].

For curved nanoparticles such as fullerenes, carbon onions, or carbon nanotubes the intrinsic curvature induced excess surface energy $E^{(S)}$ [57] has to be considered. In [57] both *ab initio* and MC simulations have shown that the excess surface energy can be well fitted by a power law $E^{(S)} \sim r^{\beta}$, where r is the radius of the curved structure. The values obtained for the fitting parameter β range from -1.40 to -2.51 depending on the type of nanostructure considered, see Fig. 25.6.

Due to the high computational costs *ab initio* calculations could only be performed for fullerenes up to the C_{240}, while MC simulations could extend this range up to C_{5120}. The MC simulations also revealed that for curved structures like fullerenes the 4-atom-bond torsion contribution is by far the largest contribution to the total energy albeit its small force constant. Due to the presence of the excess surface energy
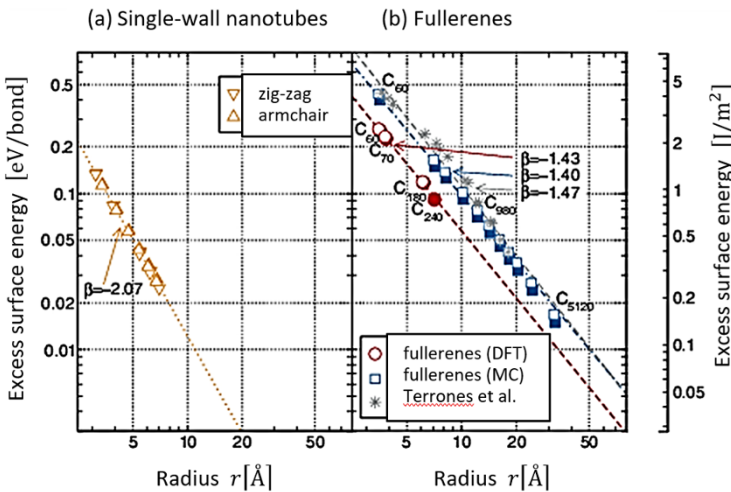
Fig. 25.6: Double logarithmic plot of excess surface energy vs radius: (a) the zigzag (down triangle) and armchair (up triangle) SWNTs from the DFT calculations, (b) fullerenes as calculated by *ab initio* (circles) Figure adapted with permission from Ref. [57]. Copyrighted (2010) by the American Physical Society.

a surface stress $\sigma^{(S)}$ develops as a "plane hydrostatic" stress state. For spherical particles the Shuttleworth equation [69]

$$\sigma^{(S)} = E^{(S)} + \frac{\mathrm{d}E^{(S)}}{\mathrm{d}\varepsilon^{(S)}}$$

holds, where $\varepsilon^{(S)}$ is the strain in each circumferential direction. For a first estimate the second term of this relation can be neglected leading to $\sigma^{(S)} = E^{(S)}$. Note that $E^{(S)}$ and $\sigma^{(S)}$ are physically different quantities possessing the same unit (force per unit length). In a finite element model $\sigma^{(S)}$ can be taken into account by applying an external pressure

$$p^{(S)} = \frac{2\sigma^{(S)}}{r}.$$

As can bee seen from Fig. 25.6 the excess surface energy, and consequently the surface stress, decreases fast with increasing radius r. Therefore, it is only of relevance for small carbon nanoparticles.

25.4 Some Examples for Application of Continuum Mechanics to Nanoparticles

In the previous Section the derivation of "effective parameters" needed for investigating the stability behaviour of nanoparticles by using continuum mechanics concepts has been shown. Now, two examples for the application of this approach will be given - see also [29]

25.4.1 Carbon Crystallites

Bending experiments of polyacrylonitril (PAN) based fibres revealed a non-Hookean fibre behaviour in compression, which is related to buckling phenomena occurring in the nanostructure of the fibre [70]. The cross section of such a PAN fibre is depicted in Fig. 25.7. PAN fibres usually show a skin-core structure [71], where the outer surface is formed by a skin-like layer and randomly distributed carbon crystallites form the inner region. In [72, 73] it is assumed that these crystallites buckle if the fibre is subjected to compressive loading and in [74] fibre failure is related to crystallite buckling. Microbeam X-ray diffraction of bent carbon fibers revealed a shift of the neutral axis towards the streched area of the cross section indicating crystallite buckling [7]. These experimental results show that the mechanical behaviour of carbon fibres under compression is dominated by instability phenomena on the nano scale, i.e. crystallite buckling.

To get further insight into the mechanisms determining the compressive behaviour of PAN fibres a continuum mechanical study on the stability of carbon crystallites

under compressive loading was performed in [30]. For this purpose a continuum shell model of a single crystallite is used and the finite element method is employed for solving the arising boundary value problem. In the following the modelling assumptions used and the results obtained in [30] are briefly discussed.

In [30] the layers of the crystallite, schematically shown in Fig. 25.7, are assumed to be oriented parallel to the fibre axis and modelled as thin elastic plates with $E = 5.5\,\text{TPa}, \nu = 0.19,$ and $0.066\,\text{nm}$), interacting with each other by vdW interactions and covalent interlayer bonds. For the crystallite dimensions parallel and perpendicular to the fibre axis $L_{a\parallel} = 4.32\,\text{nm}$ and $L_{a\perp} = 3.87\,\text{nm}$, respectively, are used being in good agreement with experimental values [72, 74]. The vdW interactions between adjacent layers are considered using the pressure-distance-relation given in Eqn. (25.8). The equilibrium vdW distance $\alpha_{\text{eq}} = \sigma$ is chosen as $\sigma = 0.344\,\text{nm}$ giving a good approximation of experimental values ranging from $0.339\,\text{nm}$ to $0.356\,\text{nm}$ [6, 72]. The crystallite is assumed to consist of eight layers resulting in a total width of $L_c = 2.512\,\text{nm}$ which is in the range of experimentally determined values [74]. Furthermore, covalent interlayer bonds connecting two adjacent layers (see Fig. 25.7) are taken into account. Possible sources of such bonds are vacancies or interstitial atoms [75] within the layers or dangling bonds at their edges [75]. In [76] it is shown that covalent interlayer bonds constrain sliding between nanotube walls and that the load transfer between the tubes is best if the bonds are uniformly distributed. Covalent interlayer bonds may also be an explanation of the "compared to graphite" increased shear modulus of carbon crystallites in PAN fibres observed in [6]. For the sake of simplicity, in [30] the interlayer bonds are modelled as trusses with their axial stiffness being far larger than the membrane stiffness of the layers. It is assumed that the bonds at the edges and in the interior of the crystallite are similar and that they locally reduce the interlayer distance to $d_c = 0.258\,\text{nm}$ [75]. Two different distributions of the interlayer bonds are investigated where (i) the bonds are distributed over the whole crystallite (including the edges) and (ii) the bonds are distributed only along the edges.

To get a reasonable representation of the self-equilibrated stress state in the layers due to interlayer bond formation the bonds are first introduced with an initial length of

$$d_c^{(0)} = 0.344\,\text{nm}.$$
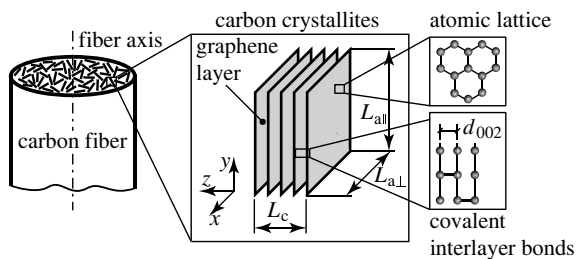
Fig. 25.7 Nanostructure of PAN-based carbon fibres. Figure adapted and reproduced with permission from [30].
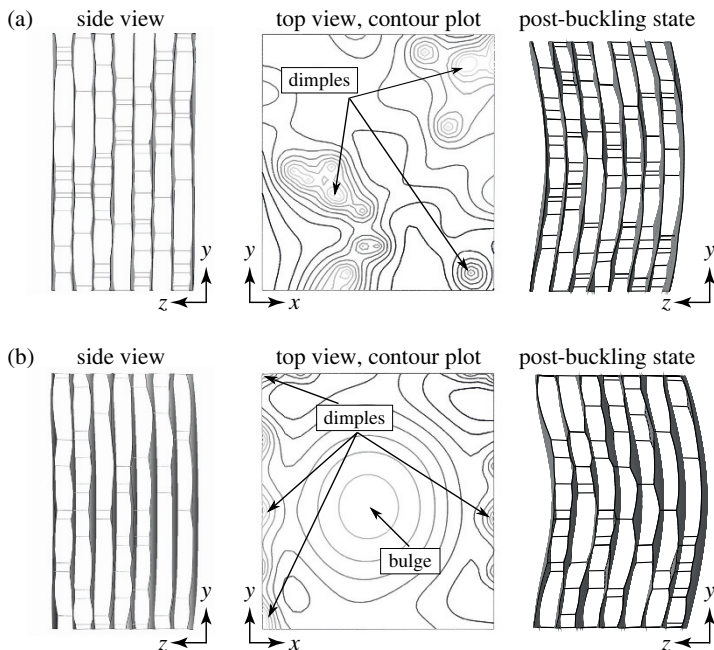
Fig. 25.8: Deformation states of carbon crystallites with their interlayer bonds being randomly distributed over the whole crystallite (a) or being located only at the edges (b). The side view of the deformation state after the formation of the interlayer bonds and the corresponding contour lines of the z-displacements of the uppermost layer are depicted on the left side and in the middle, respectively [30]. The right figure shows the post-buckling state due to the applied axial displacement. Figures on the left side and in the middle are adapted and reproduced with permission from [30]..

Then the bonds are subjected to a virtual temperature change, ΔT, reducing their length from $d_c^{(0)}$ to $d_c = 0.258$ nm, where the boundary conditions are chosen in a form to constrain the crystallite as little as possible. The deformations of the crystallite obtained by this initial step are illustrated in Fig. 25.8 (left and middle). The vdW interactions between adjacent layers prevent a uniform distance reduction leading to the formation of dimples at the interlayer bond locations. If the bonds are randomly distributed within the whole crystallite the layers remain almost parallel to the fibre axis (y-axis) and only local dimples form, see Fig. 25.8 (a). In contrast to this deformation pattern a pre-bending deformation in the form of an overall bulge can be observed if the interlayer bonds are located only at the edges, as shown in Fig. 25.8 (b). This bulge leads to a misalignment of the whole crystallite with respect to the fibre axis, resulting in a larger geometrical imperfection in terms of structural stability analysis notations.

The different deformation states obtained after the initial step lead to different behaviours of the crystallites when subjected to compressive loading. The axial compression is applied via prescribed displacements u_y in direction of the fibre
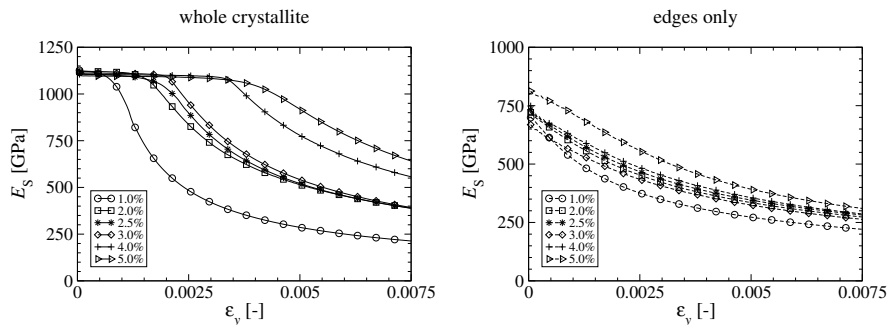
Fig. 25.9: Secant modulus E_S in compression in dependence on the different proportions of covalent interlayer bonds, expressed in terms of % of bonded pairs of atoms; for interlayer bonds distributed randomly in the whole crystallite (a), see [30], and for bonds distributed at the edges only (b). Figure (a) reproduced with permission from [30].

axis, where all layers are assumed to be subjected to the same axial displacement at the upper edge. The obtained post-buckling states of the compressed crystallites are depicted in Fig. 25.8 (right). The distribution of the interlayer bonds has no significant influence on the character of the post-buckling shape. In both cases an overall bending deformation occurs and no layer separation can be observed. Although the post-buckling behaviour seems to be independent of the distribution of interlayer bonds, the load-displacement behaviour shows a strong dependency on the bond distribution and also on the amount of interlayer bonds. Figure 25.9 shows the obtained secant modulus E_S of the crystallites depending on the amount of interlayer bonds and the distribution of the bonds. If the interlayer bonds are distributed over the whole crystallite, secant moduli in the range of 1076 GPa to 1158 GPa are obtained for the pre-buckling state. E_S remains almost constant until buckling occurs, where the critical strain increases substantially with the amount of interlayer bonds. If the interlayer bonds are located only at the edges of the crystallite much lower secant moduli ranging from 670 GPa to 812 GPa are obtained and no constant regime of E_S is observed. E_S decreases with increasing compressive strain and is almost independent of the amount of interlayer bonds. It can be concluded that covalent bonds randomly distributed over the whole crystallite have a stabilizing effect, whereas interlayer bonds located only at the edges lead to a reduction of the axial stiffness of the crystallites already for small compressive loads. Comparison with experimental values of the secant modulus (1140 ± 40 GPa [6]) show that it is more likely that interlayer bonds form within the whole crystallite and not only at the edges. The reduction of the secant modulus after the onset of buckling observed for this distribution of interlayer bonds is a possible explanation for the shift of the neutral axis observed experimentally for bent PAN fibres. Generally it can be said that with the used continuum shell model the behaviour of carbon crystallites can be well predicted. Although the crystallite model includes some simplifications it can serve as basis for further investigations regarding the compressive behaviour of carbon fibres.
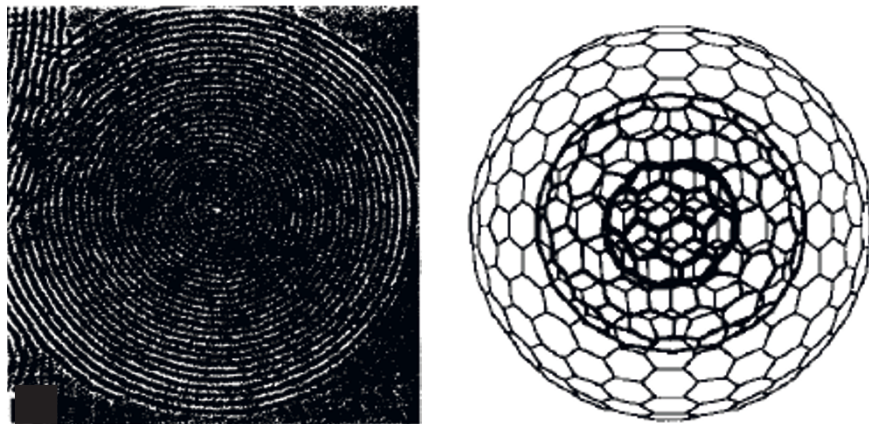
25.4.2 Carbon Onions

Carbon onions have first been discovered by Iijima in 1980 [25]. They are almost spherical in shape and consist of a number of concentric graphene-like carbon layers. Figure 25.10 shows a transmission electronmicrograph and a sketch of the atomic structure of this kind of carbon nanoparticles, respectively.

Today several production techniques are available for producing carbon onions including the intense electron irradiation of soot [16], electron irradiation of graphite at elevated temperatures ($\geq 300°$) [14, 77], annealing of diamond nanoparticles [78, 79], high pressure transformation of single-crystal graphite [80], using a radio frequency plasma process [81, 82], or synthesis by decomposition of phenolic resin [83].

Carbon onions are not only of scientific interest but are also promising candidates for practical applications, e.g., as fillers in nanocomposites, especially for electronics applications due to their high electron density [8, 18, 19], as additives in lubricants [78], or as solid lubricants [84]. In all of these applications the size of the particles is of major interest.

In reality carbon onions can consist only of a few layers [17, 78], be of intermediate size [77, 80], or consists of many layers [85, 86] with diameters up to 50 nm. The size of the onions seems to depend on the production technique, the precursor material [86], as well as on the annealing temperature and dose [14, 87, 88]. Based on this information the questions arise whether or not the size of carbon onions is limited or if the particles can be grown to an arbitrary number of layers. These questions are intensively addressed in [31]. The main modelling assumptions and results discussed therein are briefly reviewed in the following.

Fig. 25.10: Transmission electron microscope (TEM) micrograph of a carbon onion (left) taken with permission from [77], and the atomic structure of carbon onions (right) taken with permission from [17].

All investigations in [31] are based on the theory that the size of carbon onions is limited by the occurrence of a structural instability. These instability is stated to be evoked by the formation of an additional layer on an already existing onion. The carbon onions are assumed to consist of perfectly spherical and concentric layers which posses the same number of atoms as so-called icosahedral fullerens [15, 89, 90]. These assumptions are admissible as some of the existing production techniques lead to rather facetted onion layers [12, 80, 82, 83] which are comparable to fullerens. This facetted particles can then be transformed to spherical ones by intense irradiation where the degree of sphericity depends on the irradiation temperature [14, 16, 77]. The increased sphericity can, e.g., be explained by the formation of additional pentagonal rings or so-called Stone-Wales defects in the layers being not necessarily caused by the loss of atoms in the layers [91, 92].

The assumption of perfect spericity of the carbon onions is exploited by using an axi-symmetric model leading to low computational requirements. The axi-symmetry is admissible for the pre- as well as for the post-buckling state, see, e.g., [93, 94]. The layers are modelled using thin shells with

$$E = 4840\,\text{GPa}, \nu = 0.19 \quad \text{and} \quad h = 0.075\,\text{nm}.$$

This set of shell parameters has shown to give reasonable results for the mechanical properties of single fullerene layers [95]. The vdW interactions between the layers are described using the pressure-distance relation given in Eqn. (25.9) for graphene which neglects the sphericity of the particles. This simplification seems to be admissible as due to the relatively high stiffness of the innermost layers, buckling most likely occurs in the outer regions of the onions where the curvature effect within the vdW interactions is only of minor importance [10]. The parameter sets used in the vdW model are summarized in Table 25.1.

The carbon onion is assumed to grow from the inside to the outside imitating the growth scenario observed in [96] and [26]. In the growth model the individual layers are added sequentially starting with the innermost layer. As each of the layers is assumed to be an icosahedral fullerene the number of atoms n_i forming a layer i can be computed as $n_i = 60i^2$ [13], where $i = 1$ corresponds to the innermost layer. The radius $R^{(0)}$ of a layer is related to the number of its atoms n_i by [97]

$$R^{(0)} = a^{(0)}\sqrt{0.103374\,n_i - 0.424548}$$

whith $a^{(0)}$ being the carbon-carbon bond length. Therefore, the radii of the onion layers are not arbitrary leading to a distance α between an already existing onion

Table 25.1: Nonlinear vdW models used in the stability analysis of carbon onions.

Parameter Set	σ in nm	ϵ in eV	C_0 in GPa
PS1 (values from [64])	0.3415	0.00239	4.79
PS2 (values from [65])	0.3345	0.00319	6.26

and a newly formed layer that is usually different from the equilibrium distance α_{eq} of the vdW interactions. As a consequence the vdW interactions become active introducing compressive stresses in the new layer and a tensile stress contribution in all layers underneath, respectively. The excess surface energy, causing membrane compressive stresses in the layers, introduce significant contributions to the stress states only in small, i.e. in the most inner fullerenes (compare Fig. 25.6 and [57]) and can be neglected in the growth limit considerations [31, 98]. The boundary value problem arising when a new layer is added to an existing onion is solved using the finite element method.

The self-equilibrated stress state introduced by the vdW interactions may lead to the occurrence of a structural instability. Therefore, a buckling analysis is performed after each added layer in order to check whether or not the carbon onion has grown to its critical size. The corresponding eigenvalue problem is defined as

$$\left(\underline{\underline{K}}_N + \bar{\lambda}_N^j \Delta\underline{\underline{\bar{K}}}_N\right)\underline{\bar{\Phi}}_N^j = \underline{0} \qquad (25.14)$$

with $\underline{\underline{K}}_N$ being the stiffness matrix of the N-layered onion in its equilibrium state including the vdW interactions. The matrix $\Delta\underline{\underline{\bar{K}}}_N$ represents the change in the stiffness of the onion due to an external pressure $p_N^{(\text{ext})}$ applied to the outermost layer. The variables $\bar{\lambda}_N^j$ and $\underline{\bar{\Phi}}_N^j$ are the eigenvalues and the corresponding eigenvectors, respectively. For this model the smallest eigenvalue $\bar{\lambda}_N^1$ is the factor by which the pressure $p_N^{(\text{ext})}$ has to be multiplied to bring the N-layered onion to its critical state. The external pressure $p_N^{(\text{ext})}$ is required as perturbation load in the eigenvalue analysis and must not necessarily have a physical meaning. It is defined as the critical pressure of the newly added layer without the supporting layers underneath reading [99]

$$p_N^{(\text{ext})} = \frac{2Eh^2}{\sqrt{3(1-\nu^2)}(R_N^{(0)})^2}$$

where $R_N^{(0)}$ is the radius of the newly added layer. The choice of $p_N^{(\text{ext})}$ as critical pressure of the layer is not based on necessity but provides information about the effect of bedding due to the inner layers. An eigenvalue $\bar{\lambda}_N^1 \leq 1$ means that the external pressure leading to buckling of the onion is smaller than the critical pressure of the outermost layer. The growth limit of the onion is indicated by $\bar{\lambda}_N^1 = 0$ meaning that no external pressure is required to bring the onion to its critical state and that the self-equilibrated stress state introduced by the vdW interactions is sufficient to cause buckling.

Figure 25.11 (left) shows the results of the eigenvalue analysis for the different parameter sets used in the continuum vdW model, see Table 25.1. For a low number of layers $\bar{\lambda}_N^1$ first increases to values far larger than 1. This indicates that the critical pressure of the onion is larger than the critical pressure of the outermost layer, i.e. the outermost layer is sufficiently supported by the layers underneath to prevent buckling. After a certain number of layers is reached the inner layers still support the outermost

layer but the supporting effect is reduced with every additional layer. An eigenvalue $\bar{\lambda}_N^1 = 0$ is not reached as the algebraic system describing the boundary value problem becomes ill-conditioned (the stiffness matrix $\underline{\underline{K}}_N$ approaches a singularity). The maximum number of layers reached depends strongly on the LJ-parameters used in the continuum vdW model. The largest onion obtained in the analysis has about 72 layers, which is close to experimental observations [77]. In Fig. 25.11 (right) an example of a buckling mode is depicted, revealing that the outermost layers start to buckle whereas the innermost layers remain almost unaffected. This is because only
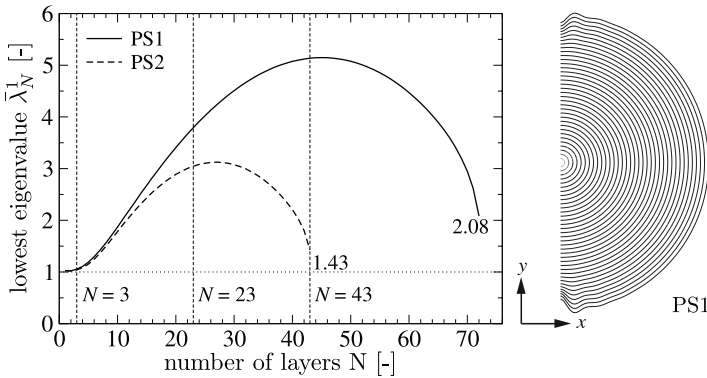
Fig. 25.11: Lowest eigenvalue $\bar{\lambda}_N^1$ versus the current number of layers N forming the carbon onion (left), where the different curves correspond to the different parameter sets used in the continuum vdW model, see Table 25.1. The right figure shows an example of a buckling mode of a carbon onion where only every second layer is shown.

the outermost layers of the onion are under compression, see Fig. 25.12, where the number of layers under compression increases during the growth of the onion.

The continuum mechanics simulations of the growth process of carbon onions show that the occurrence of a structural instability is a possible explanation for the limited size of this kind of nanoparticles. The self-equilibrating stress state leading to
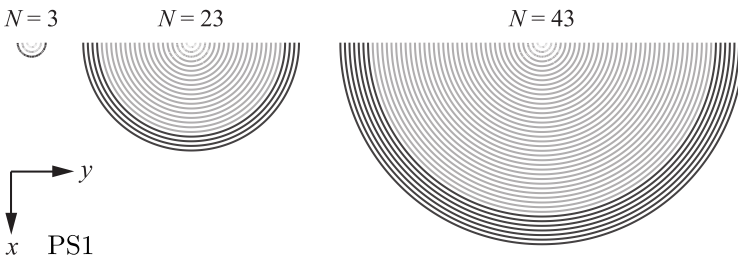
Fig. 25.12: Number of layers under compression (black) and tension (grey) for onions of different sizes.

this instability emerges due to accommodation of misfitting carbon layers during the growth process and is introduced by the vdW interactions between the layers. The obtained critical sizes of the onions are highly sensitive to the interlayer distances and compressive constants used in the vdW model and, thus have a rather qualitative than a quantitative character. Furthermore, some other effects, such as interlayer bonds or other combinations of fullerens can lead to much larger layer numbers. Nevertheless, the used models clearly indicate a growth limit of carbon onions and can serve as basis for further investigations concerning the growth of such particles.

25.5 Conclusion

In this review paper an overview on methods and models for simulating the stability behaviour of nanoparticles is provided. In particular the rather unclear situation regarding "effective" structural mechanical properties, such as Young's modulus, Poisson's ratio, and thickness of graphene layers is clarified.

In two examples the application of continuum mechanics concepts for studying the stability behaviour of nanoparticles has been demonstrated and it is shown that such carefully performed simulations can help in explaining and interpreting experimental observations at the micro and nano level.

In this sense, it could be shown that the difference of the longitudinal Young's modulus of carbon fibres between compression and tension is caused by buckling of the nanocrystallites forming the fibre when loaded in compression. Furthermore, the appearance of an instability has been identified as a possible answer to the question what limits the size of carbon onions.

References

[1] Cadelano E, Palla PL, Giordano S, Colombo L (2009) Nonlinear Elasticity of Monolayer Graphene. Physical Review Letters **102**:235,502
[2] Geim A (2009) Graphene: Status and prospects. Science **324**:1530–1534
[3] Geim A, Novoselov K (2007) The rise of graphene. Nature Materials **6**:183–191
[4] Novoselov K, Geim A, Morozov S, Jiang D, Zhang Y, et al SD (2004) Electric field effect in atomically thin carbon films. Science **306**:666–669
[5] Zhang DB, Akatyeva E, Dumitrica T (2011) Bending Ultrathin Graphene at the Margins of Continuum Mechanics. Physical Review Letters **106**:255,503
[6] Loidl D, Peterlik H, Müller M, Riekel C, Paris O (2003) Elastic moduli of nanocrystallites in carbon fibers measured by in-situ X-ray microbeam diffraction. Carbon **41**:563–570

[7] Loidl D, Paris O, Burghammer M, Riekel C, Peterlik H (2005) Direct observation of nanocrystallite buckling in carbon fibers under bending load. Physical Review Letters **95**:225,501

[8] Baughman R, Zakhidov A, de Heer W (2002) Carbon nanotubes – the route toward applications. Science **297**:787–792

[9] Iijima S (1991) Helical microtubules of graphitic carbon. Nature **354**:56–58

[10] Pantano A, Parks D, Boyce M (2004) Mechanics of deformation of single- and multi-wall carbon nanotubes. Journal of the Mechanics and Physics of Solids **52**:789–821

[11] Yakobson B, Brabec C, Bernholc J (1996) Nanomechanics of carbon tubes: Instabilities beyond linear response. Physical Review Letters **76**:2511–2514

[12] Kroto H, Heath J, O'Brien S, Curl R, Smalley R (1985) C60: Buckminster-fullerene. Nature **318**:162–163

[13] Tang A, Huang F (1995) Stability rules of icosahedral (Ih or I) fullerenes. Chemical Physics Letters **247**:494–501

[14] Banhart F, Ajayan P (1996) Carbon onions as nanoscopic pressure cells for diamond formation. Nature **382**:433–435

[15] Kroto H (1992) Carbon onions introduce new flavour to fullerene studies. Nature **359**:670–671

[16] Ugarte D (1992) Curling and closure of graphitic networks under electron-beam irradiation. Nature **359**:707–709

[17] Ugarte D (1995) Onion-like graphitic particles. Carbon **33**:989–993

[18] Macutkevic J, Seliuta D, Valusis G, Banys J, Kuzhir P, et al SM (2009) Dielectric properties of onion-like carbon based polymer films: Experiment and modeling. Solid State Sciences **11**:1828–1832

[19] Stankovich S, Dikin D, Dommett G, Kohlhaas K, Zimney E, Stach E, Piner RD, Nguyen ST, Ruoff RS (2006) Graphene-based composite materials. Nature **442**:282–286

[20] Poothanari MA, Pottathara YB, Thomas S (2019) Chapter 8 - carbon nanostructures for electromagnetic shielding applications. In: Thomas S, Grohens Y, Pottathara YB (eds) Industrial Applications of Nanomaterials, Micro and Nano Technologies, Elsevier, pp 205–223

[21] Sakhaee-Pour A, Ahmadian M, Vafai A (2008) Applications of single-layered graphene sheets as mass sensors and atomistic dust detectors. Solid State Communications **145**:168–172

[22] Sakhaee-Pour A, Ahmadian M, Vafai A (2008) Potential application of single-layered graphene sheet as strain sensor. Solid State Communications **147**:336–340

[23] Berger C, Song Z, Li T, Li X, Ogbazghi A, Feng R, Dai Z, Marchenkov A, Conrad E, First P, de Heer W (2004) Ultrathin epitaxial graphite: 2D electron gas properties and a route toward graphene-based nanoelectronics. The Journal of Physical Chemistry B **108**:19,912–19,916

[24] Wu Y, Yu T, Shen Z (2010) Two-dimensional carbon nanostructures: Fundamental properties, synthesis, characterization, and potential applications. Journal of Applied Physics **108**:071,301

[25] Iijima S (1980) Direct observation of the tetrahedral bonding in graphitized carbon black by high resolution electron microscopy. Journal of Crystal Growth **50**:675–683

[26] Chuvilin A, Kaiser U, Bichoutskaia E, Besley N, Khlobystov A (2010) Direct transformation of graphene to fullerene. Nature Chemistry **2**:450–453

[27] Los J, Pineau N, Chevrot G, Vignoles G, Leyssale J (2009) Formation of multi-wall fullerenes from nanodiamonds studied by atomistic simulations. Physical Review B **80**:155,420

[28] Hartmann MA, Todt M, Rammerstorfer FG, Fischer FD, Paris O (2013) Elastic properties of graphene obtained by computational mechanical tests. European Physical Society Letters **103**:68,004

[29] Todt M, Toth F, Hartmann M, Holec D, Cordill M, Fischer F, Rammerstorfer F (2014) Computational simulation of instability phenomena in nanoparticles and nanofilms. Computational Technology Reviews **10**:89–119

[30] Todt M, Rammerstorfer FG, Paris O, Fischer FD (2010) Nanomechanical studies of the compressive behavior of carbon fibers. Journal of Material Science **45**:6845–6848

[31] Todt M, Bitsche RD, Hartmann MA, Fischer FD, Rammerstorfer FG (2014) Growth limit of carbon onions - A continuum mechanical study. International Journal of Solids and Structures **51**:706– – 715

[32] Schwarzbart M, Steindl A (2013) Buckling of a supported annular plate with a non-euclidean metric. In: Altenbach H, Morozov NF (eds) Surface Effects in Solid Mechanics: Advanced Structured Materials 30, Springer-Verlag, Berlin Heidelberg

[33] Shima H (2012) Buckling of carbon nanotubes: A state of the art review. Materials **5**:47–84

[34] Annin BD, Baimova YA, Mulyukov RR (2020) Mechanical properties, stability, and buckling of graphene sheets and carbon nanotubes (review). Journal of Applied Mechanics and Technical Physics **61**:834–846

[35] Dion M, Rydberg H, Schröder E, Langreth D, Lundqvist B (2004) Van der Waals density functional for general geometries. Physical Review Letters **92**:246,401

[36] Grimme S (2004) Accurate description of van der Waals complexes by density functional theory including emprical conditions. Computational Chemistry **25**:1463–1473

[37] Hohenberg P, Kohn W (1964) Inhomogeneous electron gas. Physical Review **136**:B864–B871

[38] Kohn W, Sham LJ (1965) Self-consistent equations including exchange and correlation effects. Physical Review **140**:A1133–A1138

[39] Landau DP, Binder K (2014) A Guide to Monte-Carlo Simulations in Statistical Physics. Cambridge University Press

[40] Tersoff J (1988) Empirical Interatomic Potential for Carbon, with Applications to Amorphous Carbon. Physical Review Letters **61**:2879

[41] Brenner DW (1990) Empirical potential for hydrocarbons for use in simulating the chemical vapor deposition of diamond films. Physical Review B **42**:9458

[42] Brenner DW, Shenderova OA, Harrison JA, Stuart SJ, Ni B, Sinnott SB (2002) A second-generation reactive empirical bond order (REBO) potential energy expression for hydrocarbons. Journal of Physics: Condensed Matter **14**:783

[43] Sun C, Liu K (2008) Combined torsional buckling of multi-walled carbon nanotubes coupling with axial loading and radial pressures. International Journal of Solids and Structures **45**:2128–2139

[44] Yao X, Han Q, Xin H (2008) Bending buckling behaviors of single- and multi-walled carbon nanotubes. Computationa Material Science **43**:579–590

[45] Li C, Chou T (2003) A structural mechanics approach for the analysis of carbon nanotubes. International Journal of Solids and Structures **40**:2487–2499

[46] Sakhaee-Pour A (2009) Elastic properties of single-layered graphene sheet. Solid State Communications **149**:91–95

[47] Ansari R, Rouhi H (2012) Analytical treatment of the free vibration of single-walled carbon nanotubes based on the nonlocal flugge shell theory. Journal of Engineering Materials and Technology **134**:011,008

[48] Arash B, Wang Q (2012) A review on the application of nonlocal elastic models in modeling of carbon nanotubes and graphenes. Computational Materials Science **51**:303–313

[49] Chang T (2010) A molecular based anisotropic shell model for single-walled carbon nanotubes. Journal of the Mechanics and Physics of Solids **58**:1422–1433

[50] Wu J, Hwang K, Huang Y (2008) An atomistic-based finite-deformation shell theory for single-wall carbon nanotubes. Journal of the Mechanics and Physics of Solids **56**:279–292

[51] Wu J, Peng J, Hwang K, Song J, Huang Y (2008) The intrinsic stiffness of single-wall carbon nanotubes. Mechanics Research Communications **35**:2–9

[52] Xin Z, Jianjun Z, Zhong-can Q (2000) Strain energy and Young's modulus of single-wall carbon nanotubes calculated from electronic energy-band theory. Physical Review B **62**:13,692–13,696

[53] Lee C, Wei X, Kysar J, Hone J (2008) Measurement of the elastic properties and intrinsic strength of monolayer graphene. Science **321**:385–388

[54] Zhang P, Huang Y, Geubelle P, Klein P, Hwang K (2002) The elastic modulus of single-wall carbon nanotubes: a continuum analysis incorporating interatomic potentials. International Journal of Solids and Structures **39**:3893–3906

[55] Huang Y, Wu J, Hwang KC (2006) Thickness of graphene and single-wall carbon nanotubes. Physical Review B **74**:245,413

[56] Shenderova OA, Zhirnov VV, Brenner DW (2002) Carbon Nanostructures. Critical Reviews in Solid State and Materials Sciences **27**:227

[57] Holec D, Hartmann MA, Fischer FD, Rammerstorfer FG, Mayrhofer PH, Paris O (2010) Curvature-induced excess surface energy of fullerenes: Density functional theory and Monte Carlo simulations. Physical Review B **81**:235,403

[58] McDonald I (1972) NpT-ensemble Monte Carlo calculations for binary liquid mixtures. Molecular Physics **23**(1):41–58

[59] Kalosakas G, Lathiotakis NN, Galiotis C, Papagelis K (2013) In-plane force fields and elastic properties of graphene. Journal of Applied Physics **113**(13):134,307

[60] Rammerstorfer F, Daxner T (2009) Berechnungs- und Design-Konzepte für den Leichtbau. In: Degischer HP, Lüftl S (eds) Leichtbau, Wiley-VCH, pp 14–49

[61] Kang JW, Lee S (2013) Molecular dynamics study on the bending rigidity of graphene nanoribbons. Computational Materials Science **74**:107–113

[62] Kysar JW (2008) Direct comparison between experiments and computations at the atomic length scale: a case study of graphene. Scientific Modeling and Simulation SMNS **15**:143–157

[63] Kelly B (1981) Physics of Graphite, Advanced Science Publishers, pp 79–80

[64] Lu W, Liu B, Wu J, Xiao J, Hwang K, et al SF (2009) Continuum modeling of van der Waals interactions between carbon nanotube walls. Applied Physics Letters **94**:101,917

[65] Zhang H, Wang L, Wang J (2007) Computer simulation of buckling behavior of double-walled carbon nanotubes with abnormal interlayer distances. Computational Materials Science **39**:664–672

[66] London F (1930) Zur Theorie und Systematik der Molekularkräfte. Zeitschrift für Physik **63**:245–279

[67] Hamaker H (1937) The London–van der Waals attraction between spherical particles. Physica IV **10**:1058–1072

[68] Todt M, Rammerstorfer FG, Fischer FD, Mayrhofer PH, Holec D, Hartmann MA (2011) Continuum modeling of van der Waals interactions between carbon onion layers. Carbon **49**:1620–1627

[69] Fischer F, Waitz T, Vollath D, Simha N (2008) On the role of surface energy and surface stress in phase-transforming nanoparticles. Progress in Materials Science **53**:481–527

[70] Hawthorne H (1993) On non-Hookean behavior of carbon fibers in bending. Journal of Material Science **28**:2531–2535

[71] Paris O, Peterlik H (2009) The structure of carbon fibres. In: Eichhorn S, Hearle J, Jaffe M, Kikutani T (eds) Handbook of textile fibre structure, vol 2, Woodhead Publishing Limited, Cambridge, UK

[72] Oya N, Johnson D (2001) Longitudinal compressive behaviour and microstructure of PAN-based carbon fibres. Carbon **39**:635–645

[73] Nakatani M, Shioya M, Yamashita J (1999) Axial compressive fracture of carbon fibers. Carbon **37**:601–608

[74] Dobb M, Guo H, Johnson D, Park C (1995) Structure-compressional property relations in carbon fibres. Carbon **33**:1553–1559

[75] Telling R, Ewels C, El-Barbary A, Heggie M (2003) Wigner defects bridge the graphite gap. Nature Materials **2**:333–337

[76] Byrne E, Letertre A, McCarthy M, Curtin W, Xia Z (2010) Optimizing load transfer in multiwall nanotubes through interwall coupling: Theory and simulation. Acta Materialia **58**:6324–6333

[77] Banhart F, Füller T, Redlich P, Ajayan P (1997) The formation, annealing and self-compression of carbon onions under electron irradiation. Chemical Physics Letters **269**:349–355

[78] Joly-Pottuz L, Matsumoto N, Kinoshita H, Vacher B, Belin M, et al GM (2008) Diamond-derived carbon onions as lubricant additives. Tribology International **41**:69–78

[79] Tomita S, Burian A, Dore J, LeBolloch D, Fujii M, Hayashi S (2002) Diamond nanoparticles to carbon onions transformation: X-ray diffraction studies. Carbon **40**:1469–1474

[80] Blank V, Denisov V, Kirichenko A, Kulnitskiy B, Martushov SY, Mavrin B, Perezhogin I (2007) High pressure transformation of single-crystal graphite to form molecular carbon onions. Nanotechnology **18**:345,601

[81] Du AB, Liu XG, Fu DJ, Han PD, Xu BS (2007) Onion-like fullerenes synthesis from coal. Fuel **86**:294–298

[82] Fu D, Liu X, Lin X, Li T, Jia H, Xu B (2007) Synthesis of encapsulating and hollow onion-like fullerenes from coal. Journal of Material Science **42**:3805–3809

[83] Zhao M, Song H, Chen X, Lian W (2007) Large-scale synthesis of onion-like carbon nanoparticles by carbonization of phenolic resin. Acta Materialia **55**:6144–6150

[84] Hirata A, Igarashi M, Kaito T (2004) Study on solid lubricant properties of carbon onions produced by heat treatment of diamond clusters or particles. Tribology International **37**:899–905

[85] Wesolowski P, Lyutovich Y, Banhart F, Carstanjen H, Kronmüller H (1997) Formation of diamond in carbon onions under MeV ion irradiation. Applied Physics Letters **71**:1948–1950

[86] Zwanger M, Banhart F, Seeger A (1996) Formation and decay of spherical concentric-shell carbon clusters. Journal of Crystal Growth **163**:445–454

[87] Banhart F (1997) The transformation of graphitic onions to diamond under electron irradiation. Journal of Applied Physics **81**:3440–3445

[88] Redlich P, Banhart F, Lyutovich Y, Ajayan P (1998) EELS study of the irradiation-induced compression of carbon onions and their transformation to diamond. Carbon **36**:561–563

[89] Klein D, Seitz W, Schmalz T (1986) Icosahedral symmetry carbon cage molecules. Nature **323**:703–706

[90] Tang A, Huang F (1995) Theoretical study of multishell fullerenes. Physical Review B **52**:17,435–17,438

[91] Terrones H, Terrones M (1997) The transformation of polyhedral particles into graphitic onions. Journal of the Physics and Chemistry of Solids **58**:1789–1796

[92] Wang B, Wang H, Chang J, Tso H, Chou Y (2001) More spherical large fullerenes and multi-layer fullerene cages. Journal of Molecular Structure **540**:171–176

[93] Drmota M, Scheidl R, Troger H, Weinmüller E (1987) On the imperfection sensitivity of complete spherical shells. Computational Mechanics **2**:63–74

[94] Sato M, Wadee M, Iiboshi K, Sekizawa T, Shima H (2012) Buckling patterns of complete spherical shells filled with an elastic medium under external pressure. International Journal of Mechanical Sciences **59**:22–30

[95] Todt M, Rammerstorfer FG, Hartmann MA (2014) Continuum shell models for closded cage carbon nanopraticles. In: Pietraszkiewicz W, Górski J (eds) Shell Structures: Theory and Applications, Taylor & Francis Group, London, UK, pp 149–152

[96] Füller T, Banhart F (1996) In situ observation of the formation and stability of single fullerene molecules under electron irradiation. Chemical Physics Letters **254**:372–378

[97] Voytekhovsky Y (2003) A formula to estimate the size of a fullerene. Acta Crystallographica A **59**:193–194

[98] Todt M, Rammerstorfer FG, Hartmann MA, Paris O, Fischer FD (2011) Shell-models for multi-layer carbon nano-particles. In: Altenbach H, Eremeyev V (eds) Advanced Structured Materials: Shell-like Structures, Springer-Verlag, Berlin, pp 585–602

[99] Pflüger A (1975) Stabilitätsprobleme der Elastostatik. Springer-Verlag, Berlin

Chapter 26
Spectral Domain Approach for the Numerical Modeling of Elastodynamic Fields in Layered Structures

Thomas Voglhuber-Brunnmaier and Bernhard Jakoby

Abstract We review the concept and utilization of a semi-numerical method based on Stroh's formalism for modeling elastodynamic fields in stratified (layered) media and demonstrate its application to selected problems comprising linear piezoelectric, elastic, and liquid domains thus illustrating its versatility. Particular features of this method, which is based on the Boundary Element Method (BEM) are the representation of the considered fields in a spectral domain obtained by implementing a spatial Fourier transform in two dimensions. By doing so, Green's functions required for the BEM model can be established for layered structures fully considering the interface discontinuities associated with such geometries such that these interfaces between the layers do not have to be discretized anymore.

26.1 Introduction

In this contribution, we review a method related to the well-known Boundary Element Methods (BEMs), e.g., treated in [1, 2], where a spectral representation utilizing a spatial Fourier transform is employed. Generally, the Boundary Element Method in comparison to the Finite Element or the Finite Difference Methods requires only discretization of boundaries rather than volumes (see Fig. 26.1). This significant simplification comes at the cost of the construction of Green's functions describing the fields to a point excitation. Such Green's functions are particularly simple in uniform regions but can be involved if media boundaries are present. In classical BEM the simulation domain is thus split into sub-domains featuring uniform media each and the different sub-domains are then coupled imposing appropriate boundary conditions. The method reviewed here (see also [3]) considers uniformity only in two

Thomas Voglhuber-Brunnmaier · Bernhard Jakoby
Institute for Microelectronics and Microsensors, Johannes Kepler University Linz, 4040 Linz, Austria,
e-mail: thomas.voglhuber-brunnmaier@jku.at, Bernhard.Jakoby@jku.at

Finite Element Method (FEM)   Boundary Element Method (BEM)
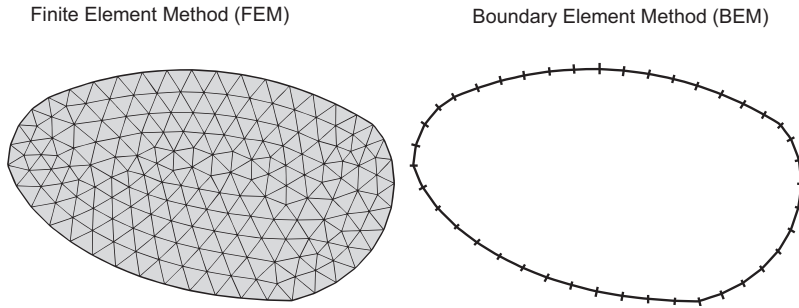
Fig. 26.1: Discretizations using finite elements (left) and boundary elements (right).

spatial directions (which we will label x and y), yet allows some material parameter variation in a third direction (z), where only piecewise constant material parameters are required, in short, we are considering layered geometries. The effects of the layers can be incorporated in the used Green's functions such that the interfaces between the layers need not be discretized. Compared to using Finite Element Methods, BEM approaches also represent a distinct benefit when layered structures with high aspect ratios are modeled[1]. This can be illustrated using the example of modeling resonant fluid sensors for viscosity measurement, where this approach is very efficient. Here, the fluid of density ρ and dynamic viscosity η to be characterized is brought in contact with a surface of the sensor vibrating harmonically in-plane thus exciting shear waves in the fluid, whose penetration depth depends on the viscosity of the fluid. In particular, the amplitude decays according to $\exp(-|z|/\delta)$ in the surface-normal direction z with δ denoting the characteristic penetration depth given by [5, 6]

$$\delta = \sqrt{\frac{2\eta}{\rho\omega}}. \tag{26.1}$$

For instance, in the case of a conventional 330 μm thick quartz disk vibrating at 5 MHz in the so-called thickness-shear mode, the penetration depth δ becomes approx 250 nm when it is immersed in water ($\rho = 1000$ kg/m^3, $\eta = 1$ mPa s). In comparison to the typical lateral dimensions of such a device (e.g., 12.7 mm diameter), the aspect ratio associated with relevant changes of the variables (e.g., displacement) is therefore approx. 50000, which is difficult to handle in a finite element implementation.

---

[1] We note that special elements can be used to tackle this issue, see, e.g., [4]

26.2 Modeling

26.2.1 Governing Equations

In the following, the governing equations of linear elasticity, electromagnetism, and piezoelectricity are provided.

26.2.1.1 Linear Elastodynamics

The equations of elastodynamics are given by Newton's second law of motion in differential form and the elastic constitutive equations, which, in continuum form, can be written as [7]

$$\rho \ddot{\boldsymbol{u}} = \nabla \cdot \boldsymbol{T}, \quad \boldsymbol{T} = \boldsymbol{c} : \boldsymbol{S}, \quad \boldsymbol{S} = \nabla_{\mathrm{s}} \boldsymbol{u}. \tag{26.2}$$

The quantities $\boldsymbol{T}$, $\boldsymbol{S}$, and $\boldsymbol{u}$ denote stress and strain tensor and the mechanical displacement vector, respectively. Material constants are mass density ρ and linear stiffness tensor $\boldsymbol{c}$. The operators $\nabla \cdot ()$ and $\nabla_{\mathrm{s}}()$ denote divergence and symmetric gradient. The double dot product indicates summation over pairs of indices.

26.2.1.2 Electrodynamics

Electrodynamics are governed by Maxwell's Eq. (26.3) and the constitutive Eq. (26.4)

$$\nabla \cdot \boldsymbol{D} = \varrho, \quad \nabla \times \boldsymbol{E} = -\frac{\partial \boldsymbol{B}}{\partial t}, \quad \nabla \cdot \boldsymbol{B} = 0, \quad \nabla \times \boldsymbol{H} = \boldsymbol{J} + \frac{\partial \boldsymbol{D}}{\partial t}, \tag{26.3}$$

$$\boldsymbol{D} = \boldsymbol{\varepsilon} \cdot \boldsymbol{E}, \quad \boldsymbol{B} = \boldsymbol{\mu} \cdot \boldsymbol{H}. \tag{26.4}$$

The vector field quantities $\boldsymbol{D}, \boldsymbol{E}, \boldsymbol{B}, \boldsymbol{H},$ and $\boldsymbol{J}$ denote electric displacement, electric field, magnetic flux density, magnetic field, and current density, respectively. For lower frequencies, the electric field $\boldsymbol{E}$ can often be considered as being approximately curl-free (i.e., no significant fields $\partial \boldsymbol{B}/\partial t$ are present) such that it can be expressed in terms of the gradient of a scalar potential φ (i.e., the quasistatic approximation [8])

$$\boldsymbol{E} = -\nabla \varphi. \tag{26.5}$$

26.2.1.3 Piezoelectric Media

In piezoelectric media, mechanical stresses and deformations are linked to electric field and polarization, which, for the linear case, can be represented by expanding the constitutive equations of electrostatics and elasticity by coupling them in terms of a third-rank piezoelectric stress tensor $\boldsymbol{e}$ [7]

$$T = c^E : S - e : E, \quad D = e : S + \varepsilon^S \cdot E. \tag{26.6}$$

The superscripts E and S denote that the respective quantity is measured under a constant electric field or constant strain. By combining Eqs. (26.2), (26.5), and (26.6) and considering no free charges ϱ and current densities J present within the material, the complete set of equations describing the dynamics of a piezoelectric element is obtained as

$$\rho \ddot{u} = \nabla \cdot \left(c^E : \nabla_s u \right) + \nabla \cdot (e : \nabla \varphi), \tag{26.7}$$

$$0 = \nabla \cdot (e : \nabla_s u) - \nabla \cdot \left(\varepsilon^S \cdot \nabla \varphi \right).$$

These are four coupled partial differential equations (PDE) of second order in u and φ. In the following, the most general examples will refer to problems involving piezoelectric media, where, as a special case, also an introductory electrostatic problem is considered. In the following treatment, we will thus in general consider the case of piezoelectric media if not noted otherwise.

26.2.2 Dimensional Analysis and Scaling

26.2.2.1 Non-Dimensionalization

The approach most often employed to enhance numerical stability is to introduce non-dimensional variables, e.g.,

$$u = u_0 u', \varphi = \varphi_0 \varphi', \rho = \rho_0 \rho', c = c_0 c', \varepsilon = \varepsilon_0 \varepsilon', \nabla = \nabla'/L_0, \nabla_s = \nabla'_s/L_0, t = t_0 t', \tag{26.8}$$

where the primed quantities are dimensionless variables and the scales $c_0, \varepsilon_0,$ and e_0 are chosen such that the matrices in Eq. 26.17 are of similar magnitude. When moving into the spectral domain, the associated scaled wavenumbers (spatial-spectral variables) $k'_x = k_x L_0$ and $k'_y = k_y L_0$, as well as the scaled angular frequency (temporal-spectral variable) $\omega' = \omega t_0$ should be close to 1. It is, therefore, suitable to choose $L_0 \approx \lambda/2\pi$ where λ corresponds to the expected dominant wavelength, and $t_0 = 1/\omega$. By furthermore demanding the following relations

$$\frac{e_0^2}{c_0 \varepsilon_0} = 1, \quad \frac{\varepsilon_0 \varphi_0}{e_0 u_0} = 1, \quad \frac{L_0^2 \rho_0}{t_0^2 c_0} = 1, \tag{26.9}$$

the resulting equations are of the same form as Eq. (26.7)

$$\rho' \frac{\partial^2 u'}{\partial t'^2} = \nabla' \cdot \left(c'^E : \nabla'_s u' \right) + \nabla' \cdot (e' : \nabla' \varphi'), \tag{26.10}$$

$$0 = \nabla' \cdot (e' : \nabla'_s u') - \nabla' \cdot \left(\varepsilon'^S \cdot \nabla' \varphi' \right).$$

Considering the usual range of parameters, a reasonable choice for the scaling factors for instance is

$$u_0 = 10^{-12}\,\text{m}, \quad c_0 = 10^{12}\,\text{N/m}^2, \quad e_0 = 1, \varphi_0 = 1\,\text{V}, \quad \varepsilon_0 = 10^{-12}\,\text{F/m}, \quad (26.11)$$

$$\rho_0 = 10^4\,\text{kg/m}^3, \quad L_0 = 10^{-2}\,\text{m}, \quad t_0 = 10^{-6}\,\text{s}.$$

26.2.2.2 Scaling of Physical Units

Numerical stability can also be enhanced by scaling the physical base units by attaching an arbitrary number to the required four base SI-units kilogram (s_{kg}), meter (s_{m}), second (s_{s}), and Ampere (s_{A}). All physical quantities enter the computation multiplied by these numbers. For instance, if a voltage of 1V is prescribed at an electrode, one sets the potential to $\varphi' = 1V\,s_{\text{kg}}s_{\text{m}}^2 s_{\text{A}}^{-1} s_{\text{s}}^{-3}$. After the computation was performed, the results are scaled back. The calculated displacement $\boldsymbol{u}$ due to an electrode potential is obtained by $\boldsymbol{u} = \boldsymbol{u}'/s_{\text{m}}$. This approach features four degrees of freedom such as the non-dimensionalization above, but the adjustment of the scales is not as straightforward. However, this method has the valuable property of disclosing unit errors in the computation code very conveniently, because if the four scales are varied, the back-scaled computation results must not change.

26.2.3 Conversion to Ordinary Differential Equations

The PDE in Eq. (26.10) are reduced to a system of ordinary differential equations (ODE) by performing a partial Fourier transform ($i = \sqrt{-1}$) with the transformation pair in Eqs. (26.12) and (26.13)

$$\tilde{f}(k_x, k_y, z, \omega) = \iiint_{-\infty}^{\infty} f(x, y, z, t)e^{-i(\omega t - k_x x - k_y y)}\,dx\,dy\,dt, \qquad (26.12)$$

$$f(x, y, z, t) = \frac{1}{(2\pi)^3} \iiint_{-\infty}^{\infty} \tilde{f}(k_x, k_y, z, \omega)e^{i(\omega t - k_x x - k_y y)}\,dk_x\,dk_y\,d\omega. \quad (26.13)$$

Upon Fourier transform from $\{x, y, z, t\} \rightarrow \{k_x, k_y, z, \omega\}$, differential operators can be replaced using the substitutions

$$\partial/\partial x \rightarrow -ik_x, \quad \partial/\partial y \rightarrow -ik_y, \quad \text{and} \quad \partial/\partial t \rightarrow i\omega. \qquad (26.14)$$

Application of this transform to the governing equations for fields in piezoelectric media, in a straightforward manner thus yields a system of ODEs of order two and dimension four with matrices $\boldsymbol{P}$ and $\boldsymbol{Q}$, which are not specified in more detail at this point:

$$\frac{\partial^2 \tilde{\psi}'}{\partial z^2} = \boldsymbol{P} \cdot \frac{\partial \tilde{\psi}'}{\partial z} + \boldsymbol{Q} \cdot \tilde{\psi}' \quad \text{with} \quad \tilde{\psi}' = \begin{bmatrix} \tilde{u} \\ \tilde{\varphi} \end{bmatrix}. \tag{26.15}$$

By applying a suitable transform, the second derivatives can be replaced using elements of the stress tensor and the dielectric displacement associated with the normal direction z yielding a system of dimension 8×8

$$\frac{\partial \tilde{\psi}}{\partial z}(k_x, k_y, z, \omega) = \boldsymbol{A}(k_x, k_y, \omega) \cdot \tilde{\psi}(k_x, k_y, z, \omega) \tag{26.16}$$

with

$$\tilde{\psi} = [\tilde{u}_x, \tilde{u}_y, \tilde{u}_z, \varphi, \tilde{T}_{xz}, \tilde{T}_{yz}, \tilde{T}_{zz}, \tilde{D}_z]^{\mathrm{T}}.$$

As it turns out, the field variables gathered in the vector $\tilde{\psi}$ exactly represent the field components that are subject to interface conditions when crossing interfaces between regions filled with different materials with a surface normal oriented in z direction (the so-called axis of stratification). This becomes useful when considering layered structures. In the following, the matrix $\boldsymbol{A}$ is given by

$$\boldsymbol{A}(k_x, k_y, \omega) = \begin{bmatrix} \boldsymbol{P}_{\mathrm{A}}^{-1} \boldsymbol{P}_{\mathrm{B}}^{\mathrm{T}} & \boldsymbol{P}_{\mathrm{A}}^{-1} \\ \boldsymbol{P}_{\mathrm{B}} \boldsymbol{P}_{\mathrm{A}}^{-1} \boldsymbol{P}_{\mathrm{B}}^{\mathrm{T}} + \boldsymbol{P}_{\mathrm{C}} & \boldsymbol{P}_{\mathrm{B}} \boldsymbol{P}_{\mathrm{A}}^{-1} \end{bmatrix}, \tag{26.17}$$

$$\boldsymbol{P}_{\mathrm{B}} = \mathrm{i} k_x \boldsymbol{P}_{\mathrm{B}x} + \mathrm{i} k_y \boldsymbol{P}_{\mathrm{B}y},$$

$$\boldsymbol{P}_{\mathrm{C}} = k_x^2 \boldsymbol{P}_{\mathrm{C}xx} + k_x k_y (\boldsymbol{P}_{\mathrm{C}xy} + \boldsymbol{P}_{\mathrm{C}xy}^{\mathrm{T}}) + k_y^2 \boldsymbol{P}_{\mathrm{C}yy} - \omega^2 \boldsymbol{P}_{\mathrm{C}tt},$$

$$\boldsymbol{P}_{\mathrm{C}tt} = \mathrm{diag}\left([\rho, \rho, \rho, 0]\right),$$

$$\boldsymbol{P}_{\mathrm{A}} = \begin{bmatrix} c_{55} & c_{45} & c_{35} & e_{35} \\ c_{45} & c_{44} & c_{34} & e_{34} \\ c_{35} & c_{34} & c_{33} & e_{33} \\ e_{35} & e_{34} & e_{33} & -\varepsilon_{33} \end{bmatrix}, \quad \boldsymbol{P}_{\mathrm{B}x} = \begin{bmatrix} c_{15} & c_{14} & c_{13} & e_{31} \\ c_{56} & c_{46} & c_{36} & e_{36} \\ c_{55} & c_{45} & c_{35} & e_{35} \\ e_{15} & e_{14} & e_{13} & -\varepsilon_{13} \end{bmatrix},$$

$$\boldsymbol{P}_{\mathrm{B}y} = \begin{bmatrix} c_{56} & c_{46} & c_{36} & e_{36} \\ c_{25} & c_{24} & c_{23} & e_{32} \\ c_{45} & c_{44} & c_{34} & e_{34} \\ e_{25} & e_{24} & e_{23} & -\varepsilon_{23} \end{bmatrix}, \quad \boldsymbol{P}_{\mathrm{C}xx} = \begin{bmatrix} c_{11} & c_{16} & c_{15} & e_{11} \\ c_{16} & c_{66} & c_{56} & e_{16} \\ c_{15} & c_{56} & c_{55} & e_{15} \\ e_{11} & e_{16} & e_{15} & -\varepsilon_{11} \end{bmatrix},$$

$$\boldsymbol{P}_{\mathrm{C}xy} = \begin{bmatrix} c_{16} & c_{12} & c_{14} & e_{21} \\ c_{66} & c_{26} & c_{46} & e_{26} \\ c_{56} & c_{25} & c_{45} & e_{25} \\ e_{16} & e_{12} & e_{14} & -\varepsilon_{12} \end{bmatrix}, \quad \boldsymbol{P}_{\mathrm{C}yy} = \begin{bmatrix} c_{66} & c_{26} & c_{46} & e_{26} \\ c_{26} & c_{22} & c_{24} & e_{22} \\ c_{46} & c_{24} & c_{44} & e_{24} \\ e_{26} & e_{22} & e_{24} & -\varepsilon_{22} \end{bmatrix},$$

which is also particularly useful when considering the fields within a single layer of a layered structure (again assuming z to be the axis of stratification). Considering layered media of this type, all material parameters do not show any dependence with respect to x and y and, within such a layer, also not with respect to z. The independence with respect to x and y particularly simplifies the problem as the material parameters can then be treated as constant when performing the Fourier transform. By considering usual material parameter ranges and field amplitudes, it

is apparent that they differ by up to 20 orders of magnitudes. Appropriate scaling as outlined in Sec. 26.2.2 is therefore necessary to avoid numerical instability.

26.2.4 Equation System and Green's Function

The solution of the ODE system in Eq. (26.16) can be composed by the eigenvalues λ_i and the eigenvectors $\boldsymbol{v}_i$. This becomes obvious when a solution ansatz featuring a z-dependence proportional to $\exp(\lambda z)$ is made, which directly yields a matrix eigenproblem. Using the matrix $\boldsymbol{X}(z)$ to denote the fundamental matrix, we may thus write for the complete solution

$$\tilde{\boldsymbol{\psi}}(z) = \sum_{i=1}^{8} \boldsymbol{v}_i e^{\lambda_i z} c_i = \boldsymbol{X}(z) \cdot \boldsymbol{c} \quad \text{with} \quad \boldsymbol{X}(z) = \boldsymbol{V} \cdot \text{diag}([e^{\lambda_1 z}, \dots, e^{\lambda_8 z}]), \quad (26.18)$$

which represents a superposition of all possible solutions associated with the eight eigenvalues and eigenvectors with thus far unknown expansion coefficients c_i. For layered problems, this general solution can be established for each layer and the expansion coefficients can be determined from interface and boundary conditions. If the layered structure is bounded by a half-space, radiative boundary conditions, e.g., for infinite air half-spaces above and below the layered structure, can be established by setting up a reduced fundamental matrix of dimension 8×4 which incorporates only the outward decaying field components (i.e., the ones featuring an outward decaying Poynting vector). Doing so, we may write

$$\tilde{\boldsymbol{\psi}}(z) = \sum_{i=1}^{4} \boldsymbol{v}_i' e^{\lambda_i' z} c_i = \boldsymbol{X}^{\text{rad}}(z) \cdot \boldsymbol{c}^{\text{rad}} \tag{26.19}$$

with

$$\boldsymbol{X}^{\text{rad}}(z) = \boldsymbol{V}' \cdot \text{diag}([e^{\lambda_1' z}, e^{\lambda_2' z}, e^{\lambda_3' z}, e^{\lambda_4' z}]).$$

For multilayered material systems consisting of N layers, the interface conditions are

$$\boldsymbol{X}_{n+1}(-d_{n+1}/2) \cdot \boldsymbol{c}_{n+1} = \boldsymbol{X}_n(d_n/2) \cdot \boldsymbol{c}_n + \Delta\tilde{\boldsymbol{\psi}}_n \quad \forall n = 0, \dots, N-1. \tag{26.20}$$

This condition enforces continuity of the field components represented in $\tilde{\boldsymbol{\psi}}(z)$ at each interface if the term $\Delta\tilde{\boldsymbol{\psi}}_i$ vanishes. The latter represents a "source term" that can account for discontinuities due to sources embedded at the interfaces (see the discussion below). Note that in the above representation, local coordinate systems were used, where $z_i = 0$ is defined at the center of the respective layer i. In the case of infinite half-spaces, the local coordinate origin is defined at the interface itself. These local coordinates were introduced, since using a global thickness coordinate would result in strongly differing magnitudes of the fundamental matrices, and are therefore numerically problematic.

In Eq. (26.20), the term $\Delta\tilde{\psi}_i$ represents a "source term" causing a discontinuity of the field's components represented in $\tilde{\psi}$ across the interface. Of particular physical relevance is the discontinuity of the mechanical stresses contained in $\tilde{\psi}$ (i.e., $\tilde{T}_{xz}, \tilde{T}_{yz}, \tilde{T}_{zz}$), which are equivalent to surface force densities ($\tilde{f}_x, \tilde{f}_y, \tilde{f}_z$, also known as tractions) acting at the interface. Similarly, a discontinuity in the vertical component of the dielectric displacement $\tilde{D}_z$ is equivalent to an electrical surface charge density $\tilde{\varrho}$ located at the interface. For the investigated applications, the piezoelectric elements are excited by time-harmonic currents applied to conductive paths at the faces of the piezoelectric material, i.e., no interfacial stress sources are considered between the layers. As an example, a typical problem featuring a single piezoelectric layer with an electrically grounded and mechanically fixed underside and electrodes on the topside (adjacent to a halfspace $z > d_2$ filled with air) is shown in Fig. 26.2. To solve for the fields associated with this problem, the matrices describing the spectral domain fields in the piezoelectric layer and the half-space above are established as discussed before and the interface conditions are enforced by setting up the following matrix equation:

$$\begin{bmatrix} \tilde{X}_1^{\mathrm{rad}}(0) & -\tilde{X}_2(d_2/2) \\ 0 & \tilde{X}_2^{\mathrm{BC}}(-d_2/2) \end{bmatrix} \begin{bmatrix} c_1^{\mathrm{rad}} \\ c_2 \end{bmatrix} = - \begin{bmatrix} \Delta\tilde{\psi} \\ 0 \end{bmatrix}. \tag{26.21}$$

The source terms at the air/piezo interface are collected in $\Delta\tilde{\psi}$ and the boundary conditions at the lower face of the piezoelectric layer (at $z = 0$) are implemented by selecting the components which should be identical zero (i.e., the first 4 elements of $\tilde{\psi}_2$, see Eq. (26.16)), i.e.,

$$\tilde{X}_2^{\mathrm{BC}} = \tilde{X}_2[1\ldots4, 1\ldots8], \tag{26.22}$$

which means that $\tilde{X}_2^{\mathrm{BC}}$ represents the upper half (first four rows) of the matrix $\tilde{X}_2$. Although the air half-space could be well replaced by a mechanical zero stress condition at low frequencies, it has to be considered for the electrical field which extends
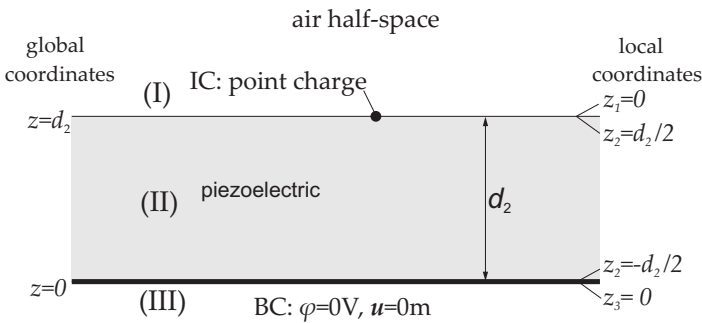
Fig. 26.2: Layer of piezoelectric material with air-halfspace above. At the air/piezo interface the fields are continuous, except for the jump in dielectric displacement caused by a point charge.

largely into the surrounding air. Solving Eqs. (26.21) for surface displacements and potential at the top side of material (II) yields therefore the dyadic spectral Green's functions relating the surface displacements u_x, u_y, u_z and the potential φ to the surface force vector $[\tilde{f}_x, \tilde{f}_y, \tilde{f}_z]^T$ and the charge $\tilde{\varrho}$ at the piezo/air interface (which excite these responses) as

$$
\begin{bmatrix} \tilde{u}_x \\ \tilde{u}_y \\ \tilde{u}_z \\ \tilde{\varphi} \end{bmatrix} = \begin{bmatrix} \tilde{G}_{ux;fx} & \tilde{G}_{ux;fy} & \tilde{G}_{ux;fz} & \tilde{G}_{ux;\varrho} \\ \tilde{G}_{uy;fx} & \tilde{G}_{uy;fy} & \tilde{G}_{uy;fz} & \tilde{G}_{uy;\varrho} \\ \tilde{G}_{uz;fx} & \tilde{G}_{uz;fy} & \tilde{G}_{uz;fz} & \tilde{G}_{uz;\varrho} \\ \tilde{G}_{\varphi;fx} & \tilde{G}_{\varphi;fy} & \tilde{G}_{\varphi;fz} & \tilde{G}_{\varphi;\varrho} \end{bmatrix} \cdot \begin{bmatrix} \tilde{f}_x \\ \tilde{f}_y \\ \tilde{f}_z \\ \tilde{\varrho} \end{bmatrix}.
\tag{26.23}
$$

When considering piezoelectric devices such as sensors, most often no external time-harmonic forces but only electrical currents are applied. Therefore, only the Green's functions for surface charges have to be considered:

$$
\begin{bmatrix} \tilde{G}_{ux;\varrho} \\ \tilde{G}_{uy;\varrho} \\ \tilde{G}_{uz;\varrho} \\ \tilde{G}_{\varphi;\varrho} \end{bmatrix} = \tilde{X}_2(d_2/2) \cdot c_2.
\tag{26.24}
$$

To calculate these (and other) Green's functions, the source vector $\Delta\tilde{\psi}$ (appearing in Eq. (26.21)) in this case is set to

$$
\Delta\tilde{\psi} = [0,0,0,0,0,0,0,1]^T,
\tag{26.25}
$$

where the 1 represents a constant spectral surface charge over all wavenumbers which corresponds to a unit point charge in the spatial domain, which, in turn, is the proper excitation term for these Green's functions.

26.2.5 Electrical Field Calculation

In the time-harmonic spatial domain, the electric surface charge and the electric potential are related by the convolution integral

$$
\varphi(x,y,d_2/2,\omega) = \iint G_{\varphi;\varrho}(x-x',y-y',\omega)\varrho(x',y',d_2/2,\omega)dx'dy',
\tag{26.26}
$$

since the lateral spatial uniformity of the structure (i.e., the independence of the material parameters from x and y) imposes a lateral translation invariance. This means that if a particular source distribution is shifted laterally by some distance, the associated fields generated by these sources shift by the same distance. If we consider the case that some portions of an interface (between layers and/or half-spaces) are

covered by conducting electrodes[2], the electric potential at each of these electrodes will be constant and surface charges will only appear in electrode-covered regions. By applying voltages to the electrodes (e.g., to generate mechanical deformations in the structure by virtue of piezoelectricity) the potential at the electrodes is prescribed and the electrode charge has to be determined. The relation between potential and charge can be described by the above convolution integral. Thanks to the properties of the Fourier transform, in the spectral domain the convolution is replaced by a simple multiplication

$$\tilde{\varphi}(k_x, k_y, d_2/2, \omega) = \tilde{G}_{\varphi;\varrho}(k_x, k_y, \omega)\tilde{\varrho}(k_x, k_y, d_2/2, \omega), \qquad (26.27)$$

which is exploited for the electrostatic field computation by the so-called method of moments as will be described below.

26.2.5.1 Method of Moments

In electrodynamics, a common approach for solving field problems is using the methods of *mean weighted residuals*, which is also known by the term *method of moments (MoM)* [9]. Here, the charge distribution is approximated by a set of trial (or basis) functions $B_i(x, y)$ with corresponding Fourier transform $\tilde{B}_i(k_x, k_y)$:

$$\varrho(x, y) = \sum_{i=0}^{\infty} a_i B_i(x, y) \ \circ\!\!-\!\!\bullet \ \tilde{\varrho}(k_x, k_y) = \sum_{i=0}^{\infty} a_i \tilde{B}_i(k_x, k_y). \qquad (26.28)$$

The expansion coefficients a_i are determined by the potentials prescribed at the electrodes. The derivation of Green's function and therefore the application of the MoM is particularly efficient in the spectral domain. Starting point is therefore the inverse Fourier transform of Eq. (26.27) (omitting the arguments $d_2/2$ and ω for notational simplicity) and the expansion of the charges in Eq. (26.28) yielding

$$\varphi(x, y) = \frac{1}{4\pi^2} \sum_{i=0}^{\infty} a_i \int_{-\infty}^{\infty} \int_{-\infty}^{\infty} \tilde{G}_{\varphi;\varrho}(k_x, k_y) \tilde{B}_i(k_x, k_y) e^{-i(k_x x + k_y y)} dk_x dk_y. \quad (26.29)$$

As the expansion of the charge distribution is an approximation of the real (unknown) charge distribution, the above potential cannot be expected to match the required (prescribed) potential at the electrodes everywhere on the electrodes. To fulfill these boundary conditions at least in an averaged sense, the equation is therefore multiplied (weighted) by the functions $T_j(x, y)$ (often also referred to as test functions) and integrated with respect to x and y. The resulting integrals over x and y on the right-hand side concern the test functions $T_j(x, y)$ and the exponential $e^{-i(k_x x + k_y y)}$ which can be written as the conjugated Fourier transform of the testing

---

[2] We adopt the approximation that these electrodes can be considered as infinitely thin, perfectly conducting, and massless.

functions[3], yielding

$$
\underbrace{\int\limits_{-\infty}^{\infty}\int\limits_{-\infty}^{\infty} T_j(x,y)\varphi(x,y)dxdy}_{b_j}
$$

$$
= \sum_{i=0}^{\infty} a_i \underbrace{\frac{1}{4\pi^2}\int\limits_{-\infty}^{\infty}\int\limits_{-\infty}^{\infty} \tilde{G}_{\varphi;\varrho}(k_x,k_y)\tilde{B}_i(k_x,k_y)\tilde{T}_j^*(k_x,k_y)dk_xdk_y}_{M_{ij}}.
$$
(26.30)

Evaluating the integrals (which is straightforward as they run over the known weighting and trial functions), a linear equation system is obtained which can be solved for the expansion coefficients a_i from which, in turn, the spatial charge distribution $\varrho(x,y)$ can be calculated using Eq. (26.28):

$$
b_j = M_{ij}a_i \rightarrow a_i = \left(M^{-1}\right)_{ij} b_j.
$$
(26.31)

The integrals in Eq. (26.30) may also be represented by inner product notation for convenience:

$$
\ll T_j\varphi \gg = \frac{1}{4\pi^2}\sum_{i=0}^{\infty} a_i \ll \tilde{G}_{\varphi;\varrho}\tilde{B}_i\tilde{T}_j^* \gg.
$$
(26.32)

The Galerkin method and point-matching (collocation) are two common variations of the method. Although the trial and weighting functions can be independently chosen, in the so-called Galerkin method, due to advantages in terms of accuracy and convergence [10] equal sets are chosen:

$$
\ll B_j\varphi \gg = \frac{1}{4\pi^2}\sum_{i=0}^{\infty} a_i \ll \tilde{G}_{\varphi;\varrho}\tilde{B}_i\tilde{B}_j^* \gg.
$$
(26.33)

In the point matching method, the potential φ is enforced to match the boundary conditions at discrete points x_j and y_j only, i.e.,

$$
\varphi(x_j,y_j) = \frac{1}{4\pi^2}\sum_{i=0}^{\infty} a_i \ll \tilde{G}_{\varphi;\varrho}\tilde{B}_i e^{-i(k_xx_j+k_yy_j)} \gg.
$$
(26.34)

Point-matching is known as being less accurate [10] on average but can be implemented very efficiently using the fast Fourier transform (FFT). The calculation of the M matrix, requires two-dimensional infinite integrals, generally with a highly oscillating kernel for which generally no closed-form representations are available thus representing the major numerical cost of the method. For handling this problem,

---

[3] The conjugate results from the minus sign in the exponential.

several options can be considered, depending on properties of the Green's function and the computational domain. E.g., for periodic problems with periods L_x and L_y in the lateral directions, the Fourier integral can be replaced by a Fourier series yielding for the MoM:

$$
\underbrace{\frac{1}{L_x L_y} \int_{-L_x/2}^{L_x/2} \int_{-L_y/2}^{L_y/2} T_j(x,y)\varphi(x,y)\,dx\,dy}_{b_j}
$$
$$
= \sum_{i=0}^{\infty} a_i \underbrace{\sum_{m=-\infty}^{\infty} \sum_{n=-\infty}^{\infty} \tilde{G}_{\varphi;\varrho}(k_m,k_n)\tilde{B}_i(k_m,k_n)\tilde{T}_j^*(k_m,k_n)}_{M_{ij}},
\tag{26.35}
$$

with $k_m = 2\pi m/L_x$ and $k_n = 2\pi n/L_y$.

For the numerical implementation, the wavenumbers and the trial functions have to be truncated. The best choices for the trial functions are functions that already approximate the expected solution to a certain degree and whose wavenumber spectrum decays fast.
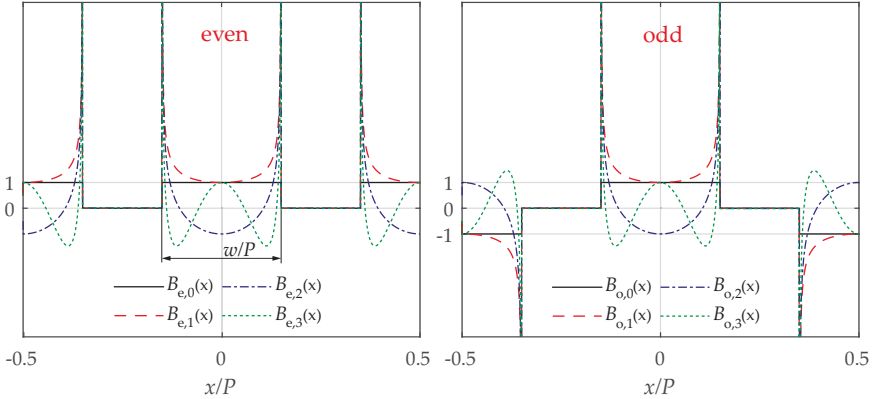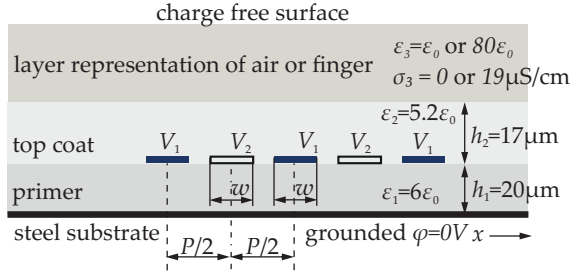
26.3 Examples

In the following, the application of the methods outlined above is illustrated using a selection of problems including electrostatic, elastodynamic, and piezoelectric systems, where more details can be found in the references provided. We start with a quasi-electrostatic example of interdigitated electrodes buried in isotropic dielectric media.

26.3.1 Electrical Capacitance Calculation of Interdigital Capacitors

Screen-printed, interdigital capacitors implemented in polymer coatings of steel substrates for touch-sensitive applications first presented in [11] are discussed in this example. A simple numerical method for the calculation of the electrical characteristics for an idealized periodic sequence of electrodes for the structure shown in Fig. 26.3 is presented. A special feature of this example is the use of global trial functions (shown in Fig. 26.4) instead of functions with local support (e.g., triangles) and the simple implementation of periodicity by using a Fourier series instead of Fourier integrals. Furthermore, the implementation of an even/odd analysis is simple and allows a full analysis of different electrical contact schemes, as shown in Fig. 26.5 (right). The layer composition comprises a polymeric primer layer on a steel substrate

Fig. 26.3 Interdigital capacitor included in coatings of metal substrates. The period is $P = 1.8$ mm and the electrode width $w = 0.45$ mm.

charge free surface

$\varepsilon_3 = \varepsilon_0$ or $80\varepsilon_0$
$\sigma_3 = 0$ or $19\,\mu$S/cm

layer representation of air or finger

$\varepsilon_2 = 5.2\varepsilon_0$

top coat V_1 V_2 V_1 V_2 V_1 $h_2 = 17\,\mu$m

primer w w $\varepsilon_1 = 6\varepsilon_0$ $h_1 = 20\,\mu$m

steel substrate $P/2$ $P/2$ grounded $\varphi = 0$V $x \longrightarrow$

Fig. 26.4: First four trial functions for even and odd mode. © 2017 IEEE. Reprinted, with permission, from [11]. .
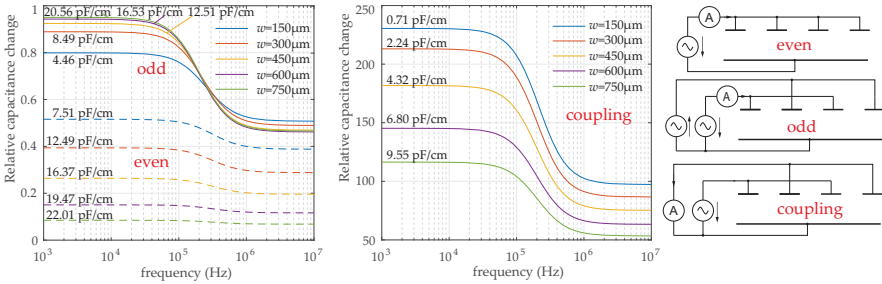
Fig. 26.5: Relative capacitance changes from air to water (simulating touching finger). The changes of even and odd capacitance (left) are comparably small, but large for the coupled capacitance (middle). The given capacitance values are per finger pair of varying finder width w for the water-covered ($\sigma = 1.9$ mS/m and $\varepsilon = 80\,\varepsilon_0$) case at low frequency (1 kHz). © 2017 IEEE. Reprinted, with permission, from [11]. The right figure shows the measurement arrangements for even, odd, and coupling mode operations..

with electrode fingers on top, covered by a polymeric top coating layer. The layer above the top coat is either air or loaded with an ohmic-permittive material that mimics a touching finger.

The method outlined above is reduced to the 2D quasi-electrostatic case (magnetic fields are neglected) and an even/odd field analysis is performed. By superimposing the results for even and odd analysis a so-called coupling mode is realized, i.e., where the left fingers are driven (e.g., by a voltage generator) and the current from the right fingers shunted to the ground is measured. This mode has shown to be of extraordinary sensitivity for detecting a touching finger [12].

For the numerical model, the materials are considered non-piezoelectric and no mechanical forces are prescribed. The piezoelectricity tensor $\boldsymbol{e}$ in Eq. (26.17) is therefore set to 0, and the governing equations for the electrical part degenerate to

$$\boldsymbol{D} = -\varepsilon\nabla\varphi \quad \text{and} \quad \nabla\cdot\boldsymbol{D} = 0. \tag{26.36}$$

The system matrix according to Eq. (26.36) is obtained by selecting only elements 4 and 8 yielding for $\boldsymbol{A}$ from Eq. (26.17)

$$\frac{\partial}{\partial z}\begin{bmatrix} \tilde{\varphi} \\ \tilde{D}_z \end{bmatrix} = \begin{bmatrix} 0 & -1/\varepsilon \\ k^2\varepsilon & 0 \end{bmatrix} \cdot \begin{bmatrix} \tilde{\varphi} \\ \tilde{D}_z \end{bmatrix} \quad \text{with} \quad k^2 = k_x^2 + k_y^2. \tag{26.37}$$

The finite length of the fingers in y-direction is disregarded by setting wavenumber k_y to zero, which is associated with infinitely long fingers. The resulting capacitances are then obtained as quantities per unit length in y-direction. The eigensystem to Eq. (26.37) is $\lambda_{1,2} = \pm ik$ and $\boldsymbol{v}_{1,2} = [\pm 1, i\varepsilon k]^T$. The spectral Green's functions[4] $\tilde{G}$ for the multilayered structure can be determined by the global matrix method [13], or more straightforwardly by assembling individual layers exemplarily shown in Fig. 26.6. Layer n transforms the underlying layers represented by Green's function $\tilde{G}_{n-1}$ according to

$$\tilde{G}_{\mathrm{L}} = \frac{\varepsilon_n\tilde{G}_{n-1}k + \tanh(h_nk)}{\varepsilon_nk(1 + \varepsilon_n\tilde{G}_{n-1}k\tanh(h_nk))}. \tag{26.38}$$

The complete Green's function is obtained by reciprocal addition of the upper ($\tilde{G}_{\mathrm{U}} = \tilde{G}_{n+1}$) and lower Green's function, i.e.,

$$\tilde{G} = (\tilde{G}_{\mathrm{U}}^{-1} + \tilde{G}_{\mathrm{L}}^{-1})^{-1}. \tag{26.39}$$

Fig. 26.6 The Green's function $\tilde{G}$ a the upper interface of layer n is determined by reciprocal adding of functions seen above ($\tilde{G}_{\mathrm{U}}$) and below ($\tilde{G}_{\mathrm{L}}$).

---
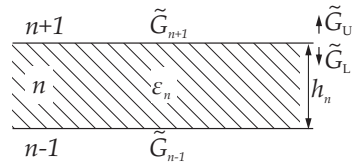
[4] The subscripts are dropped, i.e., $\tilde{G} = \tilde{G}_{\varphi;\varrho}$.

The interdigitated structure is P-periodic. This is conveniently implemented in the spectral domain representation using a Fourier series at the discrete wavenumbers $k_m = 2\pi m/P$ for integer m. For this simple problem, global trial functions yielding fast convergence are used, which provide already remarkable accuracy if only, e.g., two trial functions are used (see, e.g., the demo code in [14]). In Fig. 26.4 the first four trial functions for even and odd mode are shown. They represent scaled periodical repetitions of the rectangular function for order $i = 0$ and of the form $T_{2(i-1)}(x)/\sqrt{1-x)^2}$ $\forall i \in \{1, 2, \dots\}$, where $T_p(x)$ denotes the Chebyshev polynomials of order p. The n-th Fourier coefficient for trial function i is given by

$$\tilde{B}_{\text{e/o},0;n} = \sin(\alpha n\pi)/n\pi(1 \pm (-1)^n), \tag{26.40}$$

$$\tilde{B}_{\text{e/o},i;n} = (-1)^{i-1}\frac{\alpha\pi}{2}J_{2(i-1)}(\alpha n\pi)(1 \pm (-1)^n), \; i = 1,2,\dots \tag{26.41}$$

with $\alpha = w/P$ and J_p denoting the Bessel function of first kind and order p. Using the $+$ sign in the equations gives the even functions (e), using $-$ the odd ones (o).

$$b_{\text{e/o},j} = \frac{1}{P} \int\limits_{-P/2}^{P/2} B_{\text{e/o},j}(x)\varphi(x)dx, \tag{26.42}$$

$$M_{\text{e/o},ij} = \sum_{n=-\infty}^{\infty} \tilde{G}(2\pi n/P)\tilde{B}_{\text{e/o},i;n}\tilde{B}_{\text{e/o},j;n}^* \tag{26.43}$$

The expansion coefficients for even and odd mode $a_{\text{e/o},i}$ are calculated by using Eq. (26.31) and subsequently the charge density is evaluated with Eq. (26.28) from which the capacitances are calculated by integration over one electrode divided by the driving voltage. The authors showed in [11] by even/odd analysis that for capacitive touch sensor applications the measurement of a coupling capacitance as shown in Fig. 26.5 is most sensitive in terms of relative capacitance change from air to a highly permittive and moderately conductive (σ) applied layer, which is also verified experimentally in [12]. The low-pass frequency dependence, caused by the corner frequency of the conductive-permittive overlayer, shows that the best sensitivities are achieved using lower oscillation frequencies.

26.3.2 Vibrating Fluid Sensor

In this example the application of the spectral method to a fluid cell covered by vibrating elastic membranes, as shown in Fig. 26.7a and published in detail in [15], is discussed. The interesting features of this example are that the system matrix A and the eigensystems are given by simple expressions for isotropic materials. The fluid is modeled by the same formalism using equivalent complex-valued elastic material properties which is equivalent to using Navier-Stokes equations with neglected convective components. This approach is therefore valid for vibration velocities
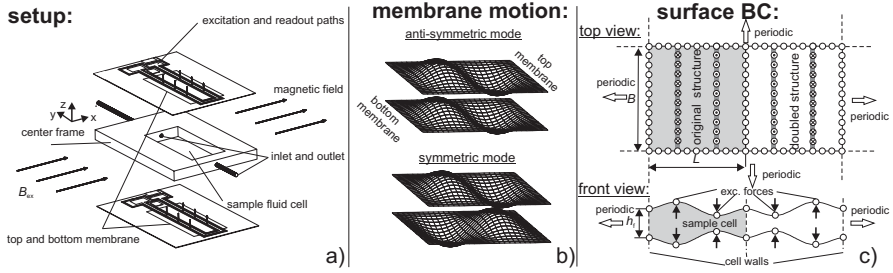
Fig. 26.7: a) A sample cell ($5.6 \times 12 \times 1 \text{mm}^3$) is covered by Lorentz force actuated (for (2,1)-mode excitation, i.e., 2/1 anti-nodes in x/y-direction) and inductively read out membranes ($50 \mu \text{m}$ PMMA). b) Membrane deflection for the two principal excitations. c) Artificial periodization for the implementation of rigid cell walls by periodic boundary conditions in the lateral directions and zero displacement constraint at the boundaries of each cell. © 2013 Elsevier. Reprinted, with permission, from [15].

much lower than the speed of sound and Reynolds numbers much below the critical values [16]. The walls of the center frame (see Fig. 26.7a) that limit the fluid cell in the lateral directions are implemented by an artificial periodization which realizes a no-flow condition by a periodic boundary condition. Also, an even/odd analysis is performed, but for this example, it concerns the normal and not the lateral direction, i.e., there is a symmetric and an anti-symmetric membrane motion, as depicted in Fig. 26.7b. The even and odd cases are therefore realized by two different Green's functions instead of different sets of trial functions as in the example in Sect. 26.3.1. The membranes carry separate conductive paths for Lorentz-force excitation and inductive readout, that excite membrane deflections as shown in Fig. 26.7b. With driving currents in equal direction on both membranes an anti-symmetric mode with predominately vertical fluid vibration is realized, while changing the polarity e.g., of driving current in the path at the bottom membrane, a symmetric mode with mostly horizontal fluid oscillation is realized (see Fig. 26.8). For the analysis, only the mechanical resonance of the structure is analyzed. This means that the electrodynamical interactions between driving and readout paths (predominantly cross-talk) are not considered at this point. However, they can be added in the
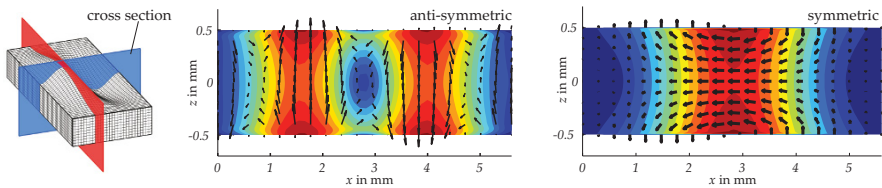
Fig. 26.8: Flow fields calculated at the cross-section shown left, for anti-symmetric (middle) and symmetric mode (right).

electrical domain when the mechanical resonance is described by an equivalent RLC circuit. These details are discussed, e.g., in [17].

The considered materials are isotropic and either elastic solids or viscous fluids. Therefore, only the six mechanical variables with zero piezoelectricity and permittivity $e = 0, \varepsilon = 0$ are used. The elements of the symmetric $(c_{ij} = c_{ji})$ isotropic stiffness tensor are best described by the elastic Lamé parameters λ and μ by setting

$$c_{11} = c_{22} = c_{33} = \lambda + 2\mu \quad c_{44} = c_{55} = c_{66} = \mu, \quad c_{12} = c_{13} = c_{23} = \lambda, \quad (26.44)$$

yielding for the system of ODEs $\partial\tilde{\boldsymbol{\psi}}/\partial z = A\tilde{\boldsymbol{\psi}}$ with $\tilde{\boldsymbol{\psi}} = [\tilde{u}_x, \tilde{u}_y, \tilde{u}_z, \tilde{T}_{xz}, \tilde{T}_{yz}, \tilde{T}_{zz}]^{\mathrm{T}}$ the compact matrix

$$A = \begin{bmatrix} 0 & 0 & \mathrm{i}k_x & 1/\mu & 0 & 0 \\ 0 & 0 & \mathrm{i}k_y & 0 & 1/\mu & 0 \\ \mathrm{i}k_x\lambda/\alpha & \mathrm{i}k_y\lambda/\alpha & 0 & 0 & 0 & 1/\alpha \\ k_x^2\gamma + k_y^2\mu - \rho\omega^2 & k_xk_y\beta & 0 & 0 & 0 & \mathrm{i}k_x\lambda/\alpha \\ k_xk_y\beta & k_x^2\mu + k_y^2\gamma - \rho\omega^2 & 0 & 0 & 0 & \mathrm{i}k_y\lambda/\alpha \\ 0 & 0 & -\rho\omega^2 & \mathrm{i}k_x & \mathrm{i}k_y & 0 \end{bmatrix}, \quad (26.45)$$

with $\alpha = 2\mu + \lambda, \quad \beta = \mu(1 + 2\lambda/\alpha)$ and $\gamma = 4\mu(1 - \mu/\alpha)$.

For this case, also a compact form for the eigensystem can be determined as shown in [18]. A reduction of dimensions of the global matrix approach is obtained by exploiting the symmetry of the layer composition and performing a decomposition in a symmetric and anti-symmetric membrane deflection (see [15]). Alternatively to the global matrix approach, the dyadic Green's function can also be determined by assembling, similar to the electrostatic example in Sect. 26.3.1. For this purpose, the generalized acoustic impedance matrix approach (see, e.g., also [19–21]) can be efficiently used. The viscous fluids can be represented for small steady-state time-harmonic vibrations by using equivalent complex-valued elastic Lamé parameters given by

$$\mu = \mathrm{i}\omega\eta \quad \text{and} \quad \lambda = \frac{1}{\xi} - \frac{2}{3}\mathrm{i}\omega\eta, \quad (26.46)$$

with η and ξ denoting the dynamic shear viscosity and the adiabatic compressibility coefficient, respectively. These equivalent parameters are determined by rearranging the time-harmonic linearized Navier-Stokes equations [16] using the Stokes hypothesis [22]. The structure is considered periodic, in $x-$ and $y-$directions. For the implementation of the rigid cell walls, however, the fundamental period is taken twice the actual sensor dimension in x-direction. The rigid cell walls are then implemented by a symmetric boundary condition, where excitation in adjacent periods is mirrored in x-direction, and repeated in y-direction. Due to the expected smooth variations of the displacement fields, point-matching provides reasonable accuracy and can efficiently be implemented by using the discrete two-dimensional fast Fourier transform.

To assess the accuracy and to validate the approach of enforcing boundary conditions by mirrored excitation, simplified problems for which the modeshapes and

vibration frequencies are known from literature, are studied. A single elastic beam (density $\rho = 1190$ kg/m^3, Young's modulus $E = 3$ GPa, length $l = 5.6$ mm, thickness h) is compared to the Euler-Bernoulli beam theory. Simulated and theoretical eigenmodes are compared in Fig. 26.9a, where the dots denote the collocation points of the numerical method. The results of the BEM converge to the EB theory for very thin beams (i.e., large l/h). In Fig. 26.9b the plate modes for the actual dimensions $l \times b = 5.6 \times 12$ mm^2 are shown. A comparison with the resonance frequencies for plates e.g. given in [23] shows a similar degree of deviation as observed for the beams.

In Fig. 26.8 the simulated displacement fields within the sensor cell are shown for the two principal excitation modes. The fluid is sheared stronger in the symmetric excitation mode and therefore the Q-factor which is closely related to energy dissipation, increased with fluid viscosity. The anti-symmetric mode is better suited for density measurements because the fluid motion is mainly in the direction of the elastic membrane and acts therefore as additional mass with smaller shear gradients. A strongly influential degree of freedom is the height of the fluid cell. By decreasing it, the resonance characteristics shift qualitatively as indicated by the arrows in Fig. 26.10. The low Q-factors of the vibration, even at low fluid viscosities, is a consequence of the internal damping of the polymeric membrane material (PMMA), which has been added to the simulation by complex-valued elasticity to meet the experimentally observed values.
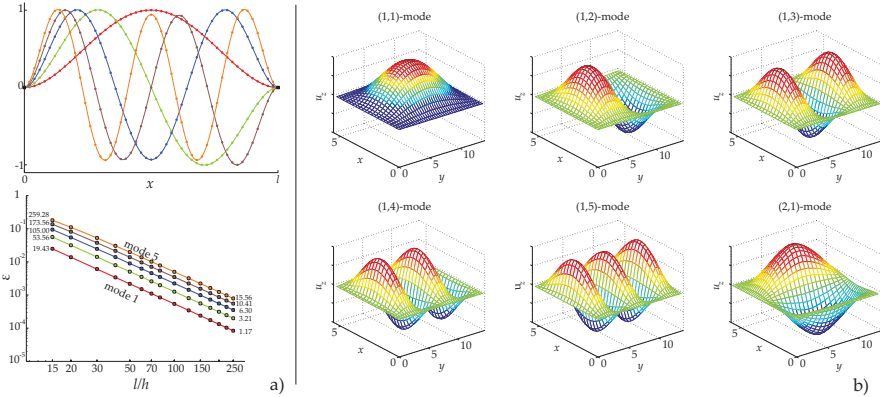
Fig. 26.9: a) Comparison of eigenmodes of Euler-Bernoulli beam theory (solid line) and the numerical method (points) for the first five modes shown in the upper figure. Shown below are the relative deviations between EB theory and the numerical method. The numbers to the left and right are the eigen frequencies in kHz of the respective mode for the extremes $l/h = 15$ and $l/h = 250$. b) Eigenmodes for a single elastic plate. The mode used in the actual application is the (2,1)-mode.
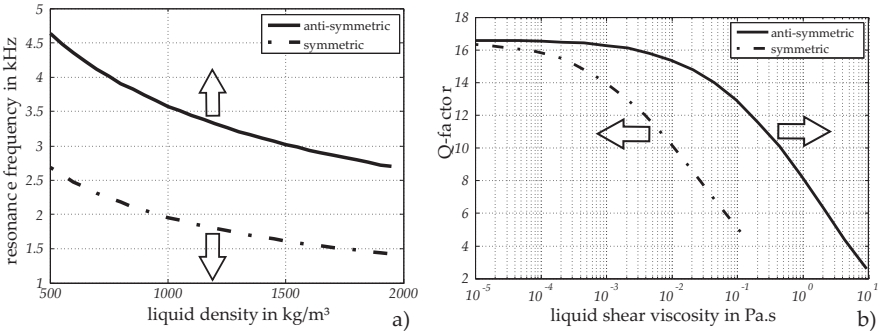
Fig. 26.10: a) Resonance frequency for varying fluid densities at a viscosity of η =1mPas. b) Q for varying viscosity at constant fluid density $\rho = 1000$kg/m^3. When the cell height is decreased, the curves shift qualitatively as indicated by the arrows. © 2013 Elsevier. Reprinted, with permission, from [15].

26.3.3 Piezoelectric Fluid Sensor

The spectral method is used to model resonant piezoelectric fluid sensors where the full anisotropy of the piezoelectric disk is implemented and local square trial functions are utilized. The fluid is modeled by equivalent complex-valued elastic constants such as in Sect. 26.3.2, before.

A sketch of a piezoelectric disk element where electrodes arranged on both major faces generate electric fields in the thickness direction in the crystal is shown Fig. 26.11a. This thickness field excitation (TFE) is the common mechanism used in quartz crystal resonators which typically oscillate in the lower MHz range. The fundamental resonance frequency is determined by a standing half-wave in the thickness direction. These resonators are therefore also known as bulk acoustic wave (BAW) devices, which are either designed for shear or extensional vibration by
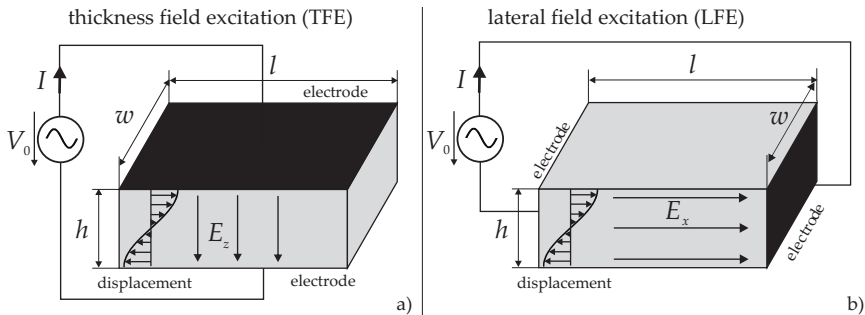
Fig. 26.11: a) Thickness field excitation (TFE): electrical fields in thickness direction excite waves propagating in thickness direction. b) Also lateral fields can excite thickness modes..

material selections and crystal cut orientation. Shear-resonators are commonly used
for clock generation in electronic circuits, but they can also be used as fluid sensors
simply by removing the metal enclosure of a commercially available component
and bringing one side into contact or immersing the whole disk into the test fluid.
The electrical impedance spectrum measured between both electrodes, each of area
A, for a single-sided fluid loading is derived using a one-dimensional model of a
h thick piezoelectric layer with effective scalar material parameters $\rho, c, e,$ and ε,
reading [24]

$$Z_{\text{el}}(\omega) = \frac{1}{\mathrm{i}\omega C}\left(1 + \frac{k_m^2}{\alpha}\frac{\mathrm{i}Z_{\text{f}}\sin(\alpha) - 2Z_{\text{p}}(1-\cos(\alpha))}{Z_{\text{p}}\sin(\alpha) - \mathrm{i}Z_{\text{f}}\cos(\alpha)}\right), \qquad (26.47)$$

where $C = A\varepsilon/h$ represents the static capacitance, $\alpha = \omega h/v_{\text{p}}$ the phase constant,
and $k_m^2 = e^2/(c^*\varepsilon)$ the electromechanical coupling factor. The phase velocity is
$v_{\text{p}} = \sqrt{c^*/\rho}$ with $c^* = c + e^2/\varepsilon$, i.e., the piezoelectrically stiffened elastic constant.
$Z_{\text{p}} = \sqrt{c^*\rho}$ denotes the characteristic acoustic impedance (i.e., stress to particle
displacement velocity of the form $Z = -T/v$) of the piezoelectric material and Z_{f}
a respective impedance of the fluid loading. Eq. (26.47) describes one of three
thickness modes which are either the slow or fast shear or the extensional mode, each
with different resonance characteristics, determined by the selected piezoelectric
material and thickness. The mechanical impedance of a fluid with density ρ_f and
viscosity η_f is for the shear mode $Z_f = \sqrt{\mathrm{i}\omega\eta_f\rho_f}$. Therefore, only the product of
density times dynamic viscosity of the fluid enters the electrical impedance spectrum
in Eq. (26.47), such that both quantities can not individually be determined from
measured impedance spectra.

Alternatively, a thickness vibration can also be generated by lateral field excitation
(LFE) as shown in Fig. 26.11b. From the 1D model, the admittance spectrum $Y_{\text{el}}(\omega)$
can be derived for the LFE modes, reading [8]

$$Y_{\text{el}}(\omega) = \mathrm{i}\omega C\left(1 - \frac{K_m^2}{\alpha}\frac{\mathrm{i}Z_{\text{f}}\sin(\alpha) - 2Z_{\text{p}}(1-\cos(\alpha))}{Z_{\text{p}}\sin(\alpha) - \mathrm{i}Z_{\text{f}}\cos(\alpha)}\right), \qquad (26.48)$$

where for the calculation of coupling constant ($K = e^2/(c\varepsilon)$), phase constant (α)
and characteristic impedance of the piezoelectric material (Z_{p}), the regular elastic
stiffness c instead of c^* is used. The effective permittivity and piezoelectricity values
parameters are different for LFE, and with it, also the coupling strengths. A practical
realization for TFE is shown in Fig. 26.12a) where the electrical field is well-confined
to the piezoelectric disk and the 1D model is a reasonably accurate representation[5].

For practical LFE sensors the electrodes are arranged at one side of the disk as
shown in Fig. 26.12b. The wanted electrical fields in lateral direction are accompanied
by unwanted thickness fields extending into the surrounding media. The electrical
properties of the liquid affect the mechanical resonance characteristics, as they
influence also the electric field distribution within the piezoelectric disk. All these

---

[5] Subtle effects such as spurious pressure wave generation due to lateral displacement gradients
cause by the limited excitation area are for instance analyzed in [25].
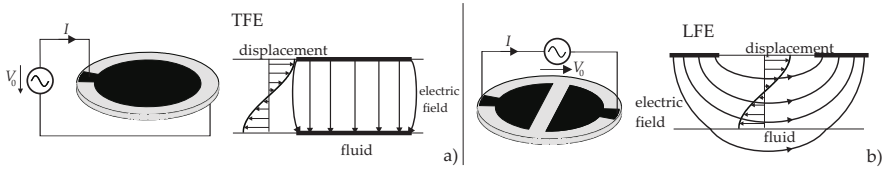
Fig. 26.12: a) Conventional thickness field excited (TFE) piezoelectric disk with confined fields. b) One-sided electrodes for excitation with lateral fields (LFE). © 2014 IEEE. Reprinted, with permission, from [26].

effects can conveniently be studied using the spectral method which yields a so-called full-wave model, i.e., it includes all three bulk waves and also all higher harmonics. For an efficient use of the spectral method, the piezoelectric material is considered infinitely extended in the lateral directions, thus neglecting the free boundary conditions at the edge of the disk, which in fact exclude some spurious modes associated with standing surface waves. The spectral electrostatic Green's function $\tilde{G}_{\varphi;\varrho}(k_x, k_y, \omega)$ is generated using the approach outlined in Sect. 26.2. It represents the electrical potential caused by a point charge at the electrode area. The fluid in contact with the plain face of the piezoelectric disk is modeled by the same approach but with piezoelectricity tensor $\boldsymbol{e}$ set to zero. Fluid conductivity σ_f is implemented by a complex-valued isotropic dielectricity tensor $\boldsymbol{\varepsilon}_f = \boldsymbol{I}(\varepsilon - \mathrm{i}\sigma_f/\omega)$, with $\boldsymbol{I}$ denoting the identity matrix. The method of moments is employed using square trial functions as shown in Fig. 26.13a. The weights are determined such
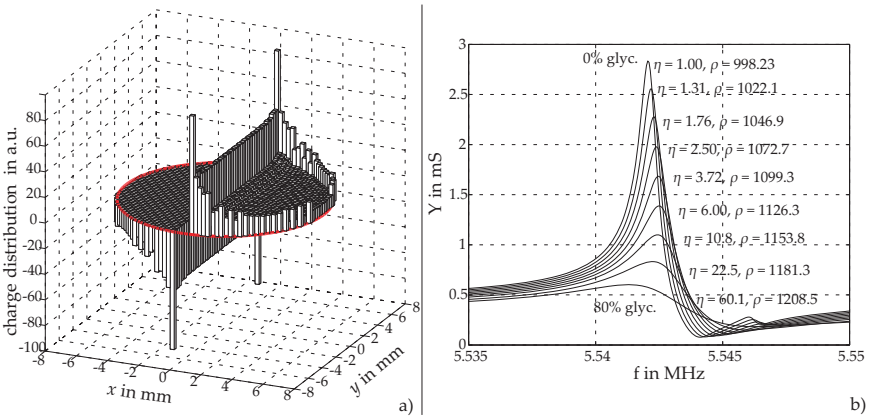
Fig. 26.13: a) Charge distribution on electrodes for square element discretization. b) Simulated electrical admittance spectra for different water/glycerol mixtures. Higher viscosity (higher glycerol content) results in stronger damping. The units of viscosity η and density ρ are mPa s and kg/m^3, respectively. © 2014 IEEE. Reprinted, with permission, from [26].

that the electrical potential equals on average the prescribed electrode potential.

Fig. 26.13a shows the thus obtained charge distribution. The charge accumulations at the electrode edges are typical and can be considered a cause of the repelling forces of equal charges that can move freely on the electrode. Admittance spectra for a lithium tantalate (LiTaO$_3$ YXl -16.51°) piezoelectric disk material that is particularly suitable for LFE with a water/glycerol layer of 0.1 mm thickness are shown in Fig. 26.13b. An equivalent electrical circuit according to Fig. 26.14 with parameters derived from the simulation can be established. It can be shown that for highly conductive liquids, such as watery solutions, the application of thick liquid layers results in diminishing lateral fields and increased thickness fields. For thicker conductive fluid layers, the device, therefore, acts more like two TFE than one LFE device. This can also be observed by considering the static capacitance of the sensors over fluid height. In Fig. 26.14 the active LFE region is shown for different piezoelectric materials.
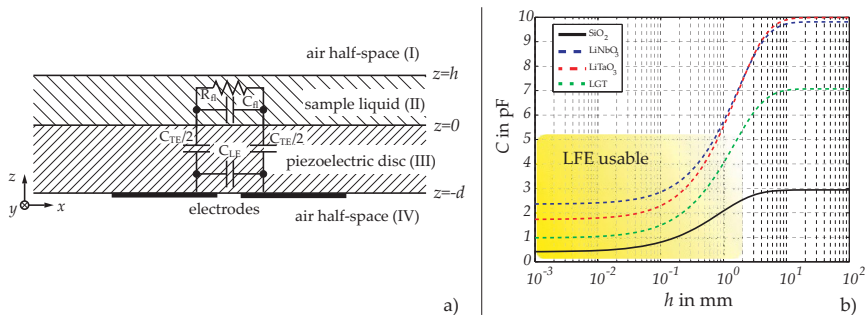
Fig. 26.14: a) Four-layer model of the simulated structure. b) Variation of static capacitance with heights h of a water layer for different materials suitability for LFE. © 2014 IEEE. Reprinted, with permission, from [26].

References

[1] Brebbia CA (1978) The boundary element method for engineers. Pentech Press Ltd. Plymouth

[2] Katsikadelis JT (2016) The boundary element method for engineers and scientists: theory and applications. Academic Press

[3] Jakoby B (2008) Efficient semi-numerical analysis of acoustic sensors using spectral domain methods - a review. Meas Sci Technol **19**:052,001

[4] Meindlhumer M, Pechstein A, Jakoby B (2022) Mixed finite elements applied to acoustic wave problems in compressible viscous fluids under piezoelectric actuation. Acta Mechanica **233**(5):1967–1986

[5] Landau LD, Lifshitz EM (1987) Fluid Mechanics: Volume 6 (Course Of Theoretical Physics). Butterworth-Heinemann

[6] Jakoby B, Beigelbeck R, Keplinger F, Lucklum F, Niedermayer A, Reichel EK, Riesch C, Voglhuber-Brunnmaier T, Weiss B (2010) Miniaturized sensors for the viscosity and density of liquids-performance and issues. IEEE T Ultrason Ferr **57**(1):111 –120

[7] Auld BA (1973) Acoustic Fields and Waves in Solids: Vol 1. John Wiley, New York

[8] Rosenbaum JF (1988) Bulk Acoustic Wave Theory and Devices. Artech House, Boston

[9] Harrington RF (1992) Field Computation by Moment Methods. IEEE Press

[10] Boyd JP (2000) Chebyshev and Fourier Spectral Methods, 2nd edn. DOVER Publications

[11] Voglhuber-Brunnmaier T, Sell JK, Jakoby B (2017) Semi-numeric model of capacitive touch sensors integrated into coatings of metallic substrates. In: 2017 IEEE SENSORS, IEEE, pp 1–3

[12] Enser H, Sell JK, Kulha P, Hilber W, Jakoby B (2018) Printed transducers embedded in polymer coatings. e & i Elektrotechnik und Informationstechnik

[13] Lowe MJS (1995) Matrix techniques for modeling ultrasonic waves in multilayered media. Ultrasonics, Ferroelectrics and Frequency Control, IEEE Transactions on **42**(4):525 –542

[14] Voglhuber-Brunnmaier T, Sell JK, Jakoby B (2017) Interdigitated capacitor calculation for capacitive touch sensor applications, https://www.mathworks.com/matlabcentral/fileexchange/64226-interdigitated-capacitor-calculation-for-capacitive-touch-sensor-applications

[15] Voglhuber-Brunnmaier T, Heinisch M, Reichel EK, Weiss B, Jakoby B (2013) Derivation of reduced order models from complex flow fields determined by semi-numeric spectral domain models. Sensors and Actuators A: Physical **202**:44–51

[16] Beigelbeck R, Jakoby B (2004) A two-dimensional analysis of spurious compressional wave excitation by thickness-shear-mode resonators. Journal of Applied Physics **95**(9):4989–4995

[17] Heinisch M (2015) Mechanical resonators for liquid viscosity and mass density sensing. PhD thesis, Université de Bordeaux; Johannes-Kepler-Universität (Linz, Autriche)

[18] Voglhuber-Brunnmaier T, Jakoby B (2012) Efficient spectral domain formulation of loading effects in acoustic sensors. Sensors and Actuators A: Physical **186**:38–47

[19] Biryukov S (1985) Impedance method in the theory of elastic surface-waves. Soviet Physics Acoustics - USSR **31**(5):350–354

[20] Tanuma K, Tanuma K (2007) Stroh formalism and Rayleigh waves. Springer

[21] Zhang VY, Dubus B, Collet B, Destrade M (2008) Piezoacoustic wave spectra using improved surface impedance matrix: Application to high impedance-contrast layered plates. The Journal of the Acoustical Society of America **123**(4):1972–1982

[22] Schlichting H, Gersten K (2016) Boundary-layer Theory. Springer

[23] Blevins RD, Plunkett R (1980) Formulas for natural frequency and mode shape. Journal of Applied Mechanics **47**(2):461

[24] Kino GS (2000) Acoustic Waves: Devices, Imaging, and Analog Signal Processing. Prentice-Hall

[25] Lindenbauer T, Jakoby B (2005) Fully three-dimensional analysis of tsm quartz sensors immersed in viscous liquids. In: Proc. IEEE Sensors, pp 1249–1252

[26] Voglhuber-Brunnmaier T, Beigelbeck R, Jakoby B (2014) Semi-numeric boundary element method for piezoelectric fluid sensors using a fourier spectral approach. In: SENSORS, 2014 IEEE, IEEE, pp 594–597